CHEMICAL AND MINERALOGICAL CHARACTERIZATION OF MICRO-INCLUSIONS IN DIAMONDS

Thesis by

Oded Navon

In Partial Fulfillment of the Requirements

for the Degree of

Doctor of Philosophy

California Institute of Technology

Pasadena, California

1989

(Submitted January 4, 1989)

ACKNOWLEDGEMENTS

I would like to thank Professors G.J. Wasserburg and Ed Stolper for their guidance. Professor Wasserburg encouraged me to come to Caltech and supported me the best way possible, even at times when he was not convinced of the usefulness of some of my scientific pursuits. He did his best to instill in me the fundamentals of experimental science and of scientific thought and analysis. Professor Ed Stolper is thanked for his trust and friendship, and for setting an example I wish I would be able to follow.

Dr. Ian Hutcheon, Professor George Rossman and Dr. John Armstrong shared their expertise and their amazing laboratories. They are thanked for teaching me how to use and understand the complex instruments, and for doing it ever so patiently. Long discussions with Dr. Hutcheon about the probe, about writing and about submitting are greatfully acknowledged. I have benefited from discussions and classes with many other faculty members. I would particularly like to thank Professors Sam Epstein, Dave Stevenson, Hugh Taylor, Peter Wyllie, Joseph Kirschvink and Yuk Yung, and Drs. Dimitri Papanastassiou and Mark Allen.

Drs. Herbert Palme and B. Spettel of the Max Planck Institute, Mainz kindly analyzed some diamonds in their INAA lab. George Guthrie and Dr. David Veblen of the John Hopkins University, Baltimore shared their TEM data. Dr. R. Wilson of Hughes Research Laboratories, Malibu, kindly implanted some diamond samples. Discussions with Drs. John Gurney, Mark Kurz, Frank Richter and Steven Koonin were very helpful; they are thanked for their advice and interest.

Interactions with the students and the post-doctoral fellows of the Geology and Geochemistry options were most valuable. I wish to thank all students and post-doctoral fellows for creating the unique atmosphere I enjoy so much, and for creating an almost non-competitive environment within this competitive institute. I would particularly like to thank Rob Ripperdan for being such a great officemate, Dave Bell for teaching me everything I know about diamonds and kimberlites, Joel Blum and Dave Pickett for teaching me English, Phil Ihinger for all the help in the lab, and Larry Edwards, Ben Frisch, Robin Chang, Gerry

Fine, Lynn Silver, Sally Newman, Dave Scott, Jen Blank, Mike Carroll, John Beckett, Glen Mattioli, Carol Prentice, Tom LaTourrette, and Janet Teshima for discussion, help and friendship.

Priscilla Piano is thanked for always being there at the right moment. Lindsey Hedges, Kathie Venturelli, Chris Price and George Yamamoto for the technical support. Joseph Zitron and Barouch Staniatsky are thanked for teaching me the secrets of diamond cutting.

Diamonds samples were kindly provided by Dr. C.T. Pillinger, Dr. J.W. Harris of DeBeers, Mr. P. Chevalier of Sibeka, Mr. C.B. Smith of CRA Exploration, Mr. J. Borden, and Mr J. Zitron. Professor Joseph Kirschvink was generous in letting me use his laser printer.

Last, I wish to thank my family for their everlasting love and support.

ABSTRACT

Secondary-ion mass spectrometry (SIMS), electron probe analysis (EPMA), analytical scanning electron microscopy (SEM) and infrared (IR) spectroscopy were used to determine the chemical composition and the mineralogy of sub-micrometer inclusions in cubic diamonds and in overgrowths (coats) on octahedral diamonds from Zaire, Botswana, and some unknown localities.

The inclusions are sub-micrometer in size. The typical diameter encountered during transmission electron microscope (TEM) examination was 0.1-0.5 μm. The micro-inclusions are sub-rounded and their shape is crystallographically controlled by the diamond. Normally they are not associated with cracks or dislocations and appear to be well isolated within the diamond matrix. The number density of inclusions is highly variable on any scale and may reach 10^{11} inclusions/cm^3 in the most densely populated zones. The total concentration of metal oxides in the diamonds varies between 20 and 1270 ppm (by weight).

SIMS analysis yields the average composition of about 100 inclusions contained in the sputtered volume. Comparison of analyses of different volumes of an individual diamond show roughly uniform composition (typically ±10% relative). The variation among the average compositions of different diamonds is somewhat greater (typically ±30%). Nevertheless, all diamonds exhibit similar characteristics, being rich in water, carbonate, SiO_2, and K_2O, and depleted in MgO. The composition of micro-inclusions in most diamonds vary within the following ranges: SiO_2, 30-53%; K_2O, 12-30%; CaO, 8-19%; FeO, 6-11%; Al_2O_3, 3-6%; MgO, 2-6%; TiO_2, 2-4%; Na_2O, 1-5%; P_2O_5, 1-4%; and Cl, 1-3%. In addition, BaO, 1-4%; SrO, 0.7-1.5%; La_2O_3, 0.1-0.3%; Ce_2O_3, 0.3-0.5%; smaller amounts of other rare-earth elements (REE), as well as Mn, Th, and U were also detected by instrumental neutron activation analysis (INAA). Mg/(Fe+Mg), 0.40-0.62 is low compared with other mantle derived phases; K/Al ratios of 2-7 are very high, and the chondrite-normalized Ce/Eu ratios of 10-21 are also high, indicating extremely fractionated REE patterns.

SEM analyses indicate that individual inclusions within a single diamond are roughly of similar composition. The average composition of individual inclusions as measured with the

SEM is similar to that measured by SIMS. Compositional variations revealed by the SEM are larger than those detected by SIMS and indicate a small variability in the composition of individual inclusions. No compositions of individual inclusions were determined that might correspond to mono-mineralic inclusions.

IR spectra of inclusion-bearing zones exhibit characteristic absorption due to: (1) pure diamonds, (2) nitrogen and hydrogen in the diamond matrix; and (3) mineral phases in the micro-inclusions. Nitrogen concentrations of 500-1100 ppm, typical of the micro-inclusion-bearing zones, are higher than the average nitrogen content of diamonds. Only type IaA centers were detected by IR. A yellow coloration may indicate small concentration of type IB centers.

The absorption due to the micro-inclusions in all diamonds produces similar spectra and indicates the presence of hydrated sheet silicates (most likely, Fe-rich clay minerals), carbonates (most likely calcite), and apatite. Small quantities of molecular CO_2 are also present in most diamonds. Water is probably associated with the silicates but the possibility of its presence as a fluid phase cannot be excluded. Characteristic lines of olivine, pyroxene and garnet were not detected and these phases cannot be significant components of the inclusions. Preliminary quantification of the IR data suggests that water and carbonate account for, on average, 20-40 wt% of the micro-inclusions.

The composition and mineralogy of the micro-inclusions are completely different from those of the more common, larger inclusions of the peridotitic or eclogitic assemblages. Their bulk composition resembles that of potassic magmas, such as kimberlites and lamproites, but is enriched in H_2O, $CO_3^{=}$, K_2O, and incompatible elements, and depleted in MgO.

It is suggested that the composition of the micro-inclusions represents a volatile-rich fluid or a melt trapped by the diamond during its growth. The high content of K, Na, P, and incompatible elements suggests that the trapped material found in the micro-inclusions may represent an effective metasomatizing agent. It may also be possible that fluids of similar composition are responsible for the extreme enrichment of incompatible elements documented in garnet and pyroxene inclusions in diamonds.

The origin of the fluid trapped in the micro-inclusions is still uncertain. It may have been formed by incipient melting of a highly metasomatized mantle rocks. More likely, it is the result of fractional crystallization of a potassic parental magma at depth. In either case, the micro-inclusions document the presence of highly potassic fluids or melts at depths corresponding to the diamond stability field in the upper mantle. The phases presently identified in the inclusions are believed to be the result of closed system reactions at lower pressures.

PREFACE

This thesis presents the chemical and mineralogical characterization of micro-inclusions in diamonds, and constitutes the main project of my Ph.D. program. Summaries of research programs with which I have been involved during the earlier phases of my doctoral work are given in sections C.1 and C.2 of Appendix C. These sections include two original articles. The first examines whether self-shielding of UV radiation in oxygen may explain the observed anomalous relationship between the three isotopes of oxygen in primitive meteorites. The second article examines some geochemical consequences of melt percolation in the upper mantle and models melt evolution during percolation by treating the upper mantle as a chromatographic column. Also included in Appendix C (section C.3) is a short article which summarizes the thesis research. Appendix B describes the results of an effort to determine the isotopic composition of carbon in diamonds by use of the ion microprobe.

TABLE OF CONTENTS

Acknowledgement ii

Abstract iv

Preface vii

Table of contents viii

Chapter 1 Introduction 1

Chapter 2 Diamonds and their mantle environment 3

- 2.1. The mantle environment 3
  - 2.1.1. The sub-continental mantle 3
  - 2.1.2. Kimberlites 6
  - 2.1.3. Lamproites and their relation to kimberlites 10
- 2.2. Diamonds 12
  - 2.2.1. Morphology 13
  - 2.2.2. Internal structure 14
  - 2.2.3. Carbon isotopic composition 14
  - 2.2.4. Nitrogen and the IR spectrum of diamonds 15
  - 2.2.5. Other impurities 16
  - 2.2.6. Inclusions 20

Chapter 3 Previous studies of micro-inclusion-bearing diamonds 25

- 3.1. Morphology and internal structure 25
- 3.2. Chemical studies 27
- 3.3. Isotopic composition 31
- 3.4. Infrared spectroscopy 33

Chapter 4 The samples 34

- 4.1. Sample description 34
  - 4.1.1. Size 34
  - 4.1.2. Color 35
  - 4.1.3. Morphology 35

4.1.4. Internal structure 38

4.1.5. Cracks 42

4.2. Sample preparation 43

4.2.1. Sawing 43

4.2.2. Polishing 43

4.2.3. Cleaning 44

4.2.4. Mounting 47

Chapter 5 Electron microprobe analysis 48

5.1. Experimental method 48

5.1.1. Instrumental procedure 48

5.1.2. Blank correction and analytical error 49

5.1.3. Data reduction 51

5.1.4. Summary 57

5.2. Results 57

Chapter 6 Secondary ion mass spectrometry 59

6.1. Experimental method 59

6.1.1. Instrumentation 60

6.1.2. Instrumental conditions 64

6.1.3. Mass interferences 64

6.1.4. Machine background and detection limits 76

6.1.5. Analytical procedure and data reduction 78

6.1.6. The analysis of heterogeneous samples 80

6.2. The determination of relative ion-yields 86

6.2.1. EPMA -SIMS correlations 87

6.2.2. Graphite - glass mixtures 101

6.2.3. Depth profiles of ion-implanted diamonds 102

6.2.4. Comparison of ion-yield determinations 118

6.3. Results 124

6.3.1. Analysis of clear diamond material 124

6.3.2. The metal-oxide content of micro-inclusion-bearing diamonds 125

6.3.3. Summary 134

Chapter 7 Analytical scanning electron microscopy 135

7.1. Experimental method 135

7.1.1. Analytical procedure 135

7.1.2. Analytical error 141

7.2. Results 141

7.2.1. Inclusion size 141

7.2.2. The composition of individual inclusions 141

7.2.3. Variation in composition of individual inclusions 149

7.2.4. Comparison with SIMS analysis 157

7.3. Summary 160

Chapter 8 Infrared spectroscopy 161

8.1. Experimental method 162

8.1.1. Instrumental procedure 162

8.1.2. Reference spectrum 162

8.1.3. Data reduction 165

8.2. The IR spectrum of micro-inclusion-bearing zones in diamonds 166

8.2.1. Absorption by the diamond matrix 166

8.2.2. Absorption by the micro-inclusions 168

8.3. Correlation of peak intensities and band assignment 178

8.3.1. Intensity measurement and error estimation 179

8.3.2. Intensity correlations and band assignment 179

8.4. The quantification of IR data 194

8.4.1 Absorption coefficient and concentration of water 195

8.4.2. Absorption coefficient and concentration of carbonate 197

8.4.3. Absorption coefficient and concentration of apatite 197

8.4.4. Absorption coefficient and concentration of clays 197

8.5. Micro-inclusion composition - IR perspective 198

8.6. Comparison with SIMS analysis 201

8.7. Freezing and leaching experiments 209

8.7.1. Freezing 209

8.7.2. Leaching 209

8.8. Summary 212

Chapter 9 Instrumental neutron activation analysis 213

9.1. Experimental procedure 213

9.2. Results 214

9.2.1. Analytical data 214

9.2.2. Comparison with SIMS analysis 218

9.2.3. Trace element composition of micro-inclusions 220

Chapter 10 What is trapped in the micro-inclusions? 223

10.1. Quantitative determination of compositions and associated errors 223

10.2. The composition and mineralogy of the micro-inclusions 225

10.3. Syngenetic origin or epigenetic alteration? 230

10.4. Experimental constraints on the stability of mantle fluids 231

10.5. Relation of the trapped material to potassic magmas 234

10.6. Relation to metasomatic fluids 238

10.7. Relation to diamonds of the peridotitic and the eclogitic suites 238

References 242

Appendix A Sample description 252

A.1. Diamonds of the GRR set 252

A.2. Diamonds of the CTP set 254

A.3. Other GRR diamonds 255

A.4. Other CTP diamonds 256

A.5. ON Samples 256

A.6. CBS diamonds 257

Table A.1. Metal oxide concentration determined by EPMA 258

Table A.2. SIMS count-rates for correlation with EPMA concentration data 259

Table A.3. Summary of SIMS analysis 260

Table A.4. INAA data 266

Appendix B Ion probe analysis of carbon isotopic composition of diamonds. 277

Appendix C Published articles

C.1. Self-shielding in O_2 - a possible explanation for oxygen isotopic anomalies in meteorites. (co-authored with G.J. Wasserburg), 1985, Earth Planet. Sci. Lett. **73**: 1-16. 284

C.2. Geochemical consequences of melt percolation: the upper mantle as an ion-exchange column. (co-authored with E. Stolper), 1987, J. Geol., **95**: 285-307. 300

C.3. Mantle-derived fluids in diamond micro-inclusions (co-authored with I.D. Hutcheon, G.R. Rossman and G.J. Wasserburg) 1988, Nature, **335**: 784-789. 323

Appendix D Abstracts 329

D.1. Self-shielding in O_2 - A possible explanation for oxygen isotopic anomalies in meteorites? (co-authored with G.J. Wasserburg), 1984, Lunar and Planetary Science XV, pp. 589-590, Lunar and Planetary Science Institute, Houston, Texas. 329

D.2. The upper mantle as an ion-exchange column. (co-authored with E. Stolper), 1984, Geol. Soc. Am. Abst. with Programs **16**: 608. 331

D.3. Ultrapotassic sub-micron inclusions in diamonds. (co-authored with I.D. Hutcheon, G.R. Rossman, and G.J. Wasserburg), 1987, EOS **44**: 1552 332

D.4. Sub-micron inclusions in diamonds - samples of pristine upper mantle fluids? (co-authored with I.D. Hutcheon, G.R. Rossman, and G.J. Wasserburg), 1988, Lunar and Planetary Science XIX, pp. 827-828, Lunar and Planetary Science Institute, Houston, Texas. 332

CHAPTER 1 INTRODUCTION

If "A snowflake is a letter from the sky" (Nakaga), *then "a diamond is a letter to us from the depth, and a letter more worth reading, since we can visit the sky."*

Charles Frank

Over the last 10 years Panurge has been reading letters from the sky. Encouraged by Frank's words, I have spent the last few years trying to help Panurge read these worthy letters from the depth. This thesis describes the content of a few such letters.

The idea that diamonds come from the depth was not developed until the early part of this century. De Toit (1906), Wagner (1914), and Williams (1932) concluded that kimberlites, and hence diamonds, must originate at great depth. In the late twenties and during the thirties enough thermodynamic data became available to calculate the diamond-graphite phase boundary and show that diamond is only stable at very high pressures (see review by Bundy, 1980).

The geological part of the letter is written mainly in the form of foreign phases included in diamonds. Since the early work of South African geologists (see review by Harris and Gurney, 1979), research on inclusions has benefited from the introduction of X-ray diffraction (Mitchell and Giardini, 1953) and electron microprobe (Meyer, 1967) techniques. Intense study of diamond inclusions over the last two decades has yielded a wealth of important geological information about the composition, the P-T conditions, the structure, and the age of the sub-continental lithosphere.

Surprisingly, although carbon transport in the mantle is thought to be dominated by migration of fluids (volatile-rich fluids or melts), no conclusive, direct observation of fluid inclusions in diamond has been reported (Roedder, 1984). Several studies have suggested the presence of gases, melt, or volatile components in microscopic (or sub-microscopic) inclusions in some diamonds (Giardini and Melton, 1975; Fesq et al, 1973; Bibby, 1979; Chrenko et al., 1973). However, no detailed characterizations of such inclusions have been attempted.

Fluid inclusions in diamonds would carry important geological information. Many mantle rocks show evidence of interaction with fluids, and mantle fluids are important in the transport of incompatible and volatile elements from the mantle into the crust and the atmosphere. However, direct observations of deep mantle fluids are scarce (Pasteris, 1987), and their exact nature is still debated (Ryabchikov, 1986; Eggler, 1987; Erlank et al. 1987).

Because of its mechanical strength and chemical inertness, diamond is probably the best material available for transporting mantle fluids to the surface. Except for carbon and nitrogen (and possibly hydrogen and oxygen), no other element is likely to react with the diamond matrix; therefore, the inclusions may be expected to retain the original bulk composition of the trapped fluid.

The study reported here is concerned with the chemical and mineralogical characterization of micro-inclusions of the type found in some cubic diamonds and in overgrowths (coats) on the clear, inclusion-free cores of coated diamonds (variety II and VI, respectively, Orlov (1977)). Most of this report (chapters 4-9) is devoted to a description of the analytical techniques employed and the resulting data. The geological implications of the results are discussed in chapter 10.

CHAPTER 2 DIAMONDS AND THEIR MANTLE ENVIRONMENT

Diamonds are found mainly in two unique rock types: kimberlites and lamproites. Both rocks are the result of violent eruptions which transport material from the deepest levels sampled by terrestrial volcanism, 150-200 km. Both types of rocks are found mainly on stable cratons that have not been deformed since the Precambrian (Dawson, 1980). Diamondiferous kimberlites are usually confined to the older Archean cores of cratons. The three diamondiferous lamproites known to date are found in the mobile belts surrounding the old parts of the cratons (see Fig 2.1).

Kimberlites and their relation with the sub-continental mantle have been the focus of few recent publications. Extensive information on related subjects can be found in Mitchell (1986), Nixon (1987), Menzies and Hawkesworth (1987), Glover and Harris (1985), and most recently, Janse et al. (1988). Only a brief review of the main geological features pertaining to diamonds and their mantle environment is given in this introduction.

Section 2.1 describes the structure, mineralogy and geochemistry of the subcontinental mantle, the petrology and geochemistry of kimberlites and lamproites, and the types of xenoliths they sample. Section 2.2 reviews the current data about diamond morphology and chemistry and the mineralogy and composition of mineral inclusions in diamonds.

2.1. THE MANTLE ENVIRONMENT

2.1.1. THE SUB-CONTINENTAL MANTLE

The crust-mantle boundary below old cratons is located at a depth of approximately 50 km. Below old cratons, a relatively cold and brittle lithosphere extends to depths of 150-200 km (Boyd and Gurney, 1986; Given and Helmberger, 1980). The lithosphere-asthenosphere boundary occurs at shallower levels below the mobile belts surrounding the old cratons. The geothermal gradient in the subcratonic lithosphere (shield geotherm) of 40 mW/m^2 corresponds to temperatures of ~1100°C at the lithosphere-asthenosphere boundary (Pollack and Chapman, 1977). Geothermobarometry of lherzolite nodules and diamond inclusions from kimberlites (Boyd and Gurney, 1986), as well as geophysical evidence (Anderson and

Figure 2.1. World map showing the locations of kimberlites and lamproites.

Map is modified after Janse (1984). Only lamproites sensu stricto are shown (after Bergman, 1987). Three lamproite localities in northern Antarctica are not shown.

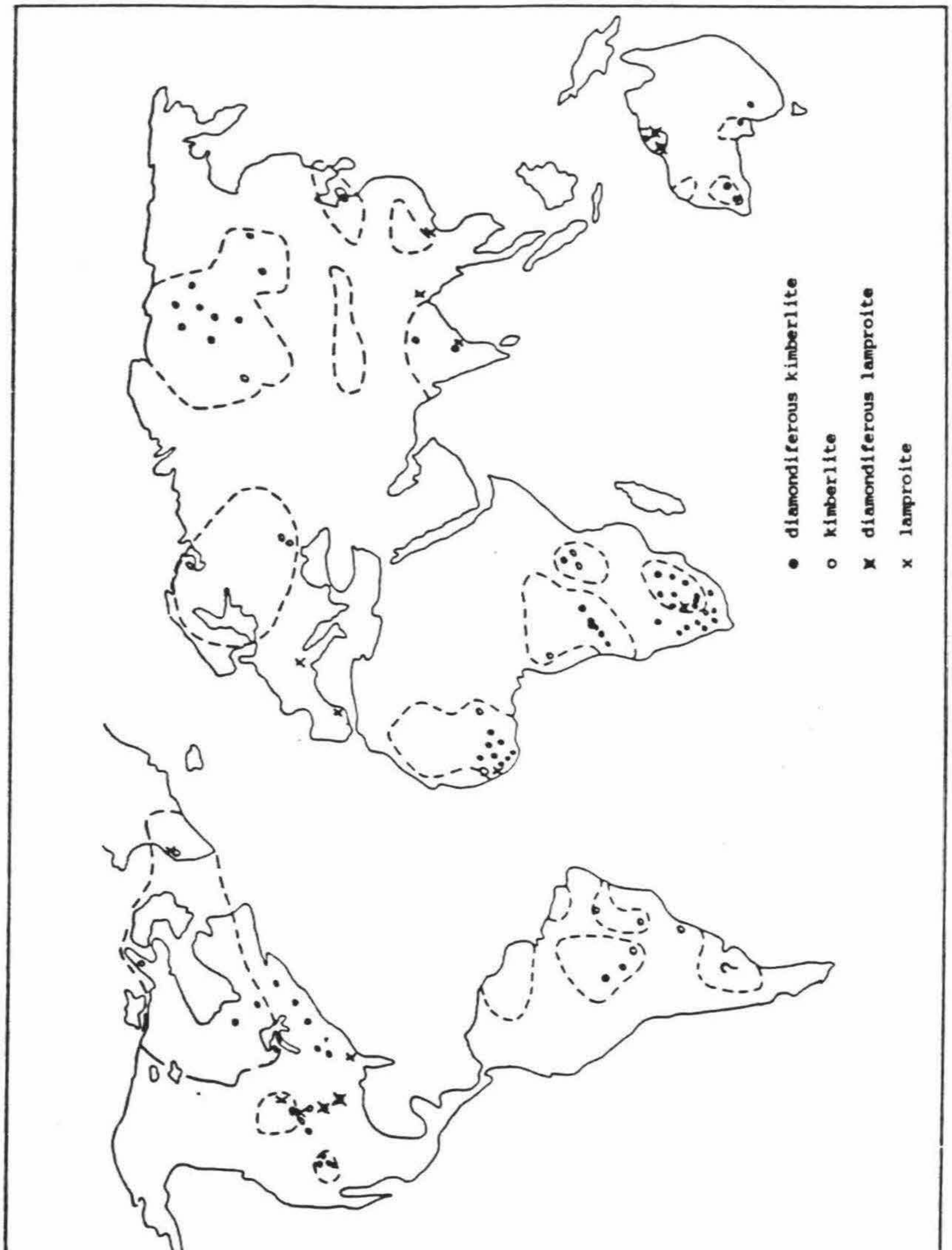
● diamondiferous kimberlite
o kimberlite
✖ diamondiferous lamproite
x lamproite

Bass, 1984), suggest higher gradients in the asthenosphere.

Xenoliths trapped in kimberlites and basalts indicates that harzburgites, with subordinate dunite and depleted lherzolites (depleted in basaltic elements, e.g., Al, Ca, Fe, Na) are the main rocks of the lithospheric mantle. Olivine (ol) is the most abundant mineral and is commonly accompanied by orthopyroxene (opx). Clinopyroxene (cpx) and garnet (gar) or spinel (sp) are present in small amounts. The upper levels of the asthenosphere are also sampled and consist of more fertile lherzolites, closer in composition and geochemistry to peridotites of the oceanic mantle.

Isotopic evidence (Richardson et al., 1984) suggests that the lithosphere below the southern African Kaapvaal craton reached its present thickness at Archean times. The reason for the greater depletion of lithospheric as compared with asthenospheric rocks may be a larger degree of initial melting due to extraction of komatiites during the Archean (Boyd, 1987) compared with extraction of basalt from oceanic or asthenospheric mantle. Another alternative is that during the Archean, faster plate motion led to subduction of hotter oceanic lithosphere. Extensive melting of that lithosphere produced a depleted, hot, light residue that underplated the continents (Nixon and Davies, 1987).

In spite of its depletion in "basaltic" elements, xenoliths of the lithospheric peridotites sampled by kimberlites show enrichments in incompatible elements. Isotopic data show that this enrichment postdates the depletion event so that the rocks still show a depleted isotopic signature (Erlank et al., 1987). The enrichment is commonly believed to be relatedrelated to an open system alteration of the depleted upper mantle rocks by fluids or melts flushing through the lithosphere (mantle metasomatism).

2.1.2 KIMBERLITES

Kimberlites are the major source of diamonds. They are found in most of the Precambrian cratons that are older than 1500 m.y. The kimberlites themselves may be younger, the oldest known kimberlite giving an age of 1600 m.y. (Kuruman province, Suoth Africa; Bristow et al. 1986), and the youngest 20-30 m.y. (Colorado plateau). Older, diamond-bearing alluvial deposits indicate even older kimberlitic occurrences (up to 2400 m.y.).

According to Clement et al. (1984), kimberlite "...is a volatile-rich, potassic, ultrabasic igneous rock which occurs as small volcanic pipes, dykes and sills...". The mineralogy is complex, as the rock is a hybrid rock containing abundant xenoliths, megacrysts and macrocrysts trapped in the original melt. "The matrix contains, as prominent primary phenocrystal and/or groundmass constituents, olivine and several of the following minerals: phlogopite, carbonate (commonly calcite), serpentine, clinopyroxene (commonly diopside), monticellite, apatite, spinels, perovskite, and ilmenite...".

The relation between the composition of the primary magma at depth and the erupting kimberlitic magma is not simple. On its way to the surface the primary melt accumulates xenoliths and xenocrysts from the conduit wall. A fluid phase separates at shallow depth and may either react with the kimberlite or partially escape together with dissolvable components. Finally, reactions of the hot kimberlite with ground water may further alter the composition of the kimberlite.

It is thus no surprise that the chemical composition of kimberlites is highly variable (Smith et al., 1985). Nevertheless, it has been shown to be characterized by high content of both compatible (e.g., Mg, Cr, Ni, Co) and incompatible (e.g., K, Rb, P, Zr, Nb, Ba, LREE) elements (Dawson, 1980).

Smith (1983, 1985) used radiogenic isotopes and whole rock geochemistry to distinguish between two groups of kimberlite. His classification of group I and group II kimberlites roughly correspond to the classification of Wagner (1914) and Dawson (1967) of "basaltic" and "micaceous" kimberlites respectively. Group I kimberlites are characterized by distinct radiogenic-isotope compositions (Smith, 1983). Present day values for ϵ_{Sr} vary from -20 to +10 and ϵ_{Nd} from +6 to -2, reflecting a time-integrated depletion of incompatible elements of their source regions. Values for $^{208}Pb/^{204}Pb$ range from 18.5 to 20.0 and are radiogenic. All ranges are similar to those observed in ocean island basalts. Kimberlites of this group are phlogopite-poor, perovskite-rich, and contain zircon and ilmenite. Group II kimberlites have abundant phlogopite in their groundmass, are poor in perovskite, and have no ilmenite or zircon (Smith et al., 1985). Isotopically they are more enriched than group I kimberlites. values of ϵ_{Sr} = 40-60 and ϵ_{Nd} = -6 to -10 reflect time-integrated enrichment of their sources. $^{208}Pb/^{204}Pb$ varies from 17.2 to 17.7 (Smith et al., 1983). Major element compositions show broad similarity to that of group I (Table 2.1), but K and Rb are more abundant in group II and Ti concentration is higher in group I. At present, group II kimberlites are only known from South Africa.

Xenoliths are present in most kimberlites. Apart from the high and low temperature lherzolites, harzburgites and dunites mentioned earlier, xenoliths of eclogitic mineralogy (gar+cpx with rare accessory phases) are also found. Many peridotite xenoliths show the effects of metasomatism (an open system alteration of the chemistry and/or mineralogy of the rock). Most commonly, metasomatism leads to enrichment of the rock in incompatible trace elements. In many cases the introduction of water leads to the formation of hydrous phases such as mica and/or amphibole. Gurney and Boyd (1980) and Menzies et al. (1987) distinguished two styles of metasomatism. The first leads to enrichment of the rock in Ti and Fe and is suggested to be the consequence of the interaction of the rock with a melt. The other style is characterized by K-enrichment and high K/Ti ratios. Menzies and co-workers suggest that the metasomatizing agent in this case is a hydrous fluid.

Large megacrysts (up to a few tens of cm size) or xenocrysts of single crystal olivine, orthopyroxene, clinopyroxene, garnet, ilmenite, phlogopite, and (rarely) zircons commonly occur in kimberlites. Based on their chemistry, the megacrysts can be divided into Cr-poor and Cr-rich suites, of which the former is more common. Large variation in Mg/Fe ratios of olivines and other phases, LREE enriched REE- patterns and Nd and Sr isotopic ratios intermediate between those of MORB and OIB suggest an asthenospheric origin for the Cr-poor suite (Harte and Gurney, 1981; Schulze, 1987; Jones, 1987).

The relationship of the megacrysts with the host kimberlite is still debated. Harte and Gurney (1981) and Schulze (1987) suggest that the megacrysts grew from proto-kimberlitic liquids and were later sampled by another kimberlite that brought them to the surface. Jones (1987) suggested that megacrysts formed from melts of picritic or alkali-basalt composition

Table 2.1. Average composition of kimberlites and lamproites.

	I	II	III	IV	V	VI	
SiO_2	38.4	53.3	33.5	40.8	44.5	55.1	All major elements are in wt% of the volatile-free fraction
TiO_2	2.6	3.0	3.0	1.1	3.9	6.0	
Al_2O_3	4.7	9.1	3.0	3.2	3.9	8.6	
FeO	11.3	6.3	13.3	9.4	8.7	6.8	
MnO	0.2	0.1	0.2	0.2	0.1	0.1	
MgO	28.7	12.1	30.4	33.4	26.8	8.0	
CaO	11.3	5.8	13.8	6.7	5.3	3.3	
Na_2O	0.5	1.4	0.2	0.1	0.5	0.6	
K_2O	1.4	7.2	0.9	3.6	4.4	10.3	
P_2O_5	0.9	1.3	1.3	1.2	1.8	1.0	
H_2O	6.6	2.7	8.5	6.0	6.3	3.0	wt% of the total.
CO_2	5.6	2.8	6.8	3.6	0.4	0.5	
Ba	1000	5120	912	3000	10334	9871	ppm
Rb	65	272	38	135	479	275	
Sr	740	1530	935	1140	1312	1184	
Pb			9	30	50	52	
Th	16	46	23	30	60	23	
U	4	5	5	5	2	3	
Zr	250	922	309	290	1133	1144	
Nb	110	95	191	120	184	123	
Y	22	27	23	16	16	20	
La	150	240	111	200	421	292	
Ce	200	400	187	350	734	435	
Nd	85	207	96	145			
Sm	13	24					
Eu	3.0	4.8					
Gd	8	13					
Tb	1	1.4					
Yb	1.2	1.7					
Lu	.16	.23					
Sc	15	17	17	20	21	14	
V	120	123	131	85	85	210	
Cr	1100	580	1165	1800	1006	348	
Ni	1050	420	1031	1400	1004	346	
Co	77	37	81	85	70	33	
Cu			69	30	56	66	
Zn			67	60	71	77	
Ga			6	6	4	17	
S					425	514	
F					4756	2655	
Cl					116	154	

I, Average kimberlite, II, Average lamproite (Bergman, 1987); III, group I kimberlites, IV, group II kimberlite (Smith et al., 1985); V, average of 89 Australian olivine lamproites, VI, 100 when they reached the asthenosphere-lithosphere boundary. He further suggested that as a result of megacryst crystallization and assimilation by lithospheric material, the primary basaltic melts evolved into kimberlitic composition.

The MARID (mica-amphibole-rutile-ilmenite-diopside) suite of xenoliths (Dawson and Smith, 1977; Dawson, 1987b) is another distinctive suite of phlogopite dominated xenoliths. Dawson and Smith suggested that the MARID assemblage is igneous in origin and was crystallized from kimberlite-like magma within the lithosphere. Recently Waters (1987) suggested that this suite of xenoliths are the product of high pressure crystallization of lamproite-like rocks.

Macrocrysts are relatively large (0.5 to 10 mm) anhedral crystals set in the finer-grained kimberlite groundmass. Olivine is the main macrocryst, but phlogopite, ilmenite, spinel, garnet, clinopyroxene, and orthopyroxene may also be found. Their origin is debatable; Clement et al. (1984) suggest that they are xenocrysts derived from mantle rocks, whereas other authors have advocated a cognate origin for some. Crustal xenoliths from various depths are also trapped in the kimberlites during their eruption.

It is obvious, even from this brief overview, that the origin of kimberlites is no simple issue. The interested reader may turn to the final chapter of Mitchell (1986) for a comprehensive review of the different hypotheses. However, in the final section he will read: "The reader seeking a comprehensive scheme of kimberlite petrogenesis as a conclusion to this chapter is likely to be disappointed." The main reason for this, says Mitchell, is: "our complete ignorance of the composition of primitive kimberlitic magma." It is my hope that the characterization of the material trapped in diamond micro-inclusions may shed some light on this issue.

2.1.3. LAMPROITES AND THEIR RELATION TO KIMBERLITES

Lamproites and kimberlites are the only two igneous source rocks for diamonds. The two rock types are distinct, but show many similarities in their mineralogy, geochemistry and eruption style. The occurrence, mineralogy, and geochemistry of lamproites has been reviewed recently by Bergman (1987), Foley et al. (1987), and Dawson (1987a). The brief summary given here relies on these reviews and on the comprehensive study of Australian lamproites (Jaques et al. 1984, 1986).

Lamproites are K- and Mg- rich rocks (typically K_2O>5%, MgO>5%) with high K_2O/Al_2O_3 (>0.8, molar ratio), and high K_2O/Na_2O (>4, molar ratio). Their mineralogy is characterized by titanian phlogopite, clinopyroxene, K-rich Al-poor amphiboles, olivine, leucite, and sanidine. Based on the relative abundances of olivine and leucite Jaques et al. (1984) distinguished between olivine and leucite lamproites. Xenoliths are less abundant in lamproites than in kimberlites. Biotite clinopyroxenites and pyroxenites are the common mantle-derived xenoliths in lamproites. Lherzolites are rare.

Lamproites have erupted since the Precambrian. The diamondiferous Argyle lamproite is 1130 m.y. old (Skinner et al.,1985), the nearby Allendale lamproites are of Miocene age, and the youngest lamproite eruptions in the Leucite Hills, Wyoming are 1 m.y. old. Most lamproites occur in old cratonic regions. However, whereas kimberlites are most abundant in the cores of the cratons, lamproites are commonly found in the old mobile belts surrounding the cores. A few lamproites are associated with younger orogenic terrains, e.g., in the Hercynian or the Alpine orogenic belts.

An average lamproitic composition and the average compositions of Australian olivine- and leucite-lamproites are given in table 2.1. There is a gradual and continuous change in composition from group I kimberlites, to group II, to olivine lamproites, and, finally, to leucite lamproites (Dawson, 1987a; Jaques et al., 1984). In comparison to kimberlites, lamproites have lower CaO and FeO and CO_2 content and higher K_2O, Na_2O, SiO_2, and TiO_2 (Jaques et al, 1984, 1986; Bergman, 1987). Incompatible trace elements are more enriched in lamproites and REE patterns are more fractionated. Compatible element concentrations are somewhat lower than those of kimberlites.

Nd and Sr isotope compositions of lamproites indicate derivation from old enriched sources. Nd is less radiogenic than bulk-earth; Sr is highly radiogenic (McCulloch 1983). The wide range spanned by lamproites includes that of group II kimberlites and led Smith (in

Bergman, 1987) and Bergman (1987) to suggest that group II kimberlites and olivine lamproites are one and the same. Bergman (1987) also pointed out the similarity between the compositions of lamproites and the MARID suite of xenoliths in kimberlites (c.f. Waters, 1987) as an additional indication of the close association between lamproites and kimberlites.

The petrogenesis of lamproites is commonly assumed to be a mantle process and not the result of crustal contamination. The low Ca, Fe, and Al content of lamproite suggests a depleted mantle source, such as dunite or harzburgite. The high content of incompatible trace elements and the isotopic composition of Nd and Sr indicate a later enrichment of the source in incompatible elements. Alternatively, it is possible to produce a lamproitic composition by preferential melting of phlogopite and some accessory phases in a previously metasomatized source (Bergman, 1987).

2.2. DIAMONDS

Diamond is the high pressure polymorph of elemental carbon. The diamond structure is cubic, with each atom connected to its four closest neighbors by four carbon-carbon single bonds 1.54 Å in length and with energies of $5.8 \cdot 10^{-19}$ J (83 kcal/mole). This tetrahedral network of short, strong bonds results in a dense (3.515 gr/cm^3), hard material. Diamond is the hardest material known and one of the best heat conductors. Due to its large band gap, 5.48 eV, diamond is an excellent insulator. However, even a low concentration of boron may lead to semiconductivity in nitrogen-free diamonds. Nitrogen-bearing diamonds show considerable photoconductivity under UV radiation.

Although at low pressures it is thermodynamically unstable relative to graphite, diamond is extremely inert and cannot be chemically attacked at room pressure and temperature. In an inert atmosphere graphitization takes place only at 1800° K. In air, diamond starts developing a black coating at 900° K and is attacked at 700° K only by strong oxidants, e.g., molten $NaNO_3$. Diamond may also be dissolved in some molten metals, e.g., iron or nickel, or react to form stable carbides. An extensive summary of the physical properties of diamond can be found in Field (1979). Recently, Harris (1987) has reviewed the physical, chemical and isotopic research on diamonds.

2.2.1. MORPHOLOGY

Natural diamonds appear in a variety of crystal forms. The usually occurring forms are octahedral, cubic and dodecahedral. Crystals of irregular forms may be the result of resorption of a single crystal or of aggregation of diamond microcrystals. Orlov (1977) suggests that most single crystal diamonds grow in the octahedral form (Orlov variety I). This form develops when diamonds grow layer by layer near equilibrium conditions (Sunagawa, 1984).

Natural diamonds do not develop growth layers on either {110} or {100}. The {110} faces are the result of stepped {111} growth and show striations parallel to <110>. Diamonds of cubic forms (Orlov varieties II and III) are the result of non-faceted growth and are rough (Sunagawa, 1984). Synthetic diamonds show faceted, smooth octahedral and cubic faces. Sunagawa (1984) suggests a different growth mechanism under the high temperatures and high carbon solubility prevailing during the growth of synthetic diamonds from metalic melts. In view of the difference in crystal habit of natural and synthetic diamond it is unsafe to infer the growth conditions of natural cuboid crystals (Haggerty, 1986) from the growth habits of synthetic diamonds at different pressures and temperatures.

Dissolution of diamond surface commonly leads to the development of rounded surfaces. According to Sunagawa, most dodecahedral diamonds are the result of dissolution of octahedral diamonds. Dissolution may also lead to the formation of pits on the diamond surface. Triangular pits (trigons) are common on the octahedral {111} faces. They are typically about 100 μm in size and may have a flat or pointed (pyramidal) bottom. Lang (1979) and Sunagawa (1984) both conclude that these trigons are the result of preferential dissolution of the diamond around the outcropping of dislocations on the diamond surface. Square pyramidal pits found on many cuboid faces are also interpreted as etch pits. Dissolution may also lead to the formation of channels. Channels develop most frequently along cleavage or glide plane (Orlov, 1977), but in many cases the channels are irregular and cannot be associated with any specific crystal plane. Commonly they are about 100 μm wide and a few hundred μm long.

Pure diamond is colorless. Nitrogen impurities may produce yellow or yellow-green colors. Blue diamonds owe their color to trace amounts of boron in nitrogen free crystals and are rare. The source of the brown and pink colors is unclear; however, brown diamonds commonly show high strain and deformation.

2.2.2. INTERNAL STRUCTURE

Single crystal octahedra of diamonds frequently show complex internal structures. Differences in cathodo-luminescence intensity and color (Lang, 1979), in resistance to etching (Seal, 1965), or in charging and electron backscattering during SEM examination (DeVries, 1983) all reveal concentric bands in sections cut through the diamond. The source of banding is probably variations in nitrogen concentration and speciation (see Section 2.2.5). Commonly the bands are parallel to the {111} planes. This pattern, according to Sunagawa, is the result of layer by layer growth in which the growth rates and the rate of incorporation of lattice impurities changes alternatively during the process of growth.

Some diamonds, including the cuboid and the coated diamonds studied here, reveal more complex internal structure. Using x-ray topography, Lang and co-workers have defined two main structural types: a mixed-habit growth texture and a fibrous texture. (The x-ray section topographs are photographs of x-rays reflected at a Bragg angle from a section across the diamond. See Frank and Lang (1965) and Lang (1979) for short and detailed descriptions of the technique.) The differences between the two textural types can also be observed by optical, UV, and cathodoluminescence microscopy. The description of the two types is given in Chapter 3.

2.2.3. CARBON ISOTOPIC COMPOSITION

Diamonds show a wide range of carbon isotope compositions, ranging from $\delta^{13}C = +5\%$ to -34.4% (Sobolev et al., 1979; Galimov, 1984). This range spans almost the full range of crustal carbon and is at present commonly attributed to heterogeneity of carbon reservoirs in the mantle. It must be noted, however, that most diamonds fall within a more limited range of $\delta^{13}C$ = -3 to -9% (Galimov, 1984). Diamonds with peridotitic inclusions (see section 2.2.5) fall only within this range, with the most frequent values being between -4 and -6%o. Diamonds with eclogitic inclusions span a larger range ($\delta^{13}C$= -26 to +3%), but most fall between -5 and -8% (Sobolev et al., 1979; Deines et al., 1987).

Deines et al. (1984, 1987) noticed a correlation between the chemical composition of eclogitic mineral inclusions in diamonds and the isotopic composition of the host diamonds. They suggested that the ^{13}C-depleted diamonds were formed in deeper mantle levels in a source region characterized by higher Fe, Mn and Al and lower Mg, Ca, Si and nitrogen compared with ^{13}C-rich diamonds. Galimov (1984) also distinguished between the two groups of eclogitic diamonds. Based on their morphology and nitrogen speciation, he suggested that the diamonds depleted in ^{13}C (his group ß with $\delta^{13}C$ = -20 to -7%) were formed at higher levels than those with heavier carbon (group α_3, $\delta^{13}C$ = -5 to -10%). He further suggested that peridotitic diamond (group α_2) originated from even deeper levels.

Zoning in the isotopic composition of carbon within single diamonds is usually limited to less than 0.5% (Kaminsky et al., 1978). Javoy et al. (1984) reported variations of up to 2.2% between fragments of octahedral diamonds from Zaire and larger variations were found between the core and the coat of coated diamonds (Zwart et al., 1983). The latter will be discussed in Chapter 3.

2.2.4. NITROGEN AND THE IR SPECTRUM OF DIAMONDS

The IR spectrum of a pure diamond (type IIa) is presented in Figure 8.1.a (Chapter 8). No absorption bands are present below 1330 cm^{-1} in the one-phonon region. This is because the diamond crystal is highly symmetric and monovalent and no first order change in electric dipole moment is produced by any of the vibrational modes. The main peaks at 1975, 2025, 2160, and 2490 cm^{-1} are due to two phonon absorption (Robertson et al., 1934); weaker, three phonon absorption gives rise to the wide bands at 3240 and 3580 cm^{-1}.

Impurities disturb the symmetry and give rise to one phonon absorption. Nitrogen is the most abundant impurity in diamond; it forms several types of IR-active centers, which are the basis for diamond classification (Table 2.2). In most diamonds (type IaA) nitrogen is present as a pair of atoms replacing two adjacent carbon atoms and gives rise to the type A spectrum (Fig 2.2.a, Table 2.2). Type IaB diamonds carry larger aggregates of nitrogen atoms (Davies, 1975) and show characteristic absorption features (type B, figure 2.1.b.) Single nitrogen atoms are present in some natural diamonds (type Ib) and in most synthetic diamonds giving rise to type C spectrum (figure 2.2.c.) Additional spectral types have been recently defined (Clark and Davey, 1984), but they are not yet associated with a particular nitrogen center. Absorption at ~1370 cm^{-1} is due to the presence of nitrogen containing platelets (Sobolev et al., 1968) and is common in diamonds of type Ia. The IR absorption coefficients of the A, B and C centers were determined and are also summarized in Table 2.2.

Harris et al. (1975) first suggested, based on geologic evidence, that single nitrogen atoms can react to form more stable nitrogen pairs and that the reaction may proceed to form larger aggregates, and finally, platelets. Evans and Qi (1982) studied the kinetics of the first two reactions. The second order reaction of single nitrogens to form nitrogen pairs has an activation energy of 5±0.3 eV. Evans and Qi estimated the time needed for 20% aggregation in a diamond containing 30 ppm nitrogen (relatively low concentration) at 1000°C to be of the order of 10^5 years. At 900°C the process would take $6x10^6$ years. The formation of larger aggregates is a much slower process.

2.2.5. OTHER IMPURITIES

Bibby (1982) and Sellschop (1979) reviewed the many studies that examined the impurity content in natural diamonds. Boron and hydrogen are the only other elements (beside nitrogen) that enter the diamond structure. Boron was shown (Chrenko, 1971) to be the donor in semiconducting diamonds. Hydrogen gives rise to sharp IR absorption bands at 3107 and 1405 cm^{-1} (Runciman and Carter, 1971). Other elements reported in diamonds are most likely associated with inclusions.

Table 2.2. Diamond types and IR spectral types.

a. Classification of diamond type

Type I	Contain nitrogen	**Type II**	No detected nitrogen
Type Ia	Aggregated nitrogen centers	**Type IIa**	Insulator contains no boron
Type IaA	Nitrogen pairs		
Type IaB	Larger aggregate		
Type Ib	Single nitrogen centers	**Type IIb**	Semiconductor contains <1 ppm boron

b. IR absorption characteristics.

Diamond type	**IaA**	**IaB**	**Ib**
Main IR lines (cm^{-1})	1282,1212 1095,1010 480	1330,1175 1095,1010	1130,1344
IR spectral type[1]	**A**	**B**	**C**
Platelet	may be present	present	no platelet
Absorption[2] Coefficient	300±20[3]	230[4]	400[5] 2500[6]

1. As defined by Clark and Davey (1984).

2. Absorption coefficients in ppm^{-1}cm^{-1}

3. Kaiser and Bond (1957), Lighttowlers and Dean (1964).

4. Sobolev and Lisoyvan (1974).

5. Chrenko et *al*. (1971).

6. Sobolev et *al*. (1969).

Figure 2.2. IR spectra of diamonds with different aggregations of nitrogen (modified from Davies, 1984).

a. IR spectrum of diamond with single nitrogen centers (diamond type - Ib, spectral type - C)

b. IR spectrum of diamond with paired nitrogen centers (diamond type - IaA, spectral type - A)

c. IR spectrum of diamond with nitrogen aggregates and platelet (diamond type - IaB, spectral type - B)

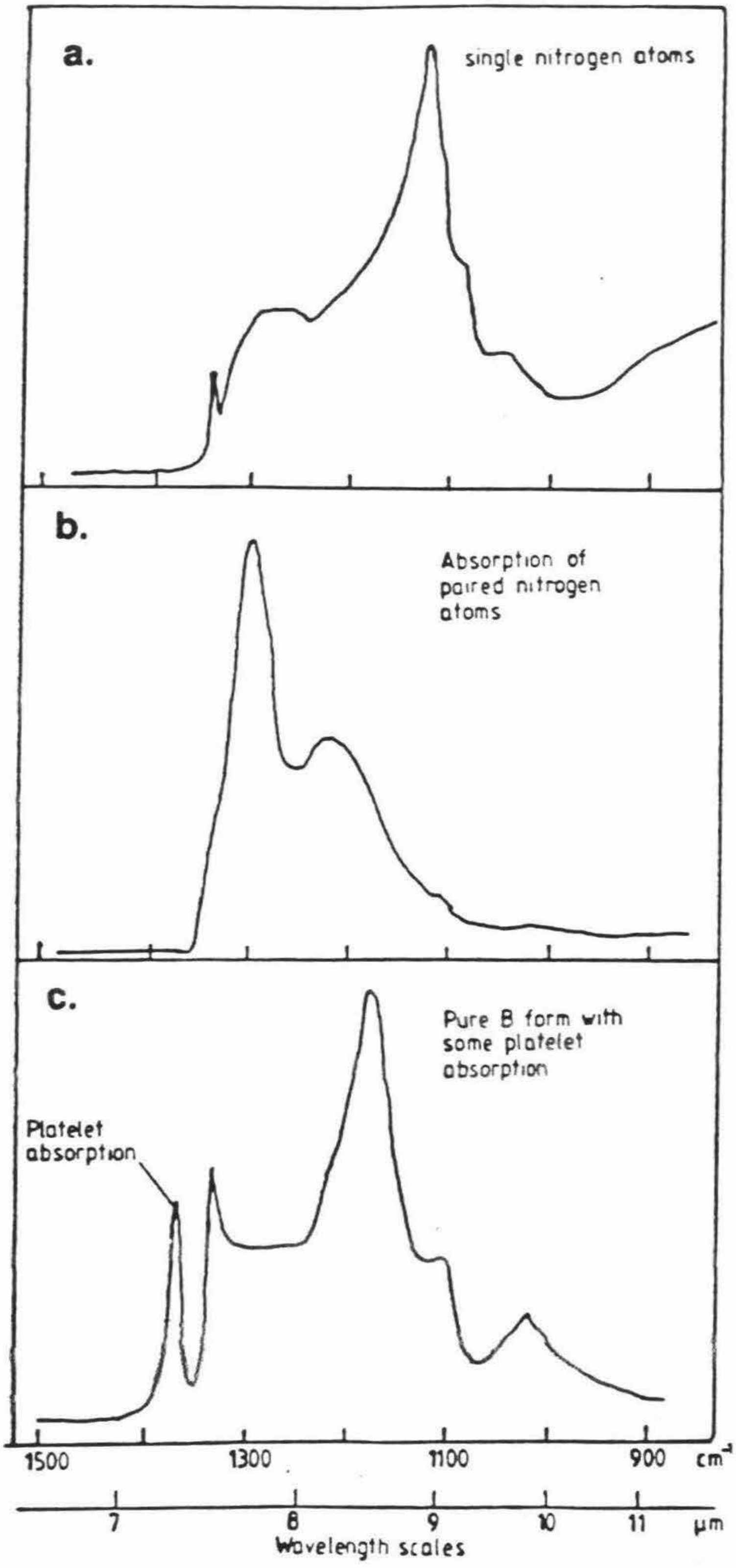
a.
single nitrogen atoms
b.
Absorption of paired nitrogen atoms
c.
Pure B form with some platelet absorption
Platelet absorption
1500
1300
1100
900
cm⁻¹
7
8
9
10
11
µm
Wavelength scales

2.2.6. INCLUSIONS

Inclusions in diamonds provide mineralogical, chemical, and isotopic information about their source region in the upper mantle. Meyer and Tsai (1976), Harris and Gurney (1979), and Meyer (1987) reviewed the results of the extensive study of mineral inclusions in diamonds. Inclusion-bearing diamonds are common, with the typical inclusion size being on the order of 100 μm. In many cases the shape of the inclusions is crystallographically controlled by the diamonds, and the inclusions may have a cubo-octahedral symmetry. Irregular inclusions or inclusions that have retained their own crystal form also occur. Most inclusions are mono-minerallic; bi- and polyminerallic inclusions are rare.

A distinction is usually made between proto- or syngenetic inclusions and inclusions of epigenetic origin. The common criterion is whether the inclusion is well encapsulated within the diamond or is connected by cracks to the surface. The minerals found in syngenetic inclusions fall into two main suites: peridotitic (or ultramafic) and eclogitic. Sulfides, olivine and orthopyroxene are the predominant peridotitic minerals, with lesser abundance of garnet, chromite, clinopyroxene and, rarely, ilmenite, zircon, native iron and magnesio-wustite. Garnet, clinopyroxene and sulfides are the main eclogitic inclusions with minor kyanite, rutile, corundum, coesite, ilmenite, sanidine, zircon, and mica. Syngenetic inclusions which could not be associated with the above suites may contain: amphibole, magnetite, apatite, ferro-periclase, and moissanite.

Except for a few rare cases (Gurney, 1986), inclusions of the two suites do not coexist in a single diamond, but different diamonds containing either peridotitic or eclogitic inclusions are commonly found in single kimberlites. The proportion of diamonds with either eclogitic or peridotitic inclusions in a kimberlite varies widely for different kimberlites. The composition of the mineral inclusions is highly similar for widely separated localities, widely different geological time, and different host rocks (kimberlites or lamproites).

Peridotitic diamond inclusions are often high in magnesium and low in calcium. This rather depleted composition is accompanied by strong enrichment of many incompatible elements (Richardson et al., 1984; Shimizu and Richardson, 1987; Shimizu et al., 1987).

Eclogitic inclusions are characterized by higher alkali content compared with common mantle eclogite minerals. Minerals of similar composition are also found in diamondiferous eclogite xenoliths.

Coexisting mineral pairs in diamonds enable the estimation of the pressure and temperature at the diamond source region at the time of its formation. Temperatures in the range of 950-1350°C were calculated for peridotitic inclusions. Similar variations, but generally higher temperatures, were obtained for eclogitic inclusions. Pressure can only be estimated for the peridotitic suite assemblages; it varies between 45 and 65 kbar. These P-T conditions indicate that peridotitic diamonds were formed "in the diamond stability field, under conditions that lie close to the predicted ambient shield geotherm and to the peridotite solidus" (Boyd and Gurney, 1986) (see Figure 2.3). These pressures and temperatures are most plausibly those prevailing close to the base of the lithosphere at depths between 150 and 200 km. Garnet-clinopyroxene solid solution, which is expected to occur only at pressures exceeding 50 kbar, is found in inclusions within diamonds from the Monastery Mine, South Africa, suggesting an even deeper source of ~450 km (Moore and Gurney, 1985) for their host diamond.

The ages of a few diamonds have been determined from the radiogenic isotope composition of their inclusions. Following the early work of Welke et al. (1974) some Pb and Nd model and isochron ages have been determined (Tab. 2.3). The model ages of most dated diamonds are substantially older than the emplacement age or the model age of the host kimberlite. The large difference between the isochron ages of Argyle diamonds and the Argyle lamproite also clearly indicates a xenocrystic relation between the diamonds and the kimberlite.

Figure 2.3. The diamond stability field.

a. The carbon phase diagram (from Muncke, 1979).

b. The relation of the diamond-graphite boundary (solid line), the shield geotherm (40 mW m^{-2}, short dashed line, and the wet peridotite solidus (long dashed line). Also shown are pressure and temperature determination for xenoliths from Northern Lesotho (Finnerty and Boyd, 1987). The ruled area represents the equilibration condition for 29 olivine-garnet pairs in diamond inclusions from the Finch mine S.A. (Boyd and Gurney, 1986). The P-T conditions recorded by the diamond inclusions led Finnerty and Boyd (1987) to suggest that garnet grew under subsolidus conditions.

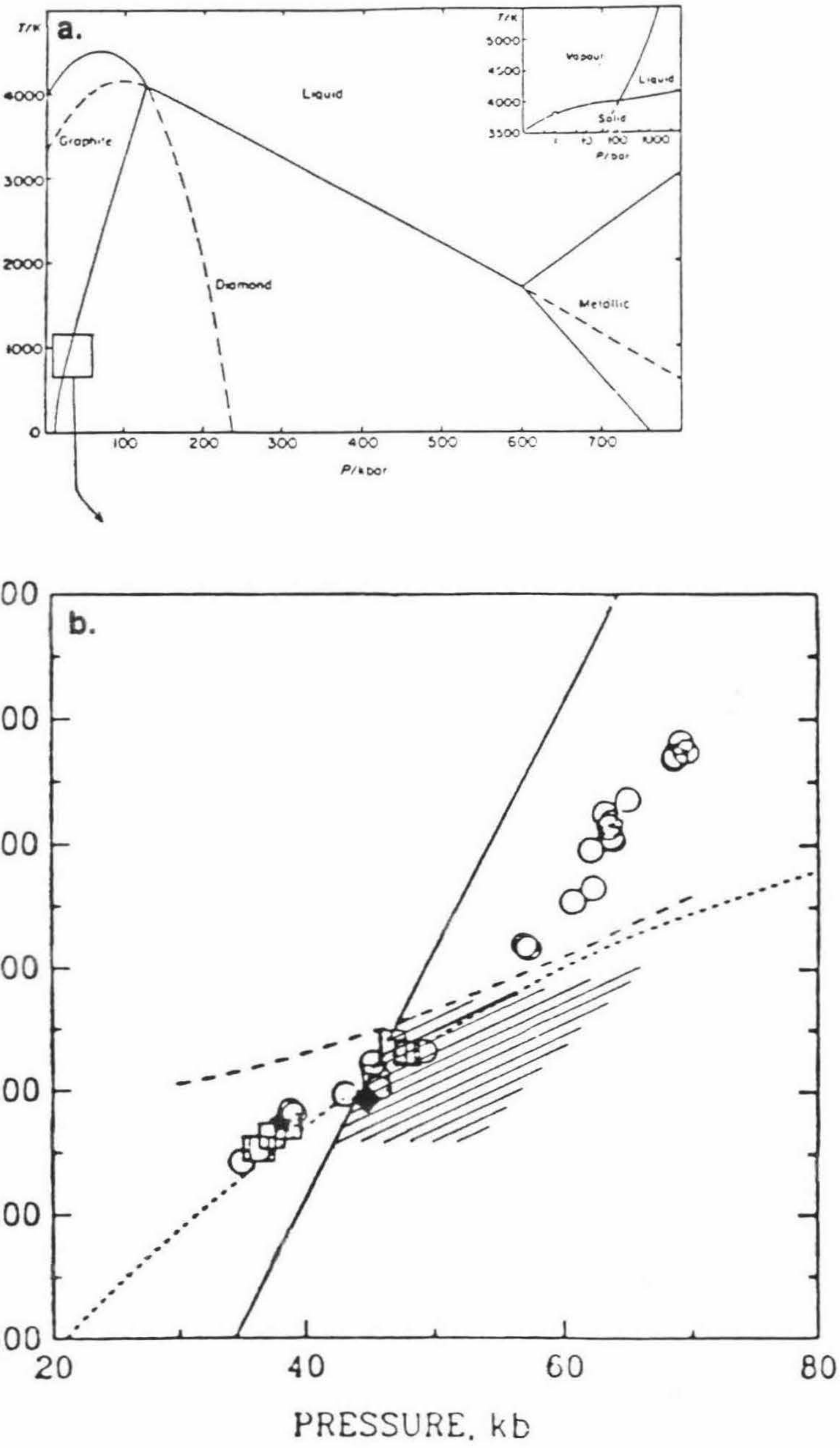
T/K
a.
4000
3000
2000
1000
0
100
200
300
400
500
600
700
P/kbar
Graphite
Liquid
Diamond
Metallic
T/K
5000
4500
4000
3500
Vapour
Liquid
Solid
1
10
100
1000
P/bar
b.
1800
1600
1400
1200
1000
800
600
20
40
60
80
PRESSURE, kb

Table 2.3. Isotopic dating of diamond inclusions.

Kimberlite	Age (m.y.)	Inclusions	Age (m.y.)	Comments	Ref
Premier	1180±30	Black (sulfides?)	1200	Pb model age.	1
Premier	1180±30	Eclogitic garnet+cpx	1150±60	Gar-cpx isochron age	3
Finsch	120	Black (sulfides?)	>2000	Pb model age	1
Finsch	120	Peridotitic garnets	~3300	Nd model age, composite sample	2
Finsch	120	Eclogitic garnets	1670±40	Nd model age, single diamond	4
Kimberley	90	Black (sulfides?)	>2000	Pb model age	1
Kimberley	90	Peridotitic garnets	~3300	Nd model age	2
Argyle	~1130	Eclogitic garnet+cpx	1580±60	Gar-cpx isochron age	3

1. Kramers (1979); 2. Richardson et al.(1984); 3. Richardson (1986); 4. Smith (1986)

CHAPTER 3 PREVIOUS STUDIES OF MICRO-INCLUSION-BEARING DIAMONDS

Since the introduction of x-ray analytical methods to the study of inclusions in diamonds (Meyer and Boyd, 1968) most of the attention has been devoted toward the study of the discrete, mineral phases included in single-crystal diamonds (see Sec. 2.2.6). The material included in other crystal forms of diamonds as well as micro-inclusions in single-crystal diamonds has been the subject of very few studies.

In this chapter I review the previous studies of micro-inclusion-bearing diamonds of the types investigated here, namely cubic[1] and coated diamonds of varieties III and IV of Orlov (1977) respectively. Micro-inclusions occurring in more perfect single crystal diamonds appear to be related to the inclusions studied here and are also included. Mineral inclusions have also been found in polycrystalline aggregates (Trueb and Barrett, 1972 and references therein). The size and the nature of these inclusions is unclear and they are not included in this summary.

3.1. MORPHOLOGY AND INTERNAL STRUCTURE

In his excellent review of diamond mineralogy, Orlov (1977) describes the two diamond varieties studied here:

> *Variety III includes "cubic crystal and crystals showing a combination of forms (octahedron + rhombic dodecahedron + cube) ... that are sub-transparent, colorless or with different hues of grey, sometimes almost black and opaque. Parallel and irregular groups are typical and also penetration twins of spinel type. Variety III crystals have a rather complex internal structure: a colorless transparent zone in the center, the outer part showing microscopic inclusions. These inclusions are responsible for the gray and dark colorations of the crystals. Because of the many defects in the outer zone, dissolution at the crystal faces produces large number of fine etch figures".*
>
> *Variety IV. "Some diamond crystals show a zonal structure, clearly visible to the naked eye when the crystal is cleaved. Such crystals are known in the literature as coated diamonds as they display an outer zone around a quite different inner core. This "coat" is usually dull, milky-white, grayish, or with slight yellow or green coloration, while the core is usually a transparent crystal. The coat has a specific structure which can be seen by x-ray diffraction*

---

[1] Natural faceted growth on cubic planes is extremely rare. Natural "cubic" diamonds are in fact cuboids. However, as the term "cubic" is largely used in the literature and is less cumbersome to use, I will use the term "cubic" throughout the thesis.

> *techniques. Plane-faced coated diamond crystals may vary in external configuration: octahedra with even faces or with stepped development, or cubes and combination of crystal forms (octahedron + rhombic dodecahedron + cube). Dissolution at the crystal faces gives rise to countless etch figures, usually pitting the whole surface of the face. Far reaching dissolution converts plane-faced crystals into rounded forms."*

The first detailed microscopic examination of coated diamonds was reported by Custers (1950). He noted that the boundary between octahedral cores and their coats is usually sharp and that, in many cases, the outer layer of the coat is inclusion-free and consists of pure diamond.

Shah and Lang (1963) were the first to apply x-ray topography to the study of the internal structure of micro-inclusion-bearing diamonds. Kamiya and Lang (1965) studied the structure of coated diamonds and Moore and Lang (1972) studied the structure of cubic diamonds; the results were reviewed by Lang (1974, 1979). Inclusions were found in the cuboid growth zones of coated and cubic diamonds and also in the cuboid growth zones of "center-cross" diamonds.

Center-cross diamonds and some cubic diamonds show a mixed-habit growth texture (Lang, 1979). They consist of sectors of faceted growth parallel to (111) together with non-faceted growth sectors, which, on the average, are parallel to (100) directions. In some cases, the (111) growth takes over in the later stages of growth and the diamond morphology is octahedral. In other cases the cubic planes extend to the surface and the diamond is cubic in shape.

X-ray topographs of coats of coated diamonds and of many cubic diamonds show a fibrous texture (Kamiya and Lang, 1965). The fiber diameters vary from 10 μm down to the resolution of the technique (~1 μm). Their average orientation is parallel to the <111> direction but individual fibers may be misoriented by up to 0.5°. The fibers join to form lamellae parallel to the {110} planes (Orlov et al., 1982). Branching of the fibers leads to the formation of cuboid surfaces that become dominant as the diamond grows (Moore and Lang, 1972).

Orlov (1977) suggested that the outer morphology of coated diamonds is determined by the relative thickness of the coat. As the coat grows in thickness the octahedral faces keep their original area while the cubic faces grow larger in area (fig. 3.1). If the core diamond is small compared with the final size, the final shape of the diamond is that of a cube. Orlov (1977) also noted that in many cases diamonds of variety III have a transparent, colorless, cross-like region and suggested that these diamonds also commenced their growth as octahedral diamonds. However, in those diamonds, as well as in few coated diamonds, no sharp boundary occurs between the octahedral and the cubic zones.

Seal (1966a) reported inclusions of up to 5 μm in size on the etched surface of a coated diamond. He also described (Seal, 1966b) transparent but birefringent inclusions of 1-3 μm size in some type I diamonds with cross-like features in their centers, including a sample from the Kimberley area, South Africa. He estimated the number density of inclusions as 1-4x10^8 inclusions/cm^3.

3.2. CHEMICAL STUDIES

Chesley (1942) analyzed diamond ash by atomic absorption spectroscopy and recorded the presence of a variety of elements in many diamonds including some coated and cubic diamonds. Gnevushev and Kravtsov (1960) found higher levels of Mg, Al, Si, Ca, and Fe in the yellow outer region of a diamond than in the inner clear core. Kamiya and Lang (1964) used x-ray fluorescence and detected the presence of MgO and SiO_2 in diamond coat. Using an electron microprobe, Seal (1966a) detected Si and oxygen in the diamond coat. The Si/O ratio varied from one inclusion to the other, and in one inclusion K and Ca were detected. Seal (1966b) also reported the presence of O, Si, Al, Ca, Mg, S, and possibly Fe in inclusions he found in some type I diamonds. Prinz et al. (1975) found "fluffy, filamentous material" in two diamonds from Zaire. The approximate composition obtained by electron microprobe analysis of this small, thin and rapidly volatilized phase was: SiO_2, 67%; TiO_2, 2.5%; Al_2O_3, 14-17%; FeO, 2-3%, MgO, 1%; Na_2O, 0.2-2.5%; K_2O, 8.5-10%. White dense clouds of particles were also observed by Harris (1968), but, in both cases the description of

Figure 3.1. Coated diamonds.

a. When the coat is thin, the octahedral shape is still preserved. The {100} faces start to develop and are commonly covered with pyramidal pits. Triangular pits (trigons) are ubiquitous on the octahedral faces, and the dodecahedral faces show striations. In cross-section, the boundary between the core and the coat is commonly sharp. The Core is transparent and the coat is translucent and show concentric zoning.

b. When the coat is thick, the octahedral faces are relatively small. Normally, they retain their original size or are smaller. The cuboid faces parallel to {100} are better developed. In most diamond they are less regular than in the figure and show higher relief, channels, and large pits. The {111} and {011} faces are less well developed.

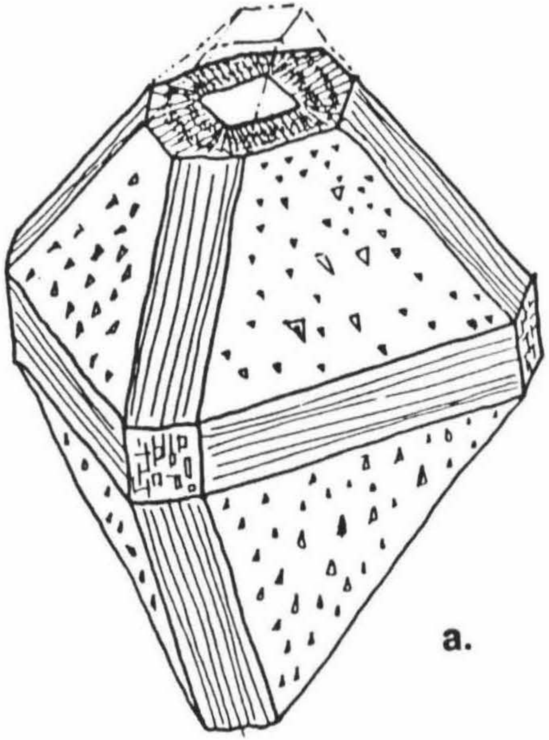

a.

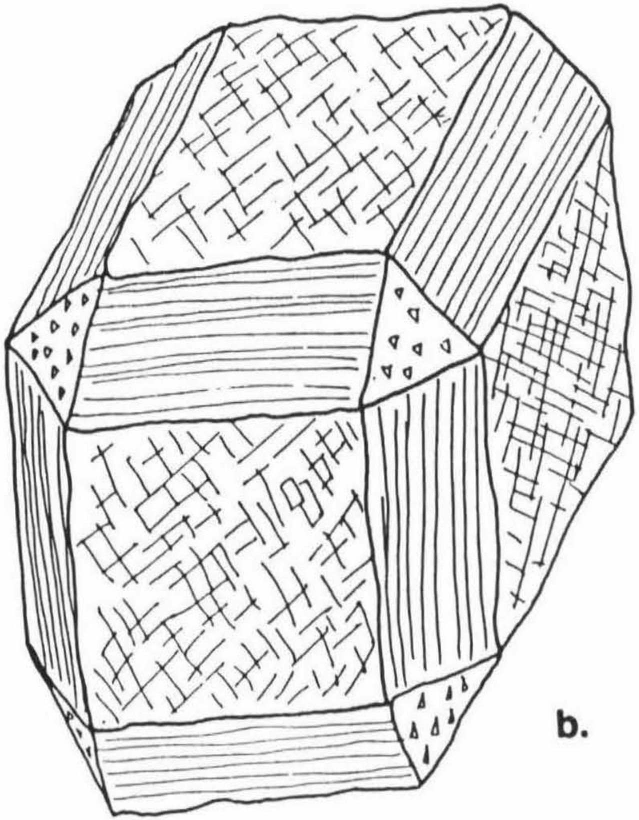

b.

the diamond is not given. The above composition is roughly that of K-feldspar; Bulanova and Argunov (1985) reported the finding of discrete inclusions of K-feldspar in the core and the coat (?) of a Siberian coated diamond.

Lang and Walmsley (1983) used transmission electron microscopy (TEM) to directly study the structure and mineralogy of the micro-inclusions in a coated diamond. They found sub-rounded inclusions of 0.1-1 μm size, that contained apatite and Si- and K-rich "non-faceted" material.

Radioactivation analyses of trace elements in diamonds by Kodochigov and co-workers during the late sixties and early seventies (as summarized in Orlov, 1977) yielded the first quantitative results of the impurity content for coated diamonds. They detected Si, 100 ppm; Na, 1-14 ppm; Cr, 25-31 ppm; Mn, 0.12 ppm; Cu, 0.06 ppm; and La 1.4 ppm. Mg, Al, Fe, Ti, P, and Pt were also detected. Bibby (1979) used instrumental neutron activation analysis to study the trace element composition of a single coated diamond of unknown origin as well as some other South African diamonds. Following the method developed by Glazunov et al. he used stepwise dissolution of the diamond to study the radial distribution of impurities in the diamonds. The core of the coated diamond was found to contain only ppb levels of Na, K, La, Ce, and Sm. The coat had a much higher impurity content; similar levels were also found in an irregular, greenish diamond from South Africa. Fe was the most abundant element with concentrations of 10-50 ppm in the coated diamond and 10-70 ppm in the green diamond. Na concentrations varied between 1-8 and 10-43 ppm in the two diamonds. K varied between 3-2.4 and 1.7-4 ppm with K/Na ratios of 0.3-0.5 and 0.1-0.2 for the two diamonds. Ba, 1-4 ppm and the light REE, 1-2 times chondritic, were found in the coated diamond. The REE patterns show light REE enrichment with La/Yb ratios of ~12 and Ce/Eu ratios of ~3. The green diamond contained 1-8 ppm Ba, but La levels were much lower (<0.1 chondriditic abundance). Few tens of ppb of Co, Cr, Sc, and Th were found in the coated diamond; the green diamonds contained less Sc and Th and much higher levels of Ni, Co, Cr, and Mn.

Bibby interpreted his result as indicating the presence of melt inclusions in the two diamonds. Based on the good intercorrelation of K, Na, Ba, and the REE and their poor correlation with Sc, Cr, and Mn, he suggested the presence of carbonate in the inclusions. He also interpreted the radial variations of Ba/Sc ratios in terms of increasing carbonate component towards the surface of the diamond. The presence of Co at ppb levels in all diamonds led Bibby to suggest that sulfide inclusions were present in all diamonds. The presence of submicroscopic inclusions of silicate melt and sulfides in diamonds was suggested earlier by Fesq et al. (1973, 1975).

Recently, Akagi and Masuda (1988) have used isotope dilution mass spectrometry to determine REE concentrations in a few Zairian cubic diamonds. They found much steeper REE patterns than those reported by Bibby. REE fractionation is extreme and the patterns resemble those of kimberlites (with concentrations in the diamonds being 10^3 to 10^4 times lower than in kimberlites).

3.3. ISOTOPIC COMPOSITION

Swart et al. (1983) measured carbon isotopic compositions of coated diamonds of unknown origin (most probably, Zaire). They found that the core and coat have different isotopic compositions. Their data also indicated variations of up to 1.16%% between the outer and inner core in one of the diamonds they analyzed. Similar results were obtained by Galimov (1984) and Boyd et al. (1987). Boyd et al. summarized the carbon isotopic data for coated diamonds from Zaire and Siberia. They showed that the isotopic composition of carbon in the coats of all diamonds falls within a narrow range between δ^{13}C= -6 and -8 %%. Boyd and Pillinger (1988) reported that coats of diamonds from Sierra Leone, Angola, and Botswana also fall within this limited range. The cores span a wider range of compositions varying between δ^{13}C= -5 to -9% for the Zairian samples and -4.5 to -16.9% for the Siberian diamonds. No correlation was found between the compositions of the cores and the coats, and Boyd et al. (1987) suggested that the two were formed in different events.

Cubic diamonds from Zaire show the same range of carbon isotopic composition as the coats (Javoy et al., 1984, Boyd et al., 1987). Zoned cubes from Siberia also fall in the same range (-6 to -7.2, Galimov, 1984). Other cubic Siberian diamonds span a wider range.

Forty-three cubic diamonds from central Yakutia kimberlites fall between -5 to -17% (Still, 39 of them are in the -5 to -10% range). Cubic diamonds of Orlov variety II (green-yellow, transparent, with paramagnetic nitrogen centers) fall between -6 and -20% . In this group, most of the diamonds are lighter then $\delta^{13}C$=-10% .

Eight published analyses of the helium isotopic composition of opaque, cubic or rounded Zairian diamonds (Ozima et al., 1985; Honda et al., 1987; Ozima and Zashu, 1988) define a narrow range in $^3He/^4He$ ratios, 4-13x10^{-6}, compared with total range of 0.1-316x10^{-6} measured in other diamonds (Ozima et al., 1985). This limited range suggests a relatively uniform source region for the diamonds.

Zashu et al. (1986) observed a good correlation between ^{40}Ar and K concentration in Zairian cubic diamonds. If interpreted as an isochron this correlation corresponds to an age of 6±0.3 b.y. Zashu et al. considered the possibility that the correlation is the result of "incorporation of variable amounts of unknown component which had a constant $^{40}Ar/K$ ratio [which contained] excess ^{40}Ar relative to in situ ^{40}K, to give the extraordinary old age." Such a constraint, they argued, would require "that the unknown component was in a fluid state to ensure the homogenization necessary to give a constant $^{40}Ar/K$ ratio, and to acquire excess ^{40}Ar from outside the system." However, these authors later argue that the fact that good correlation is also observed between $^{40}Ar/^{36}Ar$ and $K/^{36}Ar$ indicated that this is not the case and trapped fluid cannot explain the two correlations.

Close examination of figure 1 in their paper shows that the ^{40}Ar versus K line passes through the origin. When this is the case, the $^{40}Ar/^{36}Ar$ versus $K/^{36}Ar$ must preserve the correlation. Indeed this second correlation line also passes through the origin. The data can be perfectly explained by incorporation of different amounts of argon rich fluid into the diamond micro-inclusions described in this thesis. The major element composition of the trapped material is relatively homogeneous (±15%) and Ar/K ratios are also expected to be relatively uniform. The data of Zashu et al. show $^{40}Ar/K$ of 9±5x10^{-4} cm^3STP per 1 gr K. This variation is somewhat higher than that observed for the major elements.

Subsequent studies of Ar and K isotopic composition in Zairian cubic diamonds (Takigami et al., 1988; Podosek et al., 1988) are also in agreement with the trapped fluid explanation. Isotopic compositions of other rare gases in Zairian cubic diamonds were recently reported by Ozima and Zashu (1988).

3.4. INFRARED SPECTROSCOPY

Comparison of the IR spectra of a core and a coat of a coated diamond (Chrenko et al., 1973) revealed some additional lines in the spectrum of the coat. While the core exhibited a normal type Ia + platelets spectrum, the coat revealed bands at 3400, 1640, 1430, 1000, 880 and 835 cm^{-1}. The platelet peak at 1370 cm^{-1} was absent in the spectrum of the coat. The lack of platelet absorption in the spectrum of the coat was noted earlier by Angress and Smith (1965). The coat spectra recorded by Angress and Smith also show bands at ~1000, 880, and 835 cm^{-1}.

Chrenko et al., (1973) suggested that the extra bands are due to the presence of an included phase or phases in the coat, rather than being the result of isolated ionic or molecular species in the diamond lattice. They assigned the 3400 and 1640 cm^{-1} bands to the presence of hydrated phase and the 1430 and 880 cm^{-1} to a carbonate phase; they also suggested that the 835 cm^{-1} feature together with a broad band at 1360 cm^{-1} are due to the presence of nitrates; no assignment was suggested for the 1000 cm^{-1} band.

Similar bands were observed in coated diamonds from the Udachnaya kimberlite (Orlov et al., 1978) and in cubic diamonds of variety III (Plotnikova et al., 1985).

CHAPTER 4 THE SAMPLES

More than 100 diamonds were examined during the course of this study. Appendix I contains the descriptions of 56 analyzed samples. Most of the effort was devoted to the study of two sets of diamonds, rich in micro-inclusions. Six coated octahedral diamonds and eight cubic diamonds from the collection of Dr. G.R. Rossman are referred to as the GRR set. Samples GRR 1501 through GRR 1530 were purchased from Mr. David New (Eugene, Oregon). They are probably from a single locality, most likely Zaire, although their exact source is uncertain. The morphology and color of these diamonds are typical of Zairian diamonds (J.W. Harris, personal communication). Diamond GRR 1155 is also considered to be of Zairian origin. Diamond GRR 861.2 is from an unknown source.

Polished wafers of center sections (parallel to (001)) of eleven coated diamonds from a collection contributed by C.T. Pillinger of the Open University, UK, are referred to as the CTP set. Most of the CTP samples were studied for their carbon and nitrogen isotopic composition and their nitrogen speciation by Boyd et al. (1987), who presented short descriptions and photographs of the sections. Diamond CTP 6268 is from the Jwaneng mine, Botswana; CTP MM1 is from the Mbuji-Mayi mine in East Kasai, Zaire. The other diamonds of the CTP set were selected from the "bulk" Zaire production and their exact source locality is not known.

4.1. SAMPLE DESCRIPTION

4.1.1. SIZE

The cubic diamonds of the GRR set vary in weight between 11-55 mg (1.6-3 mm edges). The octahedral samples are larger, 50-132 mg (3-4 mm edges). Some of the wafers of the CTP set are from somewhat larger octahedra, up to 7 mm. This range in size represents only a portion of the range spanned by natural, inclusion-bearing diamonds. It is unlikely that the composition of the micro-inclusions depends on size.

4.1.2 COLOR

Most of the coated diamonds of the GRR set are yellow-green in color, with variations from pale green to yellowish-green through green and to brown- or grey-green. The cubes are yellow-green or milky, pale green. The diamonds of the CTP set were only examined as thin wafers (0.5 to 1 mm), the coats are commonly brown to grey-brown. CTP L3 and CTP L4 are yellow.

Microscopic examination of sections of the diamonds shows that, in most cases (e.g., GRR 1504, CTP LB), the diamond matrix is colorless and the source of the color is due to the color of the micro-inclusions. In few diamonds (e.g., CTP L3, CTP L4) parts of the coat are yellow due to the intrinsic color of the diamond; the inclusions appear as dark, brown particles in a yellow background.

It has been suggested that the intrinsic yellow-green color of coated diamonds is due to the presence of single nitrogen centers (Orlov, 1977, p.12; Galimov, 1984). Observations presented here show that this is not always the case and that microscopic examination is needed to determine the source of the color of the inclusion-bearing zones. The possible presence of single nitrogen centers in the diamonds studied here is discussed in section 8.2.1. in relation to the IR spectra of these diamonds.

4.1.3. MORPHOLOGY

All of the diamonds of the GRR and the CTP sets are euhedral in shape. The octahedral diamonds consist of a transparent core, coated by a transluscent to opaque overgrowth, commonly called a "coat". The octahedral faces are well developed. However, the edges are not sharp and some diamonds exhibit well developed, cubic and dodecahedral surfaces, parallel to the (001) and (110) planes respectively (Fig. 4.1). Sections cut through these crystals reveal that the cores have only octahedral faces. The other faces are the result of the growth of the coats and are better developed in diamonds with thicker coats (e.g., Fig. 4.2). Many of the coated octahedra have large pits (~1 mm in size) which may go through the coat and penetrate the core.

Figure 4.1. An octahedral coated diamond with some development of cubic and dodecahedral planes.

Photograph taken through Nikon binocular microscope.

Figure 4.2. A polished section of CTP LB.

The transparent core is an octahedral diamond and the core-coat boundary is sharp, indicating that the core was a euhedral octahedron at the commencement of the growth of the coat. New faces parallel to the cubic (001) planes developed during the formation of the coats, their traces on the section plane make 45° angles with the trace of the octahedral faces. Two intersecting zoning patterns can be observed in the coat. One is perpendicular to the outer faces of the diamond, and the other is concentric. The first pattern is formed by arrays of small microscopic inclusions, located between elongated, inclusion-free zones. The concentric banding is the result of higher inclusion density at the same radial position. The concentric bands represent growth stages of the diamond. Transmitted light, Nikon binocular, scale bar = 1 mm.

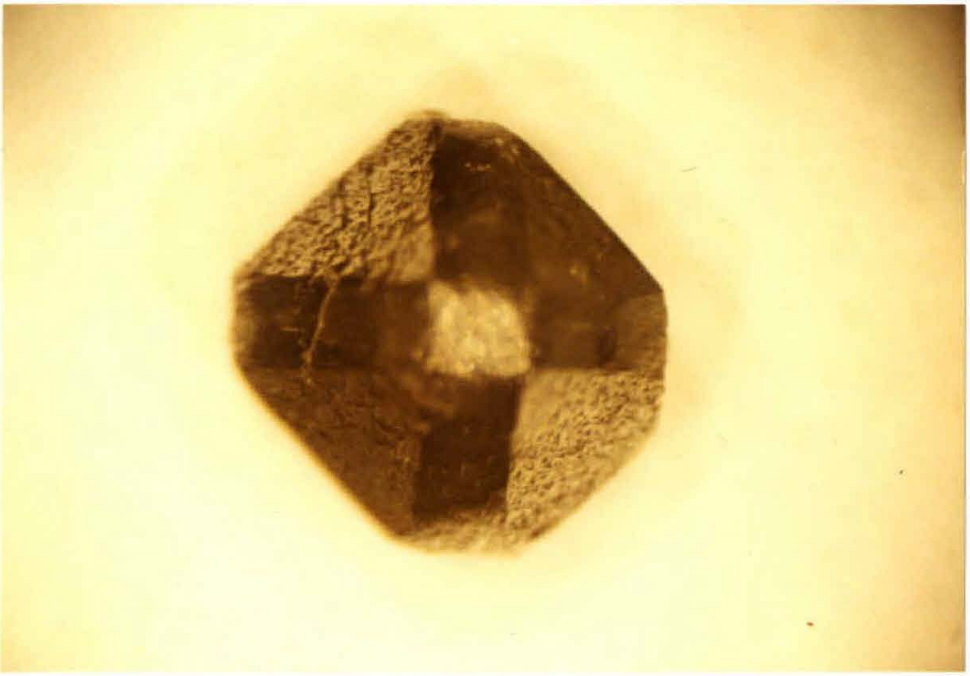

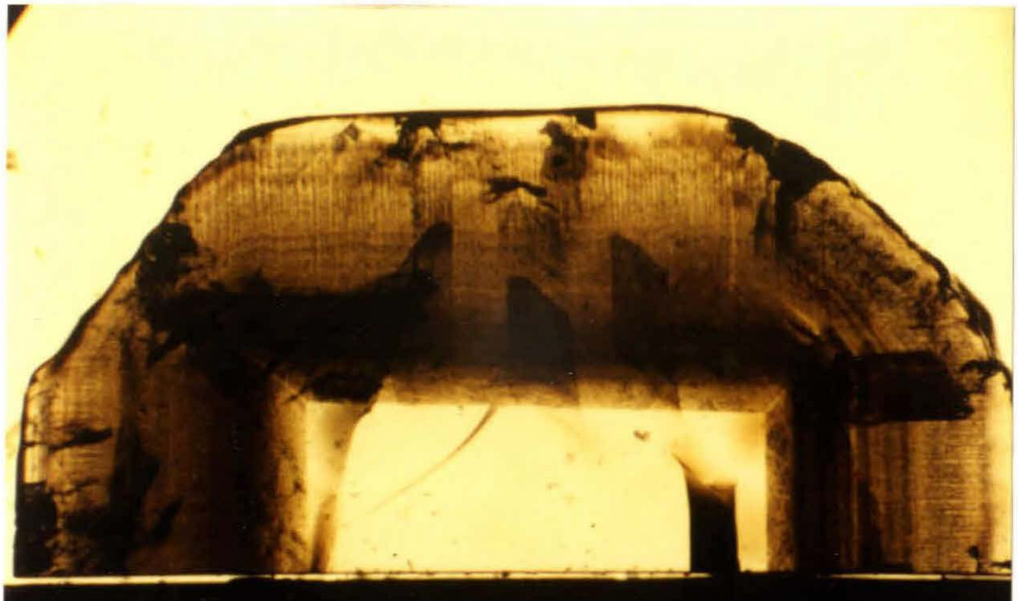

The surface morphology of the octahedral (111) and the cubic (001) faces is quite different. The octahedral faces have low relief, and are flat on a mm scale. On a smaller scale, they are populated by abundant, triangular pit (trigons). Trigons may be found in any size between 1 μm and 1 mm; they frequently overlap each other and fully cover the whole area of the octahedral faces. Their origin has been debated for a long time. Recent studies commonly suggest that they are the result of surface etching and are not formed during growth (Sunagawa, 1984). When present, the dodecahedral faces, (110), show striations parallel to the edge (<$^{-}$110> direction), but are otherwise smooth. The cubic (001) faces are similar in their morphology to those of cubic diamonds and are described in the following paragraph.

The cubic diamonds are not perfect cubes. Angles as low as 75-80° were observed between adjacent faces in some diamonds. The (001) faces of both cubic and coated diamonds are usually of higher topographic relief and irregular appearance. In some cubic diamonds the faces are concave with the centers lower than the rims. In other cases the face is relatively flat and the rims consist of few steps along <110>. Square, pyramidal pits with faces parallel to (111) are common, square positive pyramids are rare. Channels are common on the cubic faces; most are sub-parallel to the face diagonals and are a few hundred μm deep.

4.1.4. INTERNAL STRUCTURE

Optical examination of the micro-inclusion-rich zones reveals the same general characteristics described in earlier studies, as discussed in Chapter 3. Inclusion size is smaller than 1 μm. SEM (this study) and TEM (Lang and Walmsley, 1983, G.Guthrie, personal communication) suggest 0.1-0.5 μm as the common size range. The inclusions are sub rounded and appear to be completely enclosed within an optically continuous diamond matrix. TEM examination reveals that the shape of the inclusions is crystallographiclly controlled by the diamond and that normally, the inclusions are not associated with cracks or dislocations. The number density of inclusions is highly variable on every scale from micrometers to milimeters (figs. 4.2-4.4). The maximum number density is estimated (optically) to be $\sim 10^{11}$ inclusions per cm^3. The coated diamonds are usually of higher density than the cubic ones;

Figure 4.3. High magnification of the core-coat boundary of diamond GRR 1504.

Individual inclusions are sub-micron in size. The few larger, dark features are due to chipping of the diamond surface during polishing. Photograph plane is (001), transmitted light, blue filter, Zeiss microscope, scale bar = 10μm.

Figure 4.4. High magnification of the core-coat boundary of diamond ON ZIZ 74.

The diamond was cleaved parallel to the core-coat boundary and the fragment that includes all the coat plus a thin layer of core was polished almost parallel to the (111) plane. The sample was placed with the translucent coat facing down so that it was possible to view the core-coat boundary through the transparent core. Notice the grouping of inclusions along the <110> direction in the lower half of the photograph. Two triangular forms are marked with small "T"s at the upper part of the photograph.

Photograph plane is close to (111); transmitted light, Zeiss microscope, scale bar = 10μm.

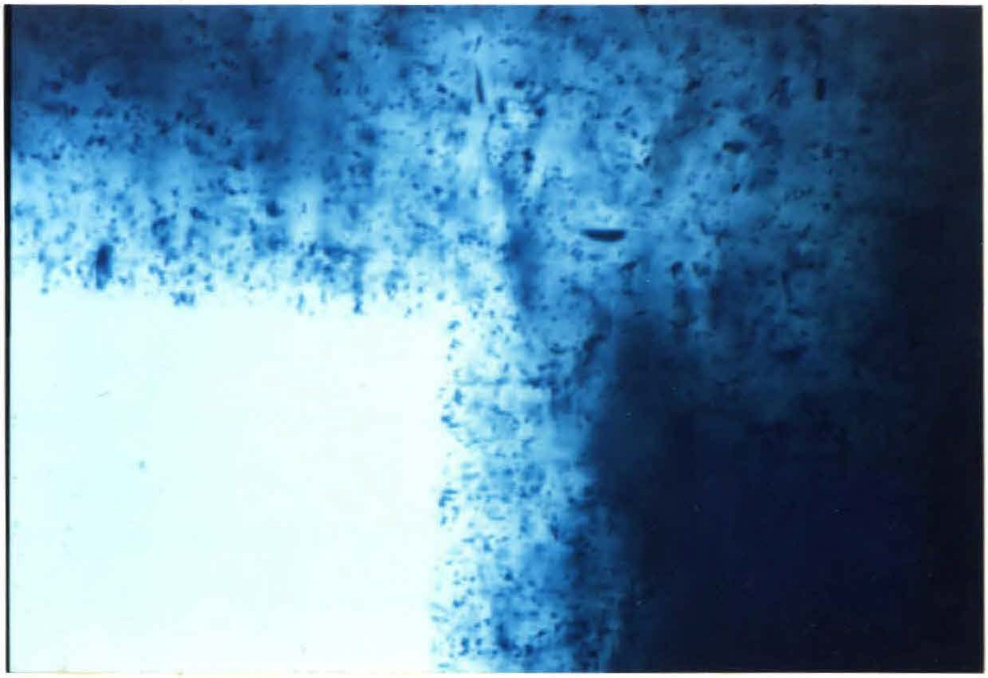

the core-coat boundary is usually the most populated region.

In many cases, (e.g. diamond CTP LB, fig. 4.2) the inclusions are arranged in radial, nearly parallel arrays of isolated inclusions, separated by 20-80 μm thick, inclusion-free regions (Custers, 1950). Focusing on deeper and deeper levels, it is possible to see how these arrays of inclusions surround elongated, inclusion-free zones of transparent diamond material. It seems likely that these elongated inclusion-free zones correspond to the fibers revealed by x-ray topography of coated diamonds (Kamiya and Lang, 1965). If so, the inclusions are located between those fibers. The thickness of these "fibers" in CTP LB, 20-80 μm is in agreement with the fiber diameters recorded by Kamiya and Lang. The radial arrays can be observed in some cubic diamonds; however, in many cubic diamonds the inclusions seem to be randomly distributed on a scale of up to 100 μm, and the only zoning pattern observed is the concentric bands. It is possible that the diamonds that show no radial arrays are of the "mixed habit growth" texture rather than the "fibrous" texture (Moore and Lang, 1972; see Section 3.1). It was not possible to verify this possibility by optical examination. An x-ray topograph may be needed in order to classify the cubic diamonds according to this criterion.

All the diamonds studied exhibit concentric zoning. In Figure 4.2 it can be recognized as darker parallel zones throughout the coat, the darker bands are the result of a higher number density of inclusions; the inclusion size does not seem to be different in the dense and less dense zones. The number of bands and the density contrast between the darker and lighter bands vary between samples. Diamond CTP L3 exhibits two distinct coat layers, separated by a transparent, inclusion-free zone.

In all the diamonds studied, the core-coat boundary intersects the polishing plane along a straight line. The transition from core to coat is sharp and occurs over less than 1 μm (Figs. 4.2, 4.3). The sharp, straight boundary suggests that the surface of the diamond prior to the growth of the coat was flat with no deep pits or rounded faces that are commonly found in natural uncoated octahedral diamonds (section 2.2.1). Flat triangular forms were found during optical examination of ON ZIZ 74. This sample consists of a whole octahedral face, cleaved from a large coated diamond. After polishing the cleaved face, it was possible to focus through the transparent core, down to the core-coat boundary (Fig. 4.4).

The arrangement of the inclusions on the (111) surface (normal to the "fiber" direction) is not random, but rather, the inclusions are concentrated to form arrays. Some arrays are linear and parallel to <110> (Fig. 4.4, lower center). This arrangement may be related to the branching of fibers in the <110> direction (Orlov, 1982). Other arrays are curved and oriented randomly. The two triangular forms at the upper part of the figure (marked T) may represent flat triangular etch pits on the surface of the uncoated core. The whole boundary is in focus, indicating that this "fossil" trigon was much flatter than the trigons that cover the outer face of the coated diamond.

4.1.5 CRACKS

The coated and the cubic diamonds almost always contain many cracks (Fig 4.2). Many small cracks are internal and do not appear to reach the surface of the diamond. The relation between the cracks and the inclusions was examined optically and it was concluded that the inclusions were formed before the cracks. In no case was the inclusion zoning pattern disturbed by cracks. Cracks that extend from the coat into the core do not affect the sharp core-coat boundary. Nor is there any relationship between the inclusion density and the cracks.

In many cases the cracks contain impurities, either in the form of brown or green films, or as opaque particles. The amount of material is small. A SIMS analysis over an exposed crack coated with a green film in the core next to the coat of diamond GRR 1504 detected only 10 ppm of material rich in Fe, Ca and Na (two last analyses of Table I.3) as compared with the adjacent inclusion-rich region that contains about 500 ppm of metal oxides. IR spectra of crack bearing cores showed normal diamond spectra. In any case, the use of microbeam techniques enabled the analysis of crack-free areas in all diamonds. Exceptions are some IR analyses where cracks cover a small portion of the analyzed area. Being a bulk analytical method, cracks could not be avoided in the course of the INA analyses.

4.2. SAMPLE PREPARATION

Diamond is the hardest material known, and its sawing and polishing take some effort and skill. By working along the softer directions of the diamond crystal it is possible to saw diamond by diamond powder dressed over a thin brass blade and to polish it with diamond powder dressed over a cast iron wheel.

Sample cleaning is relatively simple as diamonds are inert to all acids. All diamonds are acid cleaned as part of the mining and sorting operation. When received, each was weighed, measured and optically inspected. Most of the diamonds were obtained as rough uncut diamonds. Prior to their analysis, the diamonds had to be sawn, polished and cleaned.

4.2.1. SAWING

Selected samples were sent for sawing by either a diamond- dressed brass blade (J.R. Precision, New York), or by laser (Dialase, New York). All the diamond were cut parallel to the softer, cube (001) plane to ensure easy blade-sawing and polishing. Cubic diamonds were sawn in half; a square pyramid was cut at about one third the size of the octahedral diamonds. Five inclusion-rich diamonds (GRR 861.2, GRR 1155, GRR 1503, GRR 1508, GRR 1515 and all the micro-inclusion free diamonds were polished directly without sawing.

4.2.2 POLISHING

Most diamonds were polished at Caltech, using a commercial diamond polishing table with 14" cast iron wheel dressed with diamond powder in glue. The softest direction is from the center of the (001) face outward, along the <100> and <010> directions. Diamond GRR 1508 was polished parallel to (110), a plane of intermediate hardness. Diamond ON ZIZ 74, that was cleaved along a (111) plane (the common cleaving plane and the hardest polishing plane), was polished by slightly tilting it off the (111) plane.

A complete description of polishing techniques can be found in Watermeyer (1982). For this study, a relatively simple polishing was necessary, in order to establish two parallel surfaces. Diamonds are mounted in 3-8 mm diameter dops using a mixture of 95% asbestos + 5% boric acid. The dop is mounted on a holder, known as "tang" in the diamond industry (Fig. 4.5). The diamonds are pressed into the wet asbestos mixture and then are carefully lowered towards the rotating wheel (~2500 RPM). During polishing, the asbestos becomes hot and dries, firmly holding the diamonds without shattering. After the first face is polished the diamond is remounted and the other side is polished to produce two parallel surfaces. Alignment of the reflections of a light source from the inner and outer surfaces is sufficient to produce faces that are parallel to better than 1°. Opaque diamonds are difficult to align and must be taken out, measured and remounted for correcting the alignment as necessary.

I tried to substitute other materials for the asbestos. Silver solder can stand the high temperatures that may occur during polishing (the diamond may turn red-hot if the wrong crystallographic direction is put against the wheel). The hold of the diamond by the silver solder is somewhat weaker than that of the asbestos. Epoxy resins burn and lose their grip on the diamond; plaster of Paris shatters and breaks.

4.2.3. CLEANING

The polished wafers were first cleaned ultrasonically in dilute acetic acid to remove the bulk of the asbestos. They were then cleaned overnight in warm (~70°C) HF + HCl and rinsed with deionized (DI) water and propanol for IR study. Organic contaminants from handling and from the sticky tape used to mount the diamonds were removed by acetone and the samples were again cleaned by HF + HCl, DI water and propanol. The wafers were then mounted in epoxy in metal holders and finally cleaned with DI water, propanol, and reagent grade ethanol and freon. They were then dried in a vacuum desiccator and coated with carbon for SEM and EPMA analysis, or with gold, for SIMS analysis. When necessary, the carbon or gold coat was removed using 0.25 μm diamond paste followed by an additional final cleaning.

Diamonds for INAA were similarly cleaned by HF+HCl and rinsed by DI water, propanol and reagent grade ethanol and were sealed in precleaned polyethylene containers.

Figure 4.5. The diamond polishing table.

The 14" wheel is dressed with diamond powder that has been impregnated into the iron. The darker part carries the coarser powder and is used for polishing. The lighter part carries a finer powder and is used for the final finishing of the facet. The diamond is held by the tripodal "tang." The front leg includes a dop, which holds the diamond, and a short brass rod that allows for tilting the dop and the diamond.

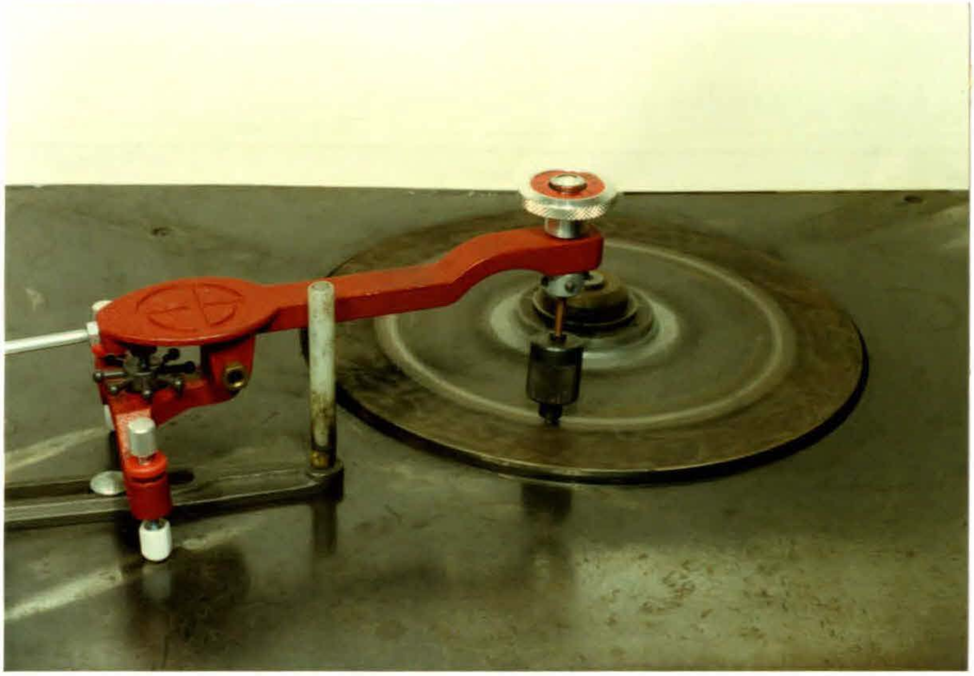

4.2.4. MOUNTING

The diamond wafers were mounted in epoxy in steel, and later in brass sleeves. At this stage no further polishing was possible and the wafers had to be mounted parallel to the sleeve face. The wafer was placed on a glass slide and the pre-polished sleeve was placed, face down, around it. Each was independently pressed against the glass and the sleeve was filled with warm epoxy. Bubbles were extracted by vacuum pumping and the sample was cured over night. The sleeve was taken out of the vice and the glass slide was removed. Ideally, the diamond was fully exposed and only light polishing with 0.25 μm diamond paste was needed to take excess epoxy off the sleeve. In a few cases, however, the glass slide stuck to the epoxy and had to be ground away. Careful polishing was needed to produce a smooth surface upon the first exposure of the pre-polished diamond surface. In a few cases the diamond was slightly tilted and only a part emerged out of the epoxy at the end of polishing. The ion-implanted diamonds were spring loaded into a brass holder with an aperture. This technique is by far the easiest and was found to yield good results. A thick gold coating ensured good conductance.

CHAPTER 5 ELECTRON MICROPROBE ANALYSIS

The concentration of impurities in micro-inclusion-bearing diamonds is of the order of 0.1% (Orlov, 1977; this study), and the bulk concentrations of the major elements found in these inclusions are in the range of tens to hundreds of ppm. Such concentrations are close to the detection limit of the electron probe micro analyzer (EPMA). Individual analyses are, thus, bound to be of low precision (error of the order of a few tens of percent). Analysis of micrometer size inclusions poses some additional problems in applying the common correction procedures (the translation of x-ray counting rates into concentrations). In spite of the analytical difficulties, useful data were obtained from the EPMA analyses. The relatively low precision of the data makes it hard to derive conclusions directly from individual EPMA analysis. However, combining the data fran 40 analyses, it was possible to use the concentrations derived from the EPMA analysis to construct working curves (EPMA concentrations against SIMS count-rates) for the conversion of SIMS intensities to concentrations. In addition the EPMA gave a fair estimation of the average composition of the micro-inclusions and put some constraints on the concentrations of phosphorus (which was not measured by the SIMS).

Section 5.1 describes the experimental details and discusses the uncertainties due to counting statistics, sample heterogeneity, and simplifying assumptions in the correction procedure. As the main use of the EPMA analysis of the diamonds was to establish the data base for calibrating the SIMS, the results are only briefly discussed in Section 5.2. A more detailed discussion is given in the context of the SIMS-EPMA correlations (Section 6.2.1.).

5.1. EXPERIMENTAL METHOD

5.1.1. INSTRUMENTAL PROCEDURE

Data were collected on a JEOL 733 EPMA using a 50 nA, 15 kV beam defocused to a 20 μm diameter spot. Na, Mg, Al, and Si were analyzed using TAP crystals and methane/argon-gas-flow, proportional counters. K, Ca, and Ti were analyzed using PET crystals and Fe using a LiF crystal, both with xenon-gas proportional counters. Data on P were collected using a PET crystal with a gas-flow proportional counting. In order to achieve long counting times and to reduce the buildup of contamination over the analysis spot, each data point consists of four adjacent spots covering an area of 40x40 μm. Peak and background counting time varied between 200-300 seconds per element on each of the four spots. Background intensity was determined by averaging two intensity measurements at energies above and below the peak position.

5.1.2. BLANK CORRECTION AND ANALYTICAL ERROR

Two gem-quality, inclusion-free diamonds were cleaned, mounted, carbon-coated, and analyzed in the same manner in order to monitor the blank levels. High blank levels (peak above background at 50 nA) were found only for Si (6 cps) and K (2 cps). Al showed a small, but consistent negative blank (< 1 cps), probably due to non-linear background. Blank was also determined by analyzing two graphite rods (Ultra Carbon, Bay City, MI). The rods were only polished on a clean paper, but were otherwise untreated. One of the rods was carbon-coated together with the diamonds and showed similar blank levels. The blank levels on the other, uncoated rod were only 3 cps at 50 nA, suggesting that coating is the source for most of the silicon blank. The source of the small K blank is not clear. The blank levels are considered reliable as repeated analysis of the gem diamonds during EPMA sessions recorded relatively constant blank levels at the values summarized here.

Peak intensities were first corrected for background and then for blank (peak-background of the gem diamonds). The corrected intensities were compared against pure oxide or silicate standards to obtain K-ratios. (K-ratios are defined as $(\text{cps/nA})_{\text{sample}}/(\text{cps/nA})_{\text{standard.}}$)

The peak, background and blank levels measured during the analysis of point 32 of diamond CTP 6268 are summarized in Table 5.1. Even in this sample, which is relatively rich in impurities, the uncertainty due to counting statistics is up to 50% of the peak intensities for minor elements. For the more abundant elements sample heterogeneity becomes the dominant source of uncertainty. The micro-inclusion-rich zones in all diamonds are heterogeneous on any scale (see Section 4.1.4) and this is well reflected in the intensity

Table 5.1. Peak, background and blank intensities for point 32 of CTP 6268.

	SPOT	Na	Mg	Al	Si	P	K	Ca	Ti	Fe
Peak intensity[1]	1	3917	5903	8344	24175	902	5236	3909	5862	1680
	2	3839	5465	8222	24889	836	4859	3448	5759	1600
	3	3853	5892	8314	23540	891	5372	3929	5914	1703
	4	4066	6172	8643	28777	907	6545	4490	584	1985
Background intensity	1	3651	5140	8142	17277	802	3015	2952	5547	1311
	2	3756	5233	8276	17291	777	3043	3094	5628	1350
	3	3712	5344	8150	17360	829	3087	2997	5778	1391
	4	3652	5248	8032	17597	799	3065	3078	108	1360
Peak-background	1	266	763	202	6898	100	2221	957	315	369
	2	83	232	-54	7598	59	1816	354	131	250
	3	141	548	164	6180	62	2285	932	136	313
	4	414	924	611	11180	108	3480	1412	476	625
Average of all 4 spots		226	617	231	7964	82	2451	914	265	389
Blank[2]		12	-94	-255	1316	12	597	42		
Blank corrected intensity		214	711	486	6648	70	1854	872	265	389
Standard deviation calculated from counting statistics[3]		109	131	161	250	51	110	102	117	68
Measured standard deviation[4]		127	259	240	1923	22	621	375	143	142

1. All intensities are in actual number of counts collected for 250 seconds at 50 nA.
2. Blank determined on gem diamonds that were cleaned and coated with the other diamonds.
3. Geometrical sum of square-root contributions from peak, blank and their background.
4. Standard deviation of the net intensities of the four spots analyzed. For the major elements (e.g., Si, K, Ca) the measured standard deviation of the intensities at the four points of each analysis is significantly greater than that calculated from counting statistics, suggesting the samples are heterogeneous on the scale analyzed.

variation between the four adjacent spots of an analysis. In samples with a lower content of impurities, counting statistics become the dominant source of uncertainty.

The effect of contamination build-up during the relatively long analysis was studied and was found to be negligible at the levels of precision for the analysis. The nine elements studied are counted by five spectrometers. By alternating the order of measurement of the two elements on each spectrometer, it was possible to compare the analyses in which the element was measured on a fresh sample with those where it was counted after 500 seconds of contamination build up. No systematic difference was found. Similarly, no difference was found in the case of Fe, which was counted twice on the same spectrometer during each analysis.

5.1.3. DATA REDUCTION

A full ZAF correction (Armstrong 1988) was used to reduce the data. The correction program employed the absorption correction of Armstrong (1982), the atomic number correction of Love et al. (1978) and the fluorescence correction of Reed (1965). Simple oxides and silicates were used as standards. Although the standards are different in composition from the diamonds, their affect on both electron scattering and x-ray emission does not differ by much from that of the diamond carbon matrix (Part A of Table 5.2). The total ZAF correction for the elements studied relative to their standards is less than 5% for Mg, Al, Si, P, K, and Ca, and less than 17% for Na, Ti and Fe. The applicability of such corrections to the analysis of micro-inclusions will be discussed later.

The main difficulty in applying existing correction procedures to micro-inclusion analysis is the heterogeneous distribution of the oxides within the diamond. The procedures all assume a homogeneous matrix. Before using them one has to decide which is the best model for describing the matrix that interacts with the electrons and the x-rays. Two end-member approximations are possible: 1) a pure carbon matrix with a trace amount of randomly dispersed oxygen and metal atoms, and 2) a pure oxide matrix of the same composition as the oxide fraction in the diamonds. The first approximation is accurate in the limit of

Table 5.2. Comparison of ZAF corrections assuming either carbon or oxide matrix.

A. Assuming 100% carbon matrix.

Element	Absorption correction	Fluorescence correction	Atomic number correction	Total correction
Na	0.78	1.01	1.06	0.83
Mg	0.92	1.00	1.06	0.97
Al	0.90	1.01	1.06	0.96
Si	0.92	1.00	1.05	0.97
P	0.92	1.00	1.08	0.99
K	0.92	1.00	1.08	1.00
Ca	0.96	1.00	1.08	1.03
Ti	0.98	1.00	1.15	1.13
Fe	0.99	1.00	1.17	1.15

B. Assuming 100% oxide matrix.

Element	Absorption correction	Fluorescence correction	Atomic number correction	Total correction
Na	1.25	1.00	0.98	1.22
Mg	1.29	0.99	0.97	1.25
Al	1.16	1.00	0.98	1.13
Si	1.11	1.00	0.97	1.07
P	1.20	0.99	0.99	1.19
K	0.99	0.98	0.99	0.97
Ca	1.05	1.00	0.99	1.03
Ti	1.05	1.00	1.05	1.10
Fe	1.01	1.00	1.06	1.07

C. Ratio of the two total ZAF corrections

	(carbon/oxide)
Na	0.68
Mg	0.78
Al	0.85
Si	0.90
P	0.83
K	1.03
Ca	1.00
Ti	1.03
Fe	1.08

D. Difference in calculated compositions assuming:

	i. carbon-matrix	ii. oxide-matrix
Na_2O	3.00	4.09
MgO	4.00	4.81
Al_2O_3	4.00	4.38
SiO_2	45.00	46.53
P_2O_5	2.00	2.24
K_2O	18.00	16.26
CaO	12.00	11.18
TiO_2	4.00	3.61
FeO	8.00	6.92

inclusions that are much smaller than the electron-excited volume analyzed by the probe. The other becomes accurate as the size of the inclusions exceeds the x-ray penetration and emission volumes. Unfortunately, the size of the inclusions is intermediate, 0.1-1 μm, compared with an electron penetration depth of ~1.7 μm (J. Armstrong, personal communication of Monte Carlo simulations).

The pure carbon model should give a fairly good approximation for the atomic number correction, Z, which included the back scatter and stopping power corrections. As all the inclusions lie below the surface, the amount of back scattered electrons is governed by the carbon matrix. The dominant energy loss mechanism for the electrons is by interaction with the carbon matrix. Energy loss during x-ray production in the inclusions themselves is, of course, better approximated by the pure oxide model. The fluorescence correction, F, is negligible. The absorption correction must, therefore, be underestimated by the pure carbon model, as absorption by the oxides in the inclusions is stronger than in a pure carbon matrix. It is difficult to calculate exactly the magnitude of this effect; however, a rough approximation can be calculated using the expression:

$$I_Z/I_0 = \exp[-(\mu/p) \cdot pZ]$$

where I_Z is the intensity at distance Z from the x-ray source; I_0, the initial x-ray intensity; (μ/p), the mass absorption coefficient and p, the density. Ratios of intensity attenuation in a carbon sphere relative to an oxide sphere are given for two different radii in Table 5.3. It is assumed that all the x-ray intensity is produced in the center of spherical inclusions. Densities used are 3.5 and 2.7 g/cm^3 for the diamond and the inclusions respectively; mass absorption coefficients are from Goldstein et al. (1981). Outside the inclusion, the pure carbon matrix accurately models the physical situation and, thus, the ratio is a good approximation for the amount by which the pure carbon model underestimates the absorption correction.

The results show that the deviation from pure carbon absorption is small for elements heavier then Si. The lighter elements are underestimated by the carbon model and the effect may reach 20% for sodium in 1 μm size inclusions. Average inclusions are ~ 0.5 μm in size

Table 5.3. Absorption of x-ray radiation in carbon and in oxide matrices.

Element	(μ/p) Carbon matrix	(μ/p) Oxide matrix	I_{oxide}/I_{carbon} Z=0.25 μm	 Z=0.5 μm
Na	1534	3673	0.89	0.80
Mg	905	2308	0.93	0.86
Al	557	1537	0.95	0.90
Si	356	1063	0.96	0.92
K	57	324	0.98	0.97
Ca	42	400	0.98	0.95
Ti	24	287	0.98	0.97
Fe	9	117	0.99	0.99

and are affected to a lesser extent.

The correction factors for the pure oxide approximation are presented in part B of Table 5.2. The magnitude of the correction depends on the composition of the oxide matrix. The composition used in calculating the factors of part B is given in column i of part D. During runs the program iterates by normalizing the concentration of the oxide fraction to 100%. The pure oxide model must, therefore, underestimate the atomic number correction, and probably overestimate the magnitude of the absorption correction. The real answer lies between the two extremes, probably closer to the pure carbon model, which was used to reduce the data.

The errors introduced by the simple modeling of the matrix must be smaller than the differences between the two extremes presented above. Part C of Table 5.2. shows the ratio of the total corrections under the two models; large effects may be expected mainly in the case of elemental ratios of light versus a heavy element. Part D shows the effect of the two corrections on the final composition: if the results obtained by the pure carbon model are those of column (i), then, using the pure oxide approximation would yield the composition of column (ii). The total oxide concentration estimated by the pure oxide model is ~7% higher than those obtained by the pure carbon model (the results of column (ii) were renormalized to 100%).

In order to check the accuracy of the pure carbon approximation and the ZAF correction as a whole, a graphite-glass pellet containing 2% glass of known composition was analyzed (see Section 6.2.2 for a detailed description of its preparation). A sample of the glass itself was also analyzed during the same day. Table 5.4 compares the composition of the pure glass with the composition of the glass in the pellet, as obtained by using the two models. The concentrations of each of the five elements was calculated using the correction program with either the "pure carbon" model (actually it assumes 98% carbon and 2% dispersed oxides), or by the "pure oxide" model. The glass composition was calculated by normalizing the concentration of the five elements to the total concentration of all five. The total concentration is also given.

Table 5.4. Comparison of correction procedures: Average composition of glass in glass-graphite pellet.

	Na_2O	Al_2O_3	SiO_2	K_2O	FeO	Total conc.
Pure glass[1]	5.0[2]	18.0	65.7	9.1	2.2	98.9
Glass in pellet-carbon matrix model[2]	4.7	16.7	67.2	9.1	2.3	1.88
Stan. dev.[3]	8%	2%	1%	3%	16%	
Difference from pure glass[4]	-5%	-7%	2%	1%	3%	
Glass in pellet-oxide matrix model[5]	5.4	16.4	67.8	8.3	2.0	2.10
Stan. dev.	8%	1%	3%	16%	29%	
Difference from pure glass	8%	-9%	3%	-8%	-10%	

1. Oxide proportions in the pure glass. Four analyses were averaged and renormalized to 100% for comparison with the composition of the glass in the graphite-glass pellets. The average value of the totals of the four analyses is given in the last column.
2. Analyses of graphite pellet containing 2% glass. The results of 24 analyses were corrected using the carbon matrix model (see text). The last column shows the average total concentration of oxides, corresponding to the average glass content of the pellet. The average proportions of the oxides in the glass were calculated by normalizing each analysis to 100% and averaging the proportion of each element for the 24 analyses.
3. Standard deviation of oxide proportion in the 24 analyses. Last column, standard deviation of the total oxide content of the pellets for the 24 analyses.
4. The difference between the composition of the glass in the pellets and that of the pure glass (in % relative to the composition of the pure glass).
5. The same data base, corrected using the oxide matrix model. The format is the same as for the carbon matrix model.

The results obtained by either model are within two standard deviations from the composition of the pure glass, except for Al, which for some unknown reason is lower in the pellet. The pure carbon model gives a closer match and, as predicted, gives a somewhat lower estimate of the sodium content. The average total concentration of all oxides is somewhat lower than the gravimetric determination, nevertheless, the difference is well within the large standard deviation of the absolute glass content of the pellet.

5.1.4 SUMMARY

The uncertainties introduced by the choice of matrix are smaller than the uncertainties due to counting statistics and the heterogeneous distribution of inclusions in the samples. However, the main use of the EPMA data is in the calibration of SIMS counting rates. While the random errors in counting rates affect the precision but not the accuracy of the SIMS-EPMA correlations, the errors introduced by the correction procedure **do** affect the accuracy of the correlations.

In practice, the pure carbon approximation is used for ZAF correction procedures. After the concentrations of the elements are estimated, oxygen is calculated by stoichiometry and carbon is added to bring the total to 100%. As the total oxide concentration is ~ 0.1%, the next iteration is carried out assuming an almost pure carbon matrix. This procedure is expected to slightly underestimate the concentration of the light elements and the total concentration of trapped oxides in the diamonds.

5.2. RESULTS

Ten diamonds were analyzed using the EPMA. Metal oxide concentrations vary from a few thousand ppm down to the detection limit of the probe. Most diamonds exhibit similar compositions with SiO_2 and K_2O being the main constituents. Assuming that all oxides are contained in the micro-inclusions, the composition of the metal oxide fraction was calculated by normalizing the total metal oxide concentrations to 100%. The average compositions of the micro-inclusions in the analyzed diamonds vary between the following ranges: SiO_2, 35-62 wt%; TiO_2, 0-8%; Al_2O_3, 3-12%; FeO, 5-16%; MgO, 2-6%; CaO, 2-17%; Na_2O, 0-6%;

K_2O, 7-23%. The variation among analyses of different zones of individual diamonds is between 6 and 25% for the abundant elements such as Si or K and is around 30-60% for elements which are close to their detection limit, e.g., Ti, Na or Mg. P_2O_5 was detected in most diamonds where it was analyzed, and comprises 0-3% of the metal oxide fraction of the inclusions. FeO was largely affected by contamination in early analyses. The source of the contamination was steel from the steel holders in which the diamonds were mounted. When the diamonds were removed and mounted in brass holders no contamination was observed.

SIMS analysis produced a more precise data set which is the base for the discussion of the chemical composition of the micro-inclusions. Further discussion of the EPMA data is given in the next chapter in relation to the SIMS-EPMA correlation. The EPMA data used for the calibration of the SIMS is summarized in Table A.1 of Appendix A.

CHAPTER 6 SECONDARY ION MASS SPECTROMETRY

The high sensitivity of the Secondary Ion Mass Spectrometer (SIMS), or ion microprobe as it is commonly called, makes it ideal for chemical analysis of trace elements (c.f. Shimizu and Hart, 1982). The good spatial resolution of the probe enables the examination of chemical heterogeneities within single mineral grains. In this study, the SIMS was used to analyze trace element abundances in diamonds. As will be shown, the good quality of the data obtained allows comparison of the chemical composition of the impurities in different micro-inclusion-bearing diamonds, as well as between different zones of individual diamonds. Section 6.1 describes the experimental detail. Mass interferences from abundant molecular species containing C, H and O are few and easy to resolve. Other interferences are shown to be negligible in the almost pure carbon matrix. The heterogeneous distribution of the inclusions leads to variability in the absolute concentrations of the different elements in the analyzed volumes but does not affect the determination of the average compositions of the oxide fraction. The main experimental problem was the determination of the SIMS ion-yields for the different elements. Section 6.2. discusses the various approaches taken and the resulting calculated ion-yields. The results of the SIMS analysis of the diamonds are described in Section 6.3.

6.1. EXPERIMENTAL METHOD

The Cameca IMS-3F consists of a double-focusing mass spectrometer with an ion-sputtering source. The double-focusing mass spectrometer (which focuses ions with different momenta and different energies) offers excellent mass and energy filtration. In many cases, interfering species of almost identical mass can be separated in the mass spectrometer and samples can be studied in situ with no need for earlier chemical separation. The ion-sputtering source enables the study of ions from a small area of the sample surface and offers high spatial resolution. In addition, the sputtering of surface atoms exposes deeper levels of the sample and offers excellent depth resolution. The instrument also permits the imaging of the geometrical distribution of a selected mass on the analyzed surface.

The in situ study of samples means that concentrations cannot be determined by isotope dilution; rather, standards of known concentrations in similar matrices must be used. In principle, ion-implantation of isotopes of the element of interest into the sample surface (Williams, 1985) may offer the same advantages as isotope dilution.

6.1.1. INSTRUMENTATION

SIMS data were obtained with PANURGE, a modified CAMECA IMS-3F (Huneke et al., 1983). A schematic illustration of the instrument is shown in Figure 6.1. Primary ions are produced in the duoplasmatron (DP in Fig. 6.1) by ionization of low-pressure oxygen gas, and negative ions are accelerated to 10 keV. No mass filtration is used, but electrons are deflected out of the beam by a weak magnetic field, in order to enable reproducible current measurements. The ions are focused by two lenses: a condenser lens, L1, that is used to adjust the primary current passing through a limiting aperture, and an objective lens that is used to focus the beam on the sample surface. A stigmator and three sets of deflectors are used to align the beam, to raster it in both x and y directions on the sample surface or to deflect it into a Faraday cup, where the ion current can be monitored before and after measurements. Finally, the ions are accelerated toward the sample (which is held at +4.5 kV) and impacted with an energy of 14.5 keV.

Secondary ions are formed as a result of the collision cascade in the first few layers of the sample. They have low average kinetic energy of a few eV and are extracted by accelerating them to 4.5 keV toward the immersion lens. Commonly, during the analysis of insulators, the accelerating voltage is offset by a few volts to compensate for positive sample charging. The transfer lenses (LT) are adjusted to extract ions from areas of 25, 150 or 400 μm of the sample. A contrast aperture located at the crossover plane (C1, see Fig. 6.1. for a description of the ion optics) prevents ions with large transverse velocities from entering the mass spectrometer (to be precise, discrimination is according to $\sqrt{m} \cdot Vo \cdot \sin\alpha$; m - mass, $Vo \cdot \sin\alpha$ - transverse velocity). An adjustable slit further limits the allowed transverse velocity in the X direction. As the mass spectrometer double-focusing condition is only to first order, this

Figure 6.1. Schematic diagram of the Cameca IMS-3F ion microprobe.

Primary ions are formed at the source in a duoplasmatron (DP), accelerated and focused on the sample by two lenses (L1, L2). Secondary ions are extracted by the immersion lens (LI). Ion trajectories are deflected in such a way that ion with the same initial energy and direction (rays 1 and 3, rays 2 and 4) appear to originate from a single point in the virtual crossover plane, C0. This plane is equivalent to the light source plane in an optical microscope. Ions originated from the same point on the sample (rays 1 and 2, rays 3 and 4) seem to originate from a single point on the virtual image plane.

The transfer lenses (LT) form a real image of the crossover plane (C1) on the entrance slit of the mass spectrometer (C1). The slit, together with the contrast aperture, limits the solid angle and the energies of the transferred ions. A field aperture is located at the image plane (I1) and limits the size of the analyzed area.

The double focusing mass spectrometer consists of an electrostatic sector (ES) and a magnetic sector (M). Only rays 1 and 3 are now followed in the scheme. Both are refocused at the crossover plan C2. Ion of different energy are well separated and the range transferred to the magnetic sector can be limited by the energy slit that is situated at this plane. The spectrometer lens (LS) refocuses the beam to form an image plane within the magnetic sector. After mass separation in the magnetic sector, the desired mass is selected by the exit slit, located on another crossover plane (C3). Ions originating from the same spot on plane C1, whether moving in different directions (rays 1 and 3) or with different energies (E_3 and E_3+ E), are refocused into C3.

The projector lenses (LP) focus the ions of the selected mass to form a real image of either the image plane or the crossover plane on the screen (S). Alternatively, the second electrostatic sector (ESA2) would deflect the ions into the entrance of the ion-counting system (IC).

(Diagram is modified from: IMS 3F - Studies of the Physical Principles. CAMECA document ML/JD 91819, published in French and translated by N. Shimizu, MIT.)

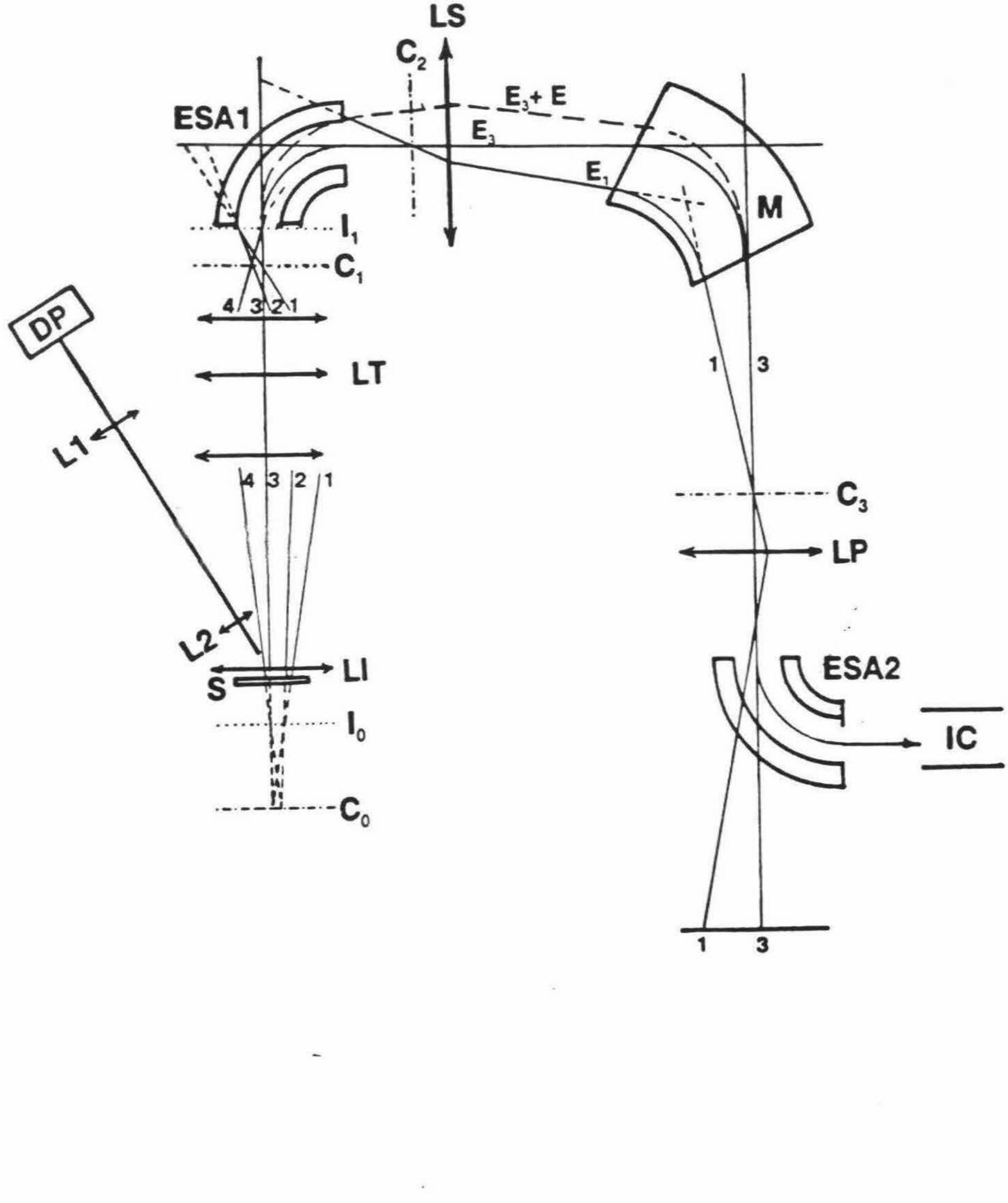
LS
C2
E3+ E
ESA1
E3
E1
M
I1
C1
4 3 2 1
DP
LT
L1
1 3
4 3 2 1
C3
LP
L2
ESA2
S
LI
IC
I0
C0
1 3

entry slit actually determines the mass resolution of the spectrometer. A field aperture in the image plane, I1, may be used to limit the size of the analyzed area.

The double focusing mass spectrometer consists of an electrostatic analyzer (ESA) which separates the trajectories of the ions according to their energies. The energy slit located in the crossover plane after the ESA (C2) can then be adjusted to select a limited range of ion energies. The spectrometer lens (LS) refocuses the ions into the magnetic sector (M), where the ions are separated according to their mass/charge ratio. The transferred range of mass/charge ratios is limited by the exit slit located at C3. The transferred ions can be focused by the projector lenses to form a real image of the image plane on a viewing screen so that the distribution of the selected isotope on the surface of the sample can be examined. Alternatively, the ion can be focused to form an image of the slit in the crossover plane. This is important in the alignment of the instrument and can be used, in principle, to measure the average intensity of the selected isotope in the analyzed area. The ion beam can also be deflected through a second electrostatic sector into the ion-counting system.

Ions are counted using a Balzers SEV217 electron multiplier operated at a gain of 10^7-10^8 electrons/ion with a potential of -3000 V at the conversion dynode. Pulses are amplified and counted by a Phillips PM 6654 programable high resolution counter.

The resolution of the mass spectrometer is determined by the combination of the entry and the exit slit and by the alignment of the ion optics. Ideally, the shape of a peak (number of ions vs. magnetic field value) at the exit boundary of the mass spectrometer can be approximated by a Gaussian with a flat top. The width of the Gaussian depends on the alignment and is a direct function of the width of the entry slit. The width of the exit slit determines the mass/charge range around the center mass selected by the mass spectrometer that is passed into the counting system. The width of the exit slit is adjusted to be about twice the full width at half maximum of the measured peak. This assures that fluctuations of ~10 ppm in the magnetic field do not displace parts of the peak out of the detection system and do not affect the accuracy of the measurement.

6.1.2. INSTRUMENTAL CONDITIONS

Primary ions	O-	
Pressure in primary column	$2\text{-}4 \cdot 10^{-6}$	torr
Primary voltage	10	kV
Primary beam aperture	#2	
Primary current	10	nA
Sample chamber pressure	$2\text{-}4 \cdot 10^{-8}$	torr
Focused beam diameter	~ 40	μm
Secondary acceleration potential	-4500	kV
Offset voltage	~ 5	V.
Image field	150	μm
Contrast aperture	#1,	widest
Field aperture	#2	
Diameter of sample area transferred by the field aperture	60	μm
Mass resolving power	2000	
Energy slit	"Open"	(FWHM ~ 50V)

6.1.3. MASS INTERFERENCES

SIMS analysis of geological samples is commonly complicated by the presence of interfering molecular ions of nearly identical masses. It will be shown that in the case of diamonds, the simple carbon matrix leads to the formation of only a few interferences which can be resolved easily.

Table 6.1 summarizes all the important interferences, together with the mass-resolving power (MRP) needed to resolve them. The necessary MRP is calculated as m/ m, where m is the mass of the species of interest, and m is the mass difference between it and the interfering species. The MRP of the machine is calculated by dividing the mass of the peak by its full width at 10% of the maximum. That means that two peaks of equal intensities, and

Table 6.1 Main mass interferences[1]

Isotope measured	**Interfering species**							
	Hydride	**MRP**	**Carbide**	**MRP**	**Oxide**	**MRP**	**Others**	**MRP**
$^{23}Na^+$			$^{11}BC^+$	1180			$^{46}Ti^{++}$	618
$^{24}Mg^+$	$^{23}NaH^+$	1905	C^+_2	1600			$^{48}Ti^{++}$	**2160**
$^{27}Al^+$	$^{26}MgH^+$	**2809**	$C_2H^+_3$ $^{12}C^{13}CH^+_2$	780 830	$^{11}BO^+$	1130	$^{54}Fe^{++}$	**2307**
$^{28}Si^+$	$^{27}AlH^+$	**2258**	$C_2H^+_4$	670	$^{12}CO^+$ $^{40}CaO^{++}$	1556 **15135**	$^{56}Fe^{++}$	**2962**
$^{39}K^+$			$^{27}AlC^+$ $^{26}Mg^{13}C^+$	**2254** 1748	$^{23}NaO^+$	1940		
$^{40}Ca^+$	$^{39}KH^+$ $^{23}NaOH^+$	**4490** 1333	$^{28}SiC^+$ C_2O^+ $^{56}FeC^{++}_2$	**2800** 1238 **8250**	$^{24}MgO^+$ $^{48}TiO^{++}_2$	**2300** **6400**	$^{40}K^+$	
$^{48}Ti^+$	$^{47}TiH^+$	**4100**	C^+_4 $^{24}MgC^+_2$	921 1294	O^+_3	1300	$^{48}Ca^+$ $^{24}Mg^+_2$	**10435** **2172**
$^{56}Fe^+$	$^{55}MnH^+$ $^{39}KOH^+$	**5138** 1778	$C_2O^+_2$	1000	$^{40}CaO^+$ $^{24}MgO^+_2$	**2478** 1600	$^{28}Si^+_2$	**2962**

[1] The isotopes considered include ^{1}H, ^{11}B, ^{12}C, ^{13}C, ^{16}O, ^{23}Na, ^{24}Mg, ^{27}Al, ^{28}Si, ^{39}K, ^{40}Ca, ^{48}Ti, ^{56}Fe.

mass difference m=m/MRP are separated by a minimum which is 20% of the maximum intensity. The contribution of one peak at the center of the other peak under such conditions is negligible. Higher resolving power may be needed to fully resolve an interfering peak that is much more intense than the measured one, whle a lower resolution may be sufficient to get rid of the interference of a less intense peak. In the following discussion of the possible interferences I use the measured relative height of the peaks in the mass-spectra measured on sample CTP L0; because the composition of the micro-inclusions in all diamonds is similar, the conclusion holds for other diamonds as well. These relative heights may change if other compositions are measured, or if the matrix is changed. For example, the intensity ratio of a metal ion and the metal-hydride ion is typically on the order of a few hundreds in silicates, but exceeds 1000 during diamond analysis.

All major interferences with molecular species comprised of carbon, hydrogen and oxygen are completely resolved at MRP=2000. However, some possible interferences from species including one or more atoms of the trace metals are not resolved at this mass resolving power. **Hydrides:** Most of the metal hydrides are unresolved from metal ions of similar masses. In order to check their abundance relative to the corresponding metal ions, high resolution mass spectra were recorded at MRPs of 2000 and 5000. The metal-to-hydride abundance ratio is not affected by the change in resolution and can be determined at MRP=5000 where the two peaks are resolved. The contribution of the hydride at the center of the metal-ion peak can be estimated from the spectrum at MRP=2000. Figures 6.2 to 6.5 present the results for masses 27, 28, 40 and 56. If present, the hydride should appear as an unresolved widening of the metal-ion peak at MRP=2000, and as a separate peak close to that of the metal ion at MRP=5000. No such peaks were observed. The intensities of the main peaks are on the order of 1000 cps at MRP=5000 and the hydride intensities must be lower then 2 cps, about three orders of magnitude weaker. It is concluded that hydride interferences are unimportant during diamond analysis.

Carbides: At MRP=2000, only $^{27}AlC^+$ and $^{28}SiC^+$ cause unresolved interferences with $^{39}K^+$ and $^{40}Ca^+$ respectively. Figure 6.4 shows the relation between the $^{40}Ca^+$ and the peak of $^{28}SiC^+$ +

Figure 6.2. High resolution mass spectrum of CTP L0: mass 27.

Secondary beam intensity (logarithmic scale) is plotted against mass. Upper plot was recorded at the mass-resolving power (MRP) used during analysis, MRP~2000; lower plot was recorded at MRP~5000 to check for masses which may be unresolved at MRP=2000.

The full scale on the X axis is 70 mamu (milli-atomic mass units). The high peak of the left is Al at mass 26.9815. The small center peak is $^{11}BO^+$ 22.7 mamu heavier than Al, the right peak is $C_2H^+_3$ 41.7 mamu heavier than ^{27}Al and possibly $^{12}C^{13}CH_2^+$, 37.7 mamu heavier than ^{27}Al and unresolved from $C_2H_3^+$. At MRP=2000 the peak width is $27 \cdot 10^3/2000=13.5$ mamu wide (at 1% of its maximum intensity), and the peaks are fully resolved. The scan at MRP~5000 does not reveal any additional peaks between the $^{27}Al^+$ and the $^{11}BO^+$ peaks. That means that the intensities of $^{26}MgH^+$ and $^{54}Fe^{++}$, which should have been resolved, are below 1 cps, more than three orders of magnitude lower than $^{27}Al^+$ intensity.

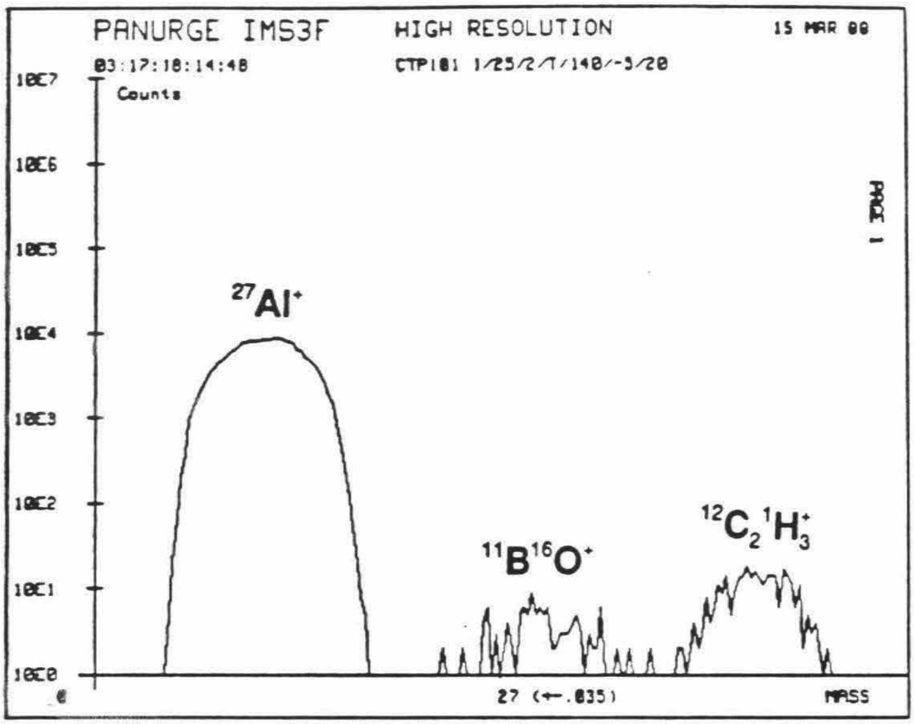
PANURGE IMS3F
HIGH RESOLUTION
15 MAR 88
03:17:18:14:48
CTP101 1/25/2/T/140/-5/20
10E7
Counts
10E6
10E5
10E4
10E3
10E2
10E1
10E0
0
PAGE 1
$^{27}Al^+$
$^{11}B^{16}O^+$
$^{12}C_2{}^1H_3^+$
27 (+-.035)
MASS

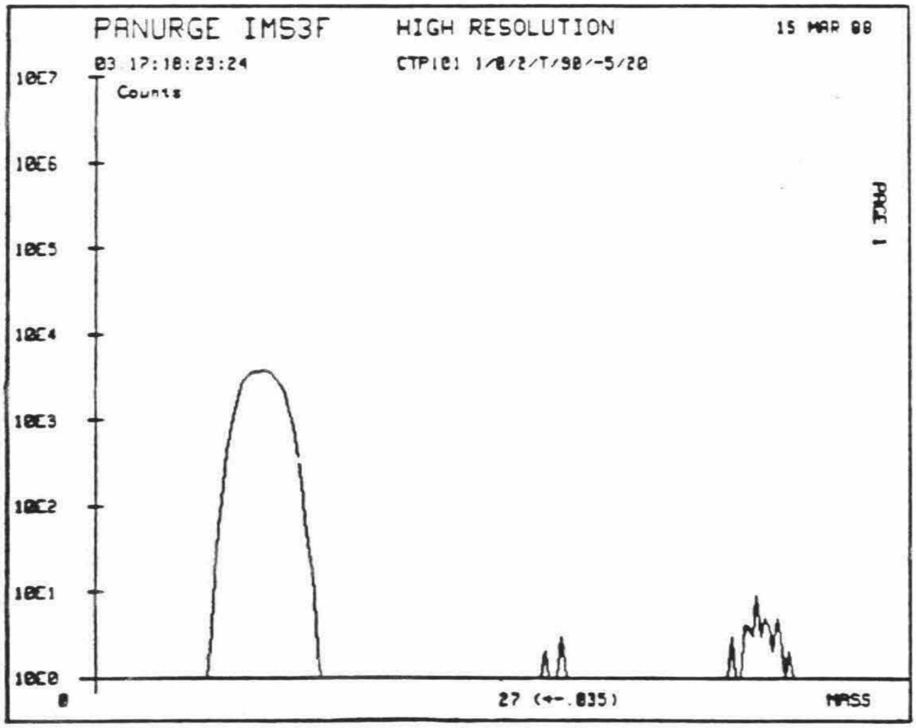
PANURGE IMS3F
HIGH RESOLUTION
15 MAR 88
03 17:18:23:24
CTP101 1/0/2/T/90/-5/20
10E7
Counts
10E6
10E5
10E4
10E3
10E2
10E1
10E0
0
PAGE 1
27 (+-.035)
MASS

Figure 6.3. High resolution mass spectrum of CTP L0: mass 28.

See detailed explanation in captions of Figure 6.2.

Full scale on X axis is 50 mamu. Left peak, $^{28}Si^+$, right peak CO^+. The two are fully resolved at MRP~2000. No additional peaks at MRP~5000.

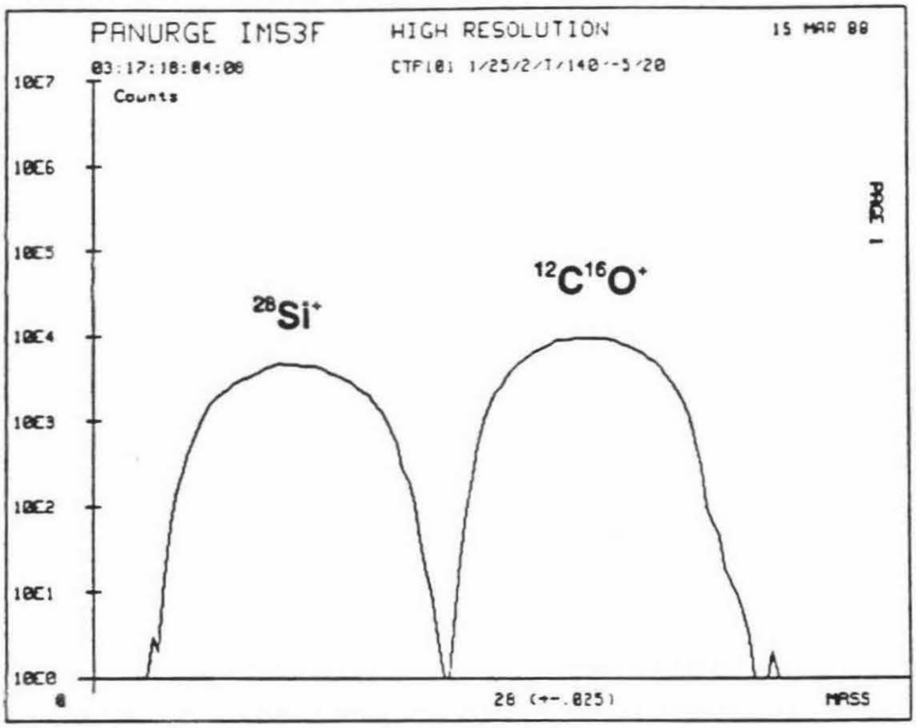
PANURGE IMS3F
HIGH RESOLUTION
15 MAR 88
03:17:18:04:00
CTF(0) 1/25/2/T/140--5/20
10E7
10E6
10E5
10E4
10E3
10E2
10E1
10E0
Counts
PAGE 1
$^{28}Si^{+}$
$^{12}C^{16}O^{+}$
0
28 (+-.025)
MASS

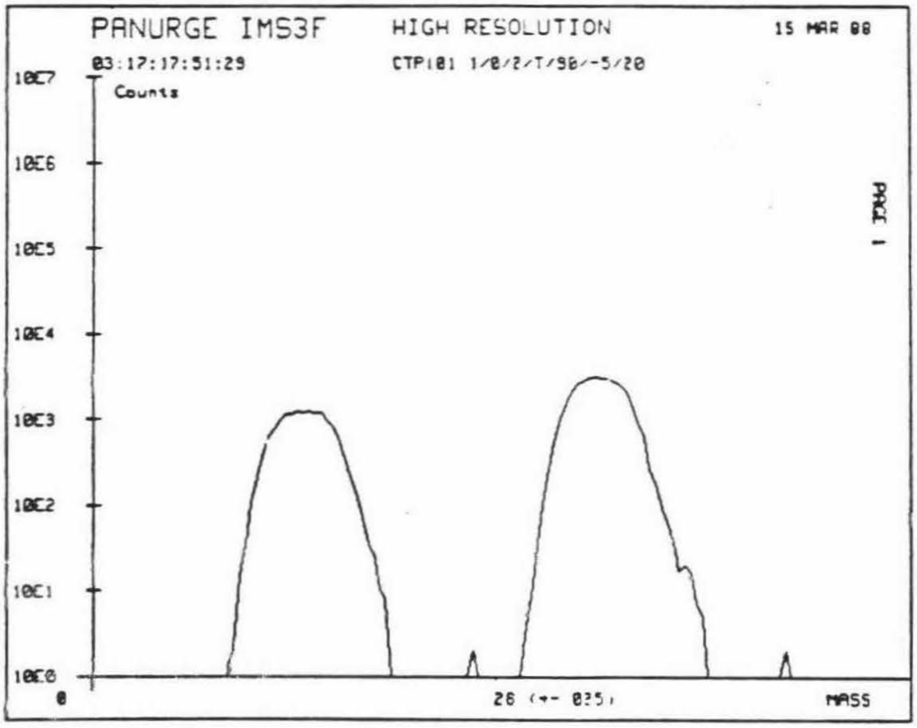
PANURGE IMS3F
HIGH RESOLUTION
15 MAR 88
03:17:17:51:29
CTP(0) 1/0/2/T/90/-5/20
10E7
10E6
10E5
10E4
10E3
10E2
10E1
10E0
Counts
PAGE 1
0
28 (+-.025)
MASS

Figure 6.4. High resolution mass spectrum of CTP L0: mass 40.

See detailed explanation in captions of Figure 6.2.

Full scale on X axis is 80 mamu. Left peak, $^{40}Ca^+$, right peak C_2O^+. Smaller center peak is due to $^{24}MgO^+$ and $^{28}SiC^+$ together (the two are unresolved even at MRP=5000). This peak is not fully resolved at MRP=2000. However, its center is 14.3 mamu away from the center of the $^{40}Ca^+$ peak center. At MRP=2000, the half-width of both peaks is 10 mamu, thus, the contribution from the small center peak is negligible. The spectrum at MRP~5000 reveals no additional peaks, indicating that KH^+ peak is of negligible intensity.

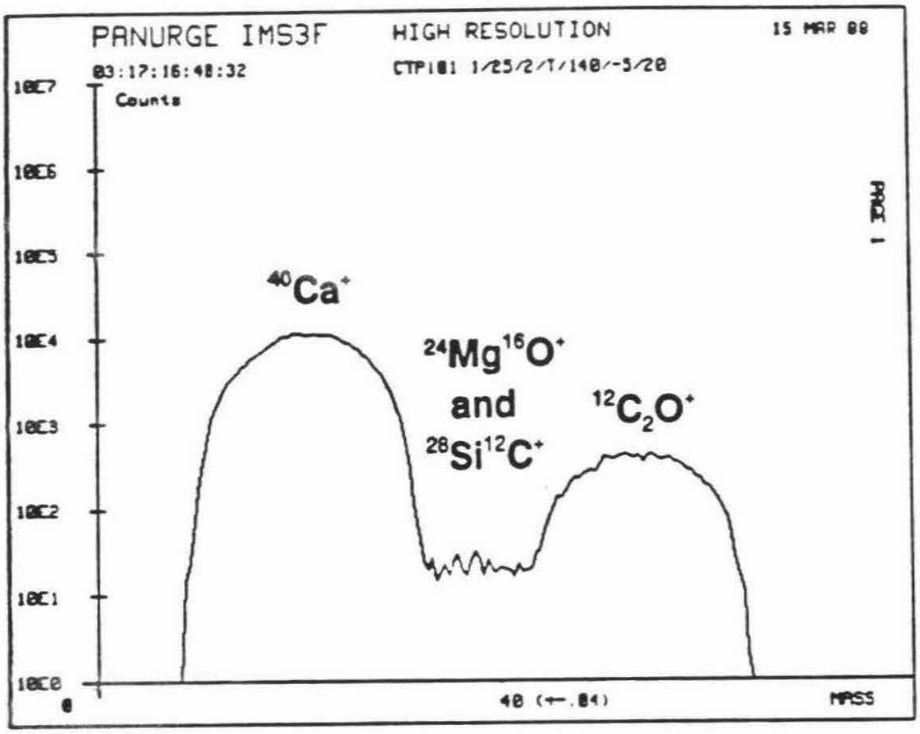
PANURGE IMS3F
HIGH RESOLUTION
15 MAR 88
03:17:16:48:32
CTP101 1/25/2/T/140/-5/20
10E7
Counts
10E6
10E5
10E4
10E3
10E2
10E1
10E0
0
40 (+-.04)
MASS
PAGE 1
$^{40}Ca^+$
$^{24}Mg^{16}O^+$ and $^{28}Si^{12}C^+$
$^{12}C_2O^+$

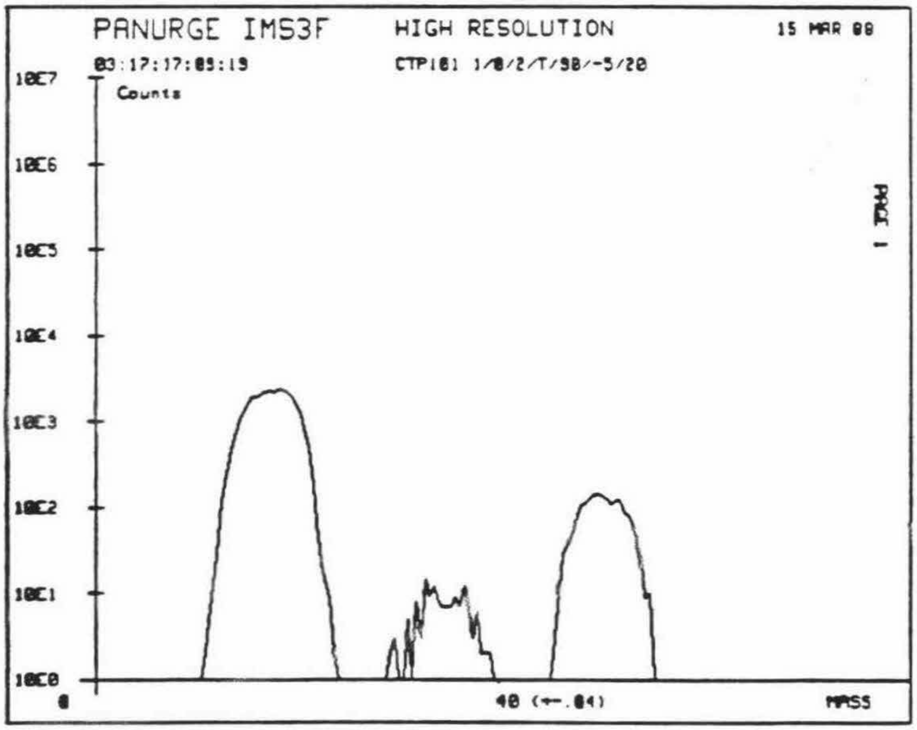
PANURGE IMS3F
HIGH RESOLUTION
15 MAR 88
03:17:17:05:19
CTP101 1/0/2/T/90/-5/20
10E7
Counts
10E6
10E5
10E4
10E3
10E2
10E1
10E0
0
40 (+-.04)
MASS
PAGE 1

Figure 6.5. High resolution mass spectrum of CTP L0: mass 56.

See detailed explanation in captions of Figure 6.2.

Full scale on X axis is 100 mamu. Left peak, $^{56}Fe^+$, right peak, $^{40}CaO^+$, 22.6 mamu heavier and only partly resolved. Still, $^{40}CaO^+$ contribution at the center of the $^{56}Fe^+$ peak is very small, as can be clearly seen in the linear plot of the mass-spectrum at MRP=2000, at the bottom figure. This situation holds true for all diamonds because the relative abundance of Ca and Fe does not vary much.

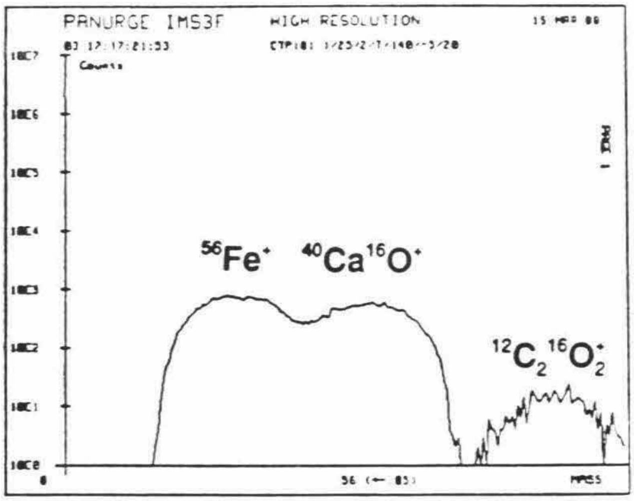
PANURGE IMS3F
HIGH RESOLUTION
15 MAR 88
03 17:17:21:53
CTP(8): 1/25/2/T/140/-5/20
Counts
10E7
10E6
10E5
10E4
10E3
10E2
10E1
10E0
0
56 (← 83)
MASS
PAGE 1
$^{56}Fe^+$
$^{40}Ca^{16}O^+$
$^{12}C_2{}^{16}O_2^+$

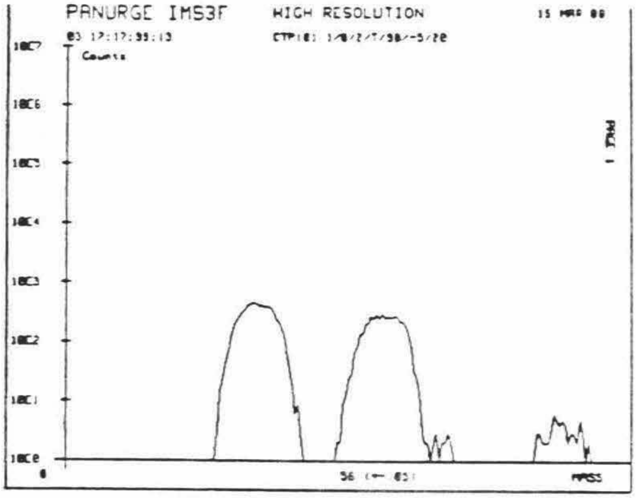
PANURGE IMS3F
HIGH RESOLUTION
15 MAR 88
03 17:17:35:13
CTP(8): 1/8/2/T/98/-5/20
Counts
10E7
10E6
10E5
10E4
10E3
10E2
10E1
10E0
0
56 (← 83)
MASS
PAGE 1

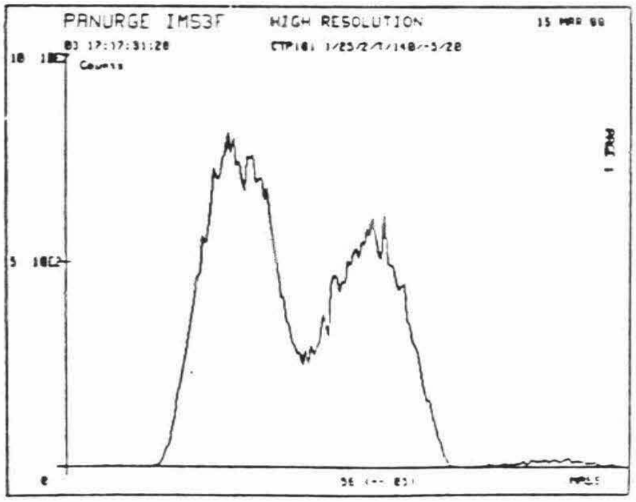
PANURGE IMS3F
HIGH RESOLUTION
15 MAR 88
03 17:17:31:20
CTP(8): 1/25/2/T/140/-5/20
Counts
10 10E2
5 10E2
0
56 (← 83)
MASS
PAGE 1

$^{24}MgO^+$ (these two do not resolve even at MRP=5000). The $^{40}Ca^+$ is almost three orders of magnitude more intense than the combined peak of the two molecular species. Their contribution at the center of the $^{40}Ca^+$ peak is, again, negligible. The same case was found for the interference of $^{27}AlC^+$ with $^{39}K^+$ (not shown); the two peaks are better resolved and the $^{39}K^+$ peak is of higher intensity. $^{54}FeC^{+}_{2}{}^{+}$ was not detected in a high resolution spectrum of mass 40 on a graphite pellet containing ~ 400 ppm Fe and no Ca. Its contribution to the $^{40}Ca^+$ peak must also be negligible.

Oxides: The case for $^{24}MgO^+$ was discussed above. The interferences of $^{40}CaO^+$ with $^{56}Fe^+$ are presented in Figure 6.5. The two peaks clearly overlap and are of approximately equal intensity. Still, as can be seen in the linear plot (Fig. 6.5c, lower spectrum), the contribution of the $^{40}CaO^+$at the peak center of the $^{56}Fe^+$ must be less than 1%. Two interfering doubly-charged oxide ions are also unresolved. Only 2 cps were counted at mass 40 on pure Ti metal and the abundance of $^{48}TiO_2^{++}$ during diamond analysis must be negligible. No independent check has been done on the relative abundance of $^{40}CaO^{++}$, which is also assumed to be negligible.

Other interfering species: No $^{56}Fe^{++}$ peak can be detected to the left of the $^{28}Si^+$ peak in Figure 6.3., and no $^{54}Fe^{++}$ was found at mass 27. $^{48}Ti^{++}$ is almost resolvable from $^{24}Mg^+$ and no $^{28}Si^{+}_{2}$ can be detected between the $^{40}CaO^+$ and the $^{56}Fe^+$ peaks at the high resolution spectra of mass 56 (Fig. 6.5). Thus, all these possible interferences may be neglected as well. The isobaric interference of $^{48}Ca^+$ with $^{48}Ti^+$ is completely unresolved. The contribution from Ca ions to Ti intensity may be calculated using the natural abundance ratio[**], $^{48}Ca/^{40}Ca=0.0019$, and the ion-yields of Ti and Ca (refer to Table 6.3, page 103). The excess Ti* (in ppm) is given by:

$$[Ti^*]_{ppm} = 0.0019[Ca]_{ppm} \cdot RIY_{Ca}/RIY_{Ti} = 0.01[Ca]_{ppm}$$

where [Ca] is the concentration of Ca in ppm, and RIY is the relative ion-yield of either Ca

---

[**] Due to machine fractionation, the actual ratio in the machine is about 10% lower.

or Ti (see Section 6.2.). This correction is usually on the order of 2-5% of the total Ti intensity. It is neglected, considering the other, larger uncertainties involved in calculating the concentrations. Similar calculations show that the contribution to the intensity of $^{40}Ca^+$ from $^{40}K^+$ amounts only to $5 \cdot 10^{-4}$ ppm Ca per ppm K and is, therefore, negligible.

6.1.4. MACHINE BACKGROUND AND DETECTION LIMITS

Machine background may be contributed by a few sources: 1) electronic noise, 2) ion reflections from inner surfaces of the machine, and 3) ionization of contaminants (which I will refer to as "blank"). Electronic noise is very low. It was monitored during all analyses by counting the intensity at the nominal mass of 11.8, where no peak is expected, for about 60 seconds. The average noise during all runs was lower then 0.1 cps, three to seven orders of magnitude lower than the count rates for the elements measured in the micro-inclusion-bearing diamonds. Broad peaks due to reflected ions do not appear to be a problem. High-resolution mass scans around the masses of interest showed background levels below 0.1 cps.

The blank is contributed to by the machine (the primary source) and contaminants on the sample. Initially, very high blank levels for the transition elements resulted from ions formed at the cathode of the duoplasmatron in the primary source. Because there is no mass filter for the primary beam, these ions are accelerated towards the sample and implanted in it. They are then sputtered out with the sample and form secondary ions. Switching to pure (99.95%) Ni cathode reduced the Fe blank from ~1200 cps to 1 cps and improved the blank of other elements as well (Table 6.2).

Blank levels were measured using gem-quality diamonds as samples. Results obtained by measuring a few natural and synthetic diamonds show similar low levels when measured with the same cathode. Using a different cathode, different levels are measured (Table 6.2). This suggests that the detected ions are contributed by the primary source and that the concentrations of the eight studied elements in gem-quality diamonds are below the detection limit of the SIMS.

The high blank levels for aluminum may be the result of machine "memory." Aluminum

Table 6.2. Blank levels for diamond analysis.

	cathode I1	**cathode II**	**pure Ni**	**10 minutes**
Counts per second				
Na	2	3	2	30
Mg	1	2	0.2	0.5
Al	130	160	85	85
Si	55	75	1	2
K	1	1	1	10
Ca	0.4	0.8	0.3	0.3
Ti	1	1	4	6
Fe	250	1150	1	2
Detection limit, ppb[2]				
Na_2O	2	3	2	30
MgO	15	29	3	8
Al_2O[3]	840	1000	550	550
SiO_2	5300	7200	100	200
K_2O	2	2	2	20
CaO	2	4	2	2
TiO_2	28	28	110	170
FeO	15200	70000	60	120

1. Cathode I and II - Ni-alloy, pure Ni - 99.96% Ni, 10 minutes - typical blank levels after rastering a 100x100 μm area with 100 nA primary beam for 10 minutes.

2. Detection limit in **ppb**, corresponding to **twice** the blank count rates and calculated using the ion-yields of Table 6.3.

metal is used during the alignment of the SIMS at the beginning of each working day. Similar Al blank was measured on ultra-pure silicon (80 cps @ 10 nA, MRP=2000). The high silicon blank during the use of the Ni-alloy cathodes may originate at the cathode itself. Fe blank was due to Fe in the Ni-alloy. Both Fe and Si blank levels decreased when the new, pure Ni cathode was used.

Each analysis was preceded by 10-15 minutes of rastering a 100x100 μm area with 100 nA primary beam. This was found sufficient to eliminate most surface contaminants. Blank determined on gem diamonds still showed a few tens of cps for Na and K (Tab. 6.2.), but this rate was trivial compared with actual count rates during measurements, so that blank correction is small for all elements except Al.

Also shown in Table 6.2 are the detection limits, obtained as twice the blank count rates divided by the ion-yields of Table 6.3 (refer to page 103). Detection limits are at the sub-ppm level for all the eight elements studied.

6.1.5. ANALYTICAL PROCEDURE AND DATA REDUCTION

Diamonds mounted in epoxy within brass or steel sleeves (see section 4.1.2.) were coated with 200-300 Å thick gold coat, inserted into steel holders and placed into the high vacuum sample chamber. After raster-cleaning (see section 6.1.3) samples were analyzed using a 10 nA O^- beam at MRP=2000. Secondary-ion intensities were measured using a computer program which switches the magnetic field to the field values corresponding to the peak centers of the selected isotopes (Huneke et al. 1983).

First, an inclusion-rich diamond is analyzed in order to ensure sufficient signal for accurate determination of peak position and shapes. Approximate magnetic field positions for the masses of interest are entered manually, and the detailed shape of the intensity peaks (ion current vs. magnetic field) is measured by stepping the magnetic field across the whole mass range of each peak. The magnetic field values at the center of each peak and at the half-height positions are recorded. Also recorded are the first derivatives of the intensity with respect to the magnetic field at the half-height positions.

Then, the program switches the field to scan through all peak-centers and half-height nominal positions in order of increasing field values. Due to the hysteresis of the magnetic field, a few cycles of switching and readjusting of the field values of the peak positions are needed before the beginning of data acquisition. Peak-centers are re-determined using the difference in intensities at the two nominal half-height positions and the pre-recorded slopes.

In order to assure accurate field positions for the first, lowest-mass peak of each cycle, the field is switched from the highest mass to a mass 0.2 amu lower than the first mass (11.8 amu in the case of carbon analysis). After 1 sec it is switched to scan through the half height, center and the other half-height of the carbon peak at mass 12 and all the other masses.

Depending on its peak intensity, each mass is counted for either 1 or 10 sec. The intensity at half-height positions is measured for 1 sec each. Runs consist of 50 or 60 cycles each and run times vary from 40 to 120 minutes. During the course of a run, field positions of all masses were found to be stable; shifts were normally on the order of a few ppm, compared with peak widths of ~ 80 ppm (FWHM at MRP=2000).

While the above procedure works well when peak intensities are high, low count rates in inclusion-poor diamonds result in statistical fluctuations, which may be interpreted by the program as shifts in peak positions. Thus, the above procedure was only used during the analysis of inclusion-rich diamonds. When diamonds with low content of included matter were analyzed, the peak positions were first determined on an inclusion-rich sample and the differences in magnetic field values of each of the masses from that of mass 12 were recorded. During the course of the following runs, only the position of the $^{12}C^+$ peak was measured and adjusted every cycle in order to compensate for possible fluctuations in the magnetic field. The peak positions of all other elements were calculated using the pre-determined dispersion values. As the widths of the peaks at 95% of maximum intensity are on the order of 30 ppm, about 3-5 times the observed shifts in peak positions, only small errors in peak intensity are introduced. All intensities were corrected for the effect of counting system dead-time using $I_c = I_m/(1-DT{\times}I_m)$. I_m is the measured intensity, I_c the corrected intensity, and DT is the dead time, which is ~17 nsec. Corrections were always very small, reaching a maximum of 0.8% in the case of K intensity in micro-inclusion-rich diamonds.

In order to correct for variations in experimental conditions, e.g., small changes in primary ion current, focusing, resolution, and counting efficiency, all count rates were normalized to the counting rate of carbon. On the average, $^{12}C^{+}$ intensity was ~ 50000 cps at 10 nA, MRP=2000. Intra-run variations of $^{12}C^{+}$ intensity were normally less than 1%; variations between runs were less than 15%. The normalized intensities are quoted as:

$I^{elem}_{norm} = I^{elem}/I^{carbon.}50000$, so that the quoted values are close to the actual count rates.

The concentrations of all metal ions were normalized against the $^{12}C^{+}$ count rate for the same cycle. The average intensity of each element was then calculated as the mean of the normalized intensities of the individual cycles. The associated standard deviations were also calculated. The average intensity was then corrected for blank as measured on gem diamonds and this final value was used to calculate ion-yields, and later concentrations of trace elements in the diamonds.

6.1.6. THE ANALYSIS OF HETEROGENEOUS SAMPLES

The trace metal atoms are not distributed uniformly throughout the diamonds. Rather, they are concentrated in the numerous micro-inclusions enclosed within the carbon matrix of the diamonds. The secondary ion intensities of K and Na were high enough to produce visible ion-images of their spatial distribution in the sample. It could be clearly seen that the intensities of both elements originated from small zones of high intensity, corresponding to the inclusions observed under the microscope.

During analysis, as the primary beam drills into the sample, it penetrates new inclusions, sputters their content and drills deeper to penetrate new ones. Figure 6.6 presents the variation of the Ca normalized intensity with time. Carbon intensity is uniform ($2\sigma<1\%$) and the variations reflect only the fluctuation in Ca intensity. Background levels are probably the result of many small inclusions being sputtered at any given moment. When larger inclusions are penetrated the intensity

Figure 6.6. Variation of $^{40}Ca^+$ with time during SIMS analysis of GRR 1155.

$^{40}Ca^+$ intensity, normalized to $^{12}C^+$ intensity, shows extreme variation during the ~1 hr analysis. The full depth sputtered was estimated using an optical microscope and assuming uniform sputtering rate, allowing for the conversion of time units (bottom) to depth (top). Each peak is attributed to the sputtering of a large inclusion. The inferred inclusion size is ~ 0.2 μm. Only Ca and C were analyzed during this run in order to obtain the detailed shape of the intensity variation. $^{12}C^+$ intensity was uniform throughout the run.

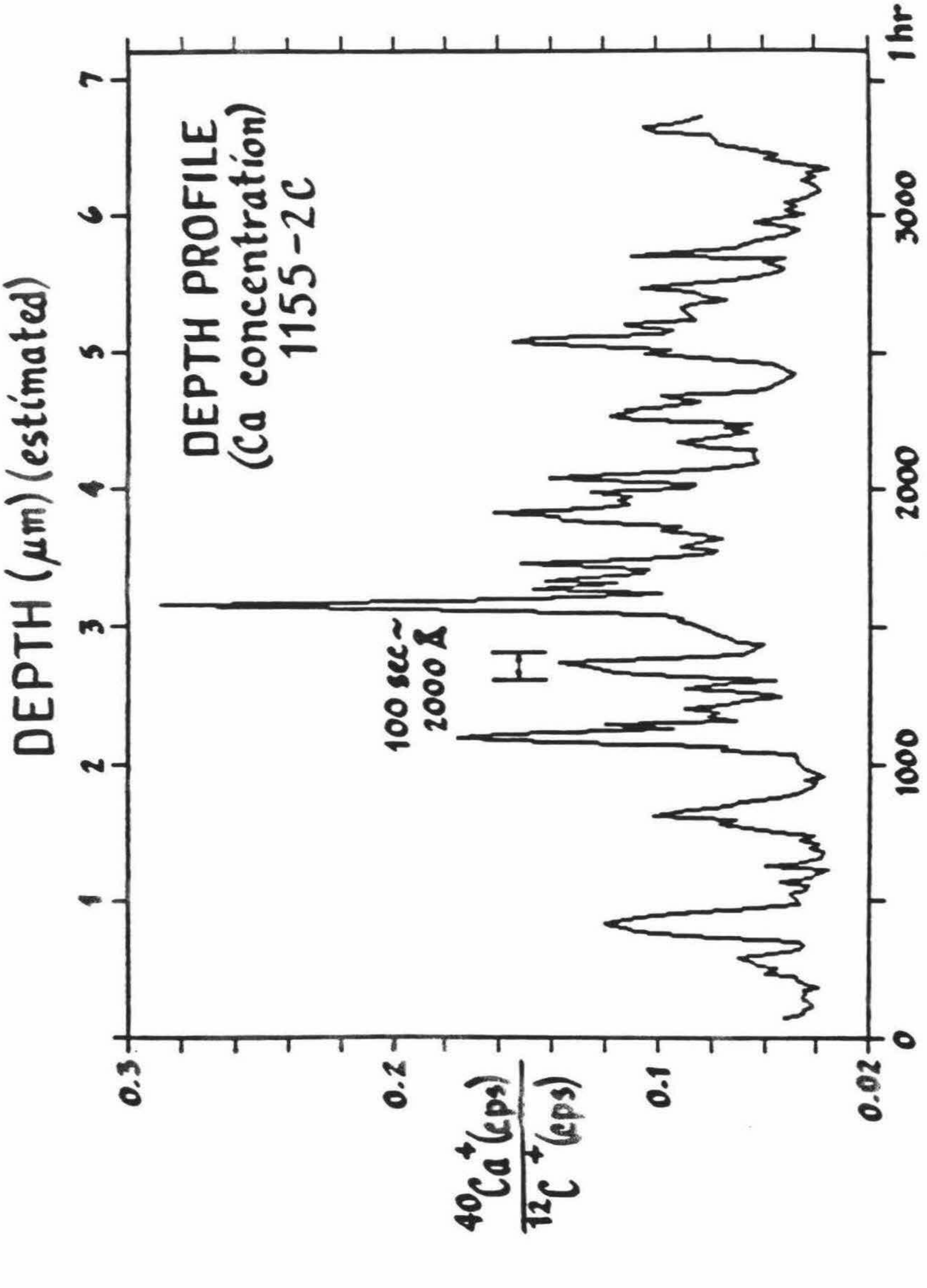
DEPTH (μm) (estimated)
1
2
3
4
5
6
7
DEPTH PROFILE
(Ca concentration)
1155-2C
100 sec ~
2000 Å
0.3
0.2
0.1
0.02
40Ca+(cps) / 12C+(cps)
0
1000
2000
3000
1hr
t (sec)

rises and then falls as the inclusion is fully digested by the beam.

Using an optical microscope I estimated the total depth excavated by the beam during this particular run to be 7 μm. Thus, the width of a single large peak corresponds to ~0.2 μm. This is in agreement with optical observations (< 1μm), and TEM observations (0.1-1 μm, Lang and Walmsley, 1983). Assuming that all the Ca is included in the micro-inclusions, the area under the curve, or the average normalized intensity, represents the total Ca concentration.

During a normal run, each element is measured at a sequentially different time. Thus, abundance ratios would vary even during analysis of homogeneous inclusions containing material of uniform composition. Because of the sharp fluctuations of the measured intensity with time, even if the intensity of one element is interpolated to the time of the measurement of the other, the ratio of the two intensities still shows scatter around the real value (see Fig. 6.7). The best estimate of intensity ratios is, in this case, the ratio of the integrated normalized intensities of the two elements, as represented by the average values for the whole run. Inhomogeneous inclusion composition will introduce additional scatter.

The standard deviation of carbon-normalized intensities of all the cycles of one run is large, typically 20-50%. This large deviation simply reflects the heterogeneity of the sample. Elemental intensity ratios of different elements vary by comparable amounts during the runs due to inhomogeneities within the inclusions themselves. However, ratios of averaged intensities for whole runs, e.g., K/Na or Si/Al, in individual diamonds show good reproducibility (Figs. 6.13, 6.14, section 6.3.2) and suggest that SIMS results can be used to obtain representative average elemental ratios.

Approximately 100 inclusions are sputtered and analyzed in the course of a single run. A few large inclusions are represented by the high intensity peaks, while the others are averaged to yield the base level (Figs 6.6, 6.15). The measured intensities are converted to absolute concentrations of the metals in the analyzed volumes. Assuming that all metals are present as oxides, and that all oxides are contained within the micro-inclusions, the total oxide concentration can be used to calculate the average composition of the metal-oxide fraction

Figure 6.7. Intensity ratios of two sequentially measured isotopes during sputtering of a homogeneous micro-inclusion.

Imagine an homogeneous micro-inclusion enclosed within a diamond. During analysis the inclusion is penetrated and the material in it is sputtered. The number of ions produced increases with time and then decreases as the inclusion is digested by the primary beam. Assuming that the ion current produced by two different isotopes is identical, the effect of the "peak switching" technique on the ratio of the measured intensities can be examined. The variation of the intensity of isotopes A and B (which may represent two different elements) has the same pattern in time (represented by the Gaussian) so that $I_A/I_B=1$ at all times. Nevertheless, because each is measured at a different time, the calculated ratio for the individual cycles deviates from the true value of 1. Element A (open square) is measured first on each cycle, element B (triangles) is second. The ratios of the intensities of B and A are clearly variable. Even if the intensity of B is linearly interpolated to the time of measurement of A ( ), the ratio B/A (crosses) deviates from the correct value of 1.

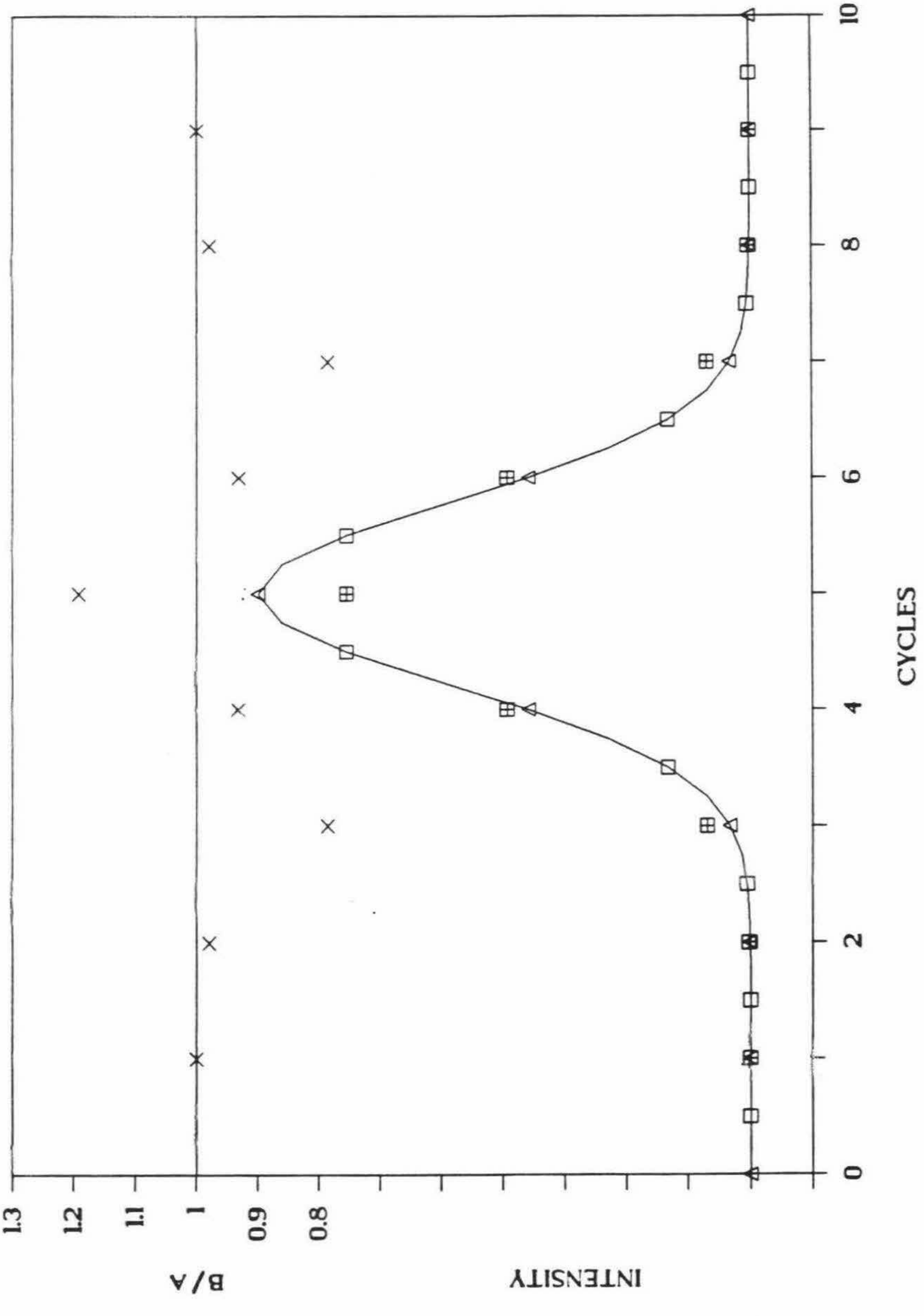
B/A
INTENSITY
1.3
1.2
1.1
1
0.9
0.8
CYCLES
0
2
4
6
8
10

in the analyzed inclusions. Other oxides, e.g., P_2O_5, SrO, BaO, or the REE oxides were detected by other techniques and usually amount to ~ 5% of the total metal-oxide content. For that reason, the eight metal oxides measured by SIMS are normalized so that their total sums to 95%.

6.2. THE DETERMINATION OF RELATIVE ION-YIELDS

A major difficulty in many geochemical SIMS applications is the determination of ion-yields, the ratio of the number of ions counted to the number of ions sputtered for a given element. For most purposes, it is sufficient to know the relative ion-yield (RIY), the ratio of the ion-yield of a given element to that of a reference element.

Both absolute and relative ion-yields have been shown to vary with matrix composition and experimental setup (Shimizu and Hart, 1982). Because of a lack of adequate physical description of this dependence and of the physics of the ion-sputtering process itself, the only way to overcome this difficulty is by analyzing standards of known composition, similar to that of the samples, under the same experimental setup.

Because diamonds containing known concentrations of the elements of interest were unavailable, ion intensities were calibrated against the concentrations of trace elements in some micro-inclusion-rich diamonds as determined by EPMA. Carbon was chosen as the reference element and thus, the RIY of an element relates the normalized secondary ion intensity (I_{el}/I_{carbon}) directly to the concentration of that element in the diamond. This correlation is described in Section 6.2.1.

In order to check this procedure, a graphite-glass "diamond analog" was prepared and analyzed. Fine powders of glass and graphite where mixed together and pressed to form a pellet with known concentrations of Na, Al, Si, K and Fe. Section 6.2.2 describes the preparation, analysis and results of this experiment. Section 6.2.3 describes the determination of RIYs by analyzing synthetic diamonds with known doses of Al, Si, Ca, Ti, and Fe implanted into their surfaces. The different techniques are compared in section 6.2.4.

6.2.1. EPMA - SIMS CORRELATIONS

The calibrations of the RIYs of Na, Mg, Al, Si, K, Ca, Ti and Fe by correlating SIMS counting rate with concentrations determined by EPMA is far from being the ideal method. It can be equated with checking the quality of a sophisticated stereo system using a tape cassette recorded on a "walkman." The main sources of error are:

a. The low sensitivity of the EPMA. As shown in Chapter 5, the concentration levels of most elements in the diamonds are close to the EPMA detection limit.

b. The heterogeneous distribution of trace atoms in the diamond matrix (micro-inclusions) as opposed to a uniform distribution of "foreign" atoms in the diamond lattice. Large standard deviations are associated with the average concentrations recorded by SIMS. Uncertainties are also introduced into the ZAF correction procedure of the EPMA data.

c. The heterogeneous distribution of micro-inclusions in the diamond (zoning). The number density of inclusions, as well as the total concentration of impurities, vary over a range of a few micrometers.

As shown in Figure 6.8, the volumes sampled by EPMA and SIMS do not completely overlap and may carry different concentrations of the elements of interest. Care has been taken to position the center of the SIMS primary beam at the center of the EPMA four-spot cluster. The contamination built during EPMA analyses (see Fig. 7.1.) helped to ensure good overlap; still, imperfect positioning introduced additional error.

Figure 6.9 presents the details of the correlation of SIMS intensities with corresponding metal-oxide concentrations determined by EPMA. The data are also tabulated in Table A.1 and A.2 of Appendix A. SIMS intensities of the analyzed **isotopes** are normalized to 50000 cps of $^{12}C^{+}$. EPMA concentrations are in ppm of the oxide of each of the elements. The result is a working curve that enables the immediate translation of the count rates to oxide concentrations. As large errors are associated with both X and Y, the algorithm of Williamson (1968) was used to determine the slopes of the best-fit lines. This algorithm

Figure 6.8 Comparison of volumes analyzed by EPMA and SIMS.

EPMA analyses x-ray from a depth of ~1.2 μm for all elements, and the four defocused-beam analyses result in four cylindrical volumes, 20μm in diameter and 1.2 μm deep (vertically hatched). The SIMS analyzes a Gaussian-shaped volume that is about 40 μm in diameter (diagonally hatched). The volumes analyzed by the two techniques are similar but not identical. Some large inclusions, or inclusion-rich zones may be sampled by only one of the techniques leading to scatter in the EPMA-SIMS correlations.

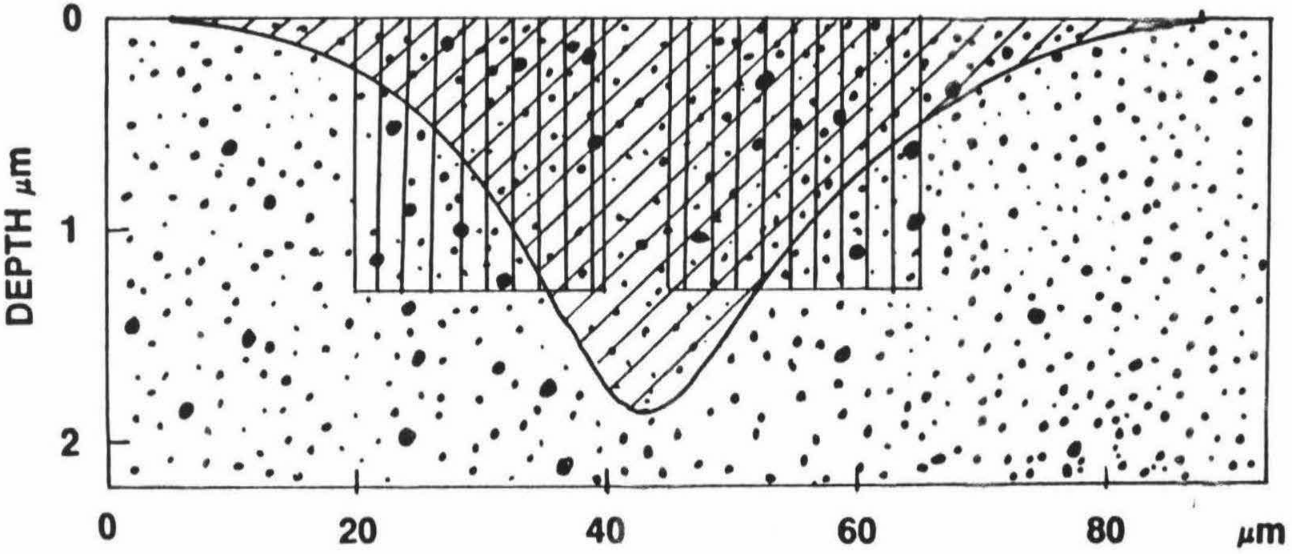
DEPTH μm
0
1
2
0
20
40
60
80
μm

Figure 6.9. EPMA-SIMS correlations for Na, Mg, Al, Si, K, Ca, Ti, and Fe.

Metal-oxide concentrations determined by EPMA analysis are plotted against normalized secondary-ion-intensities measured by SIMS. The slopes of the correlation lines are proportional to the RIYs of the elements relative to carbon and may be used to translate the SIMS raw data into concentrations. Error bars represent uncertainties due to counting statistics and sample inhomogeneity. See text for details. Triangles - results of the first two sets of EPMA and SIMS analysis. (GRR 1155; GRR 1503; GRR 1508, GRR 1515; Ni-alloy cathodes.)

squares - A later set of EPMA and SIMS analyses. (GRR 1155, GRR 1503, GRR 1508; pure Ni cathode.)

diamonds - results obtained during two sets of analyses of diamonds of the CTP set (using pure Ni cathode.)

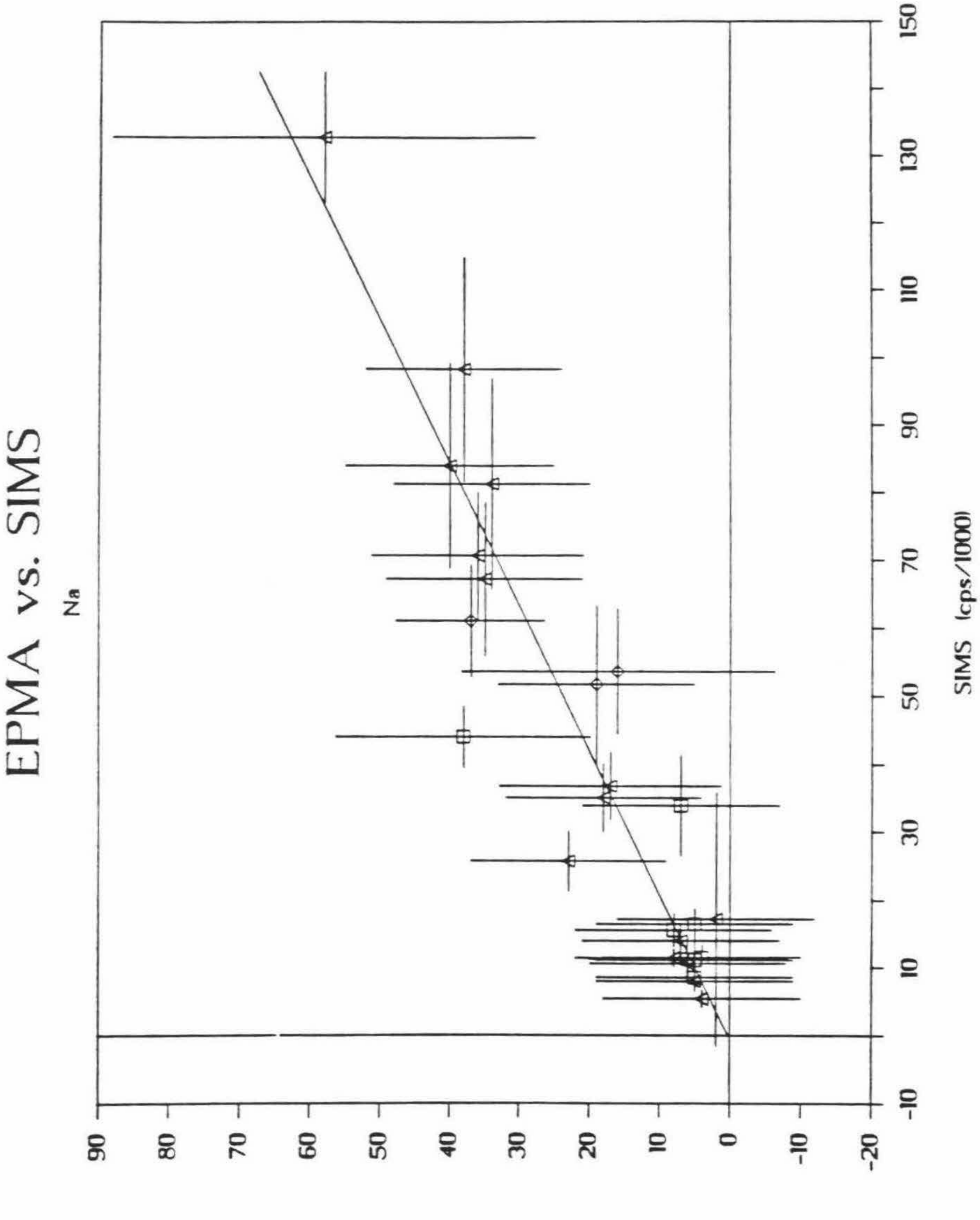
EPMA vs. SIMS
Na
SIMS (cps/1000)
EPMA (ppm)
-10
10
30
50
70
90
110
130
150
90
80
70
60
50
40
30
20
10
0
-10
-20

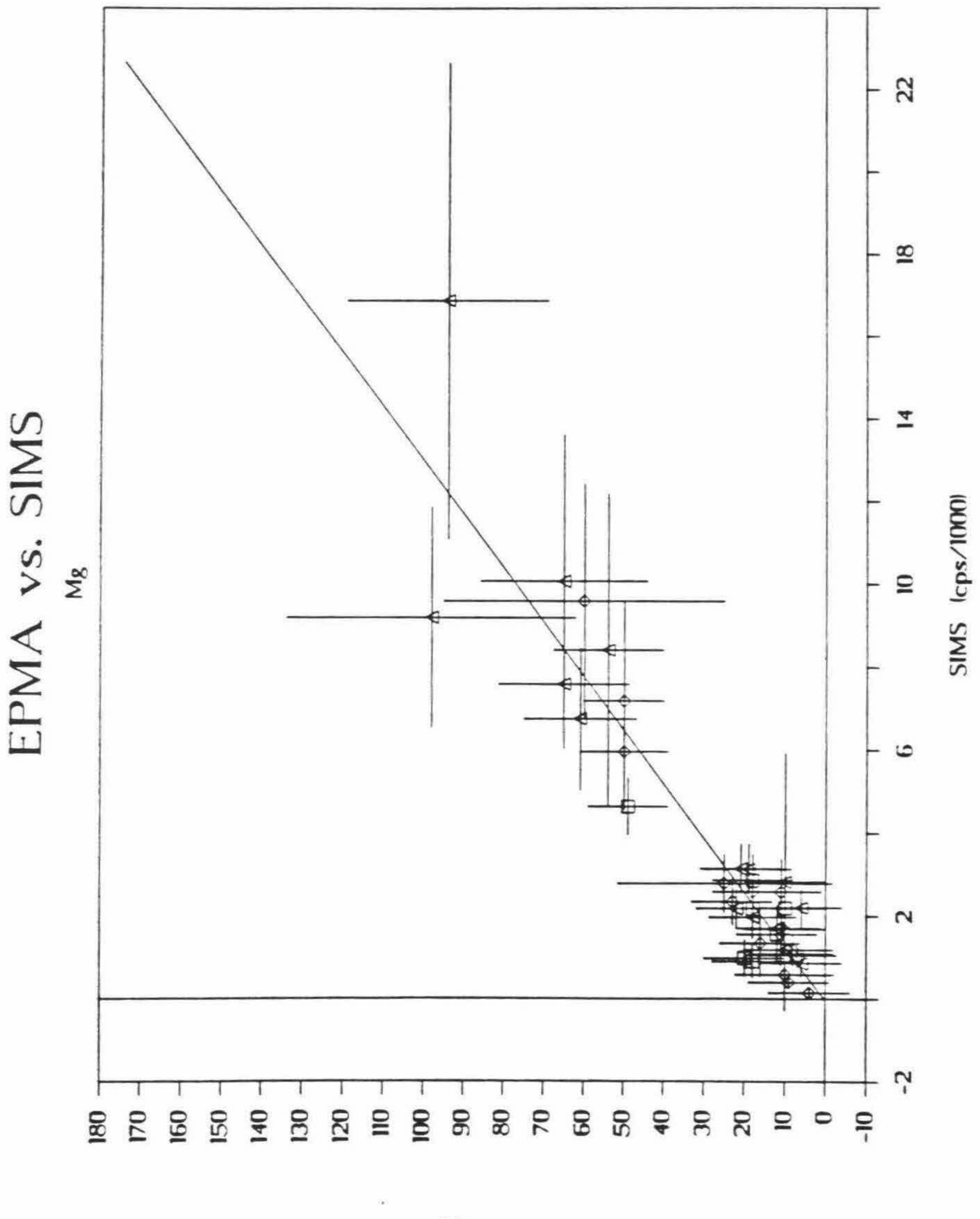
EPMA vs. SIMS
Mg
EPMA (ppm)
180
170
160
150
140
130
120
110
100
90
80
70
60
50
40
30
20
10
0
-10
SIMS (cps/1000)
-2
2
6
10
14
18
22

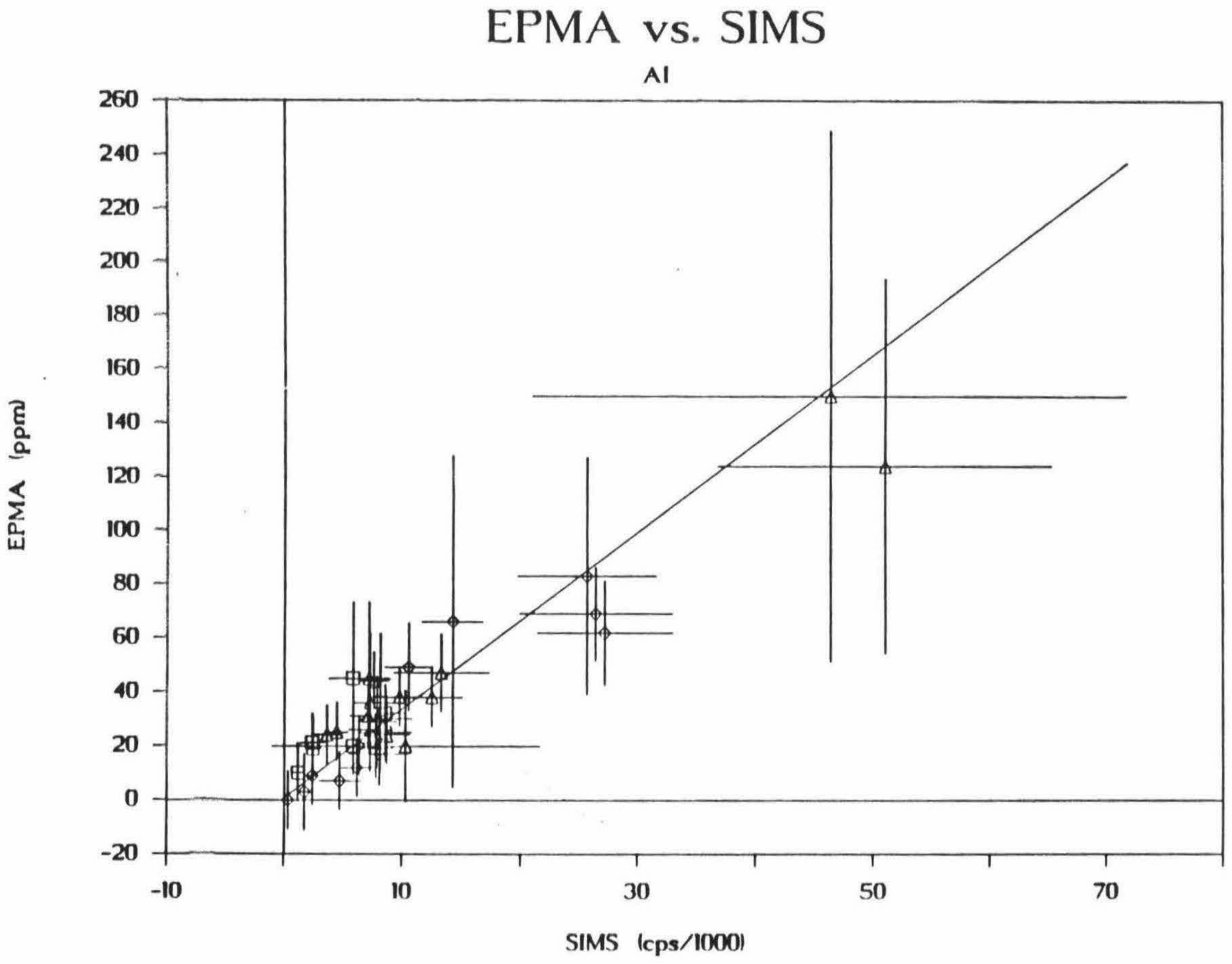
EPMA vs. SIMS
Al
EPMA (ppm)
260
240
220
200
180
160
140
120
100
80
60
40
20
0
-20
-10
10
30
50
70
SIMS (cps/1000)

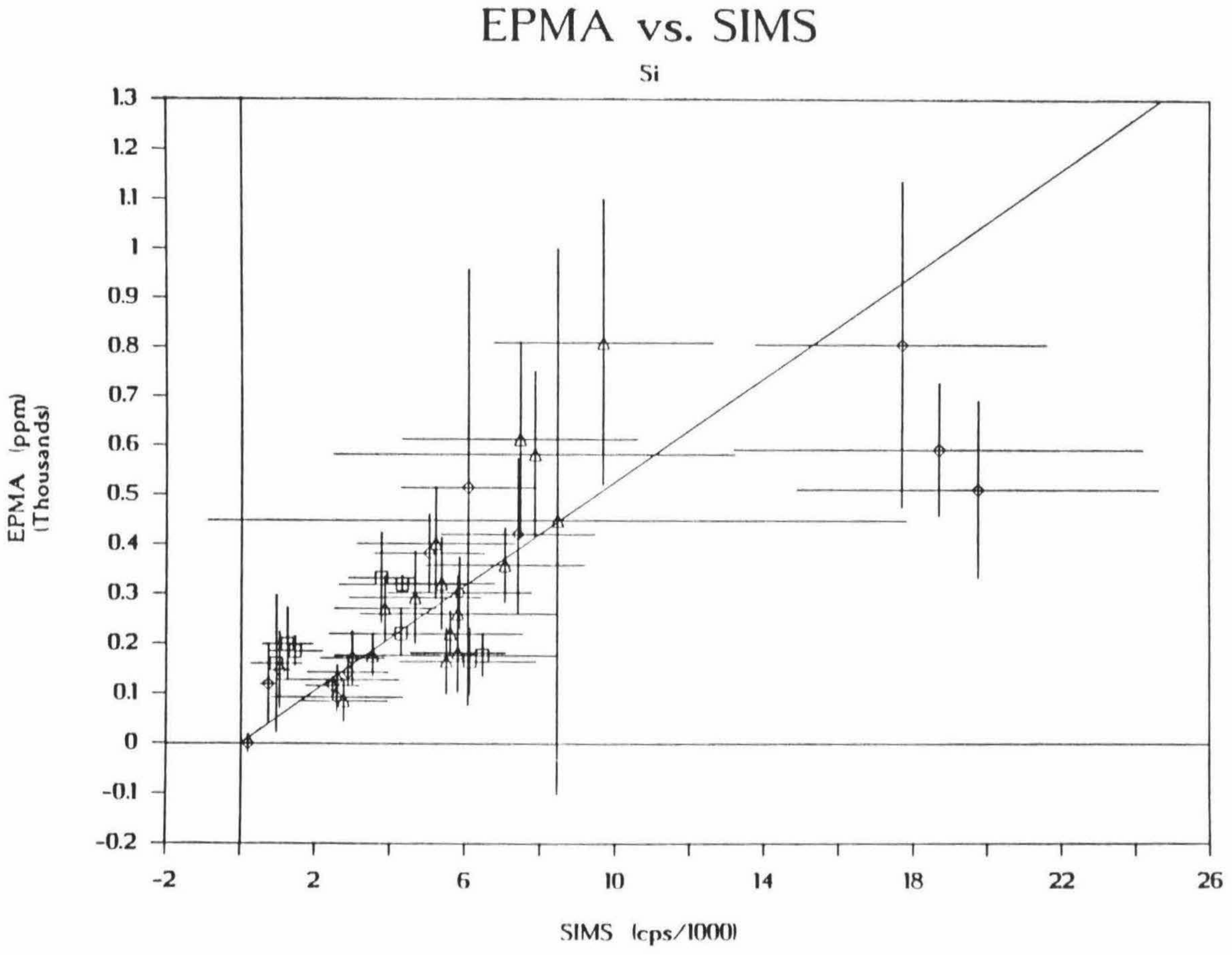
EPMA vs. SIMS
Si
EPMA (ppm)
(Thousands)
1.3
1.2
1.1
1
0.9
0.8
0.7
0.6
0.5
0.4
0.3
0.2
0.1
0
-0.1
-0.2
-2
2
6
10
14
18
22
26
SIMS (cps/1000)

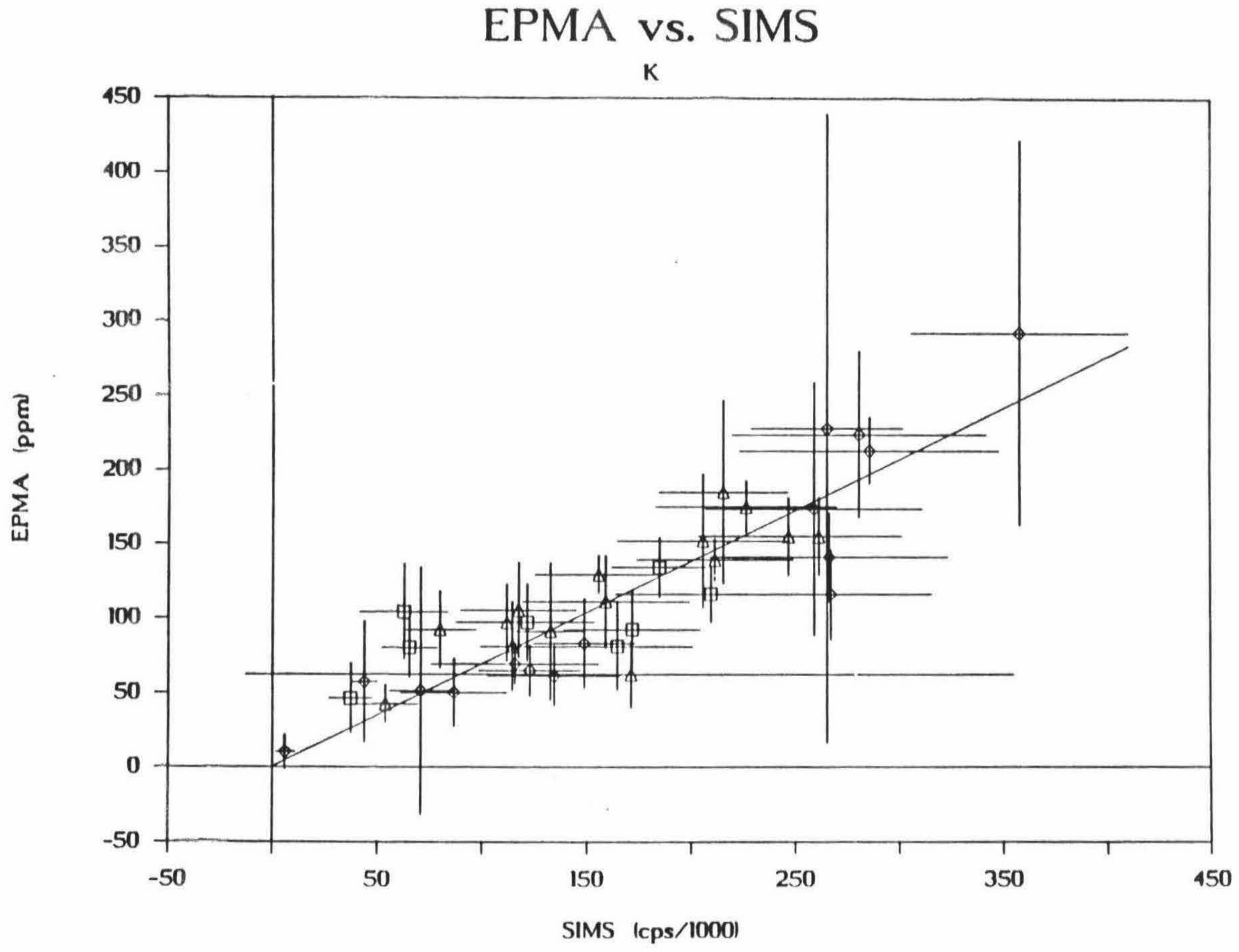
EPMA vs. SIMS
K
EPMA (ppm)
450
400
350
300
250
200
150
100
50
0
-50
-50
50
150
250
350
450
SIMS (cps/1000)

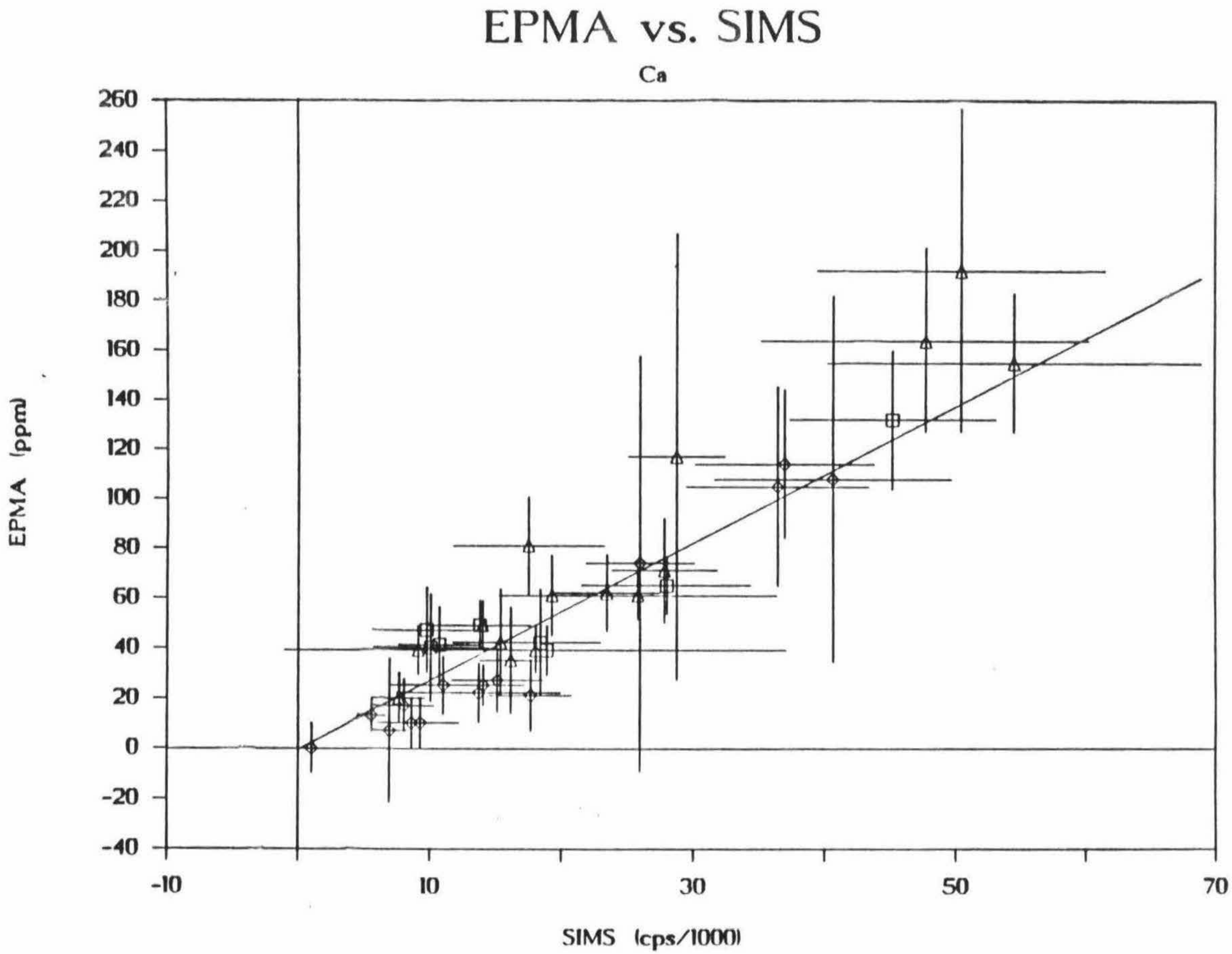
EPMA vs. SIMS
Ca
EPMA (ppm)
260
240
220
200
180
160
140
120
100
80
60
40
20
0
-20
-40
-10
10
30
50
70
SIMS (cps/1000)

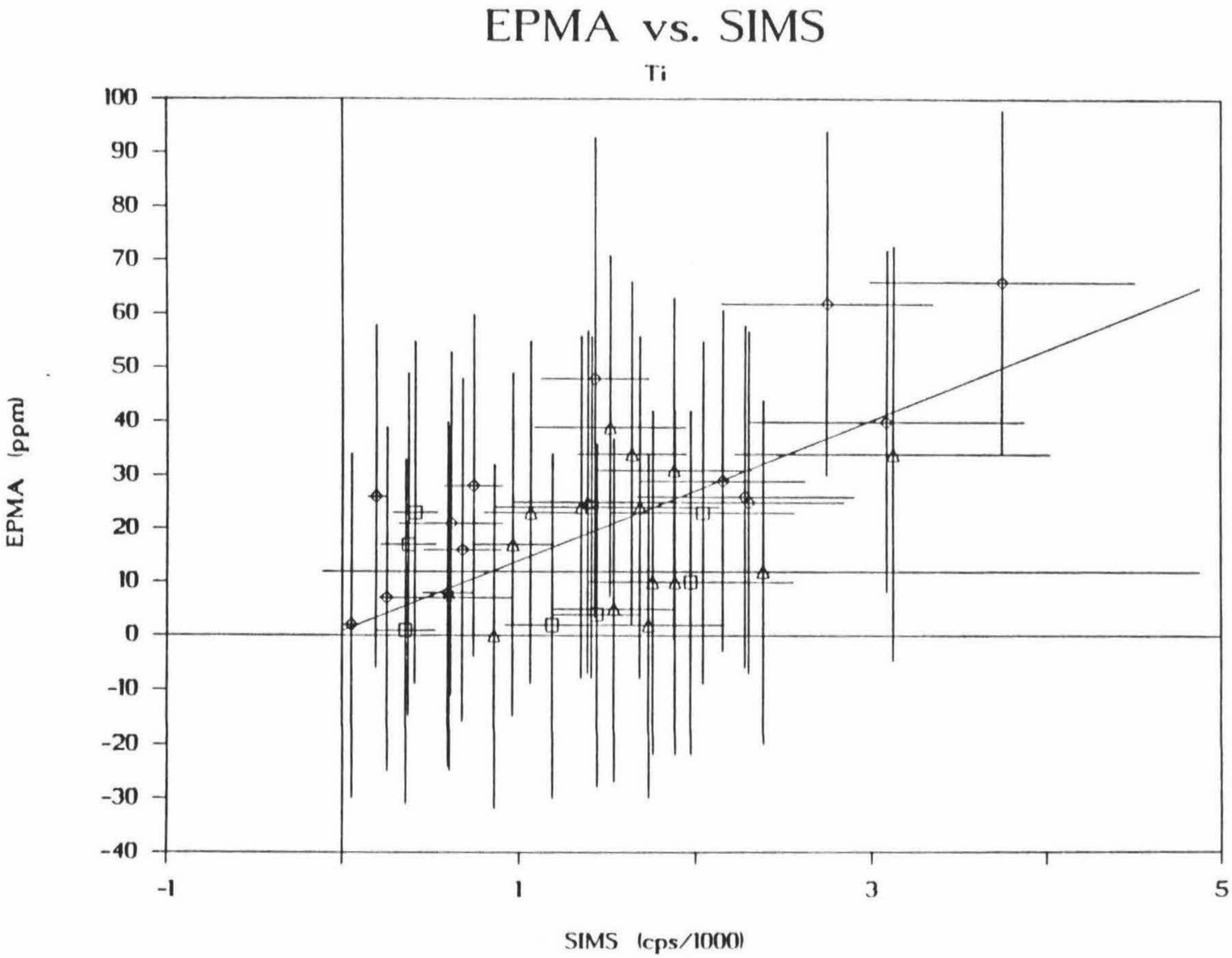
EPMA vs. SIMS
Ti
EPMA (ppm)
100
90
80
70
60
50
40
30
20
10
0
-10
-20
-30
-40
-1
1
3
5
SIMS (cps/1000)

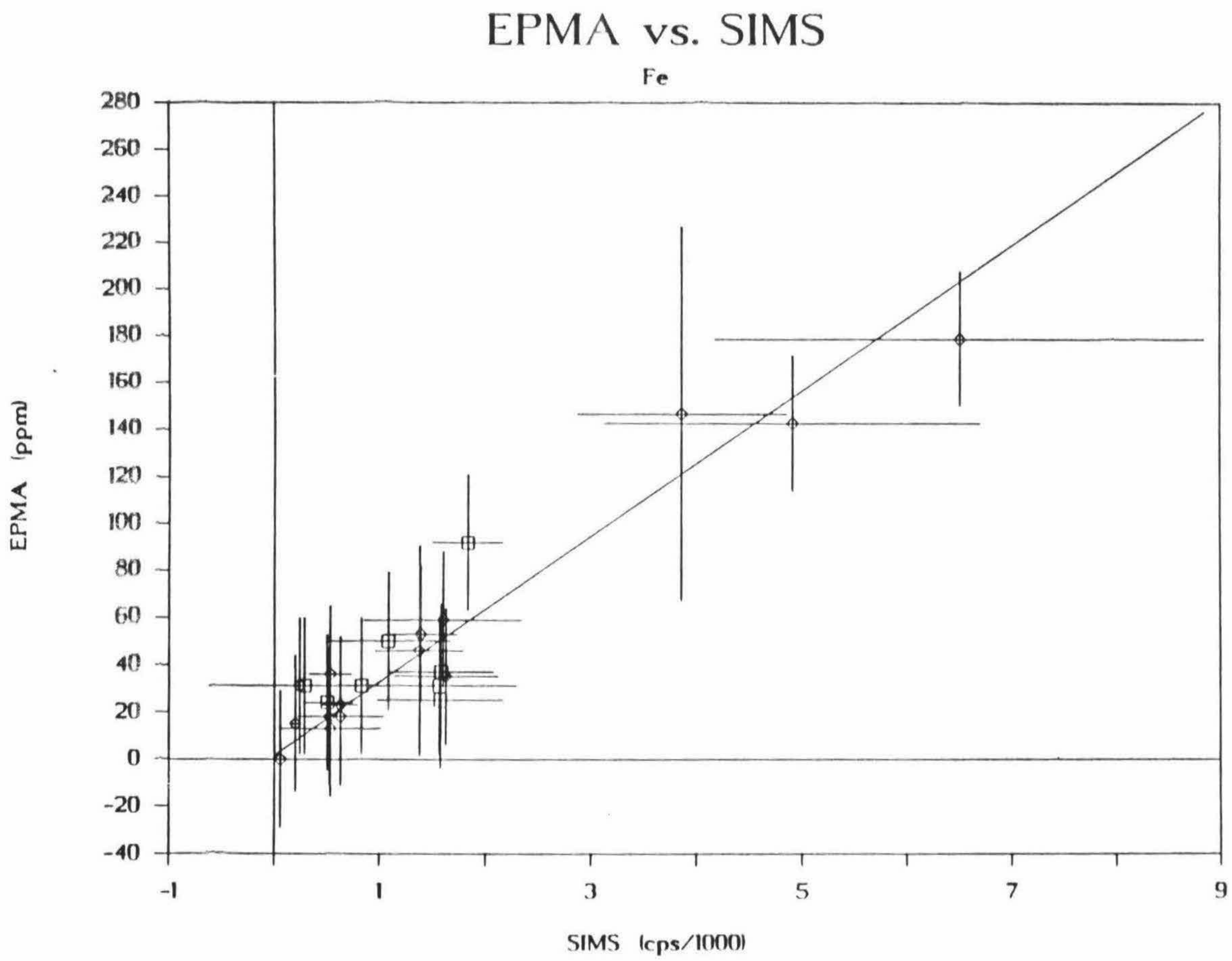
EPMA vs. SIMS
Fe
EPMA (ppm)
280
260
240
220
200
180
160
140
120
100
80
60
40
20
0
-20
-40
-1
1
3
5
7
9
SIMS (cps/1000)

weights each point according to its associated error in both the X and the Y direction.

Errors in SIMS count rates are estimated as the standard deviation of the normalized intensities of the elements in the individual cycles during the run. Errors in EPMA data are taken as the geometric sum of the square-root contributions of the peak, the blank, and their background intensities, or as the measured standard deviation of the four spot analyses of each EPMA data point (see detailed explanation in Sec. 5.1.2 and Tab. 5.1). Typically, errors due to counting statistics dominate when concentrations are low; errors due to sample heterogeneity dominate in samples with high concentration due to the inhomogeneity of these zoned samples. The correlation lines were forced towards crossing at the origin by including one blank measurement with its associated error for each of the data points.

Data were acquired during 5 different sets of EPMA and SIMS analyses. Still, the results of all sets agree with the same correlation line. All data acquired were used in the correlations except for two cases: i) Fe analyses of the two early sets of measurements, and ii) Na analysis of CTP L1, CTP L6, CTP LB, CTP MM1 and CTP Z4. Fe contamination from steel holders affected EPMA but not SIMS results (due to raster-cleaning). In addition, high Fe blank was contributed by the Ni-alloy cathodes used during the analysis of these early sets. In the case of sodium, EPMA analysis yielded exceptionallylow Na concentrations, with many analyses being lower then the blank; therefore, these results were not used in the correlation af Na data.

The large error bars for Ti are due to the large statistical errors in EPMA measurements of that low concentration element. The deviation of a few Si measurements from the correlation line may be the result of error introduced by the large blank corrections of EPMA silicon data (see Tab. 5.1).

Table 6.3 summarizes the relative ion-yields as determined from the slopes of the correlation lines and their associated errors. The slopes are expressed in units of normalized count rate per ppm oxide. These units are convenient for fast estimation of concentrations from SIMS data. Relative ion-yields are expressed in units of $(\text{cps/ppm})_{\text{elem}}/(\text{cps/ppm})_{\text{carbon}}$ (cps for the most abundant isotope, ppm of the element in the diamond). Na and K show the

Table 6.3. Relative ion-yields for trace elements in diamonds.

Element	Na	Mg	Al	Si	K	Ca	Ti	Fe
Slope[1]	2123	130	303	19	1450	364	75	32
σ_b	362	16	37	2	90	30	24	7
Intercept[2]	-551	-39	-254	-3	-811	230	-68	-56
σ_a	5064	194	529	57	3002	552	364	179
No of points[3]	40	76	76	76	76	76	76	46
Relative ion-yield[4]	57232	4322	11441	796	34942	10187	2512	811
2σ	34%	25%	25%	22%	12%	16%	63%	46%

1. Slope is in cps_{elem}/ppm_{oxide} @ 50000 cps $^{12}C^+$. σ of slope in same units.

2. Intercept with the X axis, in cps @ 50000 cps $^{12}C^+$. σ of intercept in same units.

3. Number of points, include one blank value for each data point.

4. Relative ion-yields in $(cps/ppm)_{elem}/(cps/ppm)_{carbon}$, with carbon being 10^6 ppm. 2σ in percents.

highest yields, followed by Al, Ca, and Mg. Ti, Si, and Fe have the lowest yields. Errors in the relative ion-yields are large and vary from 12% (2σ) for K to 63% in the case of Ti.

6.2.2. GRAPHITE - GLASS MIXTURES

a. Preparation of graphite-glass pellets.

A close analog to a micro-inclusion-rich diamond was prepared by mixing fine powders of silicate glass and graphite. A piece of Si, Al, K, Na and Fe bearing glass was crushed. Two fragments were mounted for EPMA analysis and the rest was ground into powder by 8 hours of grinding in an agate mortar. The glass powder was dispersed in reagent- grade acetone by shaking and ultrasonicating for 10 minutes in a glass column. The suspension was allowed to separate for 24 hours. The supernate, including particles smaller than 1 μm, was separated and mixed again ultrasonically. After 54 hours of additional separation in a glass column, the supernate that contained the extra-fine particles was removed and the precipitate was washed with 30 ml of acetone and dried in a beaker. Microscopic examination showed that ~ 95% of the particles were smaller than 1 μm with the remaining 5% in the 1-2 μm range. 12.20 mg of glass were dried at 60° under vacuum to give a final weight of 12.18 mg. The glass was mixed with dried, fine, pure graphite powder (Ultra Carbon Corporation, Bay City, Michigan, impurities < 5 ppm) to yield a mixture containing 1.987±0.007 wt% glass. The glass and the graphite were mixed ultrasonically in a vial with reagent-grade ethanol and was agitated ultrasonically until dry. One part of this 2% graphite-glass mixture was then mixed with four parts of graphite to yield a mixture with 0.398 wt% glass (referred to as the 0.4% mixture). Mixing and drying were done in the same way as for the first mixture. Using a KBr pellet presser, two pellets of each composition were prepared, as well as a pellet of pure graphite. Pellets were 5 mm in diameter and ~1.5-2.5 mm thick. Their density is estimated at ~2 gr/cm^3.

b. Analysis of graphite-glass pellets.

The five pellets were mounted in brass holders and analyzed under the same conditions as the diamonds, except for a lower primary beam current of 5 nA, which was necessary to prevent count rates in excess of 10^6 cps. Three to six points were analyzed on each sample. Run durations were about 25 minutes per point. In retrospect, this was too short a time to sample these heterogeneous samples. The standard deviation of the different cycles is up to 80% of the mean value, and the variation between the different analysis points is even higher. Still, averaging all the data for each pellet, the results for pellets of identical composition are in good agreement. These average values were used to construct the correlation lines presented in Figure 6.10. The resulting RIYs are given in Table 6.4.

The two RIY sets, those determined from the EPMA-SIMS correlations (diamond set) and those determined from the analysis of the graphite-glass pellets (graphite set), carry high associated errors, so that the differences between the two sets are actually within the error margins. However, the RIYs of the diamond set are all higher than those of the graphite set. Sodium shows the greatest difference, but as discussed in Section 5.1.3, sodium concentrations determined by EPMA are expected to be underestimated by ~10%. The resulting RIY is expected to be overestimated. If this is corrected the graphite RIYs are 18±6% lower than the diamond RIYs. The possible explanations for this difference are disscussed in Section 6.2.4.

6.2.3. DEPTH PROFILES OF ION-IMPLANTED DIAMONDS

In order to further ascertain the accuracy of the RIYs obtained from SIMS-EPMA calibration the absolute ion-yields of Al^+, Si^+, Ca^+, Ti^+ and Fe^+ were determined by depth profile analysis of ion-implanted diamonds. The use of ion-implanted samples for the calibration of SIMS ion-yields is a common technique in material analysis. A known dosage of ions of the element of interest is accelerated toward the sample and implanted into the first few micrometers of the subsurface. The depth distribution of ions is roughly a Gaussian, but a small fraction of the ions are implanted into deeper depths than expected from a Gaussian distribution (Biersack, 1987). During SIMS analysis the primary beam excavates the first few subsurface micrometers until most of the implanted ions are sputtered away. The useful yield for the implanted element can be calculated by comparing the total

Figure 6.10. SIMS analysis of graphite-glass pellets.

Normalized intensities of the five elements analyzed by SIMS are plotted against the glass content of the pellets. Using the known concentrations of the five elements the slopes of these lines can be translated to yield RIYs for Na, Al, Si,K, and Fe.

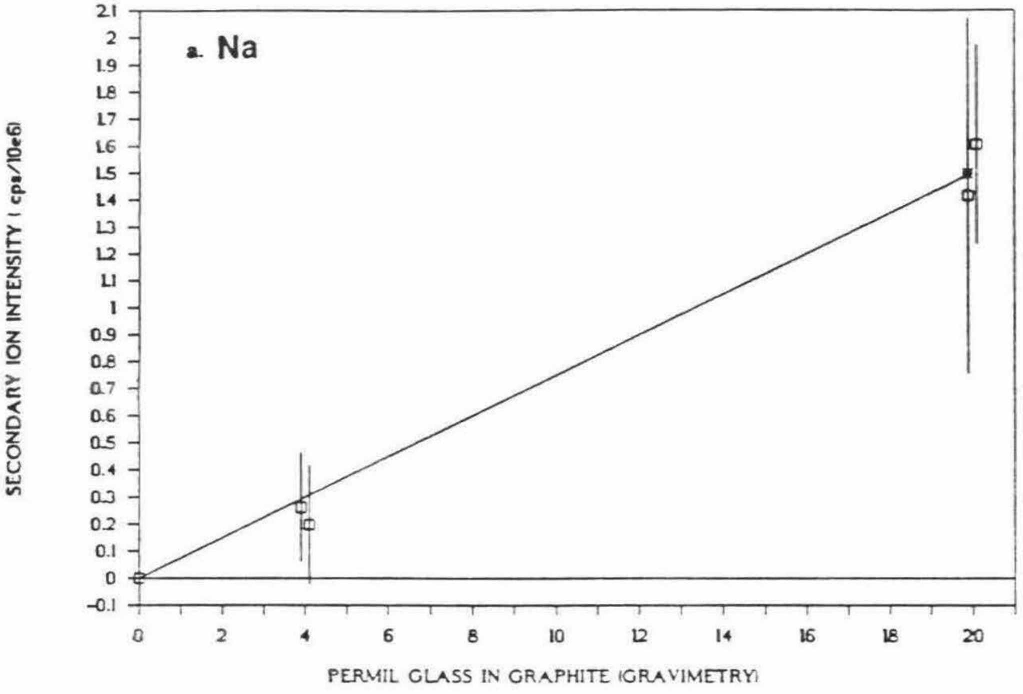
a. Na
SECONDARY ION INTENSITY (cps/10e6)
2.1
2
1.9
1.8
1.7
1.6
1.5
1.4
1.3
1.2
1.1
1
0.9
0.8
0.7
0.6
0.5
0.4
0.3
0.2
0.1
0
-0.1
0
2
4
6
8
10
12
14
16
18
20
PERMIL GLASS IN GRAPHITE (GRAVIMETRY)

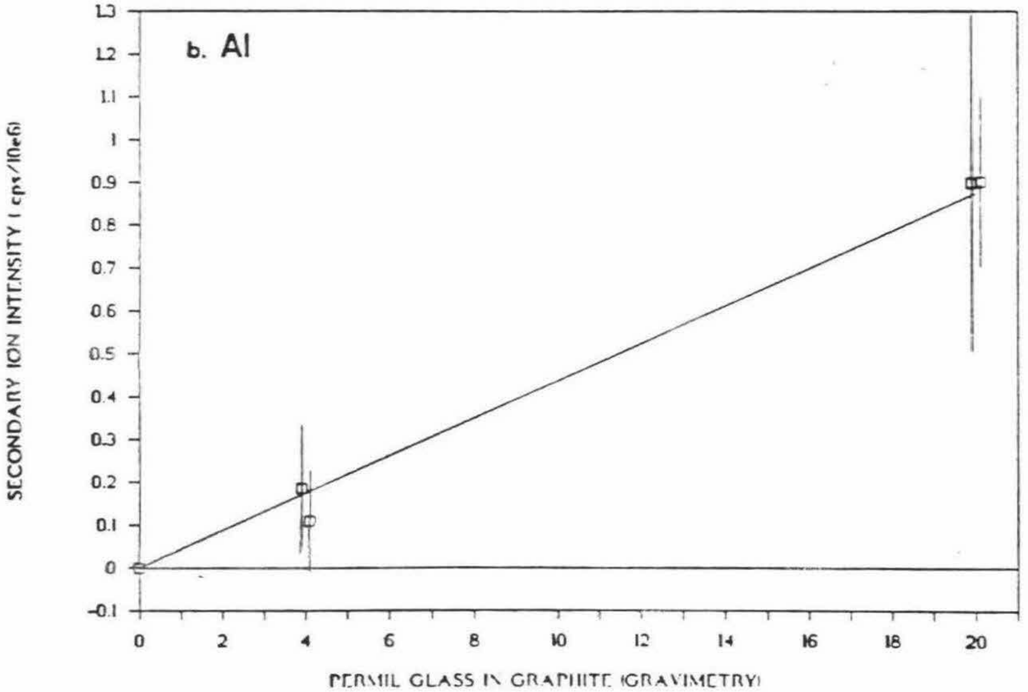
b. Al
SECONDARY ION INTENSITY (cps/10e6)
1.3
1.2
1.1
1
0.9
0.8
0.7
0.6
0.5
0.4
0.3
0.2
0.1
0
-0.1
0
2
4
6
8
10
12
14
16
18
20
PERMIL GLASS IN GRAPHITE (GRAVIMETRY)

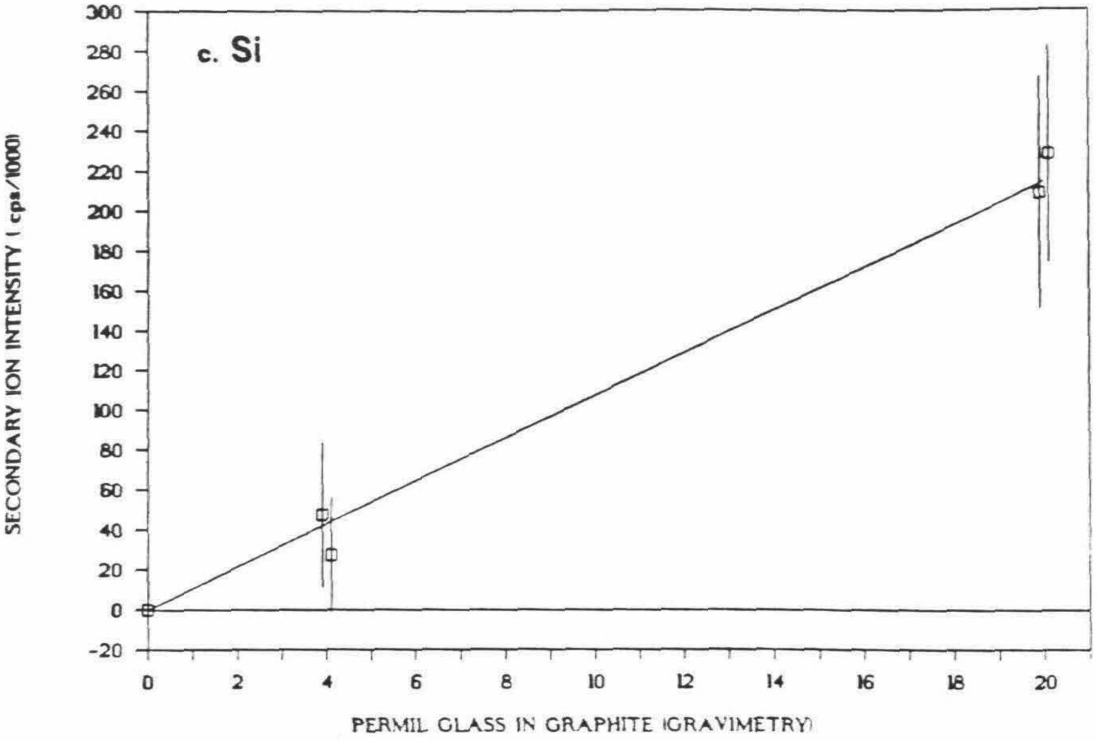
c. Si
SECONDARY ION INTENSITY (cps/1000)
300
280
260
240
220
200
180
160
140
120
100
80
60
40
20
0
-20
0
2
4
6
8
10
12
14
16
18
20
PERMIL GLASS IN GRAPHITE (GRAVIMETRY)

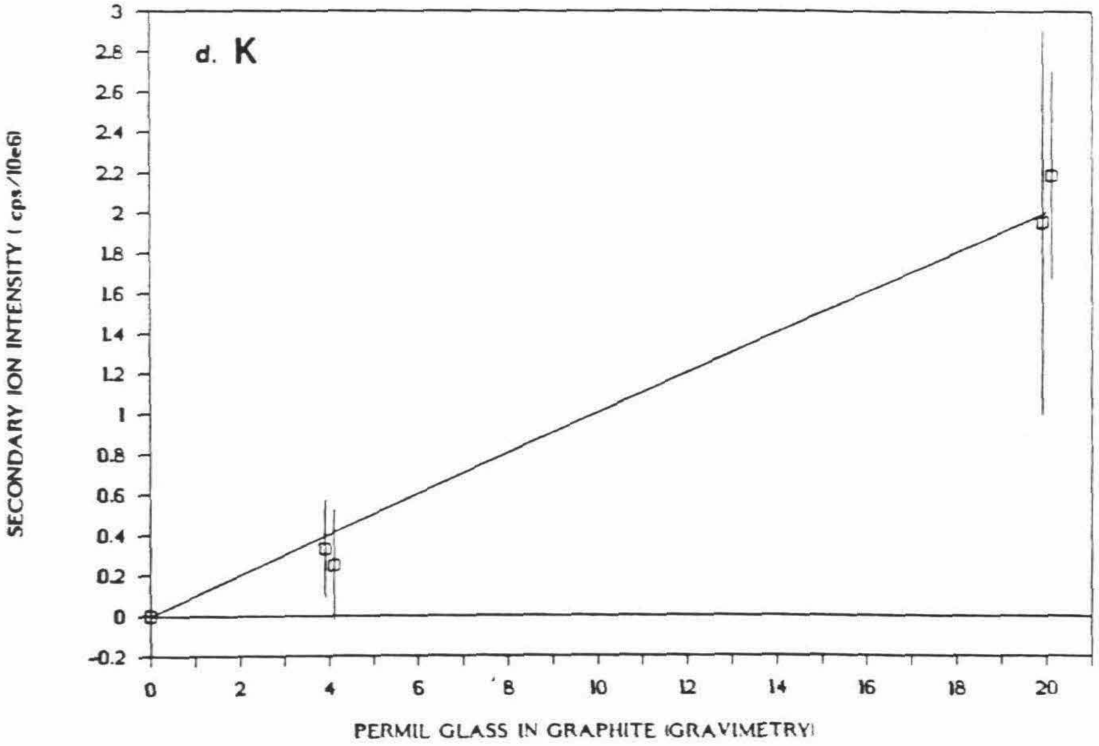
d. K
SECONDARY ION INTENSITY (cps/10e6)
3
2.8
2.6
2.4
2.2
2
1.8
1.6
1.4
1.2
1
0.8
0.6
0.4
0.2
0
-0.2
0
2
4
6
8
10
12
14
16
18
20
PERMIL GLASS IN GRAPHITE (GRAVIMETRY)

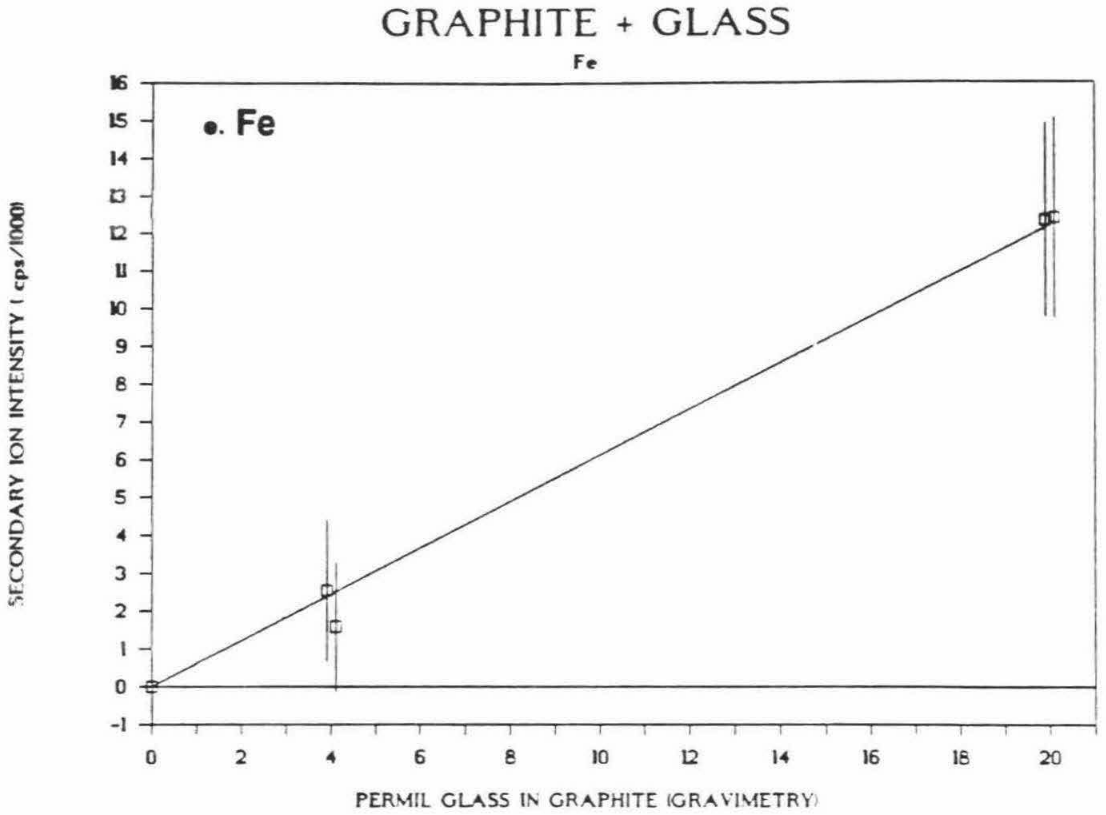
GRAPHITE + GLASS
Fe
●. Fe
SECONDARY ION INTENSITY (cps/1000)
16
15
14
13
12
11
10
9
8
7
6
5
4
3
2
1
0
-1
0
2
4
6
8
10
12
14
16
18
20
PERMIL GLASS IN GRAPHITE (GRAVIMETRY)

Table 6.4. Analysis of graphite-glass pellets.

Element	**Na**	**Al**	**Si**	**K**	**Fe**
Average intensities for the pellets (cps$_{elem}$/cps$_{carbon}$).					
2.0% a[1]	28.29 ± 47%	17.99 ± 44%	4.17 ± 28%	39.12 ± 49%	0.247 ± 21%
2.0% b	32.10 ± 23%	18.05 ± 22%	4.56 ± 24%	43.76 ± 24%	0.248 ± 21%
0.4% a	5.25 ± 77%	3.70 ± 82%	0.95 ± 77%	6.64 ± 73%	0.051 ± 73%
0.4% b	3.95 ±111%	2.18 ±110%	0.54 ±106%	4.97 ±111%	0.032 ±108%
Blank	0.00122 ± 13%	0.00017 ± 32%	0.00024 ± 21%	0.00211 ± 9%	0.00003 ± 83%
Slope[2]	14.954	8.754	2.14	20.034	0.121
σ_b	2.972	1.672	0.374	4.074	0.017
R	0.993	0.994	0.994	0.989	0.997
Glass composition[3]	5.0	18.0	65.7	9.0	2.2
RIY[4] **(pellets)**	40315 ± 40%	9191 ± 38%	697 ± 35%	26814 ± 41%	713 ± 29%
RIY (diamonds)	57232 ± 34%	11441 ± 25%	786 ± 22%	34942 ± 12%	811 ± 46%
% difference[5]	-30%	-20%	-12%	-23%	-12%

1. Samples are designated by their glass content. Blank - pure graphite pellet.

2. Slope in cps$_{elem}$/cps$_{carbon}$/wt%$_{glass}$. σ of slope in same units.

3. Glass composition by EPMA analysis of a glass fragment.

4. RIY - Relative ion-yield in (cps/ppm)$_{elem}$/(cps/ppm)$_{carbon}$. 2σ in percents.

5. % difference - between the two determination of the RIYs.

number of ions counted with the known number of implanted ions in the analyzed area. The useful yield elements in the substrate material may also be determined if the depth of the analyzed volume is known.

In the discussion that follows, the terms **"ion-yield"** or **"absolute ion-yield"** are defined as the ratio of the count-rate for the most abundant isotope of a given element divided by the concentration of that element (of natural isotopic abundance) in the sample. Here, ion-yields are measured by counts per second per ppm (cps/ppm). The term **relative ion-yield** (RIY) refers to the ratio of the ion-yield of a given element divided by that of a reference element. In this case, the reference element is always carbon and the RIY is measured in $(\text{cps/ppm})_{\text{element}}/(\text{cps/ppm})_{\text{carbon}}$. The **"useful yield"** of an element is the number of ions of a given isotope of that element counted by the SIMS divided by the number of atoms of that isotope sputtered from the analyzed area measured in counts/atom. The useful yield is a more fundamental property of the element. It is matrix-dependent; however, it is independent of the sputtering rate and the natural isotopic abundance. The ion-yield is the more practical unit in that it measured the sensitivity of SIMS for the trace element analysis.

Ion-implantation was done by Dr. Robert Wilson at the Hughes Research Laboratory in Malibu, CA. The sample was placed inside a Faraday cup and the beam was rastered over a known area within the cup. By monitoring the ion current in the cup, it was possible to calculate the total number of atoms implanted per unit area. Doses of $3\text{x}10^{13}$ or $1\text{x}10^{14}$ atoms/cm^2 of ^{27}Al, ^{30}Si, ^{40}Ca, ^{46}Ti, and ^{54}Fe+^{56}Fe were implanted into the pre-cleaned, flat, polished surfaces of three synthetic diamonds (Sumitomo Electric Co., Japan) using a 200 kV accelerating potential. The doses were monitored by placing the sample inside a Faraday cup and measuring the current flowing through the cup while rastering the beam over a known area. The uncertainty in the determination of the implantation doses are on the order of 10% (R. Wilson, pers. comm.). Before SIMS analysis, the implanted samples were cleaned in water, alcohol, and freon, coated with 500Å of gold, and spring-loaded against a brass holder with an opening aperture of 1.2 mm. A 20 nA O^- beam was rastered over a 100 μm square. Positive secondary ions were collected from a 60 μm diameter circular area in the center of the rastered square and were analyzed using a mass-resolving power of 1350. All other instrumental conditions were identical to those used during diamond analysis (Sec. 6.1.2).

Profilometry of the sputtered craters was done by Mr. R. DeSantiago at Charles Evans and Associates, Redwood City, CA, using a Tencor Alpha Step 200 with depth resolution of ~10 Å and stylus diameter of 1.5 μm. Two diagonal profiles were measured for each analysis. These two depth measurements usually agree to within a few percent, the main source of uncertainty being the roughness or the curvature of the surface.

a. The ion yield of carbon.

The craters excavated during analyses vary in depth from 0.2 to 3 μm. A typical crater is presented in the insert to Fig. 6.11. The craters are 100-130 μm wide, and become narrower with depth. The bottom is typically 60-80 μm wide and its relief is smaller than 0.05 μm in height. The depth of the craters excavated during analyses is plotted against the total sputtering time in Figure 6.11. Data shows that depth of crater increases linearly with sputtering time over the range 1×10^3 to 2.5×10^4 sec. The slope of the least-square-fit line corresponds to an average sputtering rate of 1.1 Å/sec or 0.4 μm/hr (Table 6.5). Using an average counting rate for $^{12}C^+$ of 32000 cps (Table 6.6), a useful yield of 5.3×10^{-7} count/atom was calculated for ^{12}C in diamond. In a single experiment on a graphite rod (Ultra Carbon Co., Bay City, MI), a crater of 4.5 μm depth was excavated during a $2.43 \cdot 10^4$ sec run yielding a sputtering rate of 1.8 Å/sec. This rate is 50% faster than diamond. The density of the graphite rod is only 1.33 compared with 3.51 for the diamond, so that the number of atoms sputtered per unit time is actually lower in the case of graphite. The counting rate was almost identical for diamond and graphite. That means that the useful yield is 60% higher for carbon in graphite (Table 6.6).

b. Ion yield of the implanted elements.

All implanted elements were analyzed as atomic, singly-charged ions, M^+. The profile of Ti was analyzed twice (Table 6.7). Figure 6.12a shows the results of a typical depth profile

Figure 6.11. Sputtering of diamond and graphite.

Depth of craters excavated during depth profiling of diamond and graphite samples. (Profilometry by R. De Santiago, Charles Evans and Associates, Redwood City, CA). The line represents the least-square fit to the diamond data (squares), and defines a sputtering rate of 1.1 Å/sec. The single graphite analysis (cross) falls above the line and corresponds to a sputtering rate of 1.8Å/sec.

Insert: Profilometry of a crater excavated by rastering a 20 nA O^- beam over a 100x100 μm area. The original surface of the diamond is horizontal; the rise at the left end of the profile is due to scratching and piling of the gold coat (after the analysis). Depth is measured as the difference between the left and the right markers (L,R). The value used in Table 10.1 and this figure is the average of the depths measured from two orthogonal profiles across the crater.

SPUTTERING OF DIAMOND AND GRAPHITE

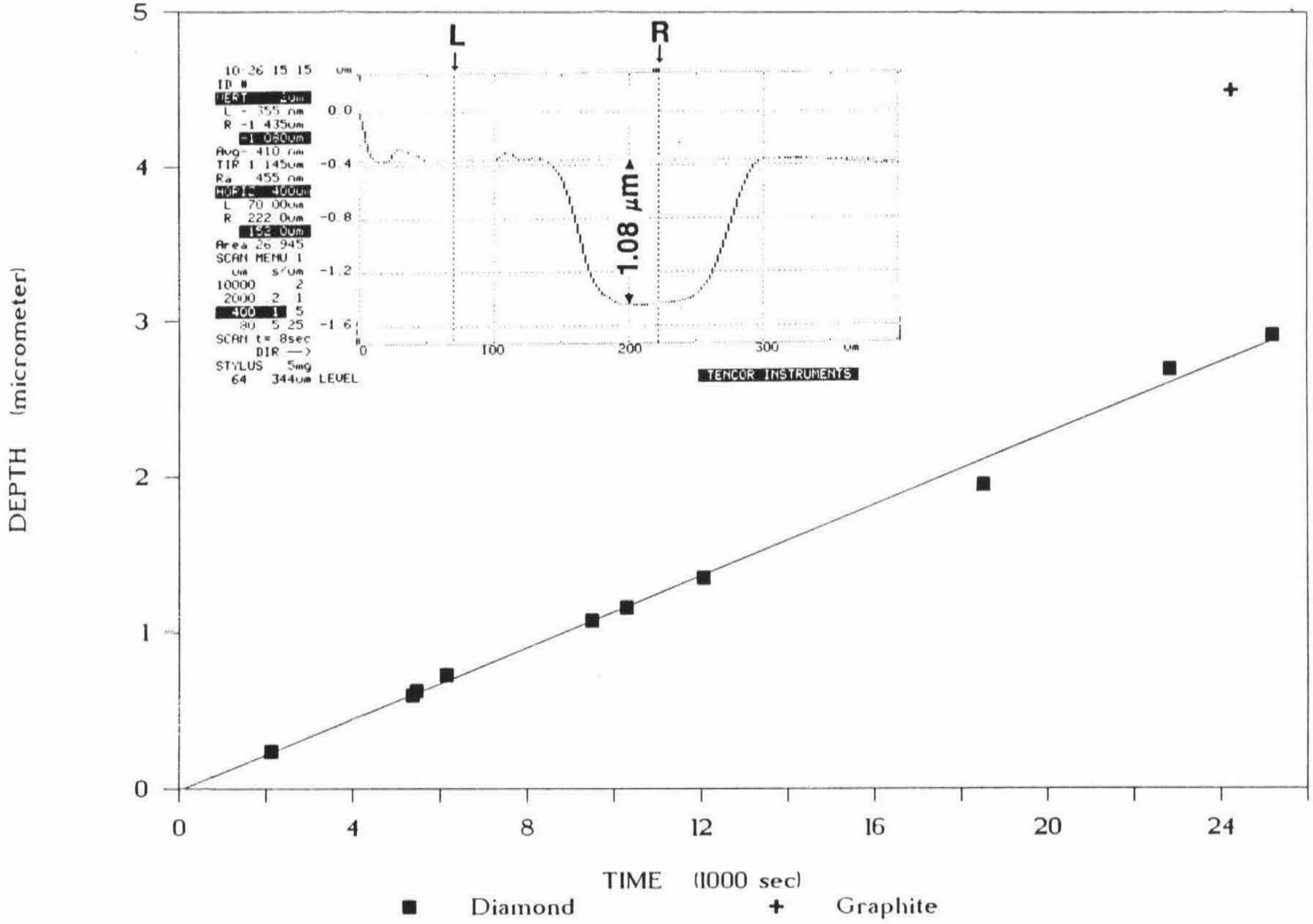

Table 6.5. Sputtering of diamond and graphite.

Sample	Material	Run Time (sec)	Depth (μm)	Avg. $^{12}C^+$ count rate (cps)	Total # of counts (10^8 counts)
ON66Al	diamond	5380	0.60	33000	1.78
ON65Si	diamond	12062	1.35	38000	4.58
ON63Ca	diamond	9485	1.08	32000	3.04
ON63Ti	diamond	10292	1.16	32000	3.29
ON63Fe	diamond	5460	0.63	38000	2.07
ON65Si	diamond	25200	2.91	31600	7.96
ON65Si	diamond	2120	0.24		
ON65Na	diamond	18520	1.95		
ON65Na	diamond	6145	0.73		
ONMMZ87	diamond	22842	2.69	28600	6.53
ON GR1	graphite	24269	4.5	31200	7.57

Table 6.6. Sputtering parameters of diamond and graphite.

Parameter	Diamond	Graphite	Units
Density	3.51	1.33[1]	gr/cm^3
Sputtering rate	1.1[2]	1.8[3]	Å/sec
Sputtering rate	0.4	0.7	μm/hr
Sputtering rate	3.9	2.5	10^{-8} gr/cm^2-sec
Counting rate	32000[4]	31000	cps
Counting rate	2.7	1.7	10^8 counts/μm
Useful yield	5.3	8.7	10^{-7} count/atom

1. Measured by weighing a 2.91 cm long piece of the graphite rod (0.25" diameter). Weight: 1.22 gr.

2. From Fig. 6.11.

3. From Table 6.5.

4. Best choice based on all sputtering experiments.

Table 6.7. Depth profile of ions implanted in diamond.

Element **Isotope** **Sample**	**Al** 27 ON66Al	**Si** 28 ON65Si	**Ca** 40 ON63CT	**Ti** 46 ON63CT	**Ti** 46 ON63CT	**Fe** 54+56 ON63Fe	**Units**
Total number of counts[1]	15.4	0.24	12.8	25.6	20.5	4.97	10^6 counts
Implanted dose dose	3	10	3	10	10	10	10^{13} atoms/cm^2
Total number of sputtered atoms[2]	8.5	28.3	8.5	28.3	28.3	28.3	10^8 atoms
Useful Yield	180	0.85	150	91	73	16	10^{-4} count/atom
Ion yield[3] (natural samples)	450	1.9	244	93	75	19	count/ppm
RIY[4]	13642	49	7631	2913	2332	509	$\frac{(count/ppm)_{el}}{(count/ppm)_{carbon}}$
Maximum count rate	13100	234	12000	32700	25260	8160	count/sec
Maximum[5] concentration	2.3	8.7	2.5	11	11	15	10^{18} atom/cm^3
Maximum concentration	29	116	48	259	250	388	ppm

1. From integration of count rate along the run, corrected for surface and background contributions.
2. Implanted dose times the analyzed area (60 μm diameter).
3. Ion yield in counts of the most abundant isotope per ppm element with natural isotopic composition. $IY=10^{-6}*UY*a*N_a*D_d*SR/W$, where UY is the useful yield; a, the fractional abundance of the main isotope; N_a, Avogadro's number; D_d, the density of diamond, SR the sputtering rate (μm/sec); and W the molecular weight of the element.
4. The relative ion-yield is calculated by dividing the ion-yield of each element by that of carbon (the average count rate on ^{12}C divided by 10^6 ppm of carbon).
5. Calculated by dividing the maximum count rate (at the center of the Gaussian by the useful yield and by the sputtering rate (cm^3/sec).

Figure 6.12. Depth profiling of Ca in diamond.

a - the variation of measured count rate of $^{40}Ca^+$ ions with time. The high initial count rates are due to surface contamination and decay after ~800 sec. At a later time the profile follows the variation in the concentration of the implanted atoms in the diamond.

b - a Gaussian closely fits the data around the maximum. Then, as a portion of the surface atoms are re-implanted into deeper levels by the primary beam, the measured profile decays more slowly than the Gaussian.

c - Count rate at the end of the run (vertical scale is expanded by a factor of 50, so that 1 unit on the graph is equivalent to 20, rather than 1000 cps).

d - an exponent closely fits the data in this region. It decays to a background rate of ~40 cps.

The total number of counts was estimated by integrating the area under the fitted Gaussian for $0 < t < 1000$ sec, and the data itself for $t > 1000$ sec, and subtracting a constant background rate of 40 cps.

DEPTH PROFILE OF Ca IN DIAMOND

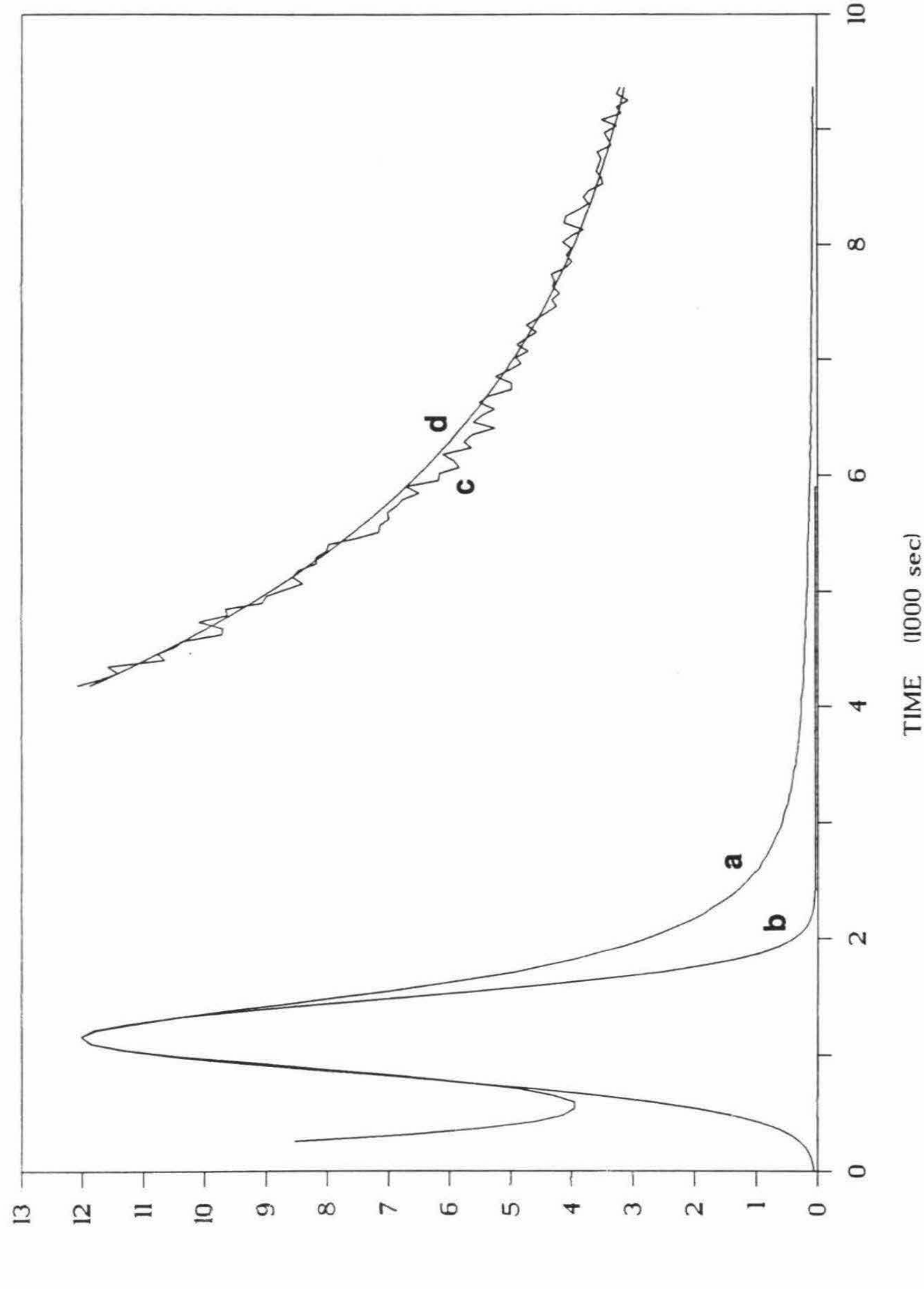

of implanted diamond; in the case shown, the implanted element is Ca. The high initial count rate is due to surface contamination. It quickly decays, and further sputtering reveals the Gaussian shape of the implantation profile. During sputtering, the primary beam re-implants the Ca atoms deeper into the sample and the Gaussian gradually turns into an exponential- decay curve. Deeply-implanted ions also contribute to the observed count rate in this region.

The total number of counts was calculated by integrating the area under the curve. Two corrections were applied to compensate for: i. the contribution from surface contamination and ii. the contribution from the measurement background. A Gaussian fit of the data was used for the first correction. The Gaussian was extrapolated to t=0, and the number of counts at the initial stage of the run was estimated by integrating under the fitted curve between t=0 and the time when maximum intensity was reached. Close agreement was obtained between the measured count rates and the Gaussian fit in the case of Ti and Fe, where surface contamination was minimal. The total correction in the case of Al, Si, and Ca analyses are on the order of 10%-18% of the total number of counts and the errors introduced by the first correction are estimated to be on the order of only a few percent. The counts past the Gaussian maximum were integrated using the data itself, and the final result was then corrected for background.

The background level was estimated by fitting an exponential-decay curve to the data at the end of the experiment and extrapolating to infinite time. Assuming that background contribution to the measured count rates is uniform throughout the run, the correction accounts for up to 10% of the accumulated counts and uncertainties in the fit may lead to a few percent error. The total error due to both corrections is smaller than 10%. The long decay time of both the surface ions and the final stages of the profile are interpreted as being due to the implantation of surface atoms.

The results are summarized in Table 6.6. Using the known dosages of implanted ions and the size of the analyzed area the total number of ions implanted into the analyzed area can be calculated and compared with the total number of ions counted to obtain the useful yield in counts/atom. In order to compare the results with those measured on natural samples the useful yield has to be converted to ion-yields by multiplying it by the sputtering rate and correcting for the different abundances of the isotopes. (Note that the ion-yield relates count rates and concentrations and is thus dependent on the sputtering rate and the density of the analyzed sample. The useful yield is independent of these parameters.) The relative ion yields (RIY) can also be calculated by dividing the ion-yields of the different elements by the ion yield of carbon during their analysis. Using the maximum count rate (at the center of the Gaussian) and the known sputtering rate, the maximum concentration of the implanted ions was also calculated.

Al and Ca have high ion-yields, on the order of 15 counts per 1000 sputtered atoms. Ti yields about 8 counts and Fe about 2 counts per 1000 atoms. Si has the lowest yield with less than 0.1 count per thousand sputtered atoms. The highest concentrations along the profile are on the order of a few tens to a few hundred ppm, comparable with concentrations in the micro-inclusion-bearing diamonds.

The total number of counts obtained during the two depth profiles of titanium differ by ~ 25%. The ion yield of carbon was similar in the two runs. Surface contamination was negligible during Ti analysis and the background correction was also small. The difference in the total number of counts is also reflected in the maximum count rate, indicating that while the ion yield of carbon remained constant during the two runs, the ion yield of Ti changed. The reason for that change is not clear.

The RIY of Al, Ca, Ti and Fe obtained from the implanted samples are within the 2σ margins of the RIYs calculated from the SIMS-EPMA correlations. Si is an exception, with the RIY obtained from ion-implantation being an order of magnitude lower than the SIMS-EPMA result.

c. Depth profile of silicates.

The sputtering rate of the micro-inclusion-bearing diamonds is similar to that of synthetic diamonds. However, it is not known whether the ionization efficiency of metals from the inclusions are controlled by the immediate oxide matrix or by the diamond matrix surrounding the inclusions. Two oxide samples, a synthetic glass and a mineral were analyzed using the same procedure in order to form a basis for comparison of the RIY from SIMS-EPMA calibration with yields in oxide matrices.

A sample of hibonite (Hibonite Madagascar) and a sample of a silica-rich glass (ON GFD) were analyzed under similar analytical conditions. A higher resolving power, MRP=2400 was needed to resolve some interferences, e.g., ^{27}AlO and ^{43}Ca or ^{27}AlH and ^{28}Si, and to reduce the intensities of some ions to below 10^6 cps (to protect the electron multiplier). The silicates charged during sputtering, and an offset of the secondary accelerating potential by 10 V during the experiment was needed in order to compensate for this.

The intensities of $^{25}Mg^+$, $^{28}Si^+$, $^{42}Ca^+$, $^{47}Ti^+$, and $^{56}Fe^+$ were measured on the hibonite sample; $^{30}Si^+$, $^{43}Ca^+$, $^{27}Al^+$ (as $^{27}AlO^+$), $^{54}Fe^+$, and $^{57}Fe^+$ were measured on the silica-rich glass. In both runs the intensity declined during the first 2-3 hours by about 15% and then increased to about 95% of the initial level. The average intensity for the whole run is about 10% lower than the intensity during the first hour.

The results are summarized in Tables 6.8 and 6.9. The sputtering rate of hibonite is lower than that of the silica-rich glass, but both are in the same range as diamond and graphite. The useful yields are similar in the hibonite and the glass (within a factor of 3), they are also comparable with those obtained for the implanted diamonds (Table 6.10). Except for Si, where a large difference was recorded between the two oxides and the implanted diamond, the ion yields show more variability than the useful yields, reflecting the different sputtering rates and densities of the different materials.

6.2.4. COMPARISON OF ION-YIELD DETERMINATIONS

The relative ion-yields (RIYs) of trace metals in diamonds were determined from SIMS-EPMA data correlation and from depth profiling of ion-implanted diamonds. RIYs were also determined for trace metals in graphite-glass mixtures. Table 6.10 summarizes the results obtained by the three methods. All show similar results which agree within the 2σ error margins. The only exception is the RIY of Si^+, where the ion-implanted sample yields a

Table 6.8. Sputtering rate of hibonite and Si-, K-rich glass.

Sample	Hibonite	Si-K-rich glass	Units
Analysis time	18530	11975	sec
Sputtered depth	1.30	2.23	μm
Sputtering rate	0.70	1.86	Å/sec
Sputtering rate	$2.7\text{x}10^{-8}$	$4.7\text{x}10^{-8}$	$\text{gr/cm}^2\text{/sec}$
Density	3.84	2.5[1]	gr/cm^3

1. Estimated based on densities of silica-rich glasses (Silver L.A. (1988) unpublished Ph.D. thesis, California Institute of Technology, Pasadena, CA)

Table 6.9. Ion yields in silicates.

	Hibonite					Silica-rich glass					
Element	Mg	Si	Ca	Ti	Fe	Si	Ca	Al	Fe	Fe	
Measured isotope	25	28	42	47	56	30	43	^{27}AlO[1]	54	57	
Main isotope	24	28	40	48	56	28	40	27	56	57	
Count rates											
Average	39971	11179	7635	17249	154268	92897	2187	1954	30949	10531	count/sec
Calculated[2]	315800	11180	1144000	171800	154300	2764000	1570000	383000	489800	449700	count/sec
Concentrations											
Wt% oxide[3]	2.28	0.49	6.76	2.86	2.89	62.3	1.9	1.5	4.8	4.8	wt%
ppm element	13700	2290	48300	17100	22400	291000	13600	3970	37000	37000	ppm
Ion-yield[4]	23	5	24	10	7	9	116	96	13	12	cps/ppm
Useful yield[5]	15	3.2	21	14	9.1	3.6	60	33	10	9.3	10^{-4} count/atom
Ion-yield[6]	99	21	102	43	30	41	497	415	56	52	cps/ppm
Useful yield	6	14	92	61	39	16	260	140	43	40	10^{-4} count/atom

1. Al was measured as ^{27}AlO. Count rate for ^{27}Al was calculated using a ratio of ^{27}Al/^{27}AlO=196 measured at lower currents.
2. Calculated count rate for the main isotope was calculated using the isotopic abundances of the measured and main isotopes.
3. From EPMA analysis.
4. Calculated count rate for the main element divided by the concentration of the element.
5. Calculated count rate for the main element divided by the number of atom of this isotope sputtered in one second.
6. The above yields multiplied by 4.3, this was found to be the ratio of the intensities at MRP=1400 and MRP=2400. The yields in these two rows can be compared with the yields in diamonds.

Table 6.10. Comparison of ion-yields from SIMS-EPMA, graphite-glass mixture and ion-implantation.

Element	Na	Mg	Al	Si	K	Ca	Ti	Fe
Relative ion-yields ($[cps/ppm]_{el}/[cps/ppm]_{carbon}$)								
SIMS-EPMA[1]	57000 (±34%)	4300 (±25%)	11400 (±25%)	800 (±22%)	35000 (±12%)	10200 (±16%)	2500 (±63%)	800 (±46%)
Graphite-glass	40000 (±40%)		9200 (±40%)	700 (±35%)	27000 (±40%)			700 (±30%)
Ion-implantation in diamond[1]			13600 (±10%)	50 (±10%)		7600 (±10%)	2600 (±10%)	500 (±10%)
Useful Yields (10^{-4} count/atom)								
Diamond (ion-implantation)			180	0.85		150	80	18
Hibonite		6		14		90	60	40
Silica-rich glass			140	16		260		40

1. RIY from SIMS-EPMA correlations are rounded from Table 6.3; RIY from graphite-glass analyses are from Table 6.4.
2. RIYs and useful yield for the ion-implanted samples are rounded from Tables 6.7 and 6.9. Errors for the results of the analysis of the ion-implanted samples (2σ) are estimated (see text).

result lower than the other two methods by a factor of 16. Comparison of the useful yields of silicon implanted in diamond, hibonite, and glass shows that the yield of Si^+ in the implanted diamond is lower relative to the oxide by a factor of 18, roughly similar to the ratio of RIYs determined from the SIMS-EPMA correlation and from ion-implantation. This difference suggests that isolated silicon atoms in a pure diamond matrix behave differently than Si in oxides. The agreement in the scaling factors also suggests that the Si in the micro-inclusions behaves like Si in an oxide matrix. This peculiarity of Si is presently not understood. In the case of the other elements, a better agreement exists between the RIYs from SIMS-EPMA and ion-implantation methods. It should be noted, however, that for those elements there exists a closer agreement between the useful yields of the metals in the oxides and in the implanted diamonds as well. For example, in the case of Ti, the RIY from ion-implantation experiments, 2500, is in close agreement with the SIMS-EPMA result, 2600. However, this similarity does not necessarily indicate that the ion-implanted sample is a good analog for the diamond. This similarity may also be due to similar ion yields in oxide and carbon matrices, as is indicated by the similar useful yields for Ti in hibonite and in the implanted diamond (60 and 80 respectively). The large differences found in the case of Si suggest that the ionization efficiency of the metals in the micro-inclusions is mainly controlled by the immediate silicate environment and less so by the carbon matrix. The similarity of the RIYs from SIMS-EPMA and ion-implantation mainly reflects similar useful yields of metals in oxides and diamonds, coupled with similar sputtering rates and densities of the ion-implanted diamonds and the micro-inclusion-bearing diamonds. Where the useful yields are different, as in the case of Si, the ion-yields for the inclusions are closer with those of oxides.

Although the RIYs from graphite-glass mixtures agree (within error) with the SIMS-EPMA results, they are systematically lower. It is possible to attribute this systematic difference to the different sputtering rate and useful yields of carbon in graphite and diamond. Table 6.6 shows that graphite is sputtered 40% more slowly than diamond (when measured in $gr/cm^2/sec$), but due to its higher useful yield the $^{12}C^+$ count rate is similar in the two materials. If the useful yields of the metal ions is similar in both cases, the relative ion-yields for the metals are expected to be lower, because less material is sputtered in the case of graphite.

As will be shown later, comparison with other techniques (INAA and IR) also suggests that the RIYs from SIMS-EPMA correlations may be underestimated. A possible source may be the cleaning procedure. All inclusions exposed during polishing are digested during acid cleaning, forming a relatively depleted layer close to the surface. The lower surface concentration affects the EPMA analyses, leading to lower average concentration. If the inclusion size is on average ~0.5 μm, then the upper 0.3 μm are almost fully leached and the concentration detected by EPMA may be more than 20% lower than the bulk concentration in the diamond in that region. In principle this should also affect the SIMS results; however, SIMS analyses were preceded by raster-cleaning the area with a 100 nA beam rastered over 100 μm size square area for 10-15 minutes. A 20 nA rastered beam sputters 1.1 Å/sec (Table 6.5). Taking into account the lower current density of the 100 nA beam, its sputtering rate during raster-cleaning is estimated as 4 Å/sec. In 10-15 minutes the upper 0.3 μm would be sputtered, so when SIMS data is collected, the average concentration of the oxide in the analyzed volume is representative of the bulk diamond. The correlation of SIMS count rates with the underestimated concentration from EPMA analysis leads to overestimation of RIYs and underestimation of concentration. This effect may also explain the difference between the RIY from SIMS-EPMA and the graphite-glass determinations.

The above effect acts similarly on all RIYs. It should not affect the accuracy of the determination of elemental ratios or of relative abundance of the different elements. Except for the underestimation of Na, and possibly Mg concentrations (see Section 5.1.3), the SIMS-EPMA correlation is expected to yield good estimation of the composition of the micro-inclusions. It probably underestimates the overall concentration of the trapped material. The underestimation of sodium relative to other elements is probably on the order of ten percent. This effect is small compared with the error resulting from the EPMA-SIMS correlation and would have only a small effect on the final results. Because of the lack of accurate estimates for this error, I chose to use the present value of the RIY from SIMS-EPMA.

It is suggested that a more accurate determination could be obtained by calibrating SIMS count rates against concentrations determined by bulk analyses of micro-inclusion-rich zones of diamonds. The RIYs from SIMS-EPMA calibration are currently the best estimate of SIMS sensitivity for analysis of micro-inclusion-bearing diamonds and are used in the conversion of SIMS count rates to concentrations.

6.3. RESULTS

SIMS analyses have been conducted on the micro-inclusion-bearing zones of 6 cubic diamonds and 9 coated diamonds, 6 cores of coated diamonds, 3 diamonds carrying visible mineral inclusions, 2 synthetic diamonds, and 3 gem-quality diamonds. The analyses of the micro-inclusion-bearing zones show broadly similar compositions. The micro-inclusions in all diamonds are rich in SiO_2, K_2O, CaO, and FeO. Total oxide content varied between 12-1450 ppm. No impurities were found in the clear diamond material of micro-inclusion-free diamonds.

6.3.1. ANALYSIS OF CLEAR DIAMOND MATERIAL

SIMS analysis of the clear, transparent diamond material in the cores of coated diamonds, colorless or yellow gem-quality diamonds, and yellow, synthetic diamonds did not detect any of the metals examined. The same is also true for the colorless, transparent diamond material between visible mineral inclusions in three inclusion-bearing diamonds. All those diamonds yielded similar low count rates, interpreted to represent the machine blank level (Section 6.1.3). The concentrations of impurities in all these diamonds are lower than SIMS detection limits (Table 6.2). The gem diamonds GRR 1162, GRR 980 and the cores of GRR 1504 and CTP L0 carry less than 10 ppb of Na, Mg, K, and Ca, < 200 ppb of Si, Ti and Fe, and < 1 ppm Al. The three diamonds with visible inclusions and the synthetic diamonds were analyzed with cathode I (Table 6.2) and higher Fe and Si detection limits are applicable.

These results are much lower than the results reported by Fesq et al. (1975). They found

160-9000 ppb of Mg, Ca and Fe, and 22-242 ppb Na during INAA analysis of composite samples, each containing 10-20 "inclusion-free" diamonds. A more detailed INAA study of individual inclusion-free diamonds (Bibby, 1979) found lower amounts, less than twice the SIMS detection limits in carefully cleaned colorless diamonds. Similar low levels were also quoted by Orlov (1977, p.36) for some cores of Russian coated diamonds. Higher levels were found by Bibby in green diamonds for which no comparable SIMS data exists. In conclusion it is suggested that the amount of material present as impurity in the diamond lattice must be at the sub-ppb level. The presence of microscopically undetected "melt" inclusions in otherwise inclusion-free diamonds, suggested by Fesq et al. (1975), could not be confirmed.

6.3.2. THE METAL-OXIDE CONTENT OF MICRO-INCLUSION-BEARING DIAMONDS

SIMS analysis of micro-inclusion-bearing zones of 15 diamonds are summarized in Table A.3 of Appendix A. The average compositions of the diamonds are presented in Table 6.11. The composition of the metal-oxide fractions of the micro-inclusions in each diamond are presented as the oxide weight percent of the eight major constituents, normalized to 95%. The remaining 5% consists, on average, of other minor oxides analyzed only by the other techniques: EPMA, analytical SEM, and INAA. The total concentration of the eight metal-oxides in the analyzed volumes is also shown. Several features are apparent in the data. The total concentration of metal-oxides is widely variable. Within a single diamond it may range from practically zero in small, inclusion-free zones within the coats or the cubic diamonds, to 1450 ppm in zones highly populated with micro-inclusions. Although not verified quantitatively, qualitative examination clearly shows that this wide range of concentrations is merely the result of the variation in the number density of inclusions in the analyzed volumes. Normally, the most populated zones of each diamond were chosen for analysis, so that the concentrations detected should be higher than average. However, this is not necessarily the case for all analyses.

The chemical composition of the different areas analyzed is broadly similar (Figs. 6.13,

Table 6.11. Average composition of the major metal-oxide in micro-inclusion-bearing diamonds.

Sample	**CTP** 6268	**CTP** L0	**CTP** L6	**CTP** LB	**CTP** Z4	**CTP** MM1	**GRR** 861.2	**GRR** 1155	**GRR** 1515	**GRR** 1517	**GRR** 1518	**GRR** 1519	**GRR** 1503	**GRR** 1504	**GRR** 1508
SiO2	30.5	38.5	41.3	32.9	66.1	41.1	47.4	51.4	43.8	28.6	40.4	43.5	33.3	40.4	40.5
TiO2	4.6	2.6	2.8	2.3	2.3	3.2	2.7	4.5	2.6	3.7	3.1	3.0	3.1	2.9	3.0
Al2O3	3.1	6.5	5.8	5.9	6.4	4.4	5.5	4.6	4.9	5.6	4.6	5.0	3.4	5.3	5.2
CaO	11.0	11.5	11.2	13.0	1.7	12.4	9.2	8.0	8.3	19.6	10.4	14.0	18.5	8.7	12.6
FeO	16.1	5.2	5.8	5.0	3.4	7.6	9.9	6.7	8.9	5.1	8.2	7.3	8.4	9.2	5.9
MgO	5.8	2.9	3.9	2.3	1.4	4.7	5.9	2.7	8.4	4.3	5.0	5.4	6.6	4.7	3.7
Na2O	2.7	3.2	3.0	3.6	1.0	4.1	3.7	1.1	5.1	2.8	3.5	3.8	3.7	2.6	2.5
K2O	21.3	24.6	21.2	30.0	12.8	17.6	12.0	16.1	13.0	25.3	19.7	13.1	18.6	21.1	21.6
Total[1]	889	406	193	227	1265	21	73	470	564	20	108	86	557	1027	463

1. Average total concentration of the above eight oxides in all volumes analyzed for each diamond (in ppm).

6.14); all are rich in SiO_2, K_2O, CaO and FeO, and carry lower amounts of MgO, Al_2O_3, TiO_2, and Na_2O. The chemical compositions of all diamond analyses fall within the following ranges: SiO_2, 27-67%; TiO_2, 2-5%; Al_2O_3, 3-7%; CaO, 2-22%; FeO, 1-17%; MgO, 2-10%; Na_2O, 1-5%; and K_2O, 10-35%. Intra-diamond variations are commonly much smaller than the full inter-diamond composition range (Figs. 6.13., 6.14., Table A.3). Thus, for example, SiO_2 varies between 27-34% in GRR 1503 or GRR 1517 compared with 50-55% in GRR 1155 and 65-67% in CTP Z4. The standard deviation (1σ) for intra-sample variation for most diamonds is smaller than 10%. Exceptions are GRR 1504, GRR 1508 and CTP LB, which show a larger scatter of about 10-20% for most elements. Fe concentrations show up to 44% scatter, mainly because of the large blank corrections in early measurements. All of these standard deviations should be compared with deviations of 21-48% for the full set of analyses.

Examination of the compositions of diamonds with extreme compositions suggests correlation between the abundances of a few of the elements. For example, high CaO content is associated with low silica and high K_2O in diamonds GRR 1517 and GRR 1503; the lowest CaO content is found in the silica rich diamond CTP Z4. Broad negative correlations between CaO and SiO_2 is found for the full data set as well. Such correlations may be an artifact of normalizing the concentration of each oxide to the total oxide content. However, weak positive correlations are also found between Na_2O/SiO_2 or K_2O/SiO_2 and CaO/SiO_2 ratios. No other correlating elemental ratios were found.

The average compositions of the analyzed zones reflect the bulk chemistry of the material trapped in the diamond. Additional information on the composition of phases in the inclusions may be derived from the examination of relative variation in ion count rates during individual runs. Figure 6.15 shows the intensity of the various elements (each normalized to its maximum intensity, in order to have them all on the same scale). The intensities of all elements follow a similar pattern in time; all rise when a large inclusion is penetrated, and go down as it is sputtered away. This similarity suggests that all elements are present in each of the large inclusions (and perhaps, in the small ones as well). Close examination reveals a somewhat independent behavior for Ca and to a lesser extent K and Na.

Figure 6.13. Al_2O_3 - Na_2O - K_2O in analysis of individual micro-inclusion-bearing zones in diamonds.

Each diamond is represented by a different symbol.

All diamonds show similar composition with K_2O/Al_2O_3 and K_2O/Na_2O ratios above 2. Analysis of different zones of individual diamonds shows a limited intra-diamond compositional variability, compared with the full range for all diamonds.

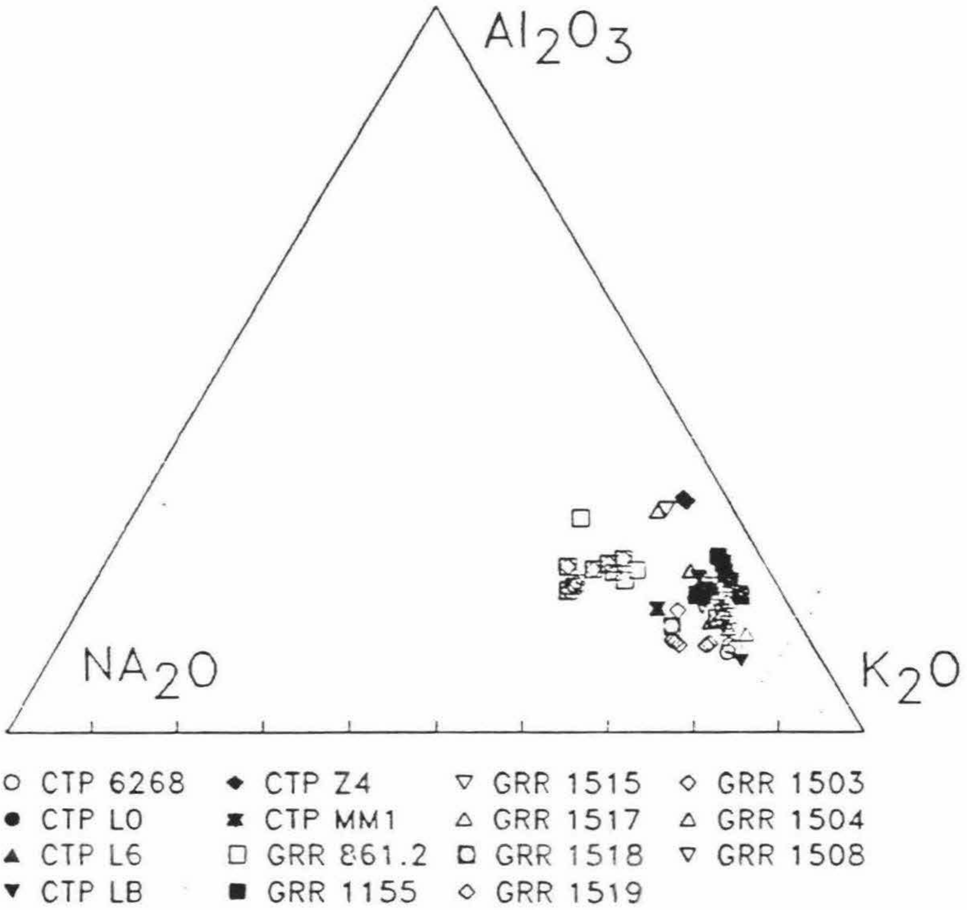
Al$_2$O$_3$
NA$_2$O
K$_2$O
○ CTP 6268
● CTP L0
▲ CTP L6
▼ CTP LB
◆ CTP Z4
✖ CTP MM1
□ GRR 861.2
■ GRR 1155
▽ GRR 1515
△ GRR 1517
□ GRR 1518
◇ GRR 1519
◇ GRR 1503
△ GRR 1504
▽ GRR 1508

Figure 6.14. SiO_2 - CaO - Na_2O+K_2O in individual analyses of micro-inclusion-bearing zones in diamonds.

Symbols as in Figure 6.13.

The range of compositions spanned by the diamonds is somewhat than in Figure 6.13. This is mainly due to variations in SiO_2/CaO and SiO_2/K_2O ratios. The $CaO/(Na_2O+K_2O)$ ratio is more uniform.

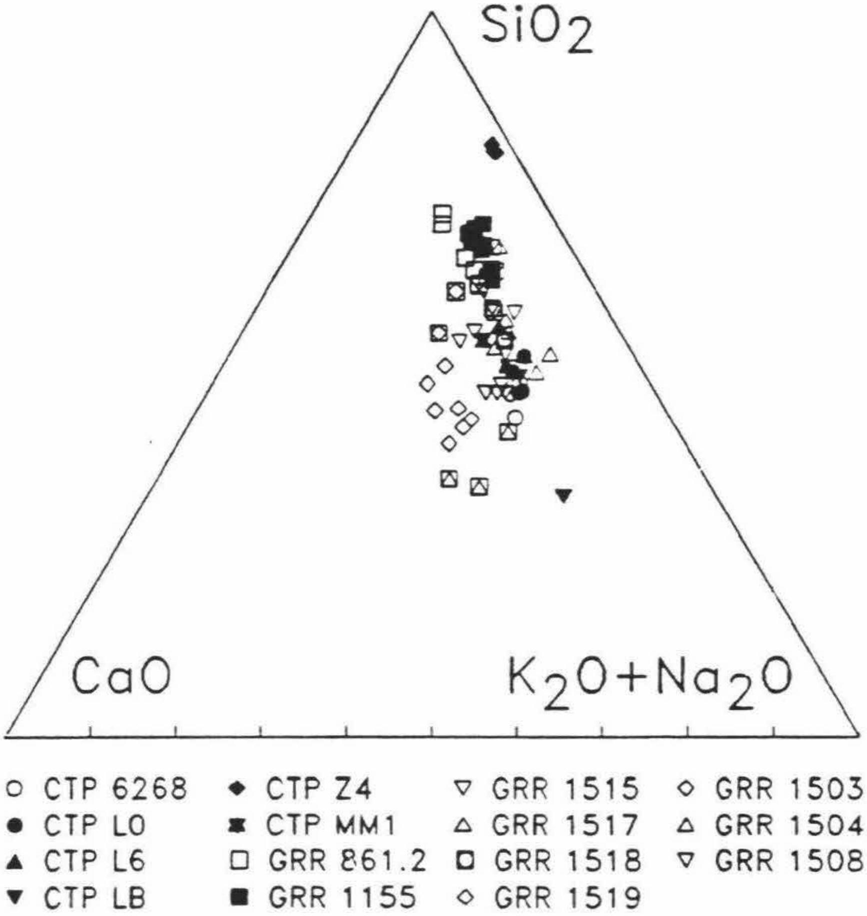
SiO2
CaO
K2O+Na2O
○ CTP 6268
● CTP L0
▲ CTP L6
▼ CTP LB
◆ CTP Z4
✖ CTP MM1
□ GRR 861.2
■ GRR 1155
▽ GRR 1515
△ GRR 1517
□ GRR 1518
◇ GRR 1519
◇ GRR 1503
△ GRR 1504
▽ GRR 1508

Figure 6.15. Variation in secondary-ion-intensities during a run.

The carbon-normalized intensities of all elements measured were re-normalized, each relative to its maximum intensity. Two main features are to be noted: 1. All elements follow similar patterns in time. The peaks are attributed to penetration and sputtered of some large micro-clusions. The base level is due to contemporaneous sputtering of many smaller inclusions. 2. Ca, Na, and K (all represented by open symbols) follow slightly different patterns in time compared with the other elements. This can be clearly viewed in cycles 25-35 where the intensity of these three elements occurs later than the others. Ca clearly shows different behavior than the other elements during cycles 37-45.

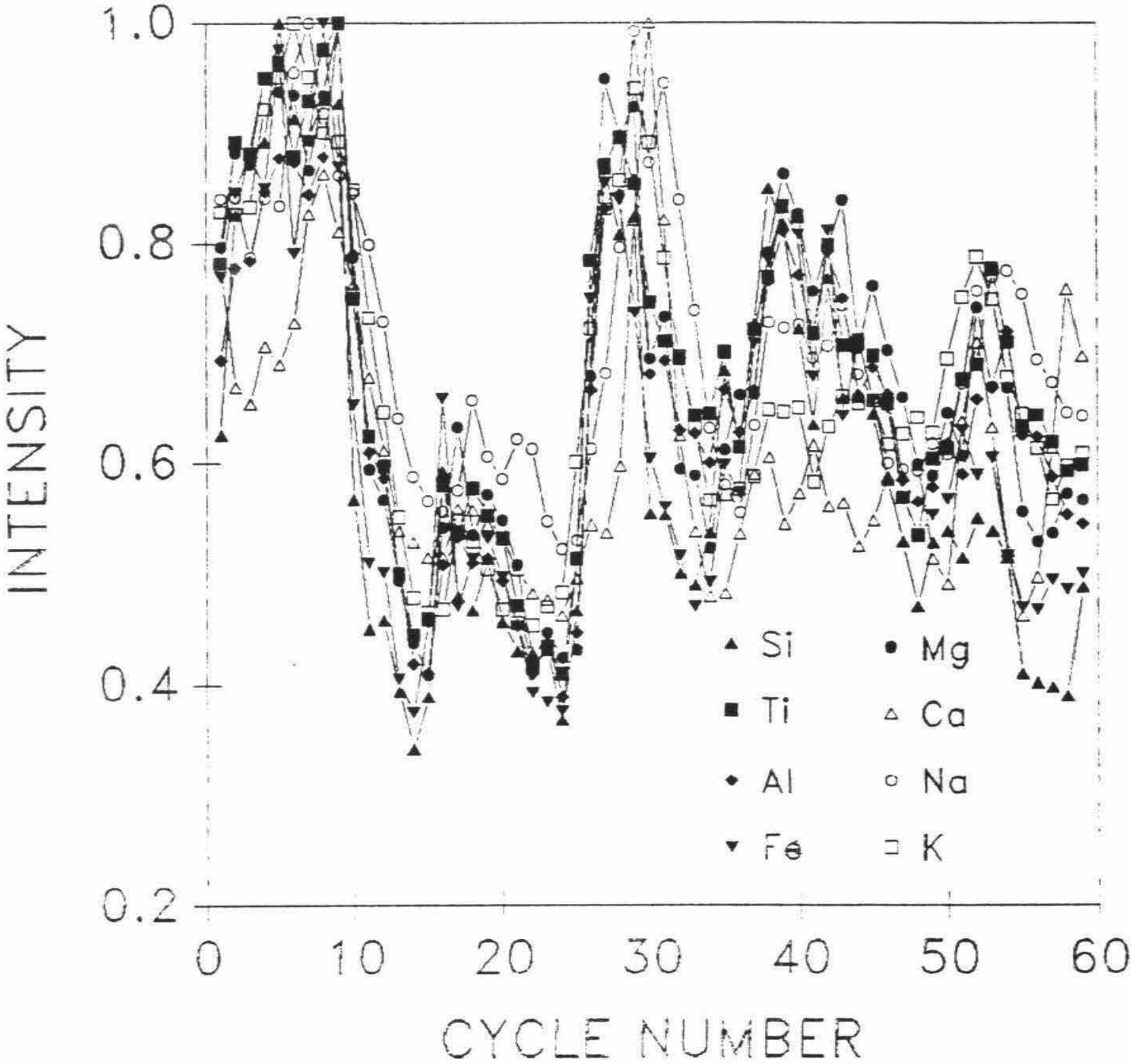
INTENSITY
CYCLE NUMBER
1.0
0.8
0.6
0.4
0.2
0
10
20
30
40
50
60
▲ Si
■ Ti
◆ Al
▼ Fe
● Mg
△ Ca
○ Na
□ K

For example, when a large inclusion is penetrated at cycle 24, all intensities rise, but Na and Ca rise a little later and together with K, their intensities are kept high 3-5 cycles after the intensities of Si, Fe, Al and Ti are back to normal levels. In addition, while plotting the intensities of all elements vs. that of Si, good correlations were observed for Al, Ti, Mg, and to a lesser extent Fe and K during individual runs. In most runs Ca or Na intensities do not correlate with Si intensity. It is suggested that Ca and Na and possibly K and Fe are associated with non-silicate phases, while the other elements are present mainly in silicate phases.

6.3.3. SUMMARY

SIMS analysis of micro-inclusion-rich zones in cubic and coated octahedral diamondsindicates a broadly similar composition for all diamonds. The average composition of the diamonds is within the following limits: SiO_2, 29-66%; TiO_2, 2-5%; Al_2O_3, 3-7%; FeO, 3-17%; CaO, 2-21%; MgO, 1-9%; Na_2O, 1-5%; K_2O, 12-30%. Intra-diamond variability is limited to about ±10% (1σ relative). The total metal-oxide concentration in the diamonds varies between 20 and 1400 ppm, reflecting the variation in the number density of inclusions. Variations of metal-ion count rates during runs suggest that all elements are present in the individual inclusions. Ca, and perhaps Na, K and Fe may be associated with non-silicate phases.

CHAPTER 7 ANALYTICAL SCANNING ELECTRON MICROSCOPY

The composition of individual inclusions was studied using energy dispersive x-ray spectrometry (EDS) on an analytical scanning electron microscope (SEM). The purpose of these analyses was to check whether:

1. The individual inclusions were mono- or poly-mineralic.
2. All micro-inclusions contained the same material, or if their compositions varied from one micro-inclusion to the other and the compositions detected by EPMA and SIMS were averages of many inclusions with a wide range of compositions. In addition it was hoped to view the morphology and internal structure of the included material.

No exposed inclusions were found on the surface of either a freshly-cleaved diamond or a polished diamond cleaned only with alcohol and freon. Imaging with both backscattered and secondary electron modes revealed only a few empty, shallow depressions, of sub-micrometer size. No foreign material was found in any of these depressions. However, sub-surface, shallow inclusions were detected, so it was possible to conduct a detailed study of the composition of individual micro-inclusions.

This chapter describes the EDS analysis of the sub-surface microscopic inclusions. Section 7.1. describes the analytical technique and the problems associated with the x-ray analysis of inclusions smaller than the size of the analyzed volume. Although the concentrations detected are close to the detection limit of the machine, and few simplifying assumptions have to be made, the 76 analyses of individual inclusions allow for definite answers to the two questions stated above. These results are discussed in Section 7.2.

7.1. EXPERIMENTAL METHOD

7.1.1. ANALYTICAL PROCEDURE

Five polished diamonds were cleaned using the normal procedure (see Section 4.2.3), mounted in epoxy in brass sleeves and coated with carbon. They were examined with a

JEOL JSM 35CF electron microscope using both secondary electron and backscattered electron microscopy. Sub-surface inclusions were found as light, cloud-like areas in both imaging modes (Fig. 7.1.). They appear somewhat sharper in the secondary electron mode but can still be distinguished from surface graphite particles (from the carbon coater) by their fuzzy contours and by comparison with backscattered electron imaging, where the small graphite particles do not show.

The inclusions were analyzed using a 0.075 nA, 15 kV beam. The beam was rastered over a 0.3x0.3 μm or larger area so that the whole inclusion was covered by the beam. Spectra were collected for 200 sec using a Tracor Northern TN5500 EDS analyzer and were deconvoluted using the Tracor Northern software. Count-rates were compared against pure oxide and silicate standards to give k-ratios that were processed using the same ZAF procedure used for the reduction of the EPMA data (section 5.1.3.).

Build-up of surface contamination spot was found to affect analysis only if the beam was not rastered. Using rastered beam, no reduction in the total impurity content was observed during eight, 50 sec long, repeated analyses of a single inclusion.

The micro-inclusions are smaller than the volume analyzed by the SEM. Thus, the correction procedure must correct for the affect of the carbon matrix on electrons and x-rays. (A detailed discussion of the correction procedure is given in section 5.1.3. in connection with the reduction of EPMA data.) Analysis of graphite-glass pellet containing 2% of fine glass powder, was compared with the EPMA analysis of the glass itself. As in the case of EPMA analysis, better agreement was obtained using the carbon matrix, rather than the pure oxide approximation (Table 7.1., see Section 5.1.3. for the details of these approximations). The ZAF correction program was adjusted to calculate the carbon content of the analytical volume by assuming that carbon completes the total of each analysis to 100%. The carbon was then included in following iterations. This procedure is similar to that employed during reduction of EPMA data.

Correction procedures employed for particle analysis do not approximate the situation in any better way. They are designed for particles in air, while here, the inclusions are in a

Figure 7.1. Sub-surface micro-inclusions in diamond GRR 1503.

a. Secondary electron imaging. The sub-surface micro-inclusions appear as small, faint, fuzzy spots (numbered). The small bright spots are carbon particles from the carbon coater. The three large spots at the bottom left are contamination spots built during previous SEM analyses. The large circles are the traces of the contamination built during earlier EPMA analysis. (In most of the EPMA analyses the circles do not overlap as in this one.) Lines running from left to right are polishing grooves.

b. Back-scattered electron imaging of the same area. The sub surface inclusions can be better recognized and the carbon grains do not appear.

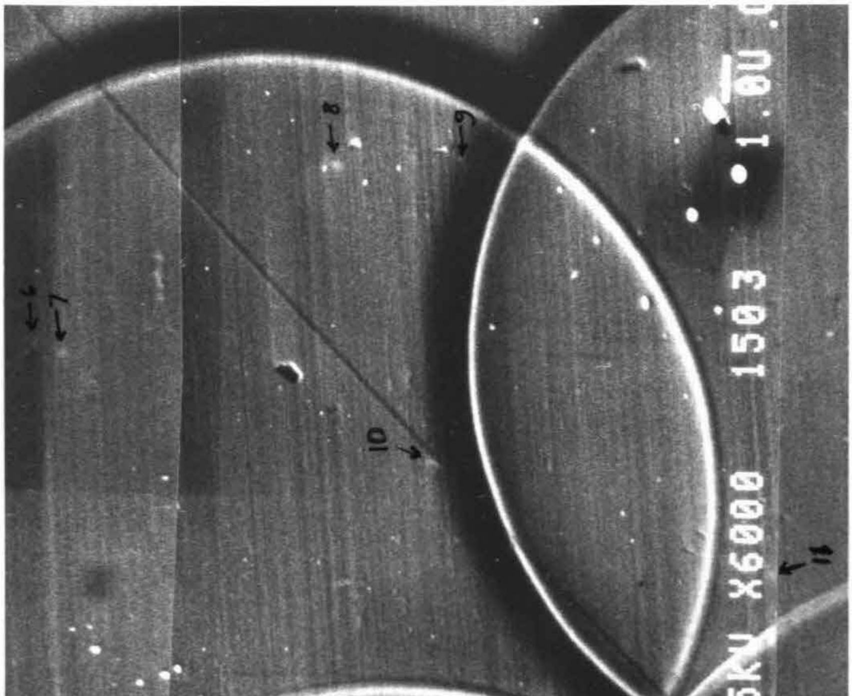
7
8
9
10
11
12
15KV X6000 1503 1.00U

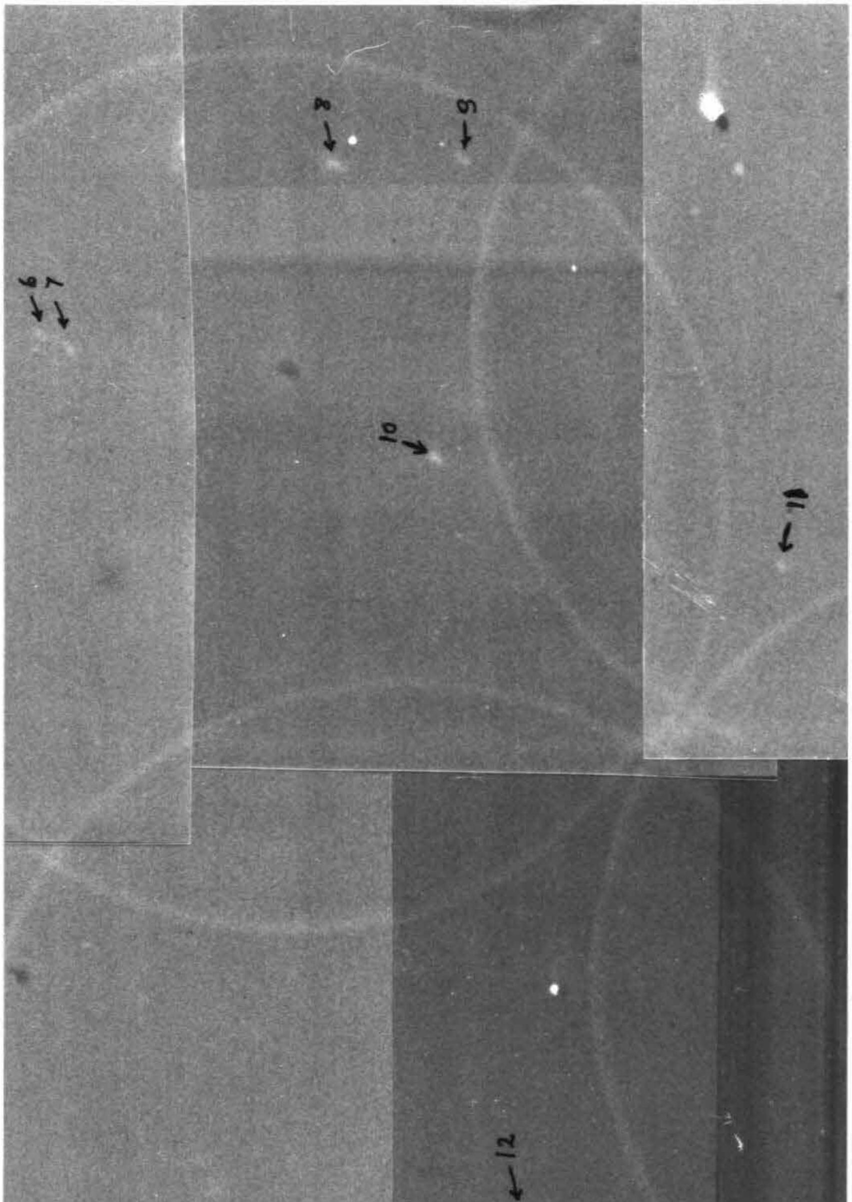
6
7
8
9
10
11
12

Table 7.1. Comparison of correction procedures for SEM data. The average composition of glass in a graphite-glass pellet.

	Na_2O	Al_2O_3	SiO_2	K_2O	FeO
Pure glass by EPMA	5.0	18.0	65.7	9.1	2.2
<u>Glass in pellet.</u>					
Carbon by difference[1]	5.0	17.7	66.2	9.2	1.9
Stan. Dev.[2]	43%	3%	5%	11%	74%
Difference from pure glass	-0.3%	-2%	1%	2%	-16%
Pure oxide[3] correction	5.6	17.4	67.0	8.5	1.6
Stan. Dev.	43%	3%	5%	11%	74%
Difference from pure glass	12%	-4%	2%	-6%	-29%

1. Average of five EDS analyses of different sub-micron glass grains on the pellet surface. Correction procedure includes carbon by assuming it completes the total weight to 100%.

2. Standard deviation of the individual analyses from the average value.

3. Average composition of the glass in the pellets obtained by correcting the raw data of the same five analyses, assuming that the whole analyzed volume is comprised of the detected oxides.

carbon matrix. Adaptation of these programs for the case of inclusions in diamond matrix was not attempted.

7.1.2. ANALYTICAL ERROR

Total oxide concentration is typically ~2-7 wt% (Tables 7.2, 7.3), and minor elements are close to their detection limit (Table 7.2). Errors are typically of the order of 0.1 wt% and result in large uncertainties, of the order of 10-60% (relative), for all elements except for Si, K and, in most cases, Ca, for which relative uncertainties are of the order of 2-10%.

7.2. RESULTS

7.2.1. INCLUSION SIZE

The results of 76 EDS analyses of micro-inclusions in five diamonds are summarized in Table 7.3. Total oxide concentrations are always much less than 100%, as the inclusions occupy only a fraction of the analyzed volume. The oxide fraction typically amounts to less than 7% of the content of that volume. Only a few analyses have higher content, up to 20% of the volume analyzed (Figure 7.2). The small number of analyses with low oxide concentrations is probably due to sampling bias; it is hard to identify small inclusions by electron microscopy. An average oxide content of 4% and an estimated total analyzed volume of ~ 2-5 μm^3 (1.5 to 2 μm electron penetration depth) yields average inclusion diameter of 0.4-0.6 μm.

7.2.2. THE COMPOSITION OF INDIVIDUAL INCLUSIONS

All inclusions are rich in Si, K, Ca and Fe. The only exception is GRR 1504.24 which contains S and Fe and will be discussed later. The composition of the micro-inclusions does not correspond to any common mineral phase, suggesting they are not monomineralic. Rather it fits the total composition inferred by a TEM study of individual inclusions in a coated diamond (Lang and Walmsley, 1983). This study revealed a multi-phase assemblage, including apatite and a Si and K rich material. A TEM study of some of the diamonds described here is underway and reveals a similar situation (G. Guthrie and D. Veblen,

Table 7.2. EDS analysis of micro-inclusion #46 in diamond GRR 1503.

element	Counts[1] ± 1σ	Concentration[2] ± 2σ	Composition[3] ± 2σ
Si	4581 ± 103	1.83 ± 0.07	36.2 ± 4%
Ti	300 ± 61	0.22 ± 0.09	4.3 ± 40%
Al	494 ± 81	0.20 ± 0.06	3.9 ± 32%
Ca	1420 ± 76	0.63 ± 0.08	12.5 ± 12%
Fe	648 ± 61	0.74 ± 0.15	14.7 ± 20%
Mg	509 ± 67	0.24 ± 0.06	4.8 ± 25%
Na	184 ± 51	0.14 ± 0.08	2.8 ± 56%
K	2190 ± 85	0.76 ± 0.06	15.1 ± 8%
P	468 ± 94	0.21 ± 0.08	4.1 ± 40%
Cl	371 ± 77	0.07 ± 0.03	1.4 ± 42%
Total		5.04	100.0

1. Counts collected during 200-second analysis.

2. Concentrations of the different elements in the analyzed volumes expressed as wt% of their oxides (Fe as FeO, P as P_2O_5). The other 94.96% of the total weight of the analyzed volume is assumed to consist of carbon.

3. Composition of the metal oxides in the inclusion, calculated by normalizing the total content of all oxides (5.04%) to 100%.composition

Table 7.3. Summary of EDS analyses. a. GRR 1503

	1503.17	1503.18	1503.19	1503.20	1503.21	1503.22	1503.23	1503.24	1503.26	1503.27	1503.29	1503.30
SiO2	16.4	21.3	25.4	16.1	26.1	29.1	21.4	17.5	24.2	20.9	21.9	30.6
TiO2	0.9	2.7	2.0	3.2	3.0	4.7	4.1	4.7	5.0	3.3	2.8	4.5
Al2O3	1.0	1.7	1.2	2.0	3.1	0.0	2.5	2.0	3.7	2.8	3.9	3.2
CaO	29.8	21.4	24.2	25.6	22.5	14.2	19.1	21.9	18.6	19.9	27.8	11.9
FeO	15.7	22.4	12.7	19.3	16.7	27.7	19.8	19.3	19.0	20.0	11.7	16.0
MgO	7.0	7.5	3.5	6.3	3.8	6.7	5.8	6.3	4.7	5.9	6.7	4.9
Na2O	3.2	3.8	2.6	3.1	4.3	2.2	5.2	5.6	3.9	4.5	3.3	4.5
K2O	13.1	14.0	12.7	13.4	16.4	6.7	15.2	13.6	12.6	13.4	13.4	19.1
P2O5	9.9	1.2	12.7	8.3	1.9	1.8	3.2	4.9	5.2	7.6	6.8	2.6
Cl	0.9	2.6	1.9	2.0	1.1	0.0	2.4	2.5	1.5	1.7	1.7	2.6
Cr2O3	0.8	1.4	1.0	0.7	1.2	4.1	0.0	1.6	0.0	0.0	0.0	0.0
SO3	1.2	0.0	0.0	0.0	0.0	2.7	1.3	0.0	1.5	0.0	0.0	0.0
Total	4.0	4.3	5.1	6.7	2.8	2.0	3.8	3.3	4.9	3.4	6.0	4.3

	1503.31	1503.31	1503.32	1503.33	1503.34	1503.35	1503.37	1503.38	1503.39	1503.40	1503.41	1503.44
SiO2	24.8	25.6	23.1	24.6	29.1	28.3	29.7	34.3	28.1	30.6	35.6	29.3
TiO2	3.6	3.1	3.4	3.4	2.2	2.8	3.2	4.2	6.4	5.5	4.7	2.3
Al2O3	2.7	2.8	3.4	2.8	1.2	2.1	3.9	3.1	0.0	0.0	2.8	4.2
CaO	18.4	19.7	17.9	18.7	19.8	19.2	16.3	14.7	14.4	15.6	9.4	16.1
FeO	21.4	21.8	24.0	20.3	20.0	18.2	13.9	16.7	20.3	25.4	18.6	17.2
MgO	7.0	6.2	6.8	6.1	4.6	5.2	5.1	3.7	5.4	2.7	4.8	5.3
Na2O	2.9	3.4	3.6	3.1	1.9	2.4	2.8	3.7	5.8	3.5	4.5	5.3
K2O	11.8	9.9	12.8	13.3	13.9	13.3	15.8	16.9	14.9	15.5	15.2	14.7
P2O5	2.8	4.4	3.5	4.1	5.1	6.6	4.9	0.0	0.0	0.0	0.0	3.0
Cl	2.4	1.4	1.5	1.3	2.1	1.8	2.5	2.7	2.0	1.2	2.5	2.5
Cr2O3	1.2	1.5	0.0	1.4	0.0	0.0	1.9	0.0	2.8	0.0	1.9	0.0
SO3	0.9	0.0	0.0	0.9	0.0	0.0	0.0	0.0	0.0	0.0	0.0	0.0
Total	6.5	5.2	5.9	4.4	3.7	5.6	3.3	3.2	2.7	2.1	2.8	3.5

1. Results are in oxide wt%, normalized to total oxide (+chloride) content = 100%

2. Actual total concentration of oxides and chloride detected in the analysis.

Table 7.3. Summary of EDS analyses: a. GRR 1503 (cont)

	1503.45	1503.46	1503.47	1503.48	1503.48	1503.49	1503.49	1503.50	1503.50	1503.52	1503.52	1503.53
SiO2	43.3	36.2	26.3	29.3	23.2	21.9	27.0	45.3	37.8	35.4	30.3	33.6
TiO2	2.9	4.3	4.8	3.5	2.0	2.7	0.0	3.2	2.2	6.4	3.4	4.3
Al2O3	5.4	3.9	2.8	2.7	1.9	3.8	5.4	5.0	4.0	3.6	3.6	5.0
CaO	7.1	12.5	18.2	15.9	21.8	22.5	17.8	5.6	8.0	3.2	12.0	8.9
FeO	16.7	14.7	15.0	12.4	17.3	24.8	21.9	15.7	13.9	21.0	15.3	13.9
MgO	5.1	4.8	5.7	4.7	6.7	5.7	4.7	3.8	1.5	2.1	2.9	2.3
Na2O	2.8	2.8	6.2	6.0	6.3	4.6	5.6	1.9	2.3	4.6	4.8	3.1
K2O	13.3	15.1	13.5	16.1	13.4	10.7	8.9	16.2	22.3	19.2	22.3	24.1
P2O5	1.9	4.1	5.5	7.2	5.4	0.0	0.0	0.0	2.8	0.0	1.4	1.6
Cl	1.4	1.4	2.1	2.3	2.2	3.3	2.9	1.8	3.5	2.2	2.1	3.2
Cr2O3	0.0	0.0	0.0	0.0	0.0	0.0	5.8	1.6	0.0	2.4	1.9	0.0
SO3	0.0	0.0	0.0	0.0	0.0	0.0	0.0	0.0	1.6	0.0	0.0	0.0
Total	5.4	5.0	4.7	5.0	2.6	1.8	1.6	4.3	3.9	2.6	3.5	5.8

1. Results are in oxide wt%, normalized to total oxide (+chloride) content = 100%

2. Actual total concentration of oxides and chloride detected in the analysis.

Table 7.3. Summary of EDS analyses. b. GRR 1504

	1504.04	1504.05	1504.06	1504.07	1504.08	1504.09	1504.10	1504.11	1504.11	1504.12	1504.13
SiO_2	35.8	40.2	44.7	44.3	43.3	43.4	36.0	44.7	57.2	25.2	41.1
TiO_2	2.6	0.0	5.0	5.6	5.1	4.9	1.4	1.7	0.0	2.5	2.6
Al_2O_3	4.0	3.1	3.4	4.6	2.7	3.2	4.2	4.3	4.3	2.6	3.3
CaO	17.0	10.3	5.0	8.9	4.4	7.7	10.0	20.6	3.2	21.8	8.6
FeO	6.8	9.4	7.7	8.9	14.3	14.5	21.2	6.4	22.5	14.0	10.2
MgO	3.0	3.7	2.7	4.2	3.0	3.7	4.1	2.1	2.3	2.2	3.5
Na_2O	3.6	4.8	6.2	2.3	4.0	1.2	2.5	1.0	3.1	3.9	2.8
K_2O	17.6	20.4	20.1	16.2	15.9	15.0	13.8	5.7	4.5	20.1	17.8
P_2O_5	6.7	5.5	3.4	3.0	3.1	4.5	3.9	13.2	3.1	4.9	6.8
Cl	2.9	2.7	1.8	2.0	2.2	2.0	1.7	0.2	0.0	2.6	1.7
Cr_2O_3	0.0	0.0	0.0	0.0	2.0	0.0	1.0	0.0	0.0	0.0	-0.0
SO_3	0.0	0.0	0.0	0.0	0.0	0.0	0.0	0.0	0.0	0.0	1.7
Total	3.2	3.5	2.1	2.2	2.1	3.5	3.8	19.2	3.3	3.6	2.5

	1504.14	1504.15	1504.16	1504.17	1504.19	1504.20	1504.21	1504.22	1504.23	1504.25	1504.24
SiO_2	41.8	52.6	40.1	36.0	38.2	39.1	42.1	22.6	47.0	43.3	3.7
TiO_2	3.9	3.8	5.2	3.3	2.8	3.2	5.6	4.0	0.0	4.7	0.0
Al_2O_3	5.0	6.6	6.4	4.4	4.3	5.0	4.3	1.9	2.8	4.5	0.7
CaO	8.2	1.5	0.7	6.2	10.4	6.0	8.9	40.7	7.3	12.2	0.0
FeO	24.5	14.8	26.4	25.3	9.2	11.5	10.0	6.3	13.1	14.7	38.8
MgO	5.9	5.5	9.0	4.8	3.5	4.6	3.8	1.5	3.7	4.3	0.6
Na_2O	1.1	1.1	1.1	1.5	4.8	4.3	2.1	0.9	3.3	2.0	1.0
K_2O	7.4	12.8	10.4	12.3	20.0	23.8	18.2	2.2	19.9	6.8	0.5
P_2O_5	2.3	0.8	0.0	3.3	3.3	0.0	2.6	18.5	0.0	6.2	2.6
Cl	0.0	0.1	0.2	0.4	3.4	2.5	2.3	0.5	2.9	0.7	0.0
Cr_2O_3	0.0	0.0	0.4	0.6	0.0	0.0	0.0	0.0	0.0	0.0	0.0
SO_3	0.0	0.5	0.0	0.0	0.0	0.0	0.0	0.9	0.0	0.7	52.1
Total	3.3	13.3	8.9	9.3	3.6	3.8	2.7	7.1	1.5	5.7	5.0

1. Results are in oxide wt%, normalized to total oxide (+chloride) content = 100%

2. Actual total concentration of oxides and chloride detected in the analysis.

Table 7.3. Summary of EDS analyses: c. GRR 1508

	1508.01	1508.02	1508.03	1508.04	1508.05	1508.06	1508.07	1508.08	1508.11	1508.13	1508.15	1508.16
SiO2	39.4	44.3	38.9	37.7	44.0	58.8	52.4	50.5	33.7	38.2	47.1	37.1
TiO2	4.4	3.1	3.7	5.6	4.3	3.5	4.1	3.1	4.2	4.3	0.0	0.0
Al2O3	5.1	5.9	2.4	7.4	5.4	6.8	5.7	7.3	4.5	4.1	3.2	5.5
CaO	14.2	5.0	12.5	10.3	7.7	3.3	4.9	4.5	14.7	10.8	10.5	18.1
FeO	10.3	6.1	3.6	6.2	9.2	3.6	9.1	0.0	10.1	8.5	5.0	5.9
MgO	2.0	2.4	3.5	2.6	3.0	1.2	1.4	3.3	4.8	3.5	6.9	0.0
Na2O	0.0	3.7	6.7	5.6	1.9	1.9	3.1	10.4	2.1	2.6	0.0	6.7
K2O	17.7	19.1	24.4	19.1	19.2	16.5	17.1	18.0	18.3	20.1	21.7	18.6
P2O5	5.1	4.0	2.5	0.0	2.7	2.1	0.0	0.0	4.0	3.6	0.0	5.3
Cl	1.8	3.6	1.8	2.8	2.5	1.5	2.2	2.8	3.6	3.0	5.6	2.8
Cr2O3	0.0	0.0	0.0	0.0	0.0	0.9	0.0	0.0	0.0	0.0	0.0	0.0
SO3	0.0	2.6	0.0	2.6	0.0	0.0	0.0	0.0	0.0	1.3	0.0	0.0
Total	1.3	1.0	1.9	2.1	3.2	4.9	3.0	1.1	3.8	4.4	0.8	1.2

Table 7.3. Summary of EDS analyses: d. GRR 1518 e. GRR 1155

	1518.01	1518.03	1518.04	1518.05	1155.31	1155.34
SiO2	9.1	64.0	41.0	40.7	35.8	41.6
TiO2	4.2	1.6	3.5	0.0	3.7	8.1
Al2O3	6.1	5.1	3.7	3.3	4.5	0.0
CaO	16.8	1.1	7.5	8.3	8.9	10.9
FeO	15.2	7.8	12.0	16.0	13.2	7.8
MgO	4.2	5.9	4.0	7.6	2.2	0.0
Na2O	4.3	2.6	7.8	5.1	1.8	9.6
K2O	23.5	11.1	16.0	13.6	17.0	17.1
P2O5	11.4	0.0	2.7	0.0	0.0	0.0
Cl	2.2	0.8	1.8	1.0	0.0	1.4
Cr2O3	3.0	0.0	0.0	4.3	12.8	3.5
SO3	0.0	0.0	0.0	0.0	0.0	0.0
Total	4.4	14.7	12.5	8.2	1.8	1.1

1. Results are in oxide wt%, normalized to total oxide (+chloride) content = 100%

2. Actual total concentration of oxides and chloride detected in the analysis.

Figure 7.2. Histogram of total oxide content in EDS analyzed volumes.

The total content of oxides (wt%) in the volumes analyzed in 76 EDS analyses of individual micro-inclusions. The detected oxide fraction depends on the inclusion size and on its depth below the surface. Inclusions that yielded less than 1% total were not included. The lower abundance of inclusions in the 1-3% range may be due to real size distribution, or due to sampling bias against these smaller (or deeper), harder-to-detect inclusions.

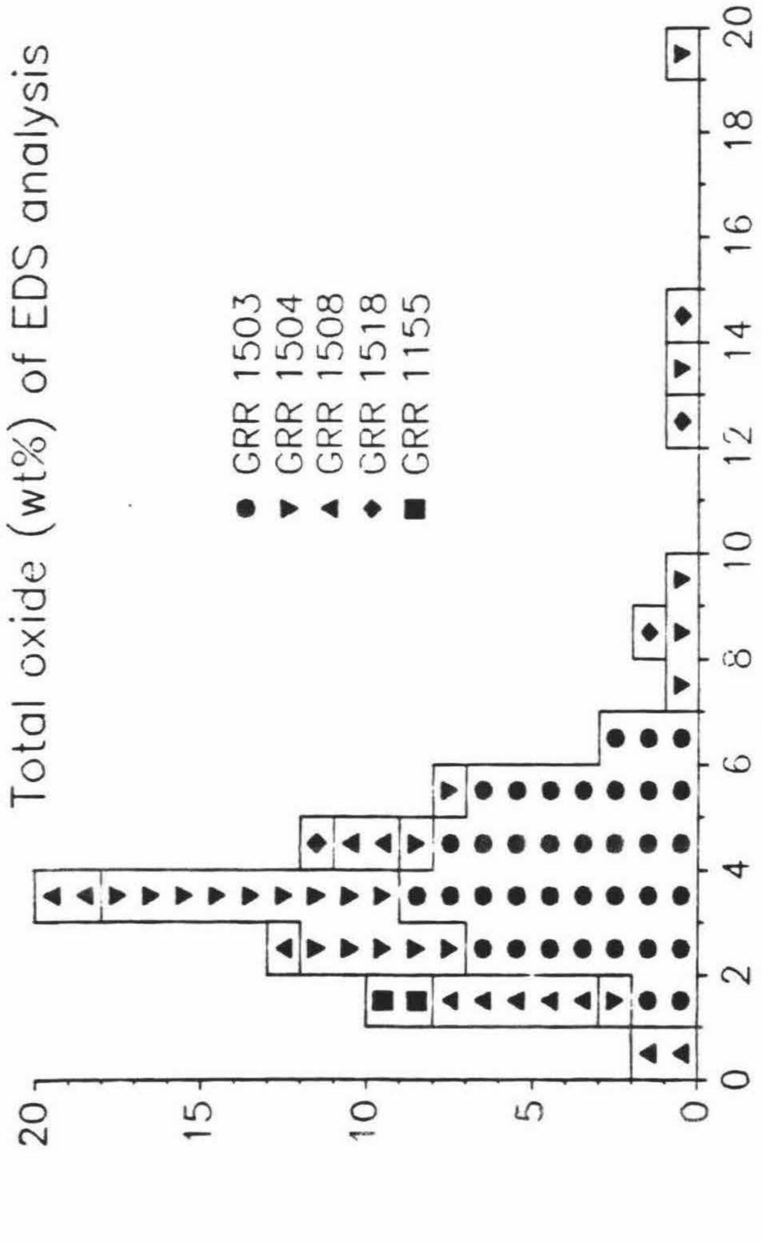
Total oxide (wt%) of EDS analysis
● GRR 1503
▼ GRR 1504
▲ GRR 1508
◆ GRR 1518
■ GRR 1155
0
5
10
15
20
0
2
4
6
8
10
12
14
16
18
20
WT % OXIDES

personal communication).

Assuming that all the elements detected are present as oxides (and chlorides), it is possible to normalize the total oxide concentration to 100% and to calculate the bulk composition of the micro-inclusions. In general, the composition of the individual inclusions shows similarities to the average composition detected by SIMS analysis. In addition, the EDS analysis reveals relatively high contents of phosphorus (typically, 2-4%; maximum 18% of the total weight of the oxide fraction) and chlorine (typically, 1-2%, up to 5%). Low concentrations of Cr and S show only in a few, otherwise normal samples. It is concluded that concentrations of Cr and S in the diamonds are below the EDS detection limit. A single inclusion was found to contain only Fe and S in proportions of $Fe_{0.83}S$. It was not possible to check this inclusion optically to see whether it is well isolated or is associated with a crack.

7.2.3. VARIATION IN COMPOSITION OF INDIVIDUAL INCLUSIONS

The range of chemical compositions revealed by the EDS analysis is much wider than that of the SIMS results. It is necessary to determine whether this wide range reflects real variation in the composition of individual inclusions (with the SIMS results representing an average), or if the range can be fully explained by the large analytical errors. I will first discuss in detail the second possibility, examining the various possible sources of error. The final conclusion is that the scatter of the EDS results cannot be due to analytical error alone. The EDS data show some real variation in the composition of individual inclusions.

The two main sources of analytical error which may produce observable variations are the low precision of the data and the errors introduced by the correction procedure.

1. Normal scatter of low precision data. Errors of up to 50% were estimated and clearly some scatter must be related to the poor statistics. However, as can be seen in Figure 7.3, although the uncertainties in Al concentrations are larger than those associated with Si or Ca, the SiO2/Al2O3 ratios show only limited scatter compared

Figure 7.3. SiO_2 - Al_2O_3 - CaO in EDS analyses of sub-surface inclusions.

The variation in SiO_2/Al_2O_3 ratios of most samples is within the 2σ limits of the analyses. The variation in SiO_2/CaO ratios is much wider, although the counting statistics predict much smaller variation. As discussed in the text, this large variation reflects, at least in part, real variation in inclusion composition.

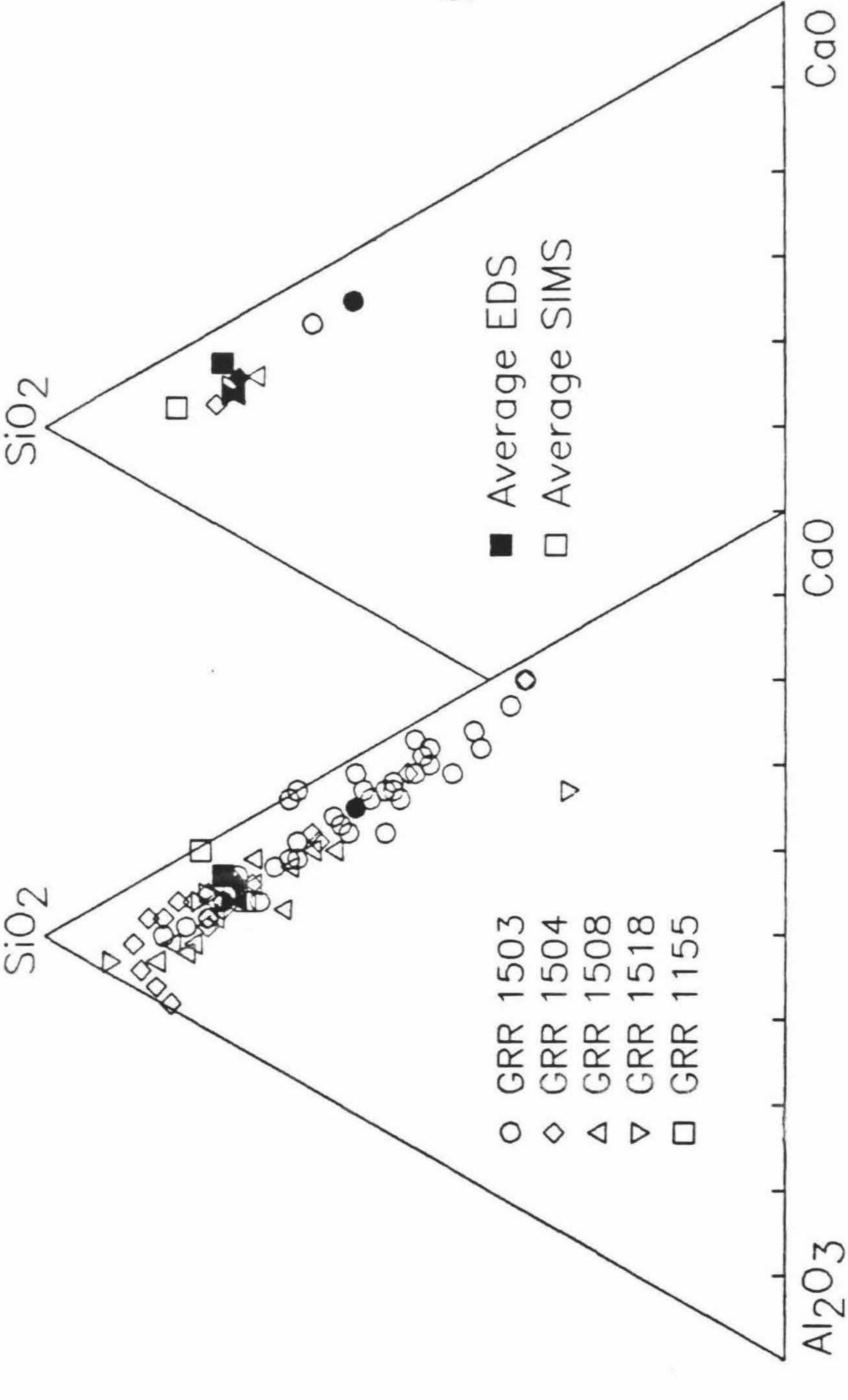
Al_2O_3
SiO_2
CaO
SiO_2
CaO
○ GRR 1503
◇ GRR 1504
△ GRR 1508
▽ GRR 1518
□ GRR 1155
■ Average EDS
□ Average SIMS

with the SiO2/CaO ratios. Thus there must be an additional cause for the wide range of compositions.

2. Differences in the geometric arrangements of individual phases relative to the EDS detector. Phases that are located closer to the surface get higher electron intensities, and the x-rays produced by them are not absorbed as efficiently as in the case of more deeply buried phases. Because the location within the micro-inclusion is random, the calculated concentration ratios for two elements associated with two different phases will vary, depending on which phase lies on top and which on the bottom. Even if two elements are associated with the same phase, differences in the mass absorption coefficients of their x-rays by the overlying layer (either another phase in the inclusion or the diamond matrix), may lead to change in the elemental ratio recorded as a function of depth. This effect should be strong in the case of pairs of light and heavy elements, e.g., K/Na, Fe/Mg.

I calculated the magnitude of these effects for two typical cases:

a) The variation of Ca/Si ratios in layered inclusions (not to be confused with "layered intrusions").

b) K/Na ratios in thin feldspar films as a function of depth.

Considering the first case, imagine two inclusions, each consisting of two thin films of equal thickness, one of calcite, the other of silica. In one inclusion the calcite is the top layer, in the other, silica. EDS analyses of the two inclusions would yield different Ca/Si ratios. The ratio of these two Ca/Si ratios can be used as a measure of the full range of apparent Ca/Si ratios, which may result from inclusions containing uniform amounts of the two phases in different geometries.

The main factors controlling the variation of the x-ray intensity reaching the detector are as follows:

i) Lower electron intensity in the bottom layer. The fraction of electrons reaching the bottom layer, covered with a top layer of thickness z and density is:

$$n_z/n_0 = 1 - 4\text{x}10^4\ zZ^{0.5} / E_0^{1.7}$$

where E_0=15 keV is the electron energy at z=0 and Z is the average atomic number. Because Z=10 for both $CaCO_3$ and SiO_2 and their densities are also similar, the magnitude of this factor is the same with either silica or calcite as the top layer. As will be shown, the effects do not cancel, but rather, are multiplied in the final ratio.

ii) Lower average electron energy in the lower phase. The x-ray production function, $\Phi(\ ,z)$, depends on the electron energy, which is lower for the bottom phase. The average electron energy, E_z, at depth z, at the upper surface of the bottom layer, was calculated by solving for E_z using:

$$z = 0.066(E_0^{1.68} - E_z^{1.68})$$

(Andersen and Hasler 1966). This lower energy was used as the initial electron energy in the thin-film, ZAF correction of Armstrong (1982). Total ZAF correction factors, ZAFCOR, were calculated for the two phases at both positions (top and bottom). Table 7.4 lists the ratio of the these corrections for the two scenarios:

$$\text{Ra} = \frac{\text{ZAFCOR}^{\text{Ca}}_{\text{calcite}}}{\text{ZAFCOR}^{\text{Si}}_{\text{calcite}}} \Big/ \frac{\text{ZAFCOR}^{\text{Ca}}_{\text{silica}}}{\text{ZAFCOR}^{\text{Si}}_{\text{silica}}}$$

where the subscript indicates the top phase and the superscript indicates the element for which the factor was calculated.

iii) While the x-rays reaching the surface of the top layer are directly detected by the EDS detector, those reaching the surface of the bottom layer can be absorbed by the top layer as well. The magnitude of this factor, ATOP, was estimated for both cases using :

$\text{ATOP}_j = I_{\text{surface}}/I_z = \exp[-(\mu/\ )^j\ z\ \csc(35°)]$ (Goldstein et al. 1981).

Table 7.4. Ratio of ZAF correction factors for Ca and Si. Calcite on top of silica vs. silica on top of calcite.

z[1] (μm)	n_z/n_0[2]	Ra[3]	$ATOP_{Si}$[4]	$ATOP_{Ca}$[5]	Final ratio[6]
0.2	0.932	0.813	0.940	0.980	1.018
0.3	0.897	0.731	0.911	0.970	1.027
0.4	0.863	0.665	0.883	0.960	1.053
0.5	0.829	0.620	0.856	0.950	1.109
0.7	0.761	0.591	0.805	0.931	1.363
0.8	0.726	0.607	0.780	0.921	1.600
1.0	0.658	0.695	0.733	0.903	2.424

1. Equal thickness, z, is assumed for both top and bottom layers.

2. The attenuation in the number of electrons during travel through the upper layer.

3. Ratio of ZAF factors for Si and Ca in top and bottom layers accounting for a lower beam energy in the bottom layer.

4. Correction for the Absorption of Si radiation by the calcite TOP layer.

5. Correction for the Absorption of Ca radiation by the silica TOP layer.

6. The over all ratio of the correction factors for Ca and Si in the two scenarios. The deviation from unity represents the full, apparent compositional variation due to the different geometries of the calcite+silica assemblage.

$(\mu/\ \ )^j$ is given by: $(\mu/\ \ )^j=\Sigma_i(\mu/\ \ )_i^j C_i$, where $(\mu/\ \ )_i^j$ is the mass absorption coefficient of x-rays of element j by the atoms of element i in the absorbing layer and C_i is the concentration of i in that layer. The magnitude of all the above factors is listed in Table 7.4 for various film thicknesses. The overall ratio of the apparent Ca/Si ratios for the two inclusions is calculated as:

$$\frac{\underline{Ca}\atop{Si_{\text{ calcite on top}}}}{\underline{Ca}\atop{Si_{\text{ silica on top}}}} = R_a \cdot \frac{\frac{1}{(n_z/n_0)_{\text{calcite}}}}{(n_z/n_0)_{\text{silica}}} \cdot \frac{\frac{1}{ATOP_{Si}}}{ATOP_{Ca}} .$$

As can be seen in Table 7.4 the correction factors cancel each other to a large extent so that the total correction expected in this case is less than 10% for layers less than 0.5 μm thick. Thus the magnitude of this effect in inclusions smaller than 1 μm is small and cannot explain the large variation in Ca/Si ratio detected by EDS analysis of the inclusions (Fig. 7.3). The second case is concerned with the K/Na ratios in thin feldspar film as a function of depth.

Due to the large difference in mass absorption coefficient for light and heavy elements of either the carbon matrix or the top part of the inclusion itself, the calculated ratio of a light and a heavy element may vary as a function of depth. This is illustrated by the calculation of the ratio of the apparent K/Na ratio to the real ratio in the case of a thin film of feldspar with 50% albite and 50% orthoclase buried below either a calcite or a carbon film of equal thickness. In this case the decrease in the number of electrons affects both Na and K in the same manner and cancels out. The attenuation of the beam energy has a minor effect on the K/Na ratio and, thus, the apparent variation of the K/Na ratio is mainly due to the different mass absorption coefficients in the upper layer. The results presented in Table 7.5. show that apparent variation of up to 25% in the detected K/Na ratio may be recorded by analyzing inclusions of uniform composition located at different depths of up to 0.5 μm below the diamond surface. The variation may reach 45% if the K and Na bearing phase is topped by

Table 7.5. **Apparent variation in K/Na ratios during EDS analysis of alkali-feldspar under varying depths of calcite and graphite.**

	z (μm)	Ra	$ATOP_{Na}$	$ATOP_{K}$	$\frac{K}{Na_z}\ \frac{K}{Na_0}$[1]
Diamond	0.2	0.997	0.877	0.995	0.879
	0.4	1.021	0.769	0.990	0.793
	0.6	1.098	0.675	0.985	0.752
	0.8	1.191	0.592	0.981	0.719
Calcite	0.2	0.997	0.772	0.990	0.777
	0.4	1.021	0.596	0.980	0.612
	0.6	1.098	0.460	0.969	0.493
	0.8	1.191	0.356	0.959	0.409
Graphite	0.2	0.996	0.907	0.996	0.906
	0.4	1.005	0.822	0.993	0.832
	0.6	1.038	0.745	0.989	0.782
	0.8	1.104	0.675	0.985	0.757

[1] Ratio of Na and K detected intensities for a 50:50 albite:orthoclase feldspar buried under varying thickness of diamond, calcite and graphite normalized to the intensity ratio detected when the same feldspar is on the surface. (See footnotes to Table 7.4. for explanation of other headings.)

calcite. Thus, the K_2O/Na_2O range of Figure 7.4 could be fully explained by analytical errors. Smaller effects are expected for elements of close atomic number. Similar effects may be expected in the case of Fe/Mg ratios.

If all inclusions are assumed to contain material of uniform composition, some of the scatter of the EDS results could be explained as the result of analytical error, due to poor counting statistics and the inability of the correction procedure to account for the variable geometries of the phases. However, some observations suggest that real variation in inclusion chemistry does occur. The scatter in CaO/SiO_2 ratio exceeds the range that can be explained by analytical error and reflects, at least in part, a real variation in the composition of the individual inclusions. Further evidence for chemical variability is revealed by examining thequality of the correlation between the concentrations of many pairs of elements. The better correlations are observed between chemically related elements, e.g., Ca vs. P, Mg vs. Ca or Si vs. Al, and are unrelated to counting statistics.

As will be shown in Chapter 8, IR data suggest the presence of a limited number of silicate, carbonate and phosphate phases. The EDS data indicate that all three groups are represented in each individual inclusion. The different compositions of individual inclusions are attributed to varying proportions of silicate, carbonate, and phosphate in each inclusion.

7.2.4. COMPARISON WITH SIMS ANALYSIS

The wide range of compositions spanned by the EDS analysis of the three well sampled diamonds (GRR 1503, GRR 1504, GRR 1508) includes, in all cases, the range spanned by the SIMS analyses of these diamonds. Still, the average composition of the inclusions in the individual diamonds, as recorded by the two techniques are, in many cases, distinct. For most elements the differences are smaller then 10% and are random. Exceptions are: Fe, which shows large-scale variation in both directions; Na, with EDS/SIMS > 1; and K, with EDS/SIMS < 1. The EDS/SIMS ratios for K and Na may be explained, in part, by the different average depth of the inclusions analyzed by EDS and by EPMA (which was used to calibrate the SIMS). The inclusions studied by EDS are on the average shallower than those filling the entire volume of an EPMA analysis. This difference would lead to lower

Figure 7.4. Al_2O_3 - Na_2O - K_2O in EDS analyses of sub-surface inclusions.

The range of composition is wider compared with the SIMS result. Symbols are as in Figure 7.3. Comparison of the average composition of the inclusions in the different diamonds as analyzed by SIMS and EPMA shows consistent shift of the SIMS result to higher K_2O/Na_2O ratios.

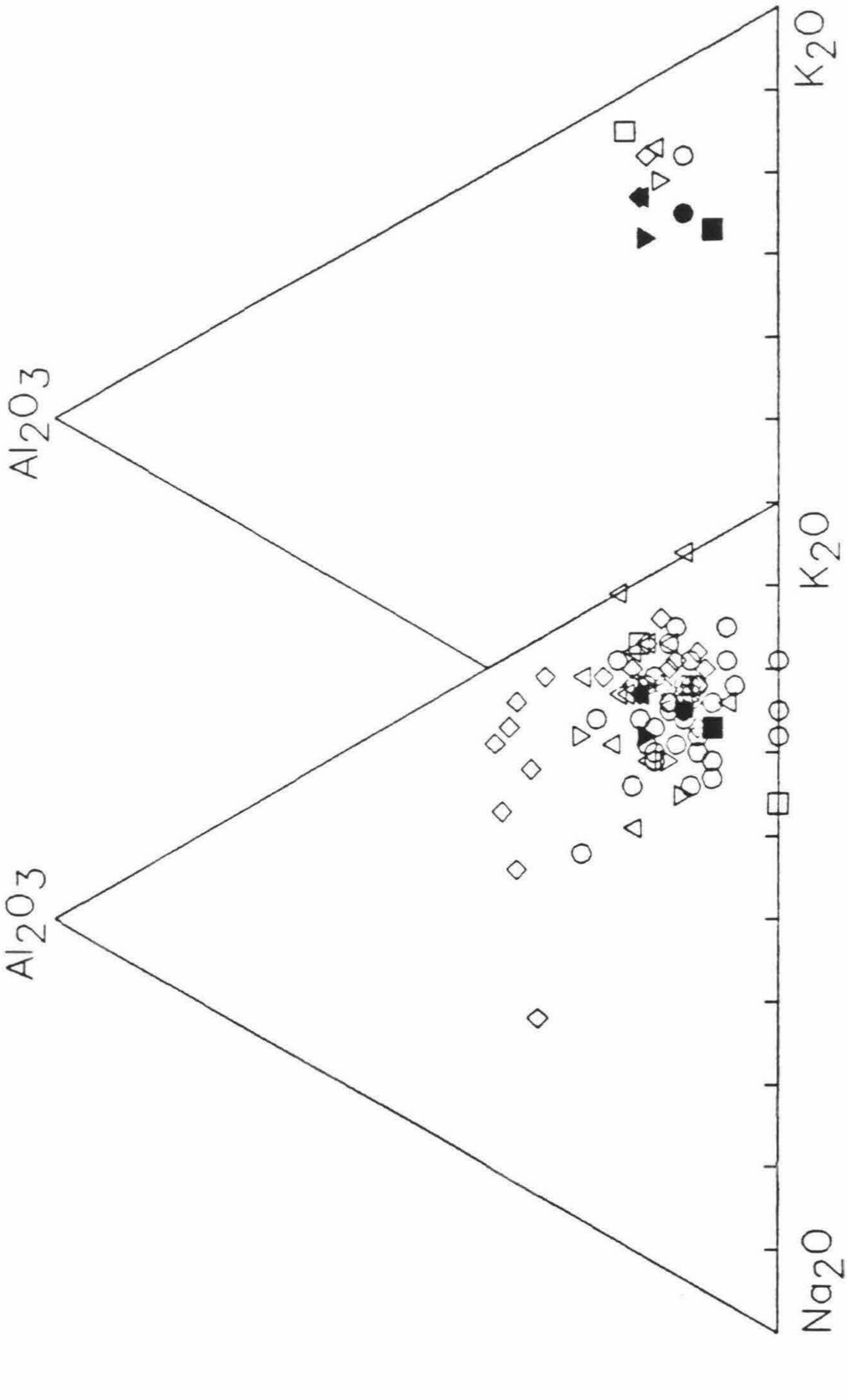
Al$_2$O$_3$
Al$_2$O$_3$
Na$_2$O
K$_2$O
K$_2$O

relative attenuation of Na intensity in the case of the EDS analysis and thus, to higher calculated concentrations.

7.3. SUMMARY

EDS analysis of individual micro-inclusions found no monomineralic inclusions. All micro-inclusions were found to contain material rich in Si, K, Ca and Fe, similar to the many-inclusions averages recorded by SIMS (this study) and to the multiphase assemblages recorded by TEM (Lang and Walmsley, 1983; G. Guthrie and D. Veblen, personal communication).

The range of compositions spanned by the micro-inclusions is large compared with the clustered SIMS averages. In some cases the observed variation in elemental ratios may be attributed to analytical uncertainties. However, the correlations between concentrations of chemically related elements and the large span in CaO/SiO_2 ratio suggest that the composition of the individual micro-inclusions do vary. It appears likely that the silicate, carbonate and phosphate minerals detected by IR (Chapter 8) are all present in all the inclusions studied. The compositional variation is attributed to varying proportions of the different phases.

Phosphorus and chlorine were detected in most inclusions and, on the average, comprise 2-5% and 1-2% of the oxide (+ chloride) fraction. Cr and sulfur are below detection limits in all the Si-, K-rich inclusions. Only one inclusion was found to contain $Fe_{0.83}S$, but it is not possible to verify whether it is isolated.

CHAPTER 8 INFRARED SPECTROSCOPY

Infrared (IR) spectroscopy enables the detection of molecular functional groups and crystalline phases through their characteristic absorption bands. In this study IR spectroscopy of diamond was used to identify:

1. The molecular functional groups and mineral phases in micro-inclusion-bearing diamonds,
2. The type of nitrogen centers in diamond, and
3. The presence of other characteristic centers (e.g., hydrogen).

The excellent sensitivity of the Nicolet Fourier Transform IR spectrometer (FTIR) enables the study of very low concentrations of absorbing species, down to the ppm level. It also enables a semi-quantitative estimation of their concentrations. IR spectrometry is important as it can distinguish and quantify various carbon carrying species, e.g., CO_2, $CO^{=}_3$, CH_4, graphite and diamond. It can also distinguish between the different nitrogen species of the diamond and between hydrogen present as C-H in the diamond lattice and hydrogen in hydrous species in the micro-inclusions.

Section 8.1 describes the experimental details and how the spectral data were reduced to obtain the spectrum due to the absorption by micro-inclusions. Section 8.2. describes the IR spectrum of the micro-inclusion-bearing zones. The spectrum of the diamond matrix is described first, followed by a description of the absorption due to the micro-inclusions. Correlations between the intensity of some of the bands in the different diamonds is a key factor in band assignment. These correlations and the possible identification of the phases in the micro-inclusions are presented in Section 8.3. Using absorption coefficients from the literature and from analysis of KBr pellets of some minerals, it is possible to estimate the concentrations of the different phases in the diamond. The choice of absorption coefficients is discussed in Section 8.4, the results are summarized in Section 8.5.

8.1. EXPERIMENTAL METHOD

8.1.1. INSTRUMENTAL PROCEDURE

IR spectra of doubly-polished diamond sections (see Section 4.2 for a description of the sample preparation) were recorded with a Nicolet 60SX FTIR at Caltech. Spectral data in the range 400-4900 cm^{-1} were recorded using a silicon carbide source, KBr beam-splitter and a liquid nitrogen cooled, HgCdTe detector. Apertures of 200-600 μm were used to collect spectra of small selected areas and to avoid cracks. A microbeam compartment allowed the focusing of high beam intensities over the aperture area, so that very good signal-to-noise ratios were obtained by collecting 1024 interferograms. Spectra were usually recorded with 2 cm^{-1} resolution. A liquid nitrogen cooled, evacuated stage with CaF_2 windows was used to collect spectra at low temperatures at the 900-4900 cm^{-1} spectral range.

8.1.2 REFERENCE SPECTRUM

In order to obtain the net absorption by the micro-inclusions, a reference spectrum of an inclusion-free diamond must be subtracted from the spectra of the inclusion-bearing zones. The diamond matrix of all the inclusion-bearing zones (in both cubic and coated diamond) show similar spectra. Nitrogen is only observed as type A. The intensity of the nitrogen peak varies both inter- and intra-diamond.

The reference spectrum was constructed by adding a type A nitrogen spectrum to a synthetic spectrum of a pure, nitrogen-free type II diamond. The intensity of the nitrogen peak is fitted so as to fully cancel the nitrogen absorption in the spectrum of the inclusion-bearing zone.

Only one small specimen, CTP 7741, of a nitrogen-free, type II diamond was available and, because of interference fringes, it yielded a noisy spectrum. A polynomial fit produced a smooth spectrum in excellent agreement with the low resolution spectrum of other type II diamonds (Clark, written communication, 1986). The fitted spectrum of CTP 7741 was used to construct the 400-1700 region of the synthetic spectrum (Fig. 8.1.a). In the 1700 to 4000 cm^{-1} spectral region, where the spectra of type II and type A diamonds are identical, five

Figure 8.1. Reference spectra.

a. Type II (nitrogen free) spectrum.

This synthetic spectrum was produced by combining the spectrum of a type II diamond in the 400-1700 cm^{-1} range, with the average of this spectrum and four type A spectra in the 1700-4000 cm^{-1} range (where type A and type II spectra are identical).

b. Type A spectrum (of GRR 1512, a type IaA diamond, solid line) compared with a synthetic type A spectrum (Clark, written communication, 1986, dashed line). The difference in the intensity of the main, 1282 cm^{-1} band is due to the non-linear absorption of this peak in the thick diamond sample. The source of the small difference in the 800-1200 cm^{-1} region is not clear. It does not resemble the spectrum of any of the other centers in diamonds (Clark, written communication, 1986). The 480 cm^{-1} band is shifted to a lower wave number compared with the spectrum of Clark.

Type II, synthetic reference spectrum

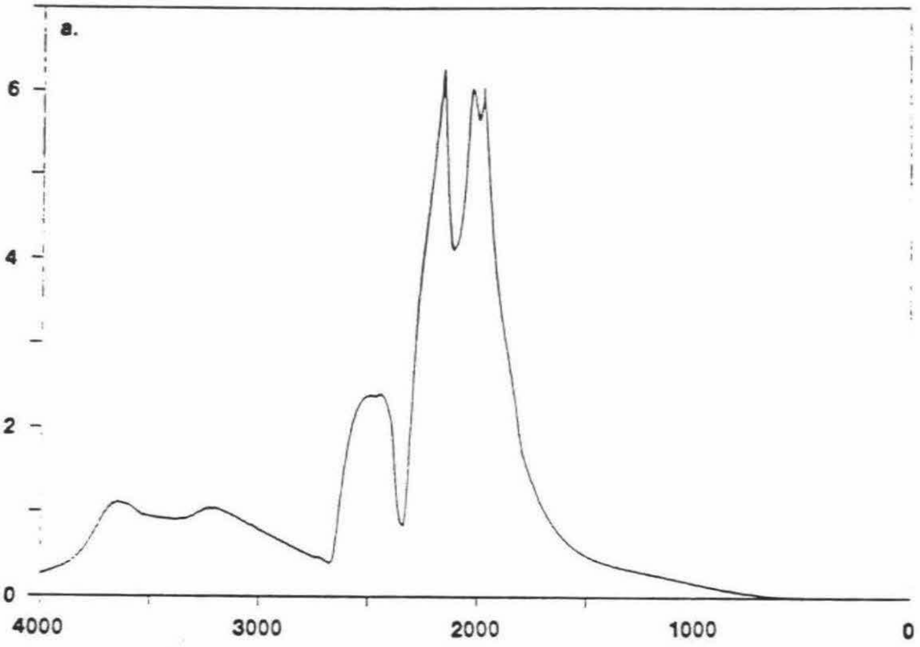

Type A spectrum

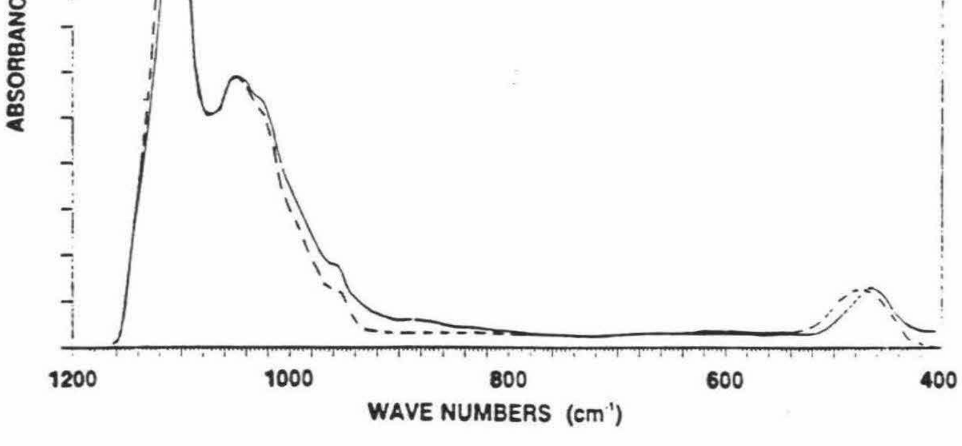

spectra (a smoothed spectrum of CTP 7741 and four type A spectra) were averaged to construct the synthetic spectrum of Figure 8.1a. All five spectra exhibit identical absorption in the 1700-2700 cm^{-1} region, but show small differences in the 2700-4000 cm^{-1} region. Trace absorbance due to hydrocarbon contamination and due to C-H modes of the diamond itself were subtracted out of the reference spectrum by fitting straight lines between 2800-3000 and 3090-3130 cm^{-1}.

The spectrum of GRR 1512, an inclusion-free cubic diamond was used as a reference type A spectrum (Fig. 8.1b). Compared with a synthetic type A end-member spectrum (Clark, written communication, 1986), GRR 1512 has a higher μ_{1212}/μ_{1282} ratio. Its low wavenumber band centers at ~480 cm^{-1}, compared with 495 cm^{-1} for the center of this band in Clark's spectrum. In all the type A and type A+B spectra I recorded, the low wavenumber band was at 480 cm^{-1}. Thus, I preferred to use the spectrum of GRR 1512 rather than the synthetic spectrum of Clark. It was verified that the difference between the spectrum of GRR 1512 and Clark's spectra is not due to the presence of an extra component in GRR 1512. The difference between the two spectra consists of a broad band between 900-1200 cm^{-1} and does not correspond to any of the other end-member diamond spectra.

8.1.3 DATA REDUCTION

All spectra were recorded with 2 cm^{-1} resolution. However, in order to enable fast processing on an AT computer, data were interpolated to produce spectra with 5 cm^{-1} between points. Next, the type II (pure diamond) and the type A (nitrogen pairs) reference spectra were subtracted and a baseline was fitted to the spectrum. The baseline absorption was manually determined at 17 points and was fitted by cubic spline interpolation. A typical baseline, of both inclusion-free and inclusion-bearing diamonds, is concave upward. It steeply declines from 400 to a minimum at ~ 1000-1500 cm^{-1} and ascends linearly in the 2000-4000 cm^{-1} region. The baseline is, however, higher and steeper for the inclusion-rich diamonds, especially in the high wavenumber region, where light scattering is significant.

The final spectrum due to the inclusions is obtained by adjusting the exact amount of type

A absorption needed to fully cancel the type A peak at 1212 cm^{-1} (the 1212 cm^{-1} peak was used instead of the 1282 cm^{-1} because, in some thick specimens, transmittance was too low for quantitative work). This final spectrum (Fig 8.2) still contains a few diamond bands: The platelet band at ~1360 cm^{-1} and the C-H bands at 1405 and 3107 cm^{-1}.

Band positions were computed using a routine provided with the Nicolet 1280 computer. This algorithm fits a cubic spline interpolation to the high resolution spectral data and calculates the absorption maxima.

8.2. IR SPECTRUM OF MICRO-INCLUSION-BEARING ZONES IN DIAMONDS

The IR spectra of the micro-inclusion-bearing zones of cubic and coated diamonds exhibit all the characteristic absorption bands of the carbon matrix, nitrogen centers and hydrogen centers found in common diamonds. In addition to these common bands the spectra exhibit bands due to absorption by the micro-inclusions.

8.2.1 ABSORPTION BY THE DIAMOND MATRIX.

The spectra of all the micro-inclusion-bearing zones studied by IR show them to be type IaA diamonds, with type A nitrogen centers as the dominant species. All other nitrogen species are at or below the detection limit. However, due to the strong type A absorption and the superposition of the micro-inclusions absorption, the detection limit for type B (aggregates) and type C (single atoms) absorption is estimated at ~1 a.u./cm. (Absorbance unit per cm; a medium with one absorbance unit transmits 10% (10^{-1}) of the incident radiation.)

Using the calibration of Kaiser and Bond (1959), nitrogen concentrations of 450-1070 ppm are estimated. Similar nitrogen concentrations were reported earlier by Seal (1965 and references therein) and by Boyd et al. (1987). The nitrogen levels in the inclusion-bearing zones are high compared with those reported for transparent, type A diamonds from South Africa (Deines et al., 1987), or Australia (Harris and Collins, 1985). No data could be found for Zairian diamonds. Platelet absorption at 1360 cm^{-1} is common in the cores of the coated diamonds.

Nitrogen concentrations for most of the diamonds of the CTP set were also measured by mass-spectrometry (Boyd et al., 1987). The concentrations they reported are ~ 10-30% higher than those determined by the IR measurements reported here. The IR spectrum of most of the diamonds of the CTP set was also measured by Boyd et al. (1987), but no intensity or IR-determined concentrations were reported. Boyd et al. did report some discrepancies between nitrogen concentration (by mass-spectrometer) and IR intensities in profiles through a core of a coated diamond. The source of this difference is not clear. The Kaiser and Bond (1957) calibration, which was used here, is based on mass-spectrometric measurements of the nitrogen content of type IaA diamonds. A later calibration of the absorption of the 1282 cm^{-1} band of type IaA diamonds against INAA and other measurements of the nitrogen content yielded absorption coefficients similar to those obtained by Kaiser and Bond (see Bibby, 1982, for a review of all analyses). It would be interesting to see whether the extensive data set of Boyd and coworkers, agrees with the old, commonly used calibration.

Other bands due to absorption by the diamond matrix are:

1370 cm^{-1}: the weak, broad band at 1370±10 cm^{-1} may be due to the presence of nitrogen platelets, or due to a characteristic absorption band of the micro-inclusions. The presence of a smaller, sharp peak at 1370 cm^{-1} in the spectra of GRR 861.2, GRR 1508, CTP L3 and CTP L4 suggests that the broad band is due to micro-inclusions, while the sharp peak is due to platelets. Intense platelet absorption was detected in most cores.

1405 cm^{-1} This small, sharp peak is due to C-H vibration in the diamond matrix (Davies et al., 1984). It is present in all diamonds except GRR 1504.

3107 cm^{-1} This sharp peak is the strongest C-H band. It is present in all diamonds. A weak absorption can be distinguished in GRR 1504 as well.

Type C absorption, single nitrogen centers: Electron spin resonance (ESR) studies have indicated the presence of variable amounts of single nitrogen centers in coated diamonds. Faulkner et al. (1965) reported concentrations of $5x10^{18}$ cm^{-1} (33 ppm), Orlov (1977) reported concentrations in excess of 1 ppm, and Galimov (1984, Fig 10) reported concentrations from sub-ppm levels to above 10^{19} cm^{-1} (66 ppm). Single nitrogen centers give rise to type C absorption spectrum as well as to a UV absorption band with a maximum at ~ 220 nm. The tail of the UV absorption band induces a yellow or green coloration. IR spectroscopy did not reveal any definite evidence for the presence of type C components in any of the yellow or green diamonds I studied. A comparison between the IR absorption spectra of two regions in the coat of CTP L3, one of intense yellow color, the other of lighter yellow, revealed a small additional shoulder at ~1130 cm^{-1}, where the type C centers have their maximum absorption. The intensity is estimated at 1-2 a.u./cm. Weaker shoulders in the spectra of CTP L4 and GRR 1504 correspond to absorbance of about 0.5-1 a.u./cm due to C centers, and the IR detection limit for the type C main band is estimated at ~ 1 cm^{-1}.

UV absorption at 220 nm is 45 times stronger than the IR absorption at 1130 cm^{-1} (Chrenko, 1971). 1 a.u./cm IR absorption would give rise to a strong UV absorption and may produce the observed yellow coloration. CTP L3 and CTP L4 exhibit varying intensities of yellow coloration in some zones of their coats. This intrinsic yellow color of the diamond matrix is not observed in other diamonds suggesting that in most diamonds the concentration of type C centers is even lower. Using the calibrations of either Sobolev et al. (1969) or Chrenko et al. (1971), a 1 a.u./cm absorption at 1131 cm^{-1} corresponds to 4 or 25 ppm of type C nitrogen respectively. Thus, even in the diamonds with the highest possible concentration of type C centers, they are limited to less than 1% of the total nitrogen content.

8.2.2 ABSORPTION BY THE MICRO-INCLUSIONS

In addition to the characteristic type A spectrum, the IR spectra of the micro-inclusion-bearing zones exhibit many additional bands. Figures 8.2b and 8.2c present a difference spectrum, obtained by subtracting the reference diamond-matrix spectrum from the spectrum of diamond GRR 1515 (both shown in Fig. 8.2a). Figure 8.3 presents the spectra of 15 other diamonds. The difference spectra of the inclusion-rich zones in all diamonds are similar and all exhibit the same bands.

Figure 8.2. IR absorption of an inclusions-bearing diamond.

a. Raw spectrum of diamond GRR 1515 (upper curve). To obtain the spectrum due to the micro-inclusions the main diamond bands were subtracted. First the reference type II spectrum (Fig. 8.1a) and then the type A spectrum adjusted to cancel the 1282 and the 1212 cm^{-1} bands. This difference spectrum (middle curve) was than corrected for baseline. The baseline absorbance was manually fitted in 17 points along the spectrum (triangles) and the baseline was then approximated by a cubic spline interpulation through these points.

b. The correction for diamond absorption was re-checked using the baseline corrected diamond spectrum (solid line) with more accurately fitted reference spectrum (dashed line). Good fit for both peaks was achieved for thin diamonds. In thick specimen, the strong peak at 1282 cm^{-1} reaches saturation and the intensity of the weaker band at 1212 cm^{-1} was used (see Fig. 8.3).

c. Absorption due to the micro-inclusions was obtained as the difference between the two spectra of a. OH, O-H stretching vibrations; CH, C-H vibrations; CO_2, absorption due to molecular CO_2; HOH, the bending mode of water; $CO_3^=$, carbonate absorption; N, the platelet mode; S, S1, S2, silicate and silicate-OH vibrations; P; apatite.

d. Detail of the low wavenumber region of B.

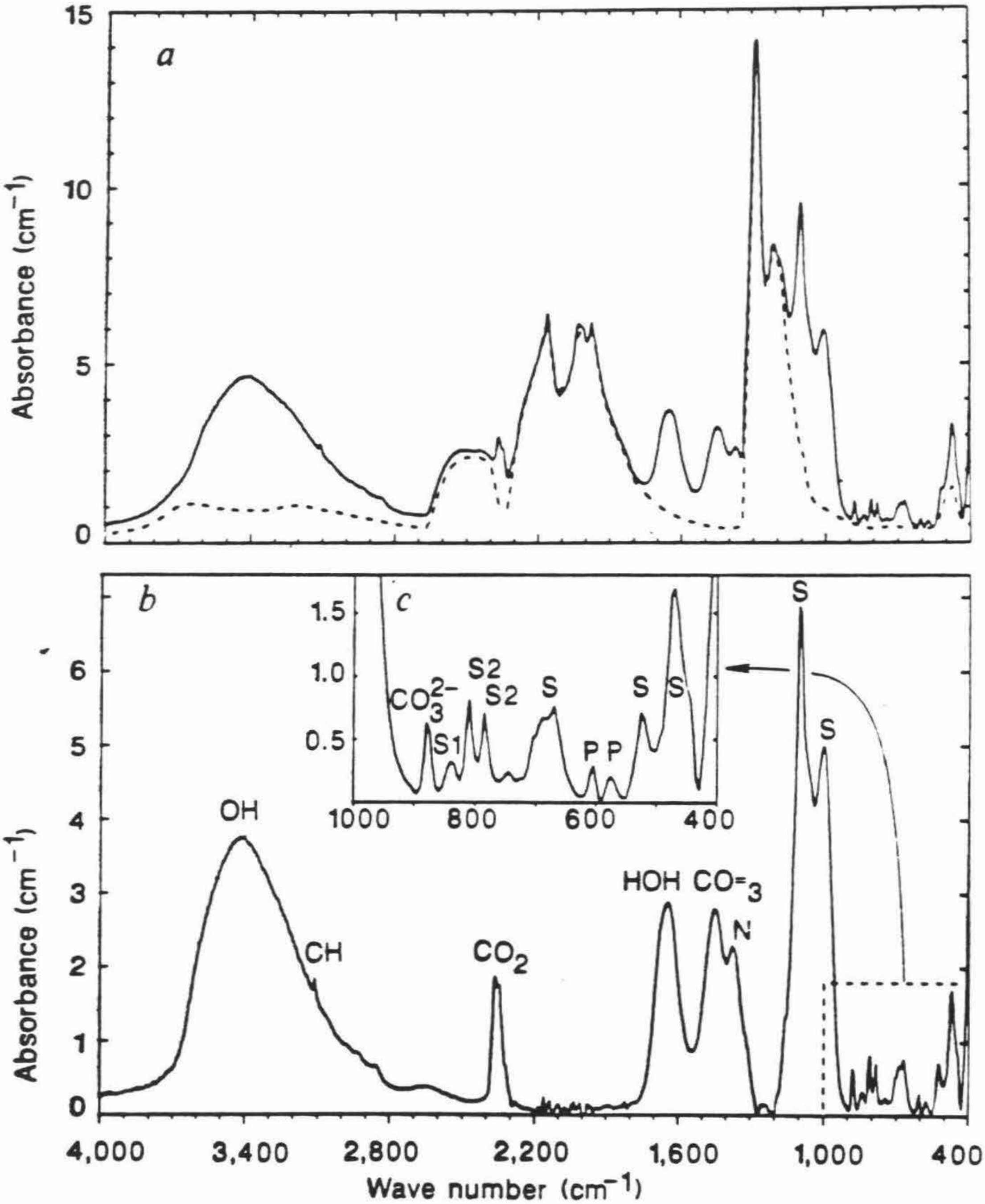
a
b
c
Absorbance (cm^{-1})
Wave number (cm^{-1})
15
10
5
0
6
5
4
3
2
1
0
1.5
1.0
0.5
1000
800
600
400
4,000
3,400
2,800
2,200
1,600
1,000
400
OH
CH
CO$_2$
HOH
CO$^=_3$
N
S
S
CO$_3^{2-}$
S1
S2
S2
S
P
P
S
S

Figure 8.3 IR absorption spectra due to the micro-inclusions in the diamonds.

Each spectrum was constructed similar to the example in Figure 8.2. Notice the change of scale in wavenumber (X-axis) at 1800 cm^{-1} and in absorbance (Y-axis) at 900 cm^{-1}. The absorbance scale on the right is for the 425-900 cm^{-1} range; the left scale is for the 900-4000 cm^{-1} range; the scale is different for each spectrum. The weak wide band around 2650 cm^{-1} is an artifact, caused by a small difference in the shape of 2600 cm^{-1} diamond band (Fig. 8.1a) between the reference spectrum and the inclusion-bearing diamonds.

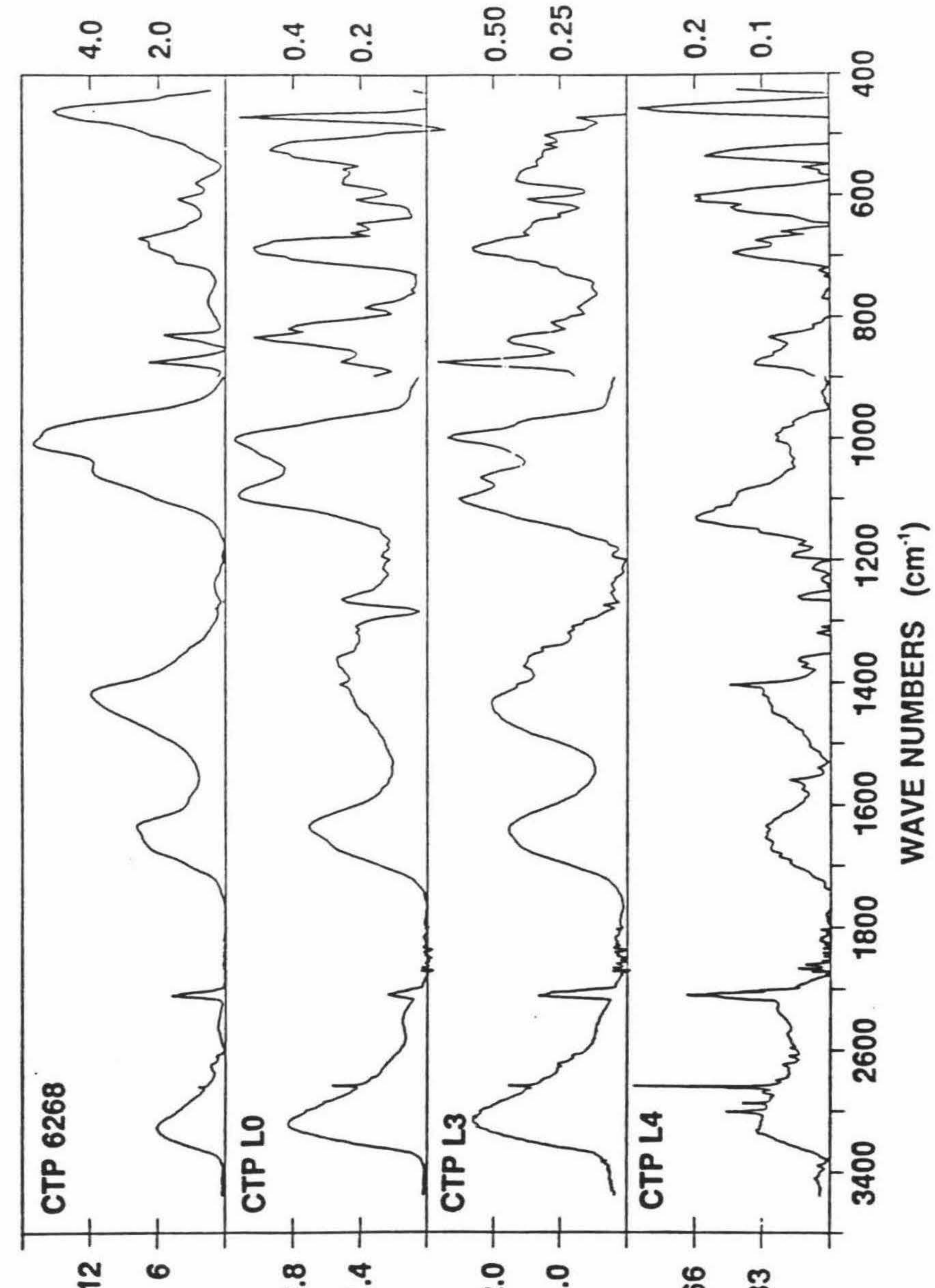
CTP 6268
CTP L0
CTP L3
CTP L4
12
6
2.8
1.4
2.0
1.0
0.66
0.33
4.0
2.0
0.4
0.2
0.50
0.25
0.2
0.1
3400
2600
1800
1600
1400
1200
1000
800
600
400
WAVE NUMBERS (cm-1)
ABSORBANCE (cm-1)

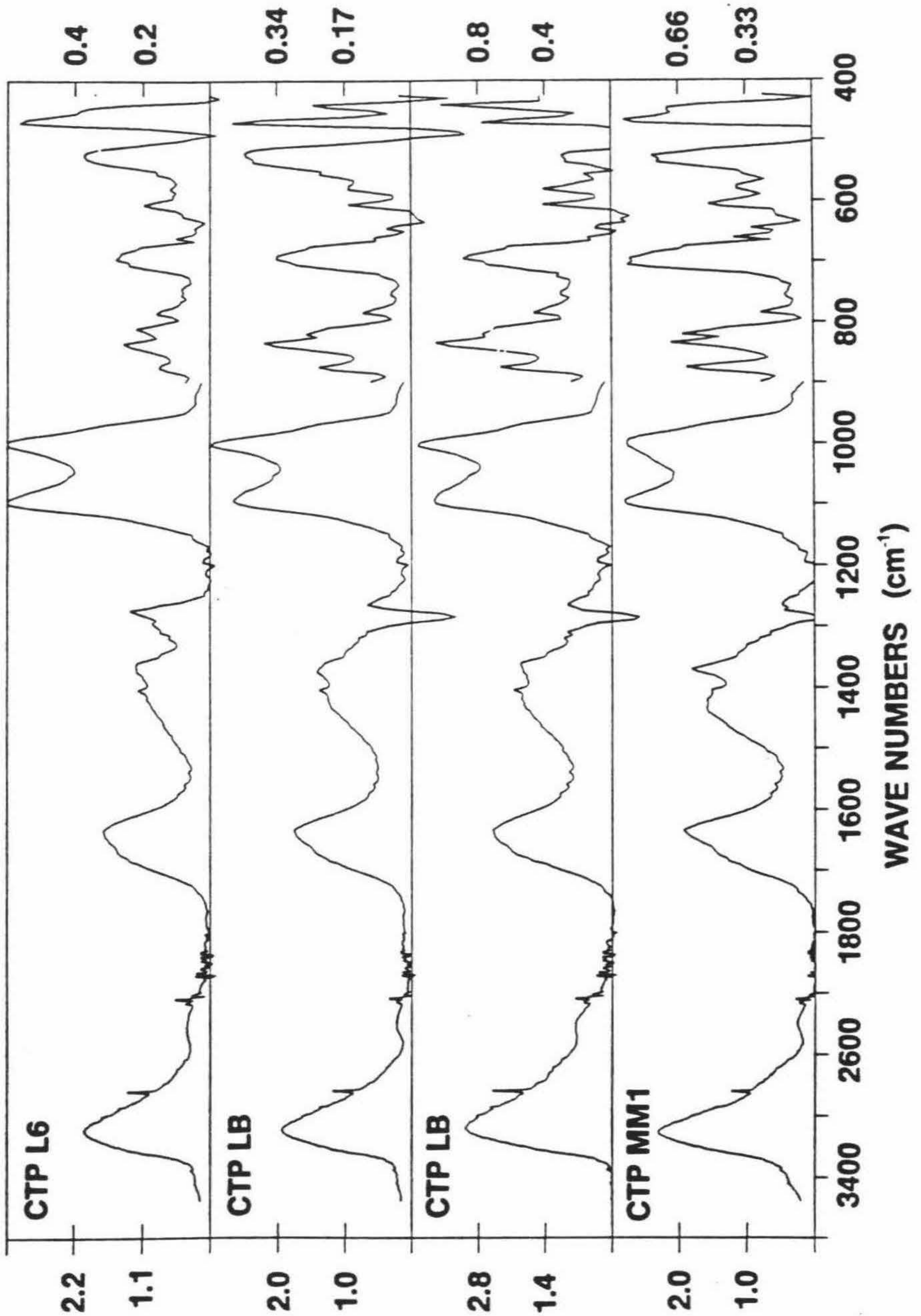
CTP L6
CTP LB
CTP LB
CTP MM1
ABSORBANCE (cm⁻¹)
2.2
1.1
2.0
1.0
2.8
1.4
2.0
1.0
0.4
0.2
0.34
0.17
0.8
0.4
0.66
0.33
WAVE NUMBERS (cm⁻¹)
3400
2600
1800
1600
1400
1200
1000
800
600
400

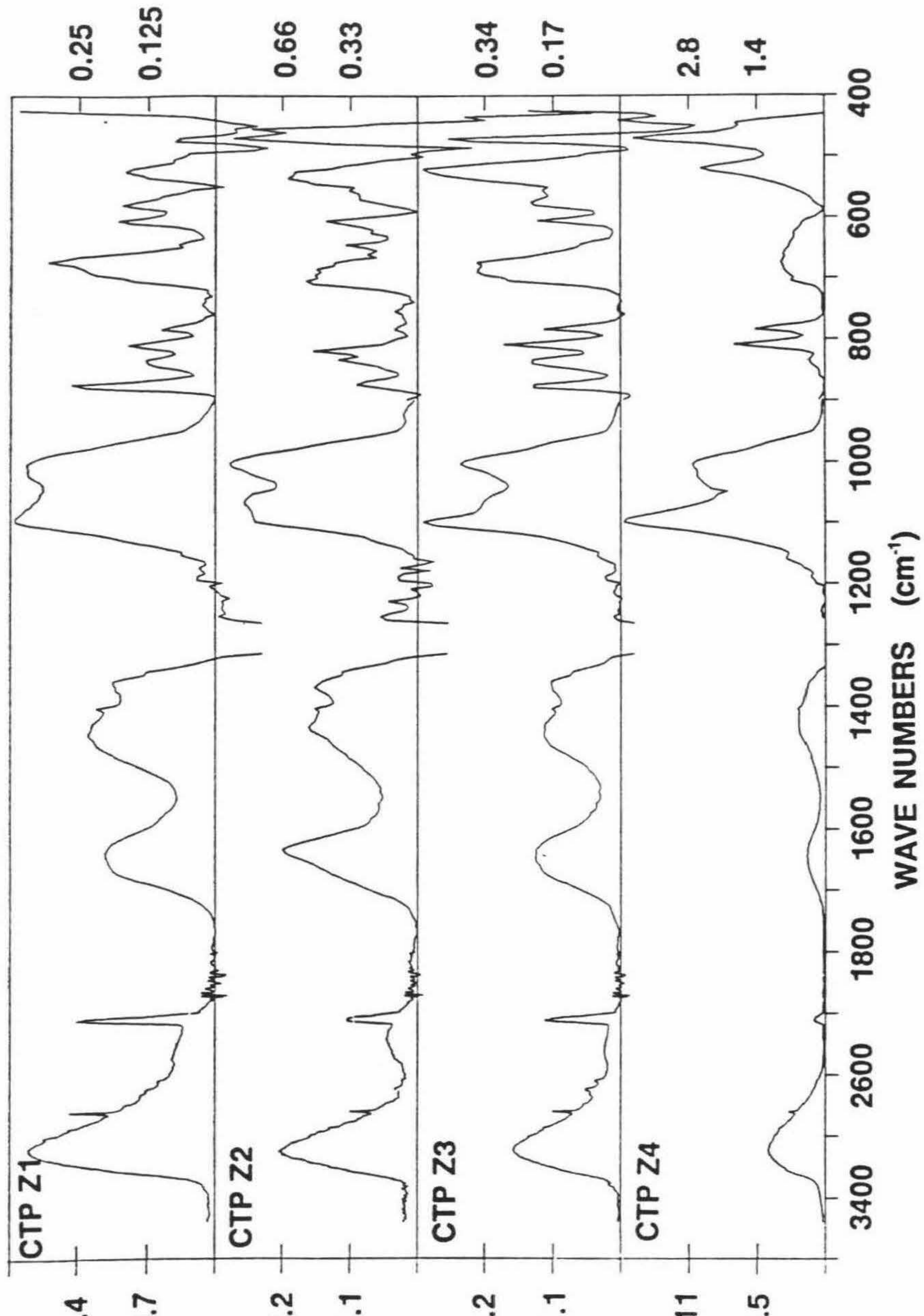
CTP Z1
CTP Z2
CTP Z3
CTP Z4
ABSORBANCE (cm⁻¹)
1.4
0.7
2.2
1.1
2.2
1.1
11
5.5
0.25
0.125
0.66
0.33
0.34
0.17
2.8
1.4
3400
2600
1800
1600
1400
1200
1000
800
600
400
WAVE NUMBERS (cm⁻¹)

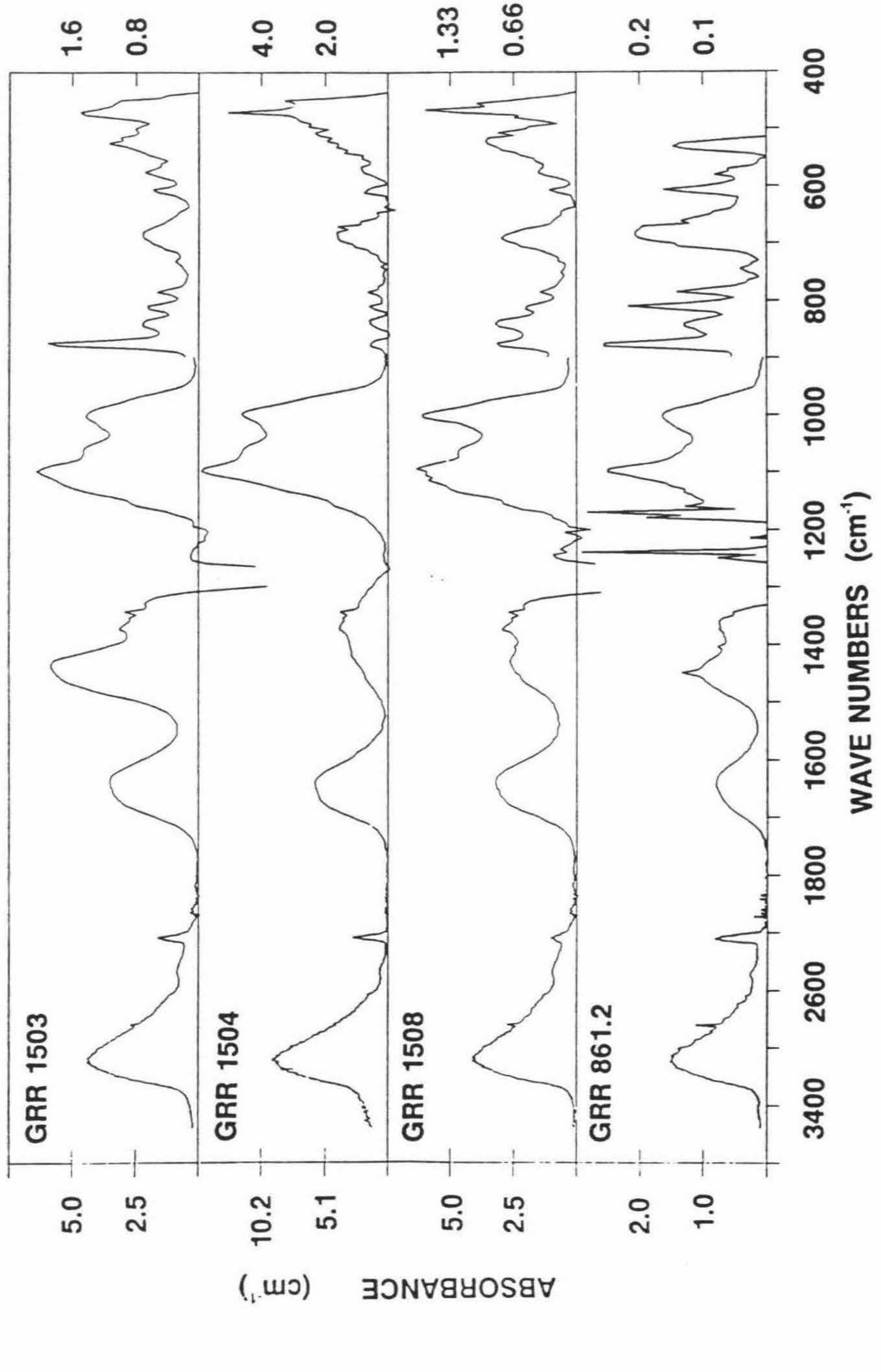
GRR 1503
GRR 1504
GRR 1508
GRR 861.2
ABSORBANCE (cm⁻¹)
5.0
2.5
10.2
5.1
5.0
2.5
2.0
1.0
1.6
0.8
4.0
2.0
1.33
0.66
0.2
0.1
3400
2600
1800
1600
1400
1200
1000
800
600
400
WAVE NUMBERS (cm⁻¹)

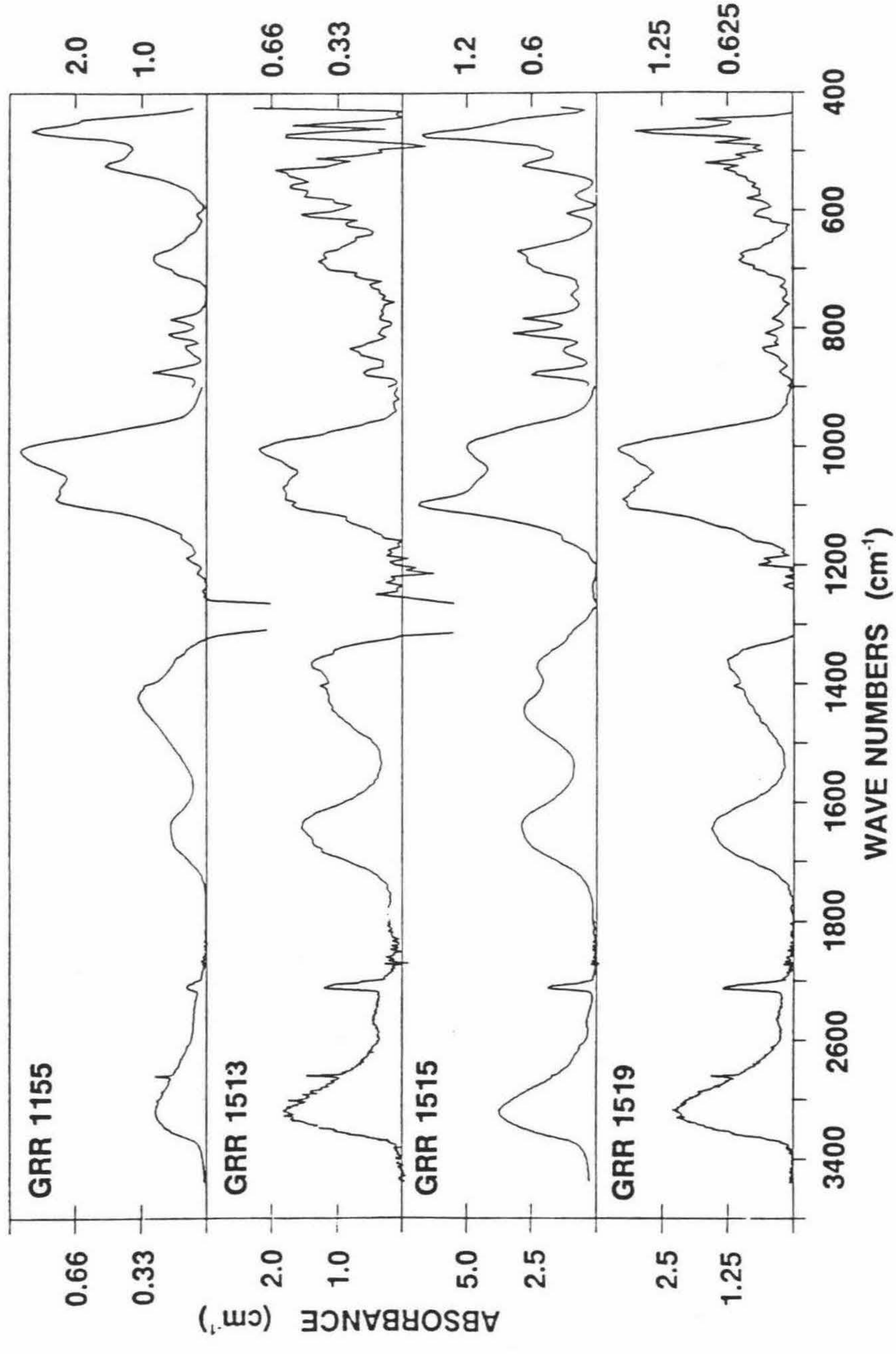
GRR 1155
GRR 1513
GRR 1515
GRR 1519
ABSORBANCE (cm^{-1})
0.66
0.33
2.0
1.0
5.0
2.5
2.5
1.25
2.0
1.0
0.66
0.33
1.2
0.6
1.25
0.625
3400
2600
1800
1600
1400
1200
1000
800
600
400
WAVE NUMBERS (cm^{-1})

475 and 525 cm^{-1}: The intensity and shape of these two bands are strongly affected by the subtraction of the type A band at 480 cm^{-1}. Still, the presence of the two bands is evident in the original, uncorrected spectra as well.

575 and 605 cm^{-1}: Two weak, narrow bands (designated by P in Fig. 8.2c). The 605 cm^{-1} is of higher intensity. The bands overlap with the stronger 525 and 685 cm^{-1} bands. CTP 6268 show the highest intensity, more than twice that of any other diamond.

685 cm^{-1}: A wide band with its center at ~ 685-690 cm^{-1} (S in Fig. 8.2.c) A side band at 670 cm^{-1} is present in many diamonds and is most prominent in CTP 6268 and GRR 1504. Another shoulder can be distinguished at ~ 700 cm^{-1}. This shoulder is present in all diamonds; it is strong in CTP MM1 and CTP Z2.

785 and 812 cm^{-1}: The two narrow bands (S2) are present in all diamonds except for CTP 6268 which only shows a wide band at ~ 770 cm^{-1}. The 812 cm^{-1} band is of somewhat higher intensity than the 785 cm^{-1}, the highest intensity (>2 times that of all other diamonds) is observed in CTP Z4. The position of this band is the same (±3 cm^{-1}) in all diamonds. CTP Z2, CTP LB and CTP MM1 exhibit an additional band at ~ 820 cm^{-1}.

840 cm^{-1}: This band (S1) is similar in shape and average height to the 812 and 785 cm^{-1} bands. However its intensity does not correlate with these of the other two bands. CTP 6268 has a strong band at 832 cm^{-1} and its 840 cm^{-1} band appears as a shoulder.

876 cm^{-1}: The position of this narrow band (CO^-) is the same (±1.5 cm^{-1} in most diamonds). In CTP Z2 the maximum occurs at 874.1 and in GRR 862.1, GRR 1515, CTP L4 and CTP Z3 it is between 878.0 and 878.6 cm^{-1}. The band is missing in CTP Z4.

1000 and 1100 cm^{-1}: These are the strongest bands in the spectrum due to the micro-inclusions. Both bands are strong in all spectra; their peak height ratio varies from one diamond to another. In most diamonds an additional shoulder appears at 1065±10 cm^{-1}. Another small band at 1190 cm^{-1} is also present in a few diamonds.

1370 cm^{-1}: This weak band (N) is either due to absorption by the micro-inclusions, or due to platelets (see Section 8.2.1).

1405 cm^{-1}: C-H vibration in the diamond matrix (see Section 8.2.1).

1430 cm^{-1}: Most diamonds show a strong wide band ($CO^{=}$) at ~ 1430 cm^{-1} and a weak band which forms a shoulder at ~ 1445 cm^{-1}. In GRR 861.2, GRR 1515 and CTP Z3, the 1445 cm^{-1} is more intense than the 1430 cm^{-1} band. These three diamonds also show shifts to higher wavenumbers in their 876 cm^{-1} band.

1640 cm^{-1}: All diamonds exhibit a broad band with a maximum at ~ 1640 cm^{-1} and a shoulder at 1670 cm^{-1} (HOH).

2350 cm^{-1}: Most diamonds show a split band with maximum at 2350 cm^{-1} (CO_2). Absorption in CTP L6, CTP LB, and CTP MM1 is below detection limit.

2850 - 2950 cm^{-1}: Weak bands, probably due to hydrocarbon, surface contamination.

3107 cm^{-1}: A sharp band (CH), related to C-H stretching vibrations in the diamond matrix (see Section 8.2.1).

3238 and 3312 cm^{-1}: Two weak bands that are also found in spectra of inclusion-free diamonds.

3420 cm^{-1}: A strong asymmetric band (OH), present in all diamonds. The position of the absorption maximum varies between 3405 and 3438 cm^{-1} in different diamonds.

8.3. CORRELATION OF PEAK INTENSITIES AND BAND ASSIGNMENT

The position and shape of a few of the bands are characteristic of known, IR-active, molecular species. The bands at 3420 and 1640 cm^{-1} are characteristic of the stretching and bending vibrations of water (Nakamoto, 1963). The bands at 1430 and 876 cm^{-1} are characteristic of the asymmetric and out of plane stretches of carbonate groups. The two bands at 1000 and 1100 cm^{-1} are typical of Si-O stretching in silicates and the peak at 2350 cm^{-1} is in the location of molecular CO_2 absorption. A good test for these assignments is the check for correlations between the intensities of all the bands assigned to any single phase in the different diamonds. Such correlation may also enable the assignment of other bands by associating them with bands already identified.

8.3.1. INTENSITY MEASUREMENT AND ERROR ESTIMATION

Although signal to noise ratios are high in most spectra, large errors are introduced during the corrections for baseline absorption and for absorption by the diamond matrix. As the magnitude of the corrections was approximately equal for all spectra, each band is assigned a fixed error in all the diamonds.

Large errors are associated with the 475 and 525 cm^{-1} bands due to the steep baseline at this low wavenumber region and due to the subtraction of the relatively large 480 cm^{-1} band of type A nitrogen in the diamond matrix. Errors are estimated as ±0.5 a.u./cm. The baseline for the 575 and 605 cm^{-1} bands was manually fitted to correct for the tails of the stronger 525 and 685 cm^{-1} bands. Errors are estimated as ±0.2 a.u./cm. Similar errors are estimated for the peak intensities of the 685, 785, 812, 840 and 876 cm^{-1} bands. Larger errors of ±0.3 a.u./cm are assigned to the intensities of the 1000 and 1100 cm^{-1} bands. No attempt has been made to deconvolve the two peaks or to correct for the shoulder at 1070 cm^{-1}. The intensity of the 1360 cm^{-1} band is highly uncertain due to the huge correction for the main nitrogen peak at 1282 cm^{-1} and the platelet absorption at 1360 to 1370 cm^{-1}; no quantitative treatment has been applied to that band. Carbonate absorption at 1430 and 1445 cm^{-1} were treated together. Errors in the maximum intensity of the 1420-1450 cm^{-1} spectral range are estimated at ±1.0 a.u./cm. Water absorption at 1640 and 1670 cm^{-1} was treated in the same way with ±0.5 a.u./cm associated error. Errors of ±0.2 a.u./cm are assigned to the 2350 cm^{-1} band. Similar errors are assigned to the sharp 3107 cm^{-1} C-H band due to smoothing of the peak during data reduction. The uncertainty in the peak intensity of the 3420 cm^{-1} water band is estimated as ±0.4 a.u./cm.

8.3.2. INTENSITY CORRELATIONS AND BAND ASSIGNMENT

Table 8.1 summarizes the intensities of the absorption band of the micro-inclusions in the different diamonds. Figures 8.4-8.9 present correlation diagrams where the intensity

Table 8.1. Band intensities in the spectrum of inclusion-bearing diamonds.

Sample	Band position in wavenumbers (cm^{-1}) 475	525	575	605	685	785	812	840	875	1000	1100	1430	1640	2350	3107	3430	1280
CTP 6268	5.08[1]	1.22	0.85	1.42	2.26	0.51	0.09	1.77	2.24	17.68	9.10	11.99	8.16	4.60	0.50	6.36	24.00
CTP L0	0.71	0.47	0.15	0.18	0.52	0.13	0.28	0.45	0.18	4.09	4.02	1.57	2.54	0.61	0.63	2.98	30.00
CTP L3	0.79	0.42	0.24	0.25	0.43	0.07	0.16	0.30	0.54	2.68	2.52	2.03	1.77	1.12	0.32	2.32	24.30
CTP L4	0.58	0.28	0.11	0.20	0.14	0.04	0.02	0.09	0.11	0.27	0.57	0.31	0.32	0.50		0.37	26.10
CTP L6	1.04	0.63	0.15	0.31	0.42	0.18	0.28	0.35	0.17	3.03	3.02	0.87	1.58	0.27	0.40	1.85	24.50
CTP LB	0.92	0.75	0.11	0.23	0.50	0.13	0.25	0.50	0.29	4.25	3.79	1.75	2.52	0.47	0.50	2.77	
CTP LB	0.62	0.32	0.17	0.17	0.31	0.09	0.20	0.36	0.20	2.90	2.66	1.32	1.80	0.55		2.20	28.80
CTP Z1	0.22	0.21	0.17	0.18	0.31	0.10	0.16	0.13	0.26	1.97	2.09	1.32	1.14	1.19	0.38	1.94	25.40
CTP Z2	1.41	0.74	0.29	0.45	0.51	0.07	0.14	0.37	0.30	3.10	2.76	1.79	2.22	0.84	0.38	2.28	27.00
CTP Z3	0.62	0.49	0.15	0.20	0.35	0.19	0.29	0.22	0.21	2.63	3.24	1.26	1.40	1.09	0.40	1.77	24.50
CTP Z4	4.31	2.66	0.28	0.41	0.86	1.45	1.91	0.34	0.02	10.77	16.39	2.13	1.47	0.79	0.60	4.60	31.70
CTP MM1	0.86	0.58	0.23	0.31	0.55	0.13	0.24	0.39	0.34	3.09	3.12	1.78	2.15	0.32	0.32	2.57	27.45
GRR 1503	1.86	1.29	0.52	0.48	0.74	0.42	0.53	0.55	1.78	4.45	6.40	5.85	3.51	1.19	0.21	4.41	22.00
GRR 1504	5.88	2.05	0.62	0.75	1.61	0.53	0.55	0.58	0.54	12.22	15.52	2.70	6.10	2.80	0.10	9.68	22.70
GRR 1508	1.90	0.96	0.24	0.26	0.80	0.29	0.37	0.66	0.59	6.10	6.38	2.65	3.22	0.53	0.40	4.20	24.00
GRR 861.2	0.60	0.35	0.08	0.16	0.21	0.14	0.22	0.13	0.26	1.64	2.51	1.33	0.79	0.72	0.35	1.53	20.00
GRR 1155	2.66	1.55	0.22	0.15	0.82	0.56	0.59	0.32	0.83	9.41	7.64	3.46	1.85	0.62	0.80	2.63	32.00
GRR 1513	0.74	0.70	0.25	0.35	0.33	0.09	0.11	0.26	0.19	2.20	1.79	1.14	1.54	0.89	0.50	1.83	25.50
GRR 1515	1.69	0.71	0.21	0.29	0.70	0.60	0.73	0.26	0.59	4.99	6.87	2.79	2.88	1.71	0.10	3.76	13.60
GRR 1519	1.60	0.83	0.19	0.28	0.51	0.20	0.26	0.29	0.13	3.35	3.26	0.87	1.56	1.13	0.50	2.31	23.30
Uncertainty[2]	0.5	0.5	0.2	0.2	0.2	0.2	0.2	0.2	0.2	0.3	0.3	1.0	0.5	0.2	0.2	0.4	1.0

1. Absorbance in cm^{-1} (absorbance units per cm).

2. See Section 8.3.1 for discussion of preferred estimation of uncertainty.

Figure 8.4. Intensity correlation of IR absorption bands in spectra of micro-inclusion-bearing diamonds.

a. The intensity of the 785 cm^{-1} band (Y axis) plotted against the intensity of the 812 cm^{-1} band (X axis) for all diamonds.

b - h. Intensity correlation between other bands.

Figures 8.5-8.9: Intensity correlation of the various peaks with the main silicate bands at 1000 and 1100 cm^{-1} and with the sum of the absorbance of the two bands.

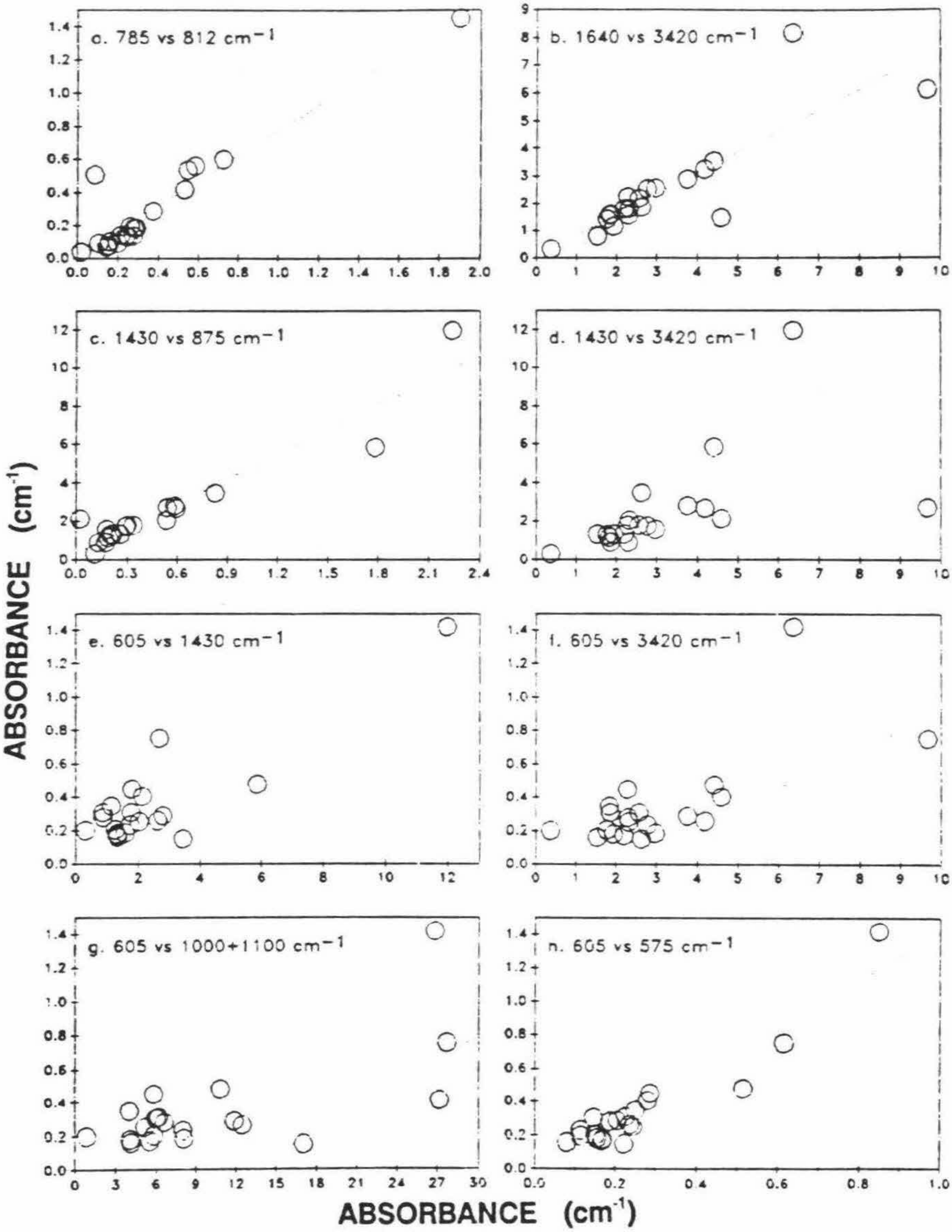
a. 785 vs 812 cm⁻¹
b. 1640 vs 3420 cm⁻¹
c. 1430 vs 875 cm⁻¹
d. 1430 vs 3420 cm⁻¹
e. 605 vs 1430 cm⁻¹
f. 605 vs 3420 cm⁻¹
g. 605 vs 1000+1100 cm⁻¹
h. 605 vs 575 cm⁻¹
ABSORBANCE (cm⁻¹)
ABSORBANCE (cm⁻¹)

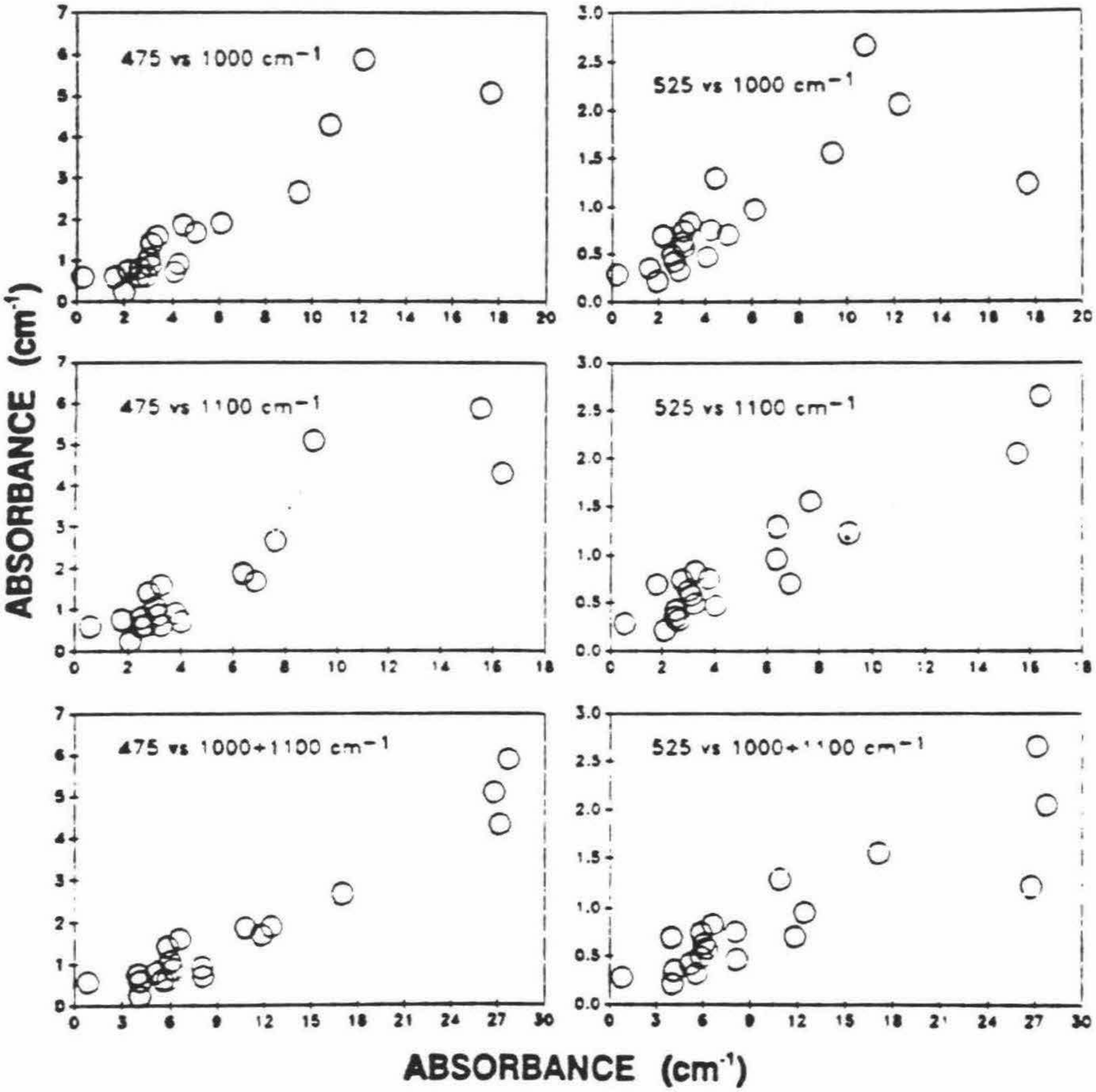
475 vs 1000 cm⁻¹
525 vs 1000 cm⁻¹
475 vs 1100 cm⁻¹
525 vs 1100 cm⁻¹
475 vs 1000+1100 cm⁻¹
525 vs 1000+1100 cm⁻¹
ABSORBANCE (cm⁻¹)
ABSORBANCE (cm⁻¹)
0
1
2
3
4
5
6
7
0.0
0.5
1.0
1.5
2.0
2.5
3.0
0
2
4
6
8
10
12
14
16
18
20
0
3
6
9
12
15
18
21
24
27
30

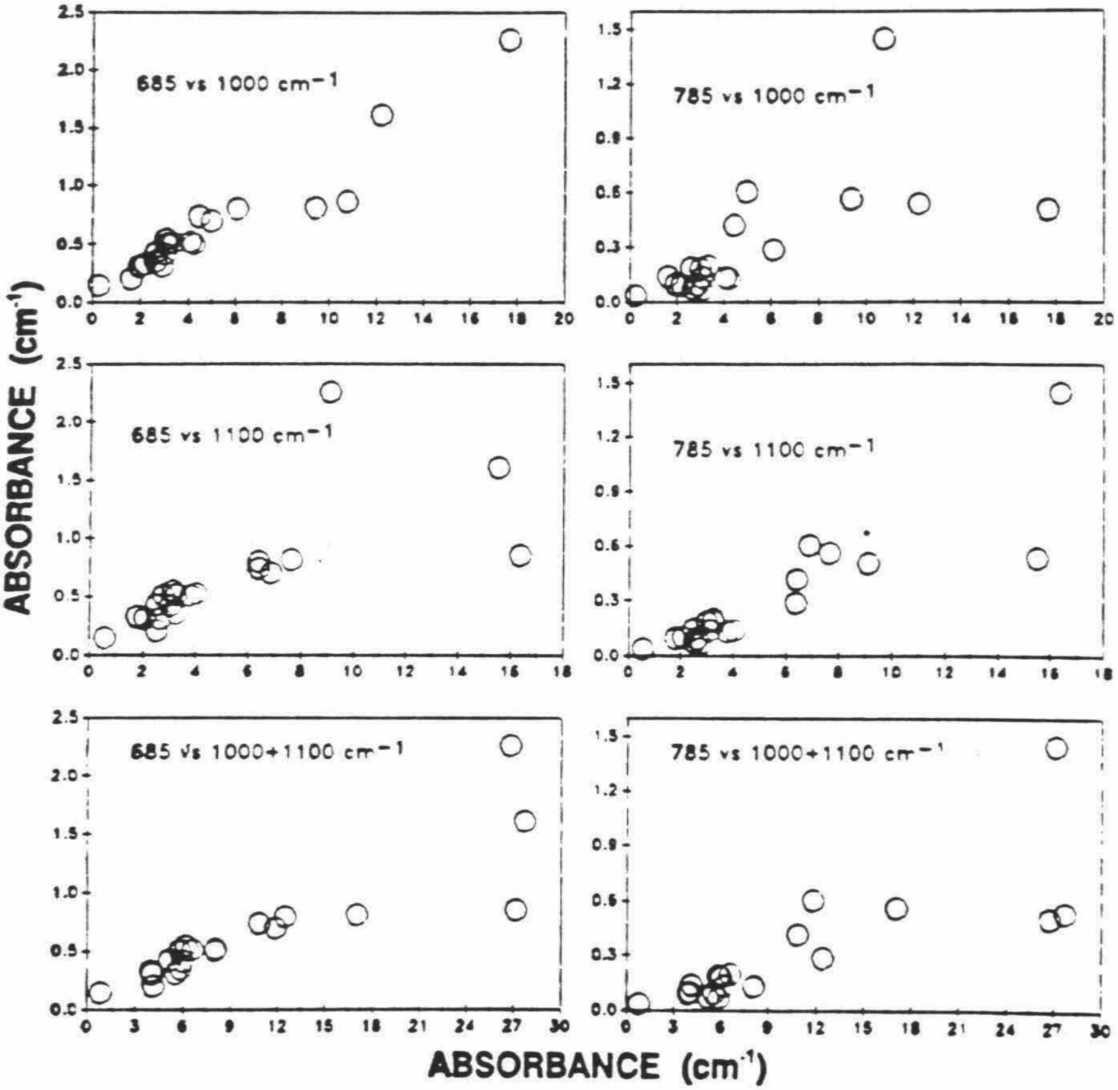
685 vs 1000 cm−1
785 vs 1000 cm−1
685 vs 1100 cm−1
785 vs 1100 cm−1
685 vs 1000+1100 cm−1
785 vs 1000+1100 cm−1
ABSORBANCE (cm⁻¹)
ABSORBANCE (cm⁻¹)
0.0
0.5
1.0
1.5
2.0
2.5
0.0
0.3
0.6
0.9
1.2
1.5
0
2
4
6
8
10
12
14
16
18
20
0
3
6
9
12
15
18
21
24
27
30

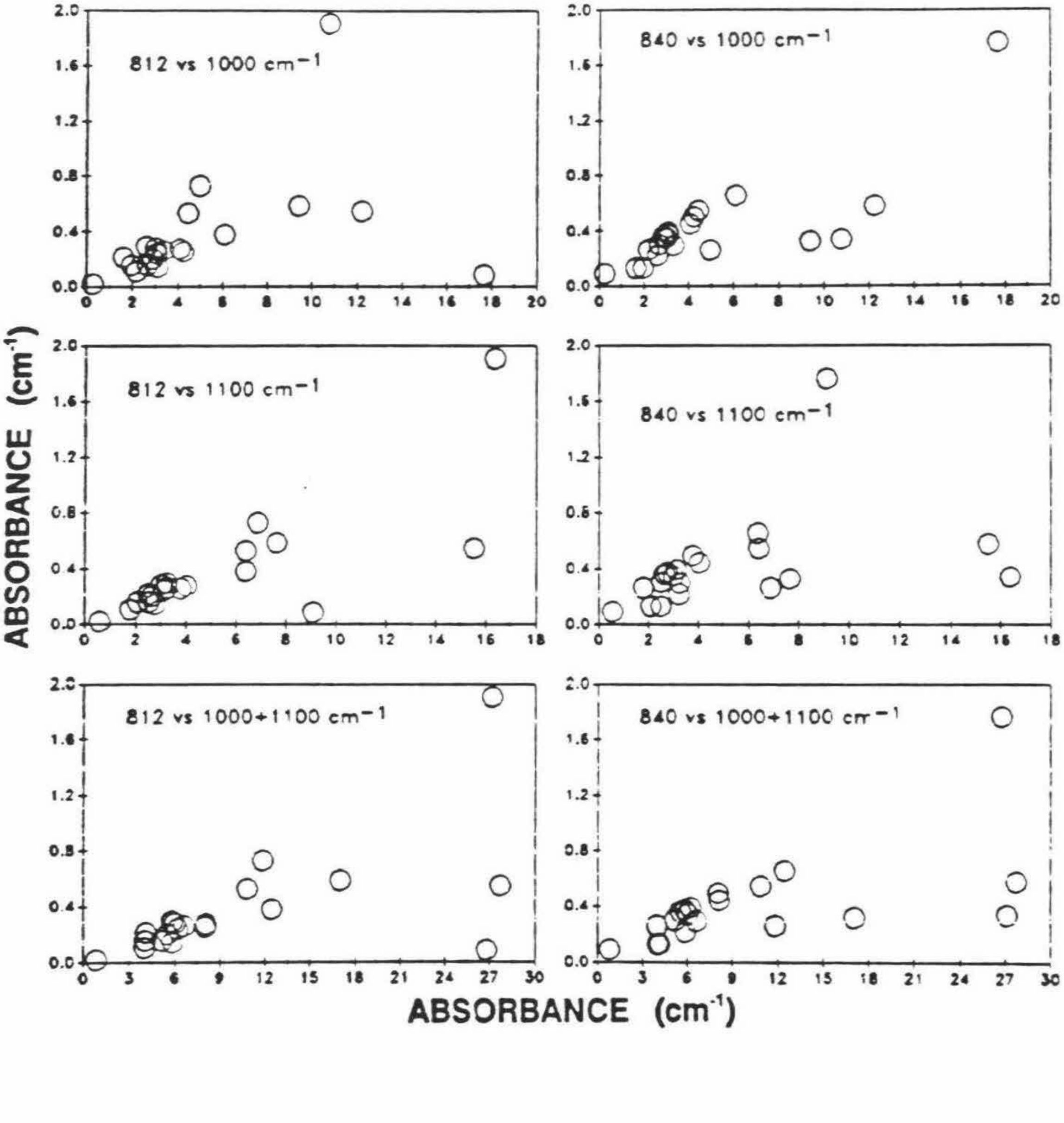
812 vs 1000 cm^{-1}
840 vs 1000 cm^{-1}
812 vs 1100 cm^{-1}
840 vs 1100 cm^{-1}
812 vs 1000+1100 cm^{-1}
840 vs 1000+1100 cm^{-1}
0.0
0.4
0.8
1.2
1.6
2.0
0
2
4
6
8
10
12
14
16
18
20
0
3
6
9
12
15
18
21
24
27
30
ABSORBANCE (cm^{-1})
ABSORBANCE (cm^{-1})

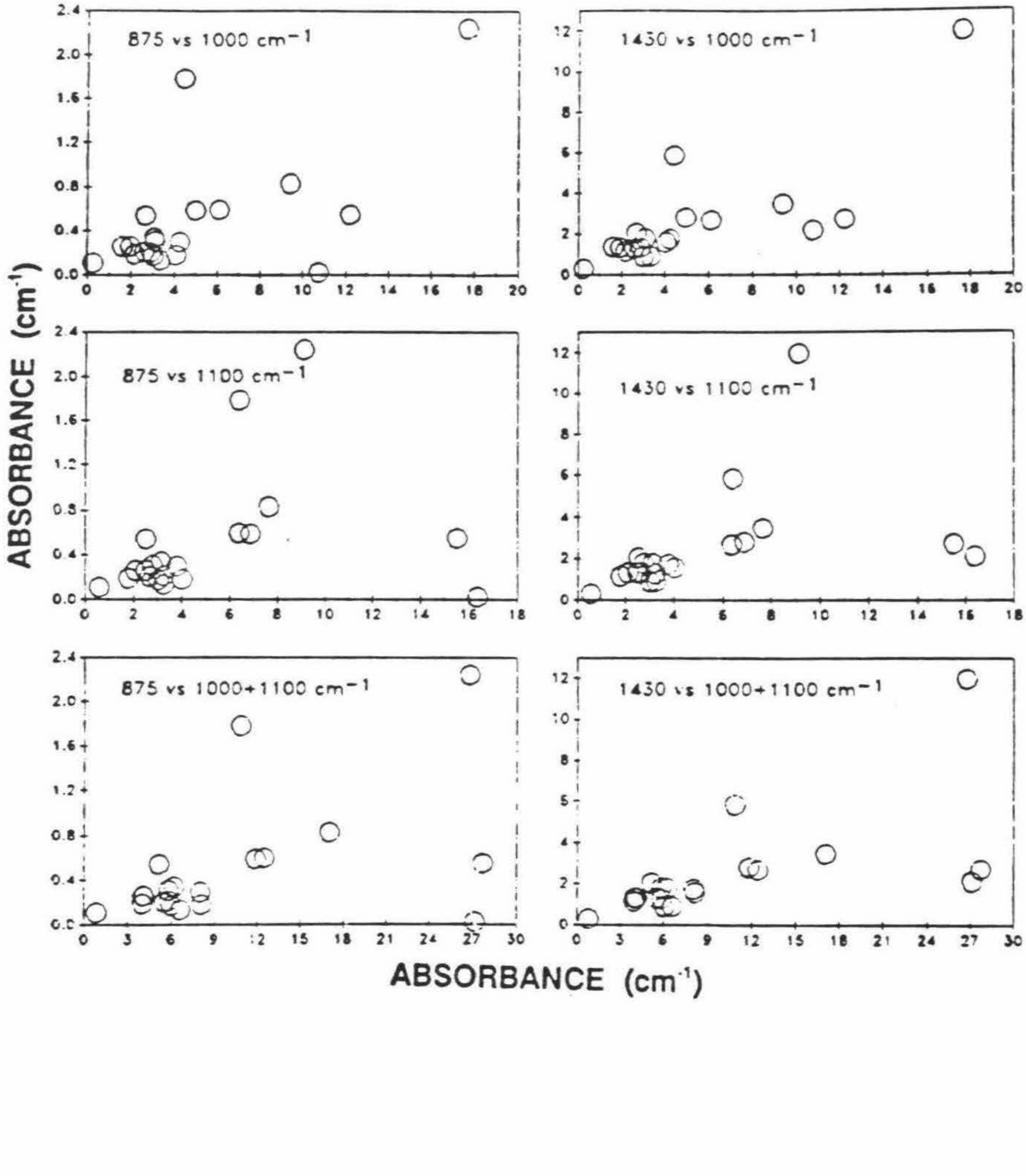
875 vs 1000 cm⁻¹
1430 vs 1000 cm⁻¹
875 vs 1100 cm⁻¹
1430 vs 1100 cm⁻¹
875 vs 1000+1100 cm⁻¹
1430 vs 1000+1100 cm⁻¹
ABSORBANCE (cm⁻¹)
ABSORBANCE (cm⁻¹)
0.0
0.4
0.8
1.2
1.6
2.0
2.4
0
2
4
6
8
10
12
0
2
4
6
8
10
12
14
16
18
20
0
3
6
9
12
15
18
21
24
27
30

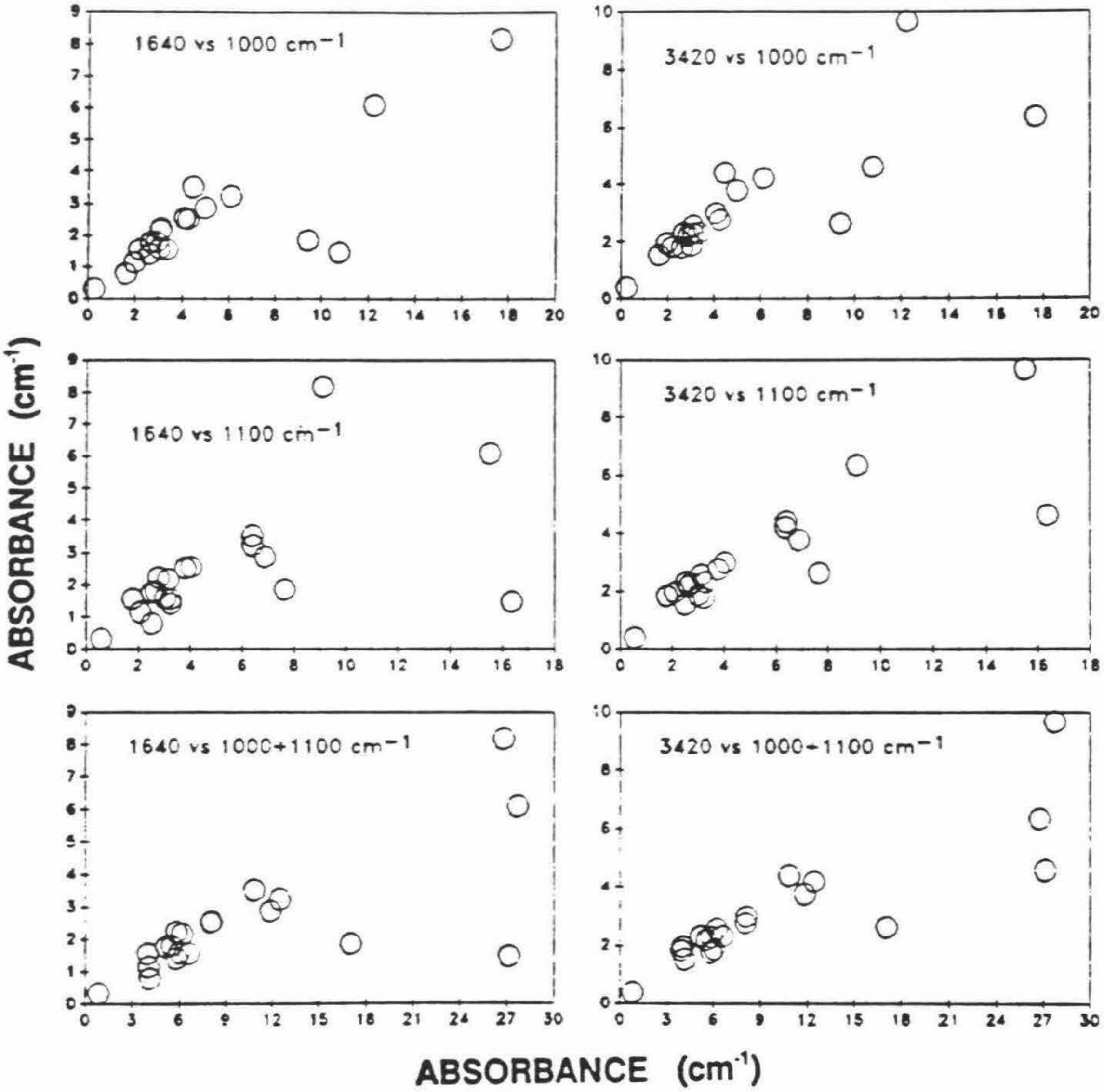
1640 vs 1000 cm⁻¹
3420 vs 1000 cm⁻¹
1640 vs 1100 cm⁻¹
3420 vs 1100 cm⁻¹
1640 vs 1000+1100 cm⁻¹
3420 vs 1000+1100 cm⁻¹
ABSORBANCE (cm⁻¹)
ABSORBANCE (cm⁻¹)
0
1
2
3
4
5
6
7
8
9
10
12
14
16
18
20
15
21
24
27
30

recorded for a specific band in all diamonds is plotted against the intensity of another band. Broad positive correlations are expected between any two bands, merely reflecting the increase in the intensities of all bands with increasing concentration of trapped material. Better correlations are expected between bands resulting from the same single phase. Indeed, the correlation between the intensities of the two water bands (Fig. 8.4a) and the two carbonate bands (Fig 8.4b) are much better than the correlation between the intensities of the water and the carbonate bands (Fig. 8.4c). Thus, it is argued that the good correlation between the intensities of the bands at 785 and 812 cm^{-1} (Fig 8.4d) suggest that both are due to one single phase.

The spectrum of minerals is commonly governed by the vibrations of the main anionic group (e.g., $SiO_4^{4-,}$ $CO_3^{=}$, PO_4^{3-}). Usually, the chemical interaction with different cations or the different crystallographic symmetry lead to characteristic modifications of the free group spectrum so that it is possible to distinguish between individual phases. In some cases, the differences between the few minerals that share the same anion group are too small and exact identification is difficult or impossible.

Apatite: The intensity of the 605 cm^{-1} band does not correlate well with the carbonate band (Fig 8.4e), the water band (Fig 8.4f) or the main silicate bands at 1000 and 1100 cm^{-1} (Fig. 8.4g). A much better correlation is observed between the intensities of the 605 and the 575 cm^{-1} bands (Fig. 8.4h). This good correlation, together with the similarity in position, shape and the relative height of the two bands with the 574 and 602 cm^{-1} bands in the powder spectrum of a Durango apatite, strongly suggest the bands are due to a phosphate phase in the micro-inclusions.

The position of the two bands is very similar to that of hydroxy- and flour-apatite (Ross, 1974). Alkali-phosphates absorb at lower wavenumbers, and in fact none of the many phosphates listed by Ross (1974) match the observed spectrum as well as those of the apatite group. The main apatite band at 1050 cm^{-1} is typically about twice the height of the 605 cm^{-1} band and is expected to be masked by the strong silicate bands.

Apatite was observed in a TEM study of a coated diamond (Lang and Walmsley, 1983).

A TEM examination of one diamond of the GRR batch, GRR 1527 (a triangular, coated diamond of spinel-type twinning), also revealed abundant, apatite-bearing inclusions (G. Guthrie, personal communication).

Carbonate: The correlation between the intensities of the characteristic carbonate bands at 1430 and 876 cm^{-1} is excellent (Fig 8.4c) and is superior to the correlation of either of these bands with the water, phosphate or silicate bands (Figs. 8.4d, 8.4e and 8.8a-e respectively).

CTP Z4, CTP 6268 and GRR 1503 deviate from the correlation line. CTP Z4 exhibits a small, but clear band at 1430 cm^{-1} but no band at 875 cm^{-1}. It does have a small band at 860 cm^{-1} which is not observed in any other diamond.

Calcite makes a close fit to the two carbonate bands of the micro-inclusions. The spectra of calcite powder in KBr pellets show bands at 1435, 875.6 and 712.6 cm^{-1}. While the position of the main band at 1430 cm^{-1} is common to many other carbonates as well, the 876 cm^{-1} line is characteristic. Dolomite absorbs at 879 cm^{-1} (measured on the FTIR), just outside the range spanned by the micro-inclusions. Magnesite, $MgCO_3$, absorbs at 887 cm^{-1} and siderite, $FeCO_3$, at 868 cm^{-1} (White, 1974); both are unlikely candidates. Examining the spectra of twenty-three Ca, Mg, Na and K carbonates and bicarbonates in White (1974), the band of only three phases, calcite, ankerite $Ca(Mg,Fe)(CO_3)_2$ and gaylusite $Na_2CO_3 \cdot CaCO_3 \cdot 5H_2O$, fall within the 874-878 cm^{-1} range spanned by the micro-inclusions. The in-plane $_4$ band of carbonates occurs at 712.6, 719, 726 and 729 cm^{-1} for calcite, gaylusite, ankerite and dolomite respectively. While many of the spectra of the micro-inclusions have a shoulder at 710-715 cm^{-1} only a few show any absorption band at 720-730 cm^{-1}. Thus, calcite appears to be the main carbonate phase in the micro-inclusions. The presence of other, additional carbonate phases (dolomite?) may be hinted at by the shoulder at 1445 cm^{-1}, the shift of the 876 cm^{-1} band to 878 cm^{-1} in the spectra of diamonds in which the 1445 cm^{-1} band is stronger than the 1430 cm^{-1} band, and by the weak absorption in the 720-730 cm $^{-1}$ region in a few of the diamonds.

Silicates: The two main bands at 1000 and 1100 cm^{-1} fall in the characteristic range of Si-O stretching vibrations in silicates. The intensities of the two peaks are only weakly correlated suggesting the presence of more than one silicate phase. CTP 6268 and CTP Z4 represent the two end-members with μ_{1100}/μ_{1000} of 0.5 and 1.5 respectively (μ being the absorbance in absorbance units at the specific wavenumber). Figures 8.6-8.8 show the correlation of other bands in the spectrum of the micro-inclusions with the 1000 and 1100 cm^{-1} bands and with the sum of their intensities.

The intensities of the 475 cm^{-1} best correlate with the sum of the intensities of the 1000 and the 1100 cm^{-1} bands (Fig. 8.6c). The position of this band is characteristic of Si-O bending vibrations. The 525 cm^{-1} band-intensities show the best correlation with the intensities of the 1100 cm^{-1} band (Fig. 8.6e), as are also the intensities of the 785 and 812 cm^{-1} bands (Fig. 8.7e, 8.8b). The only exceptions are GRR 1504 and CTP 6268. CTP 6268 completely lacks the 785 and 812 cm^{-1} bands. The intensities of the 685 and 840 cm^{-1} bands correlate best with the 1000 cm^{-1} band-intensity (Figs. 8.7d, 8.8d); exceptions are GRR 1155, GRR 1504 and CTP Z4. The intensities of the water bands at 1640 and 3420 cm^{-1} also show good correlation with those of the 1000 cm^{-1} (Figs. 8.9a,d); exceptions, again, are GRR 1155, GRR 1504 and CTP Z4. The good correlation between the intensities of the water and the silicate bands suggests the presence of a hydrated silicate phase. Absorption in the 800 cm^{-1} region is typical of metal-OH-metal vibrations of many amphiboles, micas and clay minerals (Farmer, 1974). The silicate stretching vibrations in those groups are commonly around 1000-1100 cm^{-1}. In particular, the spectrum of clays shows close resemblance to the silicate bands in the spectrum of the micro-inclusions.

Figure 8.10 show the spectra of two clay minerals: nontronite, $(1/2Ca,Na)_{0.66}Fe_4^{3+}Si_{7.34}Al_{0.66}O_{20}(OH)_4 \cdot nH_2O$, and montmorillonite, $(1/2Ca,Na)_{0.66}Al_{3.34}Mg_{0.66}Si_8O_{20}(OH)_4 \cdot nH_2O$, both belong to the smectite group and can absorb large amounts of water. Although neither matches the spectra of the micro-inclusions exactly, they show the same band structure and relative intensities. The spectrum of montmorillonite shows a band at 920 cm^{-1} which never appears in the spectrum of the micro-inclusions. This band is due to AlAlOH deformation (Russell, 1970) and is shifted to lower wavenumbers when Fe is substituted for Al. The FeFeOH band is at 818 cm^{-1} in the Fe-

Figure 8.10. IR absorption spectra of clays.

a. Nontronite (H-33b, from Manito, near Spokane, WA; CIT collection). Notice the general similarity to the spectra of the micro-inclusions. A split band at around 500 cm^{-1} is some what shifted to lower wavenumbers (460 and 493 cm^{-1}), a band at 678 cm^{-1} corresponds to the 685 $cm^{-1}$of the micro-inclusions, the weak band at 760 cm^{-1} does not correspond to a particular diamond band, however the other three bands at 785, 818, and 848 cm^{-1} are in the exact range as the three bands in the spectrum of the micro-inclusions (785, 812, 840 cm^{-1}). The main peak in the nontronite spectrum is at 1030, somewhat higher than the 1000 cm^{-1} for the main peak of the micro-inclusions. Only a weak shoulder is present at around 1100 cm^{-1}. The two water bands at ~1640 and 3420 cm^{-1} correspond to similar bands in the spectrum of the micro-inclusions. However, their relative intensity is much lower compared with the intensity of the silicate bands. The intensity of the 1640 cm^{-1} band is relatively low compared with that of the 3420 cm^{-1}, when compared with the spectra of the micro-inclusions. The band at 3630 cm^{-1} is due to O-H stretching vibrations of hydroxyl groups. The small peak at 2350 cm^{-1} is due to CO_2, either because of insufficient purging, or because it is in the clay.

b. Montmorillonite (H-26B, from Clay Spur, WA; CIT collection).

The spectrum is somewhat less similar to that of the micro-inclusions (mainly because of the bands at 620 and 918 cm^{-1}, which do not show in the spectrum of the micro-inclusions).

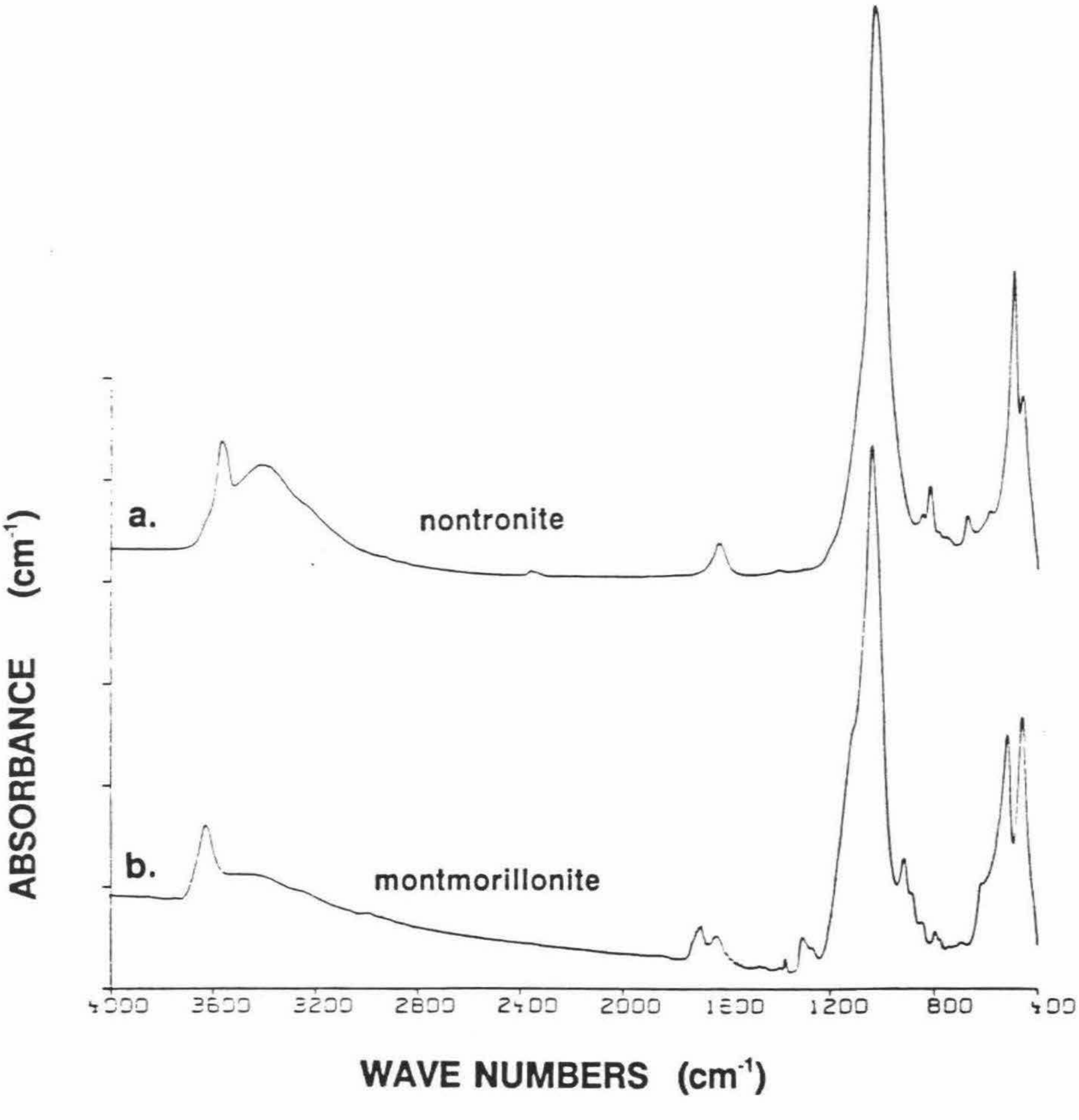
a.
nontronite
b.
montmorillonite
ABSORBANCE (cm^{-1})
4000
3600
3200
2800
2400
2000
1600
1200
800
400
WAVE NUMBERS (cm^{-1})

rich nontronite and at 812 cm^{-1} in glauconite (Russell et al., 1987). The micro-inclusions have a band at 812 cm^{-1}. These similarities make clay minerals and in particular Fe-rich clays the most probable candidates for the silicate phases in the micro-inclusions. Exact identification cannot be made based on the IR spectral data alone; hopefully, TEM data will enable a more precise determination of the silicate phases trapped in the diamonds.

The IR data can be used, however, to rule out the presence of olivine, garnet and pyroxene, as well as some other phases, as main constituents in the micro-inclusions. Absorption due to Si-O stretching in the isolated SiO_4 groups of olivine and garnet extend down to the 950 cm^{-1} region. This is not observed in the spectra of the micro-inclusions. No silicate bands are found at the 570-620 cm^{-1} range, where metal-oxygen vibrations of orthosilicates are expected. Similarly, ortho- and clinopyroxenes can be excluded based on their strong absorption in the 900-1000 cm^{-1} region.

Plagioclase and feldspars can be excluded based on their characteristic absorption in the 720-740 cm^{-1} region. The characteristic bands of quartz at 697 and 798 cm^{-1} were not observed in the diamonds. Hydrated silica and opal lack the 697 cm^{-1} band and have a broad band at 780-800 cm^{-1} and, thus, do not contradict the spectrum of the micro-inclusions. However, they show no absorption at 812 cm^{-1} while in the spectra of the micro-inclusions the 785 and the 812 cm^{-1} band intensities show excellent correlation. The common mantle amphibole, richterite, has a band at 740 cm^{-1}, and can be excluded as well. Some amphibole, e.g., tremolite, cannot be excluded based on a direct contradiction with the spectrum of the micro-inclusions, but are very unlikely to be present in the inclusions as major constituents as they cannot explain the observed correlations. Of the common micas, biotite absorbs at 720 cm^{-1} (Russell, 1987), muscovite at 754 and 935 cm^{-1} and phengite at 754 and 904 cm^{-1} (Farmer, 1974). However, the bands of phlogopite at 467, 613, 692, 814 and 1002 cm^{-1} are close enough to observed bands so that it, as well as hydrated silica, may be present in minor amounts.

Water: The position and shape of the water bands are typical of absorbed water (Stern, 1974). No sharp OH peaks are observed. This, as well as the good correlation between the intensities of the O-H stretching and the H-O-H bending modes, suggest that most water is present as water molecules rather than as hydroxyls. The presence of a bulk liquid water phase was tested by recording the spectrum of a liquid-nitrogen-cooled diamond. No characteristic shift to ice absorption at ~ 3200 cm^{-1} was observed. Figure 8.11 shows that except for some narrowing of the whole band, no shift is observed.

As discussed later, in section 8.5 the high relative water content indicated by IR is too high to be accommodated as lattice water in the phases contained in the micro-inclusions. If no bulk liquid water phase exists, then the relatively high amounts of water must be accommodated as interlayer water in clay minerals or as water absorbed on fine-grained phases.

8.4 THE QUANTIFICATION OF IR DATA

The size of the micro-inclusions dispersed throughout the diamond matrix is smaller than the wavelength of the IR radiation. This situation is similar to that in KBr pellets of finely ground powders and is ideal for quantitative work (Russell, 1974). The high refractive index of the diamond (n=2.42) ensures an almost parallel beam inside the diamond, even under the strong focusing in the microbeam chamber of the FTIR. For example, a beam with an angle of incidence of 20° is refracted and traverses the diamond at 5.6° to the normal. The high refractive index would lead, however, to multiple reflections from the diamond outer faces. About 3% of the transmitted intensity is due to multiple reflection. The multiply reflected rays travel two more times through the diamond and are absorbed to a higher extent. Over all, multiple absorption leads to 6% enhancement in absorption in the case of weak bands. Reflections from diamond - inclusion interfaces are less important, mainly because of the smaller difference in refractive indices. In a 0.5 mm thick diamond, with 1000 ppm impurities, the effective thickness of the inclusions is ~0.6 μm, corresponding to only 1-3 inclusions. The total multiple reflection (assuming normal incidence) accounts for less than 0.3% of the light.

A more serious problem may be caused by light scattering. Light scattered by the inclusions passes through a longer path-length in the diamond. As a result, the effective average path-length is increased, more light is absorbed and concentrations are over estimated.

Using data from the literature as well as from measurements of powder spectra of some carbonates and clays, I estimated the absorption coefficients for a few of the bands. Band heights rather than integrated absorption was used because of the possible errors in estimating the band width in the spectrum of the micro-inclusions. The choice of the values of absorption coefficients is discussed in the following section. The preferred values are summarized in Table 8.2.

8.4.1. ABSORPTION COEFFICIENT AND CONCENTRATION OF WATER

The shape and position of the water band at 3420 cm^{-1} suggests that most water is present as lightly bound water molecules, thus, the most reasonable value for the absorption coefficient is that of liquid water. Variations in the absorption coefficient of water in different environments are usually accompanied by shifts in the band positions. The similar position of the OH band in the spectra of the micro-inclusions and liquid water also suggests that liquid water should make a close approximation. ϵ_{3420}^{water} of 81 liter/mole·cm (Thompson, 1965) is in good agreement with the value calculated from the spectrum reported by Rossman (1988). Determination of the absorption coefficient of molecular water in rhyolitic glasses yielded ϵ_{3540}=56 (Newman et al. 1986) within 30% of the liquid water value. Using ϵ_{3420}^{water} of 81 liter/mole·cm concentration of 24-619 ppm were estimated for the diamonds studied (Table 8.2).

The relative height of the 3420 and the 1640 cm^{-1} bands in the micro-inclusions is quite different from that in pure water. Figure 8.4a indicates $\epsilon_{1640}/\epsilon_{3420}$ = 0.7; this ratio is 0.2 in pure water (Thompson, 1965; Rossman, 1988), 1 in rhyolitic glass (Newman et al., 1986) and

Table 8.2. Absorption coefficients and conversion factors for the main phases detected by IR.

Phase	**Calcite**	**Water**	**Apatite**	**clays**
Molec. wt. (gr)	100.1	18.0	502.3	~900
Wavenumber (cm^{-1})	1430	3420	605	1000
Absor. coeff. $\frac{liter}{mole \cdot cm}$	250	80	310	~2000
Component	CO_2	H_2O	P_2O_5	Water-free fraction
Conversion factor (ppm/a.u.-cm^{-1})	50	64	200	107

1. The factors for clays were calculated by averaging the results for montmorillonite and nontronite. Water was assumed to account for 90 gr of the assumed molecular weight of 900 gr (3 water molecules + 4 hydroxyl groups per unit formula).

0.37 and 0.31 in montmorillonite and nontronite, respectively, in KBr pellets (this study). It seems that most of this variation is due to changes in the absorption coefficient of the 1640 cm^{-1} and not the 3420 cm^{-1} band (G.R.Rossman, personal communication).

8.4.2. ABSORPTION COEFFICIENT AND CONCENTRATION OF CARBONATE

No absorption coefficient for the carbonate band was found in the literature. Best fit for the data of five powder spectra (G. Fine, personal communication and this work) yields $\epsilon_{1430}^{calcite}$ = 250 liter/mole·cm. Powder spectra of gaylusite (this work) and of Na_2CO_3 (G. Fine, personal communication) yield absorption coefficients of 216 and 329 liter/mole·cm respectively. Using $\epsilon_{1430}^{calcite}$ = 250 liter/mole·cm, carbonate concentrations of 23 to 877 ppm (CO_2 component of carbonate) are obtained for the diamonds studied (Table 8.2).

As in the case of water absorption, the intensity ratio of the two carbonate bands in the diamond differ from that of calcite. Figure 8.4c shows $\epsilon_{876}/\epsilon_{1430}$ =0.22, the ratio is 0.36 in calcite, 0.32 in gaylusite and 0.28 in Na_2CO_3. This variation may be the result of the sample preparation. The effect of grain-size on the measured band width and height may be substantial (Russell, 1988); the sharper 876 cm^{-1} band is more strongly affected compared with the broader 1430 cm^{-1} band.

8.4.3. ABSORPTION COEFFICIENT AND CONCENTRATION OF APATITE

A single powder spectrum of apatite yielded $\epsilon_{605}^{apatite}$ ~ 620 liter/mole·cm suggesting phosphate concentrations of 30-280 ppm apatite.

8.4.4. ABSORPTION COEFFICIENT AND CONCENTRATION OF CLAYS

The absorption coefficient of the silicate band of clays at ~1000 cm^{-1} was estimated from powder spectra of montmorillonite and nontronite. ϵ_{1030} = 2473 liter/mole-cm for nontronite, (molec. wt. = 926 gr/mole); montmorillonite (molec.wt. 809) yielded ϵ_{1040} = 1745. These absorption coefficients correspond to 97 and 117 ppm/a.u.-cm^{-1}. An average value of 107 ppm of "dry silicate" per 1 a.u./cm absorbance is used to calculate the concentration of "dry silicate" in the diamonds (Table 8.2). Corresponding "dry silicate" concentrations of 28-1900 ppm are estimated based on the IR data and the above calibration.

Nontronite and montmorillonite absorb at 1030 and 1040 cm^{-1} respectively and show only a weak shoulder at 1100. The spectrum of the micro-inclusions shows a strong absorption at both 1000 and 1100 cm^{-1}. The spectrum of the micro-inclusions indicates the presence of more than one silicate phase. Thus, the range of 28-1900 ppm, calculated using the intensity of the 1000 cm^{-1} alone, probably underestimates the **IR-determined**, "silicate" concentration. An upper bound can be estimated by using the sum of the intensities of the two bands. If this is done, the total concentration of the "dry silicate" in the diamonds falls between 90 and 3650 ppm.

8.5. MICRO-INCLUSIONS COMPOSITION - IR PERSPECTIVE

Table 8.3 presents the concentrations of water, the CO_2 component of carbonate, the P_2O_5 component of the apatite, the amount of CaO inferred from the presence of carbonate and phosphates (assuming that Ca is the sole cation in those phases) and the "dry silicate" content calculated by assigning the absorption coefficient of clays to the 1000 and 1100 cm^{-1} bands of the micro-inclusions. No correction has been applied for the longer average optical path in the diamonds.

The concentrations of all components vary over a large range, reflecting the different abundance of inclusions in the different diamonds. With the exception of diamonds CTP 6268, CTP Z4, GRR 1503, GRR 1504, which are much higher than the average, and CTP L4, which is lower, the other 15 diamonds carry a few tens ppm of P_2O_5, about 100 ppm CO_2, 200 ppm of associated CaO and 200 ppm water. "Silicate" concentrations are of the order of 400 ppm if only the 1000 cm^{-1} is taken into account and about 800 ppm when the sum of both the 1000 and the 1100 cm^{-1} absorption is used.

Taking these concentrations at face value, it is possible to deduce the composition of the micro-inclusions as inferred from the IR data. Table 8.4 lists the calculated proportions of the various components for the case in which the "dry silicate" component is calculated using

Table 8.3. Concentration of various components of micro-inclusions, as determined by IR spectrometry.

sample	H_2O[1]	CO_2[2]	P_2O_5[3]	CaO[4]	Silicate[5]	
					1000	1100
CTP 6268	407	599	284	1137	1892	974
CTP L0	191	79	37	149	438	430
CTP L3	149	101	51	196	287	270
CTP L4	24	15	40	72	28	61
CTP L6	118	44	61	136	324	324
CTP LB	178	87	47	173	455	406
CTP LB	140	66	34	129	310	284
CTP Z1	124	66	36	131	210	224
CTP Z2	146	90	90	233	332	295
CTP Z3	113	63	41	134	282	347
CTP Z4	294	107	82	243	1153	1754
CTP MM1	165	89	62	194	330	334
GRR 1503	282	292	95	498	476	684
GRR 1504	619	135	150	370	1308	1661
GRR 1508	269	133	52	238	652	682
GRR 861.2	98	67	32	128	176	269
GRR 1155	168	173	30	261	1007	818
GRR 1513	117	57	69	164	235	192
GRR 1515	241	139	57	253	534	735
GRR 1519	148	44	56	129	359	349
Average	200	122	70	248	539	555
Minimum	24	15	30	72	28	61
Maximum	619	599	284	1137	1892	1754

1. By total absorption in 3420 cm^{-1}. Assumed to include contributions from all hydrous components.

2. CO_2 component in carbonates; by total absorption at 1430 cm^{-1}.

3. P_2O_5 component of apatite.

4. CaO concentration inferred from carbonate and apatite concentrations, assuming that Ca is the sole cation.

5. Silicate concentration calculated assuming the absorption coefficient of the silicate component of the micro-inclusions is similar to that of clays (see footnote to Table 8.2).
   1000 - using the intensity of the 1000 cm^{-1} band.
   1100 - using the intensity of the 1100 cm^{-1} only (with the same conversion factor).

Table 8.4. Composition of the micro-inclusions, as inferred from IR spectrometry. Silicate concentration estimated using the 1000 cm^{-1} absorption only.

sample	H_2O[1]	CO_2	P_2O_5	CaO	Other Oxides	Total[2]
CTP 6268	9.4	13.9	6.6	26.3	43.8	4319
CTP L0	21.4	8.8	4.1	16.7	49.0	892
CTP L3	19.0	13.0	6.5	25.0	36.6	783
CTP L4	13.3	8.5	22.2	40.1	15.8	180
CTP L6	17.3	6.4	9.0	19.9	47.4	684
CTP LB	18.9	9.3	5.0	18.4	48.4	939
CTP LB	20.7	9.7	5.0	19.0	45.6	680
CTP Z1	21.9	11.6	6.3	23.1	37.1	568
CTP Z2	16.4	10.1	10.1	26.1	37.3	890
CTP Z3	17.9	10.0	6.5	21.2	44.5	633
CTP Z4	15.7	5.7	4.3	13.0	61.4	1878
CTP MM1	19.6	10.6	7.3	23.1	39.3	840
GRR 1503	17.2	17.8	5.8	30.3	29.0	1644
GRR 1504	24.0	5.2	5.8	14.3	50.6	2582
GRR 1508	20.0	9.9	3.9	17.7	48.6	1343
GRR 861.2	19.6	13.3	6.5	25.5	35.1	500
GRR 1155	10.3	10.6	1.9	15.9	61.4	1639
GRR 1513	18.3	8.9	10.8	25.5	36.7	642
GRR 1515	19.7	11.4	4.7	20.7	43.6	1224
GRR 1519	20.1	5.9	7.6	17.6	48.8	736
Average	18.0	10.0	7.0	22.0	43.0	1180
Minimum	9.4	5.2	1.9	13.0	15.8	4319
Maximum	24.0	17.8	22.2	40.1	61.4	180

1. The fraction of each of the listed components in wt% of the total.

2. Total content (ppm) calculated by summing the first five columns of Table 8.3 (silicate by the 1000 cm^{-1} absorption only).

only the absorbance of the 1000 cm^{-1} band. Table 8.5 presents the proportions calculated using the sum of the 1000 and 1100 cm^{-1} bands.

The main features rising from this exercise are:

(1) Water and carbonates account together for about 30% (1000 cm^{-1} band only) or 20% (both 1000 and 1100 cm^{-1} bands) of the total weight of the inclusions. These amounts are high, but are lower than earlier estimations (Navon et al. 1988).

(2) The total concentration of the included material in the diamonds, as suggested by IR, is much higher than the concentrations determined by SIMS.

8.6. COMPARISON WITH SIMS ANALYSIS

Figure 8.12 compares the concentration of the "dry silicate" component, as estimated by IR, with the total amount of oxide determined by SIMS. The two data sets exhibit good correlation, especially considering the different volumes sampled by each technique and the heterogeneity of the samples. This correlation indicates that both techniques analyze the same material, namely, the micro-inclusions. The slope of all three correlation lines is, however, larger than 1. When only the intensity of the 1000 cm^{-1} is used to estimate the concentration of the "dry silicate" component, the concentration estimated by IR is ~15% higher than the total oxide concentration determined by SIMS (Fig. 8.11a). If the sum of the 1000 and the 1100 cm^{-1} is used than the IR determination of the "dry silicate" concentration is 2.3 times higher than the total oxide concentration detected by SIMS (Fig. 8.11.b). Concidering that some of the oxides measured by SIMS must be incorporated in the carbonates, the discrepancy is even greater.

Similar disagreement is found between SIMS determination of CaO concentrations and the CaO calculated by assuming that Ca is the sole cation in the carbonate. Figure 8.12.a compares the two data sets; the observed positive correlation is weaker than in the case of the silicates. The IR estimation is more than three times higher than the SIMS determination. The discrepancy between IR and SIMS become larger if the CaO content inferred from the presence of apatite is also added (Fig 8.12.b). The CaO concentration estimated by IR are

Table 8.5. Composition of the micro-inclusions, as inferred from IR spectrometry. Silicate concentration estimated using the sum of the 1000 and 1100 cm^{-1} bands.

sample	H_2O[1]	CO_2	P_2O_5	CaO	Other Oxides	Total[2]
CTP 6268	7.7	11.3	5.4	21.5	54.1	5293
CTP L0	14.4	5.9	2.8	11.2	65.6	1322
CTP L3	14.1	9.6	4.8	18.6	52.8	1053
CTP L4	9.9	6.4	16.6	30.0	37.1	241
CTP L6	11.7	4.3	6.1	13.5	64.3	1007
CTP LB	13.2	6.5	3.5	12.9	64.0	1345
CTP LB	14.6	6.8	3.5	13.4	61.7	964
CTP Z1	15.7	8.3	4.5	16.6	54.9	792
CTP Z2	12.3	7.6	7.6	19.6	52.9	1185
CTP Z3	11.6	6.4	4.2	13.7	64.1	980
CTP Z4	8.1	2.9	2.2	6.7	80.0	3632
CTP MM1	14.0	7.6	5.3	16.6	56.6	1174
GRR 1503	12.1	12.6	4.1	21.4	49.8	2328
GRR 1504	14.6	3.2	3.5	8.7	70.0	4243
GRR 1508	13.3	6.5	2.6	11.7	65.9	2026
GRR 861.2	12.8	8.7	4.2	16.6	57.8	769
GRR 1155	6.8	7.0	1.2	10.6	74.3	2457
GRR 1513	14.1	6.8	8.3	19.6	51.2	834
GRR 1515	12.3	7.1	2.9	12.9	64.7	1959
GRR 1519	13.6	4.0	5.2	11.9	65.3	1085
Average	12.3	7.0	4.9	15.4	60.4	1734
Maximum	6.8	2.9	1.2	6.7	37.1	5293
Minimum	15.7	12.6	16.6	30.0	80.0	241

1. The fraction of each of the listed components in wt% of the total.

2. Total content (ppm) calculated by summing all six columns of Table 8.3 (silicate by the 1000 cm^{-1} absorption only).

Figure 8.11. Concentration of "dry silicate" in the diamonds, comparison of IR and SIMS results.

The X axes in all three graphs show the average total concentration of metal oxides in the different diamonds as determined by SIMS. Y axes show the "dry silicate" concentration in the diamonds inferred from IR spectrometry.

a. The "dry silicate" concentration in the diamond as calculated using the intensity of the 1000 cm^{-1} band only.

b. The "dry silicate" concentration in the diamond as calculated using the intensity of the 1100 cm^{-1} band only.

c. The "dry silicate" content is calculated using the sum of the intensities of the 1000 and the 1100 cm^{-1} bands (see text for details). Note that the best correlation is achieved in that case.

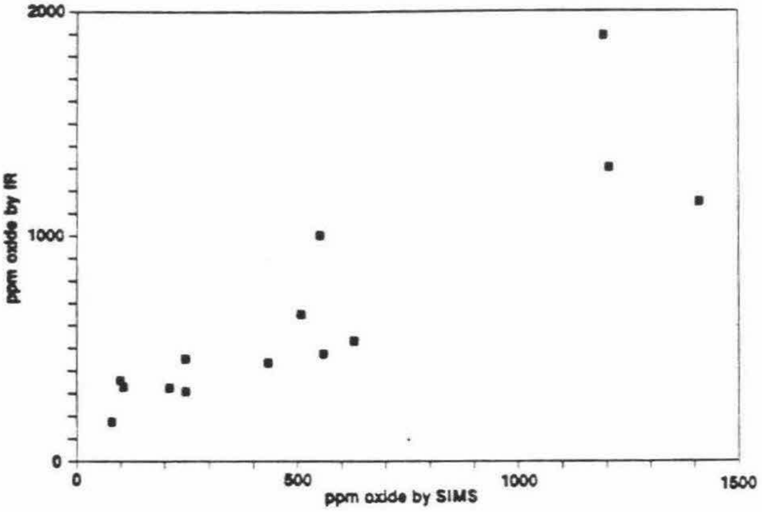
2000
1000
0
ppm oxide by IR
0
500
1000
1500
ppm oxide by SIMS

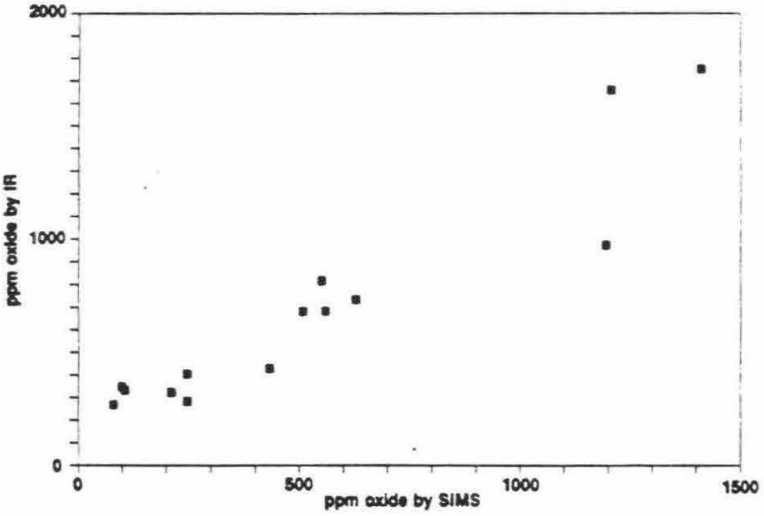
2000
1000
0
ppm oxide by IR
0
500
1000
1500
ppm oxide by SIMS

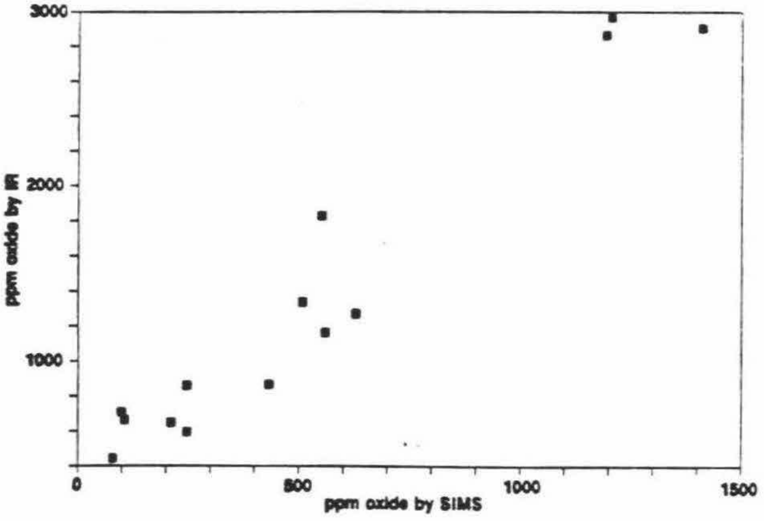
3000
2000
1000
ppm oxide by IR
0
500
1000
1500
ppm oxide by SIMS

Figure 8.12. CaO concentration in the diamonds, comparison of IR and SIMS results.

a. Comparison of the CaO inferred from calcite concentration in the diamond (assuming Ca is the sole cation in the carbonates) with CaO concentration determined by SIMS.

b. The CaO inferred from both the carbonate and the phosphate against the CaO concentration determined by SIMS.

c. The CaO inferred from the calcite concentration (same as in part a) plotted against total oxide concentration detected by SIMS. The correlation in this case is weaker than either the correlation of CaO in calcite against CaO by SIMS or the "dry silicate" concentration vs. total oxide concentration by SIMS. Thus, the correlations are not just due to variation in the number of inclusions, but rather, are related to the chemistry of the micro-inclusions.

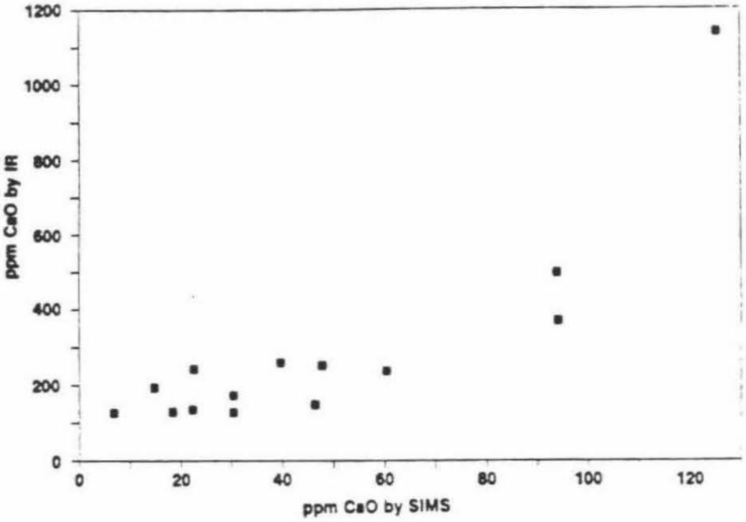
1200
1000
800
600
400
200
0
ppm CaO by IR
0
20
40
60
80
100
120
ppm CaO by SIMS

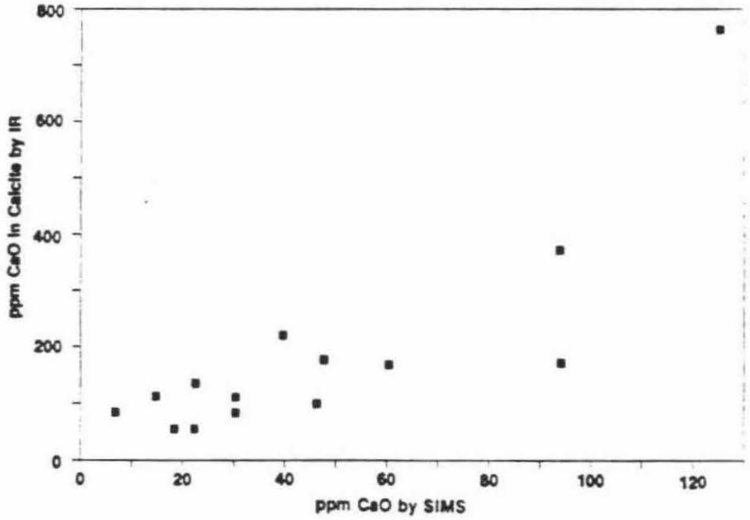
800
600
400
200
0
ppm CaO in Calcite by IR
0
20
40
60
80
100
120
ppm CaO by SIMS

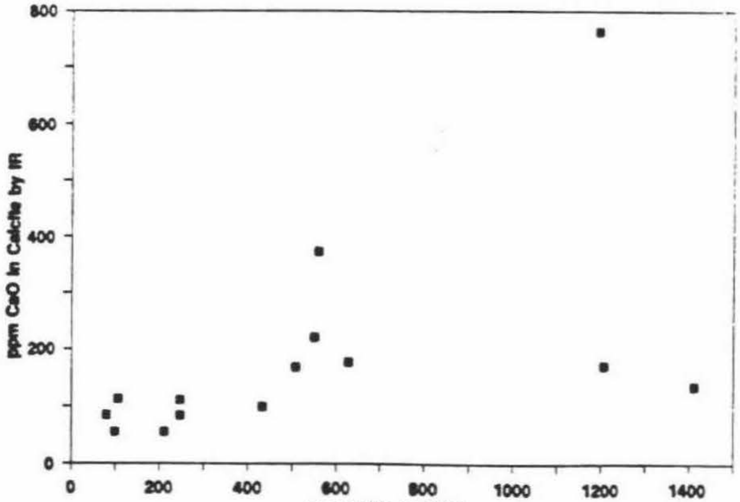
800
600
400
200
0
ppm CaO in Calcite by IR
0
200
400
600
800
1000
1200
1400
ppm oxide by SIMS

five times higher than the SIMS results. The concentrations of P_2O_5 deduced from IR data (30-300) are also much higher than those detected by EPMA (0-30).

What may be the reasons for the observed discrepancy between IR and SIMS data? Few possible sources are discussed below. At present, none of them can be singled out as the main contributor to the observed differences; a few of these posible sources can be shown to be of minor importance.

1. Errors in the determination of absorption coefficients.

Clearly, the absorption coefficients of Table 8.2 are preliminary. The absorption coefficient of apatite is based on a single measurement, silicate absorption is based on two clay samples. Still, discrepancies occur for carbonate absorption as well. In this case, absorption coefficients determined by two different operators, using different spectrometers and different samples of calcite and other carbonates, deviate by less than 30%.

2. The presence of other cations in the carbonates.

If the assumption that Ca is the sole cation in the carbonate is relaxed and Mg, Na, Fe, and K are allowed to form carbonates than, in most cases, the SIMS determined concentration of cations is sufficient to support the carbonate observed by IR. However, these cations are also associated with the silicates so they cannot be fully incorporated in the carbonate. TEM indicates the presence of dolomite and ankerite, however, IR data indicate that calcite is the main carbonate and that dolomite ankerite may only be present in minor amounts.

3. Optical path is longer than diamond thickness. As discussed earlier (Sec. 8.4) multiple reflection causes the effective optical path in diamonds to be 6% longer than the diamond thickness. Light scattering by the inclusion-diamond interfaces would enhance this effect. It is difficult to determine the effect of light scattering; it is estimated that it may lead to a few tens of percent increase in the observed absorption.

4. SIMS calibration may underestimate the concentrations of the various oxides. This effect is estimated to be of the order of 20%, it cannot account, alone, for all the observed difference between IR and SIMS.

5. The two techniques sample different volumes.

SIMS measurement only samples few hundred μm^3 from the surface of the polished diamond. IR analysis yields the average composition of the whole thickness of the diamond wafers, with total volume, about 10^5 times that of the SIMS. Since the diamonds are zoned this may lead to difference between the concentrations detected by the two techniques. However, the good correlation between "dry silicate" and total oxide concentrations (Figs. 8.11) argues that this is not the case and that the average concentrations derived from SIMS data are representative of the concentration in the bulk diamond.

6. Errors in the determination of band intensities. The good correlations between the intensities of the two carbonate bands (Fig. 8.4.c), the phosphate bands (Fig. 8.4.h), and the main silicate bands (Fig. 8.5-8.9) coupled with the extension of most of these correlation lines to the origin indicate that errors in background correction are insignificant.

None of the above can be the sole source for the observed discrepancy between IR and SIMS analysis. The last two effects, the difference in the analyzed volumes, and errors in the determination of band intensity may only increase the scatter of the results around the correlation line but should not change its slope.

A more accurate determination of the absorption coefficients and of the effect of light scattering and multiple absorption on the observed intensities can be achieved by more careful experiments.

(1) Grain size of the absorbing phases should be smaller than the wave-length of the IR radiation and comparable in size to the micro-inclusions. To achieve grain-size of $< 1\ \mu m$ it may not be enough to grind the sample; it may be necessary to separate the fine grain fraction in a separation column.

(2) The inert salt carrier should be closer in its refractive index to the diamond. The replacement of KBr (n=1.5) by TlBr (n=2.4) and the study of the effect of this replacement on the observed absorption coefficient will lead to better estimation of the absorption of IR radiation by the micro-inclusions.

(3) At present, there is no independent check on the absorption coefficient of water in the micro-inclusions. Determination of the water absorption in clays may yield such a check.

8.7 FREEZING AND LEACHING EXPERIMENTS

8.7.1. FREEZING

The spectrum of diamond ON ZIZ 74 was recorded at room temperature. The spectrum is a typical one and show all the absorption bands due to micro-inclusions. Both water and carbonate bands are clear and distinct. The diamond was placed in an evacuated, liquid nitrogen cooled cryostat with CaF_2 windows and its spectrum was recorded. Comparison of the two spectra only reveals a modest narrowing of the OH peak and a small shift of it center position. Figure 8.13 shows the two spectra together with a spectrum of an ice-covered diamond (taken after allowing some humid air into the cryostat). It clearly shows that no ice was detected under cryogenic conditions. The shift resulted by cooling is negligible compared with the large shift between water and ice and may be merely the result of the narrowing of the asymmetric peak. This negative result suggest that water is not present as bulk liquid in the micro-inclusions and is in agreement with the interpretation of the spectrum as being the result of absorbed or interlayered water. However, it is also possible that liquid water is present in the inclusion but cannot be frozen due to their high solute content and due to the small size of the water domains.

8.7.2. LEACHING

Diamond ON ZIZ 74 was split into three fragments. One fragment was heated in concentrated $HF+HClO_4$ in a closed Teflon vial at ~120°C for 22 days. The other fragment was placed in an open silver palladium capsule and was heated in a "cold seal" pressure vessel to 750°C under water pressure of 1300 bar for seven days. Internal buffering by the vesssel sets the oxigen fugasity to Ni-NiO conditions. The IR spectra of the two fragments show no difference compared with either the spectrum of the third, untreated fragment, or the spectra recorded on the two fragments before treatment. If any change did occur, it must be limited to a thin surface layer. This experiment, as well as TEM observations, indicate that the

Figure 8.13. Freezing experiment on ON ZIZ 74.

a. The spectrum at room temperature. The sharp band at 3107 cm^{-1} is due to C-H vibration in the diamond matrix.

b. The spectrum at liquid nitrogen (LN_2) temperature. The whole peak is narrower. The shoulder at ~3700 cm^{-1} is more pronounced. The weak shoulder at ~3570 which can be seen in the room temperature spectrum cannot be seen at the LN_2 spectrum.

c. a spectrum of the ice-covered diamond recorded after some air was let into the cryostat. The shift from water to ice is large. It clearly does not show in b.

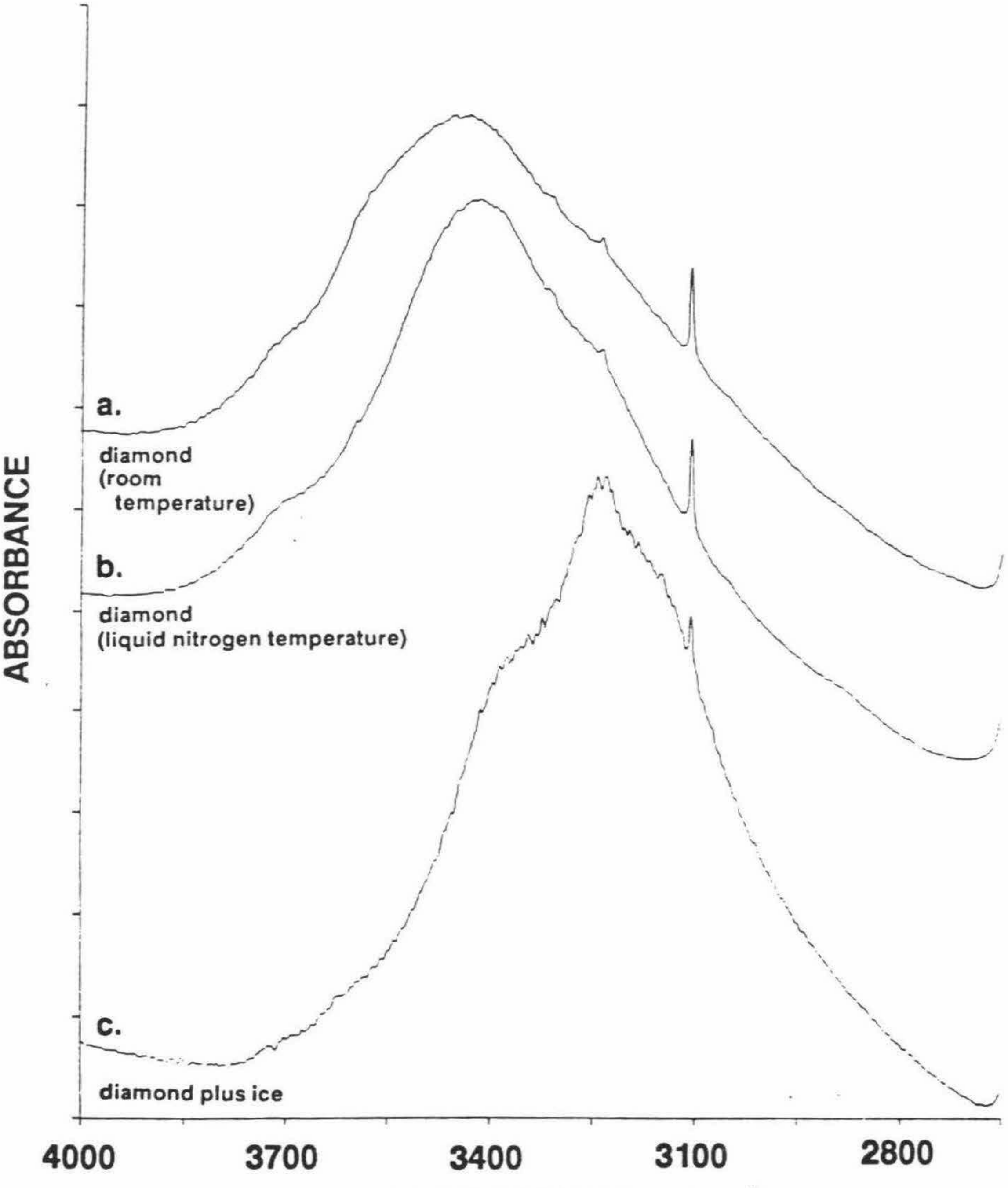
ABSORBANCE
a.
diamond
(room
temperature)
b.
diamond
(liquid nitrogen temperature)
c.
diamond plus ice
4000
3700
3400
3100
2800
WAVE NUMBERS (cm-1)

inclusions in the bulk diamond are well encapsulated and are not likely to be affected by alteration.

8.8. SUMMARY

IR spectroscopy indicates the presence of hydrous, silicate, carbonate, and phosphate phases and some molecular CO_2 in the micro-inclusions of all the cubic and the coated diamonds studied here. The silicate bands have many of the characteristic bands of Fe-rich clays, such as nontronite, glauconite and celadonite. The good correlation observed between the intensities of the water and silicate bands suggests that the water is associated with the clays. The position of the OH stretching band at 3430 cm^{-1} and the negative result of the freezing experiment suggest that water is associated with the clays as interlayered or absorbed water. The presence of a hydrous fluid phase is not supported by the data presented here. However, it cannot be excluded. High solute content and the small size of the inclusions may prevent freezing (Roedder, 1984); the good correlation of water and silicate bands may be inherited from the original material trapped by the diamonds.

The position of the carbonate bands show fits best the spectrum of calcite. Few other carbonate phases have closely relates spectra. They may be present in minor amount. Ankerite shows the highest similarity, dolomite gaylusite and perhaps few other, less common carbonate may also be present. The phosphate is most likely apatite. Other phosphate groups lack the characteristic bands at 575 and 605 cm^{-1}.

The conversion of band intensities to concentrations is still problematic. The use of absorption coefficients of water, apatite calcite and two smectite clays yields concentrations that are much higher than those determined by SIMS, for every component for which comparison is possible. Thus, at present, the average proportion of volatiles (water and carbonate) can only be estimated to be roughly between 20 and 40% of the total weight of the inclusions. Water is the main volatile species and $H_2O/(H_2O+CO_2)$ varies between 0.6 And 0.9 in molar proportions.

CHAPTER 9 INSTRUMENTAL NEUTRON ACTIVATION ANALYSIS

Instrumental neutron activation analysis (INAA) has excellent sensitivity for a large number of elements. Because the carbon matrix is not activated (Fesq et al. 1973), detection limits in diamonds are even lower than those achieved in silicate analysis. Since both SIMS and IR spectroscopy indicate that the composition of individual diamonds is relatively homogenous (within ±15%), a bulk analysis of the diamonds may be used to determine the average trace element composition of the micro-inclusions.

Ten samples were analyzed using INAA, thanks to the generous cooperation of H. Palme and B. Spettel at the Max Planck Institute for Chemistry at Mainz, Germany. The main purpose of the analysis was to verify whether it was possible to analyze small samples of micro-inclusion-bearing diamonds. The results clearly demonstrate that useful trace-element-concentration data may be obtained for ~10 mg sized samples of inclusion-bearing diamond material, using INAA. More than 50 elements were detected and the concentration of K, Na, Ba, Sr, the REE and a few other elements were determined and incorporated with the SIMS data to produce a more complete description of the chemistry of the micro-inclusions.

Section 9.1 presents the experimental details. Section 9.2. discusses the results. The data are presented in Section 9.2.1., compared with the SIMS data in Section 9.2.2., and examined in the context of the full compositional data for the micro-inclusions in Section 9.2.3.

9.1. EXPERIMENTAL PROCEDURE

Ten samples of inclusion-bearing diamonds were selected for INAA analysis. GRR 1504, 1505, 1507, 1508, and 1509 are coated diamonds. GRR 1515, 1517,1518, and 1519 are cubic diamonds. Fragments of the coated diamonds contain both core and coat material, the cubic diamonds consist solely of inclusion-bearing material. Samples GRR 1517 and 1519 are sawed halves of cubic diamonds. Sample GRR 1504 was divided into two aliquots; the lighter of the two consisted of five small fragments of almost pure coat material and the other had both core and coat with about 40% coat. The weights and the estimated percentage of the coat are listed in Table 9.1.

GRR 1508 and GRR 1515 had been previously mounted in epoxy and required special cleaning. The majority of the epoxy was removed after overnight soaking in acetone and CH_2Cl_2. Some residual material was removed mechanically using a tungsten needle. All samples were cleaned in acetone, $HCl+HNO_3$, water, HF and given a final rinse in deionized water and alcohol. An inclusion-free, crack-free gem quality diamond was cleaned in HF+HCL, water, dilute HCL, and ultra-pure water (M40) to determine the analytical blank. All the inclusion-bearing diamonds have a few cracks. GRR 1509 had several large cracks and GRR 1519 had many cracks. All samples were stored in pre-cleaned polyethylene containers and sent for irradiation in the TRIGA reactor in Mainz using the routine technique of the Mainz laboratory (Wanke et al. 1977).

9.2. RESULTS

9.2.1. ANALYTICAL DATA

Table 9.1 is a summary of the data for all elements whose concentration could be determined in the ten samples analyzed. (More detailed results, including the errors and the full list of all the elements detected, are given in Appendix A.4). Among all the elements detected, K is the most abundant and varies in concentration from 6 and 168 ppm, similar to the levels recorded by the other analytical techniques. Cl, Na, Ba, Sr, and La are present at concentrations above 1 ppm, while Mn, the remaining REE, Th, U, and Br are present at the 10-200 ppb level or higher. Sc was found at the ppb level in most diamonds; similar ppb levels of As, W, Ir, and Au were found in only a few diamonds.

The chondrite-normalized abundances of the incompatible elements in the samples are presented in Figure 9.1. The concentrations of the REE in the bulk diamond vary between 0.01 and 20 times the chondritic values. As the total concentrations of all other oxides are on the order of ~500 ppm, the REE levels in the micro-inclusions are 10-20,000 times chondritic values, indicating an extreme enrichment of REE in the micro-inclusions. All diamonds present extremely light REE (LREE)-enriched patterns. Other incompatible

Table 9.1. **Trace element concentration (ppm) in micro-inclusion-bearing diamonds.**

Sample	**GRR 1504**	**GRR 1504**	**GRR 1505**	**GRR 1507**	**GRR 1508**	**GRR 1509**	**GRR 1515**	**GRR 1517**	**GRR 1518**	**GRR 1519 LL**	**Blank DDN 20**
weight (mg)	28.57	1.682	2.094	1.054	12.207	9.29	2.587	26.149	1.212	23.414	14.014
Coat fraction[1]	0.4	0.98	0.9	0.9	0.3	0.3	1	1	1	1	1
Fe[2]	38						150	30			
Na	9.36	27.2	15.6	15.2	4.12	6.28	34.6	1.42	7.21	9.72	0.304
Cl	14.9	36.9	41	46.6	23.7	11.1	215	1.82	7.5	13.1	1.27
K	68.8	168	97.3	94.5	29.9	40.81	78.8	6.38	26.2	39.3	
Sc	0.00795				0.0039		0.028	0.00435	0.044	0.0050	
Cr							7.36				
Mn	0.341	0.795	0.453	0.287	0.136	0.193	0.664	0.0507	0.17	0.194	0.0016
Ga		0.06								0.0066	0.0045
As		0.034			0.0045			0.0021		0.0057	
Br	0.037	0.093	0.143	0.453	0.0314	0.023	0.076	0.0076		0.0294	0.011
Sr	2.56	6.28	6.76	5.94	1.09	2.13	7.68	0.375	1.7	3.20	
Ba	8.97	21.3	23.5	31.1	7.34	7.13	10.5	0.32	3.3	5.03	
La	1.1	1.92	6.52	1.28	0.34	1.62	0.932	0.0829	0.22	0.41	
Ce	1.65	2.3	10.8		0.65	2.56				0.86	
Pr			0.71		0.17	0.16				0.089	
Nd	0.52	0.61	2.8		0.31						
Sm	0.0478	0.0889	0.29	0.0243	0.02	0.0519	0.0607		0.008	0.0245	
Eu	0.011	0.0209	0.0597	0.00363	0.00455	0.0108	0.0133		0.0031	0.0051	
Dy	0.013	0.0249	0.0927		0.00359	0.0127	0.0187			0.0051	
W		0.04			0.0094					0.011	0.013
Ir						0.0023				0.0011	
Au					0.00986		0.2033				
Th		0.22				0.076					
U	0.015				0.0087					0.014	
$(La/Sm)_{chon}$	14	13	14	33	10	19	9		17	10	
$(Ce/Eu)_{chon}$	13	10	16		13	21				15	

1. Fragments of coated diamonds contained both core and coat material. The coat fraction is the eye-estimated fraction of the coat in the total volume of the sample.

2. Element concentration in ppm. Only elements for which concentrations have been determined are given in this table. See Appendix I.4 for associated uncertainties and for a complete list of all the detected elements.

Figure 9.1. Trace-element-abundance in diamond micro-inclusions.

Chondrite-normalized concentrations of trace elements in the bulk diamond. Lines connect the values of Ba and REE of each sample. (REE chondritic abundances of Nakamura, 1974. U, Th, K, Sr, Ba, Pr from Palme et al. (1981). The values of Palme et al. were multiplied by 1.34 to normalize them to the Nakamura REE values.)

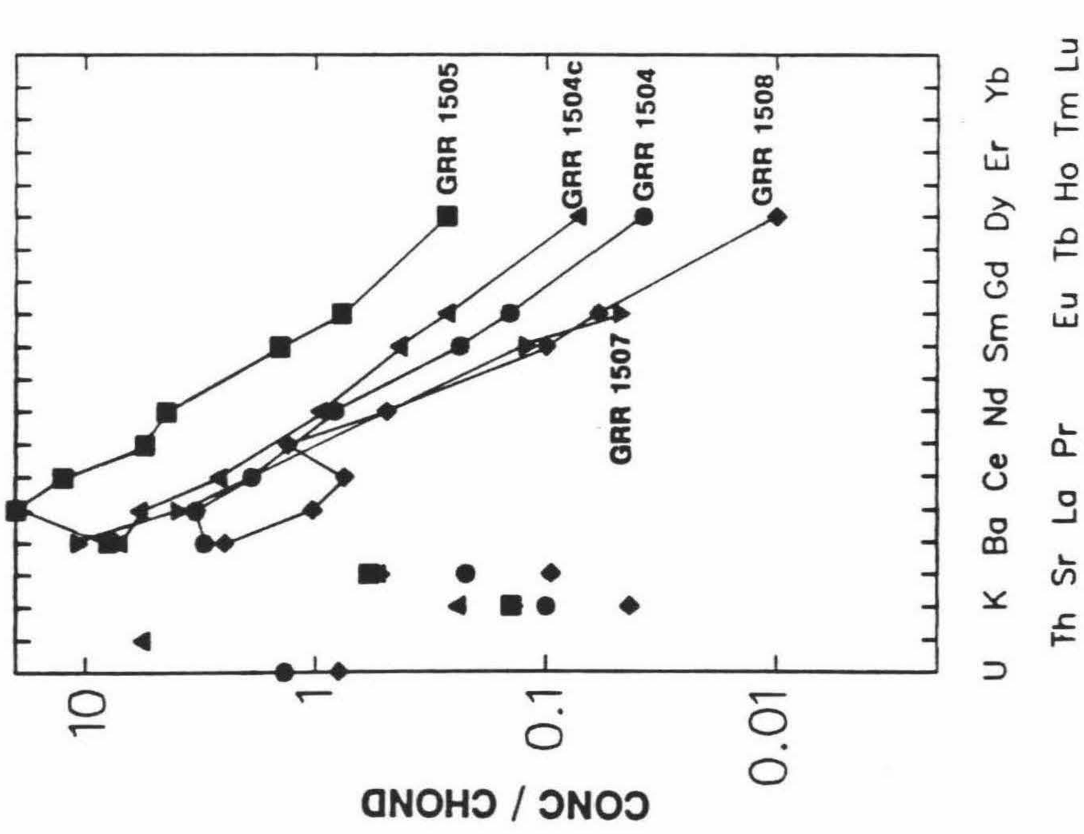
CONC / CHOND
10
1
0.1
0.01
U K Ba Ce Nd Sm Gd Dy Er Yb
Th Sr La Pr Eu Tb Ho Tm Lu
GRR 1505
GRR 1504c
GRR 1504
GRR 1508
GRR 1507

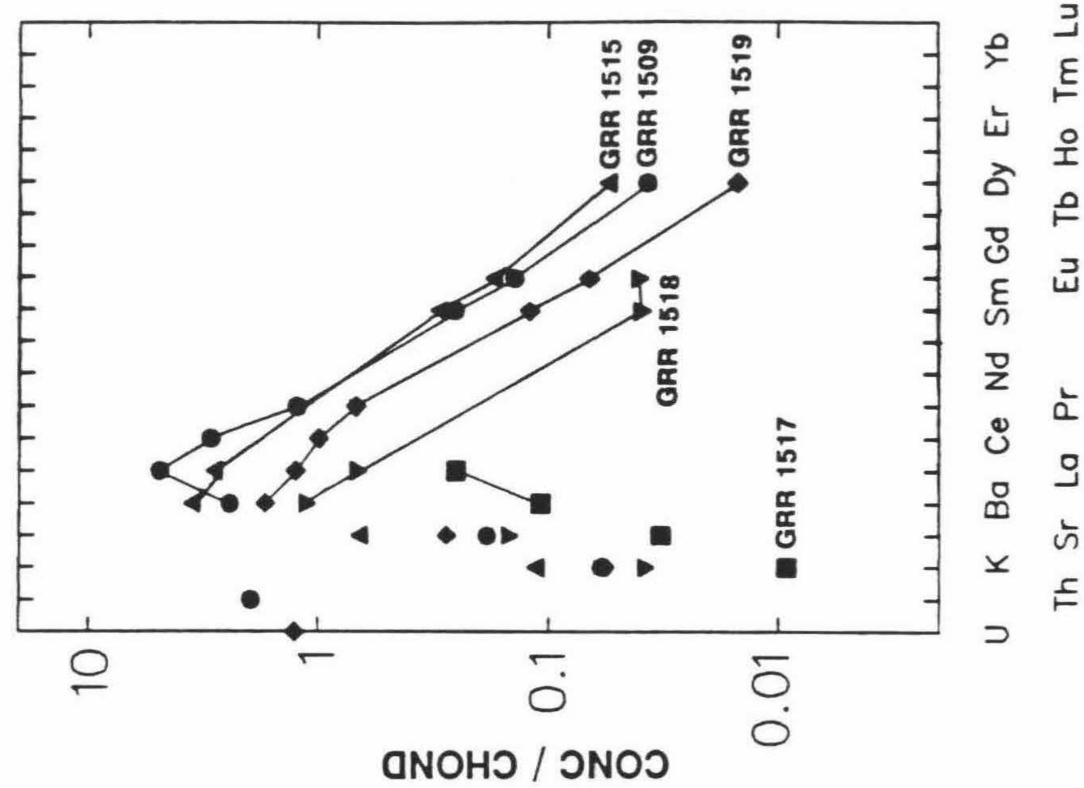
CONC / CHOND
10
1
0.1
0.01
U K Ba Ce Nd Sm Gd Dy Er Yb
Th Sr La Pr Eu Tb Ho Tm Lu
GRR 1515
GRR 1509
GRR 1519
GRR 1518
GRR 1517

elements, such as Ba, Sr, Th, and U, are also highly enriched. Ba/La ratios vary over a large range, with Ba being more enriched relative to La in a few samples and depleted in others. Similar variations have been observed in other cubic diamonds from Zaire (Akagi and Masuda, in press). Th and U concentrations are at the same levels as the LREE. Unfortunately, the abundances of these two elements were not determined in the same samples so Th/U ratios cannot be calculated. K/U ratios in the three samples for which uranium concentrations were determined range from 2800-4600. Compared with the mantle value of 10^4, these values indicate that the diamonds are 2-3 times more enriched in uranium relative to potassium. La/Sm and Ce/Eu ratios of 10-33 and 10-21 respectively also indicate extreme enrichment of incompatible elements relative to more compatible ones.

9.2.2 COMPARISON WITH SIMS ANALYSIS

Six of the diamonds were analyzed by both SIMS and INAA, making it possible to compare the concentrations of sodium and potassium determined by the two techniques. Such a comparison is useful as an independent check of the relative ion-yields used in reducing the SIMS data and of the quality of the INAA analysis. Moreover, the analysis of one or more elements by both techniques enables the incorporation of both data sets and the calculation of the trace element content of the micro-inclusions.

In Table 9.2 concentrations of K and Na are compared for the two techniques. Potassium and sodium concentrations determined by INAA are systematically higher than those determined by SIMS (except for the potassium in GRR 1504). The difference in potassium concentrations could be attributed to the fact that each technique analyzes a different volume of a heterogeneous sample. However, the systematically lower Na and K levels measured by SIMS suggest other sources of error. In addition, if all Na and K reside in the micro-inclusions, the same Na/K ratios should be detected by both techniques for the same diamond, regardless of the absolute concentration of the two elements. However, SIMS Na/K ratios are ~30% lower than the ratios obtained by INAA. Sodium concentrations recorded by SIMS are expected to be underestimated relative to potassium by ~10% (see Sections 6.2.2 and

Table 9.2. Comparison of SIMS and INAA analyses.

	GRR 1504	GRR 1504	GRR 1508	GRR 1515	GRR 1517	GRR 1518	GRR 1519
ppm K (INAA)[1]	172.0	171.4	99.7	78.8	6.4	26.2	39.3
ppm K (SIMS)[2]	194.4	194.4	89.0	64.6	4.6	18.9	9.9
SIMS/INAA	1.13	1.13	0.89	0.82	0.72	0.72	0.25
ppm Na (INAA)[1]	23.4	27.8	13.7	34.6	1.4	7.2	9.7
ppm Na (SIMS)[2]	20.6	20.6	9.0	22.4	0.4	3.0	2.5
SIMS/INAA	0.88	0.74	0.66	0.65	0.31	0.41	0.26
Na/K (INAA)	0.14	0.16	0.14	0.44	0.22	0.28	0.25
Na/K (SIMS)	0.11	0.11	0.10	0.35	0.10	0.16	0.25
SIMS/INAA	0.78	0.65	0.74	0.79	0.43	0.57	1.01
ppm Cl (INAA)[2]	14.9	36.9	23.7	215.0	1.8	7.5	13.1
Cl/K (INAA)	0.09	0.22	0.24	2.73	0.29	0.29	0.33
Na corrected for blank[3]							
ppm Na (INAA)	23.2	24.7	13.3	32.6	1.2	2.9	9.5
ppm Na (SIMS)	20.6	20.6	9.0	22.4	0.4	3.0	2.5
SIMS/INAA	0.89	0.84	0.68	0.69	0.36	1.02	0.26
Na/K (INAA)	0.13	0.14	0.13	0.41	0.19	0.11	0.24
Na/K (SIMS)	0.11	0.11	0.10	0.35	0.10	0.16	0.25
SIMS/INAA	0.78	0.74	0.76	0.84	0.50	1.41	1.04

1. Concentration in the coats of GRR 1504 and GRR 1508 are calculated by dividing the elemental concentrations by the fraction of the coat in the analyzed sample (eye-estimated before analysis).

2. Concentration in ppm of the metal in the diamond volume analyzed by SIMS.

3. Blank correction (ppm) = $\mathrm{ppm}_{\mathrm{blank}} \times \mathrm{wt}_{\mathrm{blank}}/\mathrm{wt}_{\mathrm{sample}} = 5.2/\mathrm{wt}_{\mathrm{sample}}$.

5.1.3), but the observed difference between INAA and SIMS is much larger.

One possible reason for the different concentrations recorded by the two techniques is sample contamination. Both Na and K are common surface contaminants. Prior to SIMS analysis, Na and K are efficiently removed by rastering the primary beam and sputtering away the surface layer of the area to be analyzed. This can not be done prior to INAA analysis and surface contamination may affect the INAA results leading to higher observed concentrations. The concentration of Na in the diamonds is lower than that of K. Consequently, Na concentrations are likely to be affected to a larger extent and Na/K ratios appear to be higher. The blank levels determined by analyzing an inclusion-free, crack-free gem quality diamond are low (Table 9.1, with K being below detection limit). Still, higher levels of contamination may be present in the samples analyzed due to the presence of cracks and, in some cases, possibly traces of epoxy. Diamonds GRR 1515 and GRR 1519 appear to be strongly affected by contamination. Chlorine levels detected by INAA are also high. In the case of GRR 1515 the extremely high Cl level must be the result of contamination.

In summary, contamination on surfaces and cracks may have affected the INAA analysis of Na, K, and Cl, preventing accurate comparison with the SIMS results. Potassium concentrations appear to be less affected and this element is used in relating SIMS and INAA data.

9.2.3. TRACE ELEMENT COMPOSITION OF MICRO-INCLUSIONS

Assuming that the trace elements and potassium are present only in the micro-inclusions, the trace element concentration in the micro-inclusions may be calculated by normalizing the INAA data to the K content determined by SIMS:

$$C^{i}_{inc} = C^{i}_{dia} * C^{K}_{inc}/C^{K}_{dia}$$

where C^{i}_{inc} is the concentration of element i in the micro-inclusions and C^{i}_{dia} and C^{K}_{dia} are the concentrations of element i and of potassium in the bulk diamond, respectively, as determined by INAA. C^{K}_{inc} is the content of potassium in the micro-inclusions.

Table 9.3 presents the trace-element content of the micro-inclusions. If some of the

Table 9.3. **Estimated trace-element composition of the micro-inclusions.**

	GRR 1504	**GRR 1504**	**GRR 1508**	**GRR 1515**	**GRR 1517**	**GRR 1518**	**GRR 1519**
Sc	19		23	37	143	269	13
Mn	798	762	797	867	1662	1040	496
Sr	5993	6020	6385	10033	12296	10396	8182
Ba	20997	20419	42999	13716	10493	20180	12880
La	2575	1841	1992	1217	2718	1345	1053
Ce	3862	2205	3808				2203
Pr			996				227
Nd	1217	585	1816				
Sm	112	85	117	79		49	63
Eu	26	20	27	17		19	13
Dy	30	24	21	24			13
Th		211					
U	35		51				36

Concentrations (in ppm) of the metal oxide fraction of the micro-inclusions.

potassium analyzed by INAA is due to contamination and the other trace elements are only found in inclusions, then the trace-element concentrations given here are underestimated. They are also independent of the proportions of core and coat in the analyzed samples.

All the incompatible elements are highly enriched in the micro-inclusions. Ba and Sr are present at the percent level, and La and Ce are at 1000-4000 ppm levels in the metal-oxide fraction of the micro-inclusions. All the REE, Ba, Sr, Th, and U are present at very high levels, higher than those of most kimberlites and lamproites (Smith, 1985; Bergman, 1987); Mn is lower compared with kimberlites and within the range spanned by lamproites (Bergman, 1987). The determined Sc contents are variable; the low values, 13-37, are similar to those in kimberlites, lamproites and alkali basalts.

CHAPTER 10 WHAT IS TRAPPED IN THE MICRO-INCLUSIONS?

Several analytical techniques have been employed in order to determine the composition and the mineralogy of micro-inclusions found in the cuboid growth zones of cubic and coated diamonds. The sub-micrometer size of the inclusions and their low abundance in the diamond (<0.2 volume percent) poses some analytical difficulties. Therefore, a great deal of effort was devoted to establishing analytical techniques specific to the micro-inclusions, as summarized in Section 10.1. In Section 10.2, the analytical results obtained by SIMS, EPMA, SEM-EDS, FTIR, and INAA are synthesized with the results of optical examination and with isotopic data from other studies in order to characterize the composition of the micro-inclusions. The evidence for a primary origin of the inclusions is summarized in Section 10.3; experimental constraints on the state of the matter in the inclusions are discussed in Section 10.4. The relation of the micro-inclusions to some important upper-mantle processes is discussed in Sections 10.5-10.7.

10.1. QUANTITATIVE DETERMINATION OF COMPOSITIONS AND ASSOCIATED ERRORS

The micro-inclusion-bearing regions in all diamonds are highly zoned. The number density of inclusions in the diamonds is variable on both millimeter and micrometer scales, and hence the concentrations of the different oxides may vary by more than an order of magnitude. However, the average compositions of inclusions in different volumes of a single diamond appear to be relatively uniform. Thus, in spite of the relatively low precision of oxide concentration measurements in the bulk diamond, the composition of the inclusions was determined with reasonable precision. (A limitation to this arises partly from the trace amount concentrations of the inclusions' major oxides within the actual diamonds).

EPMA analysis of diamonds with high content of inclusions (>0.1%) yields metal oxide concentrations with uncertainties on the order of 10-50%. The precision is limited by counting statistics for the less abundant elements. The best results from this technique are for the concentrations of SiO_2, K_2O, and CaO, which are the main constituents of the inclusions. Systematic errors in the correction procedure are estimated to be smaller than 10% (relative) for all of the elements analyzed except Na, for which the error should be <20%. Na and possibly Mg are underestimated by ~10% due to simplifications made in the model used for the correction procedure.

SIMS analysis yields much better precision than EPMA for the eight elements studied. The precision in the determination of metal concentrations is limited by the heterogeneity of the samples. The accuracy of the final results is limited by the knowledge of the ion-yields used during the conversion of count-rates to concentrations.

Ion-yields determined from SIMS-EPMA calibration carry associated errors (2σ) of 12-63%. Ion-yields determined by direct measurement of diamonds with implanted ions of the elements of interest are in good agreement with the SIMS-EPMA results for most elements. However, the large discrepancy in the case of Si suggests that the ionization efficiency for metals in the oxide matrix of the micro-inclusions is different from the ionization efficiency of metal atoms from the carbon matrix of the implanted diamond.

Comparison of relative ion-yields (RIYs) obtained from SIMS-EPMA correlation and from analysis of graphite-glass mixtures suggests that the SIMS-EPMA correlation underestimates the concentrations of all elements by about 20%. Underestimation of the concentrations of all metal oxides is also suggested by comparison of SIMS results with the results of INAA and FTIR measurements.

Nevertheless, the SIMS-EPMA calibration is the best available at present. It probably underestimates the concentrations of all eight metals analyzed, but if the effect is roughly the same for all metals then it should only affect the determination of absolute concentrations and not the relative composition of the trapped material. Na and possibly Mg are underestimated relative to the heavier elements due to inaccuracies in the reduction of EPMA data. This effect is expected to be smaller than 20% for Na and 10% for Mg. No correction has been applied due to a lack of an accurate estimate of the size of this effect. Elemental ratios for the heavier elements are of higher accuracy and, hence, the composition of the micro-inclusions can be determined with higher accuracy than the concentrations of the metals or their oxides in the diamond. The uncertainties are difficult to estimate. The precision can be deduced from the compositional variation between analyses of different volumes in the same diamond. If the diamond is assumed to be of homogeneous composition, then the ±20% (2σ) variation between analyses puts an upper limit on the precision. The accuracy is roughly estimated at 20% from comparison with other determinations of RIYs and with concentration determinations by other techniques.

SEM analyses of individual inclusions were corrected using the same correction procedure as the EPMA. The precision of the results is also of the order of a few tens of percent. The average compositions of the inclusions in individual diamonds determined by SEM agrees with SIMS determinations and further establishes the validity of both techniques.

Quantification of the IR data are still of very low accuracy. More accurate results must await a precise identification of the phases in the inclusions and a better determination of absorption coefficients. Good correlation is observed between IR absorbance and total oxide concentration as determined by SIMS. However, the concentrations determined by IR do not agree with SIMS results. As a result, the proportions of water and carbonate in the micro-inclusions is not well-constrained.

In spite of their low accuracy, SIMS, EPMA, and EDS analyses succeed in characterizing the main features of the chemistry of the micro-inclusions. As can be seen in Figure 10.1, the current level of accuracy is clearly sufficient to define the distinct and unique character of the micro-inclusions.

10.2. THE COMPOSITION AND MINERALOGY OF THE MICRO-INCLUSIONS

The micro-inclusions in the different diamonds are broadly of similar composition (Fig. 10.1, Table 10.1). All diamonds reported here show high contents of H_2O, $CO^{=}_3$, SiO_2, and K_2O. Composition of the metal oxide fraction of most diamonds vary within the following ranges: SiO_2, 30-53 wt%; K_2O, 12-30%; CaO, 8-19%; FeO, 6-11% (total iron as FeO); Al_2O_3, 3-6%, MgO, 2-6%, TiO_2, 2-4% and Na_2O, 1-5%, P_2O_5, 1-4%; BaO, 1-4%; SrO, 0.7-1.5%; La_2O_3, 0.1-0.3%; Ce_2O_3, 0.3-0.5%; and smaller amounts of other REE, Mn, Th and U.

Figure 10.1. Major-element abundances in diamond micro-inclusions relative to average group I kimberlite (Smith et al. 1985). Stippled area represents the results for all diamonds except CTP Z4 ( ), CTP 6268 ( ), and GRR 1515 ( ). Solid line indicates an average for lamproite (Bergman, 1987); Dashed line represents an average for group II kimberlites (Smith et al. 1985).

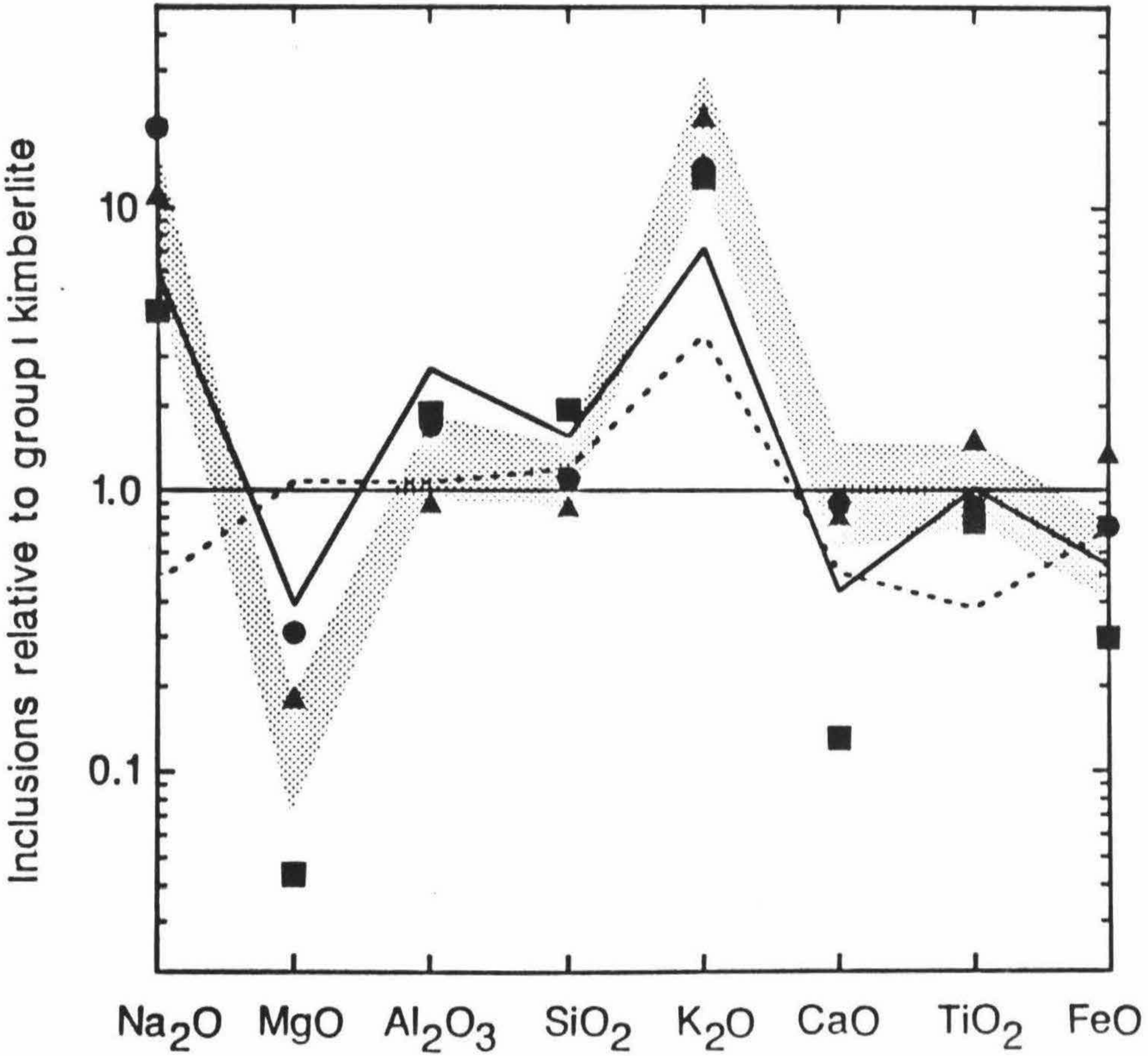
Inclusions relative to group I kimberlite
10
1.0
0.1
Na_2O
MgO
Al_2O_3
SiO_2
K_2O
CaO
TiO_2
FeO

Table 10.1. Average composition of the micro-inclusions.

	Average composition	Standard deviation	Maximum content	Minimum content	Intra-diamond deviation
SiO_2	41.3	22%	66.1	28.6	6%
TiO_2	3.1	22%	4.6	2.3	4%
Al_2O_3	5.1	18%	6.5	3.1	10%
FeO	7.5	39%	16.1	3.4	18%
MgO	4.5	39%	8.4	1.4	8%
CaO	11.3	36%	19.6	1.7	10%
Na_2O	3.1	33%	5.1	1.0	10%
K_2O	19.2	26%	30.0	12.0	8%
Total	425	88%	1265	20	28%
Mg/(Mg+Fe)	0.52				
K/(K+Na)	0.80				
K/Al	4.1				

1. Average composition of the oxide fraction of the micro-inclusions (wt%). All other elements, e.g., P, Cl, Ba are assumed to account together to 5% of the total oxide weight.

2. Total concentration of the above eight oxides in the diamond (ppm).

3. Standard deviation of the composition of the individual diamonds from the average (% relative to the average).

4. Maximum values of the proportions of the oxides in the micro-inclusions (wt%)

5. Minimum values.

6. Compositional variation within individual diamonds (1σ). Note that this variation is a factor of three smaller than the variation between different diamonds.

K_2O/Al_2O_3 ratios are very high (2-7), Mg/(Mg+Fe) are low (average ~0.5), and chondritic normalized Ce/Eu ratios vary between 10-21. SEM analyses of individual inclusions found 1-3% chlorine. No sulfur was detected, indicating that its content relative to the total oxide content is less than 1%. The amount of volatiles is not well-constrained. The average proportions of water in the micro-inclusions is estimated to be between 12-25%, and the CO_2 component of the carbonate between 7-15%. The $H_2O/(H_2O+CO_2)$ ratio varies between the different diamonds. Using the absorption coefficients of water and calcite it was estimated to vary between 0.6 and 0.9 (molar ratio).

Inclusions in three diamonds have compositions clearly distinct from that of the general population. Inclusions in CTP Z4 are much lower in CaO, MgO, K_2O and Na_2O and higher in SiO_2 (Fig. 10.1.) Inclusions in CTP 6268 (the only sample from Jwaneng, Botswana) contain 1.5 to 2 times more FeO than inclusions in other diamonds and also have high TiO_2 and MgO contents. Inclusions in GRR 1515 are rich in MgO.

The potassium content of the micro-inclusions is extremely high and is not accompanied by similar levels of Al. Most potassic magmas and minerals of mantle origin (e.g., phlogopite, leucite, sanidine) have $K/Al \leq 1$; in the micro-inclusions the ratio varies between 2-7. The highly enriched character of the inclusions is also evident from the very high levels of incompatible elements and the extreme fractionation of the REE.

SEM analyses of individual inclusions revealed no mono-minerallic inclusions. Rather, SEM analyses show that the individual inclusions contain the same Si-K-Ca-Fe-rich composition found by SIMS. The variation between the compositions of individual inclusions is in several cases larger than the analytical uncertainty and suggests limited compositional variation between inclusions in the same diamond. Nevertheless, the average composition of the inclusions in each single diamond agrees with the SIMS results.

IR spectroscopy indicates the presence of silicates, most likely Fe-bearing clay minerals or micas; carbonates, most likely calcite with possible smaller amounts of ankerite, dolomite, and gaylussite; and apatite. The presence of apatite, carbonates and a sheet silicate has been verified by TEM studies of similar diamonds (Lang and Walmsley, 1983; G. Guthrie, written communication, 1988). Strong water IR absorption indicates the presence of a hydrous phase. The good correlation between the intensities of the water and silicate absorption bands suggests that the water may be associated with the silicates. The lack of a frequency shift towards ice absorption at liquid nitrogen temperatures suggests that water is not present as a bulk aqueous phase. However, the negative result of the freezing experiment is not conclusive, as a high solute content may prevent the freezing of a possible hydrous fluid. Small quantities of molecular CO_2 are also detected by IR. Olivine, pyroxene, and garnet, which are the most common inclusions in peridotitic or eclogitic diamond, have some characteristic lines which were not detected and cannot be significant components of the inclusions.

The micro-inclusions exhibit a relatively uniform mineralogy and chemical composition, that are clearly distinct from the composition of the more common, larger, mineral inclusions of the peridotitic or eclogitic suites of diamond inclusions. The diamond hosts reveal similar textures and span a narrow range of carbon isotopic compositions. The above indicates that the micro-inclusion-bearing diamonds were all formed by similar process. The similar carbon isotopic composition of diamonds from Zaire, Siberia, Sierra Leone and Angola (Boyd and Pillinger, 1988) suggests that these diamonds are not the result of a unique and rare event, but rather, were formed by a wide-spread process.

10.3. SYNGENETIC ORIGIN OR EPIGENETIC ALTERATION?

Before any further speculations about the origin of these diamonds are made, it is important to verify whether the bulk composition of the inclusions is representative of the growth environment of the diamonds, or a product of later alteration. It is plausible that the inclusions themselves were formed within the diamond stability field. This is indicated by TEM examination which finds that in many cases the outer faces of the inclusions are crystallographically controlled by the diamond host (G. Guthrie, written communication, 1988). The concentric zoning patterns formed by the inclusions are also interpreted as growth features (Moore and Lang, 1972; Lang, 1979).

It is not possible to prove whether the chemical composition of the inclusions is primary or reflects secondary alteration. However, a few lines of evidence support a primary origin:

1. The inclusions appear to be completely enclosed within an optically continuous diamond matrix and TEM examination (G. Guthrie, written communication, 1988) has shown that they are not normally associated with cracks or dislocations.
2. INAA of sequentially etched layers of a coated Zairian diamond (Bibby, 1979) has shown that kimberlitic penetration into the diamond coat is limited to less than a few micrometers.
3. The composition of the inclusions reported here is different from either the kimberlite (fig. 10.1), or kimberlitic alteration products (e.g. magnesian clays, Kresten, 1973).

Thus, it is believed that the inclusions have retained their original bulk composition. At a later stage, perhaps during or after eruption, the original assemblage crystallized to form the current, low-temperature mineral assemblage of hydrated sheet silicates, carbonates and phosphates. The high water, carbonate, and K_2O content suggest that the material trapped in the micro-inclusions during the growth of the diamond was a melt or a water-rich, supercritical fluid.

10.4. EXPERIMENTAL CONSTRAINTS ON THE STABILITY OF MANTLE FLUIDS

The high content of volatiles and incompatible elements and the uniform average composition of the micro-inclusions suggest that the original material trapped by the diamond was a fluid (a volatile-rich fluid or a melt). Can such fluids, containing 20-40% volatiles, exist at upper mantle temperatures and pressures? Experimental data suggest that at high pressure many melts can accommodate high proportions of volatiles (water and CO_2) and that the solute content of hydrous fluids also increases with increasing pressure; some examples are given below.

Ellis and Wyllie (1980) estimated that at 50 kbar pressure in the system MgO-SiO_2-H_2O-

CO_2, a carbonate-rich melt containing 30 wt% CO_2 and 15% H_2O would coexist with forsterite, enstatite and a water-rich fluid with $H_2O/(H_2O+CO_2)=0.75$. A miscibility gap separates the carbonate-rich melt from the water-rich fluid, and extends to even higher pressures. In the system CaO-SiO_2-H_2O-CO_2 (Boettcher and Wyllie, 1969) the miscibility gap closes and a second critical point is reached at ~35 kbar and fluids with varying proportions of volatiles co-exist with aragonite and di-calcium silicate over a large range of temperatures. A second critical point is also predicted at $P<20$ kbar in the alkali-rich system H_2O - $NaAlSiO_4$ (data of Burnham, in Eggler, 1987). At higher pressures water may be dissolved in any proportion in the melt. Ryabchikov and Boettcher (1980) have estimated that the amount of solute in potassium-rich hydrous fluids in equilibrium with phlogopite + forsterite increases with increasing pressure and exceeds 50% at 30 kbar and 1000°C. Ryabchikov (1986) predicted the existence of a second critical point in the system phlogopite-peridotite-H_2O at ~35 kbar. The above data suggest that fluids with almost equal contents of volatile and non-volatile components may exist within the diamond stability field in the upper mantle. In particular, if the prediction of Ryabchikov (1986) is true, this implies that melts and fluids may be indistinguishable at the pressures of diamond formation.

At pressures below 20 kbar, the addition of CO_2 to hydrous fluids reduces the solubility of metal oxide in the fluids in equilibrium with either melt or solid assemblages (Eggler, 1987). The author is not aware of any data for higher pressure. It seems likely that at higher pressures, where carbonate becomes stable, the solubility of metal oxide in the H_2O-CO_2 should increase. The addition of CO_2 to the peridotite-H_2O system should also shift the second critical point predicted by Ryabchikov (1986) to higher pressures.

What was the state of the material trapped in the micro-inclusions? The water content of the micro-inclusions is not well constrained, thus it is not possible to infer from the relative abundance of water and carbonate whether the growing diamonds trapped a volatile-rich fluid or a melt. However, the chemistry of the metal oxide fraction can be compared with the available experimental data for melts and for hydrous fluids at high pressure.

Partial melting of a carbonated phlogopite-peridotite at pressures above 30 kbar yields melts of carbonatitic affinity (Wendlandt and Eggler, 1980). With increasing pressure the supersolidus stability of phlogopite decreases and the melt becomes more silicic and potassic. The melts are highly magnesian, and as garnet stability increases, their Al_2O_3 content should decrease. At P>50 kbar, where phlogopite is no longer stable on the solidus, Wendlandt and Eggler predict that K_2O-H_2O rich fluids may be present as an intergranular phase. The above data suggest that liquids with high volatile content, high K_2O, and low Al_2O_3 may be produced by direct melting of carbonated phlogopite peridotite at pressures of ~50 kbar. However, such liquids are expected to have high MgO content and high Mg numbers, and are probably closer in composition to kimberlites than to the micro-inclusions.

Fluids in equilibrium with solid peridotite minerals show marked depletion in MgO (Ryabchikov, and Boettcher, 1980; Schneider and Eggler, 1984). The calculated partitioning of MgO between fluid and melt is also lower relative to Al_2O_3, K_2O, or SiO_2 (Eggler, 1987). Although at low pressures there is no fractionation between Al_2O_3 and K_2O during the dissolution of phlogopite (Ryabchikov and Boettcher, 1980; Schneider and Eggler, 1984), the stabilization of garnet at high pressure may lead to enrichment of the fluid in K_2O relative to Al_2O_3. The fluid becomes preferentially enriched in sodium during the dissolution of clinopyroxene (Ryabchikov et al., 1982) or of jadeite (Ryabchikov and McKenzie, 1985).

The above data suggest that, compared with melts, hydrous fluids may be closer in composition to the micro-inclusions, especially with regard to their MgO content and K/Al ratio. However, if a second critical end point is approached or exceeded in the natural system, then melt and fluid form a "contineous" range of compositions.

A third possibility is that the micro-inclusions were not formed in equilibrium with highly magnesian peridotite, but rather, are a residual fluid (melt, vapor, or supercritical fluid) produced by fractional crystallization of a more magnesian primary fluid. Such an origin was previously suggested for the megacryst suite (Harte and Gurney, 1981; Schulze, 1987) and for the MARID xenoliths (Waters, 1987) that are found in kimberlites. Fractional crystallization would lead to a residual fluid with decreasing MgO content and Mg numbers and with strong enrichment in incompatible element content. This idea explored in the following Sections.

10.5. RELATION OF THE TRAPPED MATERIAL TO POTASSIC MAGMAS

Although some important distinctions exist between the major element composition of the micro-inclusions and of kimberlites and lamproites (fig. 10.1, 10.2) many similarities can be found as well. All three are rich in alkalies and incompatible elements; the micro-inclusions showing the strongest enrichment and most extreme fractionation between light and heavy REE. All three are also characterized by high contents of H_2O and CO_2; again, the micro-inclusions have the highest content.

The carbon isotopic composition of the diamonds of the CTP set was determined by Boyd et al. (1987) and is within the range spanned by Zairian kimberlites (Javoy et al., 1984). This similarity led Boyd et al. (1987) to suggest that the diamonds are phenocrystal to the kimberlitic melt and were formed during the accumulation and emplacement of the kimberlitic magma. Akagi and Masuda found that the Sr isotopic composition of micro-inclusions in a few cubic Zairian diamonds ($^{87}Sr/^{86}Sr = 0.7038-0.7041$) is also similar to that of Zairian kimberlites (Weis et al., 1984) and other group I kimberlites (Smith, 1983).

The similar isotopic composition of the diamonds and their host kimberlites suggests a cognate origin at depth. However, the differences in major element chemistry between the micro-inclusions and the erupting kimberlite argue against a simple phenocrystal relation between the diamonds and their host kimberlites. One would argue that the lower volatile content of the kimberlite relative to the micro-inclusions is due to volatile loss during ascent, that alkalies were also lost with the escaping volatiles, and that the high MgO content of the erupting kimberlite is due to the presence of a large proportion of xenocrysts in the hybrid rock. However, the paucity of phlogopite in the ground mass minerals of many type I kimberlites indicates that the concentration of K_2O was also low at depth, before any volatiles escaped . The high MgO content of some aphanitic kimberlites (Edgar et al. 1988) also suggests that the xenocryst-free magma is also magnesian.

It seems more plausible that the micro-inclusions and the kimberlites are genetically

Figure 10.2. The relation between the chemical composition of micro-inclusions (stippled area) and the average composition of kimberlites (K), lamproites (L), and alkali-basalt (A), all averages from Bergman, 1987).

a. Triangular plot representing all the major-elements measured by SIMS. The small stippled area at the upper right is the composition of the micro-inclusions in diamond CTP Z4 that is rich in SiO_2 and depleted in MgO and CaO.

b. The proportions of Al_2O_3 - Na_2O -K_2O in the micro-inclusions and in potassic magmas.

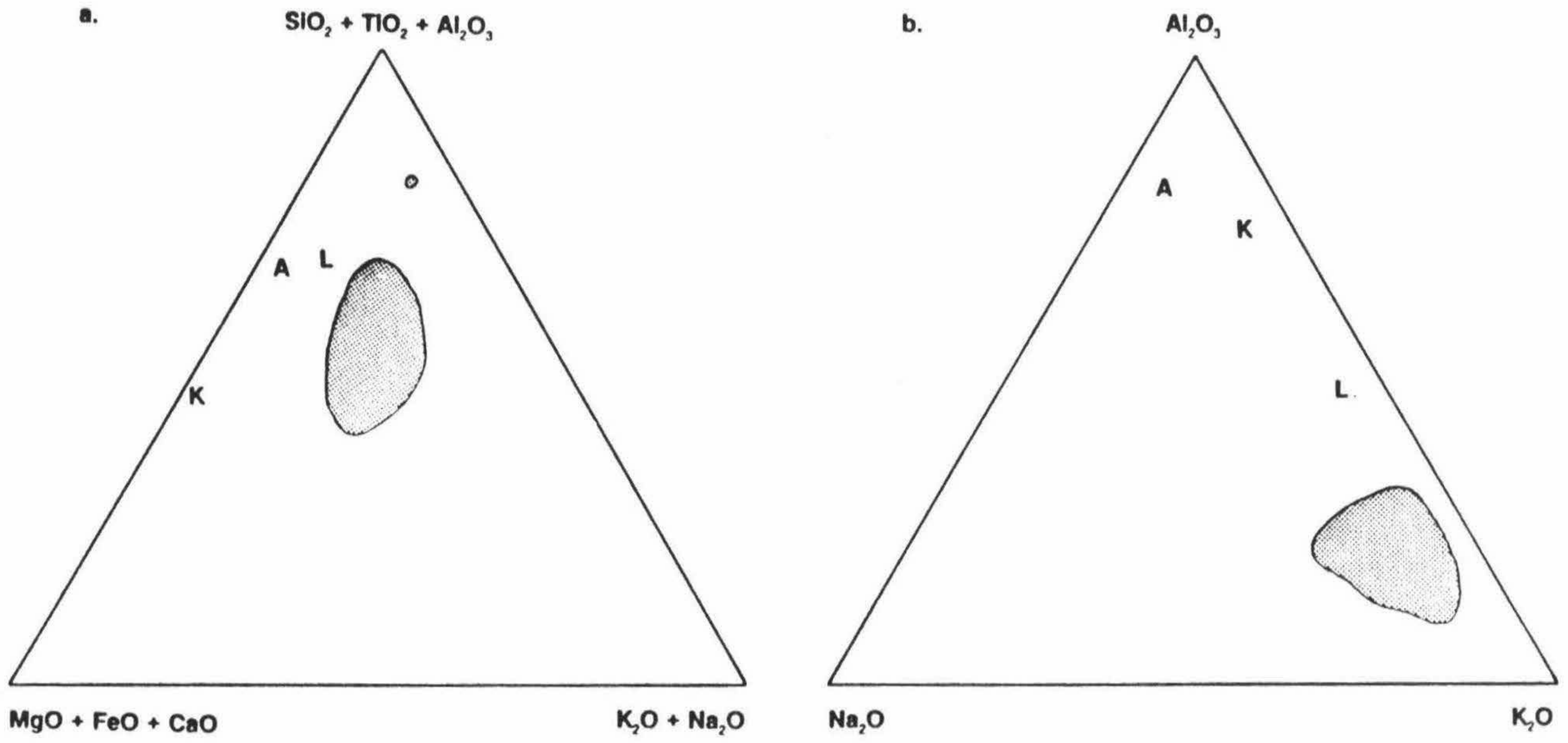
a.
SiO₂ + TiO₂ + Al₂O₃
MgO + FeO + CaO
K₂O + Na₂O
A
L
K
b.
Al₂O₃
Na₂O
K₂O
A
K
L

related to similar sources, but followed different evolutionary paths at depth. One possibility is that the micro-inclusions and the kimberlite represent different degrees of partial melt of the same source. Wyllie and Huang (1975) have suggested that at pressures above 25 kbar the first melt of a carbonated peridotite is carbonatitic and that the composition of the melt shifts towards kimberlitic composition with increasing melt fractions. It may be argued that at higher pressures incipient melting of a carbonated phlogopite peridotite is rich in K_2O and H_2O and similar in composition to the micro-inclusions and that further melting produces melts of kimberlitic affinity. The main difficulty is the high MgO content expected for melts produced by direct melting of a peridotitic source.

Another possibility is that the micro-inclusions trapped a residual fluid (melt or water rich fluid) that evolved during the fractional crystallization of a primary magma of kimberlitic affinity. Such a process was previously suggested as the source of the megacryst suite (Harte and Gurney, 1980). In this scenario the cores of the coated diamonds are xenocrysts trapped by the megacryst magma. During cooling, garnet, clinopyroxene, orthopyroxene, and olivine megacrysts crystalize and grow, and the residual liquid is strongly depleted in MgO. SiO_2, Al_2O_3, CaO, and FeO are depleted to a smaller extent and K_2O, Na_2O, TiO_2, H_2O, and CO_2 are enriched. Later, ilmenite crystallization increases the SiO_2, Al_2O_3, and CaO levels and further depletes the liquid in MgO and FeO. TiO_2 is also depleted and alkalies and volatiles are further enriched. The Mg/(Mg+Fe) ratio decreases during the crystallization sequence. The K/(K+Na) increases as Na enter the clinopyroxene in larger proportions than K. At the final stages of crystallization the residual melt is highly enriched in volatiles. The coats and the cubic diamonds grow from this melt or from a volatile-rich fluid that may separate from the melt. The diamonds and the megacrysts are then sampled by a later kimberlite that transports them to the surface.

Comparison of the Sr isotopic composition of the diamonds (0.7037-0.7050, Akagi and Masuda, 1988), diopside megacrysts (0.7027-0.7034), and the kimberlites (0.7040-0.7046, Fiermans et al., 1984) indicates that the above process must occur in an open system. The diopside megacrysts crystallized at early stages and recorded the initial composition of the magma. Assimilation of small degree of partial melt of an enriched lithospheric source by the megacryst magma could produce more radiogenic $^{87}Sr/^{86}Sr$ ratios by the time of diamond crystallization. The kimberlite also assimilated such melts during its ascent and acquired similar isotopic composition. Assimilation of enriched lithospheric melts during megacryst crystallization has been suggested by Jones (1987).

10.6. RELATION TO METASOMATIC FLUIDS

Many mantle-derived rocks document the effects of open system interaction with fluids rich in incompatible elements (mantle metasomatism). The nature of the fluid is still debated (Eggler, 1987; Erlank et al., 1987) and in most cases, no direct observation of such a fluid has been made. Menzies et al., (1987) distinguishes two types of metasomatism: one leads to enrichment of the rock in Ti, Fe, and incompatible elements and is attributed to interaction of the rock with a silicic melt; the other is characterized by strong enrichment in K and incompatible elements and high K/Ti ratios and is associated with the act of a water-rich fluid. The high solute content of the micro-inclusions, coupled with strong enrichment in K, Na, P, and incompatible trace elements, suggests that the trapped material in the micro-inclusions may represent an effective metasomatizing agent. The high volatile content assures high fluidity. Such fluids can easily percolate along wettable grain boundaries and efficiently interact with the rock.

10.7. RELATION TO DIAMONDS OF THE PERIDOTITIC AND THE ECLOGITIC SUITES

The composition of the micro-inclusions is clearly distinct from inclusions of either the peridotitic or eclogitic suites of diamond inclusions. This difference may simply reflect different environments of formation for each of the three groups of inclusions. Alternatively, it can be argued that the micro-inclusions trapped a fluid that was interacting with the larger inclusions or possibly the fluid from which they crystallized. It is possible that the larger mineral inclusions were trapped during slow diamond growth and that the micro-inclusions were trapped only during fast growth.

None of the micro-inclusion-bearing diamonds studied here was found to contain larger, discrete mineral inclusions and, except for one unclear case (see below), no such inclusions were reported to coexist with micro-inclusions in the coat of coated diamonds or in cubic diamonds. Nevertheless, one may argue that only a small number of micro-inclusion-bearing diamonds was studied and that it is easy to miss single inclusions in those opaque or translucent diamonds.

Given the lack of diamonds where both types of inclusions coexist, it is not possible to associate the micro-inclusion-bearing diamonds with either the peridotitic or the eclogitic parageneses. Some weak, indirect evidence suggests an association of the micro-inclusions with the eclogitic suite. Galimov (1984) observed that the range of carbon isotopic composition of the coats and the cubic diamonds is similar to the range of most frequent values of eclogitic diamonds. Based on this similarity, he suggested that the two populations represent one single group. It must be noted, however, that the above range is also within the range spanned by diamonds with peridotitic inclusions.

A better, but still inconclusive, case may be made for the association of the cores of the coated diamonds with eclogitic diamonds. The range of the isotopic ratios spanned by the cores is much wider than the full range of peridotitic diamonds. In one case, K-feldspar and rutile inclusions were found in the core[*] of a coated diamond from the Mir pipe, Siberia (Bulanova and Argunov, 1985). These phases were previously associated with the eclogitic paragenesis (Meyer, 1987).

Until more compelling evidence is found (for example, a diamond where an eclogitic or peridotitic inclusion is enclosed within the micro-inclusion-bearing zone, or a xenolith carrying a coated or a cubic diamond) it is only possible to speculate about the possible relation between the two types of inclusions. In the following paragraphs I discuss the

---

[*] From the description in Bulanova and Argunov (1985) it is not clear whether one of the three K-feldspar inclusions is actually enclosed within the coat. If this is the case, then it indicates a direct association of the micro-inclusion with the eclogitic suite.

possibility that the extreme enrichment of incompatible elements found in both peridotitic (Shimizu and Richardson, 1987) and eclogitic mineral inclusions (Griffin et al., 1988; Shimizu et al., 1988) can be explained by interaction of these minerals with fluids, similar in composition to that of the micro-inclusions.

Richardson et al. (1984) suggested that peridotitic garnet inclusions in diamonds equilibrated with an asthenosphere-derived melt rich in alkali, light REE and CO_2. They further suggested that the melt remained liquid until the time of diamond crystallization. However, it was later argued (Shimizu and Richardson, 1987) that the strong enrichment of light REE in these garnets is too high to be explained by equilibrium crystallization from a silicate melt. Griffin et al. (1988), using similar arguments, concluded that eclogitic clinopyroxene inclusions in diamonds from Argyle, Australia could not have crystallized directly from a silicate melt. They suggested that "... unless the clinopyroxene-melt partition coefficients for elements such as K, Rb, Sr, Pb, and U increase markedly (in many cases an order of magnitude is required) over those at low pressure, the high values of these elements in the inclusions require corresponding melts with unrealistically high concentrations."

A comparison of trace element concentrations in kimberlites and lamproites (Table 2.1) with the levels of trace elements in the micro-inclusions (Table 9.3) shows that the micro-inclusions have "unrealistically high concentrations." Potassium in the micro-inclusions is 2-10 times higher than the average kimberlite or lamproite (on a volatile-free basis), Sr is 4-10 higher, and U is 7-12 times higher. Chondrite normalized Ce/Eu ratios of 10-21 indicate steeper patterns than those of kimberlites, which are 7-10 (Fiermans et al., 1984; Mitchell, 1986). Thus, the REE patterns of the garnet inclusions studied by Shimizu and Richardson (1987) could also be explained by equilibrium crystallization from fluids similar in composition to the micro-inclusions.

More difficult to explain are the major element systematics. If peridotitic inclusions in diamonds did equilibrate with fluids of this composition, then the partitioning behavior of major elements between crystals and fluid must deviate significantly from the behavior in basaltic systems. For example, using a typical composition of a peridotitic olivine inclusion with Mg/(Fe+Mg)=0.93 (Meyer, 1987) and the average composition of the micro-inclusions (Table 10.1), we obtain $(Fe/Mg)_{olivine}/(Fe/Mg)_{fluid} = 0.07$, compared with a value of 0.3-0.4 in melting experiments using a dry peridotite (Takahashi and Kushiro, 1983). Current experimental data is insufficient to resolve this difficulty and a better understanding of the phase equilibria in peridotite-H_2O-CO_2 (and eclogite-H_2O-CO_2) at high pressures is clearly needed.

REFERENCES

Akagi, T. and Masuda, A. (1988) Isotopic studies and REE geochemistry on alluvial diamonds from Zaire. Chem. Geol. 70: 2.

Andersen, C.A. and Hasler, M.F. (1966) In Castaing, R., Deschamps, P. and Philibert, J. (eds.), "X-ray Optics and Microanalysis, Hermann, Paris, p. 310.

Angress, J.F. and Smith, S.D. (1965) The observation of defect-activated one-phonon infrared absorption in diamond coat. Phil. Mag. 12: 415-417.

Armstrong, J.T. (1982) New ZAF and α-factor correction procedures for the quantitative analysis of individual microparticles. In: K.F.J. Heinrich (ed.), Microbeam Analysis, pp. 175-180. San Francisco Press.

Armstrong, J.T. (1988) Quantitative analysis of silicate and oxide materials: comparison of Monte Carlo, ZAF and $\phi\rho z$ procedures. In: D.E. Newbury (ed.), Microbeam Analysis, San Francisco Press.

Armstrong, J.T. and Buseck, P.R. (1975). Quantitative chemical analysis of individual microparticles using the electron microprobe. Theoretical. Analyt. Chem. 47: 2178-2192.

Bergman, S.C. (1987) Lamproites and other potassium-rich igneous rocks: a review of their occurrence, mineralogy and geochemistry. In Fitton, J.G. and Upton, B.G.J. (eds.), The Alkaline Igneous Rocks, Geological Society of London, London, pp. 103-190.

Bibby, D.M. (1979) Zonal distribution of inclusions in diamond. Geochim. et Cosmochim. Acta 43: 415-423.

Bibby, D.M. (1982) Impurities in natural diamond. Chem. Phys. Carbon 18: 3-91.

Biersack, J.P. (1987) Ion ranges and energy deposition in insulators. In Mazzoldi, P. and Arnold, G.W. (eds.), Ion Beam Modification of Insulators, Elsevier, Amsterdam, pp. 1-56.

Boettcher, A.L. and Wyllie, P.J. (1969) The system CaO-SiO_2-CO_2-H_2O-III. Second critical end-point on the melting curve. Geochim. et cosmochim. Acta 33: 611-632.

Boyd, F.R. and Gurney, J.J. (1986) Diamonds and the African lithosphere. Science 232: 472-477.

Boyd, F.R. (1987) High- and low-temperature garnet peridotite and their possible relation to the lithosphere-asthenosphere boundary beneath southern Africa. In Nixon, P.H. (ed.) Mantle Xenoliths, pp. 403-412. John Wiley and Sons, New York.

Boyd, S.R., Mattey, D.P., Pillinger, C.T., Milledge, H.T., Mendelson, M. and Seal, M. (1987) Multiple growth events during diamond genesis: an integrated study of carbon and nitrogen isotopes and nitrogen aggregation state in coated stones. Earth Planet. Sci. Lett. 86: 341-353.

Boyd, S.R. and Pillinger, C.T. (1988) Carbon and nitrogen isotopes in the mantle. Chem. Geol. 70: 46.

Bristow, J.W., Smith, C.B., Allsopp, H.L., Shee, S.R. and Skinner, E.M.W. (1986) Setting, geochronology and geochemical characteristics of 1600 m.y. kimberlites and related rocks from the Kuruman Province, South Africa. In (ed.), Fourth Int. Kimberlite Conf., Extended Abstr., Geol. Soc. Aust. Abstr. Ser. No 16, Perth, Australia, pp. 112-114.

Bulanova, G.P. and Argunov, K.P. (1985) Potassic feldspar inclusions in diamond crystal from the Mir pipe. Dokl. Akad. Nauk. SSSR 284: 953-956.

Bundy, F.P. (1980) The P,T phase and reaction diagram for elemental carbon, 1979. Jour. of Geophys. Res. 85(B12): 6930-6936.

Chesley, F.G. (1942) Investigation of the minor elements in diamond. Am. Miner. 27: 21-36.

Chrenko, S.M., MacDonald, R.S., and Darrow, K.A. (1967) Infra-red spectra of diamond coat. Nature 214: 474-476.

Chrenko, R.M. (1971) Boron content and profiles in large laboratory diamonds. Nature 229: 165-167.

Clark, C.D. and Davey, S.T. (1984) Defect-induced one phonon infrared absorption in type Ia diamonds. J. Phys. C: Solid State Phys. 17: 1127-1140.

Clement, C.R., Skinner, E.M.W. and Scott Smith, B.H. (1984) Kimberlite redefined. J. Geol 92: 223-228.

Custers, J.F.H. (1950) On the nature of opal-like outer layer of coated diamonds. Am. Miner. 35: 51-58.

Davies, G. (1975) The optical properties of diamond. Chem. Phys. Carbon 13: 1-143.

Davies, G. (1984) Diamonds. Adams Hilger, Bristol.

Dawson, J.B. (1967) A review of the geology of kimberlite. In Wyllie, P.J. (ed.), Ultramafic and Related Rocks, Wiley, New York, pp. 241-251.

Dawson, J.B. (1980) Kimberlites and their Xenoliths. Springer-Verlag, Berlin.

Dawson, J.B. (1987a) The kimberlite clan relationship with olivine and leucite lamproites, and inferences for upper mantle metasomatism. In Fitton, J.G. and Upton, B.G.J. (eds.), Alkaline Igneous Rocks, Geol. Soc. London, London, pp. 95-101.

Dawson, J.B. (1987b) The MARID suite of xenoliths in kimberlite: relationship to veined and metasomatised peridotite xenoliths. In Nixon, P.H. (ed.), Mantle Xenoliths, Wiley, Chichester, pp. 465-474.

Dawson, J.B. and Smith, J.V. (1977) The MARID (mica-amphibole-rutile-ilmenite-diopside) suite of xenoliths in kimberlite. Geochim. Cosmochim. Acta 41: 309-323.

Deines, P., Gurney, J.J. and Harris, J.W. (1984) Associated chemical and carbon isotopic composition variations in diamonds from Finsch and Premier kimberlite, South Africa. Geochim. Cosmochim. Acta 48: 325-342.

Deines, P., Harris, J.W. and Gurney, J.J. (1987) Carbon isotopic composition, nitrogen content and inclusion composition of diamonds from the Robert Victor kimberlite, South Africa: Evidence for C13 depletion in the mantle. Geochim. et Cosmochim. Acta 51: 1227-1272.

De Toit, A.L. (1906) Eleventh Ann. Rep. of the Geol. Comm. of the Cape of the Good Hope.

DeVries, R.C. and Robertson, C. (1983) The internal structure of diamond by electrostatic charging in the SEM. Mat. Res. Bull. 18: 697-701.

Eggler, D.H. (1987) Solubility of Major and Trace Elements in Mantle Metasomatic Fluids: Experimental Constraints. In: M.A. Menzies and C.J. Hawkesworth (eds.) Mantle Metasomatism, Academic Press, London.

Eggler, D.H. and Baker, D.R. (1982) Reduced volatiles in the system C-O-H: Implications to mantle melting, fluid formation, and diamond genesis. In Akimoto, S., and Manghnani (eds.) High-Pressure Research in Geophysics, pp. 237-250. Center for Academic Publications, Tokyo.

Ellis, D.E. and Wyllie, P.J. (1980) Phase relations and their petrological implications in the system MgO-SiO_2-H_2O-CO_2 at pressures up to 100 kbar. Amer. Mineral. 65: 540-556.

Eppler, W.F. (1961) Inclusions in diamonds. J. Gemology 81.

Erlank, A.J., Allsopp, H.L., Haggerty, S.E., Hawkesworth, C.J., Menzies, M.A., and Rickard, R.S. (1987) Evidence for mantle metasomatism in peridotite nodules from the Bultfontein floors, Kimberley, South Africa. In Menzies and Hawkesworth (ed.) pp. 221-311.

Evans, T. and Harris, J.W. (1986) Nitrogen aggregation, inclusion equilibrium temperature and the age of diamonds. In (ed.), 4th Kimberlitic Conf.; Abstr. Ser., Geol. Soc. Australia, Perth Australia, p. 387.

Evans, T. and Qi, Z. (1982) The kinetics of aggregation of nitrogen in diamond. Proc. Roy. Soc. Lond. A381: 159-178.

Farmer, V.C. (1974) Layer silicates. In Farmer, V.C. (ed.), Infrared Spectra of Minerals, Mineralogical Society, London.

Faulkner, E.A., Whippey, P.W. and Newman, R.C. (1965) Electron spin resonance in diamond coat. Phil. Mag. 12: 413-415.

Fesq, H.W., Bibby, D.M., Erasmus, C.S., Kable, E.J.D. and Sellschop, J.P.F. (1975) A comparative trace element study of diamonds from Premier, Finch and Jagersfontein mines, South Africa. Phys. Chem. Earth. 9: 817-836.

Fesq, H.W., Bibby, D.M., Sellschop, J.P.F. and Watterson, J.I.W. (1973) The determination of trace element impurities in natural diamonds by instrumental neutron activation analysis. J. Radioanal. Chem. 17: 195-216.

Field, J.E. (ed.) (1979) The properties of diamond. Academic Press, London.

Fieremans, M., Hertogen, J., and Demaiffe, D. (1984) Petrography, geochemistry and strontium isotopic composition of the Mbuji-Mayi and Kundelungu kimberlites (Zaire). In Kornprobst, J. (ed.) Kimberlites: II, The Mantle and Crust Mantle Relationship, Developments in Petrology v.11B, pp. 107-120. Elsevier, Amsterdam.

Finnerty, A.A. and Boyd, F.R. (1987) Thermobarometry for garnet peridotites: basis for the determination of thermal and compositional structure of the upper mantle. In Nixon, P.H. (ed.) Mantle Xenoliths, pp. 381-402. John Wiley and Sons, New York.

Foley, S.F., Venlurelli, G. and Green, D.H. (1987) The ultrapotassic rocks: characteristics, classification and constrains for petrogenetic model. Earth Sci. Rev. 24: 81-134.

Frank, F.C. and Lang, A.R. (1965) X-ray topography of diamond. In Berman, R. (ed.), Physical Properties of Diamond, Calderon Press, Oxford, pp. 69-115.

Galimov, E.M. (1984) Variations in isotopic composition and inferences for diamond genesis conditions. Geokhimyva 8: 1091-1118.

Giardini, A.A. and Melton, C.E. (1975) The nature of cloud-like inclusions in two Arkansas diamonds. Amer. Mineral. 60: 931-933.

Given, J.W. and Helmberger, D.V. (1980) Upper mantle structure of northwestern Eurasia. Jour. of Geophys. Res. 85(B12): 7183-7194.

Glazunov, M.P., Kodochigov, P.N. and Orlov, Y.L. (1967) Determination of impurities and study of their distribution in diamond crystals. Isotopenpraxis 3: 168-171.

Glover, J.E. and Harris, P.G. (eds.) (1984) Kimberlite occurrence and origin: a basis for conceptual models in exploration. 298 pp. University of Western Australia, Perth.

Gnevushev, M.A. and Kravtsov, Ya.M. (1960) On the composition of impurities in Ural and Yakutian diamonds. Dokl. Akad. Nauk. SSSR 130: 154-156.

Goldstein, J.I., Newbury, D.E., Echlin, P., Joy, D.C., Fiori, C. and Lifshin, E. (1981) Scanning Electron Microscopy and X-Ray Microanalysis. Plenum, New York.

Griffin, W.L., Jaques, A.L., Sie, S.H., Ryan, C.G., Cousens, D.R. and Suter, G.F. (1988) Conditions of diamond growth: a proton microprobe study of inclusions in West Australian Diamonds. Conrib. Miner. Petrol. 99: 143-158.

Gurney, J.J. (1986) Diamonds. In (ed.), 4th Int. Kimberlite Conf.; Abst. Ser., Geol. Soc. Australia, Perth Australia.

Gurney, J.J. and Boyd, F.R. (1982) Mineral intergrowths with polycrystalline diamonds from the Orapa Mine, Botswana. Carnegie Inst. Wash. Yearbk. 81: 267-273.

Haggerty, S.E. (1986) Diamond genesis in a multiply-constrained model. Nature 320: 34-38.

Harris, J.W. (1968) The recognition of diamond inclusions. Part 1: Syngenetic mineral inclusions. Part 2: Epigenetic mineral inclusions. Industrial Diamond Review 28: 402-410,558-561.

Harris, J.W. (1987) Recent physical, chemical and isotopic research of diamond. In Nixon, P.H. (ed.), Mantle Xenoliths, Wiley, Chichester, pp. 477-500.

Harris, J.W. and Collins, A.T. (1985) Studies of Argyle diamonds. Industrial Diamond Rev. 85: 128-130.

Harris, J.W. and Gurney, J.J. (1979) Inclusions in diamond. In Field, J.E. (ed.), The properties of diamond, Academic, London, pp. 555-594.

Harris, J.W., Hawthorne, J.B. and Oosterveld, M.M. (1975) A classification scheme for diamonds and a comprehensive study of South African diamonds characteristics. Phys. Chem. Earth 9: 765-783.

Harte, B. and Gurney, J.J. (1981) The mode of formation of chromium-poor megacryst suites from kimberlites. J. Geol. 89: 749-753.

Honda, M., Reynolds, J.H., Roedder, E. and Epstein, S. (1987) Noble gases in diamonds: occurrences of solar-like helium and neon. J. Geophys. Res. 92: 12507-12521.

Huneke, J.C., Armstrong, J.T. and Wasserburg, G.J. (1983) FUN with PANURGE: High mass resolution ion microprobe measurements of Mg in Allende inclusions. Geochim. Cosmochim. Acta 47: 1635-1650.

Janse, A.J.A., (1984) Diamonds - where and when? In Glover, J.E. and Harris, P.G. (eds.) Kimberlite Occurrence and Origin: a Basis for Conceptual Models in Exploration. pp. 19-61. University of Western Australia, Perth.

Janse, A.J.A. et al.(ed.) (1988) Kimberlites and related rocks, Vol 2.: Their Mantle/Crust Setting, Diamonds and Diamond Exploration. Bleckwells, Carlton, Australia. (In press)

Jaques, A.L., Lewis, J.D., Smith, C.B., Gregory, G.P., Ferguson, J., Chappell, B.W. and McCulloch, M.T. (1984) The diamond bearing ultrapotassic (lamproitic) rocks of the west Kimberley region. In Kornprobst, J. (ed.), Kimberlites: I, Kimberlites and Related Rocks, Elsevier, Amsterdam, pp. 225- 254.

Jaques, A.L., Lewis, J.D. and Smith, C.B. (1986) The kimberlites and lamproites of western Australia. Geological Survey of Western Australia, Bull. 132: 1.

Javoy, M., Pineau, F., and Demaiffe, D. (1984) Nitrogen and carbon isotopic composition in diamonds from Mbuji Mayi (Zaire). Earth Planet. Sci. Lett. 68: 399-412.

Jones, R.A. (1987) Strontium and neodymium isotopic and rare earth element evidence for the genesis of megacrysts in kimberlites of southern Africa. In Nixon, P.H. (ed.), Mantle Xenoliths, Wiley, Chichester, pp. 711-724.

Kaiser, W. and Bond, W.L. (1959) Nitrogen, a major impurity in common type I diamond. Phys. Rev. 115: 857-863.

Kaminski, F.G., Gurkina, G.A., Ivanoskaya, I.N. and Galimov, E.M. (1978) Distribution of carbon isotopes inside the diamond crystals of different habits. In Seventh All-Soviet Symposium on Stable Isotopes in Geochemistry Abstr., Soviet Academy, Moscow, p. 221.

Kamiya, Y. and Lang, A.R. (1965) On the structure of coated diamonds. Phil. Mag. 11: 347-356.

Kresten, P. (1973) Differential analysis of kimberlite. In Nixon, P.H. (ed.) Lesoto Kimberlites. Lesoto National Development Corporation, Maseru, Lesoto.

Lang, A.R. (1974) On the growth-sectorial dependence of defects in natural diamonds. Proc. Roy. Soc. Lond A-340: 233-246.

Lang, A.R. (1978) Techniques and interpretation in x-ray topography. In Amelincky, S., Gevers, R. and Van Landuyt, J. (eds.), Diffraction and Imaging Techniques in Material Science, North Holland, Amsterdam, pp. 623-714.

Lang, A.R. (1979) Internal structure. In Field, J.E. (ed.), The Properties of Diamond., Academic Press, London, p. 674.

Lang, A.R. and Walmsley, J.C. (1983) Apatite in natural diamond coat. Phys. Chem. Mineral. 9: 6-8.

Love, G., Cox, M.G. and Scott, V.D. (1978) A versatile atomic number correction for electron probe microanalysis. J. Phys. D. 11: 7-9.

McCulloch, M.T., Jaques, A.L. and Nelson, D.R. (1983) Nd and Sr isotopes in kimberlites and lamporites from W. Australia: an enriched mantle origin. Nature 302: 400-403.

Menzies, M.A. and Hawkesworth, C.J. (1987) Mantle Metasomatism. Academic Press, London.

Menzies, M.A., Rogers, N., Tindle, A. and Hawkesworth, C.J. (1987) Metasomatic and enrichment processes in lithospheric peridotites, an effect of asthenosphere-lithosphere interaction. In Menzies, M.A. and Hawkesworth, C.J. (eds.), Mantle Metasomatism, Academic Press, London, pp. 313-361.

Meyer, H.O.A. (1967) Inclusions in diamond. Carnegie Inst. Wash. Yearbk. 66: 446-450.

Meyer, H.O.A. (1987) Inclusions in diamond. In Nixon, P.H. (ed.), Mantle Xenoliths, Wiley, Chichester, pp. 501-522.

Meyer, H.O.A. and Boyd, F.R. (1968) Inclusions in diamond. Carnegie Inst. Wash. Yearbk. 67: 446-450.

Meyer, H.O.A. and Tsai, H.M. (1976) Mineral inclusions in natural diamonds: their nature and significance. Mineral. Sci. Engineering 8: 242-261.

Meyer, H.O.A., and Tsai, H.M. (1976) Mineral inclusions in diamond: temperature and pressure of equilibration. Science 191: 849-851.

Mitchell, R.H. and Giardini, A.A. (1953) Oriented olivine inclusions in diamond. Amer. Mineral. 38: 136-138.

Mitchell, R.H. (1986) Kimberlites. Plenum Press, NewwYYork.

Moore, M. and Lang, A.R. (1972) On the internal structure of natural diamonds of cubic habit. Phil. Mag. 26: 1313-1325.

Moore, R.O. and Gurney, J.J. (1985) Pyroxene solid solution in garnets included in diamond. Nature 318: 553-555.

Muncke, G. (1979) Physics of diamond growth. In Field, J.E. (ed.) The properties of diamond. Academic Press, London.

Nakamoto, K. (1963) Infrared Spectra of Inorganic and Coordination Compounds. Wiley, New York.

Newman, S., Stolper, E.M. and Epstein, S. (1986) Measurement of water in rhyolitic glasses: Calibration of an infrared spectrometric technique. Amer. Mineral. 71: 1527-1541.

Nixon, P.H. (1987) Mantle Xenoliths. Wiley, Chichester.

Nixon, P.H. and Davies, G.R. (1987) Mantle xenolith perspectives. In Nixon, P.H. (ed.), Mantle Xenoliths, Wiley, Chichester, pp. 741-756.

Orlov, Y.u..L. (1977) The Mineralogy of Diamond. Wiley, New York.

Orlov, Y.L., Dudenko, Y.A., and Solodova, Y.P. (1978) Fibrous growth, IR spectra, and carbonate inclusions in diamond cubic crystals. Nov. Dannye. Miner. SSSR 27: 109-112.

Orlov, Y.L., Bulienkov, N.A., and Martovitsky, V.P. (1982) A study of the internal structure of variety III diamonds by x-ray section topography. Phys. Chem. Mineral. 8: 105-111.

Ozima, M. and Zashu, S. (1988) Solar-type Ne in Zaire cubic diamonds. Geochim. et Cosmochim. Acta 52: 19-25.

Ozima, M., Zashu, S., Mattey, D.P. and Pillinger, C.T. (1985) Helium, argon and carbon isotopic composition in diamonds and their implications in mantle evolution. Geochim. J. 19: 127-134.

Plotnikova, S.P., Dudenko, Yu.A., Malan'ina, R.V. and Kulakov, V.M. (1985) Internal structure and properties of varieties of diamond with cubic habit. Soviet Phys. Cryst. 30: 663-665.

Podosek, F.A., Pier, J., Nitoh, O., Zashu, S. and Ozima, M. (1988) Normal potassium, inherited argon in Zaire cubic diamonds. Nature 334(18): 607-609.

Pollack, H.N. and Chapman, D.S. (1977) On the regional variation of heat flow, geotherms, and lithospheric thickness. Tectonophysics 38: 279-296.

Prinz, M., Manson, D.V., Hlava, P.F., and Keil, K. (1975) Inclusions in diamonds. Garnet lherzolite and eclogite assemblages. Phys. Chem. Earth 9: 797-815.

Reed, S.J.B. (1965) Characteristic fluorescence correction in electron probe micro-analysis. Brit. Appl. Phys. 16: 913-916.

Reuter, W. (1972) The ionization function and its application to the electron probe analysis of thin films. In: G. Shinoda, K. Kohra and T. Ichinokawa (eds.) Proc. of the VI Intern. Conf. on X-Ray Optics and Microanalysis, Univ. Tokyo Press, pp. 121-130.

Richardson, S.H., Gurney, J.J., Erlank, A.J. and Harris, J.W. (1984) Origin of diamond in old enriched mantle. Nature 310: 198-202.

Robertson, D., Fox, J.J. and Martin, A.E. (1934) Two types of diamond. Trans. Royal Soc. Lond. A 232: 463-538.

Robinson, D.N. (1978) The characteristics of natural diamond and their interpretation. Mineral. Sci. Engineering 10: 55-72.

Roedder, E. (1984) Fluid inclusions. Reviews in Mineralogy 12, 644 pp. Mineralogical Society of America, Washington.

Ross (1974) The phosphate minerals. In Farmer, V.C. (ed.), The Infrared Spectra of Minerals, Mineralogical Society, London.

Ross, S.D. (1974) Phosphates and other oxy-anions of group 5. In Farmer, V.C. (ed.), The Infrared Spectra of Minerals, Mineralogical Soc., London, pp. 383- 422.

Rossman, G.R. (1988) Spectroscopic Methods in Mineralogy and Geology. In Hawthorne, F.C. (ed.), Reviews in Mineralogy, Mineralogical Society of America, Washington.

Runciman, W.A. and Carter, T. (1971) High resolution infra-red spectra of diamond. Solid State Comm. 9: 315-317.

Russell, J.D. (1974) Instrumentation and techniques. In Farmer, V.C. (ed.), The Infrared Spectra of Minerals, Mineralogical Society, London.

Russell, J.D. (1987) Infrared methods. In Wilson, M.J. (ed.), A Handbook of Determinative Methods in Clay Mineralogy, Blackie, London.

Russell, J.D. (1988) Infrared spectroscopy of inorganic compounds. In Willis, H. (ed.) Laboratory methods in Infrared Spectroscopy, Wiley, New York. (In press)

Russell, J.D., Farmer, V.C. and Velde, B. (1970) Replacement of OH by OD in layer silicates and identification of the vibration of these groups in infrared spectra. Miner. Mag. 37: 869-879.

Ryabchikov, I.D. (1988) Geochemical evolution of the earth's mantle. In Barsukov, ed. Science; the Twenty-seventh V.I. Vernadsky lecture, Academy of Sciences, U.S.S.R., Moscow.

Ryabchikov, I.D. and Boettcher, A.L. (1980) Experimental evidence at high pressure for potassic metasomatism in the mantle of the Earth. Amer. Mineral. 65: 915-919.

Ryabchikov, I.D. and MacKenzie, W.S. (1985) Interactions of jadeite with water at 20-30 kbar and 650 C. Mineral. Mag. 49(9): 601-603.

Ryabchikov, I.D., Schreyer, W. and Abraham, K. (1982) Compositions of aqueous fluids in equilibrium with pyroxenes and olivines at mantle pressures and temperatures. Contrib. Mineral. Petrol. 79:80-84.

Schamber, F.H., Wodke, N.F. and McCarthy, J.J. (1980) Least-squares fit with digital filter. The method and its application to EDS spectra. In Bearman, D.R., Ogilvil, R.E. and Wittry, D.B. (eds.), Eighth International Congress on X-ray Optics and Microanalysis, Pendell Publ. Co., Midland,MI, pp. 124-132.

Schneider, M.E. and Eggler, D.H. (1984) Composition of fluids in equilibrium with peridotite: implications for alkaline magmatism-metasomatism. In Kornprobst, J. (ed.) Kimberlites: II, the mantle and crust-mantle relationships. Developments in Petrology, Vol. 11B. 393 pp. Elsevier, Amsterdam.

Schulze, D.J. (1987) Megacrysts from alkalic volcanic rocks. In Nixon, P.H. (ed.), Mantle Xenoliths, Wiley, Chichester, pp. 433-452.

Seal, M. (1965) Structure in diamond as revealed by etching. Amer. Mineral. 50: 105-123.

Seal, M. (1966a) Inclusions, birefringence and structure in natural diamond. Nature 212: 1528-1531.

Seal, M. (1966b) Nature of diamond coat. Phil. Mag. 13: 645-648.

Sellschop, J.P.F. (1979) Nuclear properties in physical and geochemical studies of natural diamond. In Field, J.E. (ed.), The Properties of Diamond, Academic Press, London, pp. 108-163. Shah, G.J. and Lang, A.R. (1963) An unusual distribution of precipitants in a diamond. Min. Mag. 33: 594-599.

Shimizu, N. and Richardson, S.H. (1987) Trace element abundance patterns of garnet inclusions in peridotite-suite diamonds. Geochim. et Cosmochim. Acta 51: 755-758.

Shimizu, N., Gurney, J.J. and Moore, R.O. (1988) Trace element abundance patterns of garnet inclusions in diamonds. The Goldschmith Conf. Abstr. Vol., Geol. Soc. Am. Spec. Pub. No. 126. Washington.

Shimizu, N. and Hart, S.R. (1982) Application of the ion microprobe to geochemistry and cosmochemistry. Ann. Rev. Earth Planet. Sci. 10: 483-526.

Skinner, E.M.W., Smith, C.B., Bristow, J.W., Scott Smith, B.H. and Dawson, J.B. (1985) Proterozoic kimberlites and lamprolites and a preliminary age for the Argyle lamproite pipe, western Australia. Trans. Geol. Soc. South Africa 88: 335-340.

Smith, C.B. (1983) Pb, Sr and Nd isotopic evidence for sources of southern African Cretaceous kimberlite. Nature 304: 51-54.

Smith, C.B., Gurney, J.J., Skinner, E.M.W., Clement, C.R. and Ebrahim, N. (1985) Geochemical character of Southern African kimberlites: a new approach based on isotopic constraints. Trans. Geol. Soc. South Africa 88: 267-280.

Sobolev, E.V., Lisoivan, V.I. and Lenskaya, S.V. (1968) The relation between the "spike" extra reflection in Laue patterns of natural diamonds and their optical properties. Soviet Phys. Dokl 12: 665-668.

Sobolev, E.V. (1969) On the nature of the yellow color of diamonds. Geologiya Geofiz. Novosibirsk 12: 145-149.

Sobolev, N.V., Galimov, E.M., Ivanovskaya, I.N. and Yefimova, E.S. (1979) The carbon isotope composition of diamonds containing crystallographic inclusions. Dokl. Akad. Nauk. SSSR 249: 1217-1220.

Stern (1974) The orthsilicates minerals. In Farmer, V.C. (ed.), The Infrared Spectra of Minerals, Mineralogical Society, London.

Sunagawa, I. (1984) Morphology of natural and synthetic diamonds. In Sunagawa, I. (ed.), Material Science of The Earth Interior', Terra Scientific Publishing, Tokyo, pp. 303-330.

Swart, P.K., Pillinger, C.T., Milledge, H.J. and Seal, M. (1983) Carbon isotopic variation within individual diamonds. Nature 303: 793-795.

Takagami, Y., Ozima, M., and Zashu, S. (1988) $_{40}$Ar-$_{39}$Ar dating of a Zaire cubic diamond. EOS 69(16): 503.

Takahashi, E. and Kushiro, I. (1983) Melting of a dry peridotite at high pressures and basalt magma genesis. Amer. Mineral. 68:859-879.

Thompson, W.K. (1965) Infrared spectroscopic studies aqueous system. Trans. Farad. Soc. 16: 2635-2640.

Trueb, L.F. and Barrett, C.S. (1972) Microstructural investigation of ballas diamond. Amer. Mineral. 57: 1664-1680.

Wagner, P.A. (1914) The Diamond Fields of Southern Africa. Struik, Cape Town.

Wänke, H., Baddenhausen, H., Blum, K., Cendales, M., Dreibus, G., Hofmeister, H., Kruse, H., Jagoutz, E., Palme, H., Spettel, B., Thacker, R., and Vilcsek, E. (1977) On the chemistry of lunar samples and achondrites. Primary matter in the lunar highlands: A re-evaluation. Proc. Lunar Sci. Conf. 8th, pp. 2191-2213.

Watermeyer, B. (1982) Diamond cutting. Centaur, Johannesburg.

Waters, F.G. (1987) A suggested origin of MARID xenoliths in kimberlites by high pressure crystallization of an ultrapotassic rock such as lamporite. Contib. Miner. Petrol. 95: 523-533.

Weis, D. and Demaiffe, D. (1985) A depleted mantle source for kimberlites from Zaire: Nd, Sr, and Pb isotopic evidence. Earth Planet. Sci. Lett. 73: 269-277.

Welke, H.J., Allsopp, H.L. and Harris, J.W. (1974) Measurements of K, Pb, U, Sr and Pb isotope composition in diamonds containing inclusions. Nature 259: 35-37.

Wendlandt, R.F. and Eggler, D.H. (1980) The origin of potassic magmas: 2. Stability of phlogopite in natural spinel lherzolite and in the system $KAlSiO_4$ - MgO - SiO_2 - H_2O - CO_2 at high pressures and high temperatures. Amer. J. Sci. 280: 412-458.

White (1974) The carbonate minerals. In Farmer, V.C. (ed.), The Infrared Spectra of Minerals, Mineralogical Society, London.

Williams, A.F. (1932) The Genesis of the Diamond. Benn, London.

Williams, P. (1985) Secondary ion mass spectrometry. Ann. Rev. Mater. Sci. 15: 517-548.

Williamson, J.H. (1968) Least squares fitting of a straight line. Canad. J. Phys. 46: 1845-1847.

Wyllie, P.J. and Huang, W.L. (1976) High CO2 solubilities in mantle magmas. geology 4: 21-24.

Wyllie, P.J. and Huang, W.L. () Peridotite, Kimberlite and Carbonatite explained in the system CaO-MgO-SiO2- CO2. Geology 3: 621-624.

Zashu, S., Ozima, M., and Nitoh, O. (1986) K-Ar isochron dating of Zaire cubic diamonds. Nature 323(23): 710-712.

APPENDIX A - SAMPLE DESCRIPTION

This appendix includes the description of 56 diamonds examined during the course of this study. The morphology, color, weight, and the largest dimension of each sample are stated when known. A short summary of the preparation and analytical techniques used for each diamond is also given. Abbreviations used are: **IR** -infrared spectrometry, **SIMS** - secondary ion mass spectrometry, **EPMA** - electron microprobe, **SEM** - analytical scaning electron microscopy. **INAA** - instrumental neutron activation analysis, **CL** - cathodoluminescence. The wafer thichness and the spectral type observed are given for diamonds analyzed by IR. **GRR** - George R. Rossman, **CTP** - Collin T. Pillinger, **ON** - Oded Navon, **CBS** - Chris B. Smith. Other terms used in the descriptions are: **trigon** - a triangular etch pit, **macle** - a twinned diamond of spinel type, twinning is along an octahedral plane and results a flat, triangular diamond.

A.1. DIAMONDS OF THE GRR SET

GRR 861.2 Cubic, few large cracks throughout the diamond, greenish-brown. 51.97 mg, ~2.7 mm. Two parallel faces were polished along 001 cutting the minimal depth into the diamond. IR (2.6 mm, type IaA, micro-inclusions), SIMS. On loan to GRR from a private collector.

GRR 1155 Cubic, opaque, pale green. 11.3 mg, 1.6 mm. Polished along 001, one side deep towards the center of the diamond. SIMS, EPMA (inclusions). The single sample from a group of "Congo cubes" of unknown origin (probably Zaire).

GRR 1502 Octahedral, partly resorbed, few cracks, brown, transparent. 71.6 mg, 3.9 mm. Sawn, one half polished along 001. IR (1.193 mm, IaAB, platelets), CL (complex internal zoning). GRR 1501-1530 were brought from Mr. David New. He bought them from a private collector that stated they were bought in London and are from Orapa, Botswana. However, based on their color and morphology, it is clear they are not from Botswana and a Zairian origin has been suggested (J.W. Harris, personal comunication).

GRR 1503 Octahedral, coated, green coat, transparent colorless core. 132.2 mg, .5 mm. Polished into a wafer along the largest, 001 center plane. IR (1.008 mm, core: IaAB, platelets, coat: IaA), SIMS, EPMA, SEM, CL (complex internal structure in the core, no luminescence in the coat).

Source: see GRR 1502.

GRR 1504 Octahedral, minor development of cubic faces, coated, a large hole penetrates the core, faces are frosted, trigons on octahedral faces, green coat, colorless core. 103.3 mg, .7 mm maximum width. Laser cut along 001, upper pyramid polished into a wafer for IR (0.255 mm, core and coat: IaA, platelets), SIMS, EPMA, INAA, XRD (on coat, only the pure diamond spots. No rings due to randomly oriented inclusions). Source: see GRR 1502.

GRR 1505 Octahedral aggregated with some small crystals, minor development of cubic faces, trigons on octahedral faces, green coat, transparent core. 83.9 mg, .1 mm. Laser cut along 001, upper pyramid crushed and three large coat fragments for INAA. Source: see GRR 1502.

GRR 1507 Octahedral, trigons, green coat, colorless core. 85.6 mg, .2 mm. Sawn along 001, polished to a wafer. IR (coat: IaA, inclusions), INAA. Source: see GRR 1502.

GRR 1508 Octahedral, coated, green coat, colorless core. 110.2 mg, .1 mm. Polished into a wafer along 110. IR (core: IaAB, platelets, coat: IaA, inclusions), SIMS, EPMA, SEM, INAA, CL (core: light blue, some structure, a middle region in the outer core; coat: green). Source: see GRR 1502.

GRR 1509 Octahedral, coated, green coat, colorless core. 116.8 mg, .2 mm. Sawn, polished parallel to 100 plus one fragment of coat only. IR (1.216, 0.35 mm, core: IaAB, platelets; coat: IaA, inclusions, platelets), INAA, CL (highly zoned core). Source: see GRR 1502.

GRR 1512 Cubic, colorless, hexagonal pits. 35.7 mg, 3.2 mm. Sawing revealed an included diamond in the center of the cube, it was lost during polishing. IR (0.682 mm, type IaA). Source: see GRR 1502.

GRR 1513 Cubic, opaque, white, frosted faces, few deep pits. 7.5 mg, 3.2 mm. Sawn, polished along 100. IR (0.97±0.03, IaA, inclusions). Source: see GRR 1502.

GRR 1515 Cubic, irregular cube with sharp edges, slightly resorbed, translucent, pale green. 1.8 mg, 2.6 mm. Polished parallel to 100 down to the middle. IR (0.7 mm, IaA, inclusions, small platelet peak), SIMS, EPMA, INAA. Source: see GRR 1502.

GRR 1517 Cubic, greenish yellow, hexagonal pits on surface. 55.3 mg, 3. mm. Sawn, polished along 100. SIMS, INAA. Source: see GRR 1502.

GRR 1518 Cubic, greenish yellow, hexagonal pits, few channels. 31.1 mg, 3.2 mm. Laser cut, polished along 100. SIMS, SEM, INAA.

GRR 1519 Cubic, pale green, frosted faces, few channels. 7.7 mg, 3.2 mm. Sawn, polished along 100. IR (0.95±0.03 mm, IaA, inclusions), SIMS, INAA.

GRR 1521 Macle, coated, many trigons, few large pits, green coat. 9.8 mg, 3.3 mm. Crushed, a small fragment was mounted on a SEM holder using carbon paint and was gold coated for SEM examination. Source: see GRR 1502.

GRR 1527 Macle, coated, many trigons, one large pit reaches the transparent core; green coat. 53. mg, mm. Broken into two halves; one was crushed, and fragments of the coat were hand picked and further crushed into fine powder for TEM examination. Source: see GRR 1502.

A.2. DIAMONDS OF THE CTP SET

CTP L0 A polished wafer of a coated diamond, grey-brown coat (as viewed through the wafer), transparent core. Polished along 100. IR (0.93 mm, core: IaA, platelets; coat: IaA, inclusions) SIMS, EPMA. The wafer was adjacent to Ladder 0, studied by Boyd et al. (1988). From Zaire.

CTP L3 A polished wafer of a coated diamond, yellow double coat, with a transparent layer between the two coat layers, transparent core. Polished along 100. IR (0.9 mm, core: IaA; coat: IaA, inclusions). The wafer was adjacent to Ladder 3, studied by Boyd et al. (1988). From Zaire.

CTP L A polished wafer of a coated diamond, yellowish-green coat (as viewed through the wafer), transparent core. Polished along 100. IR (0.50 mm, core: IaA; coat: IaA, inclusions). The wafer was adjacent to Ladder , studied by Boyd et al. (1988). From Zaire.

CTP L6 A polished wafer of a coated diamond, grey-brown coat (as viewed through the wafer), transparent core. Polished along 100. IR (0.50 mm, core: IaA; coat: IaA, inclusions) SIMS, EPMA. The wafer was adjacent to Ladder 6, studied by Boyd et al. (1988). From

Zaire.

CTP LB A polished wafer of a coated diamond, grey-brown coat (as viewed through the wafer), transparent core. Polished along 100. IR (0.50 mm, core: IaA, platelets; coat: IaA, inclusions) SIMS, EPMA. The wafer was adjacent to Ladder B, studied by Boyd et al. (1988). From Zaire.

CTP MM1 (6265) A polished wafer of a coated diamond, grey-brown coat (as viewed through the wafer), transparent core. Polished along 100. IR (0.50 mm, core: IaA; coat: IaA, inclusions) SIMS, EPMA. The wafer was adjacent to Ladder MM1, studied by Boyd et al. (1988). Mbuji-Mayi, Zaire.

CTP Z1 A polished wafer of a coated diamond, grey-brown coat (as viewed through the wafer), transparent core.

IR (1.00 mm, coat: IaA, inclusions). From Zaire.

CTP Z2 A polished wafer of a coated diamond, grey-brown coat (as viewed through the wafer), transparent core.

IR (1.00 mm, coat: IaA, inclusions). From Zaire.

CTP Z3 A polished wafer of a coated diamond, grey-brown coat (as viewed through the wafer), transparent core.

IR (0.993 mm, coat: IaA, inclusions). From Zaire.

CTP Z A polished wafer of a coated diamond, grey-brown coat (as viewed through the wafer), transparent core.

IR (1.00 mm, coat: IaA, inclusions). SIMS, EPMA. From Zaire.

CTP 6268 A polished wafer of a coated diamond, grey coat (as viewed through the wafer), transparent core. IR (0. mm, core: IaA; coat: IaA, inclusions). From Jwaneng, Botswana.

A.3. OTHER GRR DIAMONDS

GRR 861.1 Octahedral, deep green color throughout the body of the diamond. 217.5 mg, ~ mm. Two small windows were polished and a low quality IR spectrum was recorded (~ mm). On loan to GRR from a private collector.

GRR 980 Cut, colorless, gem quality diamond. ~ 2 mm max diameter. SIMS, EPMA (as blank). Locality unknown.

GRR 1162 Cut, colorless, gem quality diamond. 22 mg, 3.2 mm wide. IR (0.98 mm, type IaAB, platelets), SIMS, EPMA (as blank). Locality unknown.

GRR 1166 Cut, colorless, gem quality diamond. 39.6 mg (after some additional polishing), 3.6 mm, square shape. IR (1.235 mm, IaAB, platelets), SIMS (blank). Locality unknown.

A.4. OTHER CTP DIAMONDS

CTP 3657 Colorless, polished, square chip, 0.5 mm.

IR (0.178, 0.76 mm, type IIa). Locality unknown.

CTP 3811 Colorless, polished, square chip, 0.5 mm.

IR (0.26 mm, type IIa), SIMS (isotopic composition). Locality unknown.

CTP 706 Colorless, polished, square chip, 0.5 mm.

IR (0.95 mm, type IIa). Locality unknown.

CTP 771 Colorless, polished, square chip, 0.7 mm.

IR (0.695 mm, type IIa), SIMS (isotopic composition). Locality unknown.

CTP 7772 Colorless, polished, square chip, 0.8 mm.

IR (0.00 mm, type IIa), SIMS (isotopic composition). Locality unknown.

CTP FCF 51 Colorless, cut, elongated, type IaA-IaB diamond. SIMS (isotopic composition). Locality unknown.

A.5. ON SAMPLES

ON NYZ 1 Cut, transluscent, grey. 5x3 mm. IR (1.3 mm, IaA, inclusions), polished down to .35 mm for TEM. Locality unknown.

ON NYP 15 Cut, colorless diamond with an olivine inclusion. IR (1.9 mm, IaAB). Locality unknown.

ON SDK 17 Cubo-octahedral, yelowish-green. 3.6 mg, 1.3 mm. Many black inclusions. Ir (0.96 mm, Ib). Synthetic (by G.C. Kennedy).

ON PCA 22 Rounded, colorless. 12.3 mg. IR (.775 mm, IaAB). From Prerie Creek, Arkansas, USA.

ON GCC 2 Rounded, colorless. 16.6 mg. Many inclusions, mostly colorless, few greenish grey. IR (1.20 mm, II), SIMS. From George Creek, Colorado.

ON GCC 28 Rounded, colorless. 9.2 mg. Many mineral inclusions: colorless and birefringent, greenish brown, orange-brown. IR (0.80 mm, IaAB). From George Creek, Colorado.

ON GCC 29 Rounded, colorless. 12.2 mg. Many inclusions, greenish brown, colorless, a large orange inclusion, ~250 μm. IR (1.06 mm, IaAB). From George Creek, Colorado.

ON GCC 3 Rounded, colorless. 15.8 mg. Many inclusions. IR (1.6 mm, IaAB), SIMS. From George Creek, Colorado.

ON SDS 36 Cut and polished, yellow, synthetic diamond. Color zoning. 3.2x2x1.5 mm. IR (1.51 mm, Ib), SIMS, EPMA (as blank). Sumitomo Electric Corporation, Japan.

ON ARG 0 Octahedral, resorbed, zoned with respect to resorption (two layers, outer was resorbed faster), brown. 15.7 mg, 2.1 mm. IR (0.685 mm, IaB), SIMS. Argyle, Australia.

ON ARG 1 Octahedral, slightly resorbed, few inclusions, brown. 26.5 mg. IR (1.10 mm, IaAB), SIMS. Argyle, Australia.

ON ZIZ 7 A cleaved piece of a coated octahedral diamond. The core comprises about half the thickness of the sample. 63.52 mg, 7 mm. IR (coat thickness unknown, IaA). Locality unknown, donated by Y. Zitron of Zizith Inc., New York.

LL DDN 20 A broken piece of a cut, gem diamond, colorless. 1 mg, 2.72 mm. INAA (as blank).

A.6. CBS DIAMONDS

These diamonds were received from Chris B. Smith, CRA Exploration, Australia. All diamonds are fragments of larger diamonds, that were broken by us to liberate inclusions and to study the carbon isotopic composition. They were studied by IR, and samples CBS AK1 17, 3 and 10 were analyzed for their isotopic composition by SIMS. The diamonds are characterized by their morphology, color, paragenesis, inclusions found, δ^13C, thickness and IR type.

CBS AK1 8 Macle, yellow, eclogitic, garnet, , 0.635 mm, IaAB.

CBS AK1 17 nd, yellow, eclogitic, garnet, -10.7, 1.6 mm, IaAB.

CBS AK1 27 Macle, brown, eclogitic, garnet + coesite, -9.8, 0.6 mm,IaAB.

CBS AK1 3 Macle, brown, eclogitic, garnet, -9.1, .695 mm, IaAB.

CBS AK1 10 Dodecahedron, brown, peridotitic, olivine + orthopyroxene, -7.3, no IR data.

Table A.1. Metal oxide concentration determined by EPMA.
(for correlation with SIMS data)

All concentrations in ppm (weight) of the oxides.

Sample	Point	Na2O	MgO	Al2O3	SiO2	K2O	CaO	TiO2	FeO
CTP 6268	31	19	50	30	302	213	114	40	143
CTP 6268	32	16	50	29	382	224	105	62	147
CTP 6268	35	37	60	49	420	292	108	66	179
CTP LO	31	(31)	25	66	515	228	74	48	46
CTP LO	32	(9)	16	20	127	69	22	7	13
CTP LO	33	(10)	8	12	114	65	25	8	18
CTP LO	34	(0)	10	21	170	83	21	28	23
CTP L6	31	(1)	10	9	146	57	13	7	15
CTP L6	32	(0)	11	7	92	50	25	21	18
CTP LB	31	(0)	9	3	118	51	7	26	31
CTP LB	32	(1)	8	17	142	61	27	16	36
CTP Z4	31	(0)	23	83	805	174	17	29	53
CTP Z4	32	(0)	11	69	592	141	10	26	59
CTP Z4	35	(0)	18	62	511	116	10	25	35
CTP 6265	32	(15)	4	0	0	10	0	2	0
GRR 1155	14	6	12	45	220	97	49	24	(50)
GRR 1155	16	8	18	36	164	81	42	10	(25)
GRR 1155	17	4	6	24	85	42	20	0	(25)
GRR 1155	25	2	10	20	448	62	39	12	(46)
GRR 1155	28	5	10	25	176	92	39	23	(37)
GRR 1155	29	7	6	19	182	91	35	10	(51)
GRR 1155	31	6	12	45	220	97	49	24	50
GRR 1155	32	8	18	36	164	81	42	10	25
GRR 1155	33	5	10	25	176	92	39	23	37
GRR 1503	11	34	54	24	260	155	155	31	(189)
GRR 1503	12	36	65	44	321	185	192	34	(286)
GRR 1503	13	35	61	26	292	139	164	39	(107)
GRR 1503	31	5	20	10	159	46	40	1	24
GRR 1503	32	38	49	20	332	134	132	4	92
GRR 1508	11	23	22	31	270	129	61	17	(255)
GRR 1508	12	18	19	38	358	155	62	5	(156)
GRR 1508	13	17	21	38	402	175	71	24	(90)
GRR 1508	31	4	7	19	184	80	41	23	31
GRR 1508	32	5	18	21	199	104	47	17	31
GRR 1508	33	7	18	32	319	116	65	2	31
GRR 1515	11	38	65	47	582	111	61	2	(311)
GRR 1515	12	58	94	124	809	152	117	34	(895)
GRR 1515	13	40	98	150	612	105	81	25	(786)

1. Values in paranthesis were not used in the correlations.

Table A.2. SIMS count-rates for correlation with EPMA concentration data.

All data is in cps normalized to 50000 cps for mass 12.

Sample	Point	Na	Mg	Al	Si	K	Ca	Ti	Fe
CTP 6268	31	51694	7180	8644	5846	285525	36967	3085	4906
CTP 6268	32	53577	5963	7894	5050	280535	36418	2745	3857
CTP 6268	35	60994	9588	10545	7399	358101	40632	3748	6506
CTP L0	31	(43083)	2786	14254	6080	265163	25944	1427	1377
CTP L0	32	(21539)	1353	6362	2591	115567	13683	602	530
CTP L0	33	(23497)	1093	6188	2460	122734	14025	594	523
CTP L0	34	(29348)	1680	7743	3000	148674	17630	739	630
CTP L6	31	98877)	592	2388	1051	43883	5582	251	201
CTP L6	32	(17853)	1704	4712	2580	86619	11029	613	632
CTP LB	31	(12019)	396	1726	741	70820	6966	191	237
CTP LB	32	(23957)	1192	8081	2880	134186	15106	679	533
CTP Z4	31	(28646)	2353	25651	17693	258892	8019	2154	1390
CTP Z4	32	(31549)	2581	26418	18711	266157	9307	2280	1599
CTP Z4	35	(30982)	2590	27171	19769	266914	8614	2301	1622
CTP 6265	32	(2014)	146	301	193	6036	1024	53	56
GRR 1155	14	10646	1708	7197	5611	111698	14015	1684	(1368)
GRR 1155	16	11387	1966	7325	5506	114356	15366	1755	(1504)
GRR 1155	17	5414	861	3647	2756	53929	7657	857	(656)
GRR 1155	25	17147	2821	10315	8460	171198	18002	2384	(1184)
GRR 1155	28	7986	1187	4484	3537	80034	9119	1065	(113)
GRR 1155	29	13963	2204	7787	5811	132447	16118	1881	(1070)
GRR 1155	31	11254	1565	5868	4301	121621	13776	1409	1083
GRR 1155	32	15531	2178	8176	6135	164583	18360	1972	1575
GRR 1155	33	16384	2185	8590	6467	171673	18852	2041	1580
GRR 1503	11	81266	8415	8710	5813	261206	54587	1877	(1971)
GRR 1503	12	70602	7589	7616	5381	215466	50466	1639	(1353)
GRR 1503	13	67174	6749	7302	4672	211347	47756	1514	(1318)
GRR 1503	31	8500	989	1193	955	37226	10074	356	505
GRR 1503	32	43966	4643	5855	3768	184779	45239	1439	1831
GRR 1508	11	25676	2182	7151	3871	155557	19263	964	(216)
GRR 1508	12	35030	3135	12532	7053	246661	23401	1536	(722)
GRR 1508	13	36791	3144	9814	5227	226318	27800	1349	(701)
GRR 1508	31	11464	1050	2475	1459	65458	10697	410	287
GRR 1508	32	11136	915	2407	1250	62633	9767	373	833
GRR 1508	33	33891	2862	8593	4334	209436	27961	1187	1564
GRR 1515	11	98163	10062	13295	7854	158985	25775	1733	(3547)
GRR 1515	12	132820	16874	51077	9678	205593	28697	3124	(34971)
GRR 1515	13	83936	9192	46395	7450	117261	17491	1386	(16773)

1. Values in paranthesis were not used in the correlations.

Table A.3. Summary of SIMS analysis.

Sample	CTP 6268	CTP 6268	CTP 6268	CTP 6268	CTP L0	CTP L0	CTP L0	CTP L0	CTP L0	CTP L6	CTP L6	CTP LB	CTP LB
Point	31	32	33	35	30	31	32	33	34	31	32	31	32
SiO2[1]	32.6[1]	31.4	30.7	32.9	44.6	42.4	41.0	39.3	38.9	41.8	44.8	28.6	40.6
TiO2	4.2	4.2	4.2	4.1	2.3	2.5	2.4	2.3	2.4	2.5	2.6	1.8	2.4
Al2O3	3.0	3.0	2.9	2.9	6.1	6.1	6.2	6.1	6.2	5.8	5.0	4.1	7.0
FeO	16.1	14.2	15.6	17.1	4.7	5.7	4.9	4.9	4.8	4.7	6.5	5.4	4.4
MgO	5.7	5.3	5.5	6.1	2.8	2.8	3.1	2.5	3.1	3.4	4.2	2.2	2.4
CaO	10.5	11.6	10.7	9.2	10.3	9.2	11.1	11.4	11.7	11.3	9.8	13.7	10.9
Na2O	2.5	2.9	2.8	2.4	2.8	2.6	3.0	3.3	3.3	3.1	2.7	4.1	3.0
K2O	20.4	22.4	22.5	20.4	21.7	23.7	23.4	25.1	24.7	22.4	19.3	35.1	24.3
Total[2]	917	821	1894	1150	394	732	323	320	394	128	294	132	362

1. Major oxide concentrations (wt%) in the volatile free fraction of the inclusions, calculated by normalizing the total of the eight metal oxide to 95%; on average P_2O_5, BaO, SrO and the REE account for -5% of the metal oxide fraction.

2. Total concentration of the above eight oxides in the diamond volume analyzed (in ppm).

Table A.3 Summary of SIMS analyses (cont).

Sample	CTP Z4	CTP Z4	CTP Z4	CTP MM1	CTP MM1	GRR 1503	GRR 1503	GRR 1503	GRR 1503	GRR 1503	GRR 1503	GRR 1503
Point	31	32	35	31	32	4	5	11	12	13	31	33
SiO_2	67.4	67.4	68.4	37.7	43.1	35.0	34.5	38.5	36.3	34.2	34.6	36.2
TiO_2	2.0	2.0	2.0	2.8	2.9	2.6	2.7	2.7	2.7	2.7	3.2	3.1
Al_2O_3	6.0	5.8	5.8	4.8	4.1	3.6	3.2	3.5	3.2	3.3	2.7	3.6
FeO	3.1	3.4	3.3	7.1	7.4	11.0	6.9	10.5	5.4	5.7	10.8	8.0
MgO	1.3	1.3	1.3	4.6	4.6	6.4	7.1	6.5	7.3	7.1	5.1	3.4
CaO	1.6	1.7	1.5	16.2	11.7	16.6	16.5	15.2	17.4	17.9	18.7	15.6
Na_2O	1.0	1.0	0.9	3.7	3.9	0.0	4.2	2.9	4.2	4.3	2.7	2.3
K_2O	12.6	12.3	11.8	18.1	17.3	16.7	19.9	15.2	18.6	19.8	17.3	22.7
Total	1341	1418	1477	191	23	521	862	665	758	698	141	272

Table A.3 Summary of SIMS analyses (cont).

Sample	GRR 1504	GRR 1504	GRR 1504	GRR 1504	GRR 1504	GRR 1504	GRR 1504	GRR 1504	GRR 1508	GRR 1508	GRR 1508	GRR 1508	GRR 1508
Point	11	13	14	14	15	31	32	43	4	5	11	12	13
SiO2	39.9	41.3	47.8	46.8	42.1	42.7	39.0	38.7	48.8	40.7	44.9	48.8	42.5
TiO2	2.9	2.5	2.5	2.6	2.7	2.2	2.7	2.7	2.6	2.6	2.8	2.6	2.7
Al2O3	5.8	3.8	5.0	6.5	5.3	4.2	4.3	4.1	4.6	7.6	5.1	5.3	4.9
FeO	9.8	12.7	13.0	14.2	12.1	6.5	8.3	12.1	7.6	10.1	1.5	2.9	3.4
MgO	5.0	4.6	5.1	3.9	4.3	3.8	4.9	5.0	3.2	3.5	3.6	3.1	3.7
CaO	10.4	8.6	6.3	5.2	8.1	6.9	8.7	8.4	9.3	12.7	11.4	8.3	11.6
Na2O	2.5	2.3	1.9	2.0	2.0	2.3	2.7	2.9	1.8	2.0	2.6	2.1	2.6
K2O	18.7	19.1	13.4	13.8	18.4	26.3	24.3	21.1	17.2	15.8	23.1	21.9	23.6
Total	1048	889	1639	1624	690	1234	1173	1363	747	266	440	739	627

Table 3. Summary of SIMS analyses (cont).

Sample	GRR 1508	GRR 1508	GRR 1508	GRR 1508	GRR 1508	GRR 861.2	GRR 861.2	GRR 861.2	GRR 861.2	GRR 861.2	GRR 1155	GRR 1155	GRR 1155
Point	31	32	33	41	43	2	3	4	31	32	1	6	7
SiO2	38.8	39.5	42.7	39.4	37.8	52.1	53.9	50.5	49.3	49.8	54.6	52.8	54.2
TiO2	2.7	2.8	2.8	2.7	2.6	2.3	2.3	2.4	2.4	2.5	4.0	4.2	4.2
Al2O3	4.1	4.3	3.9	4.1	4.6	6.1	5.8	6.1	4.5	4.6	4.3	4.3	4.4
FeO	6.0	6.2	10.3	4.6	8.0	6.9	5.8	8.6	5.7	7.0	7.9	8.5	7.6
MgO	3.6	3.5	4.3	4.0	3.6	5.9	6.0	5.5	5.7	5.5	2.4	2.7	2.4
CaO	13.7	12.8	11.7	14.8	12.5	8.3	8.1	8.2	9.5	8.9	7.0	7.5	7.7
Na2O	2.6	2.5	2.4	2.7	2.6	NM	NM	3.5	3.9	3.3	0.9	1.0	0.9
K2O	23.4	23.4	17.0	22.7	23.4	10.4	10.2	10.2	14.0	13.5	13.9	14.1	13.6
Total	314	617	550	189	586	82	97	60	71	92	525	533	260

Table A.3 Summary of SIMS analyses (cont).

Sample	GRR 1155	GRR 1155	GRR 1155	GRR 1155	GRR 1155	GRR 1155	GRR 1155	GRR 1515	GRR 1515	GRR 1515	GRR 1515	GRR 1515
Point	11	15	18	19	31	32	33	1	3	11	15	31
SiO2	55.9	57.2	57.2	53.4	49.6	50.5	51.0	47.0	45.0	44.3	48.9	43.7
TiO2	3.5	4.0	4.3	4.3	4.0	4.0	4.0	2.3	2.1	2.4	2.1	2.4
Al2O3	4.1	4.3	4.5	4.4	4.2	4.1	4.2	4.3	4.1	4.6	3.7	5.5
FeO	8.4	4.7	1.1	5.8	7.4	7.6	7.3	8.5	11.9	11.8	11.8	8.3
MgO	2.6	2.7	2.7	2.9	2.6	2.6	2.5	8.7	7.3	8.1	6.9	7.1
CaO	5.5	6.2	7.5	7.6	8.1	7.7	7.6	6.7	8.4	7.4	5.9	8.8
Na2O	1.0	1.0	1.1	1.1	1.1	1.1	1.1	5.0	4.8	4.9	4.8	4.5
K2O	14.0	14.8	16.6	15.6	18.0	17.4	17.4	12.3	11.3	11.5	10.9	14.7
Total	858	755	316	556	443	621	648	560	183	906	765	744

Table A.3 Summary of SIMS analyses (cont).

Sample	GRR 1515	GRR 1515	GRR 1517	GRR 1517	GRR 1517	GRR 1518	GRR 1518	GRR 1519	GRR 1519	Cracksin core of GRR 1504	
Point	31	33	31	32	33	31	32	1	2		
SiO_2	43.7	41.7	33.7	28.4	28.9	42.3	42.4	43.6	48.2	16.8	10.0
TiO_2	2.4	2.6	3.5	3.6	3.0	2.9	2.9	2.6	2.6	0.1	0.0
Al_2O_3	5.5	5.2	6.0	4.8	5.3	3.7	5.0	4.7	5.0	9.2	8.6
FeO	8.3	8.4	4.9	6.2	4.0	8.6	7.3	9.9	7.8	31.4	33.6
MgO	7.1	9.9	4.1	5.2	3.6	5.2	4.7	5.1	4.8	2.3	2.6
CaO	8.8	8.5	14.3	21.5	20.4	9.6	10.0	13.7	11.1	15.3	17.7
Na_2O	4.5	4.9	2.4	2.5	3.3	4.0	2.8	3.6	3.3	14.5	16.5
K_2O	14.7	13.9	26.1	22.9	26.6	18.7	20.0	11.9	12.3	10.3	10.9
Total	744	609	24	13	29	126	111	74	123	11	9

A.4. Analytical data sheets of instrumental neutron activation analysis.

GRR 1504
14-Dez-87 15:20
28.57mg 1.1174

	element in %	error in %
O		
Mg		
Al		
Si		
Ca	<0.05000	
Ti	<0.00340	
Fe	0.00380	(23.)

trace element in ppm --- relative error in %

Li			Ga	<0.02000		Sn			Tm		
B			Ge			Sb	<0.00300		Yb	<0.00600	
C			As	<0.01200		Te			Lu	<0.00140	
F			Se	<0.1100		J			Hf	<0.03000	
Na	9.360	(3.0)	Br	0.03700	(19.)	Cs	<0.05000		Ta	<0.03000	
P			Rb	<0.7000		Ba	8.970	(4.0)	W	<0.01000	
S			Sr	2.560	(6.0)	La	1.100	(3.0)	Re		
Cl	14.90	(6.0)	Y	< 7.500		Ce	1.650	(7.0)	Os		
K	68.80	(3.0)	Zr			Pr			Ir	<0.00100	
Sc	0.00795	(16.)	Nb			Nd	0.5200	(29.)	Pt	<0.07000	
V			Mo	<0.2000		Sm	0.04780	(4.0)	Au	<.140E-3	
Cr	<0.1700		Ru			Eu	0.01110	(3.0)	Hg		
Mn	0.3410	(3.0)	Rh			Gd	<0.2200		Tl		
Co	<0.3000		Pd			Tb	<0.01100		Pb		
Ni	< 6.000		Ag	<0.4600		Dy	0.01300	(6.0)	Bi		
Cu	<0.6000		Cd	<0.09500		Ho	<0.00620		Th	<0.1500	
Zn	<0.7000		In	<.390E-3		Er	<0.02800		U	0.01500	(33.)

Fe/Mg =
Fe/Mn = 111.4
Fe/Sc = 4780.
Ni/Co =
Sc/Yb = > 1.325
Hf/Ta =

Zr/Hf =
Nb/Ta =
Na/K = 0.1360
K /Rb = > 98.29
Rb/Cs =
K /La = 62.55

Ir/Au =
Os/Ir =
Ni/Ir =
Ba/La = 8.155
La/Yb = > 183.3
La/U = 73.33

K /U = 4587.
Th/U = < 10.00
Ir/Re =
Os/Re =
Ni/Au =

```
GRR 1504
08-Feb-88 16:10
1.682mg    1.1134

------------------------------------------------------------------------------

       element    error
        in %      in %
O
Mg
Al
Si
Ca    <0.4100
Ti    <0.05000
Fe    <0.02000

------------------------------------------------------------------------------

            trace element in ppm  ---  relative error in %

Li                  Ga 0.06000 (30.)    Sn                  Tm
B                   Ge                  Sb <0.02500         Yb <0.07000
C                   As 0.03400 (30.)    Te                  Lu <0.01900
F                   Se                  J                   Hf <0.2800
Na  27.20  (3.0)    Br 0.09300 (35.)    Cs <0.6700          Ta <0.3300
P                   Rb < 6.000          Ba  21.30  (5.0)    W  0.04000 (35.)
S                   Sr  6.280  (10.)    La  1.920  (4.0)    Re <0.01200
Cl  36.90  (8.0)    Y  < 46.00          Ce  2.300  (35.)    Os
K   168.0  (3.0)    Zr                  Pr 0.6100  (40.)    Ir <0.01300
Sc <0.03500         Nb                  Nd                  Pt
V                   Mo                  Sm 0.08890 (5.0)    Au <0.00150
Cr < 4.000          Ru                  Eu 0.02090 (5.0)    Hg
Mn 0.7950  (3.0)    Rh                  Gd                  Tl
Co < 3.000          Pd                  Tb <0.1600          Pb
Ni < 20.00          Ag                  Dy 0.02490 (8.0)    Bi
Cu < 3.000          Cd                  Ho <0.02400         Th 0.2200  (36.)
Zn < 4.000          In <0.00120         Er                  U  <0.06000

------------------------------------------------------------------------------

Fe/Mg =             Zr/Hf =             Ir/Au =             K /U  = > 2800.
Fe/Mn = < 251.6     Nb/Ta =             Os/Ir =             Th/U  = > 3.667
Fe/Sc =             Na/K  = 0.1619      Ni/Ir =             Ir/Re =
Ni/Co = < 4.348     K /Rb = > 28.00     Ba/La =  11.09      Os/Re =
Sc/Yb =             Rb/Cs =             La/Yb = > 27.43     Ni/Au =
Hf/Ta =             K /La =  87.50      La/U  = > 32.00
```

```
GRR 1505
07-Mar-88 15:17
2.094mg   1.0738

______________________________________________________________________________
        element    error
         in %      in %

O
Mg
Al
Si
Ca    <0.4200
Ti    <0.04500
Fe    <0.02000

______________________________________________________________________________
            trace element in ppm  ---  relative error in %

Li                    Ga <0.04500           Sn                    Tm
B                     Ge < 1.600            Sb <0.07000           Yb <0.06000
C                     As <0.03500           Te                    Lu <0.02000
F                     Se                    J                     Hf <0.2400
Na   15.60   (3.0)    Br 0.1430    (18.)    Cs <0.3300            Ta <0.2100
P                     Rb < 8.000            Ba   23.50   (4.0)    W  <0.04000
S                     Sr   6.760   (7.0)    La   6.520   (3.0)    Re <0.01000
Cl  41.00   (9.0)     Y                     Ce   10.80   (14.)    Os
K    97.30   (4.0)    Zr                    Pr 0.7100    (24.)    Ir <0.01000
Sc <0.02300           Nb                    Nd   2.800   (32.)    Pt < 1.100
V                     Mo                    Sm 0.2900    (3.0)    Au <0.00120
Cr < 1.600            Ru                    Eu 0.05970 (4.0)      Hg
Mn 0.4530    (4.0)    Rh                    Gd                    Tl
Co <0.6000            Pd                    Tb <0.1200            Pb
Ni < 20.00            Ag                    Dy 0.09270 (4.0)      Bi
Cu < 2.000            Cd                    Ho <0.04000           Th <0.3500
Zn < 3.800            In <0.00120           Er                    U  <0.05400

______________________________________________________________________________

Fe/Mg =               Zr/Hf =               Ir/Au =               K /U  = > 1802.
Fe/Mn = < 441.5       Nb/Ta =               Os/Ir =               Th/U  =
Fe/Sc =               Na/K  = 0.1603        Ni/Ir =               Ir/Re =
Ni/Co =               K /Rb = > 12.16       Ba/La =   3.604       Os/Re =
Sc/Yb =               Rb/Cs =               La/Yb = > 108.7       Ni/Au =
Hf/Ta =               K /La =   14.92       La/U  = > 120.7
```

```
GRR 1507
11-Apr-88 15:18
1.054mg   1.1410

      element    error
        in %     in %
O
Mg
Al
Si
Ca    <0.5100
Ti    <0.07000
Fe    <0.03300

               trace element in ppm  ---  relative error in %

Li                      Ga <0.07000         Sn                     Tm
B                       Ge < 2.700          Sb <0.03600            Yb <0.1100
C                       As <0.04500         Te                     Lu <0.03300
F                       Se < 5.500          J                      Hf <0.4000
Na   15.20   (3.0)      Br 0.4530   (13.)   Cs <0.9400             Ta <0.6800
P                       Rb < 10.00          Ba  31.10   (6.0)      W  <0.06000
S                       Sr   5.940  (13.)   La   1.280  (5.0)      Re <0.03000
Cl   46.60   (8.0)      Y                   Ce < 4.000             Os
K    94.50   (5.0)      Zr                  Pr                     Ir <0.02300
Sc <0.04000             Nb                  Nd                     Pt
V                       Mo                  Sm 0.02430  (17.)      Au <0.00190
Cr < 5.000              Ru                  Eu 0.00363  (18.)      Hg
Mn 0.2870    (4.0)      Rh                  Gd                     Tl
Co < 1.000              Pd                  Tb <0.3000             Pb
Ni < 30.00              Ag                  Dy <0.01000            Bi
Cu < 5.000              Cd                  Ho                     Th <0.2900
Zn < 5.100              In <0.00120         Er                     U  <0.1000

Fe/Mg =                 Zr/Hf =             Ir/Au =                K /U  = > 945.0
Fe/Mn = < 1150.         Nb/Ta =             Os/Ir =                Th/U  =
Fe/Sc =                 Na/K  = 0.1608      Ni/Ir =                Ir/Re =
Ni/Co = < 9.740         K /Rb = > 9.450     Ba/La =   24.30        Os/Re =
Sc/Yb =                 Rb/Cs =             La/Yb = > 11.64        Ni/Au =
Hf/Ta =                 K /La =   73.83     La/U  = > 12.80
```

```
GRR 1508
01-Feb-88 15:40
12.207mg  1.0981

        element    error
          in %      in %
O
Mg
Al
Si
Ca     <0.04500
Ti     <0.00600
Fe     <0.00500

              trace element in ppm  ---  relative error in %

Li                         Ga <0.00700          Sn                   Tm
B                          Ge <0.3400           Sb <0.00500          Yb <0.01000
C                          As 0.00450 (24.)     Te                   Lu <0.00250
F                          Se                   J                    Hf <0.04000
Na  4.120   (3.0)          Br 0.03140 (16.)     Cs <0.07000          Ta <0.05000
P                          Rb < 1.000           Ba  7.340   (3.0)    W  0.00940 (25.)
S                          Sr  1.090  (8.0)     La 0.3400   (3.0)    Re <0.00310
Cl  23.70   (5.0)          Y  < 8.000           Ce 0.6500   (27.)    Os
K   29.90   (3.0)          Zr                   Pr 0.1700   (23.)    Ir <0.00190
Sc 0.00390  (29.)          Nb                   Nd 0.3100   (42.)    Pt <0.1300
V                          Mo <0.1700           Sm 0.02080  (4.0)    Au 0.00986 (3.0)
Cr <0.3400                 Ru                   Eu 0.00455  (4.0)    Hg
Mn 0.1360   (7.0)          Rh                   Gd                   Tl
Co <0.9000                 Pd                   Tb <0.02100          Pb
Ni < 3.100                 Ag <0.4000           Dy 0.00359  (9.0)    Bi
Cu <0.4000                 Cd                   Ho <0.00600          Th <0.07000
Zn <0.5000                 In <.700E-3          Er                   U  0.00870 (32.)


Fe/Mg =                    Zr/Hf =              Ir/Au = <0.1927      K /U  =  3437.
Fe/Mn = < 367.6            Nb/Ta =              Os/Ir =              Th/U  = < 8.046
Fe/Sc = < 12821            Na/K  = 0.1378       Ni/Ir =              Ir/Re =
Ni/Co =                    K /Rb = > 29.90      Ba/La =   21.59      Os/Re =
Sc/Yb = >0.3900            Rb/Cs =              La/Yb = > 34.00      Ni/Au = < 314.4
Hf/Ta =                    K /La =  87.94       La/U  =   39.08
```

```
GRR 1509
18-Jan-88  15:16
9.29mg     1.0910

----------------------------------------------------------------------------

        element     error
          in %       in %
O
Mg
Al
Si
Ca    <0.07400
Ti    <0.00900
Fe    <0.00500

----------------------------------------------------------------------------

              trace element in ppm  ---  relative error in %

Li                       Ga <0.01000           Sn                    Tm
B                        Ge < 4.000            Sb <0.00600           Yb <0.01400
C                        As <0.00600           Te                    Lu <0.00390
F                        Se <0.6500            J                     Hf <0.07500
Na  6.280   (3.0)        Br 0.02300 (27.)      Cs <0.09000           Ta <0.08000
P                        Rb < 1.300            Ba  7.130   (4.0)     W  <0.01200
S                        Sr  2.130   (6.0)     La  1.620   (3.0)     Re <0.00400
Cl  11.10   (9.0)        Y  < 19.00            Ce  2.560   (11.)     Os
K   40.81   (3.0)        Zr                    Pr 0.1600   (30.)     Ir 0.00230 (36.)
Sc <0.00500              Nb                    Nd <0.7500            Pt <0.2100
V                        Mo <0.2000            Sm 0.05190 (4.0)      Au <.350E-3
Cr <0.6000               Ru                    Eu 0.01080 (4.0)      Hg <0.7000
Mn 0.1930   (4.0)        Rh                    Gd                    Tl
Co <0.5000               Pd                    Tb <0.02900           Pb
Ni < 16.00               Ag <0.6000            Dy 0.01270 (6.0)      Bi
Cu <0.4000               Cd                    Ho <0.00850           Th 0.07600 (22.)
Zn <0.8400               In <.460E-3           Er <0.03300           U  <0.01300

----------------------------------------------------------------------------

Fe/Mg =                  Zr/Hf =               Ir/Au = > 6.571       K /U  = > 3139.
Fe/Mn = < 259.1          Nb/Ta =               Os/Ir =               Th/U  = > 5.846
Fe/Sc =                  Na/K  = 0.1539        Ni/Ir = < 6957.       Ir/Re = >0.5750
Ni/Co =                  K /Rb = > 31.39       Ba/La =   4.401       Os/Re =
Sc/Yb =                  Rb/Cs =               La/Yb = > 115.7       Ni/Au =
Hf/Ta =                  K /La =   25.19       La/U  = > 124.6
```

```
GRR 1515
29-Feb-88 15:47
2.587mg    1.0683
```

```
       element     error
        in %       in %
O
Mg
Al
Si
Ca   <0.2200
Ti   <0.03000
Fe    0.01500     (38.)
```

```
            trace element in ppm  ---  relative error in %

Li                   Ga <0.05000         Sn                  Tm
B                    Ge < 1.900          Sb <0.01300         Yb <0.04500
C                    As <0.02100         Te                  Lu <0.01300
F                    Se < 1.000          J                   Hf <0.2000
Na  34.60   (3.0)    Br 0.07600 (32.)    Cs <0.3000          Ta <0.3200
P                    Rb < 4.500          Ba  10.50   (8.0)   W  <0.06000
S                    Sr  7.680   (8.0)   La 0.9320   (4.0)   Re <0.01400
Cl  215.0   (6.0)    Y  < 40.00          Ce < 2.000          Os
K   78.80   (4.0)    Zr                  Pr                  Ir <0.00900
Sc 0.02800 (25.)     Nb                  Nd                  Pt <0.7500
V                    Mo <0.9000          Sm 0.06070 (8.0)    Au 0.2033   (3.0)
Cr  7.360   (12.)    Ru                  Eu 0.01330 (5.0)    Hg
Mn 0.6640   (5.0)    Rh                  Gd                  Tl
Co <0.7000           Pd                  Tb <0.1000          Pb
Ni < 20.00           Ag < 1.200          Dy 0.01870 (8.0)    Bi
Cu < 2.000           Cd                  Ho <0.03000         Th <0.2500
Zn < 4.000           In <0.00230         Er                  U  <0.06000
```

```
Fe/Mg =              Zr/Hf =              Ir/Au = <0.04427    K /U  = > 1313.
Fe/Mn =  225.9       Nb/Ta =              Os/Ir =             Th/U  =
Fe/Sc =  5357.       Na/K  = 0.4391       Ni/Ir =             Ir/Re =
Ni/Co = < 14.71      K /Rb = > 17.51      Ba/La =   11.27     Os/Re =
Sc/Yb = >0.6222      Rb/Cs =              La/Yb = > 20.71     Ni/Au = < 98.38
Hf/Ta =              K /La =  84.55       La/U  = > 15.53
```

```
GRR 1517
25-Jan-88 15:05
26.149mg  1.0689
```

```
      element    error
        in %      in %
O
Mg
Al
Si
Ca   <0.02500
Ti   <0.00400
Fe    0.00305     (20.)
```

```
            trace element in ppm  ---  relative error in %

Li                    Ga <0.00400          Sn                    Tm
B                     Ge <0.1500           Sb <0.00200           Yb <0.00500
C                     As 0.00210 (36.)     Te                    Lu <0.00130
F                     Se                   J                     Hf <0.01800
Na   1.420   (3.0)    Br 0.00760 (26.)     Cs <0.04000           Ta <0.02500
P                     Rb <0.5000           Ba 0.3200   (12.)     W  0.00320 (30.)
S                     Sr 0.3750   (11.)    La 0.08290 (4.0)      Re <0.00130
Cl   1.820   (11.)    Y  < 4.000           Ce <0.3000            Os
K    6.380   (4.0)    Zr                   Pr                    Ir <.900E-3
Sc 0.00435 (18.)      Nb                   Nd <0.2500            Pt <0.08000
V                     Mo <0.1000           Sm 0.01280 (4.0)      Au <.100E-3
Cr <0.3000            Ru                   Eu 0.00280 (4.0)      Hg
Mn 0.05070 (4.0)      Rh                   Gd                    Tl
Co <0.3000            Pd                   Tb <0.01000           Pb
Ni < 1.500            Ag <0.1200           Dy 0.00372 (6.0)      Bi
Cu <0.2000            Cd <0.1600           Ho <0.00200           Th <0.03000
Zn <0.2500            In <.140E-3          Er                    U  <0.00500
```

```
Fe/Mg =               Zr/Hf =              Ir/Au =               K /U  = > 1276.
Fe/Mn =   601.6       Nb/Ta =              Os/Ir =               Th/U  =
Fe/Sc =   7011.       Na/K  = 0.2226       Ni/Ir =               Ir/Re =
Ni/Co = < 5.172       K /Rb = > 12.76      Ba/La =   3.860       Os/Re =
Sc/Yb = >0.8700       Rb/Cs =              La/Yb = > 16.58       Ni/Au =
Hf/Ta =               K /La =   76.96      La/U  = > 16.58
```

```
GRR 1518
21-Mar-88 15:28
1.212mg    1.2812
```

```
       element     error
         in %       in %
O
Mg
Al
Si
Ca   <0.5000
Ti   <0.07000
Fe   <0.03000
```

```
             trace element in ppm  ---  relative error in %

Li                   Ga <0.06000          Sn < 150.0           Tm
B                    Ge < 4.000           Sb <0.03200          Yb <0.1000
C                    As <0.04000          Te                   Lu <0.03400
F                    Se                   J                    Hf <0.4600
Na  7.210  (5.0)     Br <0.1000           Cs <0.9000           Ta <0.5100
P                    Rb < 10.00           Ba  3.300  (26.)     W  <0.04500
S                    Sr  1.700  (30.)     La 0.2200  (13.)     Re <0.1000
Cl  7.500  (35.)     Y  < 60.00           Ce                   Os
K   26.20  (11.)     Zr                   Pr                   Ir <0.01600
Sc 0.04400 (23.)     Nb                   Nd                   Pt
V                    Mo < 2.500           Sm 0.00800 (32.)     Au <0.00160
Cr < 5.000           Ru                   Eu 0.00310 (20.)     Hg
Mn 0.1700  (5.0)     Rh                   Gd                   Tl
Co < 1.000           Pd                   Tb <0.2600           Pb
Ni < 20.00           Ag                   Dy <0.01000          Bi
Cu < 4.000           Cd                   Ho                   Th <0.3000
Zn < 5.000           In <0.00200          Er                   U  <0.1300
```

```
Fe/Mg =              Zr/Hf =              Ir/Au =              K /U  = > 201.5
Fe/Mn = < 1765.      Nb/Ta =              Os/Ir =              Th/U  =
Fe/Sc = < 6818.      Na/K  = 0.2752       Ni/Ir =              Ir/Re =
Ni/Co = < 6.192      K /Rb = > 2.620      Ba/La =   15.00      Os/Re =
Sc/Yb = >0.4400      Rb/Cs =              La/Yb = > 2.200      Ni/Au =
Hf/Ta =              K /La =   119.1      La/U  = > 1.692
```

```
GRR 1519
22-Feb-88 16:00
7.412mg*  1.0054
```

```
     element    error
       in %      in %
O
Mg
Al
Si
Ca   <0.10000
Ti   <0.01200
Fe   <0.01000
```

```
              trace element in ppm  ---  relative error in %

Li                     Ga 0.02100 (35.)   Sn                     Tm
B                      Ge < 1.000         Sb <0.00700            Yb <0.02000
C                      As 0.01800 (20.)   Te                     Lu <0.00500
F                      Se <0.6000         J                      Hf <0.08000
Na  30.70   (3.0)      Br 0.09300 (13.)   Cs <0.1600             Ta <0.09000
P                      Rb < 2.000         Ba  15.90   (4.0)      W  0.03500 (21.)
S                      Sr  10.10  (4.0)   La  1.300   (3.0)      Re <0.00400
Cl  41.40   (9.0)      Y  < 16.00         Ce  2.720   (13.)      Os
K   124.0   (3.0)      Zr                 Pr 0.2800   (22.)      Ir 0.00340 (25.)
Sc 0.01570 (18.)       Nb                 Nd < 1.100             Pt <0.3000
V                      Mo <0.1500         Sm 0.07750 (3.0)       Au <.500E-3
Cr < 1.000             Ru                 Eu 0.01610 (4.0)       Hg
Mn 0.6120   (3.0)      Rh                 Gd                     Tl
Co < 0.50              Pd                 Tb <0.03500            Pb
Ni < 11.00             Ag <0.8000         Dy 0.01600 (6.0)       Bi
Cu <0.9000             Cd <0.2500         Ho <0.00900            Th <0.2500
Zn < 1.300             In <0.00100        Er                     U  0.04400 (30.)
```

```
Fe/Mg =              Zr/Hf =              Ir/Au = > 6.800     K /U  =  2818.
Fe/Mn = < 163.4      Nb/Ta =              Os/Ir =             Th/U  = < 5.682
Fe/Sc = < 6369.      Na/K  = 0.2476       Ni/Ir = < 3235.     Ir/Re = >0.8500
Ni/Co = < 13.75      K /Rb = > 62.00      Ba/La =  12.23      Os/Re =
Sc/Yb = >0.7850      Rb/Cs =              La/Yb = > 65.00     Ni/Au =
Hf/Ta =              K /La =  95.38       La/U  =  29.55
```

* By mistake, weight was taken as 7.412 instead of 23.414 and concentrations should be all corrected by dividing them by a constant factor of 3.16. (Corrected values are used in Chapter 9)

```
     LL DDN 20
   14-Mar-88 15:07
   14.014mg   1.0931

________________________________________________________________________

   element     error
    in %       in %
O
Mg
Al
Si
Ca    <0.04000
Ti    <0.00300
Fe    <0.00320

________________________________________________________________________

          trace element in ppm  ---  relative error in %

Li                     Ga 0.00450 (31.)   Sn                    Tm
B                      Ge <0.3000         Sb <0.00300           Yb <0.00800
C                      As <0.00400        Te                    Lu <0.00250
F                      Se                 J                     Hf <0.03800
Na 0.3040   (3.0)      Br 0.01100 (29.)   Cs <0.05500           Ta <0.3000
P                      Rb < 1.000         Ba <0.1600            W  0.01300 (15.)
S                      Sr <0.1000         La <0.00180           Re <0.00200
Cl  1.270   (13.)      Y  < 5.000         Ce                    Os
K  <0.2200             Zr                 Pr                    Ir <0.00180
Sc <0.00400            Nb                 Nd                    Pt <0.1000
V                      Mo                 Sm <.500E-3           Au <.120E-3
Cr <0.4600             Ru                 Eu <.700E-4           Hg
Mn 0.00160 (25.)       Rh                 Gd                    Tl
Co <0.6000             Pd                 Tb                    Pb
Ni < 1.500             Ag                 Dy <.400E-3           Bi
Cu <0.2000             Cd                 Ho <0.01000           Th <0.02500
Zn <0.4000             In <.130E-3        Er                    U  <0.00700

________________________________________________________________________

Fe/Mg =                Zr/Hf =            Ir/Au =               K /U  =
Fe/Mn = < 20000        Nb/Ta =            Os/Ir =               Th/U  =
Fe/Sc =                Na/K  = > 1.382    Ni/Ir =               Ir/Re =
Ni/Co =                K /Rb =            Ba/La =               Os/Re =
Sc/Yb =                Rb/Cs =            La/Yb =               Ni/Au =
Hf/Ta =                K /La =            La/U  =
```

APPENDIX B. SIMS ANALYSIS OF CARBON ISOTOPIC COMPOSITION OF DIAMONDS

SIMS has been used to study the isotope systematics of a variety of elements, e.g., C, N, O, Mg, Si, Ca, Ti, and Fe. The major advantages of SIMS analysis compared with thermal ionization or gas mass spectrometry is its capability to study samples in situ and the very small volumes of sample needed for the analysis. Previous carbon isotopic studies with SIMS have been concentrated on the analysis of very small samples, e.g. interplanetary dust particles (Carey et al. 1987) and microscopic carbon-containing phases in meteorites (e.g. Zinner et al. (1987). In this study, it was hoped to apply the SIMS capability for in situ analysis to the study of zoning of the carbon isotopic composition within individual diamonds.

Very little is known about zoning of carbon isotopic composition in diamond. Javoy et al. (1983), Galimov (1984), Swart et al. (1983), and Boyd et al. (1987) reported zoning of carbon isotopic composition in coated diamonds. The difference between coat and core is commonly interpreted as representing two distinct growth events. Zoning in normal, uncoated diamond is less well-documented. Javoy et al. (1983) reported variation of up to 5.3%% in small octahedral diamonds from Zaire; however, from their description it is not clear whether the diamonds are coated or not. Boyd et al. (1987) reported variations of up to 2%% in the cores of some Zairian coated diamonds. Thus, in order to study zoning patterns a precision of ~1%% is clearly needed. The full range of carbon isotopic compositions of terrestrial diamonds is ~35%%, so resolution of at least 3%% is needed for any study. This appendix reports the result of a reconnaissance study of the possibility for using SIMS for analyzing the carbon isotopic composition of diamonds.

a. Statistical considerations

About 10^7 ^{13}C ions need to be counted in order to get a statistical meaningful result with $2\sigma=1\%$. As the natural abundance of ^{13}C is about 1%%, this correspond to 10^9 ions of ^{12}C. If the setup that was used for the analysis of trace elements is used for isotopic measurements, then with an ionization efficiency of 5×10^{-7} (section 6.3.2), 10^{15} ions are needed. Using diamond density of 3.5 gr/cm^3 this corresponds to a volume of 10^3 μm^3, or if a field apperture limits the diameter of the analyzed area to 8 μm, a 20 μm deep crater needs to be excavated. This is much too deep. Thus it is clear that another carbon species, with higher ion-yield has to be found, or a different primary beam has to be employed.

b. Relative efficiencies of different carbon species

Table B.1. summarizes the results of a quick survey of the relative efficiencies of different pure carbon species under various choices of primary and secondary beam polarities. Machine fractionation was also estimated during this study. As can be seen, the best choice is the analysis of C_2 secondary ions produced by an O^- primary beam. In addition to the highest counting rate, the choice of a diatomic species ensures smaller machine fractionation (the mass difference is still 1 amu, but the masses analyzed are twice as heavy). That also means that a higher resolving power is needed to resolve the peak of heavy carbon species from the hydride of the isotopically lighter one, however, this is compensated by the double count rate expected for the rare isotope in diatomic species. (If a_{12} and a_{13} are the abundances of the two carbon isotopes than neglecting fractionation, $^{13}C^-/^{12}C^-=a_{13}/a_{12}$, while $^{12}C^{13}C^-/^{12}C_2=2a_{13}a_{12}/a_{12}^2=2a_{13}/a_{12}$.)

c. Experimental procedure

A 1-2 nA 13 kV O^- beam was focused to 5-10 μm diameter spot. Negative secondary ions were accelerated using 4500 kV potential and were collected with transfer optics corresponding to a 150μm imaged field. The smallest field aperture was used to limit the analyzed area to 8μm diameter and to minimize aberrations. No energy filtration was applied (slit open to ~50 V). In order to avoid high background levels resulting from electrons hitting the ion counter during the analysis of negative secondary ions, a low repelling voltage of 200 V was applied to the first plate of the electron multiplier. A problem associated with operating the SIMS with both primary and secondary negative polarities is the high voltage on the source (13+4.5 Kv) that resulted in frequent arcing.

d. Mass resolving power

A high resolving power is needed to resolve the interference of $^{12}C^{13}C^-$ and $^{12}C^{13}C^1H^-$ (m=4.4 mamu, MRP=5700). However, as the $^{12}C^{12}C^1H^-$ peak is only about 10%, the intensity of the $^{12}C^{13}C^-$ peak (using a cold finger to remove some hydrogen-bearing species), the contribution of the $^{12}C^{12}C^1H^-$ peak at the center of the $^{12}C^{13}C^-$ peak is very small, even at lower resolving power. Assuming that the peak shape of $^{12}C^{12}C^1H^-$ peak is similar to that of the $^{12}C_2$ peak, the drop in intensity 4.4 mamu from the center of the peak can be determined on the high intensity, well defined $^{12}C_2$ peak. At MRP=3600 the intensity drops by more than 3 orders of magnitude. That means that the contribution of the $^{12}C^{12}C^1H^-$ peak at the center of the $^{12}C^{13}C^-$ peak, 4.4 mamu away from the center of the $^{12}C^{12}C^1H^-$ peak is more than 4 orders of magnitude smaller than the intensity of the $^{12}C^{13}C^-$ peak itself and can be neglected. As a result, it was decided to use MRP=3600 in the experiments.

e. Results

The results are summarized in Table B.2. Run durations varied between 40 and 90 minutes, beam stability was reasonable and the $^{12}C^-$ count rate varied typically by 2-3% and in few runs by up to 5%. In most cases the count rate declined during the run, but in a few runs it first increased and then decreased towards the end. The $^{12}C^{13}C^-/^{12}C_2$ ratio was much more stable and the standard deviation of the mean was on the average about 2% (2σ). Examination of the 14 analyses of the carbon isotopic composition of GRR 1166 show good agreement between the first nine analyses (average $\delta^{13}C$=54.8±2.2%%). These nine analyses were performed during four different days and suggested good reproducibility. However, the last five analyses which were carried out two days later showed a substantial deviation of about 6%% from the old value. The reasons for this are not clear.

Fragments of a few of the diamonds analyzed by SIMS were previously analyzed by gas-source mass spectrometry. Figure B.1 compares the results. A general agreement between the two sets is obvious; however, differences larger than the predicted errors do occur for several samples. In conclusion, it seems that although it is relatively easy to obtain precision of ±2%%, a careful study of the effect of alignment on the magnitude of machine fractionation is needed before better precision and accuracy can be achieved. Standards should be analyzed routinely to verify the accuracy of the results.

Table B.1. Count rates and isotopic fractionation during the analysis of carbon.

Primary	Secondary	^{12}C	^{13}C	Fractionation $[\frac{(^{12}C/^{13}C)_{diamond}}{(^{12}C/^{13}C)_{PDB}} - 1] \times 10^3$
O^-	$^{12}C^+$, $^{13}C^+$	3,500	35	~ 130°/oo
O_2^+	$^{12}C^+$, $^{13}C^+$	4,100	40	~ 130°/oo
O_2^+	$^{12}C^-$, $^{13}C^-$	20,000	200	~ 130°/oo
O_2^+	$^{12}C_2^-$, $^{12}C^{13}C^-$	50,000	1,000	~ 55°/oo
O^-	$^{12}C_2$, $^{12}C^{13}C^-$	230,000	5,000	~ 60°/oo
O^-	$^{12}C^-$, $^{13}C^-$	57,000	500	-

All measurments were done using the same beam current (5 nA) and resolution (~3500). $(^{12}C/^{13}C)_{diamond}$ is the ratio of the measured count rates of the light and the heavy carbon species.

Table B.2. $\delta^{13}C$ of diamonds and associated errors.

Sample	File[1]	Count rate[2] cps Mass 24	25/24 $\times 10^2$	$\delta^{13}C$ SIMS	2σ	$\delta^{13}C$ GSMS
GRR 1166	D895A8	63900	2.1044	-53.5	3.1	
GRR 1166	D895A9	56700	2.1049	-53.8	2.6	
GRR 1166	D902B1	47236	2.1020	-55.1	2.3	
GRR 1166	D902B2	55849	2.1016	-55.2	2.1	
GRR 1166	D906B3	99131	2.1034	-54.4	2.1	
GRR 1166	D906D2	105897	2.1050	-53.7	1.6	
GRR 1166	D906D3	102719	2.0996	-56.1	1.8	
GRR 1166	D906E1	93229	2.0987	-56.5	1.3	
GRR 1166	D909B4	77777	2.1042	-54.1	2.0	
GRR 1166	D909B5	95730	2.0905	-60.2	1.7	
GRR 1166	D909F1	89024	2.0929	-59.1	1.8	
GRR 1166	D909G1	88960	2.0881	-61.3	1.6	
GRR 1166	D909H1	88015	2.0930	-59.1	1.8	
GRR 1166	D909B6	91271	2.0963	-57.6	1.7	
GRR 1503	D905A1	57591	2.0987	-56.5	2.3	
GRR 1503	D905E1	55567	2.0817	-64.2	3.4	
CTP 7772	D897B1	50000	2.0958	-57.8	1.8	-7.2
CTP 7772	D912C1	89139	2.0937	-58.8	1.6	-7.2
CTP 7741	D896B1	59000	2.1133	-50.0	1.8	-1.4
CTP FCF51	D903G1	40420	2.0853	-62.6	2.8	-5.2
CTP FCF51	D903F1	52978	2.0857	-62.4	2.2	-5.2
CTP 3811	D911A1	49212	2.0306	-87.2	2.1	-34.4
CBS AK1 17	D904A1	50917	2.0816	-64.2	2.2	-10.7
CBS AK1 17	D904A2	53810	2.0828	-63.7	2.3	-10.7
CBS AK1 34	D910A1	51348	2.0833	-65.3	2.2	-9.1
CBS AK1 104	D898A1	56400	2.0926	-59.3	2.0	-7.3
CBS AK1 104	D913B1	90019	2.0887	-61.0	1.6	-7.3
ON SDS 36	D899A1	49300	2.0684	-70.2	2.0	-24 ?
ON SDS 36	D908A2	72513	2.0479	-79.4	2.2	-24 ?
ON SDS 36	D908B1	107000	2.0483	-79.2	2.0	-24 ?
ON SDS 36	D908C1	60460	2.0536	-76.8	1.9	-24 ?

1. File number also indicate dates. D895-D899 - 2-12-87, D902-D905 - 2/15/87, D906 - 2/16/87, D908 - 2/18/87, D909-D913 - 2/20/87-2/22/87
2. Average count rate for $^{12}C_2$ during runs. Count rates higher than 75000 were obtained by using nominal primary beam currents of 2 nA. Nominal current is the sum of the ions and electrons counted by the Faraday cup.
3. Ratios of the intensities of $^{12}C^{12}C^{-}$ (mass 25) to $^{12}C_2$ (mass 24). Ratios are for the uncorrected raw data.
4. Relative to a_{13}=0.011.
5. Standard deviation of the mean 25/24 ratio.
6. Gas-source mass spectrometry. Values for the CTP and the CBS diamonds from private communication with C.T. Pillinger and C.B. Smith. SDS is a synthetic diamond. $\delta^{13}C$ is unknown and is assumed to be similar to that of a synthetic diamond measured by Boyd et <u>al</u>. (1988).

Figure B.1. Carbon isotopic composition of diamonds: comparison of SIMS and gas-source mass spectrometry results.

Gas-source mass spectrometry results are for different fragments of the same diamonds measured by SIMS. the isotopic composition of ON SDS 36 is not known. Synthetic diamonds are commonly produced from graphite which is typically of $\delta^{13}C=25\pm2\%$. Analysis of a synthetic diamond by Boyd et al. (1988) yielded $\delta^{13}C=24\pm1\%$. Vertical lines represent the errors in the SIMS analysis. The errors associated with the gas-source mass spectrometry are smaller than the symbols.

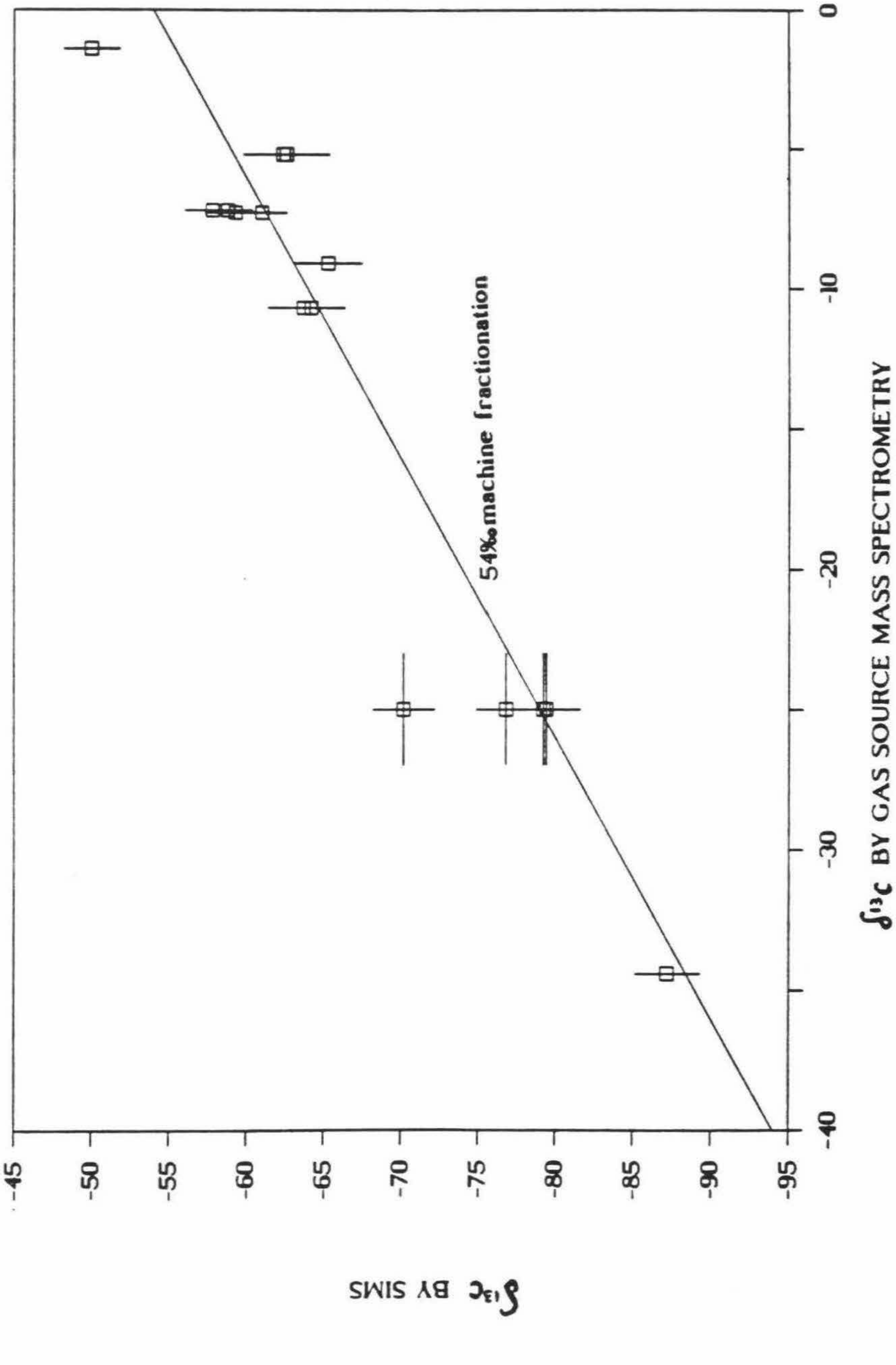
54‰ machine fractionation
δ13C BY GAS SOURCE MASS SPECTROMETRY
0
-10
-20
-30
-40
δ13C BY SIMS
-45
-50
-55
-60
-65
-70
-75
-80
-85
-90
-95

Earth and Planetary Science Letters, 73 (1985) 1–16
Elsevier Science Publishers B.V., Amsterdam – Printed in The Netherlands

[6]

Self-shielding in O_2—a possible explanation for oxygen isotopic anomalies in meteorites?

Oded Navon and G.J. Wasserburg

The Lunatic Asylum, Division of Geological and Planetary Sciences, California Institute of Technology, Pasadena, CA 91125 (U.S.A.)

Received September 24, 1984
Revised version received November 26, 1984

It is known that self-shielding of UV radiation by $^{16}O_2$ produces selective isotopic effects upon photodissociation. An analysis of this process and the chemical kinetics of isotopic exchange and trapping of O has been carried out for different gas compositions and temperatures. Calculations of the shift in ^{16}O, ^{17}O, ^{18}O abundances due to self-shielding were carried out, and it is shown that the specific rates of photodissociation J_i give $J_{17}/J_{18} \sim 1$ for column densities of O_2 between $\sim 10^{19}$ and 10^{22} molecules/cm^2 with a maximum value of $J_{17}/J_{16} = 11$ at a column density of $\sim 10^{21}$ molecules/cm^2. The O produced in this manner would have $^{17}O/^{18}O$ close to the starting material but be depleted in ^{16}O. These large shifts are quenched at temperatures higher than 500 K, or if water is present in higher concentration than O_2. Following dissociation, fast isotopic exchange reactions (e.g. $^{17}O + ^{16}O_2 \rightarrow ^{16}O + ^{17}O^{16}O$) may destroy the effect unless the atomic oxygen is efficiently trapped. Competition between trapping and exchange is shown to be of a simple mathematical form which depends on the ratio of the rate of trapping of O to the rate of exchange. Using known rate constants it is shown that trapping of anomalous O by metal atoms, hydrogen, or the O_2 itself is inefficient at pressures lower than 10^{-3} atm and normal solar abundances. Trapping on dust grains may be efficient if all oxides are present as sub-micron particles. However, the extinction of radiation by the dust is likely to quench the self-shielding effect itself. Self-shielding of radiation by O_2, may, under special conditions, lead to the production of isotopically anomalous products. However, in the light of the difficulties throughout many stages of the process, it appears to be an unsatisfactory explanation for the oxygen anomalies observed in meteorites.

The above considerations are also applied to two experiments where O is trapped by O_2 to form ozone. The isotopic shifts found in experiments by Sander et al. [10] in O_3 are compatible with the criteria developed here. The shifts found by Thiemens and Heidenreich [11,12] using a discharge cannot be explained by self-shielding of UV radiation as the pressure is below the minimum needed for self-shielding to occur. The general nature of the pressure dependence of recent discharge experiments by Thiemens and others is in agreement with the prediction of a simple kinetic model based on the production of isotopically anomalous O during dissociation of O_2, isotopic exchange of O and O_2, and ozone formation. The observed isotopic effects in O_3 produced and trapped during discharge in O_2 thus appear to be understood phenomenologically but the mechanism for selective isotopic dissociation of O_2 is still obscure and remains a fundamental problem.

Our analysis is directed toward O_2-rich environments and may only have limited applicability in the environment of the solar nebula. However, the general approach presented here is useful and may be applied to CO. It appears that selective isotopic shielding, or the mechanism which operates in the discharge experiments may still provide an explanation for some isotopic effects observed in meteorites but only if rapid trapping and isolation mechanisms (relative to exchange) can be found which apply in a low-pressure regime.

1. Introduction

Chemical or diffusional isotopic fractionation is, in most cases, mass dependent. That is, the isotopic ratio of the number of atoms of species i and j are shifted relative to an initial state (0) by the mass-dependent rule $n_i/n_j = (n_i/n_j)_0[1 + \alpha(i - j)]$. Here i and j are the atomic mass numbers and α is the effective fractionation factor. This

Div. Contribution No. 4110 (487).

0012-821X/85/$03.30

means that for the three isotopes of oxygen the enrichment of ^{18}O relative to ^{16}O during such processes is expected to be approximately twice as big as the enrichment of ^{17}O relative to ^{16}O. Using the common δ notation [*1], this yields a slope $d\delta^{17}O/d\delta^{18}O \approx 0.5$ on a three-isotope correlation diagram of $\delta^{17}O$ vs. $\delta^{18}O$.

Clayton et al. [1] found that oxygen isotopes in carbonaceous chondrites fall on a line of slope $d\delta^{17}O/d\delta^{18}O \approx 1$. No known chemical or nuclear process within the solar system was found adequate to explain this trend. Clayton et al. suggested that this trend is the result of mixing of normal solar oxygen with an exotic component, rich in ^{16}O, with $^{17}O/^{18}O$ close to normal solar oxygen or of nearly pure ^{16}O. This exotic component was inferred to have a different nucleosynthetic history from average solar system matter. The exotic oxygen was found to correspond to as much as 4% of the total oxygen nuclei, and implies a large contribution of exotic material to the solar nebula. Shifts in isotopic abundances which are not proportional to the mass difference between the isotopes (isotopic anomalies) have been found in many other elements for a variety of meteoritic samples (see [2,3] for reviews). The majority of these isotopic anomalies cannot be related to the decay of a radioactive precursor. Almost all of these effects are one to two orders of magnitude smaller than the oxygen effect, and most do not correlate with the observed isotopic anomalies of oxygen. Insofar as these isotopic anomalies are the result of stellar nucleosynthesis, they may have profound implications on the state of the protosolar nebula, the interstellar medium and the processes that contribute to it. Because of the importance of this issue, it appears useful to look for alternative processes which do not require substantial nuclear processing in stellar interiors. This approach was first tried by Arrhenius et al. [4].

Chemical processes which produce in oxygen isotopic fractionation of slope other than 1/2 are known. Open systems may produce effects which deviate from the slope 1/2 (e.g. Rayleigh fractionation process). However, as the enrichment factors in normal processes are usually of the order of few percent or much less, large deviations are achieved only when separation of the reaction products proceeds through many stages almost to completion. In this case, only a small fraction of the processed material will show a large deviation from the initial line of slope 1/2. In recent years, large isotopic enrichment factors were reported for reactions following strong vibrational excitation of N_2 and CO. Basov et al. [5] used a discharge to excite N_2 which then reacted with oxygen. They reported an enrichment factor of 20 in the abundance of ^{15}N in NO thus produced. Bergman et al. [6] reported an enrichment factor of 2.3 in the ^{13}C abundance in C_2O_3 produced by wide band laser excitation of CO. Such reactions are capable of producing large amounts of anomalous material with oxygen isotopic patterns which largely deviate from slope 1/2. No effort has yet been made to demonstrate the applicability of such processes to explain the oxygen anomalies in meteorites. Magnetic effects discriminate the zero spin ^{16}O and ^{18}O from the non-zero spin ^{17}O (e.g. [7]), but would not explain the meteoritic fractionation line.

Other photochemical reactions may also produce anomalous isotopic patterns. Due to their mass difference the isotopic species of a molecule have different vibrational and rotational frequencies. As a result, transitions between discrete states occur at different frequencies. This is the basic principle underlying isotope separation using laser sources. Natural processes may also lead to preferential activation of only one or a few of the isotopic species of a certain molecule. This can be done by (a) the strong emission line of natural sources such as the Lyman-α line of hydrogen [8] which is fortuitously absorbed only by the $^{12}C^{16}O$ species of CO; (b) mutual shielding where one molecule absorbs preferentially the radiation required for a transition by one isotopic species of another molecule, for example the shielding of ^{13}CO, $C^{18}O$, and $C^{17}O$ by the tail of one of the absorption lines of H_2 which leads to preferential dissociation of $^{12}C^{16}O$ [9]; (c) self-shielding where the most abundant isotopic species reach a larger optical depth for its absorption lines, and thus

[*1] $\delta^{*}O = 10^3\left[\dfrac{(^{*}O/^{16}O)_{\text{sample}}}{(^{*}O/^{16}O)_{\text{standard}}} - 1\right]$ where * is 17 or 18.

shielding the same isotopic molecule from dissociation at greater depth.

Self-shielding of UV radiation by ${}^{16}O_2$ in the Schumann-Runge absorption bands (175–205 nm) has been demonstrated experimentally by Sander et al. [10]. The amount of absorption is proportional to the abundance, so that as a function of path-length the more abundant (99.5%) ${}^{16}O_2$ becomes shielded much earlier than ${}^{16}O^{17}O$ or ${}^{16}O^{18}O$. Thus further photodissociation of ${}^{16}O_2$ is suppressed while sufficient radiation at other frequencies results in preferential dissociation of ${}^{16}O^{17}O$ and ${}^{16}O^{18}O$. Recently, Thiemens and Heidenreich [11,12] reported equal enrichment of ${}^{17}O$ and ${}^{18}O$ in ozone produced by an electric discharge in oxygen. They explained their results by self-shielding of ${}^{16}O_2$ and suggested that this process may explain the anomalies in meteorites.

In the present paper we investigate the production of isotopic effects in oxygen due to self-shielding of photolysing radiation by the Schumann-Runge bands (SRB) of ${}^{16}O_2$. The model studied is the simple case of incoming radiation falling on a gaseous medium of uniform composition. We calculate the enhancement of ${}^{17}O$ and ${}^{18}O$ production upon photodissociation of O_2 for various column densities, examine its dependence on temperature and the presence of other molecules, and the issue of whether the products of photolysis can be trapped and thus preserve a peculiar isotopic composition.

The general problems discussed here are of fundamental importance in atmospheric chemistry and have received extensive attention in that field. This has been of most recent interest because of large unexplained isotopic shifts in atmospheric ozone [13]. There is an extensive and expanding literature in this field which we have attempted to follow and use in our analysis.

2. Self-shielding in O_2

Oxygen is photodissociated by UV radiation following the reaction:

$$O_2 + h\nu \rightarrow O + O \tag{R-1}$$

(R-*n* refers to reactions, E-*n* to equations, and A-*n* to equations developed in the Appendix.) The photodissociation rate for isotopic species i is given by:

$$-\frac{d[{}^{i}O_2]}{dt} = [{}^{i}O_2]J_i(z) \tag{E-1}$$

$J_i(z)$ is the photodissociation rate per molecule at optical depth z. We use ${}^{i}O_2$ for the three most abundant species of oxygen: ${}^{16}O_2$, ${}^{16}O^{17}O$, ${}^{16}O^{18}O$ with $i = 16$, 17, and 18 respectively. We use ${}^{16}O^{*}O$ to denote the latter two molecules. In the subsequent analysis we will assume the oxygen to be roughly of normal isotopic composition and ignore ${}^{17}O^{17}O$, ${}^{17}O^{18}O$ and ${}^{18}O^{18}O$.

The explicit expression for $J_i(z)$ is $J_i(z) = \int_{\nu_0}^{\infty}\phi(\nu)\sigma_i(\nu)I(\nu, z)\,d\nu$. Here the product $\phi(\nu)\sigma_i(\nu)$ is the macroscopic photodissociation cross section (quantum yield for dissociation times total photon absorption cross section) and ν_0 is the dissociation threshold wave number. $I(\nu, z)$ is the radiation flux at wave number ν and depth z, and is governed by the equation:

$$I(\nu, z) = I(\nu, 0)\exp\left[-\sum_j \sigma_j(\nu)\int_0^z n_j(z)\,dz\right] \tag{E-2}$$

Here $n_j(z)$ is the number density of species j at z and the result of the integral is the column density (N_j) of species j. The sum is over all species present (the three isotopic molecules of oxygen plus other absorbing species such as H_2O or ozone).

The absorption spectrum of oxygen is the result of transitions between molecular states of different energies. The energy of the molecule can be described as a sum of electronic, vibrational, rotational and translational terms. The energy difference between electronic states is of the order of tens of thousands cm^{-1} (see Fig. 1). The bound states vibrate with discrete vibrational energies separated by few hundreds cm^{-1}, and each of the vibrational states has many rotational levels separated by a few tens cm^{-1}. At room temperature, only the first vibrational state ($v'' = 0$) of the ${}^{3}\Sigma_g^-$ ground state and its rotational levels are populated. Transitions ($'$ = excited state, $''$ = ground state) may occur to any of the vibrational states of the excited ${}^{3}\Sigma_u^+$ and ${}^{3}\Sigma_u^-$ states but only to rota-

4

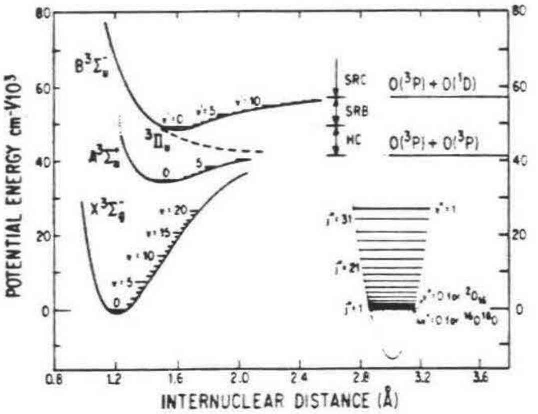

Fig. 1. Four potential curves and energy levels of O_2 (after [34]). Only three bound states of O_2: $^3\Sigma_g^-$, $^3\Sigma_u^+$, $^3\Sigma_u^-$ and one unbound state $^3\Pi_u$ are presented here. Vibrational states are numbered by their vibrational quantum number—v. Rotational levels of the $^{16}O_2$ ground state are shown in the insert in the lower right side. $^{16}O_2$ is symmetric and has only states with odd quantum number—j. $^{16}O^{17}O$ and $^{16}O^{18}O$ lack this symmetry and have twice as many states. Due to their heavier masses $^{16}O^{17}O$ and $^{16}O^{18}O$ vibrate and rotate at somewhat lower energies. Only the ground level for $^{16}O^{18}O$ is also shown. Photons of energy higher than ~41,000 cm^{-1} can excite O_2 from its ground state into the continuum of states above the dissociation limit of the $^3\Sigma_u^+$ state (the Herzberg continuum, HC) and dissociate it into two atoms in their ground state (^3P). Above 49,800 cm^{-1}, more probable transitions to the discrete states of bound $^3\Sigma_u^-$ state give rise to a line spectrum (the Schumann-Runge bands, SRB). Due to crossing into the $^3\Pi_u$ state the molecule then dissociates into two O(^{3}P) atoms. Energies above ~57,000 are higher than the dissociation limit of the $^3\Sigma_u^-$ state and the transitions are into another continuum—the Schumann-Runge continuum (SRC) where dissociation produces an O(^{3}P) atom and an excited O(^{1}D) atom.

tional levels with $j' = j'' \pm 1$. The resulting spectrum is groups of lines (bands); each consists of rotational lines (the band fine structure). Transitions to the continuum of states above the dissociation limit of the bound states lead to the continuous part of the O_2 absorption spectrum and to the dissociation of the molecule. The UV spectrum at wave numbers above the dissociation energy consists of the Herzberg continuum (HC), the Schumann-Runge bands (SRB) and the Schumann-Runge continuum (SRC). Transitions into the $^3\Sigma_u^-$ state (the SRB spectral region) lead to dissociation due to curve crossing between this state and the dissociative $^3\Pi_u$ state (see Fig. 1). The spacing between adjacent rotational lines is a few tens of cm^{-1} and the isotopic shifts of these spectral lines are also of the order of a few tens of cm^{-1}. As the width of these lines is about 1 cm^{-1} most of the $^{16}O^{17}O$ and $^{16}O^{18}O$ lines fall in the windows of the $^{16}O_2$ absorption spectrum, and each species is independently photolysed by radiation of different wave numbers. The attenuation of radiation is exponentially dependent on the column density $N_i(z)$. The photon flux in wave numbers absorbed by the $^{16}O_2$ lines is strongly attenuated, and $^{16}O_2$ is self-shielded from photodissociation. The column density of $^{16}O^{17}O$ and $^{16}O^{18}O$ is much lower, so that the flux at wave numbers absorbed by them is only weakly attenuated and their rate of dissociation is enhanced relative to $^{16}O_2$.

3. The calculations

To determine the self-shielding effect it is necessary to calculate the photodissociation rates J_{16}, J_{17} and J_{18}. J_i was evaluated following the general scheme of Cicerone and McCrumb [14]. However, we accounted for the fact that the cross section of $^{16}O^*O$ absorption lines is on the average only half that of $^{16}O_2$ and not as erroneously assumed in their paper [14]. We also used more recent spectral data for O_2 [15]. Just before the submission of our paper, Blake et al. [16] published the result of a detailed evaluation of the self-shielding effect for the earth's atmosphere. Their results are calculated for an atmospheric density and temperature profile. Our earlier estimates [17] and the results of their more detailed calculations are in good agreement. Because of this agreement, we still use the approximations used by us earlier.

We evaluate J_i for each spectral region separately so that $J_i^{\text{total}} = J_i^{HC} + J_i^{SRB} + J_i^{SRC}$. In the two continuous parts of the spectrum there are no resonances which can cause isotopic shifts. The integrals in these regions were carried out by dividing each continuum into intervals of 500–1000 cm^{-1} each. The absorption cross section and the quantum yield are those tabulated by Baulch et al. [18] for each of these intervals (we assumed $\phi = 1$

for the Herzberg continuum). When the effect of water was considered we used the data of Thompson et al. [19] for σ_{H_2O} in the SRB and SRC regions. We extrapolated these data to evaluate σ_{H_2O} in the HC region. In order to simplify the calculation we took the initial flux to be that of a black body of radius R at 5000 K and distance of $100R$. The total initial flux for each interval was evaluated using the Wien approximation of Planck's radiation law integrated over the wave number interval ν_1 to ν_2:

$$\int_{\nu_1}^{\nu_2} I(\nu, 0)\, \mathrm{d}\nu = 10^{-4} \frac{2\pi hc^2 \int_{\nu_1}^{\nu_2} \nu^3 \exp\left(\frac{hc\nu}{kT}\right) \mathrm{d}\nu}{hc(\nu_1 + \nu_2)/2}$$

where the factor of 10^{-4} is due to the distance $(100R)$ between the radiating body and the beginning of the column; h is Planck's constant; k is the Boltzmann constant; c is the speed of light. The contributions to the dissociation rate in the regions HC + SRC were then calculated by summing over the contributions of each interval:

$$\sigma_i\left(\frac{\nu_1 + \nu_2}{2}\right)\left\{\int_{\nu_1}^{\nu_2} I(\nu, 0)\, \mathrm{d}\nu\right\}$$

$$\exp\left[-\sum_j \sigma_j\left(\frac{\nu_1 + \nu_2}{2}\right) N_j(z)\right]$$

for the whole continuum.

The evaluation of the contribution of the SRB (J^{SRB}) to the dissociation rate is more involved as it contains the terms causing the isotopic effect. Large changes of σ in the vicinity of the resonance frequencies make it impossible to use the average values for σ [18]. Following Cicerone and McCrumb [14] we approximated the resonances in a band as a single square line with height equal to the average height of the absorption line and width equal to the sum of the widths of the lines at half maximum (see Fig. 2b for details). The cross section of the underlying continuum and of other absorbing molecules is averaged for each band. This approximation was checked by using these averaged values to calculate $\int_{\mathrm{band}} \sigma(\nu)\, \mathrm{d}\nu$. The results were in good agreement with the values of Yoshino et al. [15]. J^{SRB} for the $^{16}O_2$ species is then calculated by summing over the main bands, 1-0 to 12-0 (each band is referred to as v'-v''. In this case $v'' = 0$ and transitions are from the ground vibrational level of the ground electronic state). The total contribution of the SRB region to J_{16} is:

$$J_{16}^{\mathrm{SRB}}(z) = \sum_b \{\sigma_{16}(b)\Gamma(b) l_{16}(b) I(b, 0)$$

$$\times \exp - \left[\sigma_{16}(b) N_{16} + \sigma_{\mathrm{pc}}(N_{17} + N_{18}) + \sum_j \sigma_j N_j\right]$$

$$+ \sigma_{\mathrm{pc}}\left[\int_{\mathrm{band}} I(\nu, 0)\, \mathrm{d}\nu\right]$$

$$\times \exp - \left[\sigma_{\mathrm{pc}}(N_{16} + N_{17} + N_{18}) + \sum_j \sigma_j N_j\right]\Big\}$$

Here b identifies the bands; Γ is the average line width for the resonances in a band and l is the

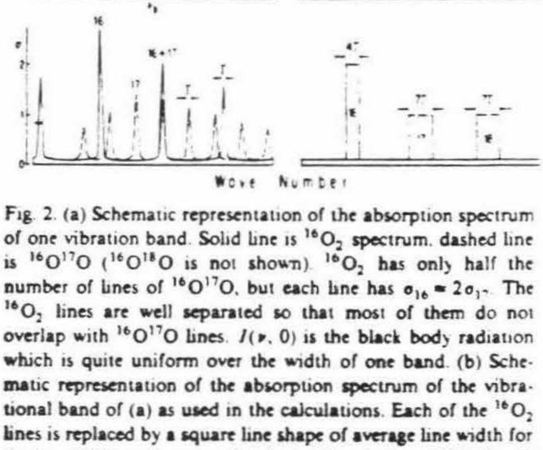

Fig. 2. (a) Schematic representation of the absorption spectrum of one vibration band. Solid line is $^{16}O_2$ spectrum, dashed line is $^{16}O^{17}O$ ($^{16}O^{18}O$ is not shown). $^{16}O_2$ has only half the number of lines of $^{16}O^{17}O$, but each line has $\sigma_{16} = 2\sigma_{17}$. The $^{16}O_2$ lines are well separated so that most of them do not overlap with $^{16}O^{17}O$ lines. $I(\nu, 0)$ is the black body radiation which is quite uniform over the width of one band. (b) Schematic representation of the absorption spectrum of the vibrational band of (a) as used in the calculations. Each of the $^{16}O_2$ lines is replaced by a square line shape of average line width for the band [40], and average height (σ) for the band ([15, fig. 6], where we included all lines below $N_{\max}$ of Yoshino et al.'s table 1). The continuous absorption cross section is averaged for each band using the average value for the lower envelop of the SRB spectrum of Yoshino et al. [15, fig. 5]. Also shown are the spectra of the other $^{16}O^{*}O$ species. In the case shown, one line of $^{16}O^{17}O$ overlaps with the $^{16}O_2$ line and is neglected. The black body photon flux $I(\nu, 0)$ (dashed line) was taken at the central wave number of the band. The solid line shows $I(\nu, z)$ at some depth z. Only those wave numbers which are absorbed by $^{16}O_2$ are substantially attenuated. At other wave numbers, including those absorbed by the less abundant $^{16}O^{*}O$, most of the initial flux is still available.

number of lines in a band; $\sigma_{16}(b)\Gamma(b)/l_{16}(b)$ is the integral of the resonances over the band as approximated by the area of the solid rectangle in Fig. 2b; σ_{pc} is the absorption cross section of the underlying pseudo-continuum. Our evaluation of σ_{pc} (see footnotes of Fig. 2b) is higher than that of Hudson and Mahle [20, fig. 1] but still much lower than σ_{pc} used by Cicerone and McCrumb [14]. $I(\nu, 0)$ is the initial flux of the black body radiation and $I(b, 0)$ is its value at the central wave number of band-b. J_{17}^{SRB} and J_{18}^{SRB} are calculated similarly using $\sigma_* = 1/2\sigma_{16}$ due to the doubled number of lines [21, p. 167]. Those $^{16}O^*O$ lines which overlap with $^{16}O_2$ lines are neglected due to the fast attenuation of radiation by $^{16}O_2$ at this wave number (Fig. 2b). The percent of these overlapping lines was evaluated using spectral data for bands 6-0 to 10-0 of the three isotopic species [22]. Nineteen percent of the $^{16}O^{17}O$ lines and 10% of the $^{16}O^{18}O$ lines are within one line width from the center of $^{16}O_2$ lines. As no data are available for other bands we assume a 15% overlap so that the number of lines is $l_{17} = l_{18} = 1.7 l_{16}$ at 300 K.

4. Results and discussion

Fig. 3 presents the results for a column of pure O_2 at 300 K. Self-shielding of $^{16}O_2$ begins at column densities of 10^{18} molecules/cm^2 where the optical depth for the more strongly absorbing bands reaches unity. Equal enhancement of $^{16}O^{17}O$ and $^{16}O^{18}O$ is predicted up to a column density of $\sim 10^{20}$ molecules/cm^2 where the column is opaque to radiation in the $^{16}O_2$ lines, but the optical depth for radiation in the spectral lines of the less abundant $^{16}O^{17}O$ and $^{16}O^{18}O$ is close to unity. As $^{16}O^{18}O$ is 5.5 times more abundant than $^{16}O^{17}O$, the effect on the two species separates at 10^{20} molecules/cm^2 when the $^{16}O^{18}O$ is better shielded than the $^{16}O^{17}O$.

The ratio of the photodissociation rate constants is presented in Fig. 4. This ratio is related to the enrichment β of the dissociated species relative to their original abundances by:

$$\beta_* = \frac{(^*O/^{16}O)_{\text{products}}}{(^*O/^{16}O)_{\text{reactants}}} - 1 = \frac{J_*}{J_{16}} - 1$$

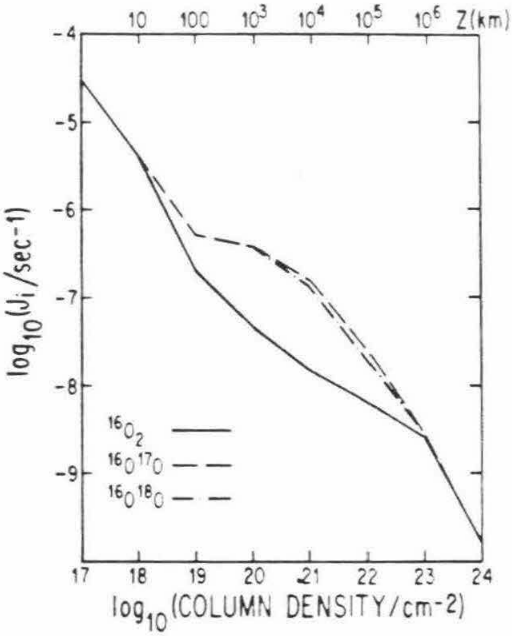

Fig. 3. The photodissociation rate constant, J, of $^{16}O_2$, $^{16}O^{17}O$ and $^{16}O^{18}O$ for various oxygen column densities. Self-shielding by $^{16}O_2$ occurs at column densities higher than 10^{18} molecules/cm^2. Column depth in km is given for O_2 density of 10^{12} molecules/cm^3.

As shown in Fig. 4, the maximum effect calculated is when $J_*/J_{16} = 11$. The actual result depends strongly upon the value of σ_{pc} (underlying the SRB). If this is large, the attenuation is sufficiently rapid as to remove the photolysing radiation that could cause an isotopic effect. Using the lower values of σ_{pc} of Hudson and Mahle [20] the maximum enrichment factor reaches a value of 40. Using the very high values of Cicerone and McCrumb [14] we obtained a value of only 2.5. In either case the isotopic effect due to self-shielding is much higher than common enrichment factors in chemical reactions at 300 K and would result in lines of slope 1 or higher on a three isotope plot. However, several factors exist which prevent an effect of that magnitude.

4.1. Other absorbing molecules

Water has a continuous spectrum in the SRB region with σ_{H_2O} similar to σ_{O_2}. The presence of

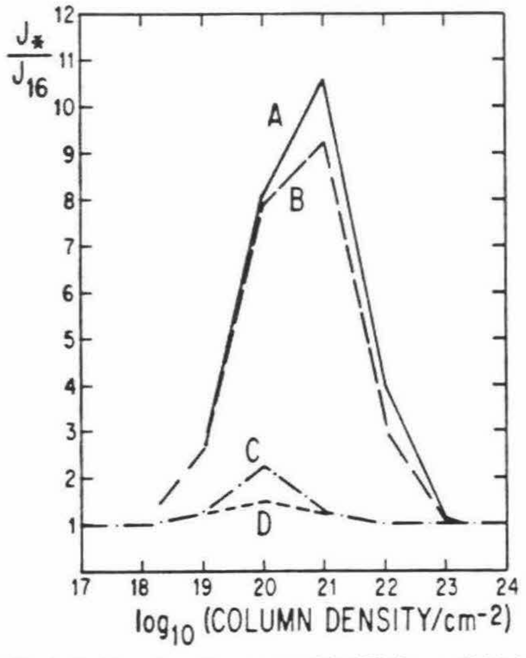

Fig. 4. J_*/J_{16}—the enhancement of the UV flux available for dissociation of $^{16}O^*O$ relative to $^{16}O_2$, for various column densities. (A) J_{17}/J_{16}, and (B) J_{18}/J_{16} both at 300 K and pure oxygen. The effect is equal at column densities lower than 10^{20} molecules/cm^2 and is larger for $^{16}O^{17}O$ at higher values due to its lower abundance. The effect dies at 10^{23} molecules/cm^2 when all bands are opaque. (C) J_*/J_{16} for a column of oxygen + water where $[H_2O] = [O_2]$. The maximum effect is only in $J_*/J_{16} = 2.3$ for both $^{16}O^{17}O$ and $^{16}O^{18}O$. (D) J_*/J_{16} for pure oxygen at 500 K. The maximum effect is 1.5 for the two species.

H_2O would thus diminish the effect of self-shielding as all wavelengths are shielded by the water absorption. Fig. 4 presents the results for equal concentrations of water and oxygen. If the H_2O concentration is 10 times that of O_2 then the maximum enrichment drops to only 0.02. Another interfering molecule is ozone, but at low densities its steady state concentration is too low and its effect is negligible. CO_2 and CH_4 have smaller cross section [23] and would have minimal effect at concentrations up to 10 times $[O_2]$. H_2 absorbs only at higher frequencies and would not effect the system. A few narrow absorption bands of CO (the Cameron bands) may disturb but not eliminate the self-shielding effect. H_2O is the main species that may efficiently suppress self-shielding of O_2 and a high $[O_2]/[H_2O]$ ratio is thus an essential condition for shielding.

4.2. Temperature

High temperatures would quench the self-shielding effect, mainly due to an increase in the population of higher vibrational and rotational energy levels. The Doppler broadening of the lines is of lesser importance as the natural line width is already broad because of the short predissociative lifetime (the time an excited molecule spends in the bound $^3\Sigma_u^-$ state before crossing to the unbound $^3\Pi_u$ state). The population ratio of $v'' = 0$, 1, 2 vibrational states is changed from $1 : 5.5 \times 10^{-4} : 3 \times 10^{-7}$ at 300 K, to $1 : 0.01 : 1.2 \times 10^{-4}$ at 500 K, and $1 : 0.1 : 0.01$ at 1000 K. This means that at 500 K $[^{16}O_2]_{(v''=1)}/[^{16}O^*O]_{(v''=0)} > 2.5$ for the 18 species and > 13 for the 17 species so that overlapping of $^{16}O^*O$ lines with $v'' = 1$ lines would result in rapid attenuation. Using the data of Hecht et al. [22] and Hudson and Carter [24] we found that ~ 25% of the $^{16}O^*O$ lines are within 1 cm^{-1} from $^{16}O_2$ $v'' = 1$ lines at 500 K. At 1000 K when $v'' = 2$ is also included, an additional 25% of the $^{16}O^*O$ lines overlap with $^{16}O_2$ $v'' = 2$ lines. The population of higher rotational levels also increases. At 300 K the population of the state with rotational quantum number $j = 31$ is 1% of the most populated level. At 500 K $j = 39$ reaches similar population levels and at 1000 K it is $j = 56$. The bands begin to overlap and $^{16}O^*O$ lines of one band may be shielded by $^{16}O_2$ lines of another band. The absorption cross section of the low j rotational lines decrease due to the more even population distribution and they are more strongly effected by the underlying pseudo-continuum. The pseudo-continuum itself increases due to better overlap between tails of the intensified lines of transitions from higher vibrational and rotational levels of the ground state. We used the analysis of Hudson and Mahle [20, fig. 1] who evaluated the contribution of the Herzberg continuum, and the overlap of the $v'' = 0$ and $v'' = 1$ lines to the underlying continuum in the SRB spectral region. At $T = 500$ K the population of $v'' = 1$ is 20 times larger than at $T = 300$ K. This affects the value of

σ_{pc} underlying bands 5-0 to 12-0 where the contribution of $v'' = 1$ is important. The lower bands are affected to a lesser extent. The enhancement factor for σ_{pc} of each band was calculated by adjusting the contribution of $v'' = 1$ in fig. 1 of Hudson and Mahle [20]. These factors were then used to correct σ_{pc} values used in our calculation for the effect of temperature. When the increase in the number of overlapping lines was also included, the final results are a maximum enrichment effect of only 1.6 at 500 K (Fig. 4), and no effect at 1000 K, where the population of $v'' = 1$ is 200 times larger than that at 300 K. In contrast, at lower temperatures σ_{pc} is smaller and an enhanced effect is expected ($J^{\bullet}/J^{16} \sim 40$ at 150 K was calculated by removing the contribution of the $v'' = 1$ to σ_{pc}).

4.3. *Isotope exchange reactions*

In the previous sections the necessary conditions for the enhanced production of $^{\bullet}\mathrm{O}$ were discussed. However, once formed, atomic oxygen may undergo rapid isotopic exchange with the molecular oxygen of the reservoir. (The appropriate rate equations are given in Appendix 1.)

$$^{16}\mathrm{O} + {}^{16}\mathrm{O}^{\bullet}\mathrm{O} \rightleftharpoons {}^{\bullet}\mathrm{O} + {}^{16}\mathrm{O}_2 \qquad \text{(R-2)}$$

The rate constant for this reaction in the forward direction was determined experimentally for $^{16}\mathrm{O}^{18}\mathrm{O}$: $k_{2f18} = 6.6 \times 10^{-12} \exp[(-554 \pm 200)/T]$ cm^3 molecule^{-1} s^{-1} [25]. This value is in good agreement with theoretical calculations [26].

If the exchange reaction reaches equilibrium then:

$$\frac{[^{\bullet}\mathrm{O}]}{[^{16}\mathrm{O}]} = \frac{[^{16}\mathrm{O}^{\bullet}\mathrm{O}]}{[^{16}\mathrm{O}_2]} \cdot \mathrm{K}_{\bullet}$$

where $K_{\bullet}$ is the equilibrium constant of (R-2). If the concentration of atomic oxygen is small so that the concentrations of the molecular species are not disturbed, then $[^{16}\mathrm{O}^{\bullet}\mathrm{O}]/[^{16}\mathrm{O}_2] = 2F_{\bullet}$ where $F_{\bullet}$ is the initial fractional abundance of $^{\bullet}\mathrm{O}$ in the O_2 before the reaction. Under these conditions the enrichment factor after the exchange reaction reaches equilibrium is:

$$\beta_{\bullet} = \frac{(^{\bullet}\mathrm{O}/^{16}\mathrm{O})_{\text{atomic oxygen}}}{\text{initial abun. in reservoir}} - 1$$

$$= \frac{2F_{\bullet}K_{\bullet}}{F_{\bullet}} - 1 = 2K_{\bullet} - 1$$

K_{18} was calculated for the 18-16 exchange [27]. We calculated K_{17} in a similar way:

$$K_{18} = 0.516 \exp(-32/T)$$

$$K_{17} = 0.508 \exp(-16/T)$$

The corresponding equilibrium β values at 300 K are $\beta_{17} = -0.037$, $\beta_{18} = -0.073$, and at 116 K are $\beta_{17} = -0.115$, $\beta_{18} = -0.217$. These results indicate mass dependent depletion of the heavy isotopes with respect to $^{16}\mathrm{O}$ if the exchange reaction can reach equilibrium and thus the exchange reaction would completely suppress the effects sought.

To preserve the self-shielding effect the atomic oxygen must therefore be removed faster than the rate of exchange. The trapping of atomic oxygen is schematically written as:

$$\mathrm{O} + \mathrm{A} \rightarrow \text{products} \qquad \text{(R-3)}$$

The rate of trapping $k_3[\mathrm{A}][^{\bullet}\mathrm{O}]$ must be faster than the rate of exchange $k_2[\mathrm{O}_2][^{\bullet}\mathrm{O}]$, or:

$$k_3[\mathrm{A}] > k_2[\mathrm{O}_2] \qquad \text{(E-3)}$$

Detailed calculations are given in Appendix 1 and the results are presented in Fig. 5. They show that a somewhat weaker condition is sufficient if the self-shielding effect is large. As can be seen in equation (A-10) of Appendix 1, the enrichment factor of $^{\bullet}\mathrm{O}$ in the trapped product depends on the relative importance of two terms:

$$\beta_{\bullet} \approx \frac{(R_{J\bullet} - 1)R_k}{1 + R_k} + \frac{2K_{\bullet} - 1}{1 + R_k} \qquad \text{(A-10)}$$

where $R_{J\bullet} = J_{\bullet}/J_{16}$ and $R_k = k_3[\mathrm{A}]/k_{2b}[^{16}\mathrm{O}_2]$. k_{2b} is the rate of (R-2) in the backward direction and can be calculated as $k_{2b} = k_{2f18}/K_{18}$. The first term must be the dominant one to give $\beta_{17}/\beta_{18} \approx 1$ (for $J_{17} = J_{18}$). At 300 K, $(2K_{\bullet} - 1)/(1 + R_k) \leqslant 0.073$ so that if $R_{J\bullet} = 10$, trapping can be two orders of magnitude slower than exchange and still preserve the isotopic effect (solid line in Fig. 5).

We have examined a few possible reactions where O can be trapped directly, or other species may be formed and trapped. Hydrogen is the most abundant molecule in the solar nebula and could trap O to form $\mathrm{H_2O}$. The first step of the mechanism is [28]:

$$H_2 + O(^3P) \rightarrow OH + H$$

$$k_4 = 3.14 \times 10^{-11} \exp(-4570/T) \text{ cm}^3 \text{ molecule}^{-1} \text{ s}^{-1} \qquad \text{(R-4)}$$

However, due to its high activation energy this reaction is too slow to compete with the exchange reaction. Under nebular pressures, water condensation occurs at $T < 200$ K so that even for $[H_2] = 10^4[O_2]$, $R_k(200\ \text{K}) = k_4[H_2]/k_{2b}[O_2] < 10^{-4}$, and trapping is inefficient. However, at higher temperatures or higher $[H_2]/[O_2]$ ratios, trapping by H_2 may be efficient. Such high $[H_2]/[O_2]$ ratios (far in excess of the solar H/O ratio) may in fact be expected if most oxygen is present as CO or as condensed water and very little is present as O_2.

Metal atoms can react with O to form oxides which have a better chance to be separated from the reservoir by condensation compared with low temperature condensibles. The trapping reaction is a three body reaction:

$$M + O + X \rightarrow MO + X \qquad \text{(R-5)}$$

where M is the metal atom and X is any third body needed to remove the excess energy. The necessary condition for efficient trapping by this reaction is:

$$k_5[X][M]/k_{2b}[^{16}O_2] \geq 0.01 \qquad \text{(E-4)}$$

The rate constants for sodium, magnesium, and iron are 10^{-33}, 10^{-32} and 10^{-32} cm^6 molecule^{-2} s^{-1}, respectively [29]. Those rates are too slow by 2-3 orders of magnitude even for a total density of $[X] = 10^{16}$ molecules/cm^3 and $[M] = [O_2]$. Reactions of metal ions with atomic oxygen are two orders of magnitude faster, but are still too slow for efficient trapping under these conditions.

Dust particles were also examined as a possible trap. Assuming spherical particles with a geometrical cross section for trapping, the rate of trapping per O atom is $k_3[A] = \sigma V n$ where $\sigma = \pi r^2$ is the cross section and V is the molecular velocity; $n = 3m/4\pi r^3 \rho$ is the number density of particles, m is the total mass of the dust per unit volume and ρ the density of a particle. The condition $k_3[A]/k_{2b}[O_2] > 0.01$ is satisfied for:

$$r < \frac{300V}{4\rho k_{2b}} \cdot \frac{m}{[O_2]}$$

Assuming all oxygen in excess of that present as CO or oxides is only present as O_2, $m/[O_2]$ can be estimated using the tabulation of Cameron [30]. The particle radius must be smaller than 1 μm. From geometrical and kinetic considerations it appears that small dust grains could thus reasonably serve as traps if the sticking efficiency is high. However, micron or sub-micron size particles absorb and scatter light with total cross section for extinction a few times their geometrical cross section [31]. Effective shielding is possible only when light extinction by the dust is weaker than light absorption by the SRB: $\sigma_{dust} n_{dust} < \sigma_{O_2}(\text{SRB})[O_2]$. Assuming a uniform mixture of gas and dust and the same cross section for light extinction and trapping of O by dust we can estimate the efficiency of trapping $R_k = \sigma_{dust} V n_{dust}/k_{2b}[O_2]$ where V is the molecular velocity. Even for $R_k =$

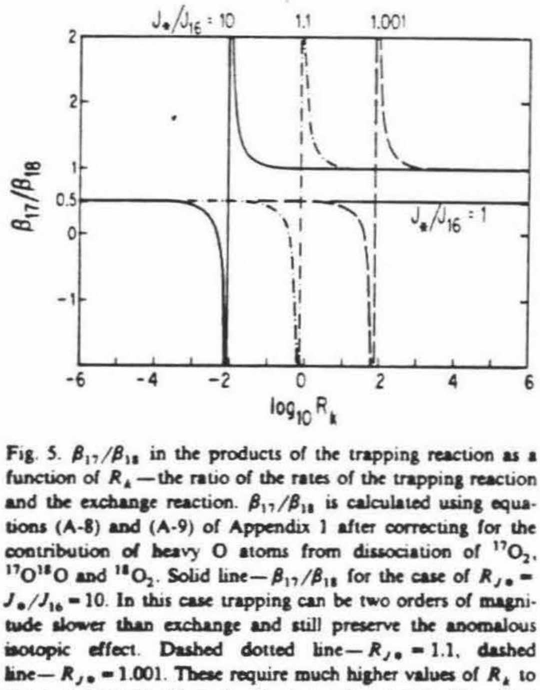

Fig. 5. β_{17}/β_{18} in the products of the trapping reaction as a function of R_k—the ratio of the rates of the trapping reaction and the exchange reaction. β_{17}/β_{18} is calculated using equations (A-8) and (A-9) of Appendix 1 after correcting for the contribution of heavy O atoms from dissociation of $^{17}O_2$, $^{17}O^{18}O$ and $^{18}O_2$. Solid line—β_{17}/β_{18} for the case of $R_{J*} = J_*/J_{16} = 10$. In this case trapping can be two orders of magnitude slower than exchange and still preserve the anomalous isotopic effect. Dashed dotted line—$R_{J*} = 1.1$, dashed line—$R_{J*} = 1.001$. These require much higher values of R_k to preserve isotopic effects in the trapped materials. No effect occurs for $R_{J*} = 1$, and $\beta_{17}/\beta_{18} = 0.5$.

0.01, we need $\sigma_{\text{dust}} n_{\text{dust}}/[O_2] = 10^{-18}$. Under this condition the optical depth for the dust reaches unity at $[O_2]_z = 10^{18}$. At this depth most of the SRB are only weakly absorbing. Further, self-shielding is strongly quenched due to the absorption of light by the dust. Under these conditions we calculated $R_{J*} < 1.01$ and $R_k = 0.01$ is not efficient enough for preserving the effect (see Fig. 5). Trapping of O atoms by dust particles is thus inefficient under conditions which allow for self-shielding to occur. However, if dust is not evenly distributed, but rather it is concentrated locally in a region where self-shielding can occur, then efficient trapping may be achieved without quenching of the self-shielding effect. This may be in local dust cloud imbedded in a larger dust free gas mass, or the boundary between gas an dust that has settled to the midplane of the solar nebular disk.

Even if a trapping species reacted fast enough to compete with the exchange reaction, other difficulties might still exist. The trapping species may react directly with molecular oxygen:

$$A + O_2 \rightarrow AO + O \qquad (R\text{-}6)$$

$$A + O_2 + X \rightarrow AO_2 + X \qquad (R\text{-}6a)$$

The products AO and AO_2 will be essentially oxygen of normal isotopic composition which will dilute the anomalous component formed by trapping of O produced through photodissociation. Thus the additional condition required is:

$$k_6[A] < J \qquad (E\text{-}5)$$

or:

$$k_{6a}[X][A] < J \qquad (E\text{-}5a)$$

Other interfering reactions may be the exchange of AO with O and O_2, photodissociation of AO and fast reactions of reactive by-products such as the H formed in (R-4). Fast condensation and separation of the product AO is thus another essential condition for efficient trapping.

5. Implications for experimental observations of isotopically anomalous ozone

The formation of ozone is another way of trapping O. The reaction is a three-body reaction:

$$O + O_2 + X \rightarrow O_3 + X \qquad (R\text{-}7)$$

where X is the third body needed to remove the excess energy, and may be any of the species present. In this case k_3, the rate constant for trapping by reaction (R-3), should be replaced by $k_7[X]$ so that the ratio of the rate of trapping to the rate of exchange is $R_k = k_7[X]/k_{2b}$ and is proportional to pressure. In pure oxygen the matrix is O_2 itself so $R_k = k_7[O_2]/k_{2b}$. The rate constant k_7 varies over a small range for different gases as the matrix. For O_2, $k_7 = 2.15 \times 10^{-34} \exp(345/T)$ [32]. If $2K_* < 1$, the singularity in β_{17}/β_{18} is at $\beta_{18} = 0$ or $R_k(J_{18}/J_{16} - 1) \approx -(2K_{18} - 1) = 0.073$ (300 K) and 0.217 (116 K). This defines the minimum condition for obtaining the anomalous pattern under discussion. This would correspond to about 1 atmosphere pressure at 300 K and 10 mm at 116 K for $J_{18}/J_{16} \sim 10$.

Both Sander et al. [10] and Thiemens and Heidenreich [11,12] sampled the oxygen atoms they produced by forming and freezing ozone. In the experiment of Sander et al. [10] efficient self-shielding of $^{16}O_2$ is expected. The broad laser source they used emitted light that is absorbed by part of the 4-0 band of the SRB where the contribution from continuous absorption is small. In this experiment a laser beam was passed through a cavity where wave lengths absorbed by $^{16}O_2$ were partially filtered out before entering an isolated absorption cell. The O_3 produced in this cell was then frozen out. The optical depth at the end of the cell (100 cm) was 12–75 for $^{16}O_2$ but lower than 0.15 for $^{16}O^{17}O$ and $^{16}O^{18}O$ so that large J_*/J_{16} is expected. Under their experimental conditions ($T = 300$ K, $P = 10$ atm) $R_k = 0.08$ so that preservation of the effect is in agreement with our predictions.

In the experiment of Thiemens and Heidenreich, O_2 was dissociated by discharge and ozone was frozen out. Anomalous isotopic effects were produced in their experiments at pressures of 6–158 mm [11,12,33].

It is clear that self-shielding of photolysing radiation cannot explain this set of experiments. The light emission in the required wavelength is extremely weak as most of the molecules excited to appropriate energies undergo dissociation and do not emit in the SRB. Anomalous isotopic effects were produced at 6 mm where the column density of their 1.7 cm diameter cell is lower than 10^{18} molecules/cm^2 and no self-shielding effect from photodissociation is expected (see Fig. 4).

However, the kinetic consideration presented in the Appendix 1 and Fig. 5 may be applied to examine the pressure dependence of that system. If the source of the special effect is in the dissociation of O_2 then the analysis given here for the nature of the effect still holds, but J_i is not simply the photodissociation rate constant but represents the rate of an undefined general dissociation mechanism which may in fact be a function of pressure. The results for the ozone experiment as a function of $[O_2]$ should then still follow the relationship of equation (A-10). Because O_3 is the trapped species whose isotopic composition is experimentally measured, the expression for β_* for O_3 should be given by substituting β'_* for β_* where $\beta'_*({}^*O^{16}O^{16}O) \approx 1/3\beta_*({}^*O)$, and:

$$\beta'_{17}/\beta'_{18} \approx \frac{(\hat{R}_{J17}-1)k_7[O_2]/k_2 + 2K_{17} - 1}{(\hat{R}_{J18}-1)k_7[O_2]/k_2 + 2K_{18} - 1} \quad \text{(E-6)}$$

Here $\hat{R}_{Ji}$ is the relative dissociation rate for an unspecified process ($X + O_2 \rightarrow 2O + Y$). These relationships predict that β'_* should approach $(2K_* - 1)/3$ at low pressures, and $(\hat{R}_{J*} - 1)/3$ at high pressures. If both $\hat{R}_{J*} - 1$ and $2K_* - 1$ are of the same sign, β'_{17}/β'_{18} should be a smooth function of pressure. However, if they have different signs, then β'_{17}/β'_{18} as a function of pressure must go through a singularity as β'_{18} changes sign. This can yield what are apparently irregular experimental results. The sequence with which β'_{17} and β'_{18} cross zero determines whether β'_{17}/β'_{18} approaches the singularity through positive or negative values. The behavior for $\beta'_{17} \rightarrow 0$ before $\beta'_{18} \rightarrow 0$ is shown in Fig. 5. The case where β'_{18} crosses zero first while $\beta'_{17} < 0$ is more complex. $\beta'_{18} = 0$ implies that $R_k = -(2K_{18} - 1)/(\hat{R}_{J18} - 1)$ so that $(\hat{R}_{J17} - 1)/(\hat{R}_{J18} - 1) < (2K_{17} - 1)/(2K_{18} - 1) \sim 0.5$ at the zero crossing. But at high pressure $\beta'_{17}/\beta'_{18} = (\hat{R}_{J17} - 1)/(\hat{R}_{J18} - 1) \approx 1$. This requires either that $\hat{R}_{J17}/\hat{R}_{J18}$ vary with pressure or that a third mechanism capable of producing positive β'_* values with $\beta'_{17}/\beta'_{18} < 0.53$ operates at medium pressure and cancels to some extent the effect of the isotopic exchange.

Through the courtesy of M. Thiemens and W. Sisk we have been provided with a report of unpublished data as a function of pressure obtained in a flow system at a given electrode configuration. At low pressure (0.5–3.5 mm) β'_* is negative and with minimum values of $\beta'_{17} = -0.038$, $\beta'_{18} = -0.072$ at 1 mm. The fractionation is mass dependent with $\beta'_{17}/\beta'_{18} \approx 0.55$. At high pressure (5–150 mm) β'_* is positive. It reaches a maximum at 43 mm where $\beta'_{17} = 0.066$, $\beta'_{18} = 0.072$. β'_{17}/β'_{18} grows constantly to values of 0.94–1. At 3.5–5 mm both β'_{17} and β'_{18} cross zero and β'_{17}/β'_{18} goes through a singularity at 4.3 mm where values between 1.1 and 0.2 were measured. For this set of experiments, β'_{18} crosses zero before β'_{17}. However, the sequence at which β'_{17} and β'_{18} cross zero is reversed for different electrode configurations (Thiemens, personal communication; [33]). The general pattern of negative β'_* with $\beta'_{17}/\beta'_{18} \approx 0.5$ at low pressure, and positive β'_* with $\beta'_{17}/\beta'_{18} \rightarrow 1$ at high pressure persists in all experiments.

These patterns may be explained by our model. The nature of the process responsible for the anomalous isotopic effect is still unclear to us. However, if it occurs upon electrodissociation of O_2:

$$^{16}O'O + e^- \rightarrow O + {}'O + e^- \quad \hat{J}_i \qquad \text{(R-1a)}$$

so that $\hat{R}_{J17} \approx \hat{R}_{J18} > 1$, then the general pattern of the pressure dependence, with β'_{17} crossing zero first is reproduced. Electron density is quenched at high pressure (> 43 mm) resulting in lower β'_* values without affecting the β'_{17}/β'_{18} values which keep approaching the high pressure value of $(\hat{R}_{J17} - 1)/(\hat{R}_{J18} - 1) \approx 1$. The case where β'_{18} crosses zero before β'_{17} cannot be explained by this simple scheme, unless $\hat{R}_{J*}$ and $\hat{R}_{J17}/\hat{R}_{J18}$ values change drastically with pressure.

An additional step, cf. the trapping reaction:

$$O + O_2^- \rightarrow O_3 + e^- \qquad \text{(R-8)}$$

seems to be a more plausible explanation.

At low pressure the two trapping reactions (R-7, R-8) cannot compete with the exchange reaction. At the cross-over (R-8) is efficient, and if it imposes $\beta'_{17}/\beta'_{18} < 0.53$ and $\beta'_* > |2K_* - 1|$, then β'_{18} crosses the zero first. $\beta'_* > 0$ is to be expected as electron attachment to the heavier isotopic species is more efficient [34]. It seems unlikely that (R-8) itself is the source of the non-mass-dependent effect, as at high pressure (R-7) is more efficient and should prevent β'_{17}/β'_{18} from approaching unity.

Thus it appears that the phenomenological characteristics of these experiments are understood; however, the actual mechanism for preferential dissociation of $^{16}O^*O$ over $^{16}O_2$ is not clear to us. We believe that charged particles and the electron density play an important role. Self-shielding of electrons with energy of 8–13 eV may be possible [35, fig. 75], but the effect, if it exists, is probably small. The various isotopic species may have different rates for the relaxation of O_2^- into the ground state of O_2 due to a fortuitous resonance between vibrational energy levels of the two states [35, pp. 469]. It is also possible that the rarer $^{16}O^*O$ molecules, when excited into high vibrational levels, do not relax as easily through collisions with the abundant $^{16}O_2$ [36]. The source of the non-mass dependent effect in the discharge experiments still remains a matter of both theoretical and possibly practical importance.

6. Conclusions

Self-shielding of UV radiation during photodissociation of $^{16}O_2$ is, in principle, capable of producing in nature a highly selective isotopic effect which is not proportional to the mass difference between the isotopes. However, many difficulties arise in applying this process to the explanation of oxygen anomalies observed in meoteorites. First it is not at all clear that O_2 is stable (or even metastable) under nebular conditions. Some workers have suggested that O_2 rather than H_2O is the main oxygen-bearing species in a system of O and H at low temperatures (~ 100 K) and a strong radiation field [37]. It is not evident that this result is valid when other elements such as C are present in solar abundance. Nonetheless, spectral and kinetic data available for O_2 enable one to examine the basic problems associated with the production and isolation of anomalous oxygen by self-shielding.

We have carried out an analysis of the isotopic shifts in O resulting from photodissociation of O_2 and obtained quantitative results of the ^{16}O depletion in this species. In this process the remaining O_2 is correspondingly enriched in ^{16}O. Low temperatures ($T < 500$ K) and low relative concentration of water ($[H_2O]/[O_2] < 1$ for any temperature) are essential conditions for effective self-shielding. If these conditions are met then it is also necessary to separate the anomalous O which is produced from the gas reservoir in order to preserve the isotopic shifts. This presents a major difficulty due to the competition between isotopic exchange reactions (which eliminate the effects) and trapping of the peculiar species. If oxygen is present at solar abundance and O_2 is the main oxygen carrying species the isotopic exchange reaction (R-2) is very efficient. Under these conditions trapping by metal atoms, hydrogen or the O_2 itself cannot compete with the exchange reaction at pressures lower than 10^{-3} atm. While trapping on dust grains may be efficient, light extinction by the dust is likely to quench the self-shielding effect in a uniform medium.

However, if, as may be expected, oxygen is carried by other species such as CO or condensed water, or if in some region of the nebula the abundance of oxygen is much lower than its bulk solar value, then the O_2 concentration is lower and isotopic exchange is less efficient. If this is achieved while the column density is still high enough and $[H_2O]/[O_2]$ low enough to enable effective self-shielding, than an anomalous isotopic pattern may be expected in the trapped product. The same may be true for trapping by dust grain distributed in an appropriate way so as to trap efficiently without quenching the self-shielding effect.

Finally, the anomalous material in meteorites shows ^{16}O enrichment whereas the products of photodissociation are depleted in ^{16}O. Thus a two-stage process is needed where the atomic oxygen produced by the photodissociation is trapped, condensed and removed to leave behind a reservoir depleted in ^{17}O and ^{18}O and relatively enriched in ^{16}O. This requires the removal of a large fraction of the anomalous O, and if the O_2

concentration is lower than its bulk solar value, cycling of large quantities of nebular gases is also needed.

Taking all of these considerations into account we believe that self-shielding of photolysing radiation by O_2 is not a satisfactory explanation for the oxygen anomalies in meteorites. However, other photochemical processes as well as self-shielding in other oxygen-bearing molecules should be considered as possible explanations for the oxygen anomalies in meteorites, and deserve further experimental as well as theoretical studies. The CO molecule seems to be a suitable candidate for such processes.

Self-shielding in CO was suggested as the source of large isotopic fractionation in molecular clouds [38]. The isotopic exchange reaction of CO is three orders of magnitude slower than that of O_2 (at 300 K [25]) and even slower at lower temperatures, so trapping may compete more successfully with isotopic exchange. This mechanism would imply correlated isotopic effects in both oxygen and carbon. Another process which may be important is vibrational relaxation following excitation by discharge or a strong radiation source [36]. The various isotopic species of CO have different vibrational and rotational energy structure. Following excitation into high vibrational levels the different isotopic species will relax at different rates. If dissociation of the excited CO molecule competes with relaxation, the final result is different dissociation rates for the different isotopic species which do not necessarily correlate with their mass difference. The large fractionation factors reported for such processes [6] may lead to formation of nearly pure ^{16}O reservoirs.

Stimulated by the work of Thiemens and Heidenreich [11,12] we carried out an extensive analysis of the isotopic shifts in O_3 resulting from dissociation of O_2 and competition between formation of O_3 and isotopic exchange reaction. The results of the self-shielding experiment of Sander et al. [10] are in agreement with the prediction of the kinetic model presented. In the case of the discharge experiments of Thiemens and Heidenreich [11,12], it was shown that self-shielding cannot be the source of the unique isotopic effects. However, the pressure dependence of the system is well explained by our simple kinetic model. Anomalous isotopic shifts are produced before or during the dissociation of O_2. At low pressure they are obliterated by the fast isotopic exchange (reaction (R-2)). At high pressure O is trapped by O_2 and a third body to form ozone (R-7). Experiments where β'_{18} crosses zero at lower pressures than β'_{17} must indicate the existence of a fourth step effective at medium pressure possibly the ozone-forming reaction of O and O_2^- (R-8). The enrichment factor observed in Thiemens' experiments seems to vary with pressure and electrode configuration and may be the sum result of a few processes operating at the dissociation stage.

While the general behavior of the system, following dissociation, appears to be understood, the fundamental question still remains as to the causal mechanism of the anomalous isotopic effect. The analysis presented here may ultimately have applicability to nebular conditions if a plausible isotopically selective dissociation and efficient trapping mechanism can be found.

Acknowledgements

We would like to thank Yuk Yung both for his scholarly criticisms and stimulating suggestion regarding charged particle reactions. Mark Allen has provided cogent criticism and useful advice. Many thanks to Steven Koonin, Onno Van Roosmalen, William Langer and Eric Herbst for discussing molecular physics with us and to Dave Stevenson, Mark Thiemens and an anonymous reviewer for their suggestions. Mark Thiemens has been generous in sharing his data and ideas from the exciting discharge experiments.

A short summary of this work was presented at the Lunar and Planetary Science Conference XV [17]. This work was supported by NSF PHY-8215500 and NASA NAG 9-43.

Appendix 1—Derivation of expression for $\delta^{16}O$ and $\delta^{18}O$

Assuming only one trapping reaction and denoting each species by its mass number, the kinetic system that has to be solved is described by:

$$^{16}O_2 + h\nu \rightarrow {}^{16}O + {}^{16}O \qquad J_{16} \tag{R-1a}$$

$$^{16}O^{17}O + h\nu \rightarrow {}^{16}O + {}^{17}O \qquad J_{17} \tag{R-1b}$$

$$^{16}O^{18}O + h\nu \rightarrow {}^{16}O + {}^{18}O \qquad J_{18} \tag{R-1c}$$

$$^{17}O + {}^{16}O_2 \rightarrow {}^{16}O + {}^{16}O^{17}O \qquad k_{2b17} \tag{R-2a}$$

$$^{18}O + {}^{16}O_2 \rightarrow {}^{16}O + {}^{16}O^{18}O \qquad k_{2b18} \tag{R-2b}$$

$$^{16}O + {}^{16}O^{17}O \rightarrow {}^{17}O + {}^{16}O_2 \qquad k_{2f17} \tag{R-2c}$$

$$^{16}O + {}^{16}O^{18}O \rightarrow {}^{18}O + {}^{16}O_2 \qquad k_{2f18} \tag{R-2d}$$

$$^{16}O + A \rightarrow \text{products } A^{16}O \qquad k_3 \tag{R-3a}$$

$$^{17}O + A \rightarrow \text{products } A^{17}O \qquad k_3 \tag{R-3b}$$

$$^{18}O + A \rightarrow \text{products } A^{18}O \qquad k_3 \tag{R-3c}$$

where we neglected isotopic exchange between $^{16}O^{17}O$ and $^{16}O^{18}O$ and the presence of $^{17}O^{18}O$, $^{17}O_2$, and $^{18}O_2$. We assume $k_{2b17} = k_{2b18} = k_{2b}$, but $k_{2f17} \neq k_{2f18}$ due to the difference in the vibrational ground level energy of $^{16}O^{17}O$ and $^{16}O^{18}O$ so that $k_{2f*}/k_{2b} = K_*$. The rates of formation for the atomic species are:

$$\frac{d[^{17}O]}{dt} = J_{17}[^{16}O^{17}O] + k_{2f17}[^{16}O^{17}O][^{16}O] - k_{2b}[^{16}O_2][^{17}O] - k_3[A][^{17}O] \tag{A-1}$$

$$\frac{d[^{18}O]}{dt} = J_{18}[^{16}O^{18}O] + K_{2f18}[^{16}O^{18}O][^{16}O] - k_{2b}[^{16}O_2][^{18}O] - k_3[A][^{18}O] \tag{A-2}$$

$$\begin{aligned}\frac{d[^{16}O]}{dt} = {} & 2J_{16}[^{16}O_2] + J_{17}[^{16}O^{17}O] + J_{18}[^{16}O^{18}O] \\ & + k_{2b}[^{16}O_2][^{17}O] + k_{2b}[^{16}O_2][^{18}O] \\ & - k_{2f17}[^{16}O^{17}O][^{16}O] - k_{2b18}[^{16}O^{18}O][^{16}O] \\ & - k_3[A][^{16}O]\end{aligned} \tag{A-3}$$

assuming a local steady state for the atomic species ($d[^{*}O]/dt = 0$) we can solve for:

$$[^{17}O] = \frac{J_{17}[^{16}O^{17}O] + k_{2f17}[^{16}O^{17}O][^{16}O]}{k_{2b}[^{16}O_2] + k_3[A]} \tag{A-4}$$

Let the ratios of $^{17}O/^{16}O$ and $^{18}O/^{16}O$ in the parcel of O_2 gas be F_{17} and $F_{18}(F_*)$ respectively. We assume that the reaction has proceeded to only a small extent so that $[^{16}O^{17}O]/[^{16}O_2] =$ $([^{16}O^{17}O]/[^{16}O_2])_0 = 2F_{17}$ and $[^{16}O^{18}O]/[^{16}O_2] = ([^{16}O^{17}O]/[^{16}O_2])_0 = 2F_{18}$. Then defining the ratios of the rates as:

$$K_* \equiv \frac{k_{2f*}}{k_{2b}}, \quad R_{J*} \equiv J_*/J_{16}, \quad R_A \equiv \frac{k_3[A]}{k_{2b}[^{16}O_2]}$$

We obtain:

$$[^{17}O] = 2F_{17}\frac{J_{17}/k_{2b} + K_{17}[^{16}O]}{1 + R_A} \tag{A-4b}$$

Similarly:

$$[^{18}O] = 2F_{18}\frac{J_{18}/k_{2b} + K_{18}[^{16}O]}{1 + R_A} \tag{A-5}$$

$$[^{16}O] = \left[(2J_{16} + 2F_{17}J_{17} + 2F_{18}J_{18})/k_{2b} + [^{17}O] + [^{18}O]\right]/[2F_{17}K_{17} + 2F_{18}K_{18} + R_A] \tag{A-6}$$

Substituting (A-4b) and (A-5) into (A-6) we can solve for the final expression for $[^{16}O]$:

$$[^{16}O] = \frac{2J_{16}(1 + R_A) + 2(F_{17}J_{17} + F_{18}J_{18})(2 + R_A)}{k_{2b}R_A(1 + 2F_{17}K_{17} + 2F_{18}K_{18} + R_A)} \tag{A-7}$$

This can now be used to find $[^{17}O]$ and $[^{18}O]$ and the enrichment factors:

$$\beta_* \equiv \left(\frac{[^{*}O]/[^{16}O]}{F_*} - 1\right)$$

$$\begin{aligned}\beta_{17} = {} & [R_{J17}R_A(1 + 2F_{17}K_{17} + 2F_{18}K_{18} + R_A)] \\ & /\left[(1 + R_A)^2 + (1 + R_A)(2 + R_A) \right. \\ & \left. \times (F_{17}R_{J17} + F_{18}R_{J18})\right] + [2K_{17}]/[1 + R_A] - 1\end{aligned} \tag{A-8}$$

$$\begin{aligned}\beta_{18} = {} & [R_{J18}R_A(1 + 2F_{17}K_{17} + 2F_{18}K_{18} + R_A)] \\ & /\left[(1 + R_A)^2 + (1 + R_A)(2 + R_A) \right. \\ & \left. \times (F_{17}R_{J17} + F_{18}R_{J18})\right] + [2K_{18}]/[1 + R_A] - 1\end{aligned} \tag{A-9}$$

For the problem under consideration $K_{17} \approx K_{18} \approx 0.5$, and F_{17}, F_{18} are smaller than 2×10^{-3} and $R_{J*} < 11$. Then for $R_{J*} > 1.002$, (A-8) and (A-9)

can be simplified to give:

$$\beta_* \approx \frac{R_{J*}R_k}{1+R_k} + \frac{2K_*}{1+R_k} - 1 = \frac{(R_{J*}-1)R_k}{1+R_k} + \frac{2K_*-1}{1+R_k} \tag{A-10}$$

When no shielding occurs $R_{J17} = R_{J18} = 1$, or when trapping is inefficient ($R_k \ll 1$) $\beta_* \approx (2K_* - 1)/(1 + R_k)$ and the effect is mass dependent. When $(R_{J*} - 1)R_k > 2K_* - 1$, $\beta_{17}/\beta_{18} \approx (R_{J17} - 1)/(R_{J18} - 1)$ so that for $R_{J17} \approx R_{J18}$ the non-mass-dependent effect is preserved and $\beta_{17}/\beta_{18} \approx 1$. The time scale τ for $[{}^*\mathrm{O}]$ to reach a quasi-steady state is $\tau \sim 1/(J_i + k_3[\mathrm{A}])$. For $R_{J*} \sim 11$, modestly efficient trapping relative to exchange requires that $R_k \equiv k_3[\mathrm{A}]/k_b[{}^{16}\mathrm{O}_2] \geq 10^{-2}$. At 300 K $k_{2b} = 10^{-12}$ cm^3 molecule^{-1} s^{-1}, then assuming $[{}^{16}\mathrm{O}_2] = 10^{12}$ molecule/cm^3 we get $k_3[\mathrm{A}] > 10^{-2}$. J_{16} is of the order of 10^{-6} to 10^{-8} (Fig. 3) so $\tau < 100$ seconds. This time is short compared with $1/J_{16} \sim 10^6$ to 10^8 seconds for the O_2 to be dissociated, so the quasi-steady state approximation is justified.

References

1 R.N. Clayton, L. Grossman and T.K. Mayeda, Component of primitive nuclear composition in carbonaceous meteorites, Science 182, 485–488, 1973.

2 G.J. Wasserburg, D.A. Papanastassiou and T. Lee, Isotopic heterogeneities in the solar system, in: Early Solar System Processes and the Present Solar System, pp. 144–191, Soc. Italiana di Fisica, Bologna, 1980.

3 F. Begemann, Isotopic anomalies in meteorites, Rep. Progr. Phys. 43(4), 1309–1356, 1980.

4 G. Arrhenius, J.L. McCrumb and N. Friedman, Primordial condensation of meteorite components—experimental evidence of the state of the source medium, Astrophys. Space Sci. 65, 297–307, 1979.

5 N.G. Basov, E.M. Belenov, L.K. Gavrilina, V.A. Isakov, E.P. Markin, A.N. Oraevskii, V.I. Romanenko and N.B. Ferapontov, Isotope separation in chemical reactions occurring under thermodynamic nonequilibrium conditions, JETP Lett. 19, 190–191, 1974.

6 R.C. Bergman, G.F. Homicz, J.W. Rich and G.L. Wolk, ^{13}C and ^{18}O isotope enrichment by vibrational energy exchange pumping of CO, J. Chem. Phys. 78, 1281–1292, 1983.

7 N.J. Turro and M.F. Chow, Magnetic isotope effect on the thermolysis of 9,10-diphenylanthracene endoperoxide as a means of separation of ^{17}O from ^{16}O and ^{18}O, J. Am. Chem. Soc. 102, 1190–1192, 1980.

8 G. Arrhenius, M.J. Corrigan and R.W. Fitzgerald, Excitation of ^{12}C^{16}O by hydrogen Lyman-α radiation: potential cause of selective ^{16}O fractionation in protostellar clouds (abstract), in: Lunar Planetary Science XI, pp. 795–797, Lunar and Planetary Science Institute, Houston, Texas, 1980.

9 A.E. Glassgold, P. Huggins and W.D. Langer, Shielding of CO dissociating radiation in interstellar clouds, Astrophys. J. (in press).

10 R.K. Sander, T.R. Loree, S.D. Rockwood and S.M. Freund, ArF laser enrichment of oxygen isotopes, Appl. Phys. Lett. 30, 150–152, 1977.

11 M.H. Thiemens and J.E. Heidenreich, III, Mass independent fractionation of oxygen: a novel isotope effect and its possible cosmochemical implications, Science 219, 1073–1075, 1983.

12 J.E. Heidenreich, III and M.H. Thiemens, A non-mass-dependent isotope effect in the production of ozone from molecular oxygen, J. Chem. Phys. 78, 892–895, 1983.

13 K. Mauersberger, Measurement of heavy ozone in the stratosphere, Geophys. Res. Lett. 8, 935–937, 1981.

14 R.J. Cicerone and J.L. McCrumb, Photodissociation of isotopically heavy O_2 as a source of atmospheric O_3, Geophys. Res. Lett. 7, 251–254, 1980.

15 K. Yoshino, D.E. Freeman, J.R. Esmond and W.H. Parkinson, High resolution absorption cross-section measurements and bands oscillator strengths of the (1.0)–(12.0) Schumann Runge bands of O_2, Planet. Space Sci. 31, 339–353, 1983.

16 A.J. Blake, S.T. Gibson and D.G. McCoy, Photodissociation of ^{16}O^{18}O in the atmosphere, J. Geophys. Res. 89, 7277–7284, 1984.

17 O. Navon and G.J. Wasserburg, Self-shielding in O_2 - a possible explanation for oxygen isotopic anomalies in meteorites?, in: Lunar and Planetary Science XV, pp. 589–590, Lunar and Planetary Science Institute, Houston, Texas, 1984.

18 D.L. Baulch, R.A. Cox, R.F. Hampson, Jr., J.A. Kerr, J. Troe and R.T. Watson, Evaluated kinetic and photochemical data for atmospheric chemistry, J. Phys. Chem. Ref. Data 9, 295–471, 1980.

19 B.A. Thompson, P. Harteck and R.R. Reeves, Jr., Ultraviolet absorption coefficients of CO_2, CO, O_2, H_2O, N_2O, NH_3, NO, SO_2 and CH_4 between 1850 and 4000 Å, J. Geophys. Res. 68, 6431–6436, 1963.

20 R.D. Hudson and S.H. Mahle, Photodissociation rates of molecular oxygen in the mesosphere and lower thermosphere, J. Geophys. Res. 77, 2902–2914, 1972.

21 G. Herzberg, Molecular Spectra and Molecular Structure, I. Spectra of Diatomic Molecules, Van Nostrand, New York, N.Y., 1950.

22 H.G. Hecht, S.W. Rabideau and R. Engleman, Jr., Isotope effects in the Schumann-Runge bands of molecular oxygen, Los Alamos Sci. Lab., Rep. No. LA-5871-MS, 10 pp., 1975.

23 H. Okabe, Photochemistry of Small Molecules, John Wiley and Sons, New York, N.Y., 1978.

24 R.D. Hudson and V.L. Carter. Absorption of oxygen at elevated temperature (300 to 900 K) in the Schumann-Runge system. J. Opt. Soc. Am. 58. 1621–1629. 1968.

25 S. Jaffe and F.S. Klein. Isotopic exchange reaction of atomic oxygen produced by the photolysis of NO_2 at 3660 Å. Trans. Faraday Soc. 62. 3135–3141. 1966.

26 A.J.C. Varandas and J.N. Murrell. Dynamics of the $^{18}O + {}^{16}O_2$ ($v = 0$) exchange reaction on a new potential energy surface for ground state ozone. Chem. Phys. Lett. 88. 1–6. 1982.

27 J.A. Kaye and D.F. Strobel. Enhancement of heavy ozone in the earth's atmosphere?. J. Geophys. Res. 88. 8447–8452. 1983.

28 R.F. Hampson. Chemical kinetic and photochemical data sheets for atmospheric reactions. Fed. Aviat. Admin. Rep. FAA-EE-80-17. 1980.

29 T.L. Brown. The chemistry of metallic elements in the ionosphere and mesosphere. Chem. Rev. 73. 645–667. 1973.

30 A.G.W. Cameron. Elemental and nuclidic abundances in the solar system. in: Essays in Nuclear Astrophysics. C.A. Barnes. D.D. Clayton and D.N. Schramm. eds.. Cambridge University Press. New York. N.Y., 1984.

31 J.M. Greenberg. Interstellar dust. in: Cosmic Dust. J.A.M. McDonnell. ed.. John Wiley and Sons. Chichester. 1978.

32 O. Klais. P.C. Anderson and M.J. Kurylo. A reinvestigation of the temperature dependence of the rate constant for the reaction $O + O_2 + M \rightarrow O_3 + M$ (for $M = O_2$, N_2, and Ar) by flash photolysis resonance fluorescence technique. Int. J. Chem. Kinet. 12. 469–490. 1980.

33 M.H. Thiemens. S. Gupta and S. Chang. The observation of mass-independent fractionation of oxygen in RF discharge. Meteoritics 18. 408–409. 1983.

34 H. Shimamori and H. Hotta. Mechanism of thermal electron attachment to O_2: isotope effect studies with $^{18}O_2$ in rare gases and some hydrocarbons. J. Chem. Phys. 81. 1271–1276. 1984.

35 G.J. Schulz. Resonances in electron impact on diatomic molecules. Rev. Modern Phys. 45. 423–486. 1973.

36 C.E. Treanor. J.W. Rich and R.G. Rehm. Vibrational relaxation of anharmonic oscillators with exchange-dominated collisions. J. Chem. Phys. 48. 1798–1807. 1968.

37 Y. Kitamura and M. Shimizu. Oxygen isotopic anomaly and solar nebular photochemistry. Inst. Space Astrophys. Sci. Komaba. ISAS RN 217. 5 pp., 1983.

38 J. Bally and W.D. Langer. Isotope-selective photodissociation of carbon monoxide. Astrophys. J. 255. 143–148. 1982.

39 P.H. Krupenie. The spectrum of molecular oxygen. J. Phys. Chem. Ref. Data 1. 423–534. 1972.

40 A.J. Blake. An atmospheric absorption model for the Schumann-Runge bands of oxygen. J. Geophys. Res. 84. 3272–3282. 1979.

VOLUME 95 NUMBER 3

THE JOURNAL OF GEOLOGY

May 1987

GEOCHEMICAL CONSEQUENCES OF MELT PERCOLATION: THE UPPER MANTLE AS A CHROMATOGRAPHIC COLUMN[1]

ODED NAVON AND EDWARD STOLPER

Division of Geological and Planetary Sciences, California Institute of Technology, Pasadena, CA 91125

ABSTRACT

As magmas rise toward the surface, they traverse regions of the mantle and crust with which they are not in equilibrium; to the extent that time and the intimacy of their physical contact permit, the melts and country rocks will interact chemically. We have modeled aspects of these chemical interactions in terms of ion-exchange processes similar to those operating in simple chromatographic columns. The implications for trace element systematics are straightforward: the composition of melt emerging from the top of the column evolves from close to that of the incipient melt of the column matrix toward that of the melt introduced into the base of the column. The rate of evolution is faster in the incompatible than the compatible elements and, as a result, the abundance ratios of elements of different compatibilities can vary considerably with time. If diffusion and other dispersive processes in the melt are negligible and if exchange between melt and solid rock is rapid, extreme fractionations may occur, and the change from initial to final concentration for each element can be through an abrupt concentration front. Integration and mixing of the column output in a magma chamber or dispersive processes within the column, in particular the incomplete equilibration between matrix and fluid due to the slow diffusion in the solid phases, may lead to diffuse fronts and smooth trace element abundance patterns in the column output. If the matrix material is not replenished, the chromatographic process is a transient phenomenon. In some geological situations (e.g., under island arcs and oceanic islands), fresh matrix may be fed continuously into the column, leading to the evolution of a steady state. Aspects of the geochemistry of ultramafic rocks, island arc lavas, and comagmatic alkaline and tholeiitic magmas may be explained by the operation of chromatographic columns.

INTRODUCTION

The importance of permeable flow during segregation and migration of melts in the earth's mantle has been emphasized in a number of recent publications (e.g., Walker et al. 1978; Stolper et al. 1981; McKenzie 1984, 1985; Richter and McKenzie 1984; Scott and Stevenson 1984, 1986; Ribe 1985). Chemical interactions must occur as melts and other fluids flow through mantle rocks with which they are not initially in equilibrium. The consequences of this interaction have been anticipated in general terms in many discussions of the evolution of alkaline basalts (e.g., Harris 1957; Green and Ringwood 1967; Hart and Allegre 1980) and KREEP-rich lunar basalts (e.g., Warren and Wasson 1979) and in considerations of the role of mantle metasomatism in influencing the compositions of melts and mantle-derived nodules (e.g., Boettcher and O'Neil 1980; Menzies 1985). Recently, Richter (1986) examined the evolution of trace elements during the segregation of melts from their compacting source regions. The goal of this paper, prompted by the recent progress in understanding the fluid dynamical aspects of porous flow through a deformable matrix, is to consider in specific terms some of the geochemical consequences of the percolation of melts and other fluids through mantle regions with which they are not in equilibrium.

---

[1] Manuscript received August 4, 1986; accepted December 1, 1986.

[JOURNAL OF GEOLOGY, 1987, vol. 95, p. 285–307]

0022-1376/87/9503-006$1.00

The essence of our treatment of melt-mantle interaction can be visualized by thinking about the well-known ion-exchange column. Fluid is continuously fed into the base of a column and percolates upward at a constant rate. The fluid is initially out of equilibrium with the column matrix, but as it flows upward, it interacts with the matrix and trends toward equilibrium with the initial matrix. After a time, the column becomes "dirty" or "used-up" and the fluid introduced at the base passes through the column with no interaction. Each element behaves differently during the fluid-matrix interaction, and hence fractionation can occur. The extreme fractionation possible via this kind of process is the reason that ion-exchange columns are so useful in laboratory settings. Both in the laboratory and in the mantle, the principal factors influencing the operation of the column with respect to each element include: its partition coefficient between melt and matrix, the fluid fraction, the column length, the flow rate, the grain size, and the diffusion coefficients in the fluid and the matrix. Such modeling has been previously applied to the study of metasomatic processes in crustal rocks (Korzhinskii 1970; Hofmann 1972) and to hydrothermal systems (Norton and Taylor 1979).

In this paper, we model the operation of a mantle "chromatographic column" using the laboratory column as a conceptual guide. We examine the evolution of trace element abundance patterns (TEAPs) in fluid and matrix during percolation, the kinds of fractionations that can occur, and their dependences on column parameters. In the first part of the paper we establish the "rules" that such a process will obey and examine some of the ways in which the products of such a column might be identified and distinguished from other fractionation processes. In the second half of the paper, we apply our modeling to three specific scenarios and show how chromatographic processes of the sort we have modeled may contribute to real rock suites. We emphasize at the outset, however, that even if this process operates in nature, it will surely do so in conjunction with many other processes (e.g., variable degrees of partial melting, crystallization, mixing, and assimilation). Thus, our treatment should be regarded as an effort to establish some of the end member effects of this process rather than a specific model of the detailed evolution of any igneous suite. Only by understanding such end members can we begin to decipher the complexities of petrogenesis.

THE IDEAL COLUMN

Imagine a mantle region containing solid rock in which fluid forms an interconnected network along grain boundaries. Properties of interest are assumed to change over a length scale that is large compared with the matrix grain size, so matrix and fluid are treated as two interacting continua. We assume that all solid phases can be represented by some average grain size and average trace element diffusivities. Major elements are not considered, and the partition coefficients for the trace elements are taken to be constants. The assumption of uniform and constant fluid fraction is equivalent to assuming either the percolation of fluid into a dry column in which the needed porosity is instantaneously established, or the preexistence of fluid in equilibrium with the matrix. Mathematically, the only difference between these two alternatives is the addition/omission of the fluid volume initially present in the column.

Consider a representative elemental volume (Bear 1972), small compared to the scale over which the average chemical and physical variables change, and large compared to the grain size. The elemental volume consists of a solid fraction of density ρ_s where the concentration of a trace element i is $C_{s,i}$, and a fluid fraction, ϕ, of density ρ_f where i is present in concentration $C_{f,i}$. Let $\bar{V}_s$ and $\bar{V}_f$ be the flow velocities of the solid and the fluid respectively, and let $\bar{D}_{s,i}$ and $\bar{D}_{f,i}$ be the diffusion coefficients of i in the two phases; then the equation describing the conservation of mass of i in the system is:

$$\begin{aligned}
&\frac{\partial}{\partial t}[\phi\rho_f C_{f,i}] + \frac{\partial}{\partial t}[(1-\phi)\rho_s C_{s,i}] \\
&+ \bar{V}_f\bar{\nabla}[\phi\rho_f C_{f,i}] + \bar{V}_s\bar{\nabla}[(1-\phi)\rho_s C_{s,i}] \\
&- \bar{\nabla}[\phi\rho_f \bar{D}_{f,i}\bar{\nabla}C_{f,i}] \\
&- \bar{\nabla}[(1-\phi)\rho_s \bar{D}_{s,i}\bar{\nabla}C_{s,i}] = 0
\end{aligned} \tag{1}$$

(Bear 1972; McKenzie 1984). The symbols used in our equations are summarized in table 1 for reference.

TABLE 1

NOTATION

t	time
ϕ	fluid fraction in the column (by volume)
ρ_s, ρ_f	densities of the solid and fluid
a	radius of grains in the column matrix
C_s, C_f	trace element concentration (by weight) in solid and fluid
C_s°, C_f°	concentration in the matrix at $t = 0$ and in the fluid introduced at the base of the column ($z = 0$)
C_{mc}, C_{mc}°	concentration in the magma chamber, concentration in the magma chamber when it is first filled
D_s, D_f	diffusivities in the solid and the fluid
$G = WV_p\phi$	flux of fluid through a two-dimensional column
$G' = W^2V_p\phi$	flux of fluid through a three-dimensional column
$K_d = C_s/C_f$	equilibrium partition coefficient (by weight) between matrix and melt
L	column length
M	volume (one-dimensional) of a magma chamber
$R = M/L$	ratio of melt volume in chamber and column
$t_c = L/V_f$	time it takes for the fluid to pass through the column
V_f	melt velocity relative to the column ($\bar{V}_f = \bar{V}_p + \bar{V}_s$)
V_p	percolation velocity of the melt relative to the matrix
V_s	matrix velocity relative to the column
w	width of the two-dimensional column
$X_f = \dfrac{\phi\rho_f}{\phi\rho_f + (1 - \phi)\rho_s K_d}$	equilibrium mass fraction of an element in the fluid
Y_f	drift of the fluid front along the y direction
Y_i	drift of the concentration front of element i along the y direction
Z	column height from bottom of column to melt front
z	distance traversed along the column

We limit our analysis to the simple cases where densities and diffusivities of solid and fluid, as well as the melt fraction, are constant and uniform. We also assume that the transport of trace elements into and out of the elemental volume by diffusion through the solid phases may be neglected compared with the other fluxes (i.e., $D_{s,i} = 0$). Omitting the subscript i, equation (1) can be rewritten as:

$$\frac{\partial C_f}{\partial t} + \frac{1 - \phi}{\phi}\frac{\rho_s}{\rho_f}\frac{\partial C_s}{\partial t} + \bar{V}_f\bar{\nabla} C_f$$
$$+ \frac{1 - \phi}{\phi}\frac{\rho_s}{\rho_f}\bar{V}_s\bar{\nabla} C_s - D_f\bar{\nabla}^2 C_f = 0. \tag{1a}$$

Consider the case of an ideal, one-dimensional column of uniform initial composition in which local equilibrium is established instantaneously and dispersive processes within the fluid are negligible (i.e., $D_f = 0$). The assumption of local equilibrium requires that at any point, $C_s = K_dC_f$, where K_d is the partition coefficient for the element of interest. Choosing the matrix as our frame of reference ($\bar{V}_s = 0$), equation (1a) can now be reduced to

$$\frac{\partial C_f}{\partial_t} + X_fV_f\frac{\partial C_f}{\partial_z} = 0 \tag{1b}$$

where

$$X_f \equiv \frac{\phi\rho_f}{\phi\rho_f + (1 - \phi)\rho_s K_d}. \tag{2}$$

X_f is the proportion of the trace element in the system that is contained in the fluid at equilibrium.

Equation (1b) describes the rate at which a point of constant concentration moves through the column:

$$\left(\frac{\partial z}{\partial t}\right)_{C_f} = X_fV_f. \tag{3}$$

Trace element concentrations are transported at lower velocities than the fluid itself. Compatible elements (high K_d, low X_f) move at a lower rate than more incompatible ones.

Suppose that a fluid with trace element concentration, C_f^o, is introduced continuously into a column with uniform trace element concentration, C_s^o. If $C_s^o/C_f^o \neq K_d$, the trace element must be exchanged between fluid and matrix, and a sharp concentration front moves through the column at a lower speed than the fluid itself. The fluid ahead of the front is in equilibrium with the original matrix ($C_f = C_s^o/K_d$); behind the front the matrix is in equilibrium with the inflowing fluid ($C_s = K_dC_f^o$).

In the case of this simple boundary condition, the front position is also easily obtainable from a simple mass balance consideration. When the fluid has traveled a distance Z up the column, the trace element content between the base of the column and the height Z must be equal to the initial trace element content of the matrix, $Z(1 - \phi)\rho_sC_s^o$, plus what was brought in by the fluid, $Z\phi\rho_fC_f^o$. Using the equilibrium concentration from the previous paragraph and the fact that the concentration front has traveled a distance z, we can express the concentrations in fluid and matrix ahead and behind the front and relate them to the total trace element content of the column between Z and the bottom:

$$\begin{aligned} z\phi\rho_fC_f^o + z(1 - \phi)\rho_sK_dC_f^o \\ + (Z - z)\phi\rho_fC_s^o/K_d \\ + (Z - z)(1 - \phi)\rho_sC_s^o = Z\phi\rho_fC_f^o \\ + Z(1 - \phi)\rho_sC_s^o. \end{aligned} \qquad (4)$$

The position of the front is then simply

$$z = X_fZ. \qquad (5)$$

Figure 1*a* presents z/Z for some trace elements with different distribution coefficients. Due to their smaller K_d values, fronts of incompatible elements move faster than those of more compatible ones. The first fluid emerging from the column is in equilibrium with the initial composition of the matrix, and its trace element concentrations are similar to those produced by incipient melting of the column matrix ($C_f = C_s^o/K_d$). This is true regardless of the fluid fraction in the column or the column length. These two factors determine only the front position and the volume of fluid in front of it. Thus, the chromatographic process is capable of producing ex-

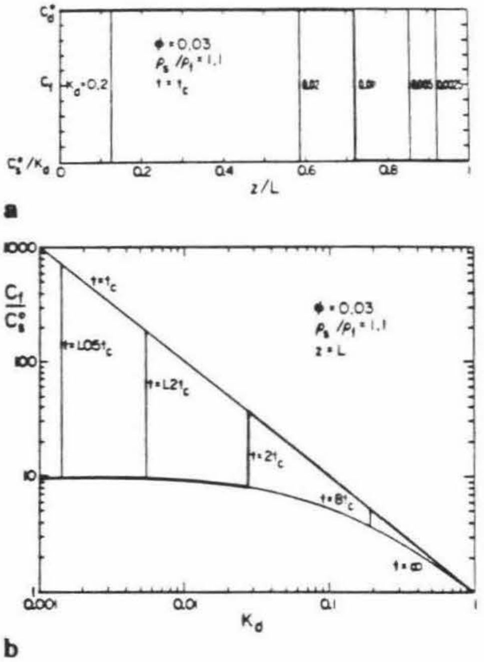

FIG. 1.—The ideal column. (*a*) Fluid concentration of five elements vs. position in the column at $t = t_c$, the time when the fluid first reaches the top of the column. Fluid with concentration C_f^o is continuously supplied at the bottom of the column (left end) and flows to the right. As fluid and matrix equilibrate, a sharp front is formed. Ahead of the front the matrix keeps its initial concentration, C_s^o, and the concentration in the fluid has changed to $C_f = C_s^o/K_d$. Behind it the fluid retains its initial composition and the concentration in the matrix has changed to $C_s = K_dC_f^o$. Column parameters and the element distribution coefficient are indicated in the figure. Concentrations are normalized to the range spanned by each element. The pattern for K_d = 0.011 is enhanced for clarification. (*b*) Trace element abundance patterns (TEAPs) in fluids emerging from the column at various times. (Concentrations are plotted against K_d; the REE in a typical peridotite would be distributed more or less evenly between $K_d \approx 0.002$ and $K_d \approx 0.50$.) In this example, melt introduced at the base of the column is produced by 10% batch melting of a source similar in composition to the column matrix. The first melt emerging at the top is identical to an infinitesimal partial melt of the column matrix. At later times the fronts of the different elements emerge from the column and their concentrations fall to the lower value of the melt introduced at the bottom. The pattern at $t = 2t_c$ is enhanced for clarification.

treme enrichments of incompatible elements that would otherwise require very small degrees of partial melting. Figure 1*b* presents the TEAP of melt emerging from a column in which the melt fraction is 3%. Regardless of the original TEAP of the melt introduced at the column base, the melt emerging from the top at $t < 1.05t_c$ ($t_c = L/V_f$ is the time it takes for a melt percolating at V_f to pass through a column of length L) has a TEAP characteristic of melt produced by incipient melting of the column matrix (for elements with $K_d >$ 0.002). Note that in figure 1*b*, concentrations are normalized to the initial matrix composition C_f°, which is not necessarily the same as the initial bulk composition of the column. In particular, if melt fraction ϕ is present in the column at $t = 0$ due to partial melting of the column matrix, then the matrix is depleted in incompatibles at $t = 0$ and the initial matrix concentration C_s° of incompatible elements will be low relative to more compatible elements. The initial matrix composition (C_s°) will only be identical to the bulk composition of the column if the melts penetrate a solid column in which melt fraction ϕ is only established during the percolation of melt through the initially dry column.

Melts emerging at later times ($t > 1.05t_c$ in fig. 1*b*) have compatible element concentrations still in equilibrium with the initial matrix composition. The incompatible elements, however, show the characteristics of the melt introduced into the base of the column. Their fronts have traveled the column, and the whole matrix has equilibrated with their initial melt composition. After sufficient volume has passed through it, the column is "used up" even for compatible elements and can no longer affect the melt composition. The column life time for each element is given by $L/(V_fX_f) = t_c/X_f$.

SMOOTHING OF THE COLUMN OUTPUT

Perhaps the most striking feature of the output of the simple column described in the previous section is the abrupt change observed in the trace element pattern as each concentration front reaches the top of the column. The absence of features of this sort in igneous suites of oceanic islands led Hofmann (1984) to conclude that chromatographic processes do not play important roles in their petrogenesis. However, several processes may lead to the production of smoother patterns in the output of mantle-scale columns. In the following sections we examine the potential of external processes acting on the products of the ideal, dispersion-free column, and of internal processes (i.e., those taking place within the column itself) for dispersing the sharp concentration fronts and for smoothing the abrupt TEAPs of the column products.

It should be emphasized that the sharp fronts shown in figure 1 are not just the result of the properties of the ideal column, but also of our choice of initial and boundary conditions. In the case discussed in the previous section, the trace element concentrations in the melt at the base of the column, $C_f^\circ(t)$ are introduced as a step function at $t = 0$. This sudden deviation from equilibrium travels through the column as a series of fronts shaped like step functions· (eq. 3). Though these conditions may be appropriate for many situations, in some environments the deviation from equilibrium between melt and matrix may evolve gradually. The initial matrix composition may change along the column length so that the melt is in equilibrium with the matrix at the base of the column and then gradually departs from equilibrium as it travels up the column. The input melt composition may also vary smoothly from equilibrium concentrations to some final $C_f^\circ(t) \neq C_s^\circ/K_d$. If these changes take place over a time or distance longer than the separation between the fronts of two consecutive elements, smooth and gradually varying TEAPs can be produced in the column output. For example, smooth variations in the melt composition introduced into the base of the column would result if early melts were produced by low degree of partial melting and later ones by progressively higher degrees, or if early melts were produced in a transition zone between the column reservoir and some other reservoir that is the source for later melts.

a. The Perfect Mixer.—One simple way of subduing sharp jumps in TEAPs is through integration and mixing of the column output. If magma is collected someplace (e.g., in a magma chamber below an impermeable layer or in an upper level crustal chamber), the TEAPs in melts coming out of such a chamber are smoothed. Consider the one-dimensional case, in which magma emerging

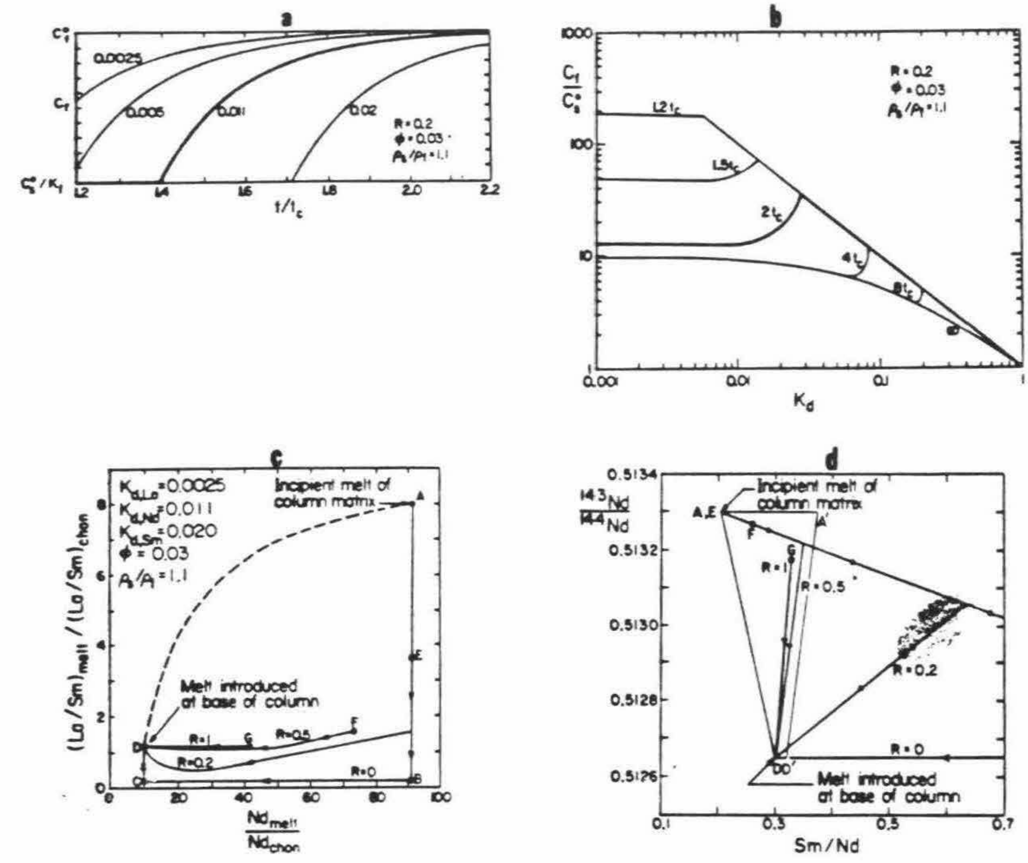

FIG. 2.—Results of collecting and mixing the column output in a magma chamber. The output of the ideal column (fig. 1) is collected and mixed in a magma chamber that is assumed to operate as a perfect mixer. The chamber discharges melt after being filled to a volume of $RL\phi$. (*a*) Concentrations of four incompatible elements in melts coming out of the chamber ($R = 0.2$) vs. time. Notice the difference from figure 1*a* where concentrations were plotted against distance. K_d values are indicated on the curves. (*b*) TEAPs of melts emerging from the chamber ($R = 0.2$) at various times. The first melt emerges at $t = (1 + R)t_c = 1.2t_c$, after passing through the column and filling the chamber. Melt and column parameters are identical to those used in figure 1*b*, but the sharp patterns are smoothed relative to the ideal case. (*c*) The evolution of La/Sm vs. Nd. Each solid curve represents the time evolution for a mixer of different volume ($RL\phi$). $R = 0$ represents the output of an ideal column. The first melt has a composition A, which corresponds to the incipient melt of matrix with chondritic concentrations. The more incompatible La is enriched with respect to Sm. When the La front arrives the ratio changes to B; when the Nd front arrives, its concentration falls to that of the melt introduced at the base of the column, C. When the Sm front arrives, the Sm concentration falls and La/Sm reaches the final value of the melt introduced at the base, D (10% melt of source with chondritic concentrations). The first composition emerging after being mixed in magma chambers of different sizes is indicated by points A, E, F, G. The evolution curves are smoothed by the effect of the chamber. In all cases, melt composition is clearly distinct from that produced by simple mixing (dashed curve). (K_d values are for a peridotite with 65% olivine, 20% orthopyroxene, 10% clinopyroxene, and 5% garnet using values from Frey et al. 1978.) (*d*) Sm-Nd evolution of melt produced by 10% batch melting of a "bulk earth" reservoir [C_f^o(Nd) = 11 ppm, C_f^o(Sm) = 3.3 ppm, ^{143}Nd/^{144}Nd = 0.51265] percolating through a column of a depleted reservoir [C_s^o(Nd) = 0.86 ppm, C_s^o(Sm) = 0.32 ppm, ^{143}Nd/^{144}Nd = 0.51330; column and mixer parameters and Sm and Nd K_d values as in fig. 2*c*]. Area A′ADD′ encloses all possible compositions resulting by simple mixing of A′, the matrix composition; A, its incipient melt; D′, the source rock; and D, its 10% melt. Note that the composition of the late melts emerging from the magma chamber may be misinterpreted as an isochron or a mixing line of D or D′ with a reservoir represented by the stippled area (for the case of R = 0.2). The composition of the first melt emerging from chambers with R = 0, 0.2, 0.5, and 1 are represented respectively by points A, E, F, and G.

from a column of length L and porosity ϕ is collected and mixed in a region above the column. The newly formed magma chamber grows to a thickness M, and then discharges magma at the same rate as it is recharged. If mixing in the chamber is perfect (i.e., occurs instantaneously), then conservation of mass for any trace element requires:

$$M\frac{dC_{mc}}{dt} = \phi V_f(C_f - C_{mc}) \qquad (6)$$

where C_f is the trace element concentration in the melt entering the chamber and C_{mc} is the concentration of the trace element in the chamber. In the case of a chamber above an ideal column, $C_f = C_s^\circ/K_d$ until the front enters the chamber at $t = t_c/X_f\lambda$ ($t = 0$ refers to when the melt is first introduced at the bottom of the column). At later times, $C_f = C_f^\circ$.

For any given size of magma chamber there is a critical value of K_d for which the volume of melt ahead of the concentration front is equal to the chamber volume:

$$M = L\phi\left(\frac{1}{X_f} - 1\right) \qquad (7)$$

More compatible elements have a larger volume ahead of their fronts, and the trace element concentration in the chamber when it is first filled is $C_{mc}^\circ = C_s^\circ/K_d$. For more incompatible elements the volume of melt ahead of the front is smaller, and C_{mc}° is given by:

$$\frac{C_{mc}^\circ - C_f^\circ}{C_s^\circ/K_d - C_f^\circ} = \frac{1}{R}\left(\frac{1}{X_f} - 1\right) \qquad (8)$$

where $R = M/L\phi$ is the ratio of melt volume in the chamber to that in the column.

In the case of a chamber above an ideal column the solution of equation (6) is a simple exponential decay to the final concentration, C_f°. In the case of the compatible elements the decay starts when the front reaches the chamber, $t = t_c/X_f$; in the case of the incompatibles the decay starts at the time the chamber is first filled, $t = t_c(1 + R)$. In both cases the time constant for decay is $M/V_f\phi = Rt_c$.

Figure 2*a* presents the results for a reservoir with $R = 0.2$ placed above the ideal column of figure 1. The sharp fronts of the ideal case are relaxed into exponential decay with time. If the concentration fronts of "consecutive" elements (e.g., La, Ce) overlap (fig. 2*a*), the sharp jumps produced by the ideal column are smoothed (fig. 2*b*). This effect is more pronounced for incompatible elements than for compatible elements.

Inspection of figures 1*b* and 2*b* shows that concentration ratios of incompatible to compatible elements can undergo extreme variations in successive melts emerging from an ideal column or from a magma chamber above such a column. These changes are illustrated in figure 2*c*. For the ideal column, the initial output has a ratio of $(C_{s,\mathrm{La}}^\circ/K_{d,\mathrm{La}})/(C_{s,\mathrm{Sm}}^\circ/K_{d,\mathrm{Sm}})$ (point A). The ratio then jumps to $C_{f,\mathrm{La}}^\circ/(C_{s,\mathrm{Sm}}^\circ/K_{d,\mathrm{Sm}})$ (B,C) and finally changes to $C_{f,\mathrm{La}}^\circ/C_{f,\mathrm{Sm}}^\circ$ (D). This path of evolution of melt composition is clearly distinct from that produced by simple mixing of the incipient melt of the column matrix with the melt introduced at the base (dashed line). Note that for small magma chambers the chromatographic process is capable of producing element ratios that cannot be explained by simple mixing of any two melts plotting at A and D; i.e., La/Sm ratios lower than that of point D can be produced.

Isotopes of the same element are equally affected by the column and evolve similarly because they have the same value of K_d. The change in isotopic ratio is the same as during simple mixing. Thus, if ^{143}Nd/^{144}Nd were plotted versus 1/Nd, a straight line would result, similar to a mixing line between incipient melt of the matrix and melt input into the base of the column. However, since ratios of elements of different compatibilities can vary widely in the output of a single column (fig. 2*c*), parent-daughter evolution diagrams can display some unusual trends. In figure 2*d*, we have constructed a Sm/Nd evolution diagram for an ideal column and various magma chamber sizes for specific choices of K_d, C_f°, C_s° and ^{143}Nd/^{144}Nd ratios for the matrix and the melt introduced at the column's base. For the ideal case ($R = 0$), the abrupt variations in Sm/Nd ratios as the two fronts arrive, coupled with the jump in the Nd isotopic ratio when the Nd front arrives, produce an extreme pattern. For the magma chamber cases, trends that resemble isochrons or mixing lines are produced. These clearly have no time significance, nor do they necessarily yield any direct information on the properties of the two components (i.e., percolating melt and matrix) being "mixed" in the chromatographic column. For example, melts along the $R = 0.2$ trend in figure 2*d* could be misinterpreted as mixing between D or D′ and a recently depleted reservoir (stippled area). Similar results are produced on a Rb/Sr evolution diagram. On an $\epsilon_{Nd} - \epsilon_{Sr}$ plot (DePaolo and Wasserburg 1976), the interaction between melts and matrix lying along the mantle array may deviate from the array, because Sr is more incompatible than Nd and ϵ_{Sr} would change faster than ϵ_{Nd}.

The ion-exchange process, softened to some extent by a "perfect mixer," can thus produce smoothly varying trace element patterns. If elements covering a wide range of compatibilities are studied, the output of this process should be distinguishable from other fractionation processes; it could be misinterpreted if only isolated parts of the data set were examined.

b. Internal Dispersive Processes.—In a realistic column, dispersive processes within the column itself could lead to diffuse fronts and smooth TEAPs in the column output. For example, chemical diffusion must occur across the concentration fronts, with the result being more dispersed, wider fronts. Mechanical dispersion, which is the result of processes such as capillarity in the tubules or the column tortuosity, mixes fluid parcels across the front and has a similar effect. Slow volume diffusion in the solid matrix may prevent local equilibrium between fluid and solid during flow and lead to dispersion of sharp concentration fronts.

Whereas an "ideal" column can be fully characterized by the melt fraction and partition coefficients, examination of dispersive processes requires knowledge of some other parameters: grain size, flow velocity, diffusivities in the fluid and the solid, and fluid viscosity. Current knowledge of most of these parameters is sufficient for us to assess the likely contributions of the various dispersive processes.

(i) Chemical diffusion in the fluid. Chemical diffusion must occur across the concentration fronts in the column, resulting in dispersed, wider fronts. In order to evaluate the magnitude of this effect, we reduce equation (1a) to the following form for a one-dimensional column, everywhere in local equilibrium, in which the matrix is chosen as the reference frame:

$$\frac{\partial C_f}{\partial t} + X_f V_f \frac{\partial C_f}{\partial z} - X_f D_f \frac{\partial^2 C_f}{\partial z^2} = 0. \quad (9)$$

Consider, as we did earlier, the case where melt with constant trace element concentration C_f° is continuously introduced at the bottom of a column of uniform composition. For these initial conditions equation (9) can be solved by the Laplace Transform, and for the case of $C_f^\circ \neq C_s^\circ/K_d$:

$$\frac{C_f - C_f^\circ}{C_s^\circ/K_d - C_f^\circ} = \frac{1}{2}\left\{\operatorname{erfc}\left[\left(\frac{V_f}{4D_f}\right)^{1/2} \frac{z - z_{\text{front}}}{(z_{\text{front}})^{1/2}}\right] + \exp\left[\frac{zV_f}{D_f}\right]\operatorname{erfc}\left[\left(\frac{V_f}{4D_f}\right)^{1/2} \frac{z + z_{\text{front}}}{(z_{\text{front}})^{1/2}}\right]\right\}. \quad (10)$$

The physical situation described by equations (9) and (10) is that of a concentration front that moves through the column with a velocity $V_f X_f$. The front, centered at $z = z_{\text{front}} = X_f V_f t$, is dispersed and is in the form of an error function. (A related case of a spike in the fluid concentration is discussed by McKenzie 1984.) The last term in equation (10), which takes care of the initial condition at $z = 0$, can be neglected for $z_{\text{front}} > 4D_f/V_f$.

The extent to which chemical diffusion can smooth TEAPs (i.e., subdue the sharp steps shown in fig. 1*b*) may be evaluated by comparing the width of the dispersed front to the separation between the fronts of two trace elements, *i* and *j*. The width of the dispersed front at the time it emerges from the column may be obtained as:

$$\Delta^{\text{diff}} = 2(z_* - z_{\text{front}}) = 4\left(\frac{D_f z_{\text{front}}}{V_f}\right)^{1/2} = 4\left(\frac{D_f L}{V_f}\right)^{1/2} \quad (11)$$

where z_* is that for which the argument in the erfc function is 1. When the front of *i* reaches the top of the column, the front of *j* is at $LX_{f,j}/X_{f,i}$. The separation between the fronts is:

$$\Delta^{\text{sep}} = L\left(1 - \frac{X_{f,j}}{X_{f,i}}\right) \quad (12)$$

and

$$\frac{\Delta^{\text{diff}}}{\Delta^{\text{sep}}} = \frac{4X_{f,i}}{X_{f,i} - X_{f,j}} \left(\frac{D_f}{V_f L}\right)^{1/2} \tag{13}$$

Dispersion of the concentration fronts is effective at smoothing trace element patterns if this ratio is greater than one. For the case of the fronts of Nd and Sm in basaltic melt percolating through peridotite, we obtain $X_{f,\text{Nd}} = 0.72$, $X_{f,\text{Sm}} = 0.58$ (using the parameters of fig. 2*c*). D_f is of the order of 10^{-6}–10^{-7} cm^2/sec (Magaritz and Hofmann 1978), so that even for low percolation velocity (1 cm/yr), diffusion is important only in columns shorter than 70 m.

We conclude, therefore, that chemical diffusion in the fluid is inefficient at dispersing the sharp fronts of the ideal column. It may be of importance in the cases of very incompatible elements (fronts are not well separated), short columns ($L < 1$ km), and low percolation velocities.

(ii) Mechanical dispersion. Mechanical dispersion may also contribute to the broadening of the concentration fronts in mantle columns. Mechanical dispersion (also called hydrodynamic dispersion; Bear 1972; Dullien 1979) is the result of processes that lead to mechanical mixing of the fluid. For example, during flow in a single tubule, capillarity and the irregular shape of the tube result in the dispersion of the front due to mechanical stirring of the fluid across the front. Fluid from the two sides of the front may also be mixed due to the different random paths of fluid parcels through the network of tubules.

It is possible to estimate the extent to which mechanical dispersion can broaden concentration fronts. Under some simplifying assumptions (Bear 1972; Dullien 1979), the effects of mechanical dispersion can be accounted for by replacing D_f in equation (9) by total dispersivity, D_f', which includes contributions from both chemical diffusion and mechanical dispersion. D_f' can be described as a function of the medium Peclet number, $Pe' = aV_f/D_f$, which is the ratio of the time it takes to travel a characteristic distance (a) by diffusion, a^2/D_f, and by advection, a/V_f.

If $Pe' < 1$, then mechanical dispersion is less efficient than chemical diffusion and $D_f' \sim D_f$ (Dullien 1979). For $Pe' > 1$, D_f' can be approximated by

$$D_f' = aV_f. \tag{14}$$

(Dullien 1979). For a typical column with $D_f = 10^{-6} - 10^{-7}$ cm^2/sec, $V_f = 0.1 - 100$ cm/yr, $a = 0.1 - 1$ cm, Pe' is between 10^{-3} and 100. Equation (13) describes the situation for $Pe' < 1$. For $Pe' > 1$, we substitute $D_f' = aV_f$ for D_f in equation (13) yielding:

$$\frac{\Delta^{\text{disp}}}{\Delta^{\text{sep}}} = \frac{4X_{f,i}}{X_{f,i} - X_{f,j}} \left(\frac{a}{L}\right)^{1/2}. \tag{15}$$

Using $X_{f,\text{Nd}} = 0.72$, $X_{f,\text{Sm}} = 0.72$ as in the previous section yields $\Delta^{\text{disp}}/\Delta^{\text{sep}} > 1$ only for $L < 4$ m. This estimate may be modified somewhat due to the effects of varying packing of grains or irregular grain geometry on dispersivity. Limited measurements and calculations suggest that increase in D_f' of two orders of magnitude is possible (Dullien 1979). However, even such enhanced dispersivities would not result in broadening of concentration fronts comparable to the separation between them for km-scale columns.

(iii) The effect of diffusion in the solid phases. Up to this point, we have simplified our analysis with the assumption of instantaneous, local equilibrium between melt and solid matrix in the column; i.e., at all points, $C_s = C_f K_d$. However, it is easy to see that this assumption will be unjustified if grain size in the matrix is large enough (or melt-solid contact is limited by the restriction of melt to tubules in partially molten systems; F. Richter, pers. comm.) or melt velocity is high enough. Suppose, for example, that the column's grain size is 1 cm and the diffusivity in the solid is about 10^{-13} cm^2/sec (e.g., rare or alkaline-earth elements in diopside and garnet at 1200°C; Freer 1981; Sneeringer et al. 1984). The time scale for equilibration would be on the order of 300,000 yrs. This may be comparable to the lifetime of a Hawaiian volcano (Shaw et al. 1980) and to the time required for basaltic melt to traverse a 10-km column of 1 cm grain size (McKenzie 1985; Scott and Stevenson 1986). The effects of slow volume diffusion in the matrix may thus be important for the kind of processes we are considering and, as we shall show, are likely to be the most important sources of dispersion.

Without the assumption of instantaneous local equilibrium, analytical solution of equation (1a) becomes difficult; C_f and C_s must now be related through a diffusion law rather than through the simple expression $C_s = C_f K_d$. We have constructed a numerical solution to equation (1a) using Fick's second diffusion law to describe the diffusion through a stationary matrix consisting of spherical grains. Diffusion and mechanical dispersion in the fluid were shown earlier to be small and have been neglected. The details of the numerical solution are described in Appendix A.

Figure 3*a* presents concentration fronts for a sample calculation when the melt has just reached the top of the column ($t = t_c$). It is clear that the slow diffusion in the solid does lead to a strong dispersion of the fronts and to a substantial overlap between fronts of different elements. Another factor contributing to the good overlap is the faster rate at which the fronts move compared with the equilibrium case (dotted lines). This faster rate of front migration results from the weaker interaction between fluid and solid. In the extreme case, when no equilibration takes place, the concentration fronts of all elements travel at the fluid velocity.

The overlap shown in figure 3*a* results in

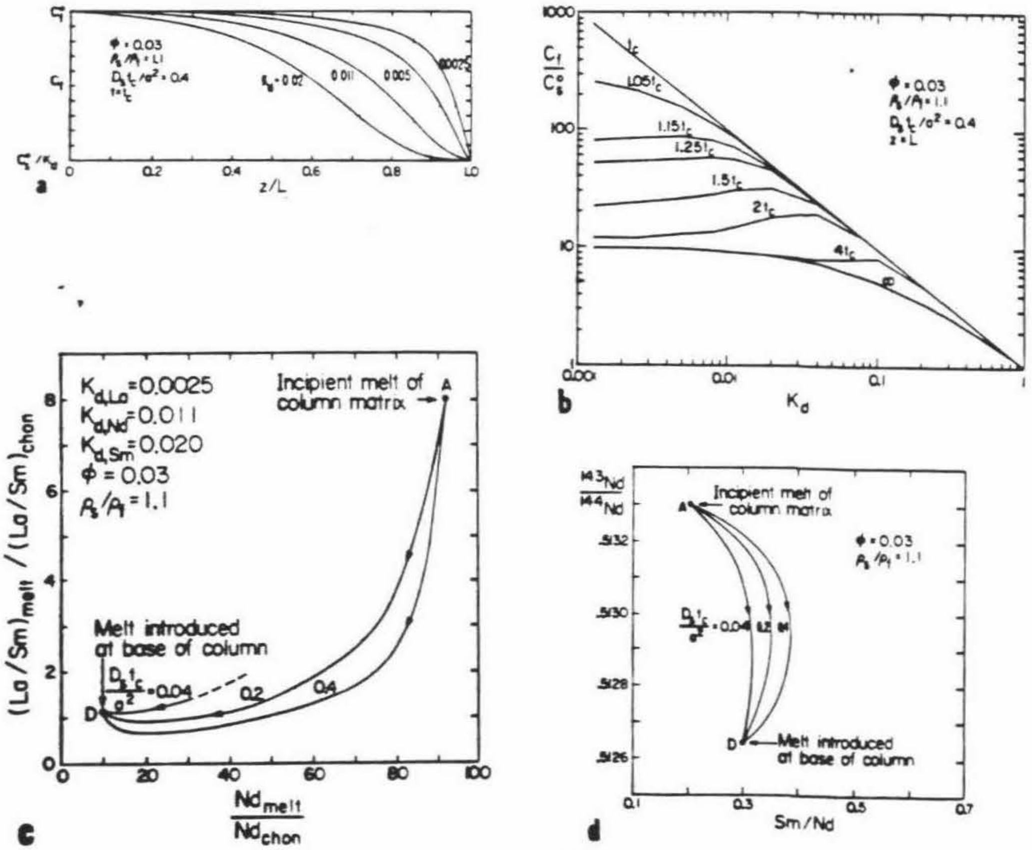

FIG. 3.—Incomplete equilibration due to slow volume diffusion in the solid. (*a*) Trace element concentrations vs. position within the column at $t = t_c$. Notice that fronts advance a larger distance than in the equilibrium case (dotted lines) and that elements of different compatibility have fronts of different width. (Column parameters and K_d values are indicated in the figure. $D_s t_c/a^2$ is the ratio of advective and diffusive time scales, which controls the column's approach to local equilibrium.) (*b*) TEAPs in fluid emerging at *L* at various times. (*c*) The evolution of La/Sm vs. Nd. Each curve represents the time evolution for a different value of $D_s t_c/a^2$. Composition of matrix and melt introduced into the column as in figure 2*c*. (*d*) Sm-Nd evolution diagram. Melt and column parameters as in figure 2*d*.

smooth TEAPs (fig. 3*b*) that change gradually with time. The characteristic features of the chromatographic column, mainly the evolution from incipient melt of the column matrix to the composition of the melt introduced into the column's base and the faster evolution of the incompatible elements, are still present.

Figures 3*c* and 3*d* show variations in incompatible to compatible element ratios and a representative parent-daughter isotope evolution diagram. Again, though the trends are smoothed, they preserve the characteristic features of the chromatographic process (compare with figs. 2*c* and 2*d*).

The shape of each front can be approximated by an error function solution similar to equation (10) where D_f is replaced by

$$``D" = \frac{a^2 V_f^2}{4\pi D_s} X_f(1 - X_f) \qquad \text{(A8)}$$

(see Appendix A). The ability of slow diffusion in the solid to produce overlap between fronts of different elements may be examined by substituting "D" into equation (13):

$$\frac{\Delta^{\text{diff}}}{\Delta^{\text{sep}}} = \frac{4X_{f,i}}{X_{f,j} - X_{f,j}} \left[\frac{a^2 V_f}{D_s L} \, \frac{X_{f,i}(1 - X_{f,i})}{4\pi}\right]^{1/2}. \qquad (16)$$

Recall that dispersion of the concentration fronts leads to smoothing of the trace element patterns if this ratio is greater than one. In the case of basaltic melt flowing through matrix with $a = 0.5$ cm at a velocity $V_f = 30$ cm/yr, we obtain for Nd ($K_d = 0.011$) and Sm ($K_d = 0.02$), $\Delta^{\text{diff}}/\Delta^{\text{sep}} > 1$ for $L < 170$ km (using column parameters of figures 2 and 3 with $D_s = 10^{-13}$ cm^2/sec; Sneeringer et al. 1984). Under these conditions $\Delta^{\text{diff}}/\Delta^{\text{sep}} > 1$ for $L < 404$ km in the case of the incompatible elements La ($K_d = 0.0025$) and Ce ($K_d = 0.05$). For the more compatible elements Yb ($K_d = 0.23$) and Lu ($K_d = 0.38$), $\Delta^{\text{diff}}/\Delta^{\text{sep}} > 1$ in columns shorter than 23 km. Thus, in km-scale columns, slow diffusion in the solid matrix is found to be efficient in dispersing the fronts and smoothing the sharp TEAPs predicted for the ideal case.

It is important to emphasize the strong dependence of equation (16) upon grain size. Since $V_f \propto a^2$ during permeable flow (Bear 1972), the parameter $a^2 V_f / D_s L$ goes as a^4. Thus, for example, if $a = 0.1$ cm, $\Delta^{\text{diff}}/\Delta^{\text{sep}} > 1$ only if $L < 270$ m (for Nd and Sm). For matrix with this grain size, the assumption of local equilibrium would be appropriate if columns are more than a few kilometers long (McKenzie 1984; Richter 1986), and smooth TEAPs would not characterize the output of such columns. If grain size is larger than a few centimeters, or if flow is in veins so that the effective "grain size" is even larger, diffusive interaction would probably be small, and melts would be little influenced by the wallrock; however, any interaction that occurred under these conditions could still be described by the treatment we have developed.

If solid and melt react so that solid phases dissolve and/or crystallize, or if recrystallization is important, then trace element transfer across the solid-melt interface would be enhanced. It was suggested by Norton and Taylor (1979) that the same mathematical scheme we have used is applicable in this case if diffusivity is replaced by transfer rate coefficients. Although very little is known of the kinetics of trace element transfer in such systems, it seems plausible that under such conditions columns could operate close to equilibrium whether melt flows along grain boundaries or in small veins.

DISCUSSION

The essence of the kind of process we envision and have described in the previous sections is as follows: melt is continuously introduced at the base of a column of rock and moves upward through it by permeable flow. The melt is initially out of equilibrium with the rock matrix, and the two interact chemically. A snapshot of the column at any time would show for each element a concentration front, above which the melt is in equilibrium with the initial matrix of the column and below which the melt is unchanged from when it was introduced into the base of the column. Above the concentration front, the matrix retains the initial column composition; below it, the matrix has changed to be in equilibrium with the melt flowing into the column. The width of the front depends on the effectiveness of dispersive processes in the column.

If we looked at a movie of the column, we would see the concentration front for each element sweeping upward, with the fronts of the more incompatible elements moving faster than those of the more compatible ones. If we sat on the top of the column and sampled the liquids that emerged, we would first collect melt identical to that of an infinitesimal degree of partial melting of the initial matrix material. As the concentration front of each element reached the top of the column (the fronts would arrive in order of increasing compatibility), we would observe the melts changing from the concentration of that element in the incipient melt of the matrix to that of the melt flowing into the column's base. Eventually, the concentration fronts of even the most compatible elements will have reached our position, and thereafter, the melts that emerge will be identical to those injected into the base of the column.

The features that should be emphasized are the rapid evolution of the incompatible elements relative to the compatible elements in the melts emerging from the column, the extreme fractionations possible via the operation of such a column, and its transient nature. These will be preserved in all incarnations of this process.

Chromatographic columns are well known for the strong chemical separations they produce. Sharp fronts are produced if local equilibrium is instantaneously established between melt and matrix, and dispersive processes are not efficient enough to broaden them. We have evaluated the dispersive effects of some internal processes such as chemical diffusion in the liquid, physical mixing across the concentration front, and incomplete local equilibrium between melt and matrix due to slow diffusion in the solid phases. We conclude that incomplete local equilibration due to slow diffusion in the solid phases is likely to be the most important and effective agent of dispersion in columns where basaltic melts percolate through mantle rocks. Chemical diffusion in the melt will play a role only if melt velocity is low or columns are shorter than a kilometer. Mechanical dispersion is not likely to be important when melt percolates along grain boundaries.

Broad fronts and smooth trace element abundance patterns may also be produced by other processes. Matrix composition, and hence the distribution coefficients between melt and matrix, may change along the column length, or input melt composition may change gradually with time, so that the deviation from equilibrium between the column and the percolating melt evolves gradually. Integrating and mixing the column products in a magma chamber can also be effective in softening the sharp fronts produced by a mantle column.

It is instructive to compare the outputs of a hypothetical mantle column and of simple mixing of the melt introduced into the base of the column with the incipient melt of the column's matrix. After all, both processes produce a continuum of melt compositions ranging between that of the incipient melt and the melt flowing into the column. The intermediate products of the two processes are, however, quite distinguishable (e.g., fig. 2*c*). Basically, in the ion-exchange process, each element can be regarded as mixing at a different rate, which is a function of the element's compatibility with respect to the matrix, with incompatible elements changing rapidly between the two end members and the compatible elements doing so slowly. Thus, although the end members of the two processes are the same, by examining the variations in a range of compatibles versus incompatibles in the intermediate members of a series of magmas, they should be readily distinguishable.

The chromatographic process has important similarities to zone refining (Harris 1957). If the volume of the refined zone is infinitesimally small and the process is repeated continuously, the results are identical to those of our equilibrium case. However, while in the case of zone refining, melt-matrix interaction is achieved by melting of the matrix and subsequent crystallization from the melt, our treatment has focused on diffusive interaction between the two media.

Caveats.—In order to bring out the main features of the chromatographic process, we have focused upon a highly schematic model of mantle processes. At this point, it is worth evaluating the degree to which actual mantle processes and conditions may deviate from these we have modeled. It seems inevitable that fluids (melts or volatile-rich supercritical fluids) will pass through country rocks with which they are not in equilibrium as they rise buoyantly. The lack of equilibrium may be the result of disequilibrium melting, migration of melts through a phase boundary (i.e., the garnet to spinel peridotite transition), or migration of melt between regions that have undergone different degrees of partial melting or between reservoirs of different chemical composition. It is less certain, however, that the melts are always able to interact chemically with country rocks as they traverse them. Flow of melt through narrow cracks may result in extensive interaction (Quick 1981) and melt percolation along grain boundaries, the flow process considered by us in our modeling of ion-exchange processes, will clearly allow the necessary interaction. On the other hand, crack propagation or diapiric rise are so rapid and the surface area to volume ratios so low that chemical interactions for these modes of magma transport are likely to be minimal, though the effects of whatever interactions do occur may be similar to those we have described.

In order to process melt quantities that are important on a regional scale, columns must be on the order of 1 km or longer. At present, it is not known whether narrow (cm-scale) veins or porous flow are stable over such distances relative to the development of larger dikes and conduits, in which chemical interaction of melts with wallrock is minimal. Also, the onset of permeability in a previously dry rock, though experimentally observed (Watson 1982), is not yet physically understood.

Perhaps the most important limitation of our modeling, and indeed of thinking about the process that we have envisioned in any geologically realistic situation, is that the only interaction between melt and matrix that we consider is *ion-exchange*. This implies the stringent limitation that, with respect to mineralogy (i.e., major elements), the fluid and the matrix are already in equilibrium when the fluid is introduced into the base of the column. If they are not, dissolution and precipitation of matrix phases or perhaps even new phases will occur.

The end member process we have described will be most relevant to scenarios in which fluids pass between regions of the mantle that have similar mineralogies (the same phases with similar major element chemistries, but not necessarily in the same proportions) but different minor and trace element characteristics. Since heat and most major elements will behave as "compatible elements," minor incompatibilities between the phase equilibria of the injected fluid and the mineralogy of the matrix will probably be adjusted by reactions occurring at the base of the column, and the end member ion-exchange process may then be relevant to the movement of the melt through the bulk of the column.

Other complexities may arise because of the pressure and temperature gradients along the column. These may lead to non-uniform composition of the initial column and to changes in the phase equilibria controlling the melt-matrix reactions. The non-uniformity of the initial column could be easily modeled by allowing for variability of the distribution coefficients with height. The effect of the pressure and temperature gradients on melt-matrix reactions is more difficult to estimate, given the paucity of relevant phase equilibrium data, and would also require specification of the pressures and temperatures throughout the column and in the melt flowing into it. Characterization of these aspects of the interaction of melt and matrix is beyond the scope of this paper, but we note that the ion-exchange process upon which we have focused will be superimposed on these phase equilibrium effects.

Geological Applications.—Up to this point, we have purposely kept the modeling and discussion rather abstract so as to emphasize the general features of the ion-exchange process and the effects of varying the parameters in the models. There are many possible situations involving different matrices, column geometries, initial melt compositions, and plumbing systems that could be modeled in detail. Rather than trying to anticipate all potential applications, we will briefly develop three geologically interesting scenarios in which ion-exchange processes might be important. Through these, we hope to demonstrate the kinds of observable geochemical features of natural suites that might reflect the involvement of km-scale chromatographic columns in mantle rocks.

a. Mantle metasomatism: U-shaped REE patterns in peridotites. Our discussion has focused on the characteristics of the liquids that emerge from hypothetical mantle-scale chromatographic columns, but the complementary evolution of the matrix composition is also of interest and may provide insights into the observed compositions of mantle-derived ultramafic xenoliths and terrains. The model that we have developed provides a framework for considering the effects of mantle metasomatism as fluids (silicate or carbonatite melts or hydrous or CO_2-rich supercritical fluids) flow through mantle rocks and alter their composition.

An example of such a process is presented in figure 4. A column, initially depleted in light REE, is penetrated by a melt highly enriched in these elements. As $C_f^\circ > C_s^\circ/K_d$, rare earth elements are transferred from the melt to the matrix. After small quantities of melt pass through the column, the fronts of the more incompatible, light REE reach the top of the column, their concentrations rise, and the matrix in this region develops U-shaped REE patterns. Later, other fronts arrive and the point of the minimum concentration moves toward the more compatible elements. After enough fluid has passed through the column, the pattern relaxes to the final equilibrium shape.

This scenario is a possible explanation for U-shaped REE patterns observed in some metasomatized peridotitic nodules (Stosch and Seck 1980; Dupuy et al. 1986) and peridotites from some ophiolitic bodies (Pallister and Knight 1981; Prinzhofer and Allegre 1985). Such peridotites could have evolved initially as residues from extensive partial melting of a typical source rock for mid-ocean ridge basalts, or as cumulates from such magmas, and developed light REE depleted patterns [similar to the patterns observed in some Kilbourne Hole nodules (Irving 1980) or in the Ronda peridotite (Frey et al. 1985)]. A later interaction of these rocks with a limited volume of light REE enriched fluid or melt could lead, according to the above scenario, to the formation of U-shaped REE patterns.

Simple mixing of an enriched component and depleted matrix could also lead to U-shaped REE patterns, but given an appropriate data set, the two processes could be distinguished. Such a data set is illustrated in figure 5, where we have plotted the REE concentrations of a suite of nodules with U-shaped REE patterns from Hoggar, Algeria (Dupuy et al. 1986). The patterns are clearly distinguishable from the linear arrays expected in the case of simple mixing. They are, however, very similar to what we would expect if a chromatographic process produced the range of observed REE patterns. The concentration fronts of the more incompatible elements move faster through the chromatographic column and their concentrations rise first. Figure 5 shows that, in accordance with the predictions of our model, the Ce and Nd concentrations in the nodules increase faster than does the concentration of the more compatible Sm, resulting in concave downward arrays. The Eu and Sm concentrations rise at comparable rates, as expected for two elements with similar K_d values. Yb and Lu concentrations (not shown) do not

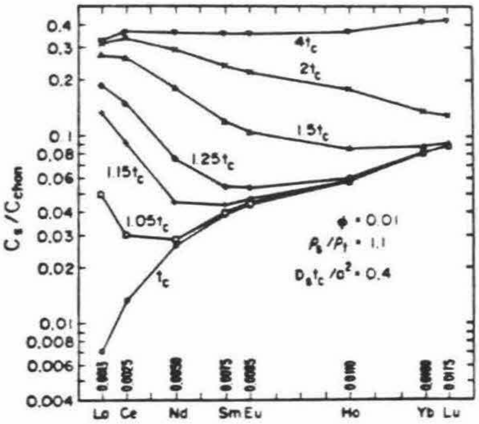

FIG. 4.—Evolution of REE abundance patterns during metasomatism of a depleted mantle infiltrated by a melt highly enriched in incompatible elements. The matrix at the top of the column retains its initial composition until the first melt reaches it at $t = t_c$. Then, since fronts of the more incompatible elements travel faster through the column, their concentrations rise earlier and a U-shaped trace element pattern evolves. If melt volume is limited ($0.05L\phi$–$0.15L\phi$ in the case shown), then interaction ends at $t = 1.05t_c$–$1.15t_c$) and these U-shaped patterns are the final ones. If more melt is available, then matrix composition will continue to evolve toward equilibrium ($t = 1.25$–$4t_c$). Melt composition is that produced by 0.1% batch melting of a source with chondritic abundance and with 65% olivine (ol) + spinel (sp), 22% orthopyroxene (opx), and 13% clinopyroxene (cpx). Matrix composition is that of a residue after a 20% batch melting of a similar source, and is composed of 74% ol, 22% opx, and 4% cpx. K_d values for the column were calculated using the values given by Frey et al. (1978) and are indicated in the figure.

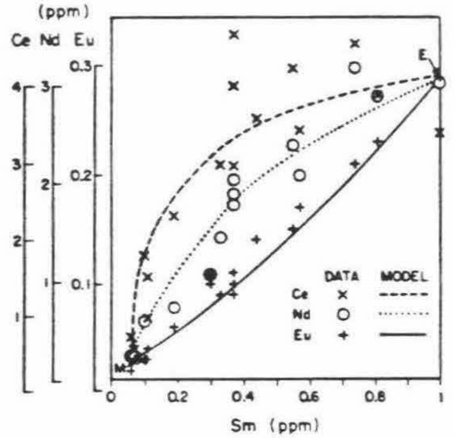

FIG. 5.—REE concentrations of peridotite nodules from Hoggar, Algeria (Dupuy et al. 1986). Concentrations of Ce, Nd, and Eu are plotted against Sm concentration (concentrations along the y axis were plotted so that end member samples plot at approximately the same position). The data array for Ce and, to a lesser degree, Nd deviate from a straight line expected for simple mixing. The concave downward patterns fit the predictions of the chromatographic model (see text). Shown for reference are the results of a model calculation for column parameters and K_d values from figure 4. Matrix composition, *M*, is that of the most depleted nodules; melt composition is in equilibrium with the most enriched samples, *E*.

correlate with Sm; this could reflect the fact that the fronts of the more compatible elements did not reach most of the nodules, in which case their concentrations would still reflect older melting events (Dupuy et al. 1986).

Lacking any information about the spatial relations of the nodules prior to eruption, we cannot estimate the size of the chromatographic column that could have produced the patterns shown in figure 5. These patterns could be the result of a large-scale column of the kind discussed above, or of a smaller-scale chromatographic process operating outward from walls of dikes that intersected the source region. Melt tapped by the matrix may have contributed to the high REE concentrations of the suite (as suggested by petrographic data; Dupuy et al. 1986). However, the correlation of the deviation from a straight mixing line with the element incompatibility strongly suggests the operation of a chromatographic process in the source region of the Hoggar peridotitic nodules.

b. Island arc magmatism: matrix cross-feeding. An obvious environment for application of the chromatographic concept is in the source regions of island arc magmas. Fluids generated in the upper parts of subducting slabs are thought to interact extensively with the overlying mantle as they flow through it. Melts which form either in the subducted slab or in the mantle wedge above it can percolate upward and interact with overlying mantle material. The chromatographic column is a useful point of reference for thinking about the nature of this interaction. A number of authors (e.g., Nicholls and Ringwood 1973; Marsh and Kantha 1978; Mysen 1979) have anticipated aspects of the consequences of this process, and Myers et al. (1985) discuss an example where they think they can see petrochemical features that have time dependencies similar to those that might be expected in the output of a chromatographic system.

In an important respect, the situation above a subducting slab will differ from the simple case upon which we have been focusing. Suppose that the source region for the fluids or melts is fixed relative to the island arc (fig. 6). The mantle wedge convects as the fluids percolate upward through it. In the context of our chromatographic column, this amounts to a continuous replenishment of the column matrix. In this section, we examine some of the consequences of this lateral movement of material into and out of the chromatographic column and suggest how this may relate to the compositions of magmas delivered to island arc volcanoes.

Consider a simple, two-dimensional model of our ideal column (local equilibrium, negligible dispersion). A column of length *L* and width *W* (fig. 6) is cross-fed by the convective flow in the mantle wedge. Fluids penetrate the column from below and percolate upward with a velocity $\bar{V}_p$. Fresh matrix is introduced on the left-hand side and passes through the column with a velocity $\bar{V}_s$. Concentration fronts migrate upward while at the same time they are carried sideward and downward with the matrix. A steady-state situation is reached after the matrix migrates the whole width of the column or when the concentration front reaches the top of the column. As shown in detail in Appendix B, fronts of incompatible elements are carried only small

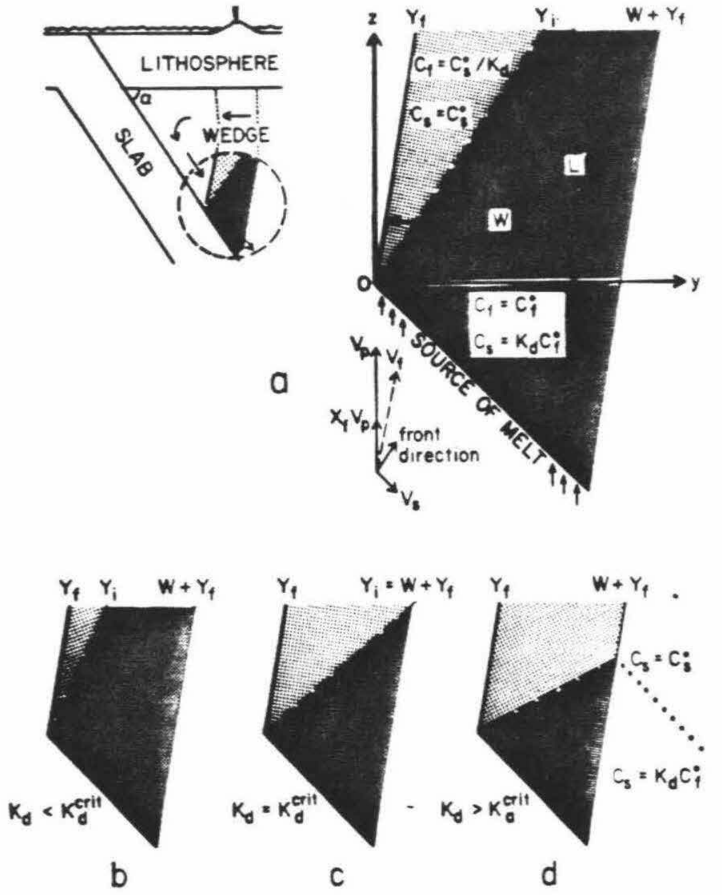

FIG. 6.—Schematic representation of matrix cross-feeding below island arcs. (*a*) Melts which form in the subducted slab or in the wedge above it percolate upward through a column of wedge material. Fresh material is introduced by convection. Melt percolates upward at velocity $\bar{V}_p$ and is moved with the matrix which is fed in at velocity $\bar{V}_s$. Melt that originates at the lower left corner of the column (0) emerges at Y_f. A concentration front of a trace element *i* travels at a lower velocity, $X_f \bar{V}_p$, is carried further by the matrix, and emerges at Y_i. Melts emerging to the left of Y_i have a composition $C_f = C_s^o / K_d$; those emerging to the right retain their initial composition, C_f^o. The position of Y_i depends on the element compatibility, and three cases are illustrated: (*b*) An incompatible element. Most of the melt emerges with the same concentration as in melt introduced into the base of the column. (*c*) $K_d = K_d^{crit}$. Y_i coincides with the right edge of the column. The concentration and isotopic composition of this element in melts emerging at the top is in equilibrium with the matrix and does not reflect the original source region. (*d*) A compatible element. Its concentration in the melt is as in (*c*). Matrix coming out of the column is zoned with respect to this element. At the lower part it is in equilibrium with the melt introduced at the bottom, $C_s = K_d C_f^o$; in the upper part the matrix has not been changed by interaction with melt.

distances with the matrix, and most of the fluids pass the column unaltered (fig. 6*b*). Fronts of compatible elements are carried through the entire column width, and the fluid emerging from the top of the column is completely altered and is in equilibrium with the original matrix composition (fig. 6*d*).

If, as a first approximation, the subduction angle, α, is taken to be zero, the critical K_d value, above which the composition of a certain element in the fluid is controlled by the wedge composition only and does not reflect the original fluid composition, is shown in Appendix B to be:

$$K_d^{crit} \approx \frac{W V_p \phi}{L V_s}. \qquad \text{(B8)}$$

$WV_p\phi = G$ is the flux of melt through the two-dimensional column, and should be equal to the rate of growth of the arc. A recent estimate of this rate (Reymer and Schubert 1984) is 30 km^2/Ma, so for a choice of $L = 10$ km and $V_s = 3$ cm/year, the critical value is $K_d^{\text{crit}} \sim 0.1$. In other words, all elements with $K_d > 0.1$ will emerge from the mantle column in equilibrium with the initial wedge composition. Only more incompatible elements will reflect contributions of other sources, i.e., the subducted oceanic crust or sediments. The choice of $L = 10$ km (i.e., the distance over which melt percolates along grain boundaries) is somewhat arbitrary. Larger values would lead to decreases in K_d^{crit} and to a greater imprint of the mantle wedge on the compositions of erupted magmas.

If the slope of the subduction zone is included in the calculation (equation B7), K_d^{crit} may be an order of magnitude lower than the value given in equation (B8) for reasonable choices of parameters. Our analysis shows that a 10-km column can significantly affect the trace element contents of melts that percolate through the wedge overlying the subducting slab. Elements such as the heavy and intermediate REE would reflect only the composition of the mantle wedge. Hf or Nd isotopes would reflect only slight contributions from other sources. Fronts of more incompatible systems such as Pb and, to a lesser degree, Sr do pass through the column, and their isotopic composition may reflect contributions from the subducted oceanic crust or sediments. The same is true for incompatible element concentrations such as Cs or Ba.

Based on our analysis, the contribution of the subducted oceanic crust and sediments is expected to be large for arcs with high ratios of growth rate over subduction velocities (G/V_s) and with shallow subduction angles (equation B7). Though other parameters must also affect the contribution of the subducted sediment component, it is interesting to note that the Lesser Antilles, where large contributions from subducted sediments have been suggested (White and Patchett 1984), is characterized by extremely high G/V_s ratio (Reymer and Schubert 1985) and relatively shallow subduction angles (45°; Molnar and Atwater 1978) compared with other arcs.

c. Comagmatic alkaline basalts and tholeiites. The nature of the relationship between comagmatic tholeiitic and alkaline basalts remains one of the most enigmatic problems in petrogenesis. One possible explanation is that alkaline magmas evolve from tholeiitic liquids by interaction with the peridotitic wallrocks that they traverse en route to the surface (e.g., Harris 1957; Green and Ringwood 1967). Recent isotopic and trace element data of tholeiitic and alkaline suites from Hawaiian volcanoes (e.g., Chen and Frey 1985) as well as from southeastern Australia (McDonough et al. 1985) indicate that both suites reflect the mixing of melts from at least two sources. Chen and Frey have suggested a model in which a tholeiitic melt formed by high degree of partial melting of an undepleted "plume" source is physically mixed with variable quantities of melt formed by low degree of partial melting of a depleted mantle similar in composition to the source regions of mid-ocean ridge basalts (MORB).

It is possible to produce similar effects by letting the melts of the plume source penetrate and percolate through an initially unmolten column of MORB source composition. The characteristics of the incipient partial melting of the MORB source reservoir are then "injected" through reaction and ion-exchange, rather than through physical mixing of magmas. The column can "mix" the two end members in all needed proportions. The resultant REE patterns would be similar to those of figures 2*b* and 3*b*. Though details would depend on the specific parameters chosen, early melts have trace element characteristics similar in important respects to Hawaiian alkaline basalts (i.e., REE patterns similar to small degrees of partial melting of the column matrix, isotopic signature dominated by the contribution of the MORB source end member). As more and more melt percolates through the column and its ability to affect melt composition is diminished, the melt composition gradually changes toward that of the tholeiitic melt being continuously introduced at the base of the column. Thus, as anticipated long ago by Harris and by Green and Ringwood, wallrock interaction is indeed capable of producing melts similar to alkali olivine basalts, at least with respect to their trace element characteristics. It is not clear that the incipient melt of the depleted column matrix has the undersaturation with respect to silica that is the defining characteristic of the alkaline suite.

Such a scenario must, however, be an extreme simplification of any possible natural plumbing system. While it may be applied to the early alkaline lavas of a Hawaiian volcano (e.g., Loihi Seamount; Moore et al. 1982) or to the formation of small alkaline volcanic centers, it clearly fails to explain certain major features of the later phases of Hawaiian volcanism. In particular, during the transition from the early alkaline stage to the main tholeiitic stage, the simple, static column is all used up. Thus the tholeiites must be, in the context of this scenario, the unmodified melt of the plume source. For this reason, we cannot easily account for the variability in trace element and isotopic composition observed in tholeiites of different Hawaiian volcanoes. More obviously, we cannot produce the enrichment of incompatible elements observed in the late transitional and alkaline phases.

In order to produce the observed sequence and to explain the late phases of Hawaiian volcanism, we must invoke the introduction of fresh column material. One mechanism for introducing fresh matrix is through cross-feeding by mantle convection (fig. 7), similar to the case presented for island arcs. During the shield-building tholeiitic stage, the high flux of plume material overcomes the replenishment of the matrix, and melt composition is barely changed from its initial tholeiitic composition. During the later stages the plume flux is weaker and the contribution of the cross-fed MORB source-like matrix is more pronounced. Using equation (B9) of Appendix B, and the estimated volcanic fluxes of Feigenson and Spera (1981), critical aspects of the geochemistry of the observed sequences of Hawaiian lavas can be reproduced by ion exchange processes. In particular, we can reproduce the same gross characteristics that Chen and Frey (1985) achieved when they postulated that during the alkalic stage the contribution of the MORB source-like matrix is of higher proportion and its composition is closer to that produced by incipient melting. Still, we cannot readily explain the variability of tholeiitic basalt compositions of different centers, since the flux of the cross-fed matrix would not be sufficient to alter significantly the composition of the plume-derived melts. Richter and McKenzie (1984) encountered a similar problem when they considered another model for the volcano plumbing system. This difficulty seems to be independent of the plumbing system chosen or the mixing mechanism of the two end members used. This, along with recent isotopic studies (e.g., Stille et al. 1983; Staudigel et al. 1984; Hegner et al. 1986), may suggest the need for additional components to account for the variability in trace elements and isotopic composition of Hawaiian tholeiites.

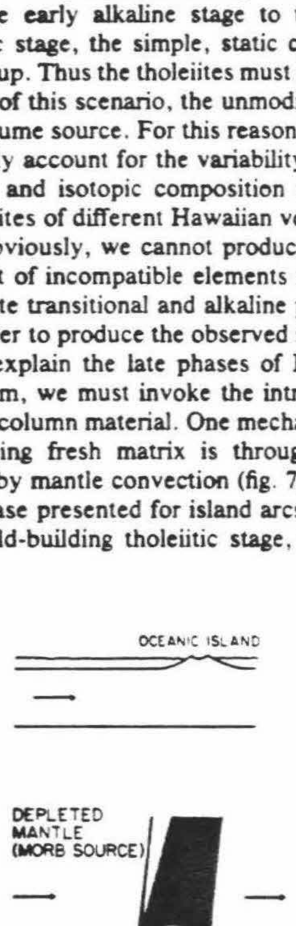

FIG. 7.—Schematic representation of cross-feeding below an oceanic island. Melt rises from a melting plume and percolates through a region of depleted mantle above the plume. Mantle convection cross-feeds fresh column material into the column region so that a steady-state situation evolves, analogous to that presented in figure 6.

CONCLUSIONS

As magmas rise from their source regions toward the surface, it is inevitable that they will traverse regions of the mantle and crust with which they are not in equilibrium; to the extent that time and the intimacy of their physical contact permit, the melts and country rocks will interact chemically. In this paper, we have suggested that regions of the mantle can be treated as chromatographic columns and that, as melts and other fluids flow through these regions, aspects of their chemical interaction can be modeled in terms of a simple ion-exchange process. The implications for trace element systematics are straightforward: The composition of melt emerging from the top of the column evolves from close to that of the incipient melt of the column matrix toward that of the melt introduced into the base of the column. The rate of evolution is faster in the incompatible than in the compatible elements and as a result the abundance ratios of elements of different compatibilities can vary considerably with time.

If diffusion and other dispersive processes in the melt are negligible and if exchange between melt and solid rock is rapid, extreme fractionations may occur, and the change from initial to final concentration for each element can be through an abrupt concentration front. The abruptness of this change may be softened by dispersive processes within the column, by gradual change with time of the composition of the melt flowing into the column, or by integrating and mixing the column output.

If the matrix material is not replenished, the chromatographic process is a transient phenomenon. However, in some geological situations (e.g., under island arcs and oceanic islands), fresh matrix may be fed continuously into the column, leading to the evolution of a steady state.

We have demonstrated that aspects of the geochemistry of ultramafic rocks and comagmatic alkaline and tholeiitic magmas might be explained by the operation of chromatographic columns. This is not sufficient to prove that such processes did play a role, since combinations of other petrogenetic processes could undoubtedly produce similar petrological characteristics. We emphasize that we consider it extremely unlikely that chromatographic columns will operate exclusive of other processes. In particular, if melt and matrix are not in thermal and major element equilibrium, crystal fractionation and/or melting of the matrix must accompany the ion-exchange processes upon which we have focused. In addition, spatial and temporal variations in source composition and in the degree of partial melting will influence the compositions of melts introduced into our hypothetical columns. Mixing, assimilation, crystal fractionation, and other magma chamber processes will typically place their marks upon the output of such columns.

Nevertheless, the raw output of a mantle chromatographic column should, according to our analysis, be easy to recognize, and though its characteristic fingerprints may be masked or mimicked by other processes, they should be identifiable, if present, through study of the temporal evolution of trace element systematics of volcanic suites, especially if elements across a wide range of compatibilities are examined.

ACKNOWLEDGMENTS.—We have benefited from discussions with D. Scott, D. Stevenson, B. Hager, F. Richter, B. Marsh, and G. J. Wasserburg, and from reviews by M. Seitz, C. Langmuir, and F. Richter. This work has been supported by NASA Grant NAG 9-105 to E. Stolper and NSF Grant EAR-84-18353 to D. Stevenson. Caltech Division of Geological and Planetary Sciences contribution number 4350.

APPENDIX A: THE NUMERICAL SOLUTION

If dispersion in the fluid is neglected so that mass transport into and out of the elemental volume is by advection only, the evolution of the trace elements in the column can be modeled using the STOP-GO algorithm (Sweed and Wilhelm 1969). The advection is represented by the GO phase in which the fluid is advanced a distance Δz. Then during the STOP phase the stationary fluid interacts with the matrix for time $\Delta t = \Delta z/V_f$.

Diffusion in the spherical grains is governed by:

$$\frac{\partial C_r(z,r,t)}{\partial t} = D_s\left[\frac{\partial^2 C_r(z,r,t)}{\partial r^2} + \frac{2}{r}\frac{\partial C_r(z,r,t)}{\partial r}\right] \quad \text{(A1)}$$

where $C_r(z,r,t)$ is the concentration at radius r within a grain located at distance z from the bottom of the column at time t. The boundary conditions are determined by the spherical symmetry and the following assumptions: (a) Grain surfaces are always in equilibrium with the fluid:

$$C_r(z,a,t) = K_d C_f(z,t) \quad \text{(A2)}$$

(b) The fluid is of limited volume so its concentration is related to the average concentration in the grain, $C_s(z,t)$, by:

$$\begin{aligned}\phi\rho_f \frac{\partial C_f(z,t)}{\partial t} &= -(1-\phi)\rho_s \frac{\partial C_s(z,t)}{\partial t}\\ &= -(1-\phi)\rho_s \frac{3}{a^3} \quad \text{(A3)}\\ &\quad \cdot \frac{\partial}{\partial t}\left[\int_0^a C_r(z,r,t) r^2 dr\right]\end{aligned}$$

(c) The fluid is homogeneous at all times; this assumption is justified because diffusion in the fluid is six to seven orders of magnitude faster than that in the solid.

Equation (A1) was solved numerically using the Crank-Nicolson algorithm. We chose to describe the change in fluid composition by equation (A3), rather than by Fick's first law, since the numerical evaluation of the integral is more accurate than the evaluation of $\partial C_s/\partial r$ at $r = a$, where a singularity may exist. Typically we used $L/\Delta z = 20$, $a/\Delta r = 75$, and updated the fluid concentration five times during each of the STOP phases. The accuracy of the numerical technique was checked by comparing the numerical and the analytical solutions for the case of static fluid and by comparing solutions obtained using different grid sizes.

The results of some sample calculations are presented in figure 3*a*, and are characterized by (a) faster migration of the fronts compared with the equilibrium case, and (b) different amounts of dispersion for fronts of different elements. The numerical solution is a function of two independent, dimensionless parameters: X_f, and $D_s t_c/a^2$ (which is the ratio of the advective (t_c) and diffusive (a^2/D) time scales).

An approximate expression for the front position in time that involves these two parameters and that will simplify application of our treatment to situations other than those we have considered may be obtained by considering the following situation: Ahead of its front, a trace element in the fluid is in equilibrium with the matrix. Behind the front, fluid concentration is constant, C_f°, and the matrix composition is controlled by a simple diffusion law (Glueckauf 1955):

$$\frac{\partial C_s}{\partial t}(z,t) = \alpha(C_f K_d - C_s) \qquad \text{(A4)}$$

where α is a parameter that includes the diffusion coefficient and other column parameters. Assuming that all fronts are sharp, and that to the first order their velocity may be taken to be constant, we can solve for $C_s(z,t)$ and calculate the average concentration in the solid behind the front:

$$\begin{aligned}\bar{C}_s(t) &= \frac{1}{z_{\text{front}}}\int_o^{z_{\text{front}}} C_s(z,t)\,dz \\ &= K_d C_f^\circ\left[1 - \frac{1 - \exp(-\alpha t)}{\alpha t}\right]\end{aligned} \qquad \text{(A5)}$$

Repeating the mass balance calculation (equation 4), we obtain

$$\frac{z}{Z} = \frac{\phi\rho_f}{\phi\rho_f + (1 - \phi)\rho_s K_d\left[1 - \dfrac{1 - \exp(-\alpha t)}{\alpha t}\right]} \qquad \text{(A6)}$$

Fitting equation (A6) against the numerical results, we obtain very good agreement (better than 7%) using:

$$\begin{aligned}\alpha &= \frac{4\pi D_s}{a^2}\cdot\frac{1 - \phi}{\phi}\frac{\rho_s}{\rho_f}K_d \\ &= \frac{4\pi D_s}{a^2}\frac{1 - X_f}{X_f}\end{aligned} \qquad \text{(A7)}$$

for $0.01 < D_s t/a^2 < 1$ and $0.1 < (1 - \phi)\rho_s K_d/\phi\rho_f = (1 - X_f)/X_f < 2$. The physical situation described by equation (A6) is that of a concentration front which moves with the melt ($V_{\text{front}} = V_f$) at $t = 0$ and relaxes to the equilibrium velocity ($V_{\text{front}} = V_f X_f$) for long times. The decay time is shorter for compatible elements than for incompatible ones.

The shape of the dispersed front can be approximated by equations of the form of equation (11) provided that: z_{front} is calculated using equations (A6) and (A7); an additional term is added in order to ensure that at the fluid front ($z = V_f t$) fluid concentration decays to the equilibrium value, $C_f = C_s^\circ/K_d$; and the diffusion coefficient of the fluid, D_f, is replaced by:

$$\text{“}D\text{”} = \frac{a^2 V_f^2}{4\pi D_s}X_f(1 - X_f). \qquad \text{(A8)}$$

Glueckauf (1955) suggested a similar expression for "D," but did not consider the faster rate of migration of the fronts compared with the equilibrium case. In a given column, elements with $X_f \sim 0.5$ ($K_d \sim \phi$) will be dispersed by the largest amount.

APPENDIX B: MATRIX CROSS-FEEDING

Consider a simple model where fluid is introduced at the bottom of a column of width W (fig. 6) and matrix is fed in a uniform velocity at an angle α to the horizontal. Such a column reaches a steady state for a certain element

$$\left(\frac{\partial C_f}{\partial t}\right)_{y,z} = \left(\frac{\partial C_s}{\partial t}\right)_{y,z} = 0 \qquad \text{(B1)}$$

either when the concentration front reaches the top of the column or after the matrix migrates across the full column width. If dispersive processes are negligible, then a simplified form of equation (1a) describes the mass balance of the advecting fluxes of trace elements by fluid and matrix flowing through the column:

$$\phi\rho_f\bar{V}_f\bar{\nabla}C_f = -(1 - \phi)\rho_s\bar{V}_s\bar{\nabla}C_s. \qquad \text{(B2)}$$

Assuming instantaneous local equilibrium, this becomes:

$$X_f \bar{V}_f \bar{\nabla} C_f = -(1 - X_f)\bar{V}_s \bar{\nabla} C_f. \qquad \text{(B3)}$$

V_f is the vector sum of the percolation velocity relative to the static matrix V_p and the matrix velocity V_s. Separating the velocities into their y and z components, substituting into equation (B3), and rearranging yields:

$$\frac{\partial C_f}{\partial z} = -\frac{V_s \cos\alpha}{X_f V_p - V_s \sin\alpha}\frac{\partial C_f}{\partial y}, \qquad \text{(B4)}$$

which means that C_f is constant along lines of slope

$$\frac{\partial z}{\partial y} = \frac{X_f V_p - V_s \sin\alpha}{V_s \cos\alpha} \qquad \text{(B5)}$$

and in particular the position of the concentration front $[C_f = C_f^\circ + 0.5(C_s^\circ/K_d - C_f^\circ)]$ also lies in this direction.

This result can also be visualized in the following way: from the time the wedge material starts its way across the column, a flux of fluid is penetrating it. While the wedge moves a distance $dy = V_f \cos\alpha dt$, the melt percolates upward by $(V_p - V_s \sin\alpha)dt$, and the front, being slower, migrates a distance $dz = (X_f V_p - V_s \sin\alpha)dt$. The combined effect is the same as given by equation (B5).

Equation (B5) can be used to calculate the front position at the top of the column (Y_i in fig. 5). If $Y_i > Y_f + W$, where Y_f is the displacement of the fluid itself along the y direction and W the width of the column, then the front does not reach the top of the column. All fluid coming out is in equilibrium with the matrix and has $C_f = C_s^\circ/K_d$. Y_i depends on X_f (equation B5) and hence on K_d. Fronts of incompatible elements may pass the column, but above a certain degree of compatibility, no matter what the input is, the output is characterized by the matrix only.

The critical K_d value can be calculated from:

$$Y_i - Y_f = \frac{LV_s \cos\alpha}{X_f V_p - V_s \sin\alpha} - \frac{LV_s \cos\alpha}{V_p - V_s \sin\alpha} < W \qquad \text{(B6)}$$

which yields

$$K_d^{\text{crit}} = \frac{WV_p \phi \rho_f}{LV_s(1 - \phi)\rho_s} \cdot \frac{\left(1 - \frac{V_s}{V_p}\sin\alpha\right)^2}{\cos\alpha + \frac{W}{L}\sin\alpha\left(1 - \frac{V_s}{V_p}\sin\alpha\right)} \qquad \text{(B7)}$$

If, as a first approximation, the subduction angle, α, is taken to be zero, then:

$$K_d^{\text{crit}} < \frac{WV_p \phi \rho_f}{LV_s(1 - \phi)\rho_s} \approx \frac{WV_p \phi}{LV_s} = \frac{G}{LV_s} \qquad \text{(B8)}$$

$G = WV_p\phi$ is the flux of melt through the two-dimensional column. In the case of the island arc, this flux is equal to the rate of growth of the arc per unit length of arc. In the three-dimensional case of hot spot volcanism (i.e., Hawaii), the column width and length have to be replaced by cross-sections in order to relate K_d^{crit} to the rate of growth.

$$K_d^{\text{crit}} = \frac{G'}{LWV_s} \qquad \text{(B9)}$$

The incompatible element composition in melts emerging from the column is only partially affected by the matrix contribution. Averaging the column output over the entire width, the average concentration of elements with $K_d < K_d^{\text{crit}}$ is

$$C_f = \frac{C_s^\circ}{K_d}\left(\frac{Y_i - Y_f}{W}\right) + C_f^\circ\left(1 - \frac{Y_i - Y_f}{W}\right). \qquad \text{(B10)}$$

From equations (B6) and (B8) it follows that

$$(Y_i - Y_f)/W \approx K_d/K_d^{\text{crit}} \qquad \text{(B11)}$$

and

$$C_f \approx C_f^\circ + \frac{C_s^\circ - K_d C_f^\circ}{K_d^{\text{crit}}} \qquad \text{(B12)}$$

for incompatible elements with $K_d < K_d^{\text{crit}}$.

REFERENCES CITED

Bear, J., 1972, Dynamics of Fluids in Porous Media: New York, American Elsevier, 764 p.

Boettcher, A. L., and O'Neil, J. R., 1980, Stable isotope, chemical, and petrographic studies of high-pressure amphiboles and micas: evidence for metasomatism in the mantle source regions of alkali basalts and kimberlites: Am. Jour. Sci., v. 280A, p. 584–621.

Chen, C. Y., and Frey, F. A., 1985, Trace element and isotopic geochemistry of lavas from Haleakalea volcano, East Maui, Hawaii: implications for the origin of Hawaiian basalts: Jour. Geophys. Res., v. 90, p. 8743–8768.

DePaolo, D. J., and Wasserburg, G. J., 1976, Nd isotopic variations and petrogenetic models: Geophys. Res. Letters, v. 3, p. 249–252.

Dulien, F. A. L., 1979, Porous Media Fluid Transport and Pore Structure: New York, Academic Press, 396 p.

Dupuy, C.; Dostal, J.; Dautria, J. M.; Girod, M., 1986, Geochemistry of spinel peridotite inclusions in basalts from Hoggar, Algeria: Jour. African Earth Sci., v. 5, p. 209–215.

Feigenson, M. D., and Spera, F. J., 1981, Dynamical model for temporal variation in magma type and eruption interval at Kohala volcano, Hawaii: Geology, v. 9, p. 531–533.

Freer, R., 1981, Diffusion in silicates minerals and glasses: a data digest and guide to literature: Contrib. Mineral. Petrol., v. 76, p. 440–454.

Frey, F. A.; Green, D. H.; and Roy, S. D., 1978, Integrated models of basalt petrogenesis: a study of quartz tholeiites to olivine melilites from southern Australia utilizing geochemical and experimental petrological data: Jour. Petrol., v. 19, p. 463–513.

———; Suen, C. J.; and Stockman, H. W., 1985, The Ronda high temperature peridotite: geochemistry and petrogenesis: Geochim. Cosmochim. Acta, v. 49, p. 2469–2492.

Glueckauf, E., 1955, Theory of chromatography: Trans. Faraday Soc., v. 51, p. 34–44.

Green, D. H., and Ringwood, A. E., 1967, The genesis of basaltic magmas: Contrib. Mineral. Petrol., v. 15, p. 103–190.

Harris, P. J., 1957, Zone refining and the origin of potassic basalts: Geochim. Cosmochim. Acta, v. 12, p. 195–208.

Hart, S. R., and Allegre, C. J., 1980, Trace element constraints on magma genesis, *in* Hargraves, R. B., ed., Physics of Magmatic Processes: New Jersey, Princeton University Press, p. 121–159.

Hegner, E.; Unruh, D.; and Tatsumoto, M., 1986, Nd-Sr-Pb isotope constraints on the sources of West Maui volcano, Hawaii: Nature, v. 319, p. 478–480.

Hofmann, A. W., 1972, Chromatographic theory of infiltration metasomatism and its application to feldspars: Am. Jour. Sci., v. 272, p. 69–90.

———, 1984, Mantle evolution by crustal recycling or by mantle metasomatism? (abs.): Terra Cognita, v. 4, p. 82.

Irving, A. J., 1980, Petrology and geochemistry of composite ultramafic xenoliths in alkalic basalts and implications for magmatic processes within the mantle: Am. Jour. Sci., v. 280A, p. 389–426.

Korzhinskii, D. S., 1970, Theory of Metasomatic Zoning (translated by Jean Agrell): Oxford, Clarendon Press, 162 p.

Magaritz, M., and Hofmann, A. W., 1978, Diffusion of Eu and Gd in basalt and obsidian: Geochim. Cosmochim. Acta, v. 42, p. 847–858.

Marsh, B. M., and Kanta, L. H., 1978, On the heat and mass transfer from an ascending magma: Earth Planet. Sci. Letters, v. 39, p. 435–443.

McDonough, W. R.; McCulloch, M. T.; and Sun, S. S., 1985, Isotopic and geochemical systematics in Tertiary-Recent basalts from southeastern Australia and implications for the evolution of the sub-continental lithosphere: Geochim. Cosmochim. Acta, v. 49, p. 2051–2068.

McKenzie, D. P., 1984, The generation and compaction of partial melts: Jour. Petrol., v. 25, p. 713–765.

———, 1985, The extraction of magma from the crust and mantle: Earth Planet. Sci. Letters, v. 74, p. 81–91.

Menzies, M.; Kempton, P.; and Dungan, M., 1985, Interaction of continental lithosphere and asthenospheric melts below Jeronimo volcanic field, Arizona, U.S.A.: Jour. Petrol., v. 26, p. 663–693.

Molnar, P., and Atwater, T., 1978, Interarc spreading and cordilleran tectonics as alternates related to the age of subducted oceanic lithosphere: Earth Planet. Sci. Letters, v. 41, p. 330–340.

Moore, J. D.; Clague, D. A.; and Normark, W. R., 1982, Diverse basalt types from Loihi Seamount, Hawaii: Geology, v. 10, p. 88–92.

Myers, J. D.; Marsh, B. D.; and Sinha, A. K., 1985, Strontium isotopic and selected trace element variations between two Aleutian volcanic centers (Adak and Atka): implications for the development of arc volcanic plumbing systems: Contrib. Mineral. Petrol., v. 91, p. 221–234.

Mysen, B. O., 1979, Trace element partitioning between garnet peridotite minerals and water rich vapor: experimental data from 5 to 30 kbar: Am. Mineral., v. 64, p. 274–287.

Nicholls, I. A., and Ringwood, A. E., 1973, Effect of water on olivine stability in tholeiites and production of silica-saturated magmas in the island arc environment: Jour. Geology, v. 81, p. 285–300.

Norton, D., and Taylor, H. P., Jr., 1979, Quantitative simulation of the hydrothermal systems of crystallizing magmas on the basis of transport theory and oxygen isotope data: An analysis of the Skaergaard intrusion: Jour. Petrol., v. 20, p. 421–486.

Pallister, J. A., and Knight, R. J., 1981, Rare earth element geochemistry of the Samail ophiolite near Ibra, Oman: Jour. Geophys. Res., v. 86, p. 2673–2697.

Prinzhofer, A., and Allegre, C. J., 1985, Residual peridotite and the mechanism of partial melting: Earth Planet. Sci. Letters, v. 74, p. 251–265.

Quick, J. E., 1981, Petrology and petrogenesis of the Trinity peridotite: an upper mantle diapir in the eastern Klamath mountains, northern California: Jour. Geophys. Res., v. 86, p. 11837–11863.

Reymer, A., and Schubert, G., 1984, Phanerozoic addition rates to the continental crust and crustal growth: Tectonics, v. 3, p. 63–77.

Ribe, N. M., 1985, The generation and composition of partial melts in the earth's mantle: Earth Planet. Sci. Letters, v. 73, p. 361–376.

Richter, F. M., 1986, Simple models for trace element fractionation during melt segregation: Earth Planet. Sci. Letters, v. 79, p. 333–344.

———, and McKenzie, D., 1984, Dynamical models for melt segregation from deformed matrix: Jour. Geology, v. 92, p. 729–740.

Scott, D. R., and Stevenson, D. J., 1984, Magma solitons: Geophys. Res. Letters, v. 11, p. 1161–1164.

———, and STEVENSON, D., 1986, Magma ascent by porous flow: Jour. Geophys. Res., v. 91, p. 9283–9296.

SHAW, H. R.; TUCSON, E. D.; and BARGER, K. E., 1980, Volcanic periodicity along the Hawaiian Emperor chain: Am. Jour. Sci., v. 280A, p. 667–708.

SNEERINGER, M.; HART, S. R.; and SHIMIZU, N., 1984, Strontium and samarium diffusion in diopside: Geochim. Cosmochim. Acta, v. 48, p. 1589–1608.

STAUDIGEL, H.; ZINDLER, A.; HART, S. R.; LESLIE, T.; CHEN, C.-Y.; and CLAGUE, D., 1984, The isotope systematics of a juvenile intraplate volcano: Pb, Nd, and Sr isotope ratios of basalts from Loihi seamount, Hawaii: Earth Planet. Sci. Letters, v. 69, p. 13–29.

STILLE, P.; UNRUH, D. M.; and TATSUMOTO, M., 1983, Pb, Sr, Nd and Hf isotopic evidence of multiple sources for Oahu, Hawaii basalts: Nature, v. 304, p. 25–29.

STOLPER, E.; WALKER, D.; HAGER, B. D.; and HAYS, J. F., 1981, Melt segregation from partially molten source regions: the importance of melt density and source region size: Jour. Geophys. Res., v. 86, p. 6261–6271.

STOSCH, H.-G., and SECK, H. A., 1980, Geochemistry and mineralogy of two spinel peridotite suites from Dreiser Weiher, West Germany: Geochim. Cosmochim. Acta, v. 44, p. 457–470.

SWEED, N. H., and WILHELM, R. H., 1969, Parametric pumping: separation via direct thermal mode: Inc. Eng. Chem. Fundam., v. 8, p. 221–231.

WALKER, D.; STOLPER, E. M.; and HAYS, J. F., 1978, A numerical treatment of melt/solid segregation: size of the eucrite parent body and stability of the terrestrial low-velocity zone: Jour. Geophys. Res., v. 83, p. 6005–6013.

WARREN, P. H., and WASSON, J. T., 1979, The origin of KREEP: Rev. Geophys. Space Phys., v. 17, p. 73–88.

WATSON, E. B., 1982, Basalt contamination by continental crust: some experiments and models: Contrib. Mineral. Petrol., v. 80, p. 73–87.

WHITE, W. M., and PATCHETT, J., 1984, Hf-Nd-Sr isotopes and incompatible element abundances in island arcs: implications for magma origins and crust-mantle evolution: Earth Planet. Sci. Letters, v. 67, p. 167–185.

Mantle-derived fluids in diamond micro-inclusions

O. Navon, I. D. Hutcheon, G. R. Rossman & G. J. Wasserburg

Division of Geological and Planetary Sciences, California Institute of Technology, Pasadena, California 91125, USA

Micro-inclusions in diamonds from Zaire and Botswana differ in composition from the more common large inclusions of the peridotitic or eclogitic assemblages. These sub-micrometre inclusions resemble potassic magmas in their composition, but are enriched in H_2O, CO_3^{2-} *and* K_2O *and depleted in MgO. This composition represents a volatile-rich fluid or melt from the upper mantle, which was trapped in the diamonds as they grew.*

The transport of volatiles and incompatible elements in the upper mantle is dominated by the migration of fluids (melts or volatile-rich fluids). Although well studied processes such as diamond genesis and mantle metasomatism have been associated with the presence of such fluids[1-3], direct evidence on deep mantle fluids is scarce and their exact nature is still debated[3,4]. Because of its mechanical strength and chemical inertness, diamond is probably the best material for transporting such fluids to the surface. Nevertheless, no conclusive, direct observation of fluid inclusions in diamonds has been reported[5]. Infrared (IR) spectroscopic studies have indicated the presence of water and carbonate in sub-micrometre inclusions in cubic diamonds[6] and in overgrowths (coats) on the clear, inclusion-free cores of coated diamonds[7]. Instrumental neutron activation analysis (INAA) of a coated diamond indicated patterns enriched in light rare-earth elements and led Bibby[8] to suggest that the inclusions contain melt. That study was unable, however, to determine the major-element composition of the included matter.

We have studied the composition and mineralogy of the micro-inclusions in cubic and coated diamonds from Zaire and Botswana, where such diamonds are commonly found. These inclusions are rich in H_2O, CO_3^{2-}, SiO_2, K_2O, CaO and FeO. Their bulk composition resembles that of potassic magmas, such

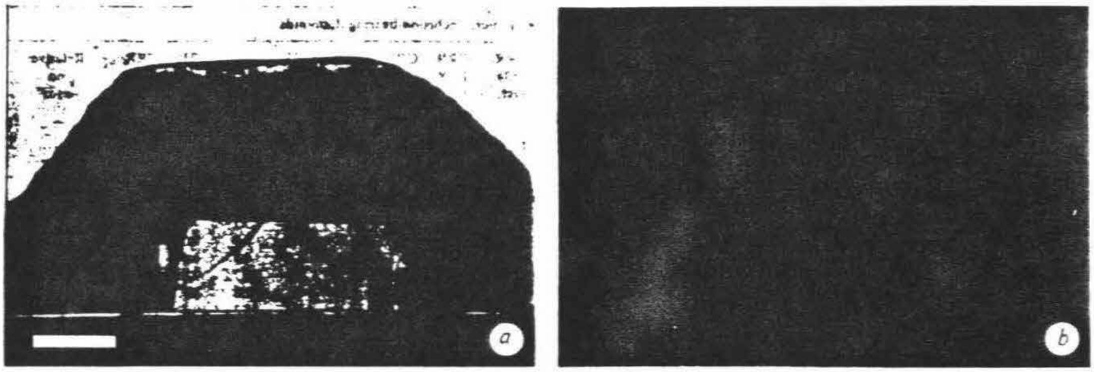

Fig. 1 Micro-inclusions in coated diamonds. *a*, A polished section of CTP LB, a coated diamond from Zaire. The transparent core is an octahedral diamond; the cuboid habit of the coat can be recognized by the development of cuboid faces at the corners. The dark parallelogram forms that run through the coat and the core are cracks. They do not disturb the concentric banding of inclusion-rich and inclusion-poor zones and are clearly late. Transmitted light, scale bar indicates 1 mm. *b*, High magnification of the core-coat boundary. Individual inclusions are of sub-micrometre size. The few larger, dark features are due to chipping of the diamond surface during polishing. Transmitted light, blue filter, scale bar represents 10 μm.

as kimberlites and lamproites, but is depleted in MgO, extremely enriched in K_2O and has a high K_2O/Al_2O_3 ratio. IR spectra indicate a mineralogical assemblage that includes hydrated sheet silicates, carbonates and phosphates; in most cases, some molecular CO_2 is also present. We infer that the bulk composition of the inclusions represents a volatile-rich fluid or melt trapped by the diamonds during their growth.

Samples and technique

The six cubic and nine coated diamonds studied here (Table 1) are translucent to opaque and vary in colour from greyish-brown to green to yellowish-green; many exhibit trigonal etch pits (trigons) and channels on their faces. The cubic diamonds fit the description of variety III and the coated diamonds are of variety IV according to the classification of Orlov[9]. X-ray topography[10,11] has shown that coats of coated diamonds and many cubic diamonds possess a fibrous internal structure in the ⟨111⟩ direction. The cores of the coated diamonds are transparent single crystals of octahedral shape.

Optical examination of the coats and the cubic diamonds reveals numerous sub-micrometre, sub-rounded inclusions, completely enclosed within optically continuous diamond (Fig. 1). In many cases the inclusions are arranged in nearly parallel arrays of isolated inclusions, perpendicular to the growth faces of the diamond. The arrays are separated by 20–80-μm thick, inclusion-free zones. In other cases the inclusions are distributed randomly. The outer rims of the diamonds are usually free of inclusions[12], while the interiors show alternating concentric bands resulting from variations in the number density of inclusions.

The diamonds were cut and polished into ~0.4–1-mm thick wafers for spectroscopic and chemical analysis. Infrared absorption spectra were obtained by Fourier transform infrared spectroscopy (FTIR); after infrared characterization the wafers were mounted in epoxy in brass holders and elemental contents were determined by electron probe microanalysis (EPMA), secondary ion mass spectrometry (SIMS) and analytical scanning electron microscopy (SEM) Fragments of some samples were analysed using INAA by the generous cooperation of B. Spettel and H. Palme at the Max-Planck-Institute für Chemie. All samples were cleaned with hot concentrated HF and HCl and were rinsed in water and ethanol to remove surface contamination. Infrared (IR) spectra were collected on a Nicolet 60SX FTIR[13] using 200–600-μm apertures. EPMA data were collected on a JEOL 733 EPMA with a 50-nA, 15-kV beam, defocused to 20 μm. Four adjacent points, covering a 40 × 40-μm area, were analysed with total counting times of 800–1,200 s. Each of the analysed areas typically contains a few hundred inclusions; an EPMA analysis therefore represents an average composition. SEM analyses of individual inclusions were made with a JEOL JSM 35CF equipped with a Tracor Northern TN-5500 energy dispersive spectrometer (EDS). A 0.075-nA, 15-kV beam was rastered over a 0.3 × 0.3-μm area centred over an inclusion. Electron probe and SEM data were reduced using a ZAF procedure[14]. The accuracy of the correction procedure was verified by analysing a graphite pellet containing 2% of glass powder of known composition.

SIMS data were obtained with PANURGE, a modified Cameca IMS-3F[15]. A 10-nA, 14.5-kV O^- beam was focused to a ~40-μm diameter spot. Positive secondary ions were analysed using a mass resolving power of $m/\Delta m = 2{,}000$, sufficient to resolve all significant molecular interferences. Detection limits were <5 parts per 10^9 for Na, Mg, K and Ca, and <500 parts per 10^9 for Al, Si, Ti and Fe; precision was much higher than that achieved by EPMA. A SIMS analysis also represents an average of a few hundred inclusions.

A key experimental issue was the determination of the SIMS ion yields, in order to calculate the concentrations of the different elements in the sputtered volumes from measured secondary ion intensities. Because diamonds containing known concentrations of the elements of interest were unavailable, ion intensities were calibrated against EPMA concentrations. Ion intensities were first normalized to the intensity of $^{12}C^+$ to correct for variations in ion yields associated with changes in operating conditions. A working curve was constructed for each element by correlating the normalized secondary ion intensities with concentrations determined by EPMA on the same inclusion-rich area of a diamond. The accuracy of the working curves was evaluated using EPMA and SIMS analyses of glass-graphite pellets containing 0.4 and 2% of glass powder of known composition. Ion yields are listed in Table 1, together with the associated 2σ errors. Errors are much larger than expected on the basis of counting statistics alone and arise chiefly from the heterogeneous distribution of inclusions in the diamonds coupled with the small difference between the analytical volumes of the EPMA and SIMS.

Each of the techniques we used samples a different volume element. The X-ray volume excitation for SEM analysis is

Table 1 Metal oxides, water and carbonate in micro-inclusion-bearing diamonds

Sample	CTP 6268 Oct.†	CTP L0 Oct.	CTP L6 Oct.	CTP LB Oct.	CTP Z4 Oct.	CTP MM1 Oct.	GRR 1503 Oct.	GRR 1504 Oct.	GRR 1508 Oct.	GRR 861.2 Cube	GRR 1155 Cube	GRR 1515 Cube	GRR 1517 Cube	GRR 1518 Cube	GRR 1519 Cube	Relative ion yields*
Source	Jwaneng, Botswana	Zaire	Zaire	Zaire	Zaire	Mbuji-Mayi Zaire	Unc.‡	Unc.	Unc.	Unk.‡	Unk.	Unc.	Unc.	Unc.	Unc.	
Points§	4	5	2	2	3	2	7	8	10	5	10	7	3	2	2	
SiO_2‖	31.9‖	41.2	43.3	34.6	67.7	40.4	35.6	42.3	42.4	51.1	53.6	45.1	30.3	42.4	45.9	800 ± 150
TiO_2	4.2	2.4	2.5	2.1	2.0	2.9	2.8	2.6	2.7	2.4	4.0	2.3	3.4	2.9	2.6	2,500 ± 1,600
Al_2O_3	2.9	6.1	5.4	5.6	5.9	4.5	3.3	4.9	4.9	5.4	4.3	4.6	5.3	4.4	4.8	11,400 ± 2,800
FeO	15.7	5.0	5.6	4.9	3.3	7.2	8.3	11.1	6.1	6.8	6.6	10.1	5.0	8.0	8.8	800 ± 400
MgO	5.7	2.8	3.8	2.3	1.3	4.6	6.1	4.6	3.6	5.7	2.6	8.0	4.3	4.9	4.9	4,300 ± 1,100
CaO	10.5	10.7	10.6	12.3	1.6	13.9	16.8	7.8	11.9	8.6	7.2	7.6	18.7	9.8	12.4	10,200 ± 1,600
Na_2O	2.6	3.0	2.9	3.5	1.0	3.8	2.9	2.3	2.4	2.1	1.0	4.8	2.7	3.4	3.4	57,000 ± 20,000
K_2O	21.4	23.7	20.8	29.7	12.3	17.7	18.6	19.4	21.1	11.6	15.5	12.4	25.2	19.3	12.1	35,000 ± 4,300
Total metal oxide (p.p.m.)¶	1,195	433	211	247	1,412	107	559	1,207	508	80	551	628	22	118	99	
H_2O (p.p.m.)#	407	191	118	140	294	165	282	619	269	98	168	241			148	
CO_2 (p.p.m.)	600	79	44	66	107	89	292	135	133	67	173	139			44	
$H_2O/(H_2O+CO_2)$ (molar ratio)	0.5	0.8	0.8	0.8	0.7	0.6	0.9	0.8	0.7	0.6	0.7			0.8		

* SIMS ion yields are in (counts per second/p.p.m.)$_{element}$/(c.p.s./p.p.m.)$_{carbon}$. Errors are estimated as 2σ of the slope of the EPMA-SIMS correlation lines.

† Oct. = coated octahedron.

‡ Unc = uncertain source, probably Zaire, according to diamond morphology (J. W. Harris, personal communication). Unk = unknown.

§ Number of SIMS analyses on each diamond.

‖ Average major oxide composition (wt %) of the volatile-free fraction of the inclusions, calculated by normalizing the total the eight metal oxides to 95%; on average, P_2O_5, BaO, SrO and the rare earth elements account for ~5% of the metal oxide fraction. Standard deviation of individual analyses from the average diamond composition is typically less than 10%.

¶ Total concentration of the above eight oxides determined by SIMS (in p.p.m.). Totals represent averages of all points analysed on each diamond. Standard deviations are typically 30%, resulting from variations in the abundance of inclusions, however it is possible that in few cases the surface analysis is not representative of the amount of matter in the whole diamond.

\# Concentration of water was calculated using $\epsilon_{3,420}$ = 80 l per mol-cm (liquid water, ref. 37). Concentration of carbonate, given in terms of p.p.m. CO_2, was estimated using $\epsilon_{1,430}$ = 250 l per mol-cm (calcite, G. Fine, personal communication). These values are believed to be representative of the absorption by the hydrous and carbonate species in the inclusions. Absorption coefficients of other carbonates (for example, Na_2CO_3, gaylucite) differ by less than 30%. The water absorption is also believed to be accurate to ~30%. The precision of the IR spectral data is ±25 p.p.m. H_2O and ±40 p.p.m. CO_2.

~2 μm in diameter, and total oxide concentration is typically a few per cent. SIMS or EPMA analyses sample the surface (1 μm depth) of a ~40-μm diameter area and total oxide concentration is a few hundred p.p.m. IR spectroscopy samples the entire wafer thickness and INAA yields element concentrations for the bulk sample. Assuming that all oxides are in the inclusions, the data are interpreted to obtain the bulk concentration of a species in a given volume (including the diamond) and the average composition of the inclusions in that volume or, in the case of SEM analysis, the composition of individual inclusions.

The constancy of both the elemental ratios from SIMS analysis and the CO_3^{2-}/H_2O ratios from FTIR analyses of individual diamonds indicate that, although the amount of trapped material is variable, the average composition of the inclusions in different zones of any one diamond is reasonably uniform. Thus, it is meaningful to compare compositional data measured by different techniques on different portions of a single diamond, as long as at least one element is measured by each technique. SIMS, SEM and INAA data can be normalized against the concentrations of K or Na that were determined by all three techniques; the comparison of SIMS and FTIR data is problematic, as we lack a common component.

Composition and mineralogy

The SIMS analyses of 15 diamonds are summarized in Table 1. The average composition of the volatile-free fraction of the micro-inclusions in each diamond is presented as the oxide weight per cent of the eight major constituents, normalized to 95%; the remaining 5% consists of other minor oxides measured only by EPMA, SEM and INAA. The total concentration of the eight metal oxides in each diamond is also shown.

Several features are apparent in the data. The total concentration of metal oxides is widely variable (20–1,270 p.p.m.), which we attribute to variation in the number density of inclusions. In contrast, the average composition of the micro-inclusions in the various diamonds is broadly similar (Fig. 2). All inclusions are rich in SiO_2, K_2O, CaO and FeO. Compositions of the metal oxide fraction in most diamonds vary within the following ranges: SiO_2, 30–53 wt %; K_2O, 12–30%; CaO, 8–19%; FeO, 6–11% (total iron as FeO); Al_2O_3, 3–6%; MgO, 2–6%; TiO_2, 2–4%; and Na_2O, 1–5%. Not shown in the table but also present are P_2O_5, 1–4%; BaO, 1–4%; SrO, 0.7–1.5%; La_2O_3, 0.1–0.3%; Ce_2O_3, 0.3–0.5%; and smaller amounts of other rare-earth elements, Mn, Th and U. K_2O/Al_2O_3 ratios are very high (2–7) and chondritic normalized Ce/Eu ratios vary between 10–21. SEM analyses of individual inclusions found 1–3% chlorine, no sulphur was detected and its content relative to the total oxide content is less than 1%.

Inclusions in three diamonds have compositions clearly distinct from that of the general population. Inclusions in CTP Z4 are much lower in CaO, MgO, K_2O and Na_2O and higher in their SiO_2 content (see Fig. 2). Inclusions in CTP 6268 (the only sample from Jwaneng, Botswana) contain 1.5 to 2 times more FeO than inclusions in other diamonds and also have high TiO_2 and MgO content. Inclusions in GRR 1515 are rich in MgO. These three samples also show distinct features in their IR spectra.

SEM analysis of individual inclusions revealed no monomineralic inclusions, but recorded the same Si, K, Ca, Fe-rich composition found by SIMS. The average composition of the inclusions in a single diamond agrees with the SIMS results.

IR spectra of inclusion-bearing zones (Fig. 3*a*) exhibit absorption bands characteristic of: (1) pure diamond; (2) type IaA nitrogen[16] (1,280, 1,220 and 480 cm^{-1}, corresponding to 500–1,100 p.p.m. nitrogen in the diamond lattice); and (3) impurities such as carbonate and water[7]. Small peaks at 1,365 (N in Fig. 3) and 3,107 cm^{-1} (C-H) are due to nitrogen platelets[16] and hydrogen[17] in the diamond matrix, respectively. The absorption features produced by the micro-inclusions were obtained as the difference between the spectra of the inclusion-bearing zones and a spectrum of clear diamond with the same amount of nitrogen. The difference spectra of the inclusion-bearing zones in all diamonds are similar and exhibit the same bands.

The intensities of the two characteristic carbonate bands at 1,430 and 876 cm^{-1} (CO_3^{2-} in Fig. 3) in different diamonds are strongly correlated. The narrow band at 876 cm^{-1} is in the same position (± 2 cm^{-1}) in all diamonds; this position is characteristic of calcite and is distinct from that in dolomite or magnesite. The two bands at 575 and 605 cm^{-1} (P) are due to phosphate absorption and are similar in position and shape to the doublet of apatite. Apatite has also been found in a TEM study of micro-inclusions in a coated diamond[18]. Molecular CO_2 is present in most but not all diamonds and gives rise to the band at 2,350 cm^{-1}. The strong bands at 1,630 and 3,420 cm^{-1} are due to H-O-H bending and O-H stretching of water, respectively. Sharp narrow bands, typical of hydroxyl groups, are not found around 3,600 cm^{-1} and must be weaker than the 3,420 cm^{-1} band, typical of the stretching vibration of molecular water. In conjunction with the relative height of the H-O-H band and the very good correlation between the intensities of the 1,630- and 3,420-cm^{-1} bands, this suggests that most water is present as H_2O molecules. No frequency shift towards ice absorption was detected at liquid nitrogen temperatures, suggesting that water is not present as a bulk aqueous phase.

The bands at 475, 525, 685, 1,000 and 1,100 cm^{-1} (S) are characteristic of silicate absorption. Their intensities are inter-correlated and are also correlated with the intensity of the water bands and of the band at 840 cm^{-1} (S1). The two bands at 785 and 812 cm^{-1} (S2) show a strong inter-correlation and a weaker correlation with the silicate bands. The S1 and S2 bands are in the spectral range characteristic of metal-OH-metal bands of micas and clay minerals. The position of all the silicate bands (S, S1, S2) and the good correlation between the intensities of the main silicate and water bands are best explained by the presence of heavily hydrated clay minerals. The presence of more than one silicate phase is indicated by the lack of correlation between the intensities of the S1 and S2 bands. The inclusions in diamonds CTP Z4 and CTP 6268 are of extreme chemical compositions (Fig. 2) and show contrasting and extreme IR spectra. CTP Z4 has intense S2 and 1,100-cm^{-1} bands. CTP 6268 has no S2 bands, but has intense S1 and 1,000-cm^{-1} bands. The intensities of the different S bands in these two diamonds do not exhibit the good correlations observed for other diamonds. The intensities of the carbonate bands, the silicate-water bands and the phosphate bands show only a weak correlation, probably because of varying proportions of the three phases in different diamonds. Olivine, pyroxene and garnet have some characteristic lines which were not detected and therefore cannot be significant components of the inclusions.

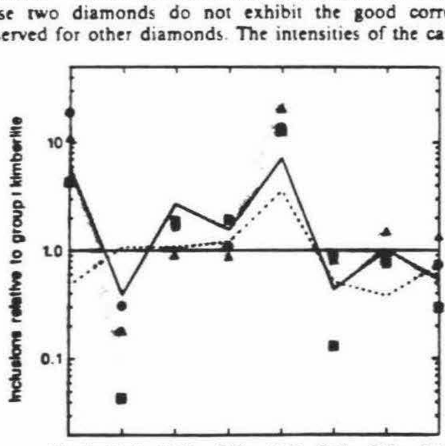

Fig. 2 Major-element abundances in diamond micro-inclusions relative to average group I kimberlite[38]. Stippled area represents all diamonds of Table 2 except CTP Z4 (■), CTP 6268 (▲) and GRR 1515 (●). Solid line indicates an average for lamproite[39]; dashed line represents group II kimberlites[38].

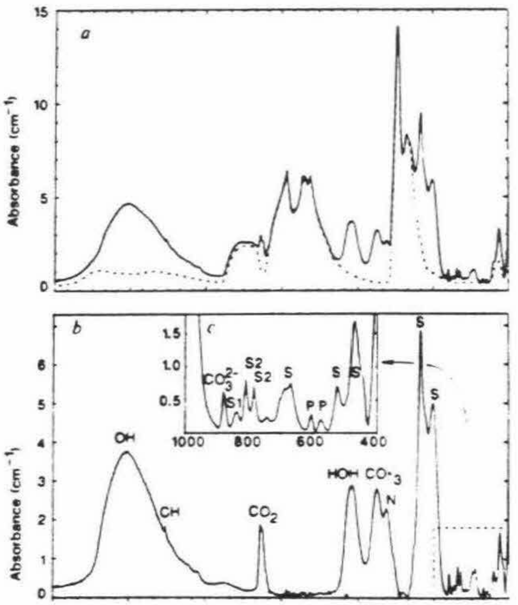

Fig. 3 *a*, IR spectrum of turbid diamond GRR 1515 (solid line) and a synthetic, composite, reference spectrum of a pure diamond plus the appropriate amount of type IaA nitrogen centres (dashed line). *b*, IR absorbance resulting from micro-inclusions in GRR 1515, obtained as the difference between the two spectra in *a*. *c*, Details of the low wavenumber region of *b*.

The total water and carbonate concentrations for each diamond studied by IR spectroscopy are presented in Table 1; concentrations of water and carbonate were calculated using absorption coefficients of pure water and calcite (see footnotes to Table 1). The concentrations of both species are quite variable, spanning the range ~44-600 p.p.m., with water being more abundant in all diamonds (molar proportions). Water-to-carbonate ratios vary among the different samples but are uniform throughout individual diamonds. As SIMS and FTIR sample different components in different volumes, an accurate determination of the relative proportions of water or carbonate in the inclusions is difficult. Accurate estimation will be achieved only when the same volume is analysed by FTIR and a bulk chemical analysis (such as INAA). At present, we can only estimate that water and the CO_2 component of the carbonate account together for ~40% of the total weight of the inclusions in most diamonds (Table 1). The absorption coefficient of molecular CO_2 depends strongly on pressure and its concentration cannot be well constrained. Rough estimates suggest that the CO_2 content is much less than the CO_3^{2-} content.

Mantle-derived fluids

Micro-inclusions in cubic and coated diamonds are rich in H_2O, CO_3^{2-}, SiO_2, K_2O, CaO and iron oxide. Their composition and IR spectra are not compatible with any single mineral phase or with any combination of the common phases present in large diamond inclusions[19] (such as olivine, garnet and pyroxene).

The bulk composition of the micro-inclusions does resemble that of potassic magmas, especially those of lamproites and group II kimberlites, but some important distinctions exist. Our estimate of the amounts of water and CO_2 (in carbonates) is almost an order of magnitude higher than the volatile content of lamproites and kimberlites. MgO is depleted and the enrichment of potassium and other incompatible elements is even higher than in lamproites or kimberlites.

The question arises as to whether the bulk composition of the inclusions is representative of the growth environment of the diamonds. The concentric zoning patterns are interpreted as growth features[10,11] and suggest that the micro-inclusions were formed during the growth of the diamonds. It is not possible to prove whether the chemical composition of the inclusions is primary or reflects secondary alteration. However, the inclusions appear to be completely enclosed within an optically continuous diamond matrix and kimberlitic penetration into the diamond coat is limited to less than a few micrometres[14]. In addition, the composition of the inclusions reported here is different from either the kimberlite (Fig. 2) or kimberlitic alteration products (for example, magnesian clays[20]). Thus we believe that the inclusions have retained their original bulk composition. The current mineral assemblage of hydrated sheet silicates, carbonates and phosphates may be the result of low-temperature, closed-system crystallization of the original trapped material.

The high content of volatiles and incompatible elements and the uniform average composition of the micro-inclusions suggest that the original material trapped by the diamond was a fluid, either a volatile-rich fluid or a melt. Can such fluids, containing ~40% volatiles, exist in the upper mantle? Ryabchikov and Boettcher[21] have shown that the amount of solute in potassium-rich hydrous fluids in equilibrium with phlogopite + forsterite increases with increasing pressure and reaches 50% at 30 kbar and 1,000 °C. Ellis and Wyllie[22] have estimated that, at 50 kbar pressure, near-solidus liquids in equilibrium with CO_2-H_2O fluid, forsterite and enstatite may contain 30% CO_2 and 15% H_2O. Based on these data and other experimental results, Eggler[4] has suggested that highly alkalic, dense hydrous fluids, similar in composition to that of the micro-inclusions, may exist at high pressures and that the miscibility gap between hydrous fluids and melts may be narrowed or closed in alkalic systems.

The high content of water and carbonate suggests that other volatile components are also enriched. Chlorine levels of 1-3 wt%, reported here, are indeed much higher than those of kimberlites (<0.1%). High levels of rare gases may also be expected and may explain the high $^{40}Ar/K$ ratios and the corresponding excessive apparent ages (6,000 Myr) observed in similar cubic diamonds from Zaire[23,24].

Many mantle-derived rocks document the effects of open-system interaction with fluids rich in incompatible elements (mantle metasomatism). The nature of the fluid is still debated[3,4], and in most cases there has been no direct observation of such a fluid. The high volatile content of the micro-inclusions, coupled with strong enrichment in K, Na, P, Ti and incompatible trace elements, suggests that the trapped material reported here may represent an effective metasomatizing agent.

Diamond formation

The similarity in composition of micro-inclusions in the coats of coated diamonds and in cubic diamonds is consistent with a common growth environment for the coats and for cubic diamonds, as suggested by the clustering of carbon isotope ratios from the two diamond types[25,26]. The isotope composition of the cores of the coated diamonds show no correlation with that of the coats[25-27], implying different growth conditions for the cores and coats.

The clear compositional distinction between the micro-inclusions and their host kimberlites[28] strongly suggest a xenocrystic relationship between the two. Thus, our data do not support the suggestion of Boyd *et al.*[26] that the cubic diamonds are phenocrysts in the kimberlitic melts that transported them to the surface. Rather, we suggest that the diamonds grew from the fluids represented by the micro-inclusions that they trapped.

The broad compositional resemblance of micro-inclusions and kimberlites may reflect a common origin at depth. As in the case of metasomatic fluids and alkaline melts, the identification of one phase as a precursor and the other as a reaction product is difficult, perhaps even impossible. Crystallization of kimberlitic or lamproitic melts at depth has been suggested as the origin of megacrysts[29] and of MARID xenoliths[30] found in kimberlites. During the final stages of such crystallization, the residue may evolve into a volatile- and incompatible-rich magma, or a supercritical fluid phase may separate[30,31]. If carbon saturation is also reached, diamonds may precipitate as well and could then trap those fluids or melts during their growth.

Two possible scenarios for the growth and emplacement of micro-inclusion-bearing diamonds have a number of common features and may have included the following events. A parental magma of kimberlitic affinity containing diamond xenocrysts (the cores) is intruded at depth into upper-mantle rocks. Towards the end of crystallization, a residual fluid, enriched in incompatible and volatile elements, would be produced. Growth of coats and cubic diamonds would trap the evolved residue as micro-inclusions. Metasomatism may occur through interaction between the residual fluid and adjacent mantle wall rocks. A later kimberlitic magma then transports the diamonds and the surrounding material to the surface. It seems likely that a requirement for a successful kimberlitic eruption is the presence of volatile-rich residues, left by earlier, unsuccessful events, which act to recharge the final kimberlite with enough volatiles to induce a violent ascent and eruption.

Alternatively, a lithic source, parental to kimberlitic rocks, undergoes incipient melting with the production of a volatile-rich fluid. This magma is intruded in a disruptive event during which growth of cubic diamonds and overgrowths on pre-existing cores (xenocrysts) occurs. This late-stage diamond growth possibly takes place rather rapidly and traps some of the volatile-rich fluid. The cores of coated diamonds represent an earlier stage of long-term growth in different mantle environments. Further melting of the parental lithic reservoir produces a kimberlitic magma which samples the surrounding rocks and may succeed in making its way to the surface, erupting as a kimberlite.

Richardson *et al.*[32] suggested that peridotitic garnet inclusions in diamonds equilibrated with an asthenosphere-derived melt rich in alkali, light rare-earth elements and CO_2. They further suggested that the melt remained liquid until diamond crystallization began. It was later argued[33], however, that the strong enrichment of light rare-earth elements in these garnets is too high to be explained by equilibrium crystallization from a silicate melt. The micro-inclusions in the diamonds we studied exhibit strongly fractionated rare-earth patterns. Chondrite-normalized Ce/Eu ratios of 10-21 indicate steeper patterns than those of kimberlites (7-10)[34]. Thus, the rare-earth patterns of the garnet inclusions could be explained by equilibrium crystallization from fluids similar in composition to the micro-inclusions.

If peridotitic inclusions in diamonds did equilibrate with fluids of this composition, then the partitioning behaviour of major elements between crystals and fluid must deviate significantly from the behaviour in dry basaltic systems. For example, using a typical peridotitic olivine inclusion with $Mg/(Fe+Mg) = 0.93$ (ref. 19) and the average composition of the micro-inclusions, we obtain $(Fe/Mg)_{olivine}/(Fe/Mg)_{fluid} = 0.07$, compared with a value of 0.3–0.4 in melting experiments using a dry peridotite[35].

Could micro-inclusion-bearing diamonds and diamonds carrying peridotitic inclusions be derived from the same source? Carbon isotope composition of coats and of cubic diamonds ($\delta^{13}C = -6$ to -8 (ref.26)) is in the same range as that found for the majority of peridotitic diamonds ($\delta^{13}C = -3$ to -8 (ref. 25). This similarity, as well as the strong incompatible-element enrichment of the inclusions in both types of diamonds, are consistent with this possibility. But although peridotitic inclusions and micro-inclusions have been found in separate Zairian diamonds, no diamond containing both types of inclusions has been reported. In addition, the peridotitic garnet inclusions studied by Richardson *et al.*[33] are much older than their host kimberlites, whereas evidence suggests a young age for the coated diamonds. The yellow colour of many coats of coated diamonds is attributed to the presence of single nitrogen centres[9]. Experimental study[36] has shown that at mantle temperatures, single nitrogen atoms would combine over a geologically short period, suggesting that the coats are close in age to their host kimberlites. Searches for macroscopic inclusions in micro-inclusion-bearing diamonds, isotope studies of the micro-inclusions and additional experimental data on potassium-rich systems will help clarify the relations of the two suites of diamond inclusions.

We thank J. T. Armstrong for his essential help in obtaining the EPMA and SEM results, H. Palme and B. Spettel for the INAA analyses, C. T. Pillinger for sharing his samples, data and enthusiasm, Ph. Chevalier of Sibeka, J. Robey of De Beers, J. W. Harris, J. Citron and J. Borden for diamonds, and D. Bell, J. Blum, G. Mattioli, E. Stolper, P. Wyllie, S. Haggerty and E. Roedder for very useful comments and reviews. A preliminary report of this work was presented earlier[40]. Funding was provided by NSF and NASA. O.N., I.D.H. and G.J.W. are at the Lunatic Asylum of the Charles Arms Laboratory (No. 4646/625).

Received 20 July, accepted 19 September 1988

1. Harte, B., Gurney, J. J. & Harris, J. W. *Contr. Miner. Petrol.* **72**, 181-190 (1980).
2. Haggerty, S. E. *Nature* **320**, 34-38 (1986).
3. Erlank, A. J. *et al.* in *Mantle Metasomatism* (eds Menzies, M. & Hawkesworth, C. J.) 221-311 (Academic, London, 1987).
4. Eggler, D. H. in *Mantle Metasomatism* (eds Menzies, M. & Hawkesworth, C. J.) 21-41 (Academic, London, 1987).
5. Roedder, E. *Rev. Miner.* Vol. 12 (Miner. Soc. Am., Washington, 1984).
6. Plotnikova, S. P., Dudenkov, Yu. A., Malan'ina, R. V. & Kulakov, V. M. *Sov. Phys. Crystall.* **30**, 663-665 (1985).
7. Chrenko, R. M., Tuft, R. E. & Strong, H. M. *Nature* **270**, 141-144 (1973).
8. Bibby, D. M. *Geochim. cosmochim. Acta* **43**, 415-423 (1979).
9. Orlov, Yu. L. *The mineralogy of the diamond* (Wiley, New York, 1977).
10. Moore, M. & Lang, A. R. *Phil. Mag.* **26**, 1313-1325 (1972).
11. Lang, A. R. in *The Properties of Diamond* (ed. Field, J. E.) 425-469 (Academic Press, London, 1979).
12. Custers, J. F. H. *Am. Miner.* **35**, 51-58 (1950).
13. Miller, G. H. & Rossman, G. R. *Phys. Chem. Miner.* **14**, 461-472 (1987).
14. Armstrong, J. T. in *Microbeam Analysis* (ed. Newbury, D. E.) 239-246 (San Francisco Press, 1988).
15. Hunke, J. C., Armstrong, J. T. & Wasserburg, G. J. *Geochim. cosmochim. Acta* **47**, 1635-1650 (1983).
16. Davies, G. *Nature* **290**, 40-41 (1981); Davies, G. *Chem. phys. Carbon*, **13**, 1-147 (1977).
17. Davies, G., Collins, A. T. & Spear, P. *Solid St. Commun.* **49**, 433-436 (1984).
18. Lang, A. R. & Walmsley, J. C. *Phys. Chem. Miner.* **9**, 6-8 (1983).
19. Meyer, H. O. A. in *Mantle Xenoliths* (ed. Nixon, P. H.) 501-522 (Wiley, New York, 1987).
20. Kresten, P. in *Lesotho Kimberlites* (ed. Nixon, P. H.) 269-279 (1973).
21. Ryabchikov, I. D. & Boettcher, A. L. *Am. Miner.* **65**, 915-919 (1980).
22. Ellis, D. E. & Wyllie, P. J. *Am. Miner.* **65**, 540-556 (1980).
23. Zashu, S., Ozima, M. & Nitoh, O. *Nature* **323**, 710-712 (1986).
24. Podosek, F. A., Pier, J., Nitoh, O., Zashu, S. & Ozima, M. *Nature* **334**, 607 (1988).
25. Galimov, E. M. *Geochimiya* **8**, 1091-1118 (1984).
26. Boyd, S. R. *et al.* *Earth planet. Sci. Lett.* **86**, 341-355 (1987).
27. Swart, K., Pillinger, C. T., Milledge, H. J. & Seal, M. *Nature* **303**, 793-795 (1983).
28. Fieremans, M., Hertogen, J. & Demaiffe, D. in *Kimberlites* I (ed. Kornprobst, J.) 107-120 (Elsevier, Amsterdam, 1984).
29. Schulze, D. J. in *Mantle Xenoliths* (ed. Nixon, P. H.) 432-451 (Wiley, New York, 1987).
30. Waters, F. G. *Contr. Miner. Petrol.* **95**, 523-533 (1987).
31. Boyd, S. R., Nixon, P. H. & Boctor, N. Z. *Contr. Miner. Petrol.* **86**, 119-130 (1984).
32. Richardson, S. H., Gurney, J. J., Erlank, A. J. & Harris, J. W. *Nature* **310**, 198-202 (1984).
33. Shimizu, N. & Richardson, S. R. *Geochim. cosmochim. Acta* **51**, 755-758 (1987).
34. Mitchell, R. H. *Kimberlites* (Plenum, New York, 1986).
35. Takahashi, E. & Kushiro, I. *Am. Miner.* **68**, 859-879 (1983).
36. Evans, T. & Qi, Z. *Proc. R. Soc. Lond.* **A381**, 159-178 (1982).
37. Thompson, W. K. *Trans. Faraday Soc.* **61**, 2635-2640 (1965).
38. Smith, C. B., Gurney, J. J., Skinner, E. M. W., Clement, C. R. & Ebrahim, N. *Trans. geol. Soc. S. Afr.* **88**, 267-280 (1985).
39. Bergman, S. C. in *Alkaline Igneous Rocks* (eds Fitton, J. G. & Upton, B. G. J.) 103-190 (Geol. Soc. spec. Publn no. 30, London, 1987).
40. Navon, O., Hutcheon, I. D., Rossman, G. R. & Wasserburg, G. J. *Lunar planet. Sci.* XIX, 827-828 (Lunar planet. Inst., Houston, 1988).

In Lunar and Planetary Science XV, p. 589 (1984)
Lunar and Planetary Institute, Houston. #462

SELF-SHIELDING IN O2 - A POSSIBLE EXPLANATION FOR OXYGEN ISOTOPIC ANOMALIES IN METEORITES? O. Navon and G. J. Wasserburg, Lunatic Asylum, Div. Geol. & Planet. Sci., Calif. Inst. of Tech., Pasadena, CA 91125

We have investigated the production of isotopic effects in oxygen due to self-shielding of photolysing radiation by the Schumann-Runge bands (SRB) of $^{16}O_2$ (175-205nm). We calculated the enhancement of ^{17}O and ^{18}O production upon photodissociation of O_2 for various optical densities, examined its dependence on temperature and presence of other molecules, and the issue of whether the products of photolysis can be trapped and prevented from exchange with O_2.

The rate of dissociation of an isotopic species i is given by:

$$-\frac{d[^iO_2]}{dt} = [^iO_2]\times j_i(z) = [^iO_2]\times\int_0^\infty \phi(\nu)\sigma_i(\nu)I(\nu,z)d\nu$$

where $[^iO_2]$ is the number density of species i; j_i is the photodissociation rate constant; $\phi(\nu)$ is the quantum yield; $\sigma_i(\nu)$ is the absorption cross section, and the photon flux $I(\nu,z)$ is $I(\nu,z)=I(\nu,0)\exp[-\Sigma\sigma_j(\nu)N_jz]$ where j includes all absorbing species, N_j the number density, and z is the column length. The spectral lines of the heteronuclear species of O_2 are shifted from those of $^{16}O_2$. As $^{16}O_2$ is the most abundant species, the radiation transmitted at the wavenumbers corresponding to its spectral lines, $I(\nu,z)$, decreases rapidly with z while more radiation is transmitted at the spectral lines of $^{16}O{*}O$ ($*$=17 or 18), and hence $j_*(z)>j_{16}(z)$ and the ^{17}O and ^{18}O rate of production is enhanced. This effect has been shown experimentally by Sander et al. (1). Thiemens and Heidenreich (2) have suggested that the equal enrichment of ^{17}O and ^{18}O in ozone they produced by discharge in O_2 is the result of this mechanism, and pointed out the possibility that isotopic anomalies of oxygen in meteorites might be explained by self-shielding.

For pure oxygen at 300K, self-shielding is effective at column densities between 10^{18}-$10^{23}cm^{-2}$ (fig. 1). Maximum effects for ^{18}O occur at $10^{20}cm^{-2}$ where $j_{18}/j_{16}=7$, whereas for the less abundant ^{17}O the maximum is at 10^{21} cm^{-2} where $j_{17}/j_{16}=10$. The effect is reduced at higher temperatures, where more lines are present in the spectrum of $^{16}O_2$. $*O$ is produced only 1.6 times as fast as ^{16}O at 500K; only a negligible effect is expected at 1000K, where most $^{16}O{*}O$ lines overlap with lines of $^{16}O_2$.

Water has a continuous absorption spectrum in the SRB zone, and its presence greatly reduces effects. The production of ^{17}O and ^{18}O are only 1.8 times that of ^{16}O when $[O_2]=[H_2O]$ (300K). For $[H_2O]/[O_2]>10$ the effect is smaller than that observed in meteorites ($j^*/j_{16}<1.045$). The ozone effect on the absorption spectrum is negligible due to its low concentration. CO and CO_2 have low absorption at 175-205nm.

While the O produced by this mechanism is anomalous, the main difficulty may lie in the physical separation of the anomalous atomic oxygen from the O_2. The O produced in the photodissociation stage: (1) $O_2 + h\nu \rightarrow O + O$ may exchange isotopically with O_2 by (2) $*O + {}^{16}O_2 = {}^{16}O + {}^{16}O{*}O$ ($k_2=6.5\times10^{-12}\exp(-554/T)$ $molecules^{-1}cm^3sec^{-1}$) (3). This exchange reaction would erase any pattern produced in the dissociation stage unless the atomic oxygen is trapped by a faster reaction, written as (3) $O + trap \rightarrow trap\text{-}O$. Thus the anomalous isotopic pattern is preserved only if (i) $k_3[trap] > k_2[^{16}O_2]$.

We examined Na, Mg, and Fe as possible trapping species. These atoms react with atomic oxygen according to: (4) $Me + O + X \rightarrow MeO + X$ (Me is a metal atom, X is any matrix species). The first-order rate constants for this reaction are: $k_4^{Na}=10^{-33}[X]$, $k_4^{Mg}=k_4^{Fe}=10^{-32}[X]$ molecules^{-1}cm^{3}sec^{-1} (4), where [X] is the total density. (i) is satisfied when $k_4[Me] > k_2[O_2]$. However, even for densities as high as $[X]=10^{16}$ cm^{-3}, the metal atoms concentration must be 10^4 greater than that of O_2 to satisfy (i). Under reasonable densities and metal atoms concentrations trapping of atomic oxygen by metal atoms is insufficient. Another difficulty may rise if the trapping species also react directly with O_2: (5) trap + O_2 $\rightarrow$ trap-O + O, (5a) trap + O_2 + X $\rightarrow$ trap-O_2 + X. The trap-O, equally enriched in the heavy isotopes formed in reactions 1 and 3, is then diluted by products of normal isotopic composition. Thus additional conditions are required: (ii) $k_5[\text{trap}] < j_1$, (iii) $k_{5a}[\text{trap}] < j_1$. In the case of Na, Mg, and Fe, reaction 5 is endothermic and thus negligible. However, in the case of Si it is exothermic and should be considered.

In summary, self-shielding by $^{16}O_2$ produces a mass-independent isotopic effect upon photodissociation in a low temperature environment with low $[H_2O]/[O_2]$. However, separation of the anomalous atomic oxygen from the main reservoir by reaction with Na, Mg, and Fe atoms is too slow to compete with the isotope exchange reaction, and no anomalous pattern is expected in the final trapped products.

The above considerations may be applied to the experiment of Thiemens and Heidenreich (2), where O is trapped by O_2 to form O_3. Using $[O_2]=5\times10^{18}$ cm^{-3} and estimating a path-length of 1 cm, the column density is just in the range for self-shielding to occur (fig. 1). If the true path-length is shorter (0.1 cm) it will not work. The atomic oxygen is trapped by the reaction: (6) O + O_2 + M $\rightarrow$ O_3 + M ($k_6=2.15\times10^{-34}(345/T)[M]$ molecules^{-1}cm^{3}sec^{-1})^2(5). In pure oxygen $[M]=[O_2]$ so that $k_2/k_6=6\times10^3\times\exp(-895/T)$ and the exchange reaction is 300 times faster than the formation of ozone. Any isotopic effect produced by dissociation is scrambled because of the exchange reaction, which closely approaches equilibrium and will not produce anomalous O_3. Thus we believe the explanation for the observed data is not in the production of anomalous O but should be looked for as an intrinsic property in the formation of ozone. It is possible that the key fractionation step involves O^+ ions.

References: (1) Sander R.K., T.R. Loree, S.D. Rockwood, S.M. Fruend (1977) App. Phys. Lett. 30, 150-152; (2) Thiemens M.H. and J.E. Heidenreich III (1983) Science 219, 1073-1075; (3) Jaffe S. and F.S. Klein (1966) Trans. Faraday. Soc. 62, 3135-3141; (4) Brown T.L. (1973) Chem. Rev. 73, 645-667; (5) Klais O., P.C. Anderson, M.J. Kurylo (1980) Int. J. Chem. Kinet. 12, 469-490. This work was supported by NSF (PHY 82-15500) and NASA (NAG 9-43). Div. Contribution #4023 (462).

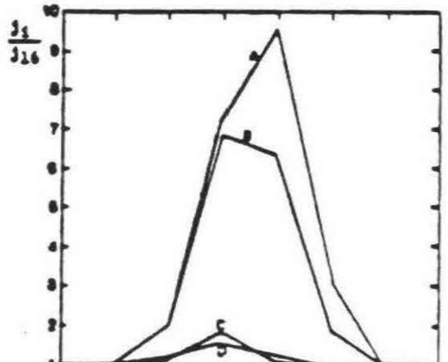

Fig. 1: Ratio of the rates of production of ^{17}O and ^{18}O vs. column density.

- A- j_{17}/j_{16} (pure oxygen, 300K)
- B- j_{18}/j_{16} (pure oxygen, 300K)
- C- $j_{17}/j_{16}=j_{18}/j_{16}$ ($[H_2O]=[O_2]$, 300K)
- D- $j_{17}/j_{16}=j_{18}/j_{16}$ (pure oxygen, 500K)

THE UPPER MANTLE AS AN ION-EXCHANGE COLUMN.

Nº 42548

NAVON, Oded, and STOLPER, Edward,
Div. of Geol. and Planet. Sci., Caltech, Pasadena, CA 91125

The evolution of trace element patterns during percolation of fluid (melt or vapor) through mantle rocks has been modeled using Glueckauf's model for ion exchange columns. While previous workers assumed instantaneous equilibration between matrix and fluid, we included the effects of diffusion in grains. As a result, diffuse concentration fronts move through the column, leading to smooth trace element patterns.

One application of this model is to the evolution of trace elements in mantle rocks metasomatized by hydrous fluids. Upward percolating fluids deposit REE into the matrix. Since LREE are strongly partitioned into the fluid, they move through the column faster than the HREE, and rocks at the top of the column develop steep LREE-enriched patterns.

A second application of our model is to the interaction between matrix and melt percolating through it. The patterns predicted by ion-exchange column modeling of such systems are different from those resulting from simple mixing or zone refining. As an example, we have considered the percolation through a "depleted" MORB-type source region of liquids formed by high degrees of partial melting of an "enriched" mantle plume. This may be relevant to the evolution of Hawaii. REE and Sr concentrations in the primary melt of the enriched source are lower than those expected for melt in equilibrium with MORB source rocks. Thus, the early melts emerging from the column are LREE enriched and have low Sr and high Nd isotopic ratios, as is observed in the Loihi seamount. Hawaiian tholeiites, with their flatter REE patterns and isotopic ratios approaching those of the plume source, can be modeled by the later melts emerging from the "dirty" column that has been altered by interaction with the melts that previously percolated through it. The late, commonly post erosional, alkalic lavas could be the result of melt percolation through fresh MORB-type source rocks that had not previously been altered by the passage of melts from the underlying plume.

Ultrapotassic Sub-micron Inclusions in Diamonds

ODED NAVON, I. D. HUTCHEON, G. R. ROSSMAN and G. J. WASSERBURG (Division of Geological and Planetary Sciences, California Institute of Technology, Pasadena, California 91125)

Ion microprobe, SEM and IR spectroscopic analyses of sub-micron inclusions in cubic diamonds and in the inclusion-rich mantles of coated diamonds reveal a composition, completely different from that of the peridotitic or eclogitic suites of "normal" diamond inclusions. The chemical compositions (oxides normalized to 100%) of inclusions in 7 diamonds from Orapa, Botswana, and 3 of unknown locality, show similar compositions: SiO_2, 30-50%; TiO_2, 2-4%; Al_2O_3, 2-10%; FeO, 10-20%; MgO, 2-7%; CaO, 6-18%; K_2O, 8-22%, Na_2O, 1-8%; and detectable P_2O_5, Cl and Cr_2O_3. Good correlations exist between Al_2O_3, TiO_2 and SiO_2, as well as between CaO, MgO, Na_2O and K_2O. IR spectra indicate the presence of water (3440, 1640cm^{-1}), carbonate(1430, 877cm^{-1}) and phosphate (606,575cm^{-1}). From available IR absorption coefficients, we estimate the inclusions are composed of 20-50% (wt) water, 10-30% carbonate and 40-70% metal oxides.

These inclusions may represent a trapped fluid or highly evolved melt broadly similar in composition to lamproites but richer in H_2O, carbonate and K_2O and lower in Mg. It is distinctly different from the host kimberlites. The high K_2O values and the presence of phosphate suggest that this trapped fluid is enriched in other incompatible elements and may be similar to fluids responsible for widespread metasomatism of the subcontinental mantle. If the inclusions are primary, then the formation process of these diamonds is different from that of diamonds associated with peridotitic or eclogitic inclusions. We infer that zoned diamonds grew in a peridotitic or eclogitic environment and were later overgrown with diamond in a lamproitic-like fluid prior to the kimberlitic eruption. The cubic diamonds may have grown completely in such fluid. The carbon isotopic sources in these two regimes of growth could be distinctive in agreement with observations by Galimov and by Pillinger. (#597) EAR 8618526.

SUB-MICRON INCLUSIONS IN DIAMONDS - SAMPLES OF PRISTINE UPPER MANTLE FLUIDS?

O. Navon, I. D. Hutcheon, G. R. Rossman and G. J. Wasserburg. Division of Geological and Planetary Sciences, Caltech, Pasadena, CA 91125.

Due to its mechanical strength and chemical inertness, diamond is probably the best material for trapping and transporting deep mantle fluids to the surface. Such fluids (either melts or supercritical fluids) are important for the transport of volatiles and incompatible elements in the mantle and control processes such as mantle metasomatism and diamond genesis.

We used ion microprobe (SIMS), electron probe (EP), SEM and IR spectroscopic analyses to examine the chemical composition of sub-micron inclusions in 4 cubic and 9 coated diamonds from Zaire, Botswana and some unknown localities. Inclusions are about 0.1-1μm in size and are concentrated in concentric bands throughout the volume of the cubic diamonds and in the mantles of the coated diamonds. The individual inclusions are isolated and their number density generally decreases toward the outer rim of the diamond. Cracks are common; however, it is clear that they were formed after the formation of the inclusions since they do not disturb the band pattern. The transition from the transparent cores to the inclusion-bearing coats is sharp. The different natures of the coat and core are also evident from X-ray and isotopic studies [1,2]. These textural features suggest that the inclusions were trapped during the growth of the diamond and are syngenetic.

IR spectra of the inclusion-rich zones (Fig. 1) indicate the presence of bound molecular water (3440 and $1640cm^{-1}$), carbonate (1430, $877cm^{-1}$), and phosphate (606, $575cm^{-1}$). Additional, still unassigned peaks are probably due to silicates (main lines at ~1000 and $\sim 1100cm^{-1}$). All the lines appear in the spectra of each diamond. Variations in the relative peak intensities indicate differences in the relative abundances of the different phases, e.g. water and carbonate. In an individual diamond, the relative peak intensities are roughly constant among the different zones; the absolute intensity of all lines may change, reflecting variation in the number density of inclusions. Using available IR absorption coefficients, we estimate that the diamonds contain 60-1000 ppm water and 20-500 ppm CO_2 (in carbonates); the $H_2O/(CO_2+H_2O)$ varies from 0.4 to 0.8.

SIMS analyses with PANURGE were performed at a mass resolving power of $m/\Delta m=2000$ and a 10nA O^- primary beam. Ion yields for each element were calculated using a working curve approach. We compared secondary ion intensities, normalized to the C^+ signal, with EP measurements on inclusion-rich diamonds. Abundances of Li, Be, B, Na, Mg, Al, Si, K, Ti, V, Cr, Mn and Fe were below detection limit, and IR detected no water or carbonate, in gem quality diamonds. SIMS and EP analyses of the inclusion-rich diamonds indicate a similar chemical composition for all diamonds. The analyses fall within the following limits: SiO_2, 30-60%; TiO_2, 2-6%; Al_2O_3, 2-10%; FeO^*, 5-22%; MgO, 2-7%; CaO, 6-18%; Na_2O, 1-8%; K_2O, 8-22%; P_2O_5, 0-3%; and detectable amounts of Cr_2O_3 and Cl. Total concentration of all the above oxides varies between 20-2000 ppm. Compositional variations follow the same pattern exhibited by the IR data. The inclusions within any individual diamond have a similar composition (Fig.2). Differences in inclusion composition are apparent among the suite of diamonds, but inclusion compositions for diamonds of similar shape and from the same locality are very similar.

SEM was used to study the composition of individual inclusions. The average composition of the inclusions in any one diamond is close to that determined by IP. More importantly, no monomineralic inclusions have been found.

Conclusions. Sub-micron inclusions in cubic and coated diamonds are completely different in composition from the peridotitic or eclogitic "normal" diamond inclusions. They are rich in water, carbonate, SiO_2, K_2O, FeO and CaO and contain smaller amounts of Na_2O, MgO, Al_2O_3, TiO_2, Cr_2O_3, P_2O_5 and Cl. Combining SIMS, IP, EP and IR data for the different diamonds, the inclusions are composed of 40-70% metal oxides, 20-50% water, and 10-30% CO_2 (in carbonates).

We suggest that these inclusions represent a quenched, trapped fluid (either a volatile-rich melt or a supercritical phase). Their composition is clearly distinct from that of kimberlites (Fig.1). Thus, the growth of these diamonds preceded the eruptive, kimberlitic event. The coated diamonds were formed in two stages. First, the transparent cores grew in a similar way to diamonds of the eclogitic or peridotitic environments; the coats grew later in contact with the potassic fluid they trapped. The cubic diamonds grew entirely during the second stage. The close relationship between cubic diamonds and the mantles of coated diamonds is also suggested by the close similarity in their $\delta^{13}C$ values [2].

Many mantle-derived nodules have been affected by metasomatism, commonly characterized by formation of hydrous or carbonaceous phases and the addition of K, Fe, Ti and incompatible elements. The high content of these components in the sub-micron inclusions suggests that the trapped material may be related to fluids responsible for the widespread metasomatism of the sub-continental mantle.

References: [1] A.R.Lang (1974) J. Cryst. Growth 24, 108; [2] E.M. Galimov (1984) GCA 8, 1091; Boyd et al. (1988) EPSL 86, 341. (#610)

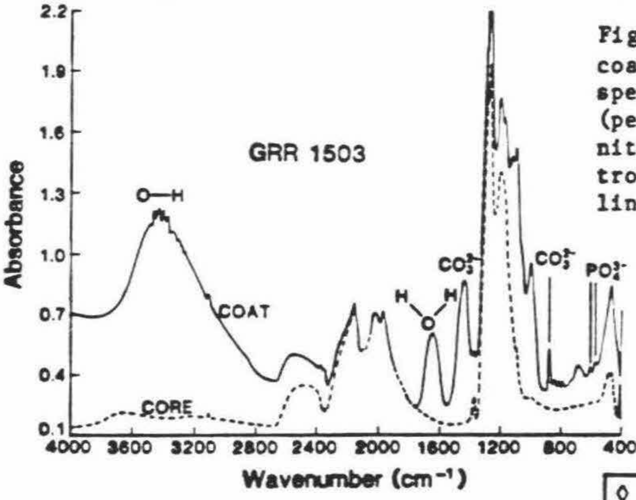

Fig. 1. IR spectra of the core and coat of a coated diamond. The core spectrum is of a normal diamond (peaks around 1100-1400 are due to nitrogen). The coat is richer in nitrogen and shows many additional lines. The higher baseline of the coat spectrum is due to light scattered by the inclusions. Sample thickness = 0.10cm.

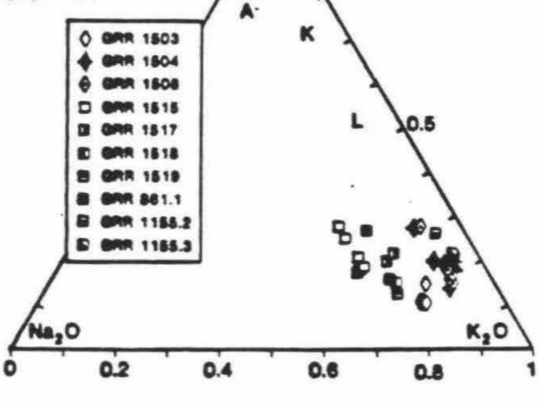

Fig. 2. Ion probe analyses of inclusion-bearing diamonds compared with average composition of some alkaline rocks (A = alkaline basalts, K = kimberlites, L = lamproites). Octahedral diamonds are shown by diamond symbols, cubic diamonds by squares. GRR1503-GRR1518 from same unknown locality; GRR1155.2, GRR1155.3 from Zaire; GRR861.1 unknown.